ISSN 0288-4534
CODEN: KONAE7

KONA

POWDER AND PARTICLE

No. 18 (2000)
Published by Hosokawa Powder Technology Foundation

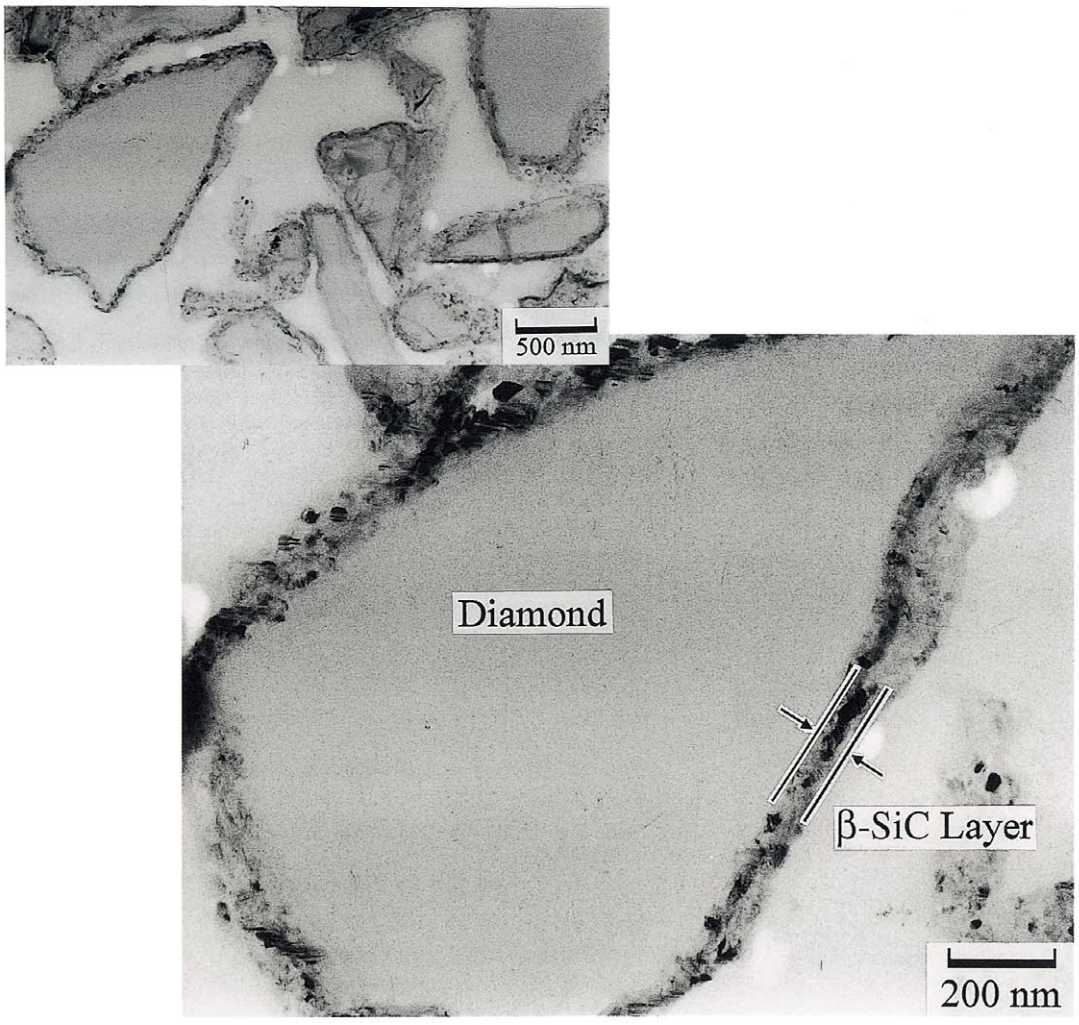

Nano-SiC Coated Diamond Particles

KONA

POWDER AND PARTICLE

KONA is a refereed scientific journal that publishes articles on powder and particle sciences and technology. KONA has been published annually since 1983 by the Hosokawa Powder Technology Foundation in Japan. KONA is distributed to researchers, members of the scientific community, universities and research libraries throughout the world.

About the Cover of Journal "KONA"

The Chinese character "粉" is pronounced "KONA" in Japanese, and means "Powder". The hand written "粉" is after the late Mr. Eiichi Hosokawa, founder of the Hosokawa Micron Corporation.

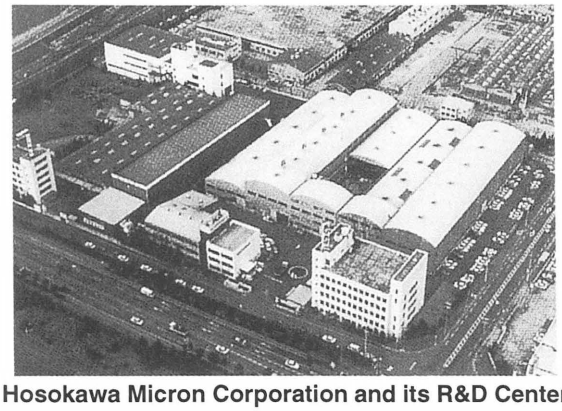

Hosokawa Micron Corporation and its R&D Center

■ **Publication Office**

Hosokawa Powder Technology Foundation (Japan) in Hosokawa Micron Corporation
No. 9, 1-chome, Shoudai Tajika, Hirakata-shi, Osaka 573 Japan

■ **Notes**

○ Hosokawa Powder Technology Foundation has entrusted the editorial duty to the editorial board organized by the Council of Powder Technology, Japan.

(Complimentary Copy)

Printed in Japan

Obituary

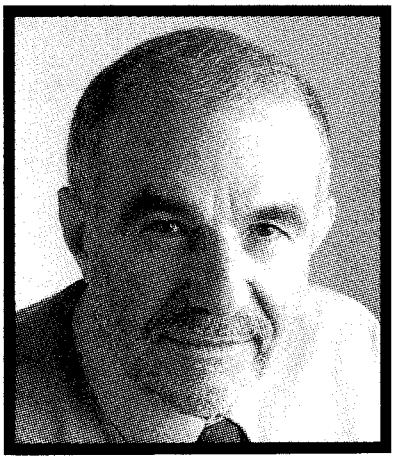

Gianfranco Ferrara, professor at the Department of Chemical, Environmental and Raw Materials Engineering of the University of Trieste, Italy, died January 12th, 2000, in Sassari (Sardinia) at the age of 71.

In the last years of his life he had liver cancer brought on by hepatitis caught during his youth. After controlling the cancer for years, he died from the rapid metathesis of said cancer.

Gianfranco Ferrara was born February 16th, 1928, in Iglesias (Sardinia). He received his degree in Minerals Engineering in 1954 at the University of Cagliari (Italy). At the same University he was appointed Research Assistant in 1955 and Assistant Professor in 1960. In 1971 he accepted a position of Professor of Mineral Processing at the University of Trieste. From 1979 to 1991 he was Chairman of the Mineral Engineering Division. He retired in 1999. That same year he was appointed "Professor Emeritus" of the University of Trieste.

As an Italian delegate, he was a member of the Steering Committee of the International Scientific Committee of the International Mineral Processing Congress. He was a member of the Editorial Board of the scientific journals Coal Preparation and KONA–Powder and Particle, and the European Editor of Minerals Engineering from 1988 to 1998. For many years, he was a consultant to the European Community for the Primary Raw Materials and Recycling research programs.

Innovative in his scientific activity, he was the progenitor of several Mineral Processing fields, particularly in Physical, as opposed to Chemical, Separation Processes. In 1954, in his Minerals Engineering degree thesis, he introduced the use of density tracers for determining the partition curve of dense medium cyclones, a technique that 30 years later was extensively applied in Australia and South Africa for laboratory and plant set-up. Now it is used worldwide.

In the years 1956-58 he developed a water-only-cyclone for the separation of heavy minerals. Later, the water-only-cyclone was used extensively in coal preparation.

In 1959 he studied the influence of recycling in separation circuits. For the first time he introduced the concept of circuit analysis. This research work was published only in Italian. Twenty years later, circuit analysis was independently studied and developed in depth by T. P. Meloy. Now Circuit Analysis is the standard tool for studying and evaluating mineral processing separation circuits.

In 1960 he developed a process of centrifugal separation using a rotating tube. This process was never used industrially. However, this idea of a flowing film separation process in a centrifugal field led to the development of other separation devices, such as the Knelson separator, the Mozley Multi-Gravity separator.

From 1964 to 1970 he was one of the leaders of the research team, directed by Mario Carta, for the study of the electric separation of minerals. The studies, both theoretical and experimental, led to the physical explanation of the triboelectric separation and to the development of new corona and triboelectric separators especially designed for treating fine particles.

In the field of process modelling, he developed with U. Preti a new kinetic-probabilistic model for the screening process, sizing. Even today his sieving model remains the most reliable model developed. Other studies of his were on modelling and simulation of integrated plant operations in mineral processing, on the use of geostatistics in modelling, and on the modelling of flowing film separation processes.

In the field of locked particles, using Meloy's 3 conservation laws, in collaboration with U. Preti and T. P. Meloy, he made important contribution to the study of mineral liberation. This work led to the prediction of the shape of locked particle size distribution that are far steeper that normal comminuted particle size distributions. Such information is now used in Circuit Analysis of Mineral Processing Circuits.

During his life, his maximum efforts were devoted to the study of dynamic dense medium separation

systems. He developed the Tri-Flo, a dynamic multi-stage dense medium separator used in more than 30 plants throughout the world (England, Germany, Italy, Greece, Spain, Canada, Brasil, South Africa, China). This device is the most precise extant dynamic dense medium separator. Thus, the Tri-Flo has been applied to difficult separations, such as processing of petalite, spodumene, feldspar and quartz. These studies were laboratory and industrial plant tests, rheology of dense medium and its modelling, design of regeneration circuits, theoretical and fluid-dynamic aspects for both cylindrical and conical cyclones, coal preparation, industrial plant results, and new perspectives and applications of the Tri-Flo Separator.

Other late studies of his were on cyclones and cyclone modelling (in collaboration with the University of Chile), particle segregation in hydrocyclones, comminution of porous materials, and separation of secondary materials and plastics. His final work was developing particle sizing methods for use on the Martian surface.

Though he never had children of his own, he is survived by his many devoted students.

T. P. Meloy
Vice Chairman of Americas Editorial Board
(West Virginia University)

The Letter from the Editor

Yasuo Kousaka
Editor-in-Chief

I am very honored to have been nominated as the Editor-in-Chief of KONA journal beginning with this issue by the Council of Powder Technology Japan after the terms of Professors Yoshioka, Jimbo and Miyanami, who made great efforts and contributions for the establishment of the present status of this journal.

When we look back upon the passing 20th century, we notice the incredible advancement of technology and at the same time its downside like the environmental problems. As for the Powder Technology, it started to be recognized as a field of technology several decade years ago and rapidly developed and advanced for the purpose of production of numerous kinds of industrial materials and also protection of the environment in the latter half of the 20th century.

The KONA journal initiated in 1983 was originally published to introduce the excellent papers written in the Japanese language to the world and now finds a good balance in the numbers of papers in the three regions of the world; namely America, Europe/Africa and Asia/Oceania. It is also distributed worldwide evenly in these regions.

Ten years after the Second World Congress Particle Technology in Kyoto in 1990, the first Asian Particles Technology Symposium APT 2000 was successfully held in December, 2000 in Bangkok, Thailand. It was strongly supported by the Society of Powder Technology, Japan and also sponsored by Hosokawa Powder Technology Foundation.

This year we lost another member of KONA editorial board, Prof. G. F. Ferrara of Univ. di Trieste, Italy and we all lament her untimely death and extend our sincere condolences heartily.

Anyway, I wish we would welcome the bright new 21st century and that we will be of assistance in distributing of good papers and reviews in the particle technology by this journal.

KONA

GENERAL INFORMATION

HISTORY OF THE JOURNAL

KONA journal has been published by the Council of Powder Technology, Japan. (CPT), from No.1 to No.12 issues, under the sponsorships of Hosokawa Micron Corporation (No.1 to No.9) and Hosokawa Powder Technology Foundation (No.10 to No.12).

The CPT has been established in 1969 as a non-profit organization to enhance the activities of research and development on powder science and technology in Japan under the sponsorship of Hosokawa Micron Corporation. In 1983, the CPT has decided to issue an international journal named "KONA", which publishes the excellent articles appeared in Japanese journals concerning powder science and technology, after translated into English, throughout the world. After the seventh volume issued in 1989, the CPT has changed its policy to internationalize the "KONA" from the 8th issue (1990) and on by incorporating the monographs originally written in English from the authors throughout the world. Immediately, the present editorial board including Asian, Americas' and European Blocks has been organized.

From the 13th issue and on, the Hosokawa Powder Technology Foundation has taken over the role of KONA publisher from the CPT and the Foundation has entrusted the editorial duty to the present KONA editorial board organized by the CPT without requesting any shift in our present editorial policies. This switching of publisher has been simply and only to make the aim and scope of the Foundation definite. Essentially no change has been observed in continuously editing and publishing this journal except in the designation on a part of the journal cover.

AIMS AND SCOPE OF THE JOURNAL

KONA Journal is to publish the papers in a broad field of powder science and technology, ranging from fundamental principles to practical applications. The papers discussing technological experiences and critical reviews of existing knowledge in specialized areas will be welcome.

These papers will be published only when they are judged, by the Editor, to be suitable for the progress of powder science and technology, and are approved by any of the three Editorial Committees. The paper submitted to the Editorial Secretariat should not have been previously published except the translated papers which would be selected by the Editorial Committees.

CATEGORY OF PAPERS

- Invited papers
  Original research and review papers invited by the KONA Editorial Committees.
- Contributed papers
  Original research and review papers submitted to the KONA Editorial Committees, and refereed by the Editors.
- Translated papers
  Papers translated into English, which were previously published in other languages, selected by the KONA Editorial Committees with the permission of the authors and / or the copyright holder.

SUBMISSON OF PAPERS

Papers should be sent to each KONA Editorial Secretariat.

- Asia / Oceania Editorial Secretariat
  T. Kawamura
  Hosokawa Micron Corporation Micromeritics Laboratory 1-9, Shoudai Tajika, Hirakata 573 JAPAN
- Europe / Africa Editorial Secretariat
  Dr. P. van der Wel or Mrs. P. Krubeck
  Hosokawa MikroPul GmbH
  Welserstr. 9-11, 51149 Köln
  Postfach 900749, 51117 Köln
  GERMANY
- Americas Editorial Secretariat
  Dr.I. Pikus or D.A. Scort
  Hosokawa Micron International Inc.
  10 Chatham Road, Summit, NJ 07901 USA

PUBLICATION SCHEDULE

KONA is published once a year.

SUBSCRIPTION

KONA is distributed free of charge to senior researchers at universities and laboratories as well as to institutions and libraries in the field throughout the world. The publisher is always glad to consider the addition of names of those who wish to obtain this journal regularly to the mailing list. Distribution of KONA is made by each Secretariat.

INSTRUCTIONS TO AUTHORS

(1) Manuscript format

- Two copies should be submitted to the Editorial Secretariat, in double-spaces typing on pages of uniform size.
- Authorship is to give author's names, and the mailing address where the work has been carried out on the title page.
- Abstract of 100-180 words should be given at the beginning of the paper.
- Nomenclature should appear at the end of each paper. Symbols and units are listed in alphabetical order with their definitions and dimensions in SI units.
- Literature references should be numbered and listed together at the end of paper, not in footnotes. Alphabetical order is accepted. Please give information as in the following examples:
  1) Carslaw, H.C. and J.C. Jaeger: "Conduction of Heat in Solids", 2nd ed., Clarendon Press, Oxford, England (1960).
  2) Howell, P.A.: US Patent, 3,334,603 (1963).
  3) Rushton, J.H., S.Nagata and D.L. Engle: AlChEJ., 10. 294 (1964).
  4) Seborg, D.E.: Ph.D. Dissertation, Princeton Univ., N.J., U.S.A. (1969).
- Original figures with each single copy should be submitted, on separate sheets. Authors' names and figure numbers are marked in the corner.
- Figure numbers and captions are listed on a separate sheet.
- Place of figure insertion is to be indicated in the margin of the manuscript.
- Tables should be typed on separated sheets.
- Submit an IBM-readable floppy disk ($3_{1/2}$) with your unformatted text file in ASCII code. If you use either WORD or WORD PERFECT—as word processing system, please add the formatted text file.

(2) Reprints

- The authors shall receive 50 free reprints. Additional reprints will be furnished when ordered with return of galley proofs.

(3) Publication policy

- All papers submitted for publication become immediately the property of the CPT and remain so unless withdrawn by the author prior to acceptance for publication or unless released by the Editor. Papers are not to be reproduced or published in any form without the written permission of the CPT.

KONA Powder and Particle No. 18 (2000)

Contents

Explanation of the Cover Photograph

Nano-SiC Coated Diamond Particles

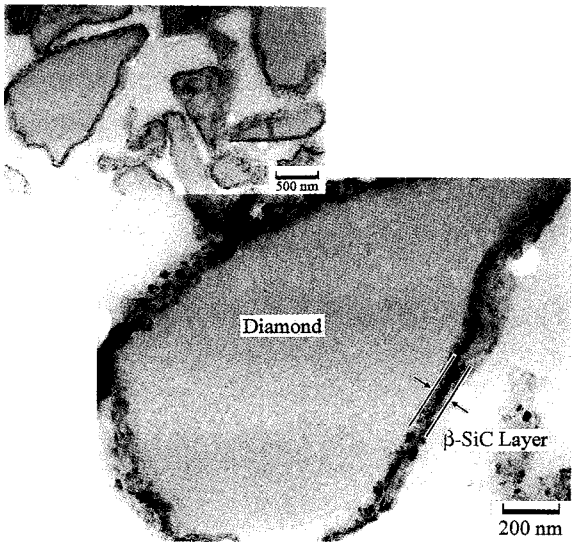

The photograph shows a TEM image of diamond particles of which surface is silicified with a dense SiC layer within 100 nm in thickness using the reaction of SiO vapor with diamond. The SiC-coated diamond powders show the starting temperature of oxidation 200°C higher than that of original diamond. Boron-doped SiC layer coated on a diamond plate shows p-type semiconducting behavior. Nano-SiC coated diamond particles, needles and plates are available for new wear resistant tools and electrodes in macro and micro machining and sensing.

By courtesy of Professor Yoshinari Miyamoto, Joining and Welding Research Institute, Osaka University, and Mr. Hideki Moriguchi, Itami Research Laboratories, Sumitomo Electric Industries, Ltd..

A Review of Breakage Behavior in Fine Grinding by Stirred-Media Milling†

R. Hogg
Department of Energy and Geo-Environmental Engineering
*The Pennsylvania State University**
H. Cho
Department of Civil, Urban & Geosystems Engineering
*Seoul National University***

Abstract

The use of stirred-media mills for grinding into the micron and submicron size range is reviewed. Mill performance and energy efficiency are discussed in the context of mill mechanics as related to mill power, material transport and flow, and particle breakage mechanisms. The development and adaptation of general size-mass balance models to fine grinding in stirred-media mills is evaluated. Specific problems in the application of the process models and, especially, in parameter estimation are described. Comparison of breakage rates and breakage distributions with those observed in coarser grinding systems reveals several similarities but some differences, particularly with respect to size-dependence. It is shown that the approach to a grinding limit can have significant effects on grinding rates and product size distributions.

Introduction

The purpose of the grinding process is to reduce particle size. In doing so, we are concerned about how to meet the objective with the minimum energy input. Obviously, a finer product requires more energy input, but the same energy input does not necessarily produce the same degree of size reduction. Grinding processes operate by applying stress to individual particles so as to induce breakage. This requires that particles first be appropriately located to receive the stress. Particle placement is relatively simple at large sizes – in jaw crushing for example – where individuals can be directly placed between the jaws. In such systems, the placement and stress application functions can be separated, with placement controlled by the feeding mechanism and stressing supplied by the motion of the jaws. This ideal approach is, unfortunately, quite impractical in fine grinding and the energy input to the mill is required to provide both functions. In the case of media milling, energy is supplied to the mill so as to agitate the media. Collisions between the media elements provide the stressing action while random motion of media and particles is relied upon to effect proper particle placement. To a considerable extent, these two functions present conflicting requirements, especially with respect to media size. Increasing media size increases the breakage stresses available per collision but decreases the number of media elements in the mill, thereby reducing the collision frequency. The best operating conditions generally involve a compromise between these requirements. An important consequence is that the process is highly inefficient in terms of energy utilization.

There are many variables that determine the ultimate outcome of the grinding process. These include material properties such as strength, hardness, brittleness, etc. The other variables are mostly related to the conditions under which particles are subjected to breakage. In the case of media milling, these include the particle loading, the feed particle size, the rotational speed, the media size, the media loading, the solids concentration, etc. In principle, operating the mill using the proper selection of these variables should ensure the production of a desired product with minimum expenditure at the desired capacity.

Energy Efficiency

As noted above, grinding processes in general are well known for their energy inefficiency. In most grind-

* University Park, PA
**Seoul, Korea
† Received: May 16, 2000

ing devices, the energy input is intended to generate stresses on the particles; compression, impact, or shear. However, the fraction of the energy input actually used for breakage is extremely low. In tumbling media mills, this percentage is said to be around 1%, with most of energy being wasted as heat. Nevertheless, the total energy input to grinding mills can often be related to the fineness of grinding. In the classical work on grinding, the fineness of the ground product, represented by some characteristic size x, has been correlated to the specific energy input E through a relationship of the form:

$$E = ax^b \quad (1)$$

where a and b are constants. Equation 1 is generally known as the Charles' Energy-Size relationship (1). In several studies on stirred ball milling [2,3,4], it was reported that the fineness of the product remains the same for a given energy input, regardless of the mill size and the operating conditions. If this is true, scale up of a stirred ball mill should be quite straightforward. However, in recent studies, this appears not to be the case and the energy efficiency is found to depend upon various operating conditions such as media size, media density, media load, slurry density, stirrer speed, and feed rate. Gao and Forssberg [5,6] investigated the effect of the above operating parameters on energy efficiency in stirred media milling. It was found that the energy utilization increases with increasing media load up to 83% of the available volume. Higher speeds naturally pulled more power and thus a higher degree of grinding could be achieved in a shorter time. But in the context of energy efficiency, lower speeds were found to be more energy efficient. In studies using media of varying density (2.5, 3.7, and 5.4 g/cm^3), the efficiency was found to increase for densities up to 3.7 g/cm, but then decreased at 5.4 g/cm^3, probably because the density was too high for the media to be fully stirred up. Also, it was found that the energy utilization decreased at a higher slurry density. The media size was found to be optimum at 0.8−1.0 mm for the grinding the particles smaller than 70 μm. Smaller media gave bimodal size distributions with coarser particles remaining unbroken. With the larger media, the particles were broken efficiently over the whole size range, giving a steeper size distribution. Overall, the authors suggested that stirred ball mills were best operated at high media loading (over 80%) using sufficiently large, but not too dense media and high rotational speed to obtain a high throughput. However, in a subsequent study [6], it was claimed that the energy efficiency was not affected significantly by the rotational speed and media load, but was most affected by the media size.

Zheng et al. [8] studied the energy efficiency of stirred media mills with pin-type stirrers in the grinding of limestone with glass beads. It was found that as the impeller speed was increased, the product surface area and energy input increased, but energy efficiency declined. The best energy efficiency and product fineness were obtained when the particles just filled the interstices between the media. As seen frequently in conventional tumbling ball mills, better grinding is achieved using smaller media size as long as they are large enough to cause particle fracture. The maximum rates of grinding were achieved when the media to feed size ratio was 12:1. However, in contrast to observations for ball milling, higher density media resulted in much higher energy consumption but did not increase the milling rate significantly. Thus, the energy efficiency was greatly reduced. Overall, the specific area increase was found to correlate with energy input through a power equation:

$$A_s = 9.27E^{0.54} \quad (2)$$

which implies that the energy efficiency was less for the higher energy input.

It is clear that there are numerous apparent inconsistencies in the literature on the energy-efficiency of stirred-media milling. For the most part, these arise from interactions among many material, equipment, and operating variables. It is generally agreed, however, that there is a clear link between energy input and product fineness. Also it is known that operating conditions play an important role. Powder and media loading and the media to particle size ratio seem to be primary factors in determining energy efficiency.

Mill Mechanics

Mill Power

The studies described above suggest that the energy input alone can not correctly predict mill performance, i.e. size reduction. Nonetheless, the power requirement for stirred ball milling is important and has been the subject of many investigations, especially aimed at scale-up. The standard treatment for the power P necessary to drive a stirrer in a Newtonian liquid operating in the turbulent regime starts with (9)

$$P = N_p N^3 D^5 \rho \quad (3)$$

where N is the rotational speed, D is the diameter of the stirrer, and ρ is the density of the liquid. N_p is the power number which depends on flow conditions and

system geometry. In stirred ball milling, the mill contains the solids being ground, the liquid (in wet grinding) and, more importantly, the grinding media. It is extremely unlikely, therefore, that the behavior would be Newtonian. Furthermore, the density in Equation 3 is no longer clearly defined. Since there is a considerable difference in the densities of the liquid and the media, there is a tendency for segregation of the media in the mill. At a low rotational speed, the media tend to settle, leading an inhomogeneous distribution of media. On the other hand, at higher rotational speeds, a vortex is formed and the media are concentrated at the wall due to centrifugal forces. Therefore, the dependency of the power draw on the rotational speed can vary significantly. Also, the movement of the media is highly dependent upon the media loading. It might be expected that the movement of the media would be more rapid at high loading, since the higher portion of media could be in direct contact with stirrers and among themselves. Therefore, it is very difficult to analyze the mill power theoretically, and it is often necessary to resort to empirical equations based on experiment. The problem with empirical equations is that they may be valid only for the particular design of the rotor. The values of the parameters, for the range of rotational speeds of interest, may depend on media loading, size, and density and slurry concentration, density, and viscosity.

Herbst and Sepulveda [2] measured power consumption for a pin-type stirred ball mill of 1 to 5 gallons, operated at 100−500 rpm, with a media size of 1/8″ to 1/4″ and density of 2.74 to 8 g/cm^3. Multiple regression of the data points resulted in

$$P = 2.55\times10^{-5}N^{1.37}V^{1.75}d_b^{0.48}\rho^{1.09} \quad (4)$$

where P=shaft power (kw), N=rotational speed (rpm), V=mill volume (gallons), d_b=diameter of media (in.), and ρ=media density (g/cm^3). A similar equation was given by Gao et al. [8], based on experiments using a 6-liter, horizontal, disk-type stirred ball mill using operating conditions of media density: 2.5−5.4 g/cm^3, slurry density: 65−75 wt.%, and stirrer speed: 805−2253 rpm. A dispersant was used at a level of 0.5−1.5 % of the solids. Their equation for power consumption, obtained by regression, was

$$P = 1.95\times10^{9}N^{1.429}\rho_s^{2.90}\rho_b^{0.18}c_d^{-0.096} \quad (5)$$

where ρ_s=slurry density (weight %), ρ_b=media density (g/cm^3), and c_d=dispersant concentration (%).

Zeng et al. [8,10] developed a method for predicting the power consumption of stirred ball milling in terms of power number and Reynolds Number. The correlation between the power number and Reynolds number was determined for various conditions. This relationship was then used to estimate the effective viscosity of the mill contents. The suggested equation for the power consumption was

$$P = C\mu N^2D^3 \quad (6)$$

where C is an impeller geometry constant and μ is the effective viscosity of the mill contents.

It should be recognized that none of these relationships take explicit account of the effects of charge segregation, etc. More realistic models will require a more detailed, quantitative understanding of the complex motion of the mill contents.

Transport and Flow

The motion of the charge, media plus powder plus liquid, in a stirred-media mill is complex and depends on mill geometry, rotational speed and the characteristics of the charge (solids/media content, density, fluid viscosity, etc.). Empirical and semi-theoretical investigations have been reported in the literature and are said to be in general agreement [12]. A detailed numerical analysis of laminar flow in a mill vessel of typical geometry with disk-type agitators indicates a relatively uniform flow field except close to the disk surfaces and the grinding chamber walls where there are high velocity gradients and, correspondingly, high energy dissipation [13]. Blecher and Schwedes [13] evaluated the motion of a single grinding bead entrained in the fluid, but the extension to a concentrated media bed has not been reported. While such studies provide some insight into the mechanics of media milling, so far they are of limited value in the analysis and prediction of mill performance. To our knowledge, discrete-element analysis, analogous to recent studies on tumbling and centrifugal ball mills [14,15], has not been attempted for stirred-media mills.

Particle Breakage

Breakage of particles occurs as a result of applied stress, which originates from energy input to the grinding device. However, as shown above, the effectiveness of the breakage action does not depend on the level of energy input alone. The nature of the energy input also plays an important role. Kwade et al. [16] have introduced the concept of energy intensity as a critical factor in determining whether or not stress application actually leads to breakage. At low stress intensities, several stressing events may be required to cause fracture. As the stress intensity increases, a

critical value is reached above which further increase does not lead to additional breakage. In any grinding process, particles are exposed to a distribution of stress intensities. The effectiveness of the process depends on the fraction of stressing events for which the stress intensity exceeds this critical level. On the other hand, excessive stress intensities, well above the critical value, lead to reduced grinding efficiency, i.e. increased specific energy.

Breakage rates are determined by the stress frequency, modified by the stress intensity, i.e. by the frequency of *adequate* stress applications. Relationships between the stress intensity and frequency and the operating conditions in stirred-media milling have been proposed [13,17]. The stress frequency f_s clearly depends on mill geometry and agitator speed and a general relationship can be expected with the form:

$$f_s \propto N\left(\frac{d_d}{d_b}\right)^2 \tag{6}$$

where N is the rotational speed and d_d and d_b are the respective diameters of the grinding chamber and the grinding beads. The stress intensity I_s can be expected to depend on agitation speed, grinding media size and density, and on the elasticity of the media and the material being ground. The latter determines the effectiveness of energy transfer between media and particles. The following specific relationship has been proposed [12,16]:

$$I_s = d_b^3 \rho_b v_t^2 \left(1+\frac{Y_s}{Y_b}\right)^{-1} \tag{7}$$

where ρ_b is the grinding bead density, v_t is the agitator tip speed, and Y_s and Y_b are the respective elastic moduli for the solid and the grinding media.

The specific grinding energy depends on the product of the stress frequency and the stress intensity, both of which vary with grinding conditions. Becker et al. [17] showed that, for a fixed energy input, there is an optimum stress intensity that provides the most size reduction. By varying the energy input using different combinations of speed, media size, and media density, they demonstrated that the optimum stress intensity decreased with increased energy input. The optimum intensity presumably reflects the critical intensity for fracture discussed above. Equation 7 indicates how it varies with media size. It would be of particular interest to establish its dependence on the size of the particles being broken. Unfortunately, the experimental procedure used in this work provides only very limited information on particle size effects, since many different sizes are being broken simultaneously.

Process Modeling

Size-Mass Balance Models

During the last three decades, mathematical modeling of grinding processes has been developed to the extent that the performance of grinding circuits can often be predicted with a reasonably high degree of precision. The models use two basic model parameters: the breakage rate function and the breakage distribution function. The breakage rate reflects the rates at which different kinds (sizes etc.) of particles are broken. The breakage distribution describes the size distribution of the fragments produced by breakage. If the breakage rates and breakage distributions are known, the product size distributions can be predicted by means of mass balances. The generalized size-mass balance model can be expressed by

$$\frac{dm_i}{dt} = -S_i m_i + \sum b_{ij} S_j m_j \tag{8}$$

where m_i is the mass of material in size class i, S_i and b_{ij} are, respectively, the breakage rate and breakage distribution for size i. Unfortunately, the determination of the breakage parameters S_i and b_{ij} is difficult, especially for the subsieve size range, which has somewhat limited the application of this approach in studies of stirred media milling.

Experimentally, the rate and distribution functions are usually determined by the so-called one-size-fraction method [18]. In this method, a narrowly sized fraction (e.g., one sieve size fraction) is prepared and subjected to grinding for various times. The fraction remaining unbroken in the starting size is used to determine the breakage rate, and the size distribution obtained for very short grinding times is used to estimate the breakage distribution. The variations in the breakage parameters with particle size are evaluated using different feed sizes. It is the difficulty of preparing precise, narrow size fractions in the sub-sieve size range that seriously limits direct estimation of the breakage parameters in ultrafine grinding.

In many cases, the specific rate of breakage for any size is found to be independent of time and the extent of grinding, i.e. the process follows first-order kinetics. There are, however, many instances of rates that either increase or decrease with time. Acceleration of breakage has been observed in wet grinding tests in tumbling ball mills and is probably due to changes in the environment inside in the mill. Deceleration of the breakage rate is often encountered in prolonged grinding and appears to result from the accumulation of fine particles, which produce some

kind of cushioning effect.

Generally, the specific rate of breakage S increases with size, but passes through a maximum and then decreases as the particles become too large to be broken efficiently by the grinding media. A typical plot of S values against the particle size is shown in **Figure 1**. This result is entirely consistent with the stress-efficiency/stress-frequency concept discussed by Kwade [12]. The maximum is probably determined by the optimum stress intensity for particle breakage. A more detailed study of the relationship between media size and particle size and critical stress intensity would be invaluable in the optimization of grinding conditions.

The relationship for the particle size range below the maximum can be fitted to a simple power function (18)

$$S_i = S_o \left(\frac{x_i}{x_o} \right)^{\alpha} \tag{8}$$

where S_i is the specific rate of breakage for particles of size x_i, x_o is a standard particle size, S_o is the specific rate of breakage at size x_o, and α is a constant.

The breakage distribution describes the fragments produced by each breakage event. It is somewhat more difficult to determine than the breakage rate because it involves measurement of the fragment size distribution before any rebreakage occurs. The form of the breakage distribution is strongly affected by the breakage mechanism. It is generally considered that there are three breakage mechanisms which are important in media milling: fracture, chipping, and abrasion [19]. Fracture refers to the complete disintegration of a particle, chipping refers to removal of fragments from edges and corners, while abrasion involves the uniform removal of surface material due to wear. Fracture leads to disappearance of the original particle, which is replaced by a complete suite of smaller fragments. Chipping and abrasion both lead to the appearance of fine particles along with the original particle, which slowly decreases in size. The chipping and abrasion mechanisms are sometimes lumped together as attrition. The fragment size distributions resulting from each of these mechanisms have a distinct, characteristic appearance as shown in **Figure 2**. In any given grinding device, all three mechanisms may take place simultaneously, but the shape of the product size distribution depends on which mechanism dominates. **Figure 3** shows a typical breakage distribution observed in a tumbling ball mill operated

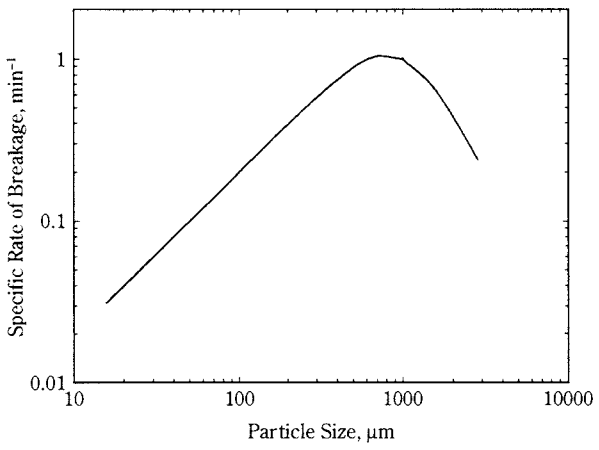

Fig. 1 Illustration of the typical variation of the specific rate of breakage with particle size.

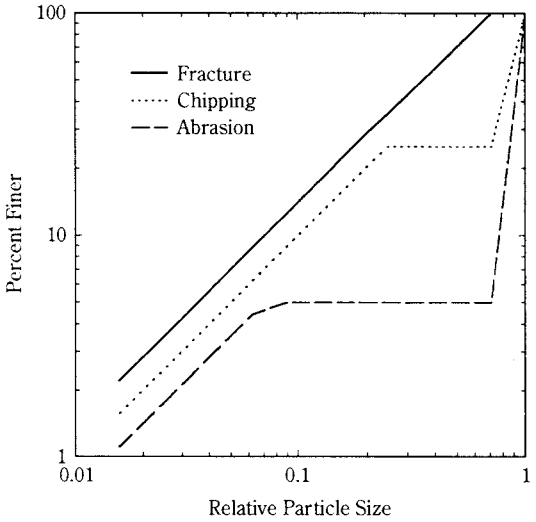

Fig. 2 Size distribution of fragments produced by different breakage mechanisms (schematic). Note that the fragments produced by chipping or abrasion include the residual core of the parent particle while, in the case of fracture, the parent disappears completely.

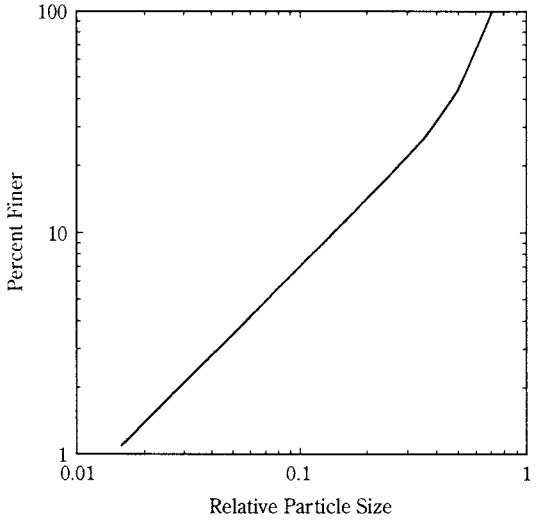

Fig. 3 A typical breakage distribution

under normal conditions. This distribution can be fitted to a double power function (18):

$$B_{ij} = \phi_j \left(\frac{x_{i-1}}{x_j} \right)^{\gamma} + (1-\phi_j) \left(\frac{x_{i-1}}{x_j} \right)^{\beta} \quad (9)$$

where B_{ij} is the cumulative breakage distribution, i.e. the fraction of the fragments produced by breaking particles of size x_j that are smaller than size x_i, ϕ_j; α, and γ are constants which may vary with the size (x_j) being broken.

In several studies, the above grinding model has been shown to be applicable to stirred ball milling [2, 20-23]. Generally, the trends in the breakage parameters were found to be similar to those for conventional, tumbling ball milling. Mankosa et al. [22,24] determined breakage rates for coals in the size range of 20×140 US mesh ground in a stirred ball mill. The grinding kinetics showed first-order behavior and for a given ball size, the breakage rates followed the trend shown in **Figure 1**. The maximum breakage rates were observed for particle sizes at about 1/20 of the ball size. The power draw was found to be higher for the larger ball sizes but, for a given energy input, the smaller ball sizes produced finer product size distributions. This indicates that the breakage distribution might be flatter for the smaller ball sizes. In a subsequent study (24), the effects of operating variables were analyzed. It was reported that the lower rotational speeds were more energy efficient. It was concluded that, at lower speeds, the balls move in a somewhat gentle manner, producing a larger effective volume for comminution. For a given specific energy input, the product size distributions were found to be essentially the same over the range of 20 to 50 wt.% solids. However, at 60% solids, the product size distribution became significantly broader than those obtained at the lower solids concentrations. This was attributed to rheological effects. When the slurry becomes too thick, the movement of media does not give proper impact on the particles. Therefore, a good portion of the large pieces still remain unbroken in the ground product, leading to a wider size distribution. It appears that the dominant breakage mechanism changes from fracture to more of an attrition type of breakage as the pulp density increases. Although not directly shown in this study, it also means that the breakage distribution may depend on the pulp density. In tumbling ball milling, grinding of higher pulp density slurries typically produces flatter breakage distributions. This effect often necessitates the use of dispersants when the slurry density and viscosity become too high or the mill contents become too fine. In their study, Mankosa et al.[24] found that the addition of a dispersant significantly improved the grinding efficiency.

Stehr et al. [21] analyzed the breakage parameters for the grinding of a 16×25 mesh coal sample in a stirred ball mill. The breakage distribution was found to have the typical form shown in **Figure 3**. However, it was considerably broader (smaller γ) than those generally observed for grinding in ball mills. This suggests that stirred ball milling produces more fines, probably because the attrition type of breakage mechanisms are more dominant in stirred ball milling. The breakage rates, which were obtained by non-linear regression, also showed a form similar to that of **Figure 1**. However, the slope of the curve was smaller (smaller α), i.e. the dependence of the breakage rate on particle size was much reduced. Overall, the experimental results, which agreed well with the kinetics model predictions, showed considerably broader product size distributions than those commonly obtained from tumbling ball mills.

Sadler et al. [3] investigated the breakage rate of 40×50 mesh dolomite ground in an attrition mill with 16×30 mesh Ottawa sand as media. The mill used had a cage-like rotor and stator type of agitation system. The breakage rate exhibited non-first order behavior, showing a decrease in rate after a short period. The initial, rapid breakage was explained by rounding of sharp edges of the particles. However, since the particle size and the media size were not much different, it is quite likely that the particles were simply too large to be crushed in the mill. The breakage rate in the later period appeared to be time independent, and to increase linearly with the cube of the agitation speed. Since the power consumption also increased with the cube of the agitation speed, it was concluded that the grinding efficiency was independent of the power input.

In many respects, the findings given in these studies are analogous to the trends frequently observed in conventional, tumbling ball milling. However, the majority of the results were based on the sieve size range and it does not necessarily follow that the same trends should continue into the sub-sieve and the micron size ranges. As noted previously, there are difficulties in directly determining the grinding kinetics model parameters for particles in the sub-sieve size range. The size-mass balance model generally used for data analysis is itself based on subdivision of the particles into narrow size intervals and determining the changes in the mass fraction in each fraction. In the sub-sieve size range, particles cannot easily be

subdivided into narrow size fractions, which makes it difficult to determine the breakage parameters experimentally. In addition, application of the model requires a consistent definition of size (usually sieve size). Fine grinding results that include size distributions obtained by combining sieve and sub-sieve (e.g., light scattering) data involve more than one size definition so that the applicability of the grinding model itself becomes questionable.

Breakage Parameters in Fine, Stirred-Media Milling

It is always possible to make estimates by extrapolating coarse grinding results into the sub-sieve size range. When the amount of the particles in the sub-sieve size range is small, this extrapolation may not produce a noticeable error in the predicted results. However, as grinding proceeds, the particles in the mill will eventually all fall in the sub-sieve size range and the predictions made by extrapolated breakage parameters may deviate substantially from the experimental results. In coarse grinding, the breakage parameters are found to be essentially independent of the extent of grinding and of the environment in the mill. There is considerable evidence, however, that this may not be true for very fine grinding; breakage parameters may change as grinding proceeds and environmental effects, due to changes in slurry rheology, become significant. Alternatively, the breakage characteristics of the particles themselves may be different in the sub-sieve range.

Recently, the authors have made considerable effort to establish reliable procedures for characterizing the model parameters in ultrafine grinding systems [25, 26]. Fine quartz (270×400 US mesh) was ground for up to 64 hours at rotational speeds ranging from 2000 to 6000 rpm in a 0.6 liter laboratory mill using 0.8–1.0 mm zirconia/silica beads as media. Examples of the product size distributions are given in **Figure 4**. Breakage rates for the feed material were obtained by direct measurement of disappearance rates. The corresponding breakage distributions were estimated from short-time product size distributions obtained by combining sieving data (at 400 mesh) with laser scattering/diffraction using an appropriate instrument-to-instrument size conversion procedure [27, 28].

The disappearance plots for the 270×400 mesh quartz feed at various rotational speeds indicated that breakage follows first-order kinetics initially, but the rates were found to increase in each case after about 2 minutes of grinding. As expected, breakage rates obtained from the short-time (<2 min) results were found to increase with rotational speed. The accelerated breakage at longer times was attributed to changes in the grinding environment inside the mill. Non-first order behavior of this kind is often observed in conventional ball milling and is generally believed to be caused by the rheological properties of the slurry, which change as the amount of fines present increases. Tangsathitkulchai and Austin [29] reported that increases in the breakage rates often occur when the slurry is rather dilute. On the other hand, breakage rates tend to decrease when the slurry becomes too thick. It appears that the media movement is hindered when the slurry becomes too viscous, suggesting that the breakage rate could decrease as the mill contents become very fine during prolonged grinding. However, this effect could not be observed directly in these tests because the original 270×400 mesh fraction disappears completely after a very short grinding time.

The product size distributions obtained for grinding times up to 64 hours at 2000 rpm were found to become progressively narrower as grinding proceeds, with a consistent steepening of the curves at sizes below about 1 μm. This effect is not generally observed in coarse grinding where the product size distributions typically shift to finer sizes in a parallel fashion. Measured surface areas, by gas adsorption and light scattering (Microtrac), were found to correlate well for grinding times up to 8 hours, which suggests that the break in the size distribution is real and is not simply an artifact resulting from the failure of the light scattering system to detect ultra-fine particles [25].

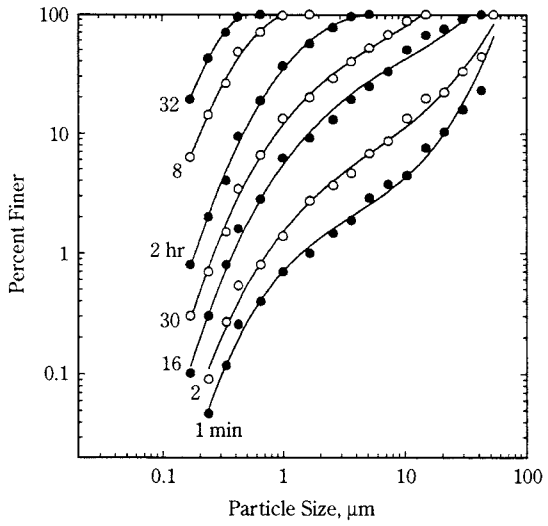

Fig. 4 Product size distributions from stirred-media milling of 270×400 US mesh quartz.

The form of the size distribution of the ground products is strongly influenced by the fragmentation process occurring at each fracture event. In coarse grinding, the breakage distributions are usually not influenced by the presence of other particles. Also, the size distributions of the fragments can often be normalized with respect to the size of the particle being broken. Consequently, the shape of the size distribution tends to be conserved even after repeated breakage events, resulting in a self-similar or self-preserving size distribution among the comminuted products [30]. However, for the data shown in **Figure 4**, the shape of the size distribution is not self-preserving but becomes progressively narrower, which suggests that the breakage distributions are not normalizable but change as a function of the size of the parent particles.

Strazisar and Runovc [31] reported that the product size distributions from grinding into the submicron size range could be represented by the log-normal size distribution and also that the distribution variance decreased for longer grinding times. This may be a consequence of the approach to a "grind limit", a limiting size below which particles cannot be broken mechanically, nor can they be produced by breakage of coarser material. As particles close to the grinding limit cease to grind, those particles still in the coarse range continue to break and the product size distribution becomes progressively narrower. Liu and Schönert [32] reported that the breakage distribution for particles undergoing bed compression could be described by a truncated log-normal distribution, i.e., one for which there is a maximum limit in particle size. For ultrafine grinding systems, extending into the submicron particle size, there is theoretical and experimental evidence of an approach to a minimum particle size [25,33]. Thus, the breakage distribution should be bounded at both the upper and lower ends. Such a distribution can be represented by a double-truncated log-normal distribution. The latter can be represented using a transformed size variable η defined by:

$$\eta = \frac{x-Y}{X-x} \tag{11}$$

where x is particle size, Y is the minimum size (the grind limit), and X is the maximum size, i.e. that of the parent particle. The form of the distribution is further defined by the median value η_{50} and the standard deviation σ of the transformed variable.

The breakage distributions shown in **Figure 5** were calculated for the 270×400 mesh feed material

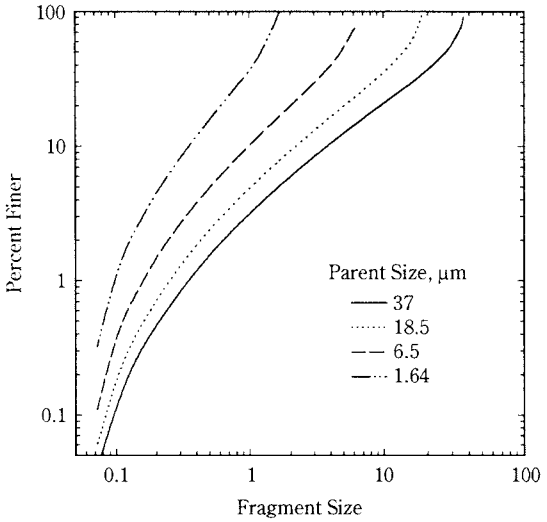

Fig. 5 Breakage distributions used to describe stirred-media milling of 270×400 mesh quartz.

(X=37 μm) based on several pairs of the product size distributions from **Figure 4** using the so-called BII method [16]. It was found that these distributions could be approximated by the double-truncated log-normal function with σ=1.75, η_{50}=1.0, and the lower limiting size Y arbitrarily set at 0.03μm.

The progressive steepening of the product size distributions noted previously implies that the standard deviation of the breakage distributions should decrease with decreasing parent size X. It was found, by trial-and-error, that the general form of the product size distributions shown in **Figure 4** was consistent with the pattern of breakage distributions shown in **Figure 5**. Simulations based on these breakage distributions agreed well with experimental data for grinding times up to 1 hour. For longer times, the simulations appeared to overestimate the extent of grinding.

The approach to a "grind limit" implied by the truncated form of the breakage distribution suggests that breakage rates may also be reduced in the finer sizes. It was postulated that the overestimates noted above were a consequence of reduced breakage rates in the fine sizes corresponding to an increase in the exponent α (Equation 9) in the submicron range. For the fine quartz particles, it was found that the data could be simulated using an exponent which increased from 1.0 in the coarse size range to 2.0 for the submicron material. This modified breakage rate is illustrated in **Figure 6**.

Reports of the specific effects of media size and density on the breakage parameters are somewhat scarce, largely due to the experimental difficulties involved in the direct measurement of breakage rates etc. at very fine sizes. In general, it appears that the trend is quite

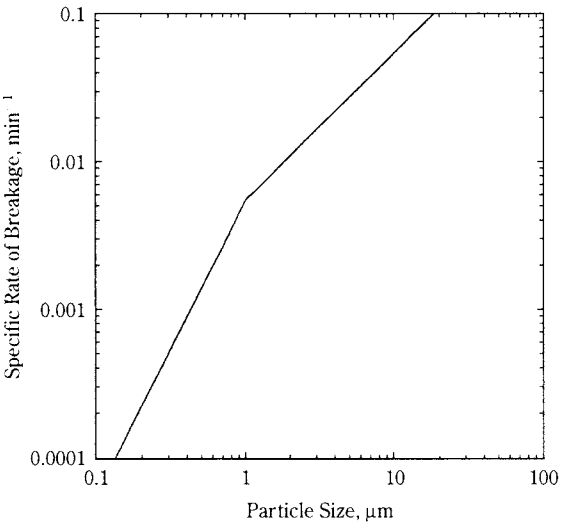

Fig. 6 Variation in breakage rate with particle size for stirred-media milling of 270×400 mesh quartz.

similar to that observed in tumbling media mills, i.e. breakage rates for a given media size increase with particle size but reach a maximum above which the media are simply too small to provide sufficient impact energy to ensure breakage. Breakage distributions seem to be relatively insensitive to media size.

Based on such data as are available and on indirect evidence from the work of Kwade et al., [11,15] and others [2,6,7,22,23,34], it appears that the trade-off between stress intensity and stress frequency becomes especially critical at ultrafine sizes. Changing media size can lead to enhanced breakage in one range of sizes but simultaneously to reduced rates for slightly coarser material. Staged stirred-media milling using progressively finer media may be a useful option for improving efficiency in ultrafine grinding. The use of a distribution of media sizes, as is the common practice in tumbling ball mills, should also be evaluated.

Conclusions

Stirred-media milling is an effective means of grinding to very fine sizes. While the process is well established commercially, much remains to be learned regarding the fundamental principles involved and the role of equipment and operating variables on grinding performance. Process design remains largely a matter of trial and error. The energy efficiency of the process is recognized to be strongly dependent on operating conditions, but there is a good deal of inconsistency in the literature with respect to the relative importance and specific effects of different variables. There is general agreement that, as with most media milling systems, the highest efficiency is obtained when the powder loading is just sufficient to fill the interstices in the media charge. It is also clear that the media size to particle size ratio is a critical factor; the optimum ratio seems to lie between 10 and 20 to 1. Understanding of mill mechanics is far from complete. Empirical and semi-empirical relationships for mill power requirements have been presented, but their ability to account for complex flow behavior etc., is questionable.

The concepts of stress intensity and stressing frequency are central to the appropriate design and operation of stirred-media mills and provide a useful way of addressing the question of media size to particle size ratio. While this approach has been shown to be consistent with general observations of product fineness etc., their relationship to breakage rates and breakage distributions has yet to be established.

The size – mass balance models have proved to be invaluable in the design and control of conventional (tumbling ball mill) grinding circuits. Several applications of these models to stirred-media milling have been reported, mostly for relatively coarse grinding. The results and the estimated model parameters are generally similar to those from tumbling mills. Due to problems with reliable parameter estimation, their application at fine (sub-sieve) sizes has been somewhat limited, but some general patterns are being established. The breakage rates and breakage distributions seem to follow the same trends with particle and media size as those observed for tumbling mills, but appear to be affected by the approach to an apparent grind limit at about 0.03–0.05 μm. Breakage rates, which normally decrease with decreasing particle size, do so more abruptly as the grind limit is approached, i.e., in the submicron size range. Breakage distributions are, by definition, bounded at the upper end by the size of the parent particle. The existence of a grind limit imposes a lower bound to the distribution as well, the result being distributions that are not normalizable with respect to the size of the parent but become progressively narrower as the parent size decreases.

Nomenclature

a	: Constant in energy-size relationship [units depend on value of exponent, a]	
A_s	: Specific surface area	[m^2/g]
b	: Exponent in energy-size relationship	[–]
b_{ij}	: Incremental breakage distribution	[–]
B_{ij}	: Cumulative breakage distribution	[–]
c_d	: Dispersant concentration	[%]

C : Impeller geometry constant
d_b : Grinding media diameter [m]
d_d : Grinding chamber diameter [m]
D : Impeller diameter [m]
E : Specific energy input [kwh/T]
f_s : Stress frequency [s^{-1}]
I_s : Stress intensity [N/m^2]
m_i : Mass of material in size interval i
N_p : Power number [−]
N : Rotational speed [rpm]
P : Mill power [kw]
S_i : Specific rate of breakage for size class i [min^{-1}]
S_o : Specific rate of breakage for standard size x_o [min^{-1}]
v_t : Agitator tip speed [m/s]
V : Mill volume [gal.]
x : Characteristic particle size [μm]
x_i : Particle size in class i [μm]
x_o : Standard particle size [μm]
X : Size of parent particle [μm]
Y : Minimum particle size (grind limit) [μm]
Y_b : Elastic modulus of grinding media [N/m^2]
Y_s : Elastic modulus of solid being ground [N/m^2]
α : Exponent in relationship between specific rate of breakage and particle size [−]
β : Exponent in expression for breakage distribution [−]
γ : Exponent in expression for breakage distribution [−]
η : Transformed size variable [−]
μ : Viscosity [Pa.s]
ρ : Density of mill contents [kg/m^3]
ρ_b : Density of grinding media [kg/m^3]
ρ_s : Density of solid being ground [kg/m^3]
ϕ_j : Constant in expression for breakage distribution for size j [−]

References

1) Charles, R.J., "Energy-Size Reduction Relationships in Comminution," Trans. AIME, 208, pp. 80-88 (1957).
2) Herbst, J.A. and Sepulveda, J.L., "Fundamentals of Fine and Ultrafine Grinding," Proceedings, The International Powder and Bulk Solids Handling and Processing Conference, Chicago, Ill, pp. 452-470 (1978).
3) Sadler, L.Y., Stanley, D.A., and Brooks, D.R., "Attrition Mill Operating Parameters," Powder Technol., 12. pp. 19-28 (1975).
4) Stehr, N. and Schwedes, J., "Investigation of the Grinding Behavior of a Stirred Ball Mill," Ger. Chem. Eng., 6. pp. 337-343 (1983).
5) Gao, M.W. and Forssberg, E., "Increasing the Specific Surface Area of Dolomite by Stirred Ball Milling," in Comminution-Theory and Practice Symposium, S.K. Kawatra (ed.), SME/AIME, Littleton, CO (1992).
6) Gao, M.W. and Forssberg, E., "A Study on the Effect of Parameters in Stirred Ball Milling," Int. J. Miner. Process., 3., pp. 45-59 (1993).
7) Gao, M.W. and Forssberg, E., "Prediction of Product Size Distributions for a Stirred Ball Mill", Powder Technol., 84., pp. 101-106 (1995).
8) Zheng, J, Harris, C.C. and Somasundaran. P, "A Study on Grinding and Energy Input in Stirred Media Mills," SME Annual Meeting, Denver, CO, March 1995.
9) Rushton, J.H., Costich, E.W. and Everett, H.J., " ," Chem. Eng. Progr., 46, pp. 395-404; 467-476 (1950).
10) Gao, M.W., Forssberg, E. and Weller, K.R, "Power Prediction for a Pilot Scale Stirred Ball Mill," Int. J. Miner. Process., 44-45. pp. 641-652 (1996).
11) Zheng, J, Harris, C.C. and Somasundaran. P, "Power Consumption of Stirred Media Mills," SME Annual Meeting, Albuquerque, NM. Feb. 1994.
12) Kwade, A., "Wet Comminution in Stirred-Media Mills – Research and its Practical Application," Powder Technol., 105, pp. 14-20 (1999).
13) Blecher, L. and Schwedes, J., (1996) "Energy Distribution and Particle Trajectories in a Grinding Chamber of a Stirred Ball Mill," Int. J. Miner. Process, 44-45, pp. 617-627 (1996).
14) Mishra, B.K. and Rajamani, R., "The Discrete Element Method for the Simulation of Ball Mills," Appl. Math. Modeling, 16. pp. 598-604 (1992).
15) Inoue, T. and Oyaka, K., "Grinding Mechanism of Centrifugal Mills – a Simulation Study Based on the Discrete Element Method," Int. J. Miner. Process, 44-45, pp. 425-435 (1996).
16) Kwade, A., Blecher, L. and Schwedes, J., "Motion and Stress Intensity of Grinding Beads in a Stirred Media Mill. Part 2: Stress Intensity and its Effects on Comminution," Powder Technol., 86, pp. 69-76 (1996).
17) Becker, M., Kwade, A. and Schwedes, J., "Influence of the Stress Intensity on the Comminution of Ceramics in Stirred Ball Mills," in Fine Powder Processing, Eds., R. Hogg, R.G. Cornwall, and C.C. Huang, Penn State University. pp. 51-58 (1997).
18) Austin, L.G., Klimpel, R.R., and Luckie, P.T., Process Engineering of Size Reduction: Ball Milling, AIME, New York, (1984).
19) Crabtree, D.D. et al., "Mechanisms of Size Reduction in Comminution Systems," Trans, SME/AIME, 229. pp. 202-210 (1964).
20) Heindenreich, E. and Kruger, G., "Investigations Concerning the Mathematical Description of Ultra-Grinding Processes," Preprints, World Congress Particle Technology, Nuremberg, FRG, pp. 695-707 (1986).
21) Stehr, N., Mehta, R.K., and Herbst, J.A., "Comparison of Energy Requirements for Conventional and Stirred Ball Milling of Coal-Water Slurries," Coal Preparation, 4. pp. 209-226 (1987)
22) Mankosa, M.J., Adel, G.T., and Yoon, R.H., "Effect of Media Size in Stirred Ball Mill Grinding of Coal," Powder Technol. 49. pp. 75-82 (1986).
23) Rajamani, R.K. and Bourgeois, F., "Energy Efficiency of

Silicon Carbide Grinding in a Stirred Ball Milling," Preprints, World Congress Particle Technology, Kyoto, Japan,. pp. 369-375 (1990).
24) Mankosa, M.J., Adel, G.T., and Yoon, R.H., "Effect of Operating Parameters in Stirred Ball Mill Grinding of Coal," Powder Technol. 59. pp. 255-260 (1989).
25) Cho, H. and Hogg, R, "Investigation of the Grind Limit in Stirred-Media Milling," Int. J. Miner. Process, 44-45, pp. 607-615 (1996).
26) Cho, H. and Hogg, R, "Breakage Parameters for Ultrafine Grinding in Stirred-Media Mills," Proceedings, XIX International Mineral Processing Congress, San Francisco, Ca, Vol. 2 pp. 53-57 (1995).
27) Austin, L.G. and Shah, I., "A Method for Inter-Conversion of Microtrac and Sieve Size Distributions," Power Technol. 35. pp. 271-278 (1983).
28) Cho, H, Yildirim, K. and Austin, L.G., "The Conversion of Sedigraph Size Distributions to Equivalent Sub-sieve Screen Size Distributions," Powder Technol. 95. pp. 109-117 (1998).
29) Tangsathitkulchai, C and Austin, L.G., "The Effect of Slurry Density on Breakage Parameters of Quartz, Coal and Copper Ore," Powder Technol., 42. pp. 287-296 (1985).
30) Kapur, P.C., "Self-Preserving Size Spectra of Comminuted Particles," Chem. Eng. Sci. 27. pp. 425-431 (1972).
31) Strasizar, J. and Runovc, F., "Kinetics of Comminution in Micro and Sub-micrometer Ranges," Int. J. Miner. Process. 44-45. pp. 673-682 (1996).
32) Liu, J. and Schönert, K. "Modelling of Interparticle Breakage," Int. J. Miner. Process, 44-45. pp. 101-115 (1996).
33) Schönert, K, "Advances in the Physical Fundamentals of Comminution, in Advances in Mineral Processing, P. Somasundaran (ed.), SME/AIME, Littleton, CO., p. 28, 1986.
34) Hogg, R., Hu, S. and Musselman, S.W., (1998) "Breakage Mechanisms in Stirred-Media Milling," Proceedings, World Congress on Particle Technology 3, Institution of Chemical Engineers, Rugby, Warwickshire, England, 1998.

Author's short biography

Richard Hogg

Richard Hogg is Professor of Mineral Processing and GeoEnvironmental Engineering at the Pennsylvania State University. He received a B.Sc. from the University of Leeds and the M.S. and PhD degrees from the University of California at Berkeley. Dr Hogg's research interests include fine particle processing, particle characterization, and colloid and surface chemistry.

Heechan Cho

Heechan Cho graduated from the Seoul National University with a B.S. degree in Mineral and Petroleum Engineering. He obtained the M.S. and Ph.D. degrees in mineral processing from the Pennsylvania State University. He has held research positions with the U.S. Department of Energy, Penn. State and the Korea Electric Power Research Institute. He is presently an assistant professor in the School of Civil, Urban & Geosystem Engineering of the Seoul National University.

Environmentally Conscious Recycling and Compositional Separation†

Shuji Owada
Department of Resources and Environmental Engineering
School of Science and Engineering
*Waseda University**

1. Soft Separation and Hard Separation

Technology which separates valuables from useless ones (and/or toxic components) is necessary in resources recycling, as can be said from old days in Japan "separation can produce resources and mixing creates wastes". Separation technologies are classified into two kinds, soft and hard separation. Soft separation (SS) is defined as the technology that does not destroy the atomic configuration of the target material while separation, in other words, can be called "solid/solid separation", which is correspondent to the "mineral processing" technologies in mining industry. Hard separation (HS) can be defined as the technology which destroy the atomic configuration, and can be called "ion/ion separation", correspondent to the "smelting and refining" technology in metallurgical industry. From the definition, it can be easily understood that the hard separation is materials- and energy-consuming process, then it is desirable that the separation in recycling is completed only by soft separation from the viewpoint of environmental harmony. However, the soft separation is the process conducted in heterogeneous system of solid particles and the hard separation is fundamentally the one in homogeneous system of ions, then the background theory is almost satisfied in the HS but not in the SS. Accordingly the reliability of separation is high in the HS and low in the SS. However, it is also the fact that the HS often becomes essential for producing high purity and functional materials from the wastes. We have to well understand the properties of the two kinds of separation technologies and make the best combination in the processing flow. Most important, however, seems to improve the reliability of the SS in recycling for the separation process to be more environment friendly. Characteristics of the two kinds of technologies are shown in **Table 1**.

* Okubo 3-4-1, Shinjuku-ku, Tokyo 169-8555 Japan
Phone: 03-5286-3319, Fax: 03-5286-3491
E-mail: owadas@mn.waseda.ac.jp
† Received: July 17, 2000

Figure 1 is a typical processing flow for the treatment of waste materials. For realization of the effective SS, the addition of many ancillary operations are required. Crushing, grinding and size classification are necessary as pretreatment, and dehydration (in the case of wet process), blending, agglomeration,

Table 1 Comparison between soft separation and hard separation

Item	Soft separation	Hard separation
Definition	Separation utilizing solid property without destroying atomic configuration	Separation by destroying atomic configuration (dissolving and/or melting)
Environmental impact	Low (material and energy saving)	High (consuming much material and energy)
Target of separation	Solid material (heterogeneous)	Ion (homogeneous in principle)
Theoretical background	There is only generic theory for the technique.	There exist theories for each technique and ion.
Reliability on separation	Low	High

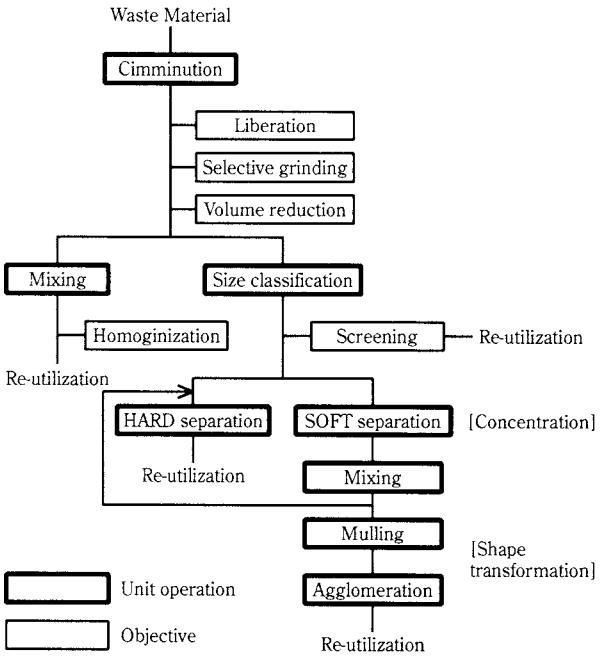

Fig. 1 A typical technological flowchart for waste treatment.

briquetting, etc. are the candidates as post-treatment. Though main role of comminution is the increase in surface area if only the HS is applied directly to wastes, the primary purpose in the SS is the liberation among compositional elements. Since comminution is highly energy consuming operation, with no more than several percentages of energy efficiency, it is not a wise way to charge large energy in this stage. Size reduction should be minimized to the extent that the liberation among components is achieved. The theoretical limit of separation efficiency of the SS is determined in the stage of size reduction, because the efficiency in the SS, of which the unit to be separated is a solid particle, is depending on the content of free particles and the existent ratio of the objective component in locked particles. Application technology must be determined also by the grain size of the feed, since each technology has applicable size range (**Figure 2**). Selective grinding is also possible if the objective component has unique grindability, compositional separation can be achieved only by size classification then, in this case. It is expected to develop new comminution technology which improves the liberation of compositional elements, such as to break preferentially the border of different phases.

The soft separation (SS) can be further classified into two kinds by the properties which are utilized in the separation process, one is bulk property and the other is surface property, as shown in **Table 2**.

Bulk property is generated from the atomic configuration of feed material which has a minimal energy level in the crystal structure, then the property is relatively stable. On the other hand, surface property is generated from unstable molecules on the surface which is exposed into the air, and the property is greatly changeable by the condition of circumstances.

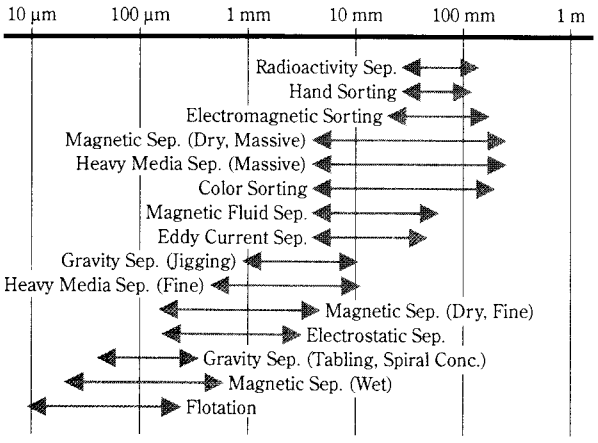

Fig. 2 Optimum size ranges for various soft separation technologies.

Therefore, in the waste processing, bulk properties are better utilized than the surface property because of the stability. However, surface properties can be artificially modified with relative ease and the improvement of separation efficiency is also expected when the separation is carried out in the controlled circumstances.

Major hard separation (HS) technologies are listed in **Table 3**. As a means for destroying atomic configuration, there are two ways, using heat and some solvents, the process of which is usually called "pyrometallurgical" and "hydrometallurgical", respectively in metal industry. In the former process, compositional separation is carried out using the difference in the affinity of objective element with some chemical compound in the molten phase. Although, the HS is conventionally applied after the concentration of an objective component using SS, the HS technologies are often carried out as pretreatment of the SS tech-

Table 2 Two kinds of soft separation technologies.

Property	Technology
<Bulk Property>	
Electromagnetic property (Reflectance)	Electronic sorting
Shape	Shape separation
Density	Heavy media separation Magnetic fluid separation (Wet) Graviry separations: Jigging, Spiral separation, Table separation, Malti-gravity separation, etc. (Dry) Gravity separations: Air table separation, Air jigging, etc.
Magnetic property	Magnetic separation
Electric conductivity	Eddy current separation
Radioactivity	Radioactivity separation
<Surface Property>	
Color, Luster, Shape, etc.	Hand sorting
Electromagnetic property (Transmittance)	Electronic sorting (incl. Color sorting)
Electric conductivity (of surface)	Electrostatic separation
Wettability	Flotation, Liquid/liquid extraction

Table 3 Major hard separation technologies

Dry (Pyrometallurgical) Processes:
<Chemical decomposition and transformation by heating>
Calcination: Oxidation, Sulfidization, Chlorination. etc.
Melting with chemical compounds
Wet (Hydrometallurgical) Processes:
<Chemical decomposition and transformation by dissolution in water and/or solvent>
Leaching, Precipitation, Cementation, Ion Exchanging, Solvent Extraction, Electrolysis, etc.

nologies especially in recycling. Since in the chlorination various metal elements are volatilized as chloride gas, compositional separation is easy only by means of solid/gas separation. Important in the pyrometallurgical process is the effective utilization of low temperature heat discharged in the processes. In the hydrometallurgical process, various technologies exist as shown in **Table 3**. It is indispensable to establish the recovery and regeneration processes of solvent as well as to develop new selective solvents. Individual technique of this category can be referred to the references[2,3].

2. Concept of Recycling and the Technologies Applied

Figure 3 shows the concept of recycling and the technologies necessary to realize each stage in the flowchart. To begin with, "Resource" (in narrow term) is acquired for our industrial system from nature. "Resource" is dressed into "Raw material" by soft separation (SS), then, the "Raw material" is transformed into "(Functional) Material" by hard separation (HS), then transformed into "Device" by fabrication, and finally producing "Product" by the application of assembly technologies. The processes from "Resource" to "Product" are called "artery industry", and "venous industry" begins with the "Waste" which is discharged from the stage of "Consumption". Here, we can choose various loops to which the waste is fed back. Of course, quantity and quality of the waste must be considered in the choice, and reasonable loop should be determined in accordance with the property of each waste. Some amount of the final waste which has too low concentration of

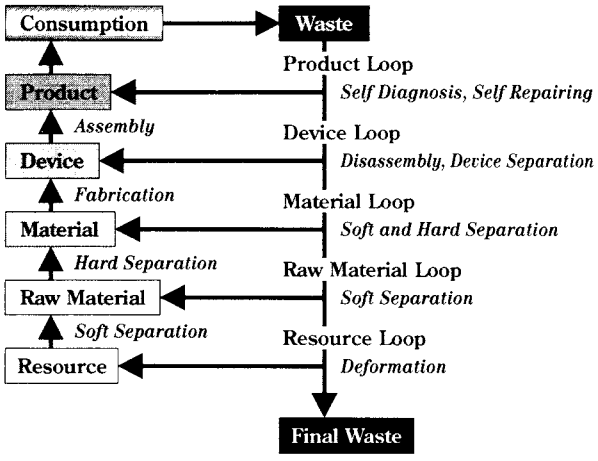

Fig. 3 Concept of recycling and technologies required in each stage.

useful component and/or too complicated structure to be recovered would be discarded into nature.

The loop which generates the least environmental impact is, no doubt, the "product and device loops" in other words "reuse" or "functional recycling". Realization of these loops is desirable in the point of utilizing the function of product, but the self-diagnostic and self-repairing techniques should be provided for the product itself, and these consideration must be paid in the stage of product design. Inspection of the function of used products and the establishment of the used item market are also required to complete these loops. At present, the examination of these techniques and systems has been made in the "Inverse Manufacturing Forum"[4], etc. The choice of "device loop" is the second best policy, when the function of product is not accepted any more. In this case, technological development of the disassembly of devices from products and separation (SS) technologies among devices by species are required. The product design to facilitate the disassembly and separation becomes also important.

In order to complete "material loop", the application of both SS and HS technologies as well as the disassembly technology is required. In the product design, the use of the structural materials having a proof to the design which is suitable for product and device recycling becomes essential, and the use of composite materials which are too complicated and hazardous constituents should be prohibited. "raw material loop" is the fed back loop of concentrated materials to the artery industry, then only the application of the SS is fundamentally required. The last stage of recycling is "resource loop" in which wastes are returned to the artery industry as "Resource" (in narrow term) by the application of simple shape transformation.

Although (a part of) waste materials which can not be recycled in either loop have to be discharged into the environment as final wastes, it becomes often necessary to reduce the volume by incineration, etc. and stabilize them not to leach toxic components, as well as detoxify the wastes. To utilize the processing (decomposition) ability in the environment (nature) is one of the most environment-friendly measures. In the cases, keeping the wastes in some disposal site for a long period, it is possible to apply some biological treatment, etc. to recover low content valuable components as "long term recycling".

It is definitely the fact that any materials and energy are transformed into dispersed and less concentrated (low level) state, if no high level material and energy is added into the system. In order to put again valu-

ables back to the low level substance once discharged, considerable amount of materials and energy must be charged. In the recycling, as is said previously, we should choose smaller loop in which the materials can be kept in high level in the process, because the high level materials were produced under the sacrifice of the emission of low level energy and waste materials which is probably a potential of environmental disruption). The advantage of the SS compared with the HS is clear from this point of view. The larger the recycling loop becomes, the greater the amount of materials and energy required for the recycling becomes. The venous industry demonstrates the true value in the case in which the environmental impact generated from recycling processes is smaller than that from artery processes. We can call this kind of recycling "Environmentally Conscious Recycling".

3. Examples of the Process Combining Soft and Hard Separation

There are two cases of combining the soft separation (SS) and hard separation (HS), 1) the SS is applied as pretreatment of the HS to reduce the total environmental impact, 2) the HS is firstly applied to the complex materials which cannot be treated by the SS, then compositional separation is realized by the following SS. Representative example of the former case is the combination of mineral processing and metallurgical processing technologies in metal producing industry. This type of combination is usually adopted in the cases that the value (price) and/or content of the objective component are low in the feed. However, there is no need in the SS stage to separate (reject) the elements which are useful as mixture in the stage of the HS. The latter is often applied to the case in which the value of the feed is relatively high but the structure is complicated. It is desirable in the case that the effect of material and energy charged in the HS process is focused selectively to the objective component.

Some examples combining both separation technologies are shown in the followings.

3.1 Processing of the shredder residue

The scrap automobiles after dismantling the engines, tires, catalysts, oils, etc. and the whole scrap home electric appliances are usually fed into shredder plant, where those are shredded and iron and aluminum are recovered by SS techniques, such as magnetic and eddy current separation. Each concentrate is sent to iron-making or smelting plant to produce ground metal by the HS, from the fact of which the effective material recycling seems to be completed. However, the residue, almost 25 wt.% of the scrap materials, is generated from the shredder plant, which is mainly composed of plastics but has been obliged to be discarded in the controlled landfill site from 1996 because of the serious concern to the leaching of heavy metal ions. The residue still contains small amount of valuable metals as well as toxic one and high calorie of the plastics is expected to be a good fuel.

Here, the process developed by The Center for ECO-Mining is introduced among many processes[6] which has been proposed until now. Flowchart of the process is shown in **Figure 4**. The shredder residue is first heated and decomposed to the residue with metals and the carbonic material that is utilized in the following stages as a fuel, while the chloride gas generated in this stage is concentrated and crystallized to be solid chloride that is planed for using as snow melting agent in cold region. Copper, lead and zinc are concentrated, respectively, by applying the SS technologies, such as magnetic, eddy current, shape separation. The copper concentrate is fed to copper smelter (by the HS) to produce ground copper, lead is further concentrated into the sintering fly ash, which is fed to lead smelter (by the HS) to produce ground lead, and zinc concentrate is gasified in the melting furnace to become distilled zinc.

This kind of processes in which the existing smelting facility is effectively utilized seems to show a smart direction of the future waste processing that is economically feasible.

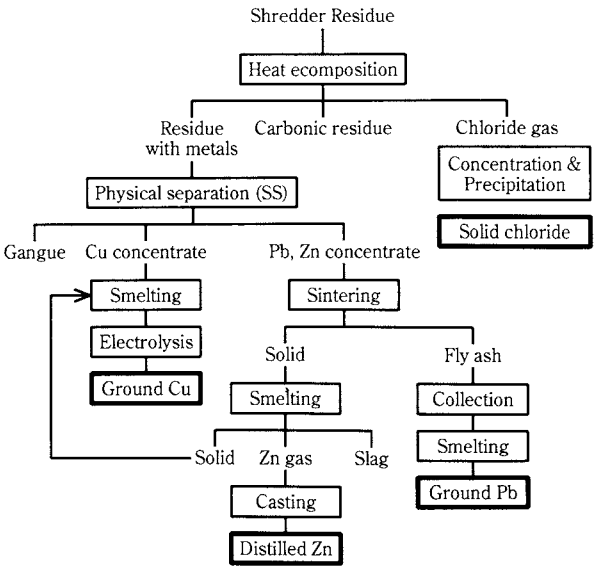

Fig. 4 A Process flow of shredder residue utilizind existing smelters.

3.2 Removal of plating film by selective oxidation

Recently, complexity increases in the structure of products and devices, then, it becomes difficult to apply the SS techniques directly to them. It would be a countermeasure to transform the atomic configuration of the objective component by the HS technology, in order to create a new structure which facilitates the following SS. This concept in the case of metal production can be called "metal laundering"[7], and seems to apply many case, for example copper removal from scrap iron, removal of surface film from aluminum can, etc.

Here, the study[8] on the removal of nickel plating film from the punching scrap of IC lead-frame which is a major scrap of copper alloys. The material has the nickel film of 3 μm thickness coated on the surface of copper plate. Since it is difficult for copper plate to be liberated from the others by simple comminution because of the ductility of metals, SS cannot be applied directly to the material. New series of processes can be proposed; 1) heating the scrap to oxidize nickel film selectively, and 2) quenching them, then giving them mechanical vibration to strip off the film. The separation can be achieved by the difference of the heat expansion rate between metal and oxide. The separation result is shown in **Figure 5**, indicating that almost 100 % removal of nickel phase can be realized in the process. However, high temperature and long time heating also accelerate the oxidation of copper phase, then the point (difficulty) is there in the determination of the conditions in which the oxidation is carried out selectively.

This kind of separation system are suitable to apply to the electronic devices, etc. the structure of which is anticipated to become more complicated.

3.3 Recovery of platinum group metals from spent automobile catalyst

Automobile catalyst (so called converter) has a function to clean up the discharged gas from automobiles, by the oxidation of HC and CO and the reduction of NO_x in the catalytic reaction of three kinds of platinum group metals (PGMs), platinum, palladium and rhodium. At present, those catalytic elements are recovered by the processes, involving fine grinding, leaching with aqua regia, selective precipitation (or solvent extraction), as well as new pyrometallurgical pretreatment process in which the PGMs are concentrated into molten copper phase. However, considering that the content of the PGMs are no more than

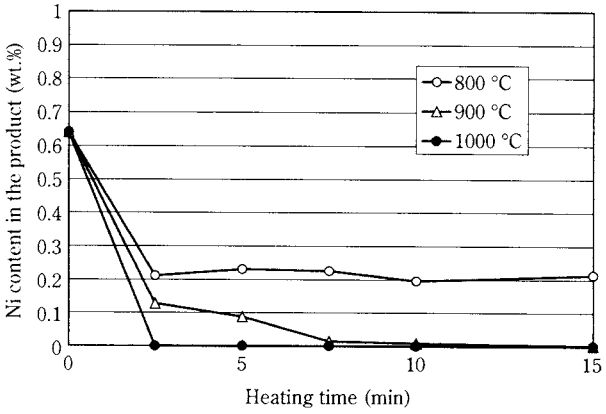

Fig. 5 Effect of temperature on the rejection of Ni in the product.

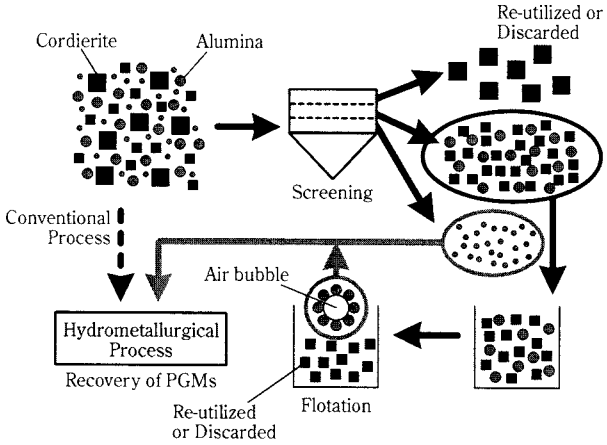

Fig. 6 New process of low energy input for the recovery of PGMs.

1 ppm in the converter, the process, leaching and/or melting all materials, might consume too much energy.

The first choice to develop new process would be the application of SS technologies as pretreatment to reduce the mass of feed to the HS process, but the particle size of the PGMs is as small as several ten nm which is too small to apply the SS technique as shown in **Figure 2**. The converter has the alumina layer containing the PGMs and coated on the substrate of cordierite ($(Mg,Fe)_2Al_3(Si_5Al)O_{18}$) with the thickness of several ten μm. It is not so difficult to separate the alumina layer from the substrate by flotation with some ionic surfactants (collectors). Then, new process can be developed as shown in **Figure 6**, involving selective grinding, screening and flotation as a series of pretreatment for the conventional HS process. This process flow will be able to reduce total energy and solvent consumption to the one thirds of that in the present flow.

References

1) S. Owada: J. Soc. Powder Technology Japan, vol.32, no.6, p.401, 1995.
2) A. Yazawa and M. Eguchi: "Hydrometallurgy and Waste Water Treatment", Kyoritsu, 1975.
3) The Section Society of Resources Recycling, MMIJ: "Resources Recycling", Nikkan-Kogyo, p.257, 1991.
4) Manufacturing Science and Technology Center: "Report on the Investigation on the Project Development for Inverse Manufacturing", 1997.
5) S. Owada: Bonanza, vol.281, no.5, p.13, 1999.
6) Clean Japan Center: "Report on the Investigation on the Treatment System of Shredder Residue", 1996.
7) N. Masuko and T. Nakamura: Prep. Fall meeting, MMIJ, p.523, 1996.
8) N. Nakamura and N. Masuko: Proc. 2nd Int. Symp. Extraction and Processing for the Treatment and Minimization of Wastes, TMS, p.523, 1996.
9) S. Owada, et.al.: Proc. 2nd Int. Symp. East Asian Resources Recycling Technology, p.69, 1993.

Author's short biography

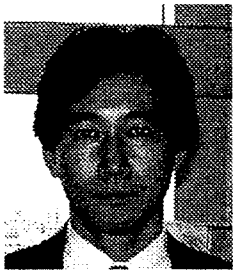

Shuji Owada

Dr. Shuji Owada is professor of Resources and Environmental Engineering, Waseda University, Tokyo Japan. He completed Doctor (of Engineering) degree in 1984 at Waseda University and has been working for the same university for 17 years. He is director of the Mining and Materials Processing Institute of Japan, director of the Resources Processing Society of Japan and member of the Recycling Engineering Committee of Science Council of Japan. His interest is in the field of resources processing and recycling especially in separation technologies, such as comminution, size classification, solid/solid and solid/liquid separation. His recent research works are 1) Liberation model considering preferential breakage between phase boundary, 2) Fractal analysis of finely comminuted particles, 3) Evaluation of grindability combining DEM simulation and fundamental experimental results, 4) Electrical disintegration of coals for improving liberation, 5) Simulation of electrostatic separation behavior, 6) Separation of commodity plastics by flotation, 7) Recycling of waste office papers, 8) Recycling of shredder residues.
He is also interested in professional accreditation system in engineering and representative member of Resources Engineering field in the Japan Accreditation Board for Engineering Education.

Fundamentals of Breakage of Aggregates in Fluids†

Ko Higashitani[1], Kenji Iimura[2] and Ivan U. Vakarelski[1]
[1] *Dept. of Chem. Eng., Kyoto Univ.*
[2] *Dept. of Chem. Eng., Himeji Institute Technology*

Abstract

Because of the industrial importance of dispersion and separation technologies, a large number of researches on the floc breakage have been carried out in various fields, but the fundamental mechanism is still poorly understood. In this review, with priority given to our works, fundamental aspects on the breakage of aggregates in fluids are overviewed theoretically and experimentally, using theories and experimental data available at present, and the future works for the better understanding are considered.

1. Introduction

Many advanced materials, such as ceramics, electronic and magnetic materials, are produced through highly concentrated colloidal dispersions. Hence knowledge of the stability of colloidal particles in fluids is fundamentally important to control the performance of final products. The mechanism of coagulation between particles has been studied extensively, mainly in the field of colloid chemistry, and is clarified fairly well, whichever the coagulation is, ortho-kinetic or peri-kinetic [1-3]. On the other hand, the mechanism to disperse coagulated particles has been poorly understood. The term "dispersed" has been used in two different ways, as illustrated schematically in **Fig. 1**. It is often used to imply that a suspension is stable such that particles do not coagulate even if they collide each other. This is essentially the problem of coagulation described above. The term is also used to describe to break up aggregates (flocs) by external forces. This is a complicated problem because aggregates are possibly deflocculated in many different ways, as illustrated in **Fig. 1**.

Since particles are essentially unstable in solutions, they are more or less aggregated when supplied in many industrial processes. These particles must be fully dispersed to make the best use of their functions, and so the breakup of aggregates has been a key technology. In general, aggregates are different each other in size, shape and strength, so that they deform and break up in different ways. Besides the breakup behavior depends also on the kind of field applied. Hence it is not easy to clarify the mechanism systematically. Nevertheless, because of the industrial importance, a large number of studies and efforts have been carried out to understand the breakup mechanism of aggregates experimentally and theoretically. The breakup process in flows is often estimated using the following population balance equation [4-8].

$$\frac{dn_{pi}}{dt} = C^b_i + C^d_i + B^b_i - B^d_i \tag{1}$$

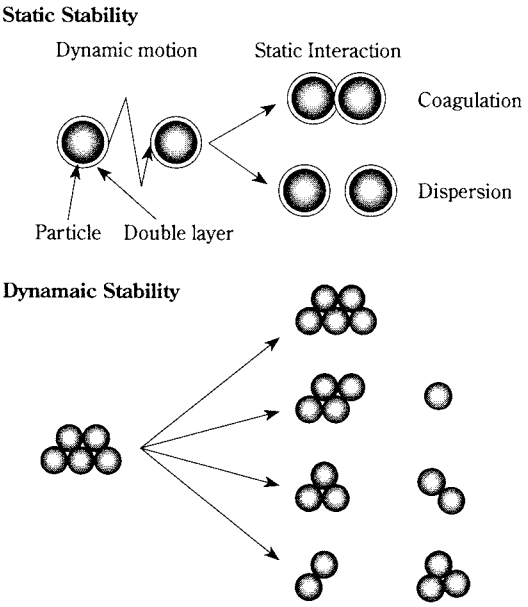

Fig. 1 Schematic drawing of the mechanism of static and dynamic stability.

[1] Yoshida, Sakyo-ku, Kyoto 606-8501 Japan
Tel. +81-75-753-5562 Fax. 81-75-753-5913
Email: higa@cheme.kyoto-u.ac.jp
[2] Shosha, Himeji 671-2201 Japan
Tel. & Fax. +81-792-67-4960
† Received: October 3, 2000

where n_p is the number concentration of particles, t is the time, C is the coagulation rate, B is the breakage rate, the subscript i stands for the i-fold particle, and superscripts b and d indicate the birth and death of aggregates, respectively. The breakage rate is usually determined such that the change of size distribution given by Eq.(1) fits experimental data. However, a few ambiguities exist in this procedure; (1) the breakage rate must be determined by subtracting the contribution of coagulation, but the coagulation rate itself is not known well when particles grow up to large aggregates of irregular shape, and (2) experiments are usually carried out in mixing vessels in which the detailed flow field is not known. It seems that more direct approach to the behavior of aggregates in flows is needed to understand fundamentally the mechanism of floc breakup, as well as the deformation and fragmentation, and to derive the breakage rate analytically.

We have been investigating the breakage of aggregates in various fields not only experimentally but also theoretically. In this review, we will overview the reliable information on floc breakage available at present, with priority given to our works. First we introduce theoretical backgrounds given by the trajectory analysis and our simulation model developed recently for the breakup in the shear and elongational flows, comparing the results with experiments reported so far. Secondly treatments for the turbulent breakage of aggregates are discussed. Thirdly experimental findings for the practically important breakage by the other fields are explained. Finally it is emphasized that the microscopic characterization of the adsorbed layer on the solid-liquid interface is important to evaluate the adhesive force between particles, which is directly related with the breakage of aggregates.

2. Breakage in Shear and Elongational Flows

The shear and elongational flows are the fundamental flows of which most complicated flows in real processes are composed. Hence the floc breakage in these flows is of fundamental importance.

As for a pair of equal spheres in slow flows, their hydrodynamic behavior is able to be evaluated rigorously by the trajectory analysis developed by Batchelor and Green [9]. This analysis was extended to evaluate the collision rate between unequal spheres by Adler [10, 11], Higashitani *et al.* [12] and Wang [13]. Then the contribution of static interactions between particles was introduced by Sonntag and Russel [14, 15] for equal spheres and by Higashitani *et al* [12] for unequal spheres. This analysis was then employed to know detailed features of doublet breakage in flows, which is briefly described below [16].

As for large aggregates of arbitrary shape, the theoretical approach seems to be extremely difficult, because of the complexity of their size, shape, strength and deformation. Adler and Milles [17] succeeded to evaluate the critical size of aggregates in a linear shear flow, but aggregates there are considered to be porous spheres which are far from real aggregates. Doi and Chen [18] simulated the motion of coagulated particles using their sticky-sphere model. In this model the hydrodynamic drag force was assumed to act on all the constitutive particles of aggregates, even though particles are not necessarily exposed to the flow. Hence this model is applicable only to small aggregates in which almost all particles are exposed directly to the fluid. Higashitani and Iimura [19] proposed a two-dimensional modified discrete element method (m-DEM) to simulate the breakup of aggregates of arbitrary shape and size, where the drag force acts only on the particle surface exposed directly to the fluid and the force propagates to the inside particles by the mechanism of DEM. Recently this model was extended to the three-dimension, and the quantitative accuracy was improved by introducing not only the effective particle surface for the hydrodynamic drag force but also the disturbance of neighboring particles on the flow field [20]. The brief explanation of this model and the comparison with experiments will be given below.

2.1 Trajectory analysis for doublets

Doublets are the simplest aggregates. Simulation of their breakup will provide the fundamental understanding for the breakup mechanism of aggregates. Here a pair of particles 1 and 2 in a flow are considered, where their radii are a_1 and a_2 respectively and $a_2/a_1(=\lambda)\leq 1$. The center of the particle 1 is taken to be the origin of coordinates and the particle 2 is positioned at $\boldsymbol{r}(r, \theta, \varphi)$, as shown in **Fig. 2**. The relative movement of the particle 2 is influenced by both the static and hydrodynamic interactions.

According to the DLVO theory [1, 2], static potentials between particles in aqueous solutions are given explicitly by the following equations. The electrostatic repulsive potential V_R between unequal spheres was derived by Hogg *et al.* [21] as follow.

$$V_R=\frac{\lambda\varepsilon a_{12}(\psi_{s1}^2+\psi_{s2}^2)}{2(1+\lambda)^2}\left[\frac{2\psi_{s1}\psi_{s2}}{\psi_{s1}^2+\psi_{s2}^2}\ln\frac{1+\exp(-\kappa a_{12}(R-2))}{1-\exp(-\kappa a_{12}(R-2))}+\ln\left[1-\exp(-2\kappa a_{12}(R-2))\right]\right] \quad (2)$$

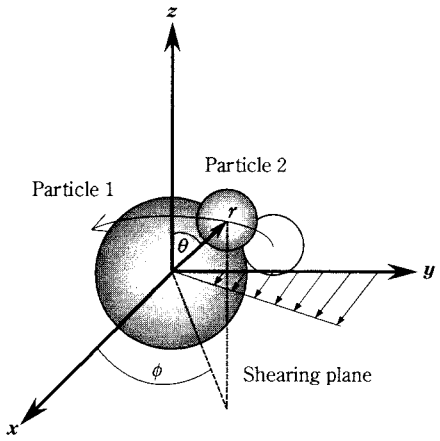

Fig. 2 Doublets in the shearing flow and coordinates.

where ε is the dielectric constant of medium, $a_{12}=(a_1+a_2)/2$, $R=|\boldsymbol{r}|/a_{12}$, and ψ_{s1} and ψ_{s2} are the surface potentials of particles 1 and 2 respectively. The reciprocal thickness of the electrical double layer, κ, given by

$$\kappa=(2n_{ion}Z^2e^2/\varepsilon kT)^{1/2} \tag{3}$$

where n_{ion} is the number concentration of ions, Z is the valency of ions, e is the elementary charge of electron, k is the Boltzmann constant and T is the temperature. The van der Waals attractive potential V_A also acts between particles, when the two surfaces are close each other.

$$V_A=-\frac{A}{6}\left[\frac{8\lambda}{(1+\lambda)^2(R^2-4)^2}+\frac{8\lambda}{(1+\lambda)^2R^2-4(1-\lambda)^2}+\ln\frac{(1+\lambda)^2(R^2-4)^2}{(1+\lambda)^2R^2-4(1-\lambda)^2}\right] \tag{4}$$

where A is the Hamaker constant which depends only on the property of the particle and medium. Another strong repulsive potential, called the Born potential V_B, acts between particles when the separation distance is less than a few Å. This repulsion is attributable to the overlap of electron clouds of atoms on surfaces. There is no general expression for this potential, but it is usually given by the following equations.

$$\begin{aligned} V_B&=\infty \quad \text{for} \quad R\leqq 2+\delta/a_{12} \\ &=0 \quad \text{for} \quad R>2+\delta/a_{12} \end{aligned} \tag{5}$$

where δ is the minimum separation which is conventionally taken to be 4Å. Then the total potential V_T is given by the sum of V_R, V_A and V_B, and the corresponding total static force $\boldsymbol{F}_T$ is given by

$$\boldsymbol{F}_T=-\frac{a_{12}dV_T}{dR}\boldsymbol{n}_r \tag{6}$$

where $\boldsymbol{n}_r$ is a unit vector defined by $\boldsymbol{r}/|\boldsymbol{r}|$.

Modifying the trajectory equation for unequal spheres by the above-mentioned static interactions, the expression for their relative movement in the flow of strain rate $\boldsymbol{E}$ and vorticity $\boldsymbol{\omega}_0$ is derived as follows.

$$\frac{d\boldsymbol{r}}{dt}=\boldsymbol{\omega}_0\times\boldsymbol{r}+\boldsymbol{E}\cdot\boldsymbol{r}-\left[\mathcal{A}\frac{\boldsymbol{rr}}{r^2}+\mathcal{B}\left(\mathbf{I}-\frac{\boldsymbol{rr}}{r^2}\right)\right]\cdot\boldsymbol{E}\cdot\boldsymbol{r}+\frac{\mathcal{C}F_T}{6\pi\mu_f a_{12}} \tag{7}$$

where $\mathbf{I}$ is the unit tensor, the coefficients $\mathcal{A}$, $\mathcal{B}$ and $\mathcal{C}$ are the dimensionless scalar functions only of R and λ given elsewhere [10, 11], and μ_f is the fluid viscosity. The rate of strain tensor $\boldsymbol{E}$ is given by $(\boldsymbol{\Gamma}+\boldsymbol{\Gamma}^T)/2$, the angular velocity $\omega_0=(1/2)\nabla\times(\boldsymbol{\Gamma}\cdot\boldsymbol{r})$. The velocity gradient tensor $\boldsymbol{\Gamma}$ is given by the following equations for the shear and elongational flows, respectively.

$$\boldsymbol{\Gamma}=\begin{bmatrix}0&\gamma_s&0\\0&0&0\\0&0&0\end{bmatrix} \tag{8}$$

$$\boldsymbol{\Gamma}=\begin{bmatrix}2\gamma_e&0&0\\0&-\gamma_e&0\\0&0&-\gamma_e\end{bmatrix} \tag{9}$$

where γ_s and γ_e are the shear and elongational rates respectively. Substituting $\boldsymbol{\Gamma}$ and $\boldsymbol{F}_T$ into Eq.(7), the trajectory equations for shear and elongational flows can be derived with the following non-dimensional parameters.

$$N_F=\frac{6\pi\mu_f a_{12}{}^3\gamma}{A} \tag{10}$$

$$N_R=\frac{\varepsilon a_{12}\psi_{s1}\psi_{s2}}{A} \tag{11}$$

N_F and N_R indicate relative intensities of the flow field and electrostatic repulsive force against the attractive force between particles respectively, where γ is either γ_s or γ_e. Solving Eq.(7) for doublets in a given flow which are initially coagulated at $R=2+\delta/a_{12}$ and $\phi=-\pi$, their relative trajectory can be determined.

It is found that trajectories in simple shear flows are able to be classified into three types as illustrated in **Fig. 3**; (a) the particle 2 rotates along a spherical orbit without detaching, (b) the particle 2 rotates along an oval-like orbit as a satellite, and (c) the particle 2 moves along an open trajectory to separate completely. This indicates that doublets belong to one of the following regions, depending on N_F and N_R: (a) the coagulation region, (b) the semi-dispersion region and (c) the dispersion region, as illustrated in **Fig. 4**. Since the boundary for N_R is essentially insensitive to the strength of flow field as shown in the figure, only the boundary for N_F is discussed below.

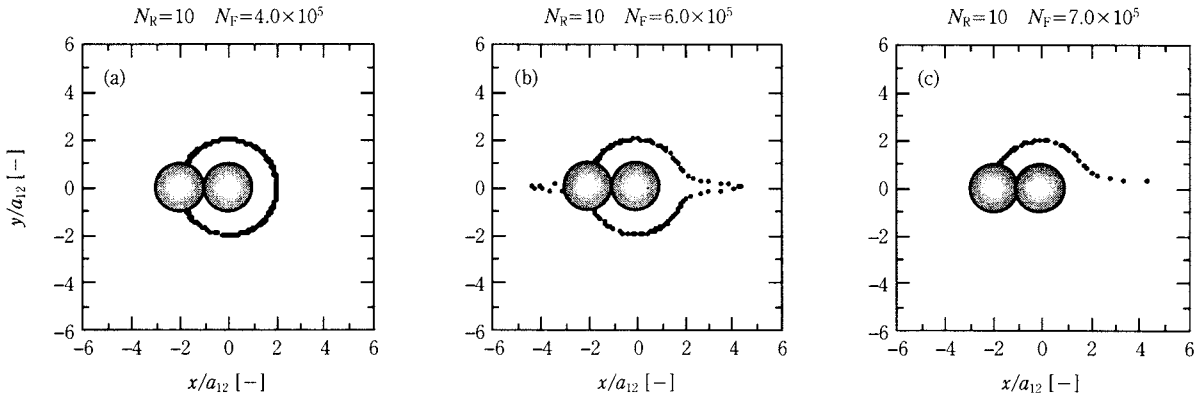

Fig. 3 Three types of relative motion of doublets in the shearing plane.

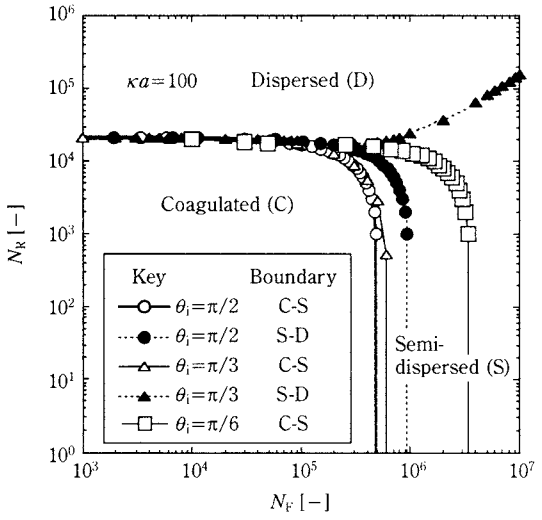

Fig. 4 Dependence of boundaries among coagulation, semi-dispersion and dispersion regions on the initial tilting angle of doublet.

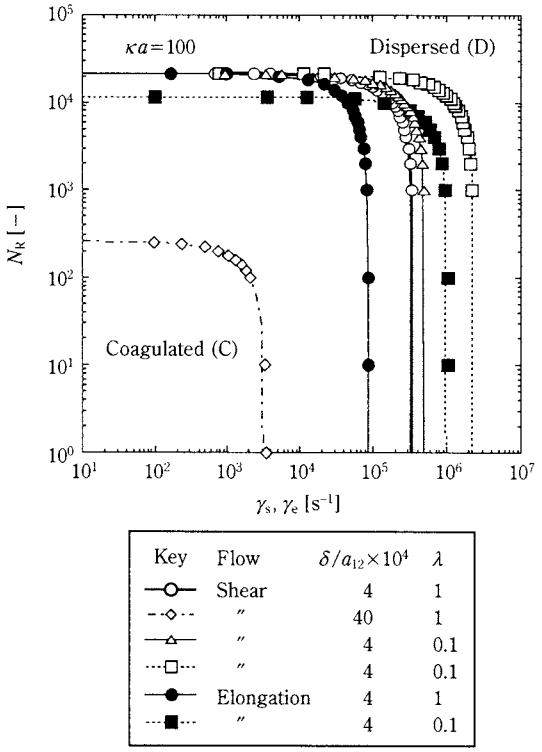

Fig. 5 Dependence of coagulation and dispersion regions on various initial conditions.

It is clear that the boundary for the semi-dispersion region depends strongly on the initial angle θ of doublets, that is θ_i. This indicates that the breakup of doublets depends sensitively on their initial angle tilting from the shearing plane of $\theta=\pi/2$. Since small disturbances always exist in real flows, particles in the semi-dispersed region will easily deviate from their orbit to an open trajectory. Hence it is plausible to assume that the boundary between coagulation and semi-dispersion regions is the practical boundary between the coagulation and dispersion. It is also clear that the boundary value of N_F becomes the smallest when $\theta=\pi/2$; doublets are most severely destroyed in the shearing plane. Hence doublets in this coagulation region can never be dispersed, while doublets outside the region may or may not be dispersed, depending on their initial conditions. In the case of uni-axial elongation flows, doublets will rotate and line up to the flowing direction before their breakage. Hence their dispersibility is not influenced by the value of θ_i and the semi-dispersion region does not exist.

Substituting various conditions into Eq.(7) for the case of $\kappa a_1=100$ and $\psi_{s1}=\psi_{s2}$, boundaries between coagulation and dispersion for doublets of unequal spheres in shear and elongation flows are calculated, where doublets are assumed to be in the shearing plane in the case of shear flow. The results are summarized in **Fig. 5**. In the case of $\lambda=1$ and $\theta_i=\pi/2$, the boundary is able to be estimated also by an analytical

equation derived by equating the adhesive force between particles with the maximum hydrodynamic dispersing force [22].

$$N_F = b[(a/\delta)^2/12 - \kappa a N_R/4] \tag{12}$$

where $b=1$ for the shear flow and $b=1/4$ for the elongation flow. This equation agrees well with boundaries shown in **Fig. 5**. These results give us the fundamental image for the behavior of aggregates in shear and elongational flows. It is especially important to know that the breakage is very sensitive to the value of the minimum separation δ, that is, the adhesive force between particles, and the tilting angle of doublets against the shearing plane θ_i.

Since the trajectory analysis is rigorous, the stability of doublets must agree with experimental results, as far as conditions assumed are experimentally satisfied. The comparison between the prediction and experiments was made extensively for equal spheres by van de Ven [23]. Doublets are sometimes used to simulate the breakup of large aggregates, assuming that their behavior are represented by that of two spheres whose size may and may not be the same, because this makes an analytical treatment possible [24, 25].

2.2 Breakage of large aggregates

Here a three-dimensional large aggregate of arbitrary shape composed of N spherical particles of radius a and density ρ_p is considered. When the aggregate is placed in a flow, the hydrodynamic drag force and torque act on the outside particles exposed directly to the flow and are propagated into the inside particles through interactions between constituent particles. This will result in the deformation and breakup of the aggregate. In the present model, the total force and torque on each particle is evaluated at time t and then the trial displacement at $t+\Delta t$ is estimated using the DEM. Repeating this procedure for all the constitutive particles, the kinetic behavior of the whole aggregate is simulated. The translational and rotational motions of a particle i in the aggregate are expressed by the following equations.

$$m\frac{d\boldsymbol{u}_{pi}}{dt} = \boldsymbol{F}_{hi} + \sum_j \boldsymbol{F}_{mij} \tag{13}$$

$$I\frac{d\boldsymbol{\omega}_{pi}}{dt} = \boldsymbol{M}_{hi} + a\sum_j \boldsymbol{F}_{mij} \times \boldsymbol{n}_{ij} \tag{14}$$

where m $(=(4/3)\pi a^3\rho_p)$ and I $(=(8/15)\pi a^5\rho_p)$ are the mass and moment of inertia of particle respectively, $\boldsymbol{u}_{pi}$ and $\boldsymbol{\omega}_{pi}$ are the velocity and angular velocity of particle i, $\boldsymbol{F}_{hi}$ and $\boldsymbol{M}_{hi}$ are the hydrodynamic drag force and torque respectively, $\boldsymbol{F}_{mij}$ is the mutual interaction force imposed on the particle i by the particle j, $\boldsymbol{n}_{ij}=\boldsymbol{r}_{ij}/r_{ij}$, $\boldsymbol{r}_{ij}=(\boldsymbol{x}_i-\boldsymbol{x}_j)$, $r_{ij}=|\boldsymbol{r}_{ij}|$, and $\boldsymbol{x}_i$ is the position vector of the center of particle i.

Because the flow field around aggregates is extremely complicated in general, it is almost impossible to evaluate the values of $\boldsymbol{F}_{hi}$ and $\boldsymbol{M}_{hi}$ rigorously. In conventional models, the drag force on the constituent particle is assumed to be given by the Stokes law for a single particle, neglecting the disturbance due to neighboring particles. This is called "free-draining approximation". In the present model, the drag force is assumed to act only on the particle surface exposed directly to the flow. This exposed area S_i, illustrated schematically in **Fig. 6**, is determined as follows. The surface of a particle is divided into 2592 sections such that the angle between the grid lines is $\pi/36$. Then a straight line is drawn to a corner of a given section from the particle center. If all the lines for four corners do not intersect with the surface of the other particles within the distance of $6a$, the section is assumed to be exposed directly to the flow. Repeating this procedure for all the sections, the exposed area S_i for particle i is determined, as illustrated as the dark sections in **Fig. 6**.

Supposing that a single particle of velocity $\boldsymbol{u}_{pi}$ and angular velocity $\boldsymbol{\omega}_{pi}$ is in an applied homogeneous flow of velocity $\boldsymbol{u}_0$ and angular velocity $\boldsymbol{\omega}_0$, the fluid

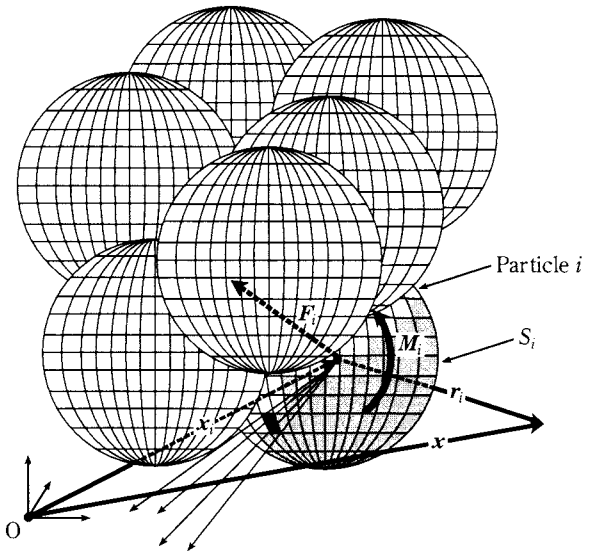

Fig. 6 Schematic drawing of the simulation model of an aggregate and the coordinate system. Dark sections on the particle i indicate sections which are regarded as exposed directly to the flow. Lines are drawn to 4 corners of each section from the particle center in order to determine whether the section is exposed to the fluid or not.

velocity $\boldsymbol{u}_f(\boldsymbol{x})$ and the corresponding pressure field $p(\boldsymbol{x})$ at an arbitrary position $\boldsymbol{x}$ around the particle is given by the following equation. [22, 26]

$$\boldsymbol{u}_f(\boldsymbol{x}) = (\boldsymbol{E}+\boldsymbol{\Omega})\cdot\boldsymbol{x} - \left(\frac{a}{r_i}\right)^5 \boldsymbol{E}\cdot\boldsymbol{r}_i - \frac{5}{2}\left(\frac{a}{r_i}\right)^3\left(1-\frac{a^2}{r_i^2}\right)\frac{\boldsymbol{r}_i\boldsymbol{r}_i\cdot\boldsymbol{E}\cdot\boldsymbol{r}_i}{r_i^2} + \left(\frac{a}{r_i}\right)^3\left(\boldsymbol{\omega}_{pi}-\boldsymbol{\omega}_0\right)\times\boldsymbol{r}_i + \frac{3a}{4r_i}\left(1+\frac{a^2}{3r_i^2}\right)\left(\boldsymbol{u}_{pi}-\boldsymbol{u}_0\right) + \frac{3a}{4r_i}\left(1-\frac{a^2}{r_i^2}\right)\frac{\boldsymbol{r}_i(\boldsymbol{u}_{pi}-\boldsymbol{u}_0)\cdot\boldsymbol{r}_i}{r_i^2} \quad (15)$$

$$p(x) = -\frac{5\mu_f a^3}{r_i^3}\frac{\boldsymbol{r}_i\cdot\boldsymbol{E}\cdot\boldsymbol{r}_i}{r_i^2} + \frac{3\mu_f a}{2r_i^3}\left(\boldsymbol{u}_{pi}-\boldsymbol{u}_0\right)\cdot\boldsymbol{r}_i \quad (16)$$

where $\boldsymbol{r}_i=\boldsymbol{x}-\boldsymbol{x}_i$, $r_i=|\boldsymbol{r}_i|$, $\boldsymbol{\Omega}$ is the vorticity tensor given by $(\boldsymbol{\Gamma}-\boldsymbol{\Gamma}^T)/2$. The velocity gradient tensor $\boldsymbol{\Gamma}$ of applied fields is given by Eqs.(8) and (9). The stress tensor $\boldsymbol{\tau}$ for a Newtonian fluid around a particle is given by

$$\boldsymbol{\tau} = -p\mathbf{I}+\mu_f\left(\nabla\boldsymbol{u}_f+\nabla\boldsymbol{u}_f^T\right) \quad (17)$$

Then the force and torque acting on the area S_i are calculated by the following equations respectively.

$$\boldsymbol{F}_{hi} = \int_{S_i}\boldsymbol{\tau}\cdot\boldsymbol{n}\big|_{r_i=a}\,dS \quad (18)$$

$$\boldsymbol{M}_{hi} = \int_{S_i}\boldsymbol{r}_i\times\boldsymbol{\tau}\cdot\boldsymbol{n}\big|_{r_i=a}\,dS \quad (19)$$

where $\boldsymbol{n}$ is the unit vector normal to the surface.

It is known that the velocity field around a particle is influenced by the neighboring particles. This effect is taken into account, as follows. The local velocity around a particle in the particle bed of porosity ε_v is given by $\varepsilon_v f(\varepsilon_v)\boldsymbol{u}_0$, where $f(\varepsilon_v)$ is a porosity function and $0\leq f(\varepsilon_v)\leq 1$. Hence we assume that the velocity $\boldsymbol{u}_0$ in Eqs.(15) and (16) may be replaced by $\varepsilon_v f(\varepsilon_v)\boldsymbol{u}_0$, using the local porosity ε_v around particles. We use the following Steinour's equation for $f(\varepsilon_v)$ [27].

$$f(\varepsilon_v) = 10^{-1.82(1-\varepsilon_v)} \quad (20)$$

The local porosity ε_v around a particle is defined as the porosity for the spherical space between the inner radius a and the outer radius $2a$.

The hydrodynamic force and torque given above will be propagated to inside particles through the inter-particle interactions. Two kinds of propagation mechanisms are considered. When particles are not contacting, they interact through the interaction forces given by the DLVO theory. Here only the van der Waals force for equal spheres given by Eq.(4) is considered for the sake of simplicity, although the electrostatic repulsive force given by Eq.(2) is able to be taken into account, if needed. On the other hand, when the particle surfaces contact or overlap each other because of the trial displacement by the DEM, a repulsive force acts because of their volume exclusion effect. The interaction due to the volume exclusion is calculated by the conventional method of DEM [28, 29].

The quantitative validity of the present model was confirmed by comparing in **Fig. 7** the dynamic shape factor Ψ_{cal} simulated by the present model with the experimental one Ψ_{exp} for well-defined rectangular aggregates composed of chromium spherical particles in the quiescent silicon oil [30]. In the comparison, two other models are introduced; 1) Model I, the so-called free-draining model, in which the hydrodynamic drag force acts on each particle as if the neighboring particles are absent, 2) Model II, in which the hydrodynamic force act only on the particle surface exposed to the flow, 3) Model III, the present model. It is clear that the hydrodynamic drag is overestimated considerably in Model I. The overestimation becomes smaller in Model II, but still the coincidence between the simulation and the experiment is not satisfactory. Values simulated by the present Model III are in a good agreement with the experimental data.

Since the proposed model is found to be quantitative enough, the model is now applied to simulate the behavior of aggregates in flows. All the aggregates I~IX employed are listed in **Table 1**, which may be classified into two kinds in terms of fractal dimension; particle-cluster (pc) aggregate of rather compact structure whose value of fractal dimension D_{fr} is 2.4, and cluster-cluster (cc) aggregate of rather loose structure whose value of D_{fr} is 1.7.

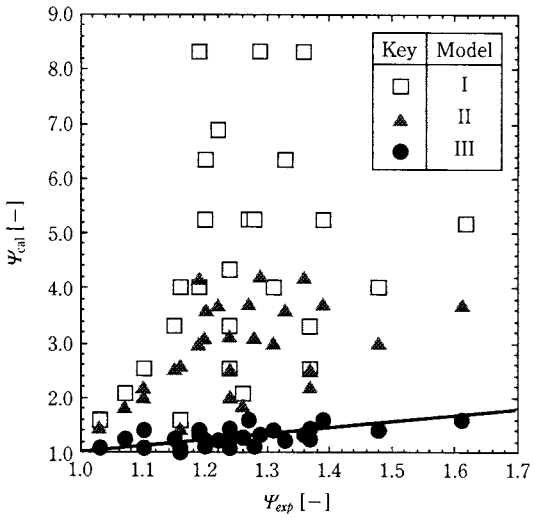

Fig. 7 Comparison of the dynamic shape factor between simulation and experiment [30].

Table 1 Parameters of aggregates employed in the simulation and estimated values of c and P.

Flow Field	Aggregate	N [−]	Type of aggregate	D_{fr} [−]	a or $a_{av}\times10^{9}$ [m]	$\delta\times10^{9}$ [m]	$c\times10^{-3}$ [−]	P [−]
Shear	I	512	pc	2.47	100	0.4	64.1	0.936
	II	256	pc	2.44	100	0.4	61.6	0.981
	III	1024	pc	2.48	100	0.4	59.1	0.875
	IV	512	pc	2.46	100	2.0	5.70	0.945
	V	512	pc	2.45	500	0.4	12.5	0.946
	VI	512	pc	2.43	500	2.0	0.850	1.04
	VII	512	cc	1.74	100	0.4	7.52	0.725
	VIII	512	pc	2.31	100 (σ_{st}=0.336)	0.4	42.1	0.881
	Exp	—	—	2.2	70	2.58	21.7	0.879
Elongation	IX	512	pc	2.47	100	0.4	111	1.60

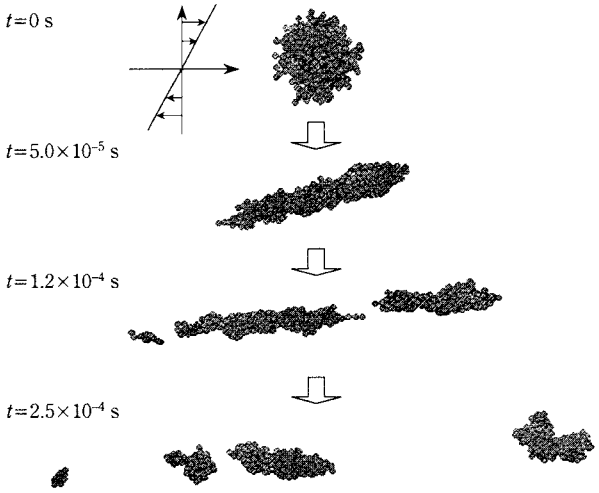

Fig. 8 Snapshots of the fragmentation of an aggregate I of in simple shear flow.

Fig. 8 shows a series of snapshots of the deformation and breakup of the pc-aggregate I composed of mono-dispersed particles in the shear flow of $\mu_f\gamma_s$= 500 Pa. It is found that the aggregate is rotated, elongated into the flow direction, and then split into smaller fragments, but not eroded one by one to single particles from the aggregate surface as in the case of the breakup by ultrasonication [31]. This splitting breakup is consistent with the photographic observation given by van de Ven [23], and also with the rupturing process of highly viscous droplets [32, 33]. Repeating the similar computation for shear flows of various intensities, the relation between the average number of particles in the final fragments $\langle i\rangle$ and the shear stress $\mu_f\gamma_s$ can be obtained. It is worth noting that a power-law relation holds between $\langle i\rangle$ and $\mu_f\gamma_s$, as follows.

$$\langle i\rangle = c(\mu_f\gamma_s)^{-P} \tag{21}$$

where values of c and P are listed in **Table 1**. It is clear that the value of P is nearly constant irrespectively of the aggregates. This implies that aggregates I~VI and VIII are fragmented essentially in the same fashion. On the other hand, the value of c varies with values of N, a, δ and the geometric standard deviation of size distribution σ_{st}. It is especially sensitive to the value of δ; the final size of fragments is very sensitive to the minimum gap between particles. This is consistent with the breakup of doublets mentioned above. It is clear that the power-law relation also holds for cc-aggregates, though the value of P is smaller than those of pc-aggregates. These results indicate that P depends mainly on D_{fr}, but not on N, a, δ and σ_{st}; the aggregates with the same D_{fr} will be broken in the similar fashion. This is consistent with the report by Yeung and Pelton [34] that the strength of aggregates does not vary with the size but with the fractal dimension.

It is examined whether the fragmentation process of aggregates may follow any scaling law or not. It is plausible to assume that the final size of fragments is determined by the balance between the adhesive force between particles and the hydrodynamic drag on particles. The ratio of the magnitudes of these forces, N_{DA}, is defined by the following equation.

$$N_{DA} = 6\pi\mu_f a^2\gamma_s \Big/ \left(\frac{Aa}{12\delta^2}\right) = \frac{72\pi\mu_f a\gamma_s\delta^2}{A} \tag{22}$$

All the data of $\langle i\rangle$ are plotted against N_{DA} in **Fig. 9**. It is important to note that almost all data for the aggregates I~VIII fall around a single line illustrated by a solid line, although the data for the pc-aggregate IV of large minimum separation and for the cc-aggregate VII of loose structure tend to deviate from the line. This line is expressed by the following equation.

$$\langle i\rangle = 27.9\times N_{DA}^{-0.872} \tag{23}$$

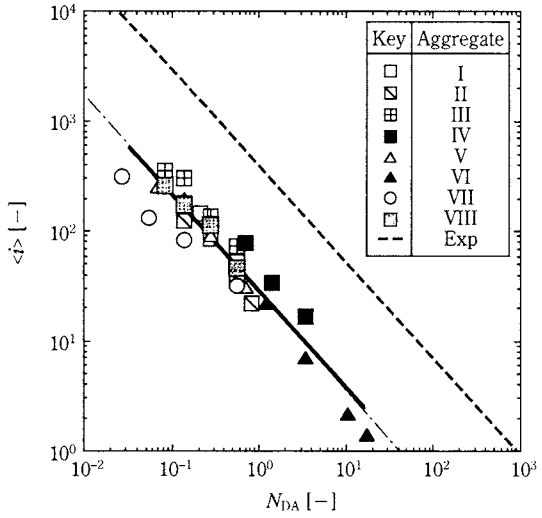

Fig. 9 Dependence of the average number of particles in a fragment on dimensionless parameter N_{DA} (Exp indicates the experimental relation given by Sonntag & Russel, the solid line indicates the best fit for simulated results, and the thin chain line indicates the experimental data for δ_{min}=0.65nm.)

This equation gives us a good tool to estimate the average size of flocs which exist stably in the shear flow, as far as the inter-particle potential is expressed by Eq.(4). According to Eq.(12), doublets should be broken at $N_{DA}=1$, but **Fig. 9** indicates that doublets exist even at $N_{DA}\sim 10$. This is because doublets which are not in the shearing plane can remain coagulated unless a higher shear field is applied.

The present simulation must be compared with quantitative experiments in which effects by re-aggregation among broken fragments are carefully avoided. Sonntag and Russel carried out experiments of the breakage of aggregates with $D_{fr}=2.2$ in the simple shear flow which are composed of mono-disperse latex particles of $a=7.0\times10^{-8}$m [14]. It is found that a power-law relation with $c=2.11\times10^{4}$ and $P=0.879$ holds between $<i>$ and $\mu_f\gamma_s$. The comparison with Eq.(23) is made by the dashed line in **Fig. 9**. We consider that the agreement between the simulation and experiments are satisfactory, because the slope is nearly the same, that is, aggregates are fragmented in the similar fashion. As for the absolute magnitude of $<i>$, the experimental value is greater. Sonntag and Russel estimated that δ is 2.58 nm, using their model. This value is much larger than the minimum surface separation widely employed, that is, 0.4 nm. But, if δ=0.65nm is assumed, their data are expressed by the thin chain line drawn in the figure and coincide extremely well with Eq.(23). We consider this value of δ is much more reasonable.

The most popular experimental approach for the aggregate breakage is to correlate the maximum diameter of aggregates d_{max} with the dissipation energy of flow ε_{dis}, as follows.

$$d_{max}\sim\gamma_s^{-2n}\sim\varepsilon_{dis}^{-n} \tag{24}$$

where n is a constant. It is reported that n=0.1 and n=0.25 for shear flows [35, 36]. The effect of re-aggregation of broken fragments is negligible in Eq.(24), because the maximum size is determined solely by the balance between the aggregate strength and the hydrodynamic dispersing force. On the other hand, the average diameter of aggregate $<d>$ will be influenced by the initial size distribution and the re-aggregation. Hence the data of $<d>$ must be carefully used in comparison. However data of $<d>$ are often expressed in the same fashion as Eq.(24), and the value of n is reported to be 0.18~0.25 in the shear flow [37]. In spite of this ambiguity, it is interesting to compare the present prediction with the experimental value. Since $<d>\propto<i>^{1/3}$, Eq.(23) predicts that $n\sim0.15$. This approximate coincidence of n value supports the validity of our simulation model.

Simulation by the present model is carried out also for elongational flows. It is found that aggregates do not rotate but are elongated to the flow direction, and then split into smaller fragments in the same manner as the shear flow. The value of $<i>$ is also expressed by Eq.(21), replacing γ_s by γ_e. Values of c and P are listed in **Table 1**. We can not find any quantitative data to compare. This is probably because the experiment for purely elongational flows is difficult. As for qualitative observation, the breakage process was observed using a four-roller device [38]. It was found that aggregates of irregular shape are split into a few fragments followed by erosion of much smaller fines, but spherical aggregates tend to be broken by erosion. The present simulation indicates that aggregates are broken by splitting, but not by erosion, which is essentially consistent with the above-mentioned observation for aggregates of irregular shape.

It is important to know which flow is more adequate to break up aggregates, shear or elongational flows. Values of $<i>$ for the aggregate I are plotted against the dissipation energy ε_{dis} in **Fig. 10** under the flow conditions which appear in usual industrial processes. The value of $<i>$ for the elongational flow is always smaller than that by the shear flow in this range. This indicates that the elongational flow is more effective and preferable to disperse coagulated particles. This result is consistent with the prediction by the trajectory analysis in **Fig. 5** and the observation by Kao and Mason [39] who claimed that the

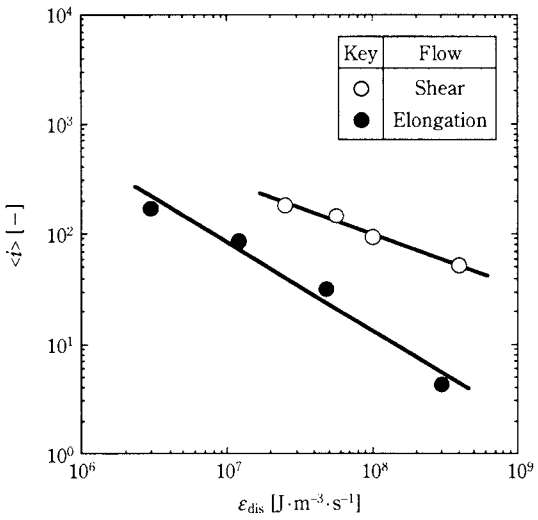

Fig. 10 Comparison between the fragment size of aggregates I in shear flow and that in elongational flow.

elongational flow is more effective for floc breakup, because the energy of flow is consumed to break up the aggregates but not to rotate them.

3. Breakage in Turbulent Flows

As for the breakage in turbulent flows, various analytical attempts have been carried out to estimate the size of broken fragments [36, 40-42]. The maximum stable size d_{max} is usually correlated with the energy dissipation of fluid ε_{dis} as follows, by equating the aggregate strength with the turbulent dispersing force.

$$d_{max} \sim K \varepsilon_{dis}^{-n} \tag{25}$$

where analytical expressions of K and n depend on the models and assumptions employed for the aggregate strength, the hydrodynamic force on aggregates in turbulence, and the breakage mechanism. The breakage mechanism is considered to depend on the relative size of aggregates to the Kolmogoroff microscale of turbulent eddies, λ_ε; aggregates are broken predominantly by the shear stress in the eddy at $d_{max} < \lambda_\varepsilon$, while they are broken by the fluctuation of pressure or tensile stress at $d_{max} > \lambda_\varepsilon$. Despite of the analytical derivation, the value of n varies greatly, that is, $n=0.25 \sim 1.0$. However, the value of $n=0.33 \sim 0.55$ reported by Tambo and Watanabe [40] and Muhle [36] seems to be the most reliable.

A large number of experiments have been performed and it is found that the power-law relation given by Eq.(25) holds. It is reported that $n=0.15 \sim 0.75$, but more often $n=0.2 \sim 0.4$ [36, 40-45]. Since experiments are usually carried out in mixing vessels, the turbulent flow is not as uniform as assumed in the derivation of Eq.(25). Nevertheless, a relatively good coincidence has been obtained.

4. Breakage by Other Fields

In practical devices to break up aggregates, very complicated fields are employed to achieve a high performance. However, important fields popularly employed may be classified into (i) the contractile flow, (ii) the rotary disk flow generated by a rotational disk and a stationary outer cylinder, and (iii) the ultrasonic field. In this section, characteristics of floc breakage by these fields are discussed and compared each other.

4.1 Breakage by orifice contractile flow

The orifice contractile flow is a converging flow into a small hole of an orifice. The fluid is contracted, accelerating abruptly just before the orifice. The flow along the centerline may be regarded as an elongational flow and the flow near the wall inside the orifice is regarded as a high shear flow. According to our experiments in which effects of re-aggregation are carefully avoided, the following features are clarified [46, 47].

(i) Most aggregates are broken in the acceleration region before the orifice and the contribution of high shear and elongational flows within and after the orifice is negligibly small.

(ii) The number of constituent particles in the maximum fragment i_{max} can be correlated with the energy dissipation of the orifice flow, ε_{dis}, independently of the orifice size and the size of constitutive particles in aggregates, as follows.

$$i_{max} \sim \varepsilon_{dis}^{-0.11} \tag{26}$$

According to the experiments by Sonntag and Russel [15], $<i> \sim Q^{-1}$, where Q is the flow rate. In the contractile flow, $\varepsilon_{dis} \sim Q^3$, so that $<i>$ is expressed as follows.

$$<i> \sim \varepsilon_{dis}^{-0.33} \tag{27}$$

Apparently further accumulation of experimental data and the detailed study by simulation are necessary to understand the breakage by the contractile flow fundamentally.

4.2 Breakage by rotary disk flow

The rotary disk flow is the flow generated by a rotary disk in a stationary cylinder, which is fundamental for commercial dispersers with rotary blades. Aggregates flow helically along the cylinder with the rotational motion by the rotor, and pass through a

high shear field in a small gap between the rotor and cylinder wall, that is, the flow is a complex flow composed of rotational, contractile and shear flows. It was found that there are two kinds of breakup mechanism [48]; (i) aggregates are broken by contractile and rotational flows at the upstream before the rotary disk, but not by the high shear flow within the gap, and (ii) aggregates are broken mainly by the shearing flow in the gap. The former mechanism is predominant when the gap between the rotor and cylinder δ_{gap} is sufficiently small, say $\delta_{gap}<2$ mm, while the latter becomes important when the gap is widely open.

In many commercial devices the gap is taken to be sufficiently small to achieve a high shear flow. The above results indicate that aggregates are broken sufficiently at the upstream by the contractile flow, before they receive a high shear in the gap, so that the thin disk is good enough to achieve a sufficient breakage.

4.3 Breakage by ultrasonic field

Ultrasonic dispersers are widely used, but there are very few systematic investigations on the floc breakage by ultrasonication. **Fig. 11** shows the dependence of i_{max} of latex aggregates in a 1M KCl solution on the frequency, the power of sonic generator W_s, the radiation time t_r and the volume of suspensions V_f, respectively [31]. It is found that all the data are expressed by single curves independently of various experimental conditions. This indicates that the degree of ultrasonic breakage is solely determined by the total sonic energy radiated to the floc solution of unit volume, $\bar{\varepsilon}_{dis}(=W_s t_r/V_f)$, as far as the size of constituent particles is the same. This is important because the degree of breakage is easily controlled by adjusting the combination of values of W_s, t_r and V_f. The dependence of i_{max} on $\bar{\varepsilon}_{dis}$ is approximately given at $\bar{\varepsilon}_{dis}<8\times10^6$ J/m^3 as follows.

$$i_{max} \sim \bar{\varepsilon}_{dis}^{-0.53} \tag{28}$$

Ultrasonication is strong enough to break up aggregates into single particles if sufficient energy is applied, but great care must be taken to the fact that sonic vibration contributes not only to the breakage of aggregates but also their coagulation.

4.4 Comparison of breakage by flow and ultrasonic fields

The comparison of size distribution of broken fragments indicates that size distributions given by contractile and rotary-disk flows are similar each other, but they differ from that given by ultrasonication. Fractions of single constituent particles and large fragments are much higher in the sonic breakage than in the breakage by fluid flows. This indicates that splitting into smaller fragments is predominant in the case of flow-induced breakage, while single particles are primarily ripped off one by one from the surface of aggregate in the case of sonic breakage, as illustrated schematically in **Fig. 12**. This difference in breakup mechanism suggests that the flow-induced breakage with the subsequent sonic breakage will be an effective procedure to break up large aggregates.

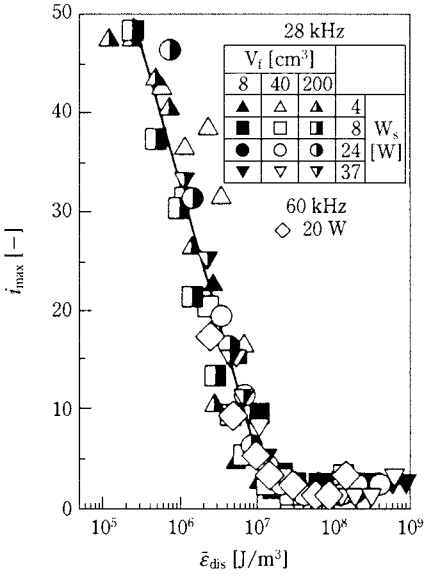

Fig. 11 Dependence of the maximum size of broken fragments on the total radiation energy.

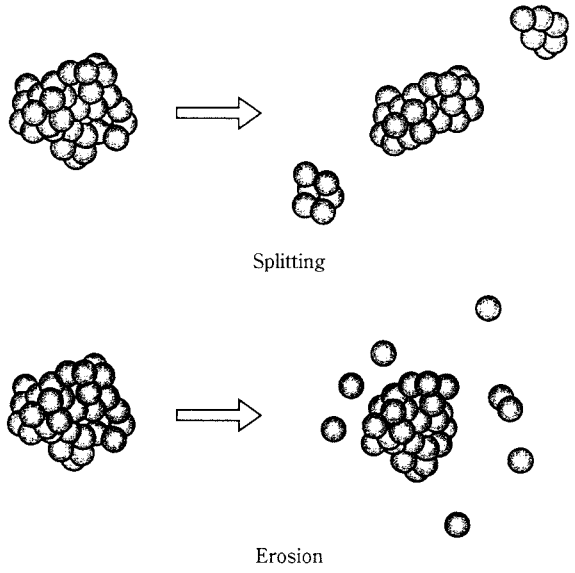

Fig. 12 Schematic drawing of breakage mechanisms; Splitting and Erosion.

5. Adhesive Force between Particles in Solutions

Finally we discuss about the adhesive force between surfaces in solutions, because the adhesive force is directly related with the breakage of aggregates. The adhesive force between particles is usually assumed to be given by the van der Waals force, without checking the adequacy. It is known that two or three layers of water molecules, ions and hydrated ions are adsorbed on the solid-liquid interface [2]. Recent measurements of adhesive forces between a plate and a particle with an atomic force microscope (AFM) indicate that the strength of adhesive force depends greatly on the microstructure of the adsorbed layer, even in such a simple solution like electrolyte solution. The characteristics are summarized as follows, and the details are given elsewhere [49, 50].

(i) The adhesive force F_{ad} depends on how much particles can break the adsorbed layer to contact directly during the contact time t_c.

(ii) The magnitude of F_{ad} depends on the hydration enthalpy of ions ΔH, as well as the electrolyte concentration C_e;. F_{ad} decreases with increasing C_e and decreasing value of ΔH. It is especially important to know that the dependence of F_{ad} on t_c varies greatly with ΔH in concentrated solutions, as shown in **Fig. 13**. This is explained as follows. Since highly hydrated cations like Li^+ form a thick but weak adsorbed layer, surfaces can contact directly to have a strong adhesion by destroying the adsorbed layer. On the other hand, because poorly hydrated cations like Cs^+ form a thin but strong adsorbed layer, the gap between surfaces at contact reduces the strength of adhesive force greatly. The mechanism is schematically drawn in **Fig. 14**.

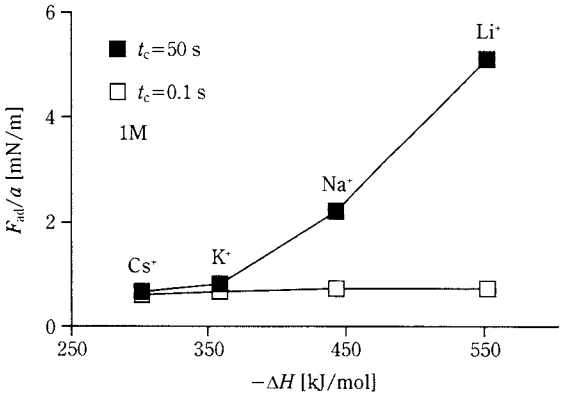

Fig. 13 Difference between the adhesive forces at t_c=0.1 and 50 s in various 1M electrolyte solutions.

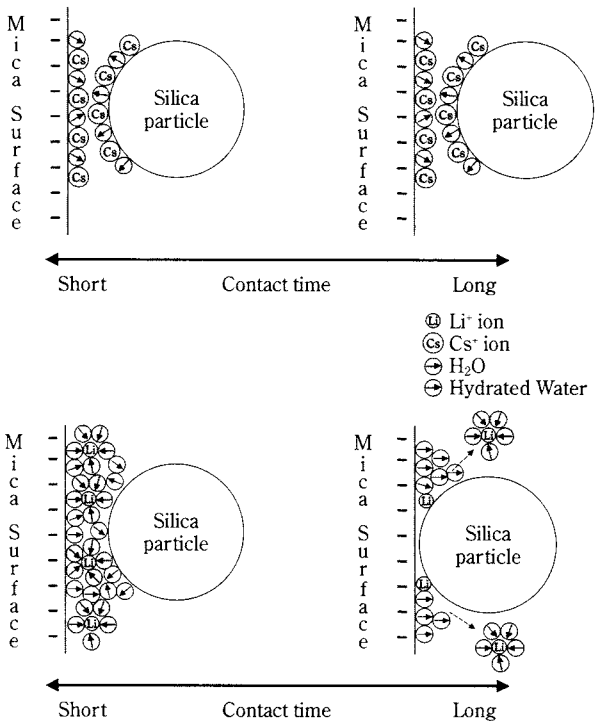

Fig. 14 Mechanism for the difference of adhesive force between cations of low and high hydration enthalpies.

6. Concluding Remarks

In this review, fundamental aspects on the breakage of aggregates in fluids are discussed from theoretical and experimental points of view, using theories and data available at present. Because of the industrial importance of dispersion and separation technologies, a large number of studies on the floc breakage have been carried out in various fields, but the coincidence between data, as well as between data and theories, is not satisfactory and the fundamental mechanism is still poorly understood, especially in turbulent breakage. This is not only because the behavior of aggregates is complicated, depending on many factors, such as their size, shape, strength and the field applied, but also because experiments have been carried out using all kinds of different experimental systems so that the data are hardly compared each other.

It seems that the floc breakage is too complicated to analyze using conventional macroscopic approaches. In order to gain more detailed information, rigorous computer simulations of aggregates in flows are deadly required. Because of recent rapid advancement of computer ability and computation method, we can expect that the hydrodynamically rigorous simulation will be possible for aggregates of arbitrary shape in the near future. At the same time, the data on the structure and strength of aggregates must be accumulated systematically to understand their characteristics from the microscopic point of view.

Nomenclature

A	: Hamaker constant	[J]
$\mathcal{A}, \mathcal{B}, \mathcal{C}$	: functions of R and λ in Eq.(7)	[−]
a	: radius of particle	[m]
a_{12}	: $(a_1+a_2)/2$	[m]
B	: breakage rate	[s^{-1}]
b	: parameter for shear and elongational flows	[−]
C	: coagulation rate	[s^{-1}]
C_e	: electrolyte concentration	[Mol]
c	: coefficient of power-law relation in Eq.(21)	[−]
D_{fr}	: fractal dimension of aggregates	[−]
d_{max}	: maximum diameter of broken aggregates	[m]
$<d>$	: average diameter of broken aggregates	[m]
e	: elementary charge of electron	[C]
$\boldsymbol{E}$	: rate of strain tensor	[s^{-1}]
$\boldsymbol{F}$	: force	[N]
F_{ad}	: adhesive force between surfaces	[N]
$\boldsymbol{F}_T$	: total force between particles	[N]
f	: porosity function of aggregates	[−]
$\mathbf{I}$	: unit tensor	[−]
I	: moment of inertia of particles	[$kg \cdot m^2$]
i_{max}	: maximum number of particles in a broken aggregate	[−]
$<i>$	: mass averaged number of particles in a broken aggregate	[−]
K	: coefficient function in Eq.(25)	
k	: Boltzmann constant	[$J \cdot K^{-1}$]
$\boldsymbol{M}$	: torque on particle	[N·m]
m	: mass of a particle	[kg]
N	: number of particles of an aggregate	[−]
N_{DA}	: ratio of hydrodynamic drag force and van der Waals force	[−]
N_F	: dimensionless intensity of flow	[−]
N_R	: dimensionless intensity of electrostatic repulsive force	[−]
n	: power of power-law relation in Eq.(24)	[−]
n_p	: number concentration of particles	[m^{-3}]
n_{ion}	: number concentration of ions	[m^{-3}]
$\boldsymbol{n}, \boldsymbol{n}_r, \boldsymbol{n}_{ij}$	: unit vector	[−]
P	: power of power-law relation in Eq.(21)	[−]
p	: static pressure	[$N \cdot m^{-2}$]
Q	: volume flow rate	[$m^3 \cdot s^{-1}$]
$\boldsymbol{r}$	: relative position vector between particles	[m]
r	: $\lvert\boldsymbol{r}\rvert$	[m]
R	: $\lvert\boldsymbol{r}\rvert/a_{12}$	[−]
S	: surface area of particle	[m^2]
T	: temperature	[K]
t	: time	[s]
t_c	: contact time between two surfaces	[s]
t_r	: radiation time of ultrasonic field	[s]
$\boldsymbol{u}_0$	: velocity of homogeneous flow field	[$m \cdot s^{-1}$]
$\boldsymbol{u}_f$	: velocity of fluid around particles	[$m \cdot s^{-1}$]
$\boldsymbol{u}_p$	: velocity of particles	[$m \cdot s^{-1}$]
V_A	: van der Waals potential	[J]
V_B	: Born repulsive potential	[J]
V_R	: electrostatic repulsive potential	[J]
V_T	: $V_A+V_R+V_B$	[J]
V_f	: volume of suspensions	[m^3]
W_s	: power of ultrasonic generator	[$J \cdot s^{-1}$]
$\boldsymbol{x}$	: position vector from origin	[m]
Z	: valency of ion	[−]

Greek

ΔH	: hydration enthalpy of ions	[J·mol]
Δt	: time step	[s]
δ	: minimum separation between particle surfaces	[m]
δ_{gap}	: gap between rotor and cylinder	[m]
ε	: dielectric constant of fluid	[$J^{-1} \cdot C^2 \cdot m^{-1}$]
ε_{dis}	: dissipation energy of flow	[$J \cdot m^{-3} \cdot s^{-1}$]
$\bar{\varepsilon}_{dis}$	: total sonic dissipation energy per unit volume	[$J \cdot m^{-3}$]
ε_v	: porosity of aggregates	[−]
ϕ	: parameter of spherical coordinate	[−]
$\boldsymbol{\Gamma}$	: velocity gradient tensor	[s^{-1}]
γ	: rate of strain	[s^{-1}]
γ_s	: shear rate	[s^{-1}]
γ_e	: elongation rate	[s^{-1}]
κ	: reciprocal thickness of the electrical double layer	[m^{-1}]
λ	: a_1/a_2	[−]
λ_ε	: Kolmogoroff microscale of turbulent eddies	[m]
μ_f	: viscosity of fluid	[−]
$\boldsymbol{\tau}$	: stress tensor	[−]
θ	: parameter of spherical coordinate	[−]
θ_i	: initial angle θ of doublets	[−]
ρ_p	: density of particles	[−]
σ_{st}	: geometric standard deviation of size distribution	[−]
Ψ_{cal}	: simulated dynamic shape factor	[−]
Ψ_{exp}	: experimental dynamic shape factor	[−]
ψ_s	: surface potential of a particle	[V]
$\boldsymbol{\Omega}$	: vorticity tensor	[s^{-1}]
$\boldsymbol{\omega}_p$	: angular velocity of particles	[s^{-1}]
$\boldsymbol{\omega}_0$	: vorticity of flows	[s^{-1}]

Subscripts

1, 2, i, j	: index of particles
ij	: index of relative relation of i to j
h	: hydrodynamic interaction between particle and fluid

m : mutual interaction between particles

Superscripts

b : birth of aggregates
d : death of aggregates

References

1) Hunter, R. J.: "*Foundations of Colloid Science, Vol. 1*," Clarendon Press, Oxford (1987).
2) Israelachvili, J. N.: "*Intermolecular and Surfaces Forces, 2nd ed.*," Academic Press, New York, 1992.
3) Ives, K. J. ed.: "*The Scientific Basis of Flocculation*," Sijthohh & Noordhoff, The Netherlands (1978).
4) Vanni, M.: "Approximate Population Balance Equations for Aggregation-Breakage Processes," *J. Colloid and Interface Sci.*, **221**, 143-160 (2000).
5) Thomas, D. G.: "Turbulent Disruption of Flocs in Small Particle Size Suspensions," *AIChE. J.*, **10**, 517-523 (1964).
6) Bowen, M. S., M. L. Brodie and R. J. Cohen: "Temporal Evolution of the Cluster Size Distribution during Brownian Coagulation," *J. Colloid and Interface Sci.*, **105**, 617-627 (1985).
7) Lu, C. F. and L. A. Spielman: "Kinetics of Floc Breakage and Aggregation in Agitated Liquid Suspensions," *J. Colloid and Interface Sci.*, **103**, 95-105 (1985).
8) Kramer, T. A. and M. M. Clark: "Incorporation of Aggregate Breakup in the Simulation of Orthokinetic Coagulation," *J. Colloid and Interface Sci.*, **216**, 116-126 (1999).
9) Batchelor, G. K. and J. T. Green: "The Hydrodynamic Interaction of Two Small Freely-moving Spheres in a Linear Flow Field," *J. Fluid Mech.*, **56**, 375-400 (1972).
10) Adler, P. M.: "Heterocoagulation in Shear Flow," *J. Colloid and Interface Sci.*, **83**, 106-115 (1981).
11) Adler, P. M.: "Interaction of Unequal Spheres. I. Hydrodynamic Interaction: Colloidal Forces," *J. Colloid and Interface Sci.*, **84**, 461-474 (1981).
12) Higashitani, K., R. Ogawa, G. Hosakawa and Y. Matsuno: "Kinetic Theory of Shear Coagulation for Particles in a Viscous Fluid," *J. Chem. Eng. Japan*, **15**, 299-304 (1982).
13) Wang, Q.: "A Study on Shear Coagulation and Heterocoagulation," *J. Colloid and Interface Sci.*, **150**, 418-427 (1992).
14) Sonntag, R. C. and W. B. Russel: "Structure and Breakup of Flocs Subjected to Fluid Stresses I. Shear Experiments," *J. Colloid and Interface Sci.*, **113**, 399-413 (1986).
15) Sonntag, R. C. and W. B. Russel: "Structure and Breakup of Flocs Subjected to Fluid Stresses III. Converging Flow," *J. Colloid and Interface Sci.*, **115**, 390-395 (1987).
16) Higashitani, K., D. Tsutsumi and K. Iimura: "Particle Behavior in Dispersion of Coagulated Particles by Shear and Elongational Flow Fields," *Proc. of China Japan Symposium on Particuology*, pp. 1-6, Beijing, China (1996).
17) Adler, P. M. and P. M. Milles: "Motion and Rupture of a Porous Sphere in a Linear Flow Field," *J. Rheol.*, **23**, 25-37 (1979).
18) Doi, M., and D. Chen: "Simulation of Aggregating Colloids in Shear Flow," *J. Chem. Phys.*, **90**, 5271-5279 (1989).
19) Higashitani, K. and K. Iimura: "Two-dimensional Simulation of the Breakup Process of Aggregates in Shear and Elongational Flows," *J. Colloid and Interface Sci.*, **204**, 320-327 (1998).
20) Higashitani, K., K. Iimura and H. Sanda: "Simulation of Deformation and Break-up of Large Aggregates in Flows of Viscous Fluids," Accepted in *Chem. Eng. Sci.*
21) Hogg, R, T. W. Healy and D. W. Fuerstenau: "Mutual Coagulation of Colloidal Dispersions," *Trans. Faraday. Soc.*, **62**, 1638-1651 (1966).
22) Russel, W. B, D. A Saville and W. R. Schowalter: "*Colloidal Dispersions*," Cambridge University Press, Cambridge (1989).
23) van de Ven, T. G. M.: "*Colloidal Hydrodynamics*," p. 532., Academic Press, London (1989).
24) Francisco, E. T., W. Russel and W. R. Schowalter: "Floc Structure and Growth Kinetics for Rapid Shear Coagulation of Polystyrene Colloids," *J. Colloid and Interface Sci.*, **142**, 554-574 (1991).
25) Yuu, S.: "Disruption Mechanism of Aggregate Aerosol Particles through an Orifice," *AIChE J.*, **29**, 191-198 (1983).
26) Dhont, J. K. G.: "*An Introduction to Dynamics of Colloids*," Elsevier, Amsterdam (1996).
27) Steinour, H. H.: "Rate of Sedimentation-Non Flocculated Suspensions of Uniform Spheres-," *I. E. C.*, **36**, 618-624 (1944).
28) Cundall, P. A. and O. D. L. Strack: "A Discrete Numerical Model for Granular Assemblies," *Geotechnique*, **29**, 47-65 (1979).
29) Soc. Powder Technol. Japan ed.: "*Funtai Simulation Nyumon*," Sangyo-Tosho, Tokyo (1998).
30) Niida, T. and S. Ohtsuka: "Dynamic Shape Factors of Regular Shaped Agglomerates and Estimation Based on Agglomerate Symmetry," *KONA*, **15**, 202-211 (1997).
31) Higashitani, K., K. Yoshida, N. Tanise and H. Murata: "Dispersion of Coagulated Colloids by Ultrasonication," *Colloids and Surf. A*, **81**, 167-175 (1993).
32) Torza, S., R. G. Cox and S. G. Mason: "Particle Motions in Sheared Suspensions," *J. Colloid and Interface Sci.*, **38**, 395-411 (1972).
33) Williams, A., J. J. M. Janssen and A. Prins: "Behaviour of Droplets in Simple Shear Flow in the Presence of a Protein Emulsifier," *Colloids and Surf. A*, **125**, 189-200 (1997).
34) Yeung, A. K. C. and R. Pelton: "Micromechanics: A New Approach to Studying the Strength and Breakup of Flocs," *J. Colloid and Interface Sci.*, **184**, 579-585 (1996).
35) Smith, D. K. W. and J. A. Kitchener: "The Strength of Aggregates Formed in Flocculation" *Chem Eng. Sci.*, **33**, 1631-1636 (1978).
36) Muhle, K.: "*Coagulation and Flocculation*," p. 355, Marcel Dekker, New York, (1993).
37) Hunter, R. J. and J. Frayne: "Flow Behavior of Coagu-

lated Colloidal Sols," *J. Colloid and Interface Sci.*, **76**, 107-115 (1980).
38) Pandya, J. D. and L. A. Spielman: "Floc Breakage in Agitated Suspension: Theory and Data Processing Strategy," *J. Colloid and Interface Sci.*, **90**, 517-531 (1982).
39) Kao, S. V. and S. G. Mason: "Dispersion of Particles by Shear," *Nature*, **253**, 619-621 (1972).
40) Tambo, N. and Y. Watanabe: "Physical Characteristics of Floc-II," *Water Res.*, **13**, 421-427 (1979).
41) Sakurai, M. and Y. Harano: "Flocculation in a Microcellulose-aluminum Sulfate Disperse System," *Int. Chem. Eng.*, **22**, 116-124 (1982).
42) Tomi, D. T. and D. F. Bagster: "The Behavior of Aggregates in Stirred Vessels," *Trans. Inst. Chem. Engr.*, **56**, Part-I, 1-8, Part-II, 9-18 (1978).
43) Francois, R. J.: "Strength of Aluminium Hydroxide Flocs," *Water Res.*, **21**, 1023-1030 (1987).
44) Leentvaar, J. and M. Rebhun: "Strength of Ferric Hydroxide Flocs," *Water Res.*, **17**, 895-902 (1983).
45) Glasgow, L. A. and X. Liu: "Response of Aggregate Structures to Hydrodynamic Stress," *AIChE J.*, **37**, 1411-1414 (1991).
46) Higashitani, K., N. Inada and T. Ochi: "Floc Breakup along Centerline of Contractile Flow to Orifice," *Colloids and Surf.*, **56**, 13-23 (1991).
47) Higashitani, K. N. Tanise, A. Yoshiba, A. Kondo and H. Murata: "Dispersion of Coagulated Particles by Contractile Flow to Orifice," *J. Chem. Eng. Japan*, **25**, 502-507 (1992).
48) Higashitani, K.: "Particle Dispersion in Liquid Sate" in *Powder Technology Handbook (K. Goto, H. Masuda, K. Higashitani, Ed.)*, p. 475, Marcel Dekker, New York (1997).
49) Vakarelski, I. U., Ishimura, K. and Higashitani, K.: "Adhesion between Silica Particle and Mica Surfaces in Water and Electrolyte Solutions," *J. Colloid Interface Sci.*, **227**, 111-118 (2000).
50) Vakarelski, I. U. and Higashitani, K.: "Dynamic Features of Short-range Interaction Force and Adhesion in Solutions," Submitted to *J. Colloid and Interface Sci.*

Author's short biography

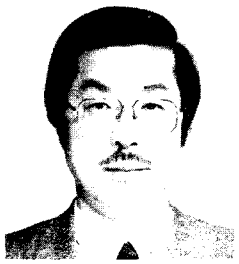

Ko Higashitani

Ko Higashitani graduated from Department of Chemical Engineering, Kyoto University, Japan in 1968. He worked on Hole Pressure Error of Viscoelastic Fluids as a Ph.D. student under the supervision of Prof. A. S. Lodge in Department of Chemical Engineering, University of Wisconsin-Madison, USA. After he received a Ph.D. degree in 1973, he moved to Department of Applied Chemistry, Kyushu Institute of Technology, Japan, as an assistant professor, and then became a full professor in 1983. He jointed Department of Chemical Engineering, Kyoto University, in 1992. His major research interests now are in the kinetic stability of colloidal particles in solutions, such as coagulation, breakup, adhesion, detachment of particles in fluids, slurry kinetics, etc. Especially he is interested in how the microstructure of particle surface is correlated with interaction forces between particles and the macroscopic behavior as particles and suspensions.

Kenji Iimura

Kenji Iimura graduated from Department of Chemical Engineering, Kyoto University, Japan, in 1995, and received a MS degree in 1997. While he is in his Ph.D. course, he moved to Himeji Institute of Technology as a research associate in 1999. His interest is the computer simulation for the behavior of coagulated particles in flow fields.

Ivan U. Vakarelski

Ivan Vakarelski graduated from Physics Department at Sofia University, Bulgaria, in 1990. Then he worked as an assistant researcher at Chemistry Department of the same University. He is currently working for a Ph.D. project in the Kyoto University, Japan. The subject of his thesis is the atomic force microscope study on the adhesion between micro-particles in solutions.

Particle Standards: Their Development and Application†

Jolyon P. Mitchell
Trudell Medical International, London, Canada

Abstract

With the increase in the importance of dispersed materials (powders, aerosols, emulsions etc.) to trade, there is an increasing awareness of the need to verify that instruments which measure particle properties, particularly size, are operating within defined limits of accuracy. As a minimum, this process requires some form of verification with reference to standard particles whose properties are known in relation ultimately to the international standards of mass and length (so-called traceability chain). In some cases, a formal calibration to establish instrument response in terms of size, shape or concentration may be required. This article reviews the particle standards that are available to establish the performance of measurement equipment, placing most emphasis on particle size, as this is the variable that is generally of most importance to industry. However, secondary properties, such as shape, density and refractive index, influence the response of many types of particle size analyzer. Attempts to provide standard materials that may enable independent assessment to be made of the effect of some of these variables on instrument performance are therefore also considered.

1. Introduction

1.1 Background

There is an increasing awareness that instruments used to measure the properties of disperse systems (powders, aerosols, particles suspended in liquid etc.) cannot by themselves provide absolute values. Quality systems, such as the ISO 9000 series [1] require that the performance of instrumentation used in the measurement of properties deemed critical to the process for which the materials under investigation are being used, be verified on a regular basis as part of a method validation process, or standard operating procedure (SOP). The intention behind this requirement is to enable measurements made on a particular product at one location to be reproducible within well-defined limits anywhere else. Standard or reference materials (RMs) that are particle-based have an important part to play in this process.

1.2 Concept of Particle Size

The definition of 3-dimensional particle size itself requires clarification before proceeding to look at particle standards. The concept of particle diameter has unambiguous physical meaning only for spherical particles. It is not possible to define a single diameter that describes the geometric size of particles that are irregular-shaped, which comprise the vast majority of cases where measurements are sought. There are many techniques that can be used to measure particle size; some are more suited to liquid-based particle systems [2] (coarse particle suspensions and colloids) and others are applicable to gas-based systems [3] (aerosols). Each technique measures a particular dimension that is dependent on the measurement principle (**Table 1**). Hawksley has postulated that there are only three fundamental diameters [4]:

- volume equivalent diameter (D_v): the diameter of a sphere having the same volume as the particle being studied
- surface equivalent diameter (D_a): the diameter of a non-porous sphere having the same surface area as the particle being studied
- drag or Stokes diameter (D_{st}): the diameter of a sphere having the same resistance to motion as the particle in question, in a fluid of the same viscosity

More recently, Scarlett [5] has presented a view that D_v is the most basic parameter to choose as the calibrating size, because it is directly proportional to the quantity of matter in the particle, regardless of shape. D_a has limited use, except in applications where surface properties (*e.g.* catalysis) are under consideration. D_{st} is not strictly a fundamental diameter, but one of a series of equivalent sphere diameters (including aerodynamic and mobility diameters) that relate to the interaction of a particle of any shape with the fluid within which it is contained. D_{st} is measured

† Received: May 16, 2000

Table 1 Particle Size Measured by Selected Analyzer Principles

Technique	Operating Principle	Weighting of Size Distribution	Remarks¶
impactors, impingers, gas- and hydro-cyclones	inertia	mass	size analysis by fractionation in several stages – measures D_{ae}
inertial spectrometers, spiral duct centrifuge	inertia	mass	size-separated particles are retained as a continuous deposit – measures D_{ae}
sedimentometers	gravity (Stokesian flow)	mass	various techniques to weigh size-separated particles – measures D_{st}
TOF analyzers	inertia (ultra-Stokesian flow)	number	TOF of individual size-separated particles measured – measures modified D_{ae}
laser (phase) Doppler systems	light scattering (phase angle)	number	Doppler 'burst' from individual particles passing through measurement zone
laser diffractometers	light scattering (Lorenz-Mie theory)	volume (mass)	'ensemble' scattering of whole particle population in measurement zone
electrical sensing zone (ESZ)	electrical resistance change	number	individual particles sized by passage through micro-orifice – measures D_v
electrical mobility analyzers	particle mobility	number	mobility of individual particles having known charge in an applied electric field
optical particle counters	angular light scattering	number	individual particles sized in terms of light scattering intensity
microscopy/image analysis	direct observation	number	individual particles sized in terms of projected area diameter (equivalent to D_v for spheres)
sieve analysis	penetration through mesh aperture	mass	fractions weighed (near-mesh technique provides link to microscopy-measured size)

¶ diameters (D_x) are defined in the text

directly by several widely used techniques that employ gravitational sedimentation as the size-separating principle, where Stokes Law applies, and:

$$U_{ts} = \frac{[\rho_b - \rho_{fl}]}{18\eta} D_{st}^2 g \qquad [1]$$

where ρ_p is the particle density and U_{ts} is the particle terminal settling velocity, ρ_b and ρ_{fl} are the particle density immersed in the fluid and fluid density respectively, η is fluid viscosity and g, acceleration due to gravity. D_v and D_{st} are related through the expression [3]:

$$D_{st} = D_v \left[\frac{\rho_p}{\chi \rho_b} \right]^{1/2} \qquad [2]$$

where χ is a correction that adjusts for the effect of 3-dimensional particle shape on sedimentation behavior (dynamic shape factor). χ is unity for spheres, and always exceeds this value for irregular-shaped particles. It may also have more than one value for certain shapes (*e.g.* spheroids), depending upon their orientation with respect to their motion in the suspending fluid [6].

Particle size analysis techniques that operate on other measurement principles measure one of several different equivalent sphere diameters (**Table 1**), each of which can ultimately be related to D_v, though not necessarily in the form of a simple relationship, such as that given by equation [2]. It follows that the response of particle size analysis equipment to irregular particles with few exceptions is modified by shape (as well as in some cases by bulk properties such as density, porosity etc.). This behavior becomes especially important when it becomes necessary to compare data from instruments that operate on different principles, a not uncommon situation. The question to be posed is 'can particle standards provide meaningful reference values to enable such comparisons to be made accurately?' The answer depends on the properties of the standards themselves, and the approach taken to verify analyzer performance (Section 1.3). Size-based standard particles are the most widely used RMs, and several options are available for their use. Reference particles which have specific non-spherical shapes (so-called 'particle shape standards' are considered separately from particles used in connection with particle sizing (Section 4.1), as their function in performance verification is fundamentally different.

1.3 Verification of Sizing Accuracy

There are two distinctly different approaches that can be taken to verify the accuracy of measurements

based on particle size, on which this article is primarily focused.

In one approach, particle standards produced from bulk powders, whose size distributions and related properties (*e.g.* density) have been corroborated by independent laboratories, are used as so-called 'certified reference materials' (CRMs). The particles may be spherical or of irregular shape, but their range of size will be chosen to encompass the measurement range of the instrument being evaluated. This process is termed performance verification. The attractiveness of this process to industry is obvious; it is usually rapid to carry out, as only a single RM is normally required for the purpose, and analyzers operating on different measurement principles can be readily compared.

Performance verification should be distinguished from instrument calibration, which is the other approach for which particle standards are widely used. The calibration process in its most generic form, involves measurement of analyzer response and associated bias conversion factor, when presented with particles having known size properties by an independent procedure that is traceable ultimately to the international standard of length. The various documented international (**Table 2**) and national (**Table 3**) standards that relate to many of the particle size analysis methods in widespread use generally call for the use of standard particles as part of the calibration or performance verification process, particularly in instances where the instrument response is not a straightforward monotonic function of particle size. Even techniques, such as laser diffractometry (low-angle laser light scattering (LALLS)), which provide volume-weighted size distribution data for spherical particles by rigorous solution of Lorenz-Mie equations [7], so that formal calibration is not strictly necessary, should ideally be validated on a regular basis with particle size-based RMs [8], or at least by the use of a suitable reticle [9]. The purpose of such measurements is as a check on the continued stability of the complete measurement system, including the software. The precise requirements for such RMs will vary from one instrument type to another. In the case of laser diffractometers, the ideal RMs should be spherical with maximum light absorption to avoid anomalous responses due to light reflection and refraction, and for examining liquid-based suspensions at least, the particle density should be close to that of the dispersion fluid [8]. Their size distribution should also be preferably uni-modal and log-normal. Röthele and Witt [8] have gone as far as to provide indicative size distributions for 3-CRMs that might be developed specifically for this class of analyzer with the following size distribution properties based on D_v:

- CRM1: range 0.1–10 μm: D^{10} 0.126 μm, D^{50} 1.00; D^{90} 7.94 μm
- CRM2: range 1.0–100 μm: D^{10} 1.26 μm, D^{50} 10 μm, D^{90} 79.4 μm
- CRM3: range 10–1000 μm: D^{10} 12.6 μm, D^{50} 100.0 μm, D^{90} 794 μm

where D^{10}, D^{50} and D^{90} are the 10^{th}, 50^{th} (median) and 90^{th} percentiles by volume (mass). Such CRMs have yet to be developed, although some of those planned by the European Community Bureau of Reference

Table 2 International Standards† Relating to Particle Size Analysis as of Jan 1, 2000

Standard	Description	Date
ISO 2591-1	Test Sieving – Part 1: Methods using test sieves of woven wire cloth and perforated metal plate	1988
ISO 3310-1	Test Sieves – Technical requirements and testing – Part 1: Test sieves of metal of metal wire cloth	1990
ISO 3310-2	Test Sieves – Technical requirements and testing – Part 2: Test sieves of metal of perforated metal plate	1999
ISO 3310-3	Test Sieves – Technical requirements and testing – Part 2: Test sieves of metal of electroformed sheets	1990
ISO 13320-1	Particle size analysis – Laser diffraction methods – Part 1: General principles	1999
ISO 13321	Particle size analysis – Photon correlation spectroscopy	1996
ISO 13317-2	Determination of particle size distribution by gravitational liquid sedimentation methods – Part 2: Fixed pipette method	in process FDIS*
ISO 13319	Particle size analysis – Electrical sensing zone method	2000
ISO 13322	Particle size analysis – Image analysis methods	in process
ISO 13762	Particle size analysis – Small angle x-ray scattering method	in process
ISO 13323	Particle size analysis – Single particle light interaction methods	in process

*FDIS=final draft international standard
†from International Standards Organization, Geneva, Switzerland

Table 3 Selected National Standards Relating to Particle Size Analysis

Standard	Description	Date
BS 3406†	Determination of particle size distribution: • Part 1: Guide to powder sampling • Part 2: Gravitational liquid sedimentation methods • Part 4: Optical microscope methods • Part 5: Electrical sensing zone method • Part 6: Centrifugal liquid sedimentation methods • Part 7: Single particle light interaction methods • Part 8: Photon correlation spectroscopy • Part 9: Filter blockage method (mesh obscuration)	 1986 1984 1993 1983 1985 1988 1997 (ISO 13321:1996) 1997
ASTM‡ F 328-98	Standard practice for determining counting and sizing accuracy of an airborne particle counter using near-monodisperse spherical particulate materials	1998
ASTM‡ F 660-83	Standard practice for comparing particle size in the use of alternative types of particle counters	1983 (rev. 1993)
ASTM‡ F 649-80	Standard practice for secondary calibration of airborne particle counter using comparison procedure	1980 (rev. 1992)
ASTM‡ F 658-87	Standard practice for defining size calibration, resolution and counting accuracy of a liquid-borne particle counter using near monodisperse spherical particulate material	1987 (rev. 1992)
JIS B 9921¶	Light scattering automatic particle counter	1989
JIS B 9925¶	Light scattering automatic particle counter for liquid	1991
DIN 66165#	Particle size analysis – Sieve analysis: General principles	1987: parts 1 and 2
DIN 66111# DIN 66115#	Particle size analysis – Sedimentation analysis: General principles – pipette method	1989 1983

† available from British Standards Institute, Milton Keynes, UK – www.bsi.org.uk
‡ available from American Society for Testing and Materials, Philadelphia, USA – www.astm.org
¶ available from Japanese Standards Association, Tokyo, Japan – www.jsa.org.jp
# available from Deutsches Institut für Normung e.V., Berlin, Germany – www.din.de

(BCR) will come close to meeting these criteria (Section 2.3).

The calibration process can be considerably more time consuming than performance verification, as it is necessary to utilize more than one RM to gauge the sensitivity of the response function to change in particle size. It is important that the properties of the RMs likely to be used for calibration purposes (particularly their shape, but also other properties that relate to the instrument response *e.g.* density in the case of techniques that measure Stokes or aerodynamic diameter) are well specified. In general, the most useful RMs for this activity will therefore be formulated from spherical, rather than irregular-shaped particles.

1.4 RM Hierarchy

It is useful to consider the hierarchy of particle size standards as having the form of an equilateral triangle (**Figure 1**), in which the international standard of length as the fundamental unit pertaining to size, forms the apex. Immediately beneath are the limited range of certified or standard reference materials (CRMs or SRMs) produced by governmental agencies, usually in partnership with industry and academia. CRMs/SRMs have been subjected to rigorous inter-laboratory evaluation by independent methods that are directly traceable to international standards, and are normally supplied with a data report in which their specification is defined. These standards are available in limited amounts and the process of certification, being labor intensive, results in their high cost. A compromise between the rigor of a formal certification process and the need for standards in appropriate quantities at reasonable cost is therefore necessary, resulting in the growth of secondary standard materials (SSMs). These calibrants are available from many sources, making them particularly useful for processes where frequent calibration is necessary or with techniques, such as sieve analysis, where rela-

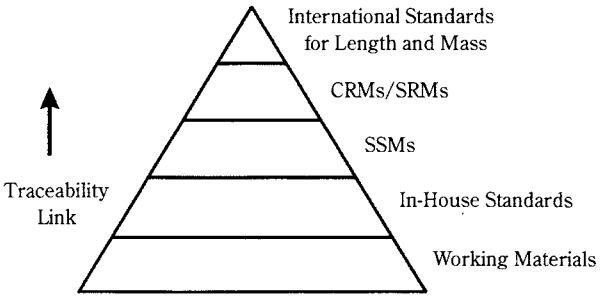

Fig. 1 Calibration hierarchy in terms of particle size standards

tively large quantities of calibrant is needed to achieve acceptable precision in the size analysis process. There is often less information available on the properties of SSMs, other than size distribution, more often than not measured by a single technique. At the lowest level in the hierarchy are so-called tertiary standards. These particles are prepared *in-situ* for calibration purposes, frequently by aerosol generation methods. The twin advantages of tertiary standards are their low relative cost (although the equipment used to create the aerosol can be expensive), and the convenience in being able to both control and vary particle size within fairly wide limits. In some cases, it may be possible to control other properties, such as shape, density and refractive index, each of which may modify the response of the equipment under calibration. Since the process is essentially local to the laboratory undertaking the calibration, inter-laboratory data are by definition unavailable. Ultimately, the traceability of the size measurements is dependent upon the calibration of size analysis equipment that is used to verify correct operation of the particle generation equipment, even in instances such as the vibrating orifice monodisperse aerosol generator (VOMAG), where the modal particle size can be predicted directly from the operating variables of the system [10] (Section 4.3).

2. CRMs/SRMs:

2.1 The Certification Process

The approach taken by the two organizations that have been responsible for almost all the particle size-based CRMs/SRMs produced to date is radically different. At the US National Institute for Standards and Technology (NIST-formerly the National Bureau of Standards), their own laboratory has been responsible for the production of ranges of SRMs with limited assistance from outside bodies. In the case of the SRMs based on uniform-sized particles (**Table 4**) [11-12, 14-17], the basic approach has been to certify by means of a so-called 'first principle' technique that is directly traceable to the international length standard, supported by one other sizing technique. Certifying techniques chosen for each of the SRMs based on uniform-sized polymer latex particles were as follows:

- optical microscopy of close-packed arrays of the larger spherical particles (SRMs having nominal D_v of 3, 10 and 30 μm) [11, 12, 14] (**Figure 2**)
- Mie angular light scattering intensity patterns, measured to size the SRM having nominal D_v of 1 μm [15]

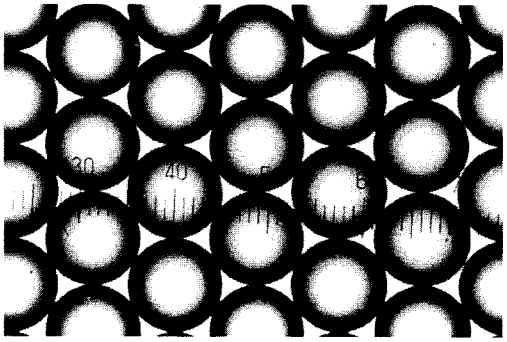

Fig. 2 Array sizing of monodisperse close-packed particles by microscopy

Table 4 Monodisperse CRMs/SRMs – Polymer (Polystyrene) Latex Particles

Code	Source	Nominal D_v (μm)	Certification Method	Reference
SRM 1961	NIST	29.64±0.06†	optical microscopy – array sizing	Hartman *et al.* [11]
SRM 1960	NIST	9.89±0.04†	optical microscopy – array sizing	Lettieri *et al.* [12]
CRM 167	BCR	9.475±0.018‡	optical microscopy – array sizing	Thom *et al.* [13]
CRM 166	BCR	4.821±0.019‡	optical microscopy – array sizing	Thom *et al.* [13]
SRM 1962	NIST	2.978±0.007†	optical microscopy – array sizing	Hartman *et al.* [14]
CRM 165	BCR	2.223±0.013‡	optical microscopy – array sizing	Thom *et al.* [13]
SRM 1690	NIST	0.895±0.008†	angular intensity light scattering	Mulholland *et al.* [15]
SRM 1691	NIST	0.269±0.007†	transmission electron microscopy	Lettieri and Hembree [16]
SRM 1693	NIST	0.101±0.002†	electrical mobility	Kinney *et al.* [17]

† based on total uncertainty (certification by single laboratory)
‡ uncertainty based on 95% confidence interval (consensus certification by several independent laboratories)

NIST SRMs are each supplied in ca. 5 cm^3 aqueous suspension at a mass concentration of about 0.5% w/v solids
BCR CRMs are each supplied in 2 cm^3 aqueous suspension: CRM 165 contains 0.02% w/v solids, CRM 166 contains 0.2% w/v solids and CRM 167 contains 1.4% w/v solids

- transmission electron microscopy, to size the SRM having nominal D_v of 0.3 μm [16] – difficulties associated with the establishment of an accurate edge defining each particle boundary and distortion at the image periphery were overcome by including 1 μm diameter spheres from the previously calibrated SRM
- electrical mobility of particles having a known charge to size the SRM having nominal D_v of 0.1 μm [17].

In addition to the certifying techniques, quasi-elastic light scattering (QELS), in which the decay of coherence of the scattered light from the particles suspended in water, was used as the second method with the SRM having a nominal D_v of 0.3 μm. Resonance light scattering, in which sharp Mie resonances were observed in the plots of scattered light intensity versus size, was used with the SRM having nominal D_v of 10 μm. Metrology electron microscopy was utilized to size the SRMs having nominal D_v of 3, 10 and 30 μm). In this secondary technique, the focused beam of a scanning electron microscope (SEM) was held stationary whist a single sphere (or row of spheres) was moved beneath the beam by means of a scanning stage. An interferometer was used to measure stage travel, whilst the SEM indicated where the leading and trailing edge of each particle passed by the beam.

The size distribution data provided for these SRMs, accurate though they are, represent the outcome of each certifying method, but are limited to measurements made within the laboratories at that single organization. In contrast, the certification process undertaken at the BCR has been by consensus measurements between several independent laboratories, also using techniques directly traceable to the international length standard. The BCR has no internal laboratory, but operates by contracts with outside organizations, almost always, but not necessarily within the European Union. The procedure is no less rigorous than that utilized by NIST, in that the certifying procedure (undertaken at each participating laboratory) is a 'first principle' method. However, there is added strength to the process by requiring corroboration of results from independent sources before certification takes place. In the case of the three sizes of uniform CRMs produced to date (**Table 4**), the certifying method has been optical microscopy of close-packed particle arrays, similar to that used by NIST with their larger sized SRMs [13]. Supporting measurements of these CRMs were also made by an individual participating laboratory using the electrical sensing zone (ESZ) method (to estimate the dispersion of particle size about the modal value – distribution skewness and kurtosis), and also by TEM (3-participants).

Similar considerations apply with the range of polydisperse CRMs also certified by the BCR (**Table 5**) [18-19] each based on a bulk sample of powder derived from materials in common use (*e.g.* quartz sand, gravel). However, the certifying techniques had to be quite different from those employed with the uniform-sized CRMs. Array sizing by optical microscopy would not work, since the particles were irregular in shape as well as varying substantially in size. Alternative methods were therefore chosen (gravitational sedimentation in liquid suspension under Stokesian flow conditions for the CRMs containing particles with D_v finer than ca. 100 μm and sieve analysis for those comprising larger particles). The certified size was therefore an equivalent sphere (Stokes) diameter (D_{st}) in cases where sedimentation in a liquid suspension was used. In the instances where sieve analysis was the certifying technique, the near-mesh procedure, in which particles held firmly in the sieve mesh are brushed out for microscopy-based size analysis, was used to establish D_v for particles close in size to the mean aperture size of each sieve. The link between D_{st} and D_v is relatively straightforward [equation 2], although the immersed particle density (ρ_b) had to be determined as accurately as possible in the dispersant medium (0.1% w/v sodium pyrophosphate in aqueous solution [19]).

2.2 Spherical or Irregular-Shaped Particles for SRMs/CRMs

Two equally valid, but distinctly different options exist when utilizing SRMs/CRMs to evaluate equipment in terms of particle size, and these options apply equally to other RMs.

In one approach that is becoming increasingly popular, standard particles that are spherical and have well-defined density as well as other relevant properties, such as refractive index, may be used. In the case of CRMs/SRMs of this type, the particles have been processed to control the primary properties of concern with the intention of being primarily used as calibrants. The CRMs/SRMs that have been prepared from polymer latex sources (**Table 4**), as well as being highly uniform in size (monodisperse), have well-defined, though not certified particle density (1.05×10^3 kg/m^3 for polystyrene) and refractive index ($m=1.59+0i$ (polystyrene)). However, they are relatively expensive and are available only in small quantities, and in limited sizes (Section 1.4).

Table 5 Polydisperse CRMs/SRMs

Code	Source	Nominal Range Based on D_v (μm)	Size Property	Material	Density¶ ($kg/m^3 \times 10^3$)	Mass per Unit (g)	Reference
CRM 132	BCR	1400 – 5000	D_v	quartz gravel†	–	700	BCR [18]
CRM 131	BCR	480 – 1800	D_v	quartz sand†	–	450	BCR [18]
CRM 130	BCR	50 – 220	D_v	quartz sand†	–	200	BCR [18]
CRM 068	BCR	160 – 630	D_v	quartz sand†	2.647	100	Wilson *et al.* [19]
CRM 069	BCR	14 – 90	D_{st}	quartz sand†	2.645	10	Wilson *et al.* [19]
CRM 067	BCR	2.4 – 32.0	D_{st}	quartz powder†	2.646	10	Wilson *et al.* [19]
CRM 070	BCR	1.2 – 20	D_{st}	quartz powder†	2.642	10	Wilson *et al.* [19]
CRM 066	BCR	0.35 – 3.50	D_{st}	quartz powder†	2.619	10	Wilson *et al.* [19]
SRM 1019b	NIST	750 – 2450	D_v	glass beads	–	200	http://oip.nist.gov/srmcatalog/tables/
SRM 1018b	NIST	220 – 750	D_v	glass beads	–	87	http://oip.nist.gov/srmcatalog/tables/
SRM 1017b	NIST	100 – 400	D_v	glass beads	–	70	http://oip.nist.gov/srmcatalog/tables/
SRM 1004a	NIST	40 – 170	D_v	glass beads	2.45	70	http://oip.nist.gov/srmcatalog/tables/
SRM 1003b	NIST	6 – 60	D_v	glass beads	2.445	25	http://oip.nist.gov/srmcatalog/tables/

D_v = volume equivalent diameter
D_{st} = Stokes diameter
† irregular shaped particles
¶ density values are uncertified – provided to relate D_v to D_{st} through equation [2] with $\chi = 1.00$

RMs may also be used to relate measurements as part of performance verification to check the collective reliability of procedure, operator and instrument (arguably the true purpose of a so-called 'reference material' [20]), rather than as calibrants *per se*. The 8-polydisperse CRMs from the BCR (Section 2.1) are available in several overlapping size ranges, in many cases encompassing about half an order of magnitude in size per CRM, and are supplied in amounts varying from 10 g (CRMs 66, 67, 69 and 70) to as much as 700 g (CRM 132). Although ρ_b for many of these CRMs was established by pyknometry, the individual particles are irregular in shape, and their optical properties are ill-defined. The four SRMs from NIST in this category all comprise spherical glass microspheres, having relatively narrow but still polydisperse unimodal size distributions.

The use of spherical SRMs/CRMs as particle standards implies that the theoretical behavior of a sphere of the material in question is known, and that for the purpose of instrument calibration a check is being made between the presumed behavior and the actual response of the equipment on test. It follows that if a particular instrument has been calibrated using spherical particles, any irregular particle that gives the same response as a spherical particle with that instrument, is presumed to have the same equivalent size (equivalent sphere diameter (Section 1.2)). Scarlett *et al.* have argued that in cases where the response of a particular instrument (*e.g.* one that operates by the ESZ principle) is proportional to the volume of each particle entering the measurement zone, calibration with spheres of known volume is no different in principle to calibration with irregular particles of known volume [20]. However, in instances where the relationship between the response function of the instrument and size is complex (especially with techniques such as laser diffractometry, that involve some form of deconvolution), true calibration may only be achievable with irregular-shaped RMs in fact, the particles which are themselves to be measured. To judge from experience where systematic comparisons of the performance of laser diffractometers from different manufacturers have been carried out using polydisperse BCR CRMs, the process still leaves much to be desired, with deviations as large as ±70% in reported size compared with certified size ob-served in some instances, albeit with excellent reproducibility [21-23]. It is interesting to note that in one study, significant deviations were also observed

with methods based on sedimentation/centrifugation of particles in liquid suspension, attributed to a variety of causes, including software error and dilution corrections [22]. The variability between techniques of similar principle has been attributed to a combination of the following factors [23]:

- poor sampling (from the 10 g bottles of powder supplied by the BCR)
- inadequate dispersion (both with surfactant and by ultrasonic methods)
- non-prescriptive analytical procedures, including statistical interpretation of data
- in the case of laser diffractometers, differences in interpretation of light scattering from the angular quartz particles (including ill-defined and variable refractive index)

The development of SOPs that describe good sample handling and analytical practices would alleviate the impact of the first three factors, but the fourth factor reflects a more fundamental limitation in the CRMs themselves.

2.3 The Planned Certification of Spherical, Polydisperse CRMs

Studies of the sort already described [19-21] illustrate that the performance verification of many types of particle size analyzers with polydisperse, irregular shaped particles is a valid procedure, notwithstanding SOP-related issues that are best defined in written procedures, such as those already published and in development through ISO (**Table 2**). However, it is increasingly recognized that it is important that the RM be homogeneous, not simply in terms of certified size distribution, but also that different samples have equivalent secondary properties within the range of particle size that is present. Such homogeneity is, in fact, essential if acceptable agreement is to be achieved, even between instruments operating on the same principle. Furthermore, it should be possible to reconcile measurements by instruments that operate on different principles on the basis of the equivalent sphere diameter, once RMs having consistent properties have been created. In response to these demands, the BCR since the late 1980s, has been pursuing the development of a new range of CRMs comprising polydisperse, spherical particles having both homogeneous and well-defined secondary properties. However, it can be argued that current demand cannot be met with the quantities of powder that were originally envisaged even if certification of these CRMs eventually takes place.

The original specification was to provide a series of CRMs, each comprising a narrow width, uni-modal and near log-normal size distribution occupying an order of magnitude in size [24]. The overall size range between 0.1 and 650 μm volume equivalent diameter was to have been encompassed by these CRMs having overlapping size ranges. On a volume (mass) weighted basis, between 5% and 95% of the spherical particles in each CRM would be within the upper and lower nominal size boundaries and the modal size would be well-defined. Most size fractions were to be produced with a uniform, measured refractive index, having the following appearances: (a) transparent – non absorbing, (b) colored – absorbing.

The development of the CRMs based on sub-micron particles were, to the author's best knowledge, not pursued beyond the initial materials sourcing stage. However, the need for these CRMs could be even more urgent now than in the early 1990s, as many techniques are being developed or extended in capability to size sub-micron particles without the necessary means to verify performance satisfactorily.

The International Fine Particle Research Institute (IFPRI) was responsible for coordinating the production of the bulk powders to manufacture the 8-CRMs comprising particles larger than 1 μm, and these materials (**Table 6**) were delivered to the BCR by the mid 1990s. They are currently sub-divided and awaiting certification by traceable techniques in accordance with the principles defined by the BCR [25]. The technical document supporting the current Call for Proposals defines the following methodology for

Table 6 Planned BCR Polydisperse, Spherical CRMs

Nominal Size Range Based on D_v (μm)	Appearance	Material
1 – 10	transparent, colorless	barium titanate glass
1 – 10	opaque, light absorbing	glassy carbon
3 – 30	transparent, colorless	barium titanate glass
3 – 30	opaque, light absorbing	glassy carbon
10 – 100	transparent, colorless	barium titanate glass
10 – 100	opaque, light absorbing	glassy carbon
150 – 650	transparent, colorless	barium titanate glass
150 – 650	opaque, light absorbing	glassy carbon

Materials supplied by the International Fine Particle Research Institute (IFPRI)

consensus certification [26]:

- 100−100 μm and 150−650 μm: sieve analysis (near mesh technique)
- 3−30 μm, 10−100 μm and 150−650 μm: optical microscopy
- 1−10 μm, 3−30 μm and 10−100 μm: gravitational sedimentation (in liquid suspension)
- 1−10 μm; 3−30 μm and 10−100 μm: ESZ analysis
- density measurements by helium or water pyknometry

In addition, each CRM is required to be characterized by non-directly traceable size analysis procedures (laser diffractometry and sedimentation methods not involving direct gravimetric assay). Finally, additional properties of importance (refractive index, porosity (if significant) and surface area (BET-method) as well as stability of the particle size distribution are to be established with their tolerances wherever possible.

It is encouraging to note that, in a study in preparation for the main certification program, inter-laboratory agreement by each of the certifying techniques proposed for the new CRMs was within ±20% of the consensus mean between 10 and 90% of each number- or volume (mass)-weighted size distribution [27]. Several RMs based on glass particles that 'mirrored' the size distributions of the proposed CRMs were sized by several independent laboratories. Great care was taken to ensure homogeneity of important particle properties (*e.g.* sphericity, density and refractive index) during manufacture of the bulk powder. Furthermore, the size distribution of the sub-divided samples of 'mirror' standards from the bulk powder sources was accomplished in the minimum number of operations by custom-made spinning rifflers. It is understood that similar rigor has been applied to the CRMs themselves.

The addition of methods to characterize the proposed CRMs with widely used techniques to the certification methods will add to their value as tools for comparing analyzers of different kinds, as a significant database will be available that is directly applicable to instrumentation in actual laboratory use. However, caution will still required in the interpretation of data from these materials. For instance, Scarlett *et al.* have observed that in cases where proprietary deconvolution techniques are used to transform measured data into a size distribution (*e.g.* laser diffractometry), compatibility between instruments operating on the same principle may not be achievable even with spherical CRMs [20]. Access to proprietary software is a commercially sensitive issue, and until international agreement can be achieved on standards for such software, each basic instrument and its attendant software must be separately specified and tested, regardless of the type of size-based CRM that is being used.

3. Monodisperse or Polydisperse Standards

A useful distinction can be made between particle standards in which the size distribution, which is almost always unimodal, is either uniform (monodisperse) or comprises a significant range of particle sizes (polydisperse). If, as a first approximation, the size distribution is represented as a log-normal function, the degree of dispersity is given by the geometric standard deviation (σ_g). A perfectly monodisperse standard would have σ_g of unity. However, a practical and widely accepted definition of monodispersity is given by $\sigma_g < 1.2$ [28]. Many CRMs/SRMs are monodisperse by this definition (**Table 4**). In addition, there are several sources of manufactured SSMs (**Table 7**), as well as a number of aerosol-based methods that can be readily implemented in the laboratory to custom-produce monodisperse particles for routine work (**Table 8**) [29-35].

Regardless of the choice or availability of spherical or irregular-shaped RMs, the decision whether to calibrate or verify particle size analyzer performance using monodisperse or polydisperse standards depends on the nature of the measurement technique. Polydisperse RMs are effective where time is of the essence, especially in instances where performance verification is all that is required. However, the presentation of the sample to the analyzer is of critical importance, if size-related bias is to be avoided. Precautions are therefore required in sample preparation [2] (especially if a sub-sample is being extracted from the bulk RM for the test), as well as in how the RM is introduced to the measurement zone of the analyzer. The latter is particularly an issue with the calibration of equipment in which a sample of the particle stream is measured, where consideration must be given to both inlet sampling bias and size-related internal losses between inlet and measurement zone [2, 3, 36]. For these reasons, the use of monodisperse particle standards has become widespread, despite the limited availability of particle sizes, at least for CRMs/SRMs. In most cases, SSMs (**Table 7**) or custom-made calibrants (**Table 8**) are satisfactory alternatives for routine calibration activities.

Certain techniques, most notably laser diffraction, provide size measurements of the whole population of particles simultaneously in the measurement zone

Table 7 Selected Sources of Secondary Standard Materials (SSMs)

SSM Type	Indicative Size Range Available (μm)	Dispersity	Source
soda-lime glass (monosphere)	20 – 200	monodisperse	Whitehouse Scientific, Waverton, Cheshire, UK www.whitehousescientific.com
soda-lime glass intermediate/broad/wide ranges	1 – 5000	polydisperse	Whitehouse Scientific, Waverton, Cheshire, UK www.whitehousescientific.com
polymer latex/silica/glass	0.020 – 1000	monodisperse†	Duke Scientific Corp., Palo Alto, CA, USA www.dukescientific.com
polymer latex (particle counter SSMs)	0.1 (10^9/ml) – 80 (3×10^4/ml)	monodisperse	Duke Scientific Cotp., Palo Alto, CA, USA www.dukescientific.com
polymer latex	0.05 – 10	monodisperse	Polysciences Inc., Warrington, PA, USA www.polysciences.com
polymer latex/silica	0.1 – 100	monodisperse/ polydisperse	Bangs Laboratories, Indianapolis, IN, USA www.bangslabs.com
polymer latex	0.038 – 91	monodisperse†	Seradyn Inc., Indianapolis, IN, USA www.seradyn.com
polymer latex (premium grade)	0.5 – 25	monodisperse	Dyno Particles a/s, Lillestrøm, Norway www.dyno.no
polymer latex	0.042 – 3.1	monodisperse	Japan Synthetic Rubber Co., Tokyo, Japan www.jsr.co.jp
polymer latex (surfactant-free)	0.014 – 6.0	monodisperse	Interfacial Dynamics Corp., Portland, OR, USA www.teleport.com

† larger sizes (D_v > ca. 50 μm) are more polydisperse

Table 8 Production of Custom Monodisperse Standard Particles by Aerosol Generation Procedures†

Method	Size Range (μm)	Materials	References
liquid atomization – vibrating orifice	1 – 50	soluble species	Berglund and Liu [10] Vanderpool *et al.* [29]
liquid atomization – spinning top/disk	2 – 50	soluble species	Walton and Prewett [30] Cheah and Davies [31]
heterogeneous vapor condensation	0.1 – 10	low-volatile substances	Sinclair and LaMer [32] Prodi [33]
electrostatic classification (EC)	0.01 – 1.0	soluble species (nebulization as dilute aerosol prior to EC)	Liu and Pui [34]

† A detailed appraisal of all methods has been given by Mitchell [35]

(so-called ensemble light scattering (**Table 1**). The performance of these instruments is most conveniently validated when a range of different particle sizes is present at the same instant, so that the use of polydisperse standards (with appropriate precautions to ensure representative delivery to the measurement zone) is more appropriate. Ideally, the size distributions of such standards should each be unimodal, and well-defined by at least one independently traceable technique between 10% and 90% of the number or mass of particulate contained in the standard. The standards should also be available in quantities appropriate for repeated use with the technique being validated. Polydisperse glass microspheres, such as the so-called 'broad-range' RMs supplied by Whitehouse Scientific Ltd. (**Table 7**), most of which were developed to mirror the size distribution properties of the proposed spherical, polydisperse BCR CRMs (Section 2.3), meet this specification.

4. Other Issues Involving Reference Particles:

4.1 Density- and Shape-Related Standards

For many techniques, calibration or performance verification with existing RMs is adequate, since the size parameter that is measured can be related to a certified diameter (D_v or D_{st}) rigorously (Section 1.2). However, for certain techniques, it may be necessary to assess performance, using particles of well-defined shape as well as size. One particular example of importance in the field of aerosol measurement serves to illustrate the rationale for density- and shape-related

standards. There are a large number of aerosol particle size analyzers (impactors, centrifuges, inertial spectrometers etc. (**Table 1**)) that measure particle aerodynamic diameter (D_{ae}) on the basis of some form of inertial separation process. The underlying assumption is that particle motion takes place under Stokesian motion (creeping flow), where the particle Reynolds number (Re_p) is less than 1.0 [3]. In this aerodynamic regime, D_{ae} is related directly to D_v, by analogy with equation [2]:

$$D_{ae} = D_v \left[\frac{\rho_p}{\chi \rho_0} \right]^{1/2} \left[\frac{C(D_v)}{C(D_{ae})} \right]^{1/2} \quad [3]$$

where ρ_p and ρ_0 are the particle density and reference density (of water) respectively, and the terms $C(D_v)$ and $C(D_{ae})$ are the Cunningham slip correction factors which become significant with sub-micron sized particles. χ is the particle dynamic shape factor, already discussed briefly in Section 1.2. When comparing aerodynamic particle size analysis equipment, the assumption is made that the techniques operate in similar regime of Re_p. However, this assumption may not always be valid, for instance, when making comparisons of traditional equipment with the group of analyzers that determine particle size scaled in terms of D_{ae} by time-of-flight between well-defined locations (TOF-aerodynamic particle size analyzers (**Table 1**)). In these instruments, Re_p is significantly greater than 1 throughout their operating range, and particle motion is therefore in the ultra-Stokesian (unsteady motion) regime. A full definition of the modified D_{ae} measured by these systems would require equation [2] to include the added mass and Basset 'history' terms that are beyond the scope of this article to define, but are attempts to describe the complex interactions between the particles and the surrounding fluid during the measurement process [37-38]. These terms require assumptions to be made that effectively void the directly traceable link between D_{ae} and D_v. The overall effect is that when the size parameter measured by such instruments is scaled in terms of D_{ae}, they exhibit significant bias associated with both particle density [39] and shape [40-41] when compared with measurements made by more traditional methods. RMs with well-defined density, shape and size are therefore ideally required to determine the bias between modified D_{ae} and true D_{ae}.

The development of particle size standards specifically to address variation in particle density has so far not been formalized into programs from which SRMs/CRMs have emerged. Instead, researchers have preferred to test the performance of equipment with monodisperse, spherical particles of known density [39-41], often assuming bulk density values for the particles from the literature and in more rigorous studies, determining density by helium or water pyknometry if sufficient mass of calibrant is available.

The situation in connection with particle shape standards until recently was similar, and the formal process of developing SRMs/CRMs has been slow to get off the ground. Part of the problem is the complexity of defining the term 'shape'. Again, taking the case of analyzers that operate on the basis of particle motion in a fluid, the dynamic shape factor (χ) appears to provide a common link to D_v in the case of instruments whose operating principle can be related to D_{st} or D_{ae} through the application of Stokes Law (see equations [2] and [3]). However, χ varies with orientation with respect to particle motion for non-spherical particles having simple geometry, such as spheroids [6]), resulting in ambiguity in the relationship between D_v and D_{st} or D_{ae} [38]. The same is true for particles of more extreme geometries (*e.g.* disks, elongated fibers, plates having large aspect ratio with respect to their thickness or chain and branched agglomerates) in the flow. In some cases the exact value of χ in the measurement zone of the analyzer being evaluated may be undefined. Under these circumstances, the concept of a shape-standard SRM/CRM with a single certified value of χ may not be meaningful. The use of cluster agglomerates containing small numbers of monodisperse, micron-sized spherical polymer latex particles which have well-defined values of $\chi_{agglomerate}$ in different orientations (**Table 9**) has hitherto been the nearest to standardization for establishing the behavior of agglomerated particles in particle size analyzers of this type [41-42]. Although attempts have been made to define shape factors for these agglomerates that are properly descriptive under other measurement principles (*e.g.* light scattering [43]), this process is fraught with difficulty.

Despite the issues that have already been outlined, several individual groups have produced their own SSMs for particular purposes, mainly based on com-

Table 9 Values of $\chi_{agglomerate}$ for Clusters of Monodisperse Spherical Particles ($\chi_{singlet}=1.00$), Based on Cheng *et al.* [40]

Number of Singlets in Agglomerate	Agglomerate Configuration	$\chi_{agglomerate}$ (long axis perpendicular to flow)	$\chi_{agglomerate}$ (long axis parallel to flow)
2	doublet	1.142	1.022
3	triplet	1.18	1.08
4	tetrahedron	1.12	1.12

pact-shaped geometry. One important route to the development of these standards has been the controlled crystal growth by forced hydrolysis of simple inorganic species in accordance with procedures developed by Matijevic and co-workers (**Table 10**) [44]. This has resulted in the development of several potential SSMs having a variety of well-defined shapes, such as cubes, rods, needles and ellipsoids [45-47]. In many cases, rigorous control of particle shape to the point at which χ can be evaluated, let alone determined as a function of particle orientation, has proved elusive. However, in at least one case it has been possible to grow monodisperse octahedral-shaped particles with D_v from 2 to 20 μm, whilst maintaining χ in the range 1.19±0.06, by altering the reaction time during which particles of sodium-ferric sulfate (natrojarosite – $NaFe_3(SO_4)_2(OH)_6$) are formed. In this case, values of χ were reported assuming orientation independence due to similarity in profile from all directions [46].

Strategies for producing SSMs based on fibers of known aspect ratio have involved a fiber extrusion process [47] and micromachining of silicon by a process widely used to mass-produce microelectronic components [48-49] (**Figure 3**). The latter process can be controlled with great precision and can be used to form a variety of particle shapes, in particular rod-like structures of variable 2-dimensional profile (aspect ratio) varying from 1 μm×1 μm (square profile) to more than 30 μm×1 μm. The chosen profile (rod or disk) is replicated millions of times by means of a mask that is used in the fabrication of the silicon dioxide particles by photolithographic etching. The etching process rounds the corners as well as slightly undercutting the profile. As a result of the latter, the thickness of the particles is limited to about 1 μm with current technology. Under the UK government-sponsored Valid Analytical Measurement (VAM) pro-

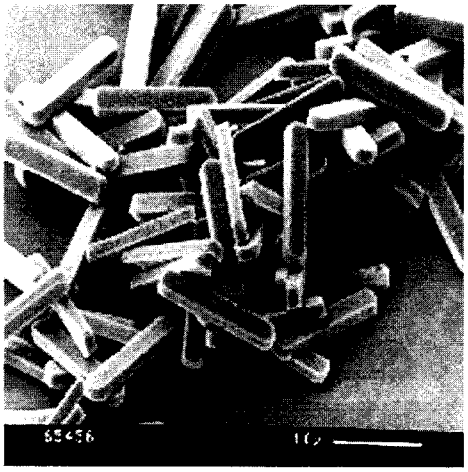

Fig. 3 Silicon Micromachined CRM Shape Standards

gram in the period 1992 to 1995, a range of 3-CRMs based on differing rectangular cross-sections was developed by AEA Technology plc in collaboration with the University of Hertfordshire [50] (**Table 11a**). 500 samples of each CRM were created, each vial containing approximately 10^6 particles. Scanning electron microscopy (SEM) was chosen as certifying method, by which an unspecified number of particles of each CRM were sized. The procedure was undertaken by a single laboratory, rather than by a consensus process, and without resort to confirmatory measurements using independent, traceable techniques. As well as providing physical dimensions, the certifying laboratory estimated indicative values of D_{ae} from a knowledge of both particle density and extremes of orientation with respect to flow, based on the model of Oseen [6] (**Table 11b**).

In principle, silicon micromachining offers such a degree of control over particle profile that a wide range of CRMs could be produced in order to simulate the behavior of fibers as well as acicular-shaped particles in analyzers. However, the current manufac-

Table 10 Production of Particle Shape Standards by Controlled Crystal Growth in Accordance with Principles Described by Matijevic [42]

Materials	Shape Description	Particle Length (μm)	References
ferric oxide	spheroidal (major/minor axes 1:1 to 3:1)	1 – 5 μm, monodisperse	Gowland and Wilshire [45]
basic copper sulfate	acicular	1 – 50 μm polydisperse	Gowland and Wilshire [45]
zinc oxide	rod	1 – 50 μm polydisperse	Gowland and Wilshire [45]
basic iron sulfate	octahedral (hexagonal projected image)	2 – 15 μm monodisperse	Gowland and Wilshire [45]
basic iron sulfate (natrojarosite)	octahedral (hexagonal projected image) ($\chi^{\dagger}$=1.19±0.06; ρ_p=3.11±0.15×10^3 kg m^{-3})	2 – 20 μm monodisperse	Marshall and Mitchell [46]
β-ferric hydroxide (akaganeite)	acicular	0.2 – 2 μm monodisperse	Marijnissen *et al.* [47]

† χ based on settling under Stokesian conditions and assumed orientation independent due to similarity of profile in all orientations

Table 11(a) Specifications of Particle Shape CRMs Developed for the UK VAM program mean±1 standard deviation

Code†	Nominal Length (μm)	Length (μm)	Width (μm)	Depth (μm)	Particles per Sample Vial ($\times 10^7$)
AEA-1001	3.0	3.09±0.10	1.67±0.08	0.96±0.09	1.00
AEA-1002	7.5	7.51±0.22	1.72±0.11	1.02±0.06	1.44
AEA-1003	12.0	12.13±0.22	1.70±0.04	1.00±0.07	2.74

Table 11(b) Indicative Values of Aerodynamic Diameter (D_{ae} (μm))‡ of Particle Shape CRMs Based on Particle Motion in Analyzer

Code†	Nominal Length (μm)	Motion Perpendicular to Major Axis	Motion Parallel to Major Axis
AEA-1001	3.0	2.89	3.14
AEA-1002	7.5	3.54	4.11
AEA-1003	12.0	3.78	4.51

† Reference Code of Supplier: Office of Reference Materials, Laboratory of the Government Chemist, Queens Road, Teddington, Middlesex, TW11 0LY, UK
‡ based on reported particle density (ρ_p) of $2.05\pm0.15\times10^3$ kg m^{-3}

turing process is expensive compared with traditional particle generation methods, and only microgram quantities in terms of mass have so far been made. The development of further CRMs of this type will therefore depend very much on user demand for shape-related standards.

4.2 Mixtures of Reference Particles

It has already been mentioned (Section 3) that a limitation when using monodisperse particles is the potential number of standards having different sizes that might be required to calibrate a particle analyzer. The ability to create 'cocktails' containing more than one monodisperse RM offers the potential both to reduce the amount of work required, and perhaps more importantly, to compare the sensitivity of an instrument (in terms of the appropriate ordinate scale (number, surface area, volume or mass)) at several different sizes simultaneously. However, this argument presupposes that the 'cocktail' RM can be prepared in a traceable way based on particle concentration as well as size.

A technique has been developed for the determination of particle number concentration in suspensions of monodisperse polymer latex particles, using a TEM calibrated by a first principle method to count individual particles carefully deposited on a flat plate [51]. The accuracy is claimed to be better than ±10% of the nominal particle number concentration. This procedure was used by the Japan Synthetic Rubber Co. (JSR) to certify a series of 4-CRMs each containing a equal blend by number concentration of 3-monodisperse particle components as a further part of the UK VAM program [52] (**Table 12**). It was intended that these standards be used for the calibration of analyzers that determine particle size weighted by number- rather than volume or mass (**Table 1**). Particle size measurements for each component were also certified by TEM. The certification process, as with the shape-based CRMs from the same source, involved a single laboratory, rather than a consensus between independent laboratories. The particle concentration was chosen to be quite low (4×10^8 particles/ml aqueous suspension). At this concentration, it was predicted that each cocktail would produce a singlet to multiplet ratio close to 0.99 when the suspensions were converted to aerosol form by pneumatic nebulization with equipment capable of generating an aqueous spray with droplets having volume median diameter of 3 μm and geometric standard deviation close to 2.0 (based on Raabe [53], assuming the droplet distribution to be log-normal).

Table 12 'Cocktail' CRMs Comprising 3-Component Monodisperse Polymer Latex Microspheres‡

Code†	Component Modal Sizes¶ Based on D_v (μm)
AEA-1004	0.1, 0.2, 0.5
AEA-1005	0.2, 0.5, 1.0
AEA-1006	0.5, 1.0, 2.0
AEA-1007	1.0, 2.0, 5.0

† Reference Code of Supplier: Office of Reference Materials, Laboratory of the Government Chemist, Queens Road, Teddington, Middlesex, TW11 0LY, UK
‡ Each vial contains 4×10^8 particles ml^{-1} in 10 ml aqueous suspension – each component is present in similar number concentration
¶ Particle sizes are nominal values without tolerances quoted in the certification report. The coefficients of variation of size quoted for each component are believed to be <4% of the modal size, based on the published specification for the unblended particles

4.3 Concentration-Based Standards

The development of standards with which to evaluate the performance of particle size analyzers in terms of the distribution axis (count (number), surface area, volume (mass)) is in its infancy. By definition, particle-gas and particle-liquid systems are unstable with time, making it impossible to create a fixed RM, in the sense of the particle standards already reviewed. Nevertheless, there is a need to be able to determine the concentration-based sensitivity of analyzers as a function of particle size within their operating ranges, especially in cases where these instruments extract samples from the bulk particle suspension. In addition, there are many particle counting instruments (*e.g.* condensation nuclei counters, nephelometers etc.) that require calibration in terms of total particle count within a given size range. Requirements for mass concentration standards also exist for instruments that collect particulate by weighing or a mass-weighted technique.

The cocktail CRMs referred to in Section 4.2 were partly intended to address this issue, and were therefore formulated so that each component was present in similar number concentration. The manufacturer (JSR) indicated that they should be stable in liquid suspension at the supplied concentration for at least 3-years following their creation, provided that the samples are stored in their unopened container at temperatures between 0 and 20°C (this limit is reduced to 6-months after opening the vial containing the particles [52]). As long as the particles are kept in suspension, or re-suspended by carefully agitating the container prior to use, agglomeration is the main process that will gradually reduce particle number concentration and at the same time lead to the formation of multiplets. This process is likely to be reduced if the suspensions are further diluted with the same suspending medium prior to use. However, to the best knowledge of the author, published data on long term stability of these CRMs is lacking, making their viability as stable concentration standards uncertain. The BCR monodisperse CRMs (**Table 4**) could be used as an alternative particle concentration standard, and although they are not certified by particle concentration, measurements made by ESZ analyzer (Coulter counter) on 1 in 100 sample vials have provided overall coefficients of variation $<\pm 2\%$ of the mean particle concentration [54]. The nominal particle concentration is 3×10^7 particles m^{-3} for each of the CRMs, corresponding to mass concentrations based on solids content of 0.2, 2.0 and 14.0 g L^{-1} for CRMs 165, 166 and 167 respectively [13].

Harfield and Bradshaw [54], in the context of establishing reference count standards for ESZ analyzers, observed that the BCR monodisperse CRMs have the smallest uncertainties of any other standard for those wanting to count particles. However, they commented that achieving concentration stability of these liquid-based suspensions is much harder to achieve than the establishment of stable and therefore certifiable particle size. Factors that have to be considered are irreversible binding of particles to the walls of containers, a process that can be offset to some extent by dilution, although the process of dilution itself introduces concerns about traceability. The accessibility to reliable particle concentration standards might be useful as a means of validating the mass integration (mass balance) method in cases where it can be applied (*e.g.* with ESZ analyzers). Here, the total volume, in instrument units, of the particles measured in a known volume of suspension is related to the known mass concentration and the immersed density of the particles, allowing the calibration (bias conversion) factor for the instrument to be calculated [55].

The use of monodisperse polymer latex particles as aerosol concentration standards imposes the added problem of creating the aerosol from the liquid suspension. Aerosols, by their nature are unstable systems compared with liquid suspensions because of the lower viscosity of the surrounding fluid [56]. It is therefore most unlikely that creation of a particle concentration standard by a single burst of aerosol formation could provide a reference particle concentration that would remain constant during the time required for performance measurements to be made. The alternative and preferred approach is to replenish the aerosol continuously in a flow-through system. Yamamoto *et al.* [57] have described such an aerosol generator, which uses a purpose-built pneumatic nebulizer (Kousaka *et al.* [58]) for suspending particles in the size range from 0.08 to 3.0 μm. They have claimed that this apparatus provides aerosols whose stability in terms of particle number concentration is $<\pm 10\%$ of the mean (9.3×10^6 particles m^{-3}) during 120 min operation with particles having D_v of 0.168 μm. Their facility probably represents the state-of-the-art in terms of measures to control particle concentration. The aerosol was passed through a charge equilibrator to minimize electrostatic charge induced agglomeration (which can be potent with aerosols), and the particle concentration was kept low to minimize Brownian agglomeration. Furthermore, the size range of operation was chosen such that loss mechanisms to the container walls (sedimentation, inertial deposition and

diffusion effects) were minimized. More recently, this system has been commercialized as the JSR-Aeromaster®. However, attempts to suspend two of the cocktail CRMs (AEA-1005 and AEA-1007) with this equipment resulted in a mixed outcome [52]. The cocktail containing the finer particles (AEA-1005) provided highly stable aerosols over the 30-minute test period, with variability of all three components within less than 5% of the mean concentration. However, a slight, but systematic increase in concentration with elapsed time was evident with the cocktail containing the coarser particles (AEA-1007). Furthermore, the efficiency of nebulization of the 2 μm and 5 μm diameter components was lower than the expected values by factors of 5 and 100 respectively, based on the concentration of each component in the original suspension. On the basis of these data, this type of nebulizer may be unsuited for the generation of aerosol concentration standards containing particles much larger than 1 μm diameter. The gradual increase in particle concentration with time appears to be related to the volatilization of the suspending fluid in the nebulizer and can be minimized by various techniques, including operation at low ambient temperature and the use of a larger secondary reservoir attached to that of the nebulizer [59]. Nevertheless, it is difficult, if not impossible to eliminate all causes of time-dependent drift in particle concentration, resulting in a gradual loss of traceability. In the end, these standards are likely to have to be used in conjunction with a validated particle concentration monitor [52].

The vibrating orifice monodisperse aerosol generator (VOMAG) is an alternative method to develop an in-house particle concentration standard for particles in the size range from about 0.5 to 50 μm volume equivalent diameter [10, 29]. The modal size of the particles (μm) that are formed is related directly to variables that are both well-defined and which can be measured by directly traceable means:

$$D_v = 10^4 \left[\frac{Q_l C_f}{10 \pi F_{vib}} \right]^{1/3} \qquad [4]$$

where Q_l is the liquid feed rate (cm^3 min^{-1}), C_f is the fractional concentration of solute in the feed liquid and F_{vib} (Hz) is the orifice vibration frequency. The lack of an empirical constant in this relationship makes it possible to derive the uncertainty in D_v directly from the uncertainties associated with Q_l, F_{vib} and C_f, free from bias, although a check should always be made of particle size and sphericity by a traceable method, such as optical microscopy [35]. Aerosols from the VOMAG are highly monodisperse (σ_g typically <1.02) and concentrations in the range 1 to 100 particles cm^{-3} are achievable, depending upon the configuration of the aerosol generator. The aerosol number concentration (N, particles cm^{-3}) can be predicted if the particle stream emerging from the vibrating orifice is introduced without losses into a flow of carrier gas (usually air ($Q_{carrier}$, L min^{-1})) and thoroughly mixed without inducing losses to the walls of the mixing chamber, since:

$$N = \frac{0.06F}{Q_{carrier}} \qquad [5]$$

Equation [4] is not continuous (*i.e.* not all conditions will give rise to a monodisperse aerosol [59]). However, under conditions where monodispersity is achieved, the relationship relating the mass- to number-concentration of particles of size D_v (μm) dispersed in Q_c (L min^{-1}) applies:

$$M = \frac{\pi \rho_p D_v^3 N}{6} \qquad [6]$$

where ρ_p is the particle density (kg m^{-3}) and M is the aerosol mass concentration (mg m^{-3}). Strictly, this relationship only links particle number- and mass-concentration in a fully traceable manner when the particle stream is perfectly monodisperse ($\sigma_g = 1.00$), but in practice the error is sufficiently small that the aerosol from a VOMAG can be used both as a mass as well as a number concentration standard.

Recently, Booker and Horton [59] have described a practical flow-through particle concentration source based on the VOMAG principle, in which care is taken to disperse the droplets by an air-jet sideways from the region of the vibrating orifice to reduce deposition at this location, as well as minimize losses in the aerosol sampling chamber due to sedimentation and inertial effects (**Figure 4**). Control of Q_l within ±0.5% at a typical feed rate of 0.2 cm^3 min^{-1} was achieved using an isocratic pump, and orifice vibration frequency was stable within ±0.01% of typical operating frequency (50 kHz). The monodispersity of the aerosol stream was monitored continuously by optical means, observing the angle at which the droplet stream was dispersed (the presence of more than one stream was indicative that the particles were no longer monodisperse)

5. Future Needs:

The development of particle-based standards experienced a period of rapid growth in the early 1990s, but of late has languished, probably as a result of the

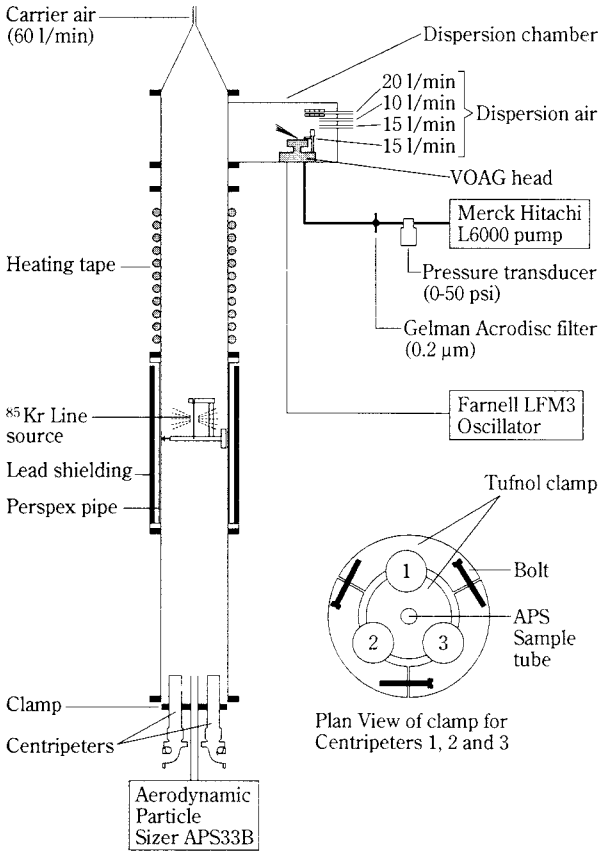

Fig. 4 Particle Concentration Standard
[from ref. 59 © UK Crown Copyright – used by permission]

withdrawal of government funding for the intensive campaigns that are needed to develop adequate RMs. Probably the most pressing need at the present time is the completion of the certification of the polydisperse, spherical CRMs by the BCR (**Table 6**), in particular to support the performance verification of the large number of laser diffractometers in use. At the time of writing, the sub-divided powders are currently in storage at the EU Institute for Reference Materials and Measurements (IRMM-JRC-Geel, Belgium), awaiting the outcome of the call for proposals to certify them by a consensus approach, as well as characterization by a variety of non-first principle size analysis methods. In the last decade, there has also been rapid growth in capability to size sub-micron sized particulates in powder, liquid suspension and in aerosol form by techniques that involve some form of deconvolution (*e.g.* PCS, laser diffractometry) or whose size-related response requires a complex transformation of raw data to the final size distribution (*e.g.* TOF aerosol analyzers). In these cases, it would be beneficial if the original intent of the BCR were to be fulfilled, so that this CRM series is extended to particle sizes at least as fine as 0.1 μm volume equivalent diameter.

The production of monodisperse, spherical SRMs/CRMs with additional certified sizes is a lower priority, since in many instances, SSMs supplied by a variety of manufacturers, as well as in-house particle generation techniques are adequate for the main use for these materials, which remains size-based calibration. Nevertheless with the emergence of nanotechnology as an important source of economic growth, there will be pressure to extend the NIST SRMs to sizes finer than 0.1 μm volume equivalent diameter. The twin challenges will be to develop adequate first-principle techniques to size nanometer particles, and to create them in sufficient quantity to be of use as RMs.

The future for particle shape standards remains uncertain, since it is not clear in most instances, how they can be used to provide unambiguous data especially when particle orientation with respect to the flow or interrogation technique (light beam in the case of optical-based techniques) cannot be defined. CRMs based on silicon micromachining are relatively easy to produce, although expensive relative to other material sources, and they probably have a role to play in the simulation of particles having extreme aspect ratios, such as fibers. It is unlikely, however, that impetus to develop more of these materials will arise unless there is sufficient demand for the current CRMs. As a footnote, the consensus method of certification is preferred over single laboratory certification, as there is an opportunity to quantify both inter-laboratory variances as well as inter-sample variances for each CRM.

Finally, the provision of adequate standards for particle concentration is most likely to come in response to those making aerosol-based measurements. Such standards are particularly important in the fields of occupational hygiene and environmental sampling where a plethora of new techniques are in the process of development. There is a need to have an understanding of both inter-technique as well as inter-instrument performance when establishing widely accepted standards, for example the PM-series for environmental particulate emission control limits in the USA. The challenge with this class of standards, is to develop systems that extend to a wide enough range of particle sizes and at the same time have minimal losses, or whose losses are accurately quantified.

Acknowledgements

The author would like to acknowledge the support of several people who provided information to help in the task of writing this review, in particular Mr. Mark

Bumiller, Prof. Brian Kaye, Dr. Ian Marshall, Mr. Mark Nagel, Dr. Graham Rideal, Prof. Brian Scarlett and Mr. Maurice Wedd.

References

1) International Standards Organization (ISO). Quality Management and Quality Assurance Standards: ISO 9001-1 (1994); ISO 9000-2 (1997); ISO 9000-3 (1997); ISO 9000-4 (1993), ISO, Geneva, Switzerland (1993-1997).
2) Allen, T. Particle Size Measurement. Fourth Edition, Chapman and Hall, N.Y., (1990).
3) Hinds, W,C. Aerosol Technology. 2nd Edition Wiley, N.Y., USA. (1999).
4) Hawksley, P.G.W. The Physics of Particle Size Measurement: Part 1 – Fluid Dynamics and the Stokes Diameter. *Br. Coal Util. Res. Assoc. Mon. Bull.*, 15(4), 105, (1951).
5) Scarlett, B. Measurement of Particle Size and Shape, Some Reflections on the BCR Reference Material Programme. *Part. Charact.*, 2, 1-6, (1985).
6) Oseen, C.W. Latest Methods and Results in Hydrodynamics. Akademische Verlag, Leipzig, Germany, (1927).
7) International Standards Organization (ISO). Particle Size Analysis: Laser Diffraction Methods, Part 1: General Principles. ISO 13320-1, (1999).
8) Röthele, S. and Witt, W. Standards in Laser Diffraction. pp. 625-642 in *Proc. PARTEC, 5th European Symp. Particle Characterization*, Nürnberg, Germany, 1992.
9) Mühlenweg, H. and Hirleman, E.D. Reticles as Standards in Laser Diffraction Spectroscopy. *Part. Part. Syst. Charact.*, 16, 47-53, (1999).
10) Berglund, R.N and Liu, B.Y.H. Generation of monodisperse aerosol standards. *Environ. Sci. Technol.*, 7, 147-153, (1973).
11) Hartman, A.W., Doiron, T.D. and Hembree, G.G. Certification of NIST SRM 1961: 30 μm Diameter Polystyrene Spheres. *J. Res. Natl. Inst. Stand. Technol.*, 96, 551-563, (1991).
12) Lettieri, T.R., Hartman, A.W., Hembree, G.C. and Marx, E. Certification of SRM 1960: Nominal 10 μm Diameter Polystyrene Spheres ('Space Beads'). *J. Res. Natl. Inst. Stand. Technol.*, 96, 669-691, (1991).
13) Thom, R., Marchandise, H. and Colinet, E. The Certification of Monodisperse Latex Spheres in Aqueous Suspensions with Nominal Diameter 2.0 μm, 4.8 μm and 9.6 μm. Commission of the European Communities (Bureau of Community Reference) Report EUR-9662-EN, Brussels, Belgium, (1985).
14) Hartman, A.W., Doiron, T.D. and Fu, J. Certification of NIST SRM 1962: 3 μm Diameter Polystyrene Spheres. *J. Res. Natl. Inst. Stand. Technol.*, 97, 253-265, (1992).
15) Mulholland, G.W., Hartman, A.W., Hembree, G.C., Marx, E. and Lettieri, T.R. Development of a One-Micrometer Diameter Particle Size Standard Reference Material. *J. Res. Natl. Bur. Stds.*, 90, 3-26, (1985).
16) Lettieri, T.R. and Hembree, G.C. Dimensional Calibration of the NBS 0.3 μm Diameter Particle Sizing Standard. *J. Coll. Interface Sci.*, 127(2), 566-572, (1989).
17) Kinney, P.D., Pui, D.Y.H., Mulholland, G.W. and Bryner, N.P. Use of the Electrostatic Classification Method to Size 0.1 μm SRM Particles – A Feasibility Study. *J. Res. Natl. Inst. Stand. Technol.*, 96, 147-176, (1991).
18) BCR, Reference Materials of Defined Particle Size, Bureau of Community Reference, Brussels, Belgium, (1992).
19) Wilson, R., Leschonski, K., Alex, W., Allen, T., Koglin, B. and Scarlett, B. Bureau of Community Reference Certification Report on Reference Materials of Defined Particle Size, Quartz: BCR No. 66–70, Commission of the European Communities (Bureau of Community Reference) Report EUR 6825 EN, Brussels, Belgium, 1980.
20) Scarlett, B., Merkus, H.G. and Meesters, G.M.H. European Progress on Calibration and Standardization for Particle Sizing. pp. 9-18 in *Liquid Particle Size Measurement Techniques: 2nd Volume, ASTM STP 1083*, eds. E.D. Hirleman, W.D. Bachalo and P.E. Felton, American Society for Testing and Materials, Philadelphia, USA, (1990).
21) Harfield, J.G., Simmons, A.W., Wenman, R.A. and Wharton, R.A. A Study of the BCR Reference Materials. pp. 349-357 in *Particle Size Analysis-85*, ed. P.J. Lloyd, John Wiley and Sons, Chichester, UK, (1985).
22) Allen, T. and Davies, R. Evaluation of Instruments for Particle Size Analysis. pp. 17-46 in *Proc. 4th Eur. Symp. Part. Charact. (PARTEC)*, ed. K. Leschonski, NMA NürnbergMesse- und Außtellungsgesellschaft mbH, Nürnberg, Germany, (1989).
23) Merkus, H.G., Bischof, O., Drescher, S. and Scarlett, B. Precision and Accuracy in Particle Sizing: Round-Robin Results from Sedimentation, Laser Diffraction and Electrical Sensing Zone Using BCR 67 and 69. in *Proc. 6th Eur. Symp. Part. Charact. (PARTEC)*, ed. K. Leschonski, NMA NürnbergMesse- und Außtellungsgesellschaft mbH, Nürnberg, Germany (1995).
24) Mitchell, J.P. Certification and Characterization of a New Range of Community Bureau of Reference Polydisperse, Spherical Certified Reference Materials, *Anal. Proc.*, 29, 508-509, 1992.
25) Standards, Measurement and Testing (SMT) Programe of the European Union (formerly BCR), Guidelines for the Production and Certification of BCR Reference Materials: Part A – Recommendations to Proposers of Reference Materials Projects. BCR/01/97-Part A, (1997), SMT Programme Research DG-CII/3, Brussels, Belgium.
26) Standards, Measurement and Testing (SMT) Programe of the European Union (formerly BCR) 1994-98. Topic 29: Certification of Polydisperse Particulate Reference Materials, now Topic II-21 (Support to the Development of CRMs), in *Measurements and Testing Newsletter*, 7(2), (1999), Measurements and Testing Generic Activity, SMT Programme Research DG-CII/3, Brussels, Belgium.
27) Rideal, G.R., Dodds, J.A., Pons, M-N., Leschonski, K., Lloyd, P.J. and Merkus, H.G. The Development of New Reference Standards for Particle Sizing Instrument Calibration. Paper 50 in *Proc. World Congress on Particle Technology 3*, UK Inst. Chem. Engrs., Brighton, UK, (1998).

28) Fuchs, N.A. and Sutugin, A.G. Generation and Use of Monodisperse Aerosols. pp. 1-30 in *Aerosol Science*, ed. C.N. Davies, Academic Press, N.Y., USA, (1966).
29) Vanderpool, R.W., and Rubow, K.L. Generation of Large, Solid Monodisperse Calibration Aerosols. *Aerosol Sci. Technol.*, 9, 65-69, (1988).
30) Walton, W.H. and Prewett, W.C. The Production of Sprays and Mists of Uniform Drop Size by Means of Spinning Disc Like Sprayers. *Proc. Phys. Soc.*, 62, 341-350, (1949).
31) Cheah, P.K.P. and Davies, C.N. The Spinning-Top Aerosol Generator – Improving the Performance. *J. Aerosol Sci.*, 15(6), 741-751, (1984).
32) Sinclair, D. and LaMer, V.K. Light Scattering as a Measure of Size in Aerosols. *Chem. Rev.*, 44, 245-267, (1949).
33) Prodi, V. A Condensation Aerosol Generator for Solid, Monodisperse Particles. pp. 169-181 in *Assessment of Airborne Particles*, eds. T.T. Mercer, P.E. Morrow and W. Stöber. C.C. Thomas, Springfield, IL, USA, 1972.
34) Liu, B.Y.H. and Pui, D.Y.H. A Sub-Micron Standard and the Primary, Absolute Calibration of the Condensation Nucleus Counter. *J. Coll. Interface Sci.*, 47, 155-171, (1974).
35) Mitchell, J.P. Aerosol Generation and Instrument Calibration. pp. 31-79 in *Physical and Chemical Properties of Aerosols*, ed. I. Colbeck, Blackie Academic and Professional, London, (1998).
36) Mark, D. Transport and Sampling of Aerosols, pp. 80-152 in *Physical and Chemical Properties of Aerosols*, ed. I. Colbeck, Blackie Academic and Professional, London, (1998).
37) Clift, R., Grace, J.R. and Weber, M.E. Bubbles, Drops and Particles, Academic Press, N.Y., USA, 1978.
38) Clift, R. Inertial, Sedimentation, Image Analysis and Electrozone Measurements of Particle Size. pp. 3-17 in *Particle Size Analysis*, ed. P.J. Lloyd, Wiley-Interscience, Chichester, UK, (1988).
39) Wang, H-C., and John, W. Particle Density Correction for the Aerodynamic Particle Sizer. *Aerosol Sci. Technol.*, 6, 191-198, (1987).
40) Cheng, Y-S., Chen, B.T., Marshall, I.A., Mitchell, J.P. and Griffiths, W.D. Behavior of Compact Non-Spherical Particles in the TSI Aerodynamic Particle Sizer Model APS33B: Ultra-Stokesian Drag Forces. *Aerosol Sci. Technol.*, 19, 255-267, (1993).
41) Cheng, Y.S., Barr, E.B., Marshall, I.A. and Mitchell, J.P. Calibration and Performance of an API Aerosizer. *J. Aerosol Sci.*, 24, 501-514, (1993).
42) Stöber, W., Berner, A. and Blaschke, R. The Aerodynamic Diameter of Aggregates of Uniform Spheres. *J. Coll. Interface Sci.*, 29, 710, (1969).
43) Chen, B.T. and Cheng, Y.S. Optical Diameters of Aggregate Aerosols. pp. 23-25 in *Aerosols*, eds. B.Y.H. Liu, D.Y.H. Pui and H. Fißan. Elsevier Science Publ. Co. Inc., N.Y., USA, (1984).
44) Matijevic, E. Production of Monodisperse Colloidal Particles. *Am. Rev. Mater. Sci.*, 15, 483-516, (1985).
45) Gowland, R.J and Wilshire, B. Standard Powders for Particle Size Analysis. pp. 99-107 in *Particle Size Analysis*, ed. N.G. Stanley-Wood, Royal Society of Chemistry, Cambridge, UK, (1992).
46) Marshall, I.A. and Mitchell, J.P. The Preparation and Characterization of Particle Shape Standards. pp. 81-90 in *Particle Size Analysis*, ed. N.G. Stanley-Wood, Royal Society of Chemistry, Cambridge, UK, (1992).
47) Marijnissem, J., Buwalda, H., Lemkowitz, S. and Bibo, H. Production of Uniform Micron and Sub-Micron Fibers for Instrument Calibration. pp. 211-216 in *Aerosols: Their Generation, Behavior and Applications and Particle Shape*, Proc. 5th Conf. UK Aerosol Society, Loughborough, UK. (1991).
48) Hoover, M.D., Casalnuovo, S.A., Lipowicz, P.J., Hsu, C.Y., Hanson, R.W. and Hurd, A.J. A Method for Producing Non-Spherical Monodisperse Particles Using Integrated Circuit Fabrication Techniques. *J. Aerosol Sci.*, 21(4), 569-575, (1990).
49) Kaye, P.H., Hirst, E. and Clark, J.M. The Manufacture of Standard Non-Spherical Particles by Silicon Micromachining. pp. 223-228 in *Aerosols: Their Generation, Behavior and Applications and Particle Shape*, Proc. 5th Conf. UK Aerosol Society, Loughborough, UK. (1991).
50) Marshall, I.A. VAM-14: Annex B (I) – Development and Use of Particle Shape Standards for Aerosol Analysis. AEA Technology Report AEA-TPD-0335, (1995).
51) Katsuta, T., Fukai, Y. and Aotani, S. Determination of the Correct Number of Polystyrene Particles in Pure Water. pp. 64-66 *in* Proc. 6th Symp. on Aerosol Science and Technology, Japan Assoc. Aerosol Sci. Technol., Japan (1988).
52) Marshall, I.A. VAM-14: Annex A – Development and Use of Cocktail Reference Materials for Aerosol Analysis. AEA Technology Report AEA-TPD-0338, (1995).
53) Raabe, O.G. The Generation of Aerosols of Fine Particles. pp. 57-110 in *Fine Particles*, ed. B.Y.H. Liu, Academic Press, N.Y., USA, (1976).
54) Harfield, J.G. and Bradshaw, A.M. A Systems Approach to Assigning a Reference Count by Coulter Counter Instrumentation to a Standard Material. Paper 49 in *Proc. World Congress on Particle Technology 3*, UK Inst. Chem. Engrs., Brighton, UK, (1998).
55) Lines, R.W. The Electrical Sensing Zone Method (The Coulter Principle). pp. 350-373 in *Particle Size Analysis*, ed. N.G. Stanley-Wood, Royal Society of Chemistry, Cambridge, UK, (1992).
56) Hidy, G.M. and Brock, J.R. The Dynamics of Aerocolloidal Systems. Pergamon Press, Oxford, UK, 1970.
57) Yamamoto, S., Aotani, S., Fukushima, N. and Kousaka, Y. Generation and Application of Uniform Aerosol of Polystyrene Particles. pp. 247-250 in *Aerosols: Science, Industry, Health and Environment*, Proc. 3rd. Int. Aerosol Conf., Kyoto, Japan, Pergamon Press, Oxford, UK. (1990).
58) Kousaka, Y., Okuyama, K., Shimada, M., Oshima, K. and Hase, T. Performance of a Nebulizer for Standard Aerosol Particle Generation. *J. Aerosol Res. Japan*, 4(4), 294, (1989).
59) Booker, D.R. and Horton, K.D. Development of Aerosol Concentration Standards. AEA Technology Report AEA-TPD-0345, (1995).

Author's short biography

Jolyon P. Mitchell

Jolyon Mitchell is currently Scientific Director of Trudell Medical International, with responsibility for all aspects of *in vitro* aerosol testing. During the past 5 years, he has built up the laboratory to the point at which more than 50 publications have been produced for the open literature, many of which have appeared in peer-reviewed journals. He is Chair of Task Group 1 (*In Vitro* Methods) of the Inhalant Drug Delivery Systems Sub-Committee of the Canadian Standards Association. This committee is currently developing a standard for testing Spacers and Holding Chambers. He is a member of the American Association of Pharmaceutical Scientists (Inhalation Technology Focus Group) and a Member of Executive Committee developing the Next Generation Impactor for the Pharmaceutical Industry. He is about to join the Editorial Advisory Board of *Journal of Aerosol Medicine*.

Since graduating from the University of Salford in the United Kingdom with a doctorate in physical chemistry in 1976, he has had approaching 20 years experience in the measurement and control of aerosols, initially as an experimentalist and more recently as coordinator of major projects involved with standards and calibration of aerosol measuring equipment. He joined the UK Atomic Energy Authority in 1980 to undertake research into the release and subsequent behavior of aerosols that might be released from severe nuclear reactor accidents. This work involved developing several measurement devices and tools for their calibration, and subsequently evolved into initiatives concerned with the development of new particle standards. As Manager of the Aerosol Science Centre, he coordinated the first phase of a UK government initiative to apply the principles of valid analytical measurement to the assessment of aerosols. He developed an interest in medical aerosols as a result of working with colleagues to develop better measurement techniques and immigrated to Canada in 1994 to join the Trudell Medical Group.

He has published more than 120 articles in the open literature, of which about 40 are in peer-reviewed journals. He has also contributed to two major books on aerosol science, writing chapters concerned with aerosol measurement techniques and calibration of aerosol measurement equipment.

Adsorption of Poly (ethylene oxide) Onto Silica at Different Solids Loadings†

Mick Bjelopavlic[1], Abbas A. Zaman[2] and Brij M. Moudgil[1]
[1] *Department of Materials Science and Engineering*
[2] *Department of Chemical Engineering*
*Engineering Research Center for Particle Science and Technology**

Abstract

The adsorption of poly (ethylene oxide) (PEO) of 7,500 MW, a hydrogen bonding polymer, onto the surface of monodisperse colloidal silica particles was investigated as a function of volume fraction of solids. Adsorption studies revealed the presence of two plateaus, which was attributed to a change in conformation from a flat, "pancake" type, to a more elongated "brush" type conformation of the adsorbed polymer, where the terminal hydroxyl groups remained bound to the silica surface. Adsorption studies also revealed that, within the concentration range studied, there was no effect upon PEO adsorption as a function of volume fraction.

Introduction

Dispersion and stabilization of particles is of fundamental importance in areas such as ceramic processing, formulation of inks and paints, cosmetics, the food industry, pharmaceuticals, and slurry transport. In order to stabilize particulate suspensions, polymers are often used as dispersing agents. Examples include the use of polyacrylic acid (PAA) to stabilize suspensions of alumina[1] and titania[2], and poly (ethylene oxide) (PEO) to disperse polystyrene latex[3] and silica[4] particles. Such systems are stabilized through steric barriers as a result of polymer adsorption[5].

As industry strives towards improved products, there is a growing need to operate at ever increasing solids loadings. This is exemplified by the direct casting methods used in the ceramics industry, where increasing solids loadings while maintaining relatively low slurry viscosities, is providing a more cost effective means of producing increasingly complex objects with low structural defects, high uniformity and good mechanical properties[6].

The challenge, therefore, is to maintain the stability of highly concentrated particulate slurries by improving the effectiveness and efficiency of polymers used as dispersants. The ability of a polymer to stabilize a given particulate suspension is directly related to the level of surface coverage, conformation and orientation of the adsorbed polymer on the particulate surface, as well as polymer molecular weight. The effect of increasing solids loadings upon these parameters, however, is not well known. The adsorption of poly (ethylene oxide) onto colloidal silica spheres, used as a model system, was therefore studied as a function of solids loading in order to gain an understanding of the pertinent polymer properties (such as adsorption density, conformation, etc.) which ultimately control the stability and viscosity of suspensions.

Experimental Section

Materials. All samples used in this investigation were prepared in an electrolyte solution of 0.01 M $NaNO_3$ containing polyethylene oxide of different concentrations. Ultra-pure water (Millipore) of specific conductivity less than 1 $\mu ohm \cdot cm^{-1}$ was used to prepare the solutions and Fisher brand NaOH was used to adjust the pH of the samples to the desired value. All reagents were of ACS grade and obtained from Fisher Scientific Co.

Silica powder of 99.9% purity was used in this study and was obtained from Geltech, Inc. This sample was used as received and had a nominal diameter of 0.5 μm, as stated by the manufacturer. Particle size analysis was performed using a Coulter LS230 laser

* University of Florida, Gainesville, FL 32611, USA
† Received: May 16, 2000

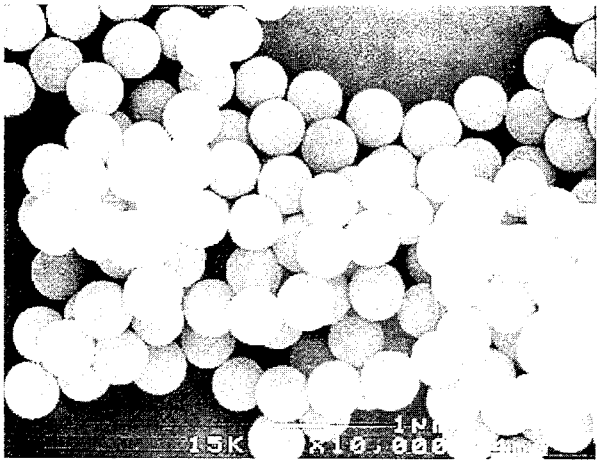

Fig. 1 SEM micrograph of 0.60 μm (diameter) silica particles.

diffraction apparatus and SEM. **Figure 1** is an SEM image of the 0.5 μm sample which indicates that the powder is monosized and the particles are spherical in shape. The experimentally measured volume average (d_{50}) particle diameter of the powder was found to be 0.6 μm. Henceforth, all particle diameters referred to in this text are the experimental, rather than the nominal values. Powder density was measured using a Quantachrome Ultrapycnometer 1000 and was found to be 2.1 $g \cdot cm^{-3}$. The BET nitrogen specific surface areas of the silica powder was measured with a Quantachrome Nova 1200 and found to be 6.22 $m^2 \cdot g^{-1}$.

Poly (ethylene oxide) (PEO) of molecular weight 7,500 was procured from Polysciences Inc. and used as received. Polymer stock solutions were prepared by mixing 4.0 g of polymer with 500 cm^{-3} of 0.01M $NaNO_3$ solution and stirring for 16 hours using a magnetic stirrer in order to achieve complete dissolution. The solutions were also covered in order to avoid decomposition of the polymer due to exposure from ultraviolet radiation. The stock solutions were then diluted to the desired concentrations using 0.01M $NaNO_3$.

Adsorption studies. All adsorption experiments were conducted at pH 9.5 using suspensions with a total volume of 10 cm^3 contained in 30 cm^3 polyethylene screw capped bottles. Depending upon the volume fraction of silica and the polymer dosage, the PEO stock solution was diluted with 0.01M $NaNO_3$ to the desired concentration and used as the suspending fluid. The required mass of dry silica was then slowly added to the PEO solution while mixing the sample by shaking and vibration. After adding all silica particles, the pH of the suspension was adjusted to 9.5 using 1M NaOH. Adjustment of pH was performed in one direction only.

After addition of silica, the suspensions were vigorously shaken by hand and the pH checked and readjusted, after which they were treated with ultrasonics in order to break up any aggregates, using a Cole-Parmer Model CV-26 water jacketed cup horn probe with Model CPX-600 Ultrasonic Processor set at 500 watts power. The suspensions were then agitated using a Burrell Model 75 Wrist Shaker for a period of 20-24 hours in order for equilibrium to be reached. During equilibration, the suspensions were treated with ultrasonics at regular intervals (for at least 30 minutes) to break up any aggregates which may have formed, and the pH checked and readjusted if required. After equilibration, the samples were centrifuged for 10 minutes at 15,000 rpm and supernatant was carefully withdrawn. The supernatant was then allowed to sit overnight in a refrigerator in order to allow the settling of any remaining particles, as tests had shown that small numbers of particles could still be present after the centrifugation process, the presence of which could adversely affect subsequent analysis.

Residual PEO concentration was measured directly in terms of organic carbon content using a Tekmar-Dorhmann Phoenix 8000 Total Organic Carbon (TOC) analyzer. The TOC analyzer was calibrated using potassium hydrogen phthalate standards of known carbon concentration to give a linear primary calibration curve. Solutions with known masses of 7,500 MW PEO were also analyzed, and within the concentration range studied (0.1-20 $mg \cdot L^{-1}$ carbon), a secondary linear calibration curve was obtained. The multiplication factor to convert from units of $mg \cdot L^{-1}$ organic carbon, to $mg \cdot L^{-1}$ of PEO, was found to match the theoretical value of 1.83 (determined from the amount of carbon in the PEO repeating unit). TOC analyses were performed in triplicate and had an experimental error of not more than ±5%.

Results

Adsorption studies of 7,500 MW PEO were performed using silica spheres at different volume fractions. The adsorption isotherm for a suspension of 50 %vol of 0.6 μm silica particles is illustrated in **Figure 2**. This shows that polymer adsorption steadily increases until a plateau is reached at approximately 0.34 $mg \cdot m^{-2}$ surface coverage. However, as the equilibrium solution concentration increases above approximately 6,000 $mg \cdot L^{-1}$, more polymer adsorbs until a second plateau is reached at 1.20 $mg \cdot m^{-2}$ surface coverage. It should be noted that the initial portion of **Figure 2** should not be taken as being indicative of a

typical high affinity type isotherm, generally associated with polymer adsorption, due to the large equilibrium concentration (C_{eq}) scale used. The **Figure 2** inset shows the initial portion of the isotherm has a rounded (as opposed to high affinity) profile, and possibly is a consequence of polydispersity[7,8] within the PEO sample used for this study.

Figure 3 shows the adsorption of 7,500 MW PEO on 0.6 μm silica spheres as a function of volume fraction for PEO doses of 2.5 mg·(g solids)$^{-1}$ and 1.0 mg·(g solids)$^{-1}$, respectively. Polymer adsorption rises steadily with increasing silica volume fraction until a plateau is reached at approximately 20% solids for both polymer doses used. In **Figure 4**, the adsorption of PEO onto silica at 2 %vol fraction is shown. As in the **Figure 2** inset, polymer adsorption increases until a pseudo plateau is reached at approximately 0.34 mg·m^{-2} surface coverage.

Discussion

Adsorption Behavior. The adsorption of 7,500 MW PEO on 0.6 μm silica as a function of solids volume fraction was studied due to the importance of understanding how increasing the solids loading would impact upon adsorption phenomena. **Figure 2** shows the adsorption of 7,500 MW PEO onto 50 %vol SiO_2. It was observed that adsorption increased until a plateau was obtained at approximately 0.34 mg·m^{-2}, which corresponds to an approximate PEO dose of 1.4 mg·(g solids)$^{-1}$ (see **Figure 2** inset).

The parking area occupied by one polymer molecule, S_{exptl}, at the plateau values was calculated from the adsorption isotherm using the formula[9]:

$$S_{exptl} = \frac{1}{\Gamma_{max}} \times \frac{10^{18}}{N_A} \quad (1)$$

where Γ_{max} is the amount adsorbed at the plateau (mol·m^{-2}; converted from units of mg·m^{-2} by dividing by polymer MW), 10^{18} is a conversion factor for m^2 to nm^2, and N_A is Avogadro's number (6.02×10^{23}). Values of S_{exptl} are summarized in **Table 1**. Additionally, the theoretical parking area, S_{theory}, for unperturbed polymer coils was calculated using the radius of gyration, R_g, for 7,500 MW PEO, which was determined from the intrinsic viscosity data published earlier by Bailey and Koleske[10]. These values are also summarized in **Table 1**.

Figure 2 shows that the first plateau is reached at a surface coverage of 0.34 mg·m^{-2}. This value is in good agreement with the earlier work of Killmann *et al.*[11] who obtained a plateau value of 0.37 mg·m^{-2} for the adsorption of 6,000 MW PEO on Stöber silica. Comparison of the values of S_{exptl} and S_{theory} in **Table 1** reveals that for the first adsorption plateau, the experimentally obtained parking area is some 20% less than the theoretical value derived from R_g. Killmann *et al.*[11],

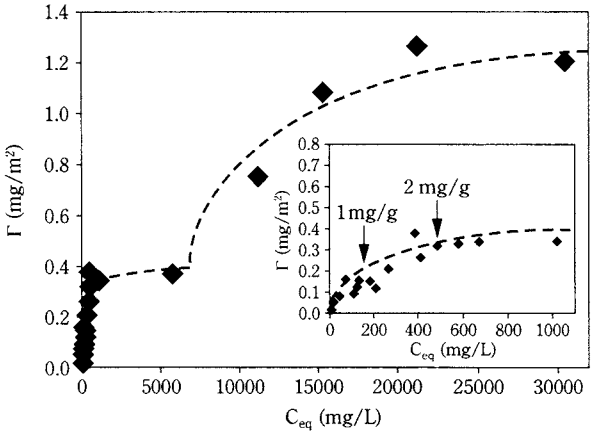

Fig. 2 Adsorption of 7,500 MW PEO onto 0.60 μm silica particles at 50 %vol. (0.01M $NaNO_3$, suspension pH=9.5).

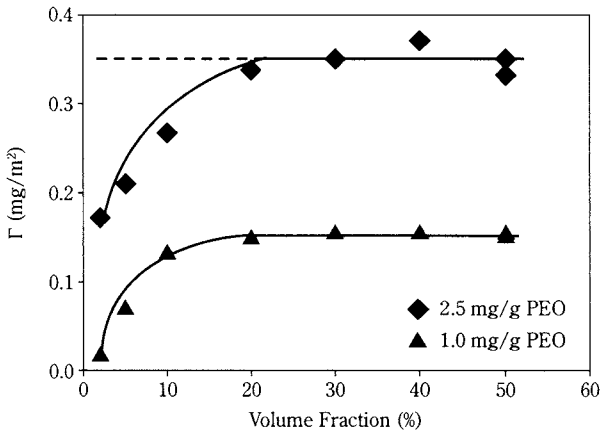

Fig. 3 Adsorption of 7,500 MW PEO onto 0.60 μm silica particles as a function of volume fraction of the particles at two different polymer dosages. (0.01M $NaNO_3$, suspension pH=9.5).

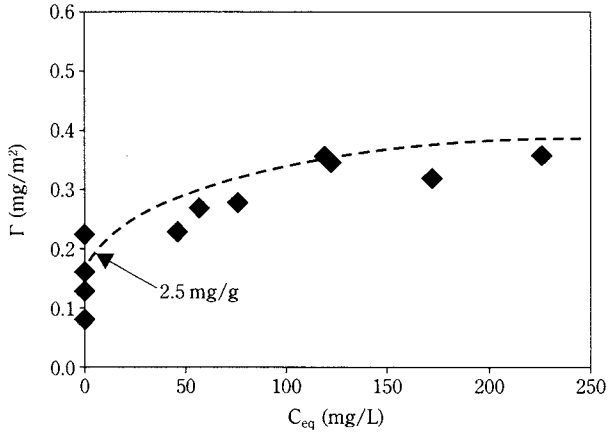

Fig. 4 Adsorption of 7,500 MW PEO onto 0.60 μm silica particles at 2 %vol. (0.01M $NaNO_3$, suspension pH=9.5).

Table 1 Γ_{max}, Radius of Gyration (R_g), and Experimental and Theoretical Parking Areas (S_{theory}) for 7,500 MW PEO on 50 %vol Fraction of 0.60 μm Silica Particles.

Plateau	Γ_{max} (mg·m^2)	S_{expt} (nm^2)	R_g (nm)	S_{theory} (nm^2)
first	0.34	36.6	3.81	45.6
second	1.20	10.4	–	–

observed that at monolayer capacity, there was a marked increase in the hydrodynamic layer thickness of PEO (of various molecular weights) adsorbed onto Stöber silica, citing this as evidence for the polymer undergoing elongation or "stretching" perpendicular to the surface. Such behavior is in agreement with the polymer adsorption theory of Scheutjens and Fleer[12,13], where the conformation of adsorbed polymers is strongly influenced by the amount adsorbed and the surface coverage, ie. competition for adsorption sites between polymer segments increases with increasing coverage. This suggests that as the amount of polymer covering the silica surface approaches the (pseudo) monolayer capacity (or first plateau), the adsorbed PEO molecules change from a flat conformation to a somewhat more elongated or "brush type" conformation.

Some idea of the conformation of the adsorbed polymer can also be obtained from examining values of adsorbed layer thickness (d), and comparing them to those for unperturbed coils in the bulk. For an unperturbed polymer coil adsorbing on a surface, the layer thickness would be two times the radius of gyration ($2R_g$). From the work of Killmann *et al.*[11], the following equation (derived from photon correlation spectrometry measurements) can be used to determine the PEO layer thickness on silica for a given molecular weight (M):

$$d = 0.018 M^{0.52} \quad (2)$$

Using Equation (2), one obtains a layer thickness value of 1.86 nm for the present study. In comparison, the corresponding value for an unperturbed coil would be equal to 7.62 nm, or twice the value of R_g (see **Table 1**). This therefore suggests that at the first plateau, the adsorbed polymer is in a flat, or "pancake" type conformation, and is significantly more coiled compared to the free polymer in the bulk. From the previous discussion, however, the adsorbed polymer also undergoes some degree of elongation perpendicular to the surface.

The various works of Killmann *et al.*[11,14-16], however, did not explore the adsorption region beyond the first plateau. The present study shows that after the first plateau was reached, more PEO adsorption occurred when the equilibrium polymer concentration increased above approximately 6,000 mg·L^{-1} (see **Figure 2**). This resulted in the observation of a second plateau region at 1.20 mg·m^{-2} surface coverage, as illustrated in **Figure 2**. To the best of the authors' knowledge, the only other occurrences in the literature of a "two plateau" adsorption isotherm for PEO on silica surfaces, was in the recent study by Trens and Denoyel[17]. These researchers examined the effect that methyl and hydroxyl end groups on PEO of various molecular weights, had upon their adsorption to fumed silica. They observed similar behavior for the adsorption of hydroxyl terminated (as used in the present study), low molecular weight PEO on fumed silica at high equilibrium concentration. From their adsorption data, these authors showed that the affinity of terminal hydroxyl groups was greater than that of the ethoxy groups, and thus argued that as more polymer adsorbed onto the surface after the first plateau was reached, the adsorbed polymer molecules would partly "stand up", fixed by one or both ends, thereby allowing for the adsorption of more PEO. This change in conformation is illustrated in **Figure 5**. Although they only considered the case of a polymer with one surface-active terminal group and make no mention of "two plateau" adsorption isotherms as is observed in the present study, this conformational change is also consistent with the work of Fleer *et al.*[7]. They state that a polymer containing both a terminal group and chain segments which have an affinity for the surface, will adsorb in a "pancake type" conformation at low surface coverages, and then change to a "brush type" conformation, attached to the surface by the terminal group, as surface coverage increases.

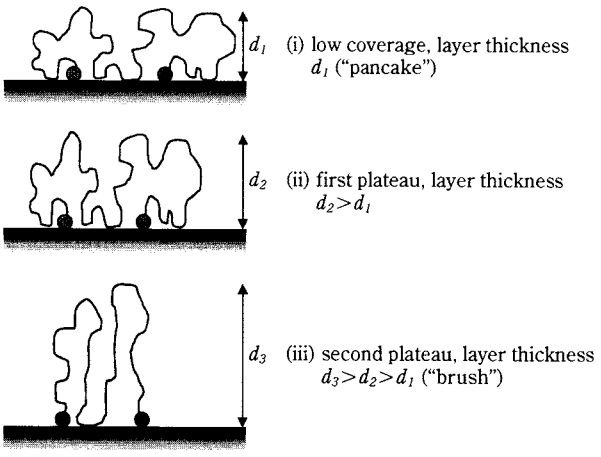

Fig. 5 Polymer conformation and layer thickness (d) at different surface coverages, where $d_1 < d_2 < d_3$.

Examination of the values of Γ_{max} and S_{exptl} for the second plateau in **Table 1** reveals the adsorbed PEO molecules occupy approximately three-and-a-half times less surface area in comparison to that occupied at the first plateau (10 nm^2 compared to 37 nm^2). This suggests that PEO undergoes significantly more elongation at surface concentrations beyond the first plateau.

Effect of Solids. From the inset of **Figure 2**, it can be seen that a PEO dose of 2.0 mg·(g solids)$^{-1}$ was sufficient for the first plateau to be reached at 50 %vol of silica. A PEO dose of 2.5 mg·(g solids)$^{-1}$ was therefore used for other volume fractions of silica, under the reasonable assumption that the plateau would also be reached in all cases. Additionally, a PEO dose of 1.0 mg·(g solids)$^{-1}$ was also used in order to be able to observe any effect of volume fraction in the more sensitive "knee" region of the adsorption isotherm. The adsorption as a function of volume fraction at the two PEO doses is illustrated in **Figure 3**, which shows that the adsorption density increases as a function of volume fraction until a plateau is reached at approximately 20 %vol. **Figure 4**, however, shows the adsorption isotherm of 7,500 MW PEO on 2 %vol SiO_2. From this diagram, it is apparent that a PEO dosage of 2.5 mg·(g solids)$^{-1}$ is insufficient for the (pseudo) plateau to be reached due to a very low number of polymer molecules being present in the system. Indeed, when the (first) plateau value is used in **Figure 3** (dashed line), it is apparent that there is no effect of volume fraction on the adsorption of PEO. This is an important observation, as previous experimental protocols for measuring the adsorption of polymers have been the same, in the past, irrespective of the solids loading of the suspension. This approach is valid for fixed (or constant) solids loadings. However, from the present experimental findings, in order to obtain equivalent surface coverages under different solids loading conditions, it is imperative to scale from one volume fraction to another with respect to the residual concentration as opposed to initial polymer dosage, as is mostly practiced. This is an important consideration for many industrial processes where the solids loadings can vary, such as flocculation and dispersion, as practiced in the ceramics and minerals processing industries.

Conclusions

The adsorption of PEO onto colloidal silica (SiO_2) spheres at different volume fractions was found to show two plateau values, the first of which was found to be consistent with those observed in previous studies employing similar polymer molecular weights (~7,500 MW). The second plateau was observed for higher equilibrium concentration values and was attributed to a change in the conformation of the adsorbed polymer molecules. The experimental evidence suggested that at low surface coverages, PEO was adsorbed in a flat, "pancake" type conformation, before changing orientation to a more elongated, "brush like" conformation at higher equilibrium concentrations, where both terminal hydroxyl groups are still attached to the silica surface.

Adsorption density measurements as a function of the solids loading studied in this work (2 %vol to 50 %vol) showed that there was no effect of volume fraction upon PEO adsorption. Rather, it was demonstrated that in order to obtain equivalent surface coverages at different volume fractions, scaling from one volume fraction to another should be done with respect to the equilibrium (C_{eq}), as opposed to the initial (C_o), polymer solution concentration.

Acknowledgement

The authors would like to acknowledge the experimental assistance of Mr. Pankaj Singh and Mr. Patrick Nguyen and helpful discussions with Professor P. Somsundaran (Columbia University). Additionally, the financial support of the Engineering Research Center (ERC) for Particle Science and Technology at the University of Florida (NSF Grant No. EEC-94-02989), and the Industrial Partners of the ERC, is also acknowledged.

References

1) Cesarano, J. and Aksay, I. A. *J. Am. Ceram. Soc.* **1988**, *71(12)*, 1062.
2) Heijman, S. G. J. and Stein, H. N. *Langmuir* **1995**, *11*, 422.
3) Liang, W., Tadros, Th. F. and Luckham, P. F. *J. Colloid Int. Sci.* **1992**, *153(1)*, 131.
4) Liu, S. F., Lafuma, F. and Audebert, R. *Colloid Polym. Sci.* **1994**, *272*, 196.
5) Napper, D. H. In *Polymer Stabilization of Colloidal Dispersions*; Academic Press: New York, 1982.
6) Sigmund, W. M., Bell, N. S. and Bergström, L. *J. Am. Cer. Soc.*, in press.
7) Fleer, G., Cohen Stuart, M. A., Scheutjens, J., Cosgrove, T., and Vincent, B. In *Polymers at Interfaces*; Chapman & Hall: London, 1993.
8) Fleer, G. J. and Lyklema, J. In *Adsorption From Solution at the Solid/Liquid Interface*; Parfitt, G. D. and Rochester,

C. H., Eds.; Academic Press: New York, 1983; Chapter 4.
9) Kim, B. S., Hayes, R. A. and Ralston, J. *Carbon*, **1995**, *33(1)*, 25.
10) Bailey, Jr., F. E. and Koleske, J. V. In *Poly (ethylene oxide)*; Academic Press; New York, 1976.
11) Killmann, E., Wild, Th., Gutling, N. and Maier, H. *Colloids and Surfaces* **1986**, *18*, 241.
12) Scheutjens, J. M. H. M. and Fleer, G. F. *J. Phys. Chem.* **1980**, *84*, 178.
13) Fleer, G. F. and Scheutjens, J. M. H. M. *Adv. Colloid Interface Sci.* **1982**, *26*, 62.
14) Killmann, E., Maier, H., Kaniut, P. and Gutling, N. *Colloids and Surfaces* **1985**, *15*, 261.
15) Killmann, E., Maier, H. and Baker, J. A. *Colloids and Surfaces* **1988**, *31*, 51.
16) Killmann, E. and Sapuntzjis, P. *Colloids and Surfaces A* **1994**, *86*, 229.
17) Trens, P and Denoyel, R. *Langmuir* **1993**, *9*, 519.

Author's short biography

Mick Bjelopavlic

Dr. Mick Bjelopavlic is a Research Associate in the Department of Materials Science and Engineering and the Engineering Research Center for Particle Science and Technology at the University of Florida, Gainesville, FL. He received his BSc in 1991 and BSc(Honors) in Physical and Inorganic Chemistry in 1992 at the University of Adelaide, Australia. He continued his graduate studies at the University of South Australia, Australia, and received a PhD in Chemical Technology. He was a Research Scientist at the Australian Water Quality Centre from 1996-98 prior to receiving a Research Fellowship at the University of Florida.
His current research interests include polymer and surfactant adsorption, particulate dispersion and flocculation, selective surfactant design, and rheology of concentrated suspensions.

Abbas A. Zaman

Dr. Abbas A. Zaman is an Assistant Professor in Engineering Research Center for Particle Science and Technology and an adjunct professor in the Department of Materials Science and Engineering at the University of Florida, Gainesville. He received his BS. and MS. in Chemical Engineering from University of Tehran, Iran. He continued his graduate studies at the University of Florida, Gainesville, and received his PH.D degree in Chemical Engineering.
His current research interests include Rheology of complex fluids, Mathematical Modeling, Numerical Methods, Computational Fluid Mechanics with application in polymers, crystal growth, suspensions, heat and mass transfer processes, and Pulp and Paper.

Brij M. Moudgil

Dr. Brij M. Moudgil is a Professor in the Department of Materials Science and Engineering, and Director of the Engineering Research Center for Particle Science and Technology at the University of Florida, Gainesville, FL. Dr. Moudgil also serves as the Director of the UF Mineral Resources Research Center. He received his undergraduate training in Metallurgical Engineering at the Indian Institute of Science, Bangalore. He continued his graduate studies at Columbia University, New York, and received M.S. and Eng.Sc.D. degrees in Mineral Engineering – Particulate Processing.
His current research interests include polymer and surfactant adsorption, dispersion and aggregation of fine particles, particulate processing for advanced materials, solid-solid and solid-liquid separations, crystal modification, and rheology of concentrated suspensions.

Effect of Surfactant and Polymer Adsorption on the Viscosity of Aqueous Colloidal Silica Dispersions under Extreme Conditions†

A.A. Zaman[1], P.K. Singh[2] and B.M. Moudgil[2]
[1] *Department of Chemical Engineering*
[2] *Department of Materials Science and Engineering*
*Engineering Research Center for Particle Science and Technology**

Abstract

The effect of surfactant and polymeric additives on the viscosity behavior and stability of aqueous colloidal dispersions of silica particles under extreme conditions (low pH, high ionic strength) has been investigated. The surfactant and polymer used as dispersing agent were $C_{12}TAB$, a cationic surfactant, and DarvanC, a commercially available polymer. It was found that the surfactant stabilized dispersions show a lower viscosity and a more uniform resistance to flow than the samples stabilized through electrostatic repulsion or polymer induced forces in the system. Stability analysis through turbidity measurements indicated that the state of the dispersion changes from an unstable regime to a stable regime above a critical concentration of $C_{12}TAB$ in the system. Viscosity measurements as a function of temperature indicates that $C_{12}TAB$ dispersing agent can further improve the flowability of the dispersion at higher temperatures

1. Introduction and Background

Stability and viscosity behavior of concentrated colloidal dispersions of solids is determined by the combined effects of different factors such as Brownian motion of the particles, hydrodynamic interactions, interparticle forces, as well as physical characteristics of the particles such as particle size, particle size distribution, and shape of the particles. Colloidal dispersions are encountered in various industrial processes such as paints, paper coatings, ceramic and minerals, chemical-mechanical polishing, and pharmaceuticals. In most of the applications, colloidal dispersions need to be stabilized against aggregation and agglomeration of the particles using stabilizing agents such as salt, surfactants, polymers, and polyelectrolytes. Particle-particle interactions arising from the adsorbed and dissolved polymers and surfactants as well as van der Waals attractive forces and electrostatic repulsive forces due to the diffuse part of the electrical double layers around the charged particles play a very significant role in governing stability and rheological behavior of colloidal dispersions.

Even though the topic of electrostatic stabilization has been extensively studied by many investigators (1-3) and the DLVO theory is now largely accepted as a classical description for stability of colloidal dispersions through electrostatic repulsion, but when surfactants and polymers are used as stabilizers, surfactant interactions and steric forces do not fit this theory leaving a problem of both experimental and theoretical interest.

Additionally, the increasing use of suspensions of nanosized particles in severe environments such as high electrolyte concentrations, high pressures, high shear and high pH levels in applications such as chemical mechanical polishing, consolidation, pumping, deaggregation, grinding, homogenization, high speed coatings, and crystal growth necessitates the development of versatile dispersants capable of dispersing the nanoparticles under severe environments. At high salt concentrations, electrostatic repulsive forces will be of very short range and do not protect the colloidal particles against coagulation. Stabilization of such dispersions may be achieved through the addition of surfactants as dispersing agents to the suspending media. It is very important to identify the conditions (dosage, pH, etc.) at which the added surfactant will stabilize the system.

Electrostatic repulsion is often applied to stabilize dispersions of solid particles at low levels of ionic strength where pH can be controlled in order to pro-

* University of Florida, Gainesville, FL 32611, USA
† Received: May 16, 2000

vide sufficient surface charge. Considering that the electrostatic repulsive energy between the suspended particles decreases as the size of the particles is decreased, a greater surface potential is required to stabilize dispersions of nanoparticulates of smaller sizes. Under these conditions, pH adjustment or addition of inorganic dispersants such as sodium silicate may not lead to a dispersion of sufficient stability against aggregation and agglomeration of the particles.

Since most of the traditionally used polymeric dispersants are similar in size to the nanoparticles, hence in the case of highly concentrated dispersions, there will be a significant increase in the effective volume fraction of the particles that may adversely affect the fluidity of the system. When polyelectrolytes are used as stabilizing agents, stability will be imparted through a combination of electrostatic and steric repulsion. At high electrolyte concentration and extreme pH conditions, these dispersants may not perform adequately due to charge neutralization and insufficient ionization.

Surfactants provide a viable alternative for stabilization of the dispersions of nanoparticles under extreme conditions due to the small thickness of the adsorbed surfactant layer, controlled adsorption, and reversibility of adsorption. Surfactants have been used in various industrial processes ranging from ore flotation, lubrication, and paint technology to enhanced oil recovery (4). Forces between surfactant coated surfaces have been measured by several investigators (5-7) in order to understand the surfactant adsorption and also to predict the nature of the aggregate formed by surfactant molecules on surfaces. Also, surfactants have been used for the dispersion of particulates in aqueous media by researchers such as Evanko et. al (8), Huang and Somasundaran (9), Colic and Fuerstenau (10), Colic and Fuerstenau (11), Koopal et al (12), Bremmell et al. (13), and Solomon et al. (14). In this work a systematic study has been performed on the role of surfactants (as dispersing agents) on stability and fluidity of colloidal aqueous silica dispersions at high electrolyte concentrations.

2. Methods

Silica powder of 99.9% purity used in this study was obtained from Geltech, Inc. The powder was used as received and had a nominal diameter of 200 nm, as stated by the manufacturer. The experimentally measured volume average (d_{50}) particle diameter (using a Coulter LS230 laser diffraction apparatus) of the powder was found to be 250 nm. Powder density and surface area were found to be 2.1 g/cm^3 and 14.62 m^2/g respectively.

Dodecyltrimethylammonium bromide (C_{12}TAB) of 99 % purity was obtained from Aldrich Chemical Company and used as received. Surfactant stock solutions of different concentrations were prepared in an electrolyte solution of 0.1 M Fisher brand NaCl and stirred using a magnetic stirrer in order to achieve complete dissolution. The surfactant dosage was calculated so that the bulk concentration of the surfactant, i.e surfactant left in the suspending fluid after adsorption onto the surface of the particles was 32 mM at all solids loading. For suspensions of 250 nm silica particles at 45 %vol and 50 %vol the surfactant concentration was determined to be 250 mM and 300 mM respectively. The CMC (critical micelle concentration) of Dodecyltrimethylammonium bromide (C_{12}TAB) was determined to be 8 mM with 0.1 M NaCl and at a value of CMC, the surfactant aggregate structure is very stable and can provide steric barrier to the agglomeration of the particles. All experiments were conducted in ultra pure water (DI) of specific conductivity less than 1 μohm/cm. Sodium chloride (NaCl) was used as background electrolyte and sodium hydroxide (NaOH) and Hydrochloric acid (HCl) were used as pH modifiers. These reagents were of ACS grade and obtained from Fisher Scientific Company.

Silica slurries were prepared by gradually adding silica powder to the electrolyte or electrolyte-surfactant solutions. The required mass of dry silica (to prepare 10 cm^3 of the suspension at a given volume fraction of the particles) was then slowly added to the solution while mixing the sample by shaking and vibration. After addition of silica, the suspensions were vigorously shaken by hand and then the pH of the samples was adjusted to 4 using HCl solution. After the pH adjustments, samples were sonicated for at least 30 minutes in order to break up any aggregates. The suspensions were then agitated using a Burrell Model 75 Wrist Shaker for a period of 16−20 hours in order for equilibrium to be reached. During equilibration, the pH of the suspensions was checked periodically and readjusted if required.

Viscosity measurements were carried out using a Paar Physica UDS 200 rheometer with a cone-and-plate geometry. All experiments were performed at 25°C and the sample temperature was controlled to within ±0.1°C using water as the heat transfer fluid. In all experiments, a cone of radius 4.30 cm with a cone angle of 0.5° (a gap size of 25 μm) was used. Viscosity measurements as a function of time (at a fixed shear rate) indicated that sedimentation of the particles and

water evaporation from the samples during experiments were negligible. To check for other possible errors (e.g, inertial and secondary flows, edge effects, etc.), some of the experiments were repeated using a cone of radius 3.75 cm with a cone angle of 1.0° (a gap size of 50 μm). The results did not change over the time period of experiments and the viscosity values measured with two different cones agreed within experimental error (±3%).

Stability analysis on the samples was performed by measuring turbidity of the dispersions as a function of time and surfactant concentration using a Hach Model 2100AN turbidimeter. The optical system of the instrument consists of a tungsten filament lamp, lenses, and apertures to focus the light, a 90° detector to monitor scattered light, a forward-scatter light detector, a transmitted light detector, and a back scattered light detector.

For turbidity measurements, samples were prepared by adding 0.05 grams of silica particles to 50 ml of suspending fluid (surfactant solutions of different concentrations in 0.1 M NaCl solution). Samples were then sonicated for 10 minutes and the pH of the dispersion was then adjusted to 4.0 using Fisher brand HCl. The suspensions were then allowed to shake for 2 hours on a wrist shaker and if needed the pH was re-adjusted to 4.0 prior to the turbidity measurements.

Zeta potential measurements were carried out using a Laser Zee Meter (Model 501) instrument supplied by PenKem Inc. Using this instrument, zeta potential is determined based on electrophoresis phenomena. In this method, the velocity of multiple particles with respect to a stationary fluid is measured in a potential gradient applied between platinum and molybdenum electrodes using a rotating prism and then used to determine the zeta potential.

For zeta potential measurements, silica slurries were prepared by adding 0.1 grams of 250 nm (diameter) silica particles to 50 ml of suspending media following the same procedure that was explained in preparing samples for turbidity measurements.

3. Results

3.1 Zeta Potential

Figure 1 presents zeta potential as a function of surfactant concentration for suspensions of 250 nm (diameter) silica particles dispersed in a 0.1 M NaCl solution (suspension pH=4). When a cationic surfactant such as C_{12}TAB is added to the dispersion of charged particles, electrical double layer around the particles and therefore, the zeta potential will be

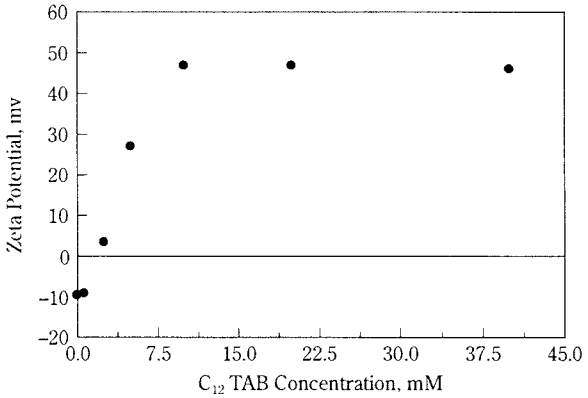

Fig. 1 Effect of C_{12}TAB concentration on the zeta potential of 250 nm (diameter) silica dispersions prepared in an electrolyte solution of 0.1 M NaCl (25°C and pH=4).

altered due to the adsorption of surfactant molecules onto the surface of the particles. It can be observed from **Figure 1** that while at low levels of C_{12}TAB concentration (less than 2.5 mM) the zeta potential values indicate a negative charge on the surface of the particles, at higher levels of surfactant concentration, silica particles will be positively charged and there will be an increase in the magnitude of the zeta potential as particles are gradually covered by surfactant molecules.

The zeta potential of the bare silica surface at pH 4.0 in the presence of 0.1 M NaCl is approximately equal to −10 mV. It can be observed that, as the amount of surfactant added to the dispersion is increased, there is no observable change in the zeta potential till a critical concentration of C_{12}TAB, which appears from the data given in **Figure 1** to be approximately equal to 0.6 mM. Beyond this concentration which is equal to critical hemi-micelle concentration (15), the original charge of the surface is neutralized by the adsorption of oppositely charged surfactant by ion pairing. The surface charge eventually acquires the same sign as the surfactant ion (positive in the case of C_{12}TAB) due to formation of bi-layers of the surfactant molecules. As the surfactant concentration is increased further (beyond 8 mM surfactant concentration), the rate of adsorption decreases due to repulsion between oncoming ions and similarly charged particle surface and finally saturation adsorption is achieved. Correspondingly, the slope of the zeta potential curve also decreases and finally the zeta potential reaches a plateau value of +45 mV.

3.2 Stability of Dilute SiO_2 Dispersions in the Presence of C_{12}TAB

Based on the DLVO theory of colloidal stability, an important factor influencing stability of aqueous

colloidal dispersions is the surface potential of the particles. The repulsive interactions between the suspended particles hinder aggregation and agglomeration of the particles providing a certain degree of stability. Effect of C_{12}TAB concentration on the stability of dilute SiO_2 dispersions prepared in an electrolyte solution of 0.1 M NaCl (suspension pH=4) was evaluated through measurement of the turbidity of the dispersion as a function of time. Turbidity of the dispersion in the absence of C_{12}TAB was very low indicating a high sedimentation rate of solids due to the presence of aggregates in the system. Above a critical concentration of C_{12}TAB in the system, there was a significant increase in the turbidity of the dispersion indicating a transition from an unstable regime to a stable regime after which the turbidity attained a constant value indicating no significant change in the stability of the system.

3.3 Shear Flow Properties

Stability and rheological behavior of colloidal dispersions can be significantly affected by the adsorption of surfactant molecules onto the surface of the particles (16). Dispersions of colloidal particle can show different rheological behavior such as shear thinning, shear thickening, yield stress, and viscoelasticity depending upon the general characteristics of the system. (17-19). **Figure 2** is a plot of viscosity as a function of shear rate for suspensions of 250 nm silica particles at solids loading of 45 %vol and 50 %vol prepared in aqueous solutions of 0.1 M NaCl containing 250 mM and 300 mM C_{12}TAB respectively (suspension pH=4). The viscosity shows changes with both shear rate and volume fraction of the particles. Both samples exhibit non-Newtonian behavior and there is no indication of shear thickening behavior over the entire range of shear rate investigated (1 s^{-1} up to 15,000 s^{-1}). While we were not able to prepare a dispersion of 50 %vol silica particles in an electrolyte solution of 0.1 M NaCl in the absence of C_{12}TAB, addition of surfactant to the suspending media made it possible to prepare a well dispersed slurry of low viscosity.

Figure 3 is a comparison between the viscosity of dispersions of 250 nm silica particles at 45 %vol prepared at two different conditions. The first sample was prepared in an electrolyte solution of 0.001 M NaCl without the addition of surfactant and the second sample was prepared in an electrolyte solution of 0.1 M NaCl and 250 mM C_{12}TAB (the pH of both samples was adjusted to 4). While the first sample is stabilized through long range electrostatic repulsion between the suspended particles, the second sample is stabilized through surfactant induced forces due to the adsorption of C_{12}TAB molecules onto the surface of the particles. There is a significant difference between the viscosity of the two samples even at very high shear rates where hydrodynamic forces are dominant. Surfactant stabilized dispersion shows a lower and a more uniform resistance against flow than electrostatically stabilized dispersion. This indicates that C_{12}TAB is a more effective despersing agent for silica slurries under extreme condition.

The data presented in **Figure 3** indicate that the differences between the viscosity of the samples are more significant at low shear rates. Suspensions of particles in shear flows experience different kind of forces such as hydrodynamic forces (including the viscous drag force and particle-particle interaction through flow field induced by neighboring particles), colloid chemical forces (including electrostatic, steric, and London-van der Waals attractive forces), forces

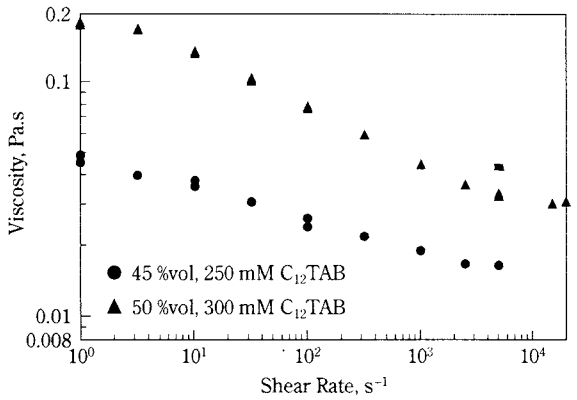

Fig. 2 Viscosity as a function of shear rate for 250 nm (diameter) dispersions of silica particles of 45 %vol and 50 %vol stabilized with C_{12}TAB (0.1 M NaCl, 25°C and suspension pH=4).

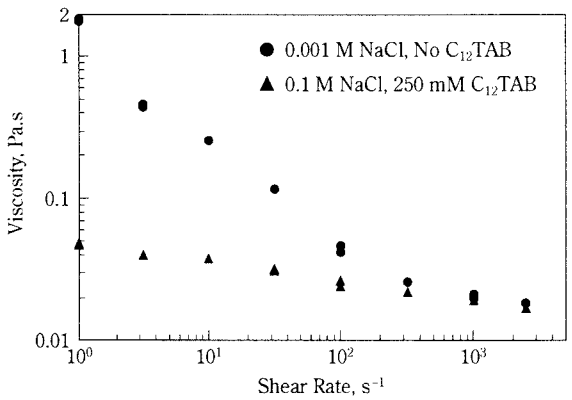

Fig. 3 Comparison between the viscosity of electrostatically stabilized (0.001 M NaCl) and surfactant stabilized (0.1 M NaCl, 250 mM C_{12}TAB) dispersions of 250 nm (diameter) silica particles of 45 %vol (25°C and suspension pH=4).

due to gravitational, inertial, electroviscous, and thermal or molecular collisional effects. The observed differences between the viscosity of the two samples indicate that interparticle forces and also type of the interactions (e.g., electrostatic versus steric) control the flow behavior of concentrated colloidal dispersion at low shear rates.

3.4 Effect of Temperature on the Viscosity and Stability of SiO_2 Dispersions in the Presence of C_{12}TAB

Figure 4 represents the effect of temperature on the viscosity of a 50 %vol dispersion of 250 nm silica particles prepared in an electrolyte solution of 0.1 M NaCl containing 280 mM of C_{12}TAB surfactant (suspension pH=4) at a shear rate of 50 s^{-1}. It can be seen that over the temperature range studied, the viscosity of the dispersion initially decreases with increasing temperature, reaches a minimum at approximately 55°C and then increases with further increase in temperature. This indicates that C_{12}TAB dispersing agent can further improve the flowability of the dispersion at higher temperatures. Increase in temperature will increase Brownian motion of the particles which is in favor of increasing the viscosity of the dispersion due to increase in number of collision between the suspended particles. On the other hand there will be a decrease in the viscosity of the suspending fluid with increasing temperature, which tends to decrease the viscosity of the dispersion over the entire range of temperature. When surfactants are present in the system, change in temperature will affect several other important factors such as intermolecular interactions between solvent and solutes (e.g, hydrogen bonding), cmc of surfactant, and micellization. It is shown by Flockhart (20) that the cmc of most ionic surfactants goes through a minimum as the temperature is increased from 0°C to 70°C. Also, it was found by Cook et el. (21) that cmc of some nonionic surfactants is minimum around 50°C. These indicate that one needs to have a clear understanding of the effect of temperature on all the above mentioned factors to be able to explain the effect of temperature on the viscosity of the dispersion. However, this needs to be further investigated.

3.5 Effect of the Type of the Stabilization on the Viscosity of Silica Dispersions

Another method that is widely used to improve the rheological properties and stability of colloidal suspensions is the addition of polymers to the system. When water soluble polymers are added to the suspension, the polymer may be adsorbed on the particle surface. The distribution of the polymer molecules in the solution is affected by particle-particle interactions producing a force whose sign and magnitude depends on the nature of the particle-polymer interaction (22). The adsorbed polymer can either stabilize or destabilize the suspension depending upon the magnitude of the repulsive forces between the adsorbed polymer molecules. Steric stabilization occurs when the repulsive forces overcome the attractive van der Waals forces acting between the particle surfaces.

The effect of DarvanC, a commercially available polymeric dispersant on the viscosity of silica suspensions is presented in **Figure 5** which is a plot of viscosity as a function of polymer dosage for aqueous silica slurries at 50 %vol (dispersed in a solution of 0.1 M NaCl and suspension pH=4) at different shear rates. It can be observed that the viscosity of the suspension initially decreases to a minimum with increasing the polymer dosage and then starts to increase with

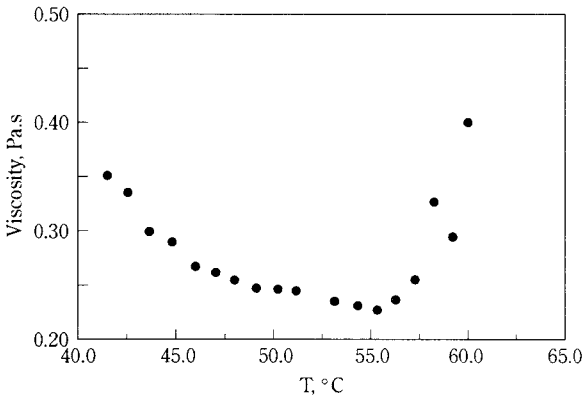

Fig. 4 Effect of temperature on the viscosity of a surfactant stabilized (0.1 M NaCl, 280 mM C_{12}TAB) dispersion of 250 nm (diameter) silica particles of 50 %vol at a shear rate of 50 s^{-1} (suspension pH=4).

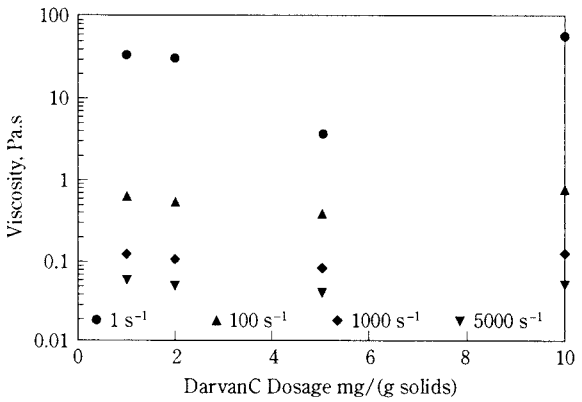

Fig. 5 Effect of DarvanC dosage on the viscosity of dispersions of 250 nm (diameter) silica particles of 50 %vol at different shear rates (0.1 M NaCl, suspension pH=4, 25°C).

further addition of polymer to the suspension. There is a critical amount of polymer (5 mg/g solids for the system under consideration) that must be added to the system to achieve minimal viscosities. It can be seen from this figure that the effect of polymer dosage on the viscosity of the system is more significant at lower shear rates as might be expected.

Figure 6 is a comparison between the viscosity of the above mentioned system with the viscosity of a dispersion of silica particles in the presence of C_{12}TAB as stabilizing agent. Even though at very high shear rates the viscosity of the two systems tends to approach a final limiting value, but surfactant stabilized dispersion shows a lower resistance to flow at low to intermediate shear rates as the viscosity of surfactant stabilized system is significantly lower than the viscosity of the dispersion in the presence of DarvanC. This indicates that C_{12}TAB surfactant is more effective than the polymeric dispersant in terms of improving the low to intermediate shear flow properties of the dispersion.

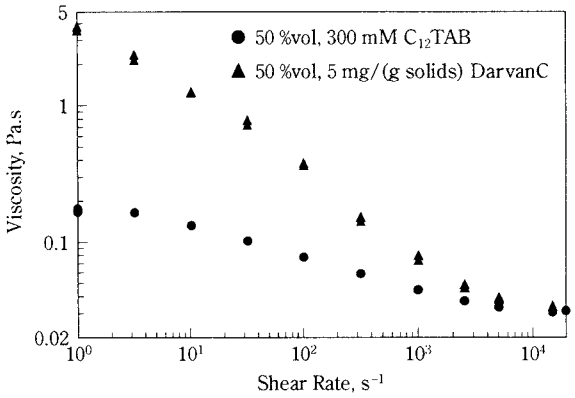

Fig. 6 Comparison between the viscosity of electrosterically stabilized (0.001 M NaCl) and surfactant stabilized (0.1 M NaCl, 250 mM C_{12}TAB) dispersions of 250 nm (diameter) silica particles of 45 %vol (25°C and suspension pH=4).

Summary

The role of surfactant and polymer adsorption on flow properties and stability of concentrated aqueous silica dispersions under extreme conditions has been investigated. DarvanC, a commercially available polymer and C_{12}TAB, a cationic surfactant were used to stabilize dispersions of silica particles under high ionic strength and low pH. It is shown that surfactant stabilized silica dispersions show a better fluidity and a more uniform resistance to flow than the samples stabilized through electrostatic repulsion or polymer induced forces in the system.

As the amount of surfactant added to the dispersion is increased, while there is no significant change in the magnitude of the zeta potential below a critical concentration of the surfactant (critical hemi-micelle concentration), the negative zeta potential of the particles will go through zero as the surfactant concentration is increased and finally will approach a final limiting value at higher surfactant concentrations. Stability analysis through turbidity measurements indicated that while sedimentation rate of the solids is very high at low levels of surfactant dosage (low turbidity), as the surfactant concentration is increased, there will be a significant increase in turbidity of the samples indicating that the state of the dispersion changes from an unstable regime to a stable regime above a critical surfactant dosage. Zeta potential measurements as well as turbidity measurements indicate that both zeta potential and turbidity will attain constant values at high surfactant concentrations.

Effect of temperature on the viscosity of 50 %vol silica dispersion prepared in the presence of surfactant was also studied. Over the temperature range studied, the viscosity of the dispersion initially decreased with increasing temperature, reached a minimum at approximately 55°C and then increased with further increase in temperature. Since change in temperature will affect several important parameters such as Brownian motion of the particles, viscosity of the suspending fluid, intermolecular interactions between solvent and solutes, cmc of surfactant, and micellization, the combined effect of temperature on all these variables should be considered to be able to explain the effect on the viscosity of the dispersion.

Acknowledgments

The authors are grateful for the financial support provided by the University of Florida Engineering Research Center for Particle Science and Technology (NSF Grant No. EEC-94-02989) and the industrial partners of ERC. Helpful discussions with Dr. D. O. Shah, Dr. Y. Rabinovich, and Mr. J. Adler are greatly acknowledged.

References

1) Derjaguin, B. V., Landau, L. D., I., *Acta Physicochim USSR*, 1941, 14, 633.
2) Verwey, E. J. W., Overbeek, J. Th. G., *Theory of stability of lyophpobic colloids*, 1948, Elsevier.
3) Israelachvili, N. J., *Intermolecular and Surface Forces*, 1985, Academic Press, London.

4) Rosen, M. J., *Surfactants and Interfacial Phenomena*, 1989, John Wiley and Sons, New York.
5) Pashley, R. M., McGuiggan, P. M., Horn, R. G., and Ninham, B. W., Journal of Colloid and Interface Science, 1988, 126(2), 569.
6) Chen, Y. L., Chen, S., Frank, C., and Israelechvilli, J., Journal of Colloid and Interface Science, 1992, 153(1), 244.
7) Rutland, M. W., and Parker, J. L., Langmuir, 1994, 10, 1110.
8) Evanko, C. R., Dzombak, D. A., and Novak Jr., J. W., Colloids and Surfaces A: Physicochemical and Engineering Aspects, 1996, 110, 219.
9) Huang, L., and Somasundaran, P., Colloids and Surfaces A: Physicochemical and Engineering Aspects, 1996, 117, 235.
10) Colic, M., and Fuerstenau, D. W., Langmuir, 1997, 13, 6644.
11) Colic, M., and Fuerstenau, D. W., Powder Technology, 1998, 97, 129.
12) Koopal, L. K., Goloub, T., Keizer, A., and Sidorova, M. P., Colloids and Surfaces A: Physicochemical and Engineering Aspects, 1999, 151, 15.
13) Bremmell, K. E., Jameson, G. J., and Biggs, S., Colloids and Surfaces A: Physicochemical and Engineering Aspects, 1999, 146, 75.
14) Solomon, M. J., Saeki, T., Wan, M., Scales, P. J., Boger, D. V., and Usui, H., Langmuir, 1999, 15, 20.
15) Wakamatsu, T., and Fuerstenau, D. W., in Adsorption from Aqueous Solution, ed. by W. J. Weber, Jr. and E. Matijevic, American Chemical Society, Washington DC, 1968, 161.
16) Chen, X., Cheng, H., and M. Jiming, Powder Technology, 1998, 99, 171.
17) Russel, W. B., J. Fluid Mech., **85**, 209-232 (1978).
18) Jeffrey, D. J., and Acrivos, A., AIChE J. 22(3), 417-432 (1976).
19) Krieger, I. M., Trans. Soc. Rheol., 7, 101-109 (1963).
20) Flockhart, B. D., Journal of Colloid and Interface Science, 1961, 16, 484.
21) Cook, E. H., Fordyce, D. B., Trebbi, G. F., Journal of Physical Chemistry, 1963, 67, 1987.
22) Russel, W. B., Saville, D. A., and Schowalter, W. R., *Colloidal Dispersions*, 1991, Cambridge University Press, New York, NY.

Author's short biography

Abbas A. Zaman

Dr. Abbas A. Zaman is an Assistant Professor in Engineering Research Center for Particle Science and Technology and an adjunct professor in the Department of Materials Science and Engineering at the University of Florida, Gainesville. He received his BS. and MS. in Chemical Engineering from University of Tehran, Iran. He continued his graduate studies at the University of Florida, Gainesville, and received his PH.D degree in Chemical Engineering.
His current research interests include Rheology of complex fluids, Mathematical Modeling, Numerical Methods, Computational Fluid Mechanics with application in polymers, crystal growth, suspensions, heat and mass transfer processes, and Pulp and Paper.

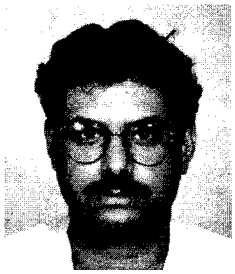

Pankaj K. Singh

Pankaj Singh is a graduate student in Materials Science and Engineering at the University of Florida. He is currently pursuing his Ph.D degree. He obtained his BTech. Degree in Materials and Metallurgical Engineering from the Indian Institute of Technology, Kanpur and his M.S degree in Materials Science and Engineering from the University of Florida. His current research is on the use of self assembled surfactant/polymer aggregates at interfaces for dispersion of nanoparticulates under severe environments such as high salt, extreme pH and high pressures.

Brij M. Moudgil

Dr. Brij M. Moudgil is a Professor in the Department of Materials Science and Engineering, and Director of the Engineering Research Center for Particle Science and Technology at the University of Florida, Gainesville, FL. Dr. Moudgil also serves as the Director of the UF Mineral Resources Research Center. He received his undergraduate training in Metallurgical Engineering at the Indian Institute of Science, Bangalore. He continued his graduate studies at Columbia University, New York, and received M.S. and Eng.Sc.D. degrees in Mineral Engineering – Particulate Processing.
His current research interests include polymer and surfactant adsorption, dispersion and aggregation of fine particles, particulate processing for advanced materials, solid-solid and solid-liquid separations, crystal modification, and rheology of concentrated suspensions.

The Production of Thin Metal Oxide Films by Spray Pyrolysis Using Supercritical CO_2-Assisted Aerosolization of Aqueous Solutions†

Scott P. Sellers, Bobbi A. Miles, and Robert E. Sievers*
Department of Chemistry and Biochemistry, University of Colorado
Ward Halverson
Spire Corporation

Abstract

Thin metal oxide films have been deposited onto various substrates, under ambient pressure, utilizing supercritical CO_2-assisted nebulization of aqueous solutions. In this process, supercritical CO_2 is contacted with an aqueous precursor solution inside a low-dead-volume tee. The resulting emulsion is allowed to expand out of a capillary restrictor, and the fine particle aerosol formed is directed toward heated substrates. Dehydration, pyrolysis and oxidation of the precursors occur at or near the surface of the substrate to form the desired metal oxide film. Thin films of zinc oxide, zinc gallate and manganese-doped zinc gallate have been prepared using this technique.

1. Introduction

Thin films of zinc oxide have recently received much attention due to their multifunctional nature. In addition to being transparent wide band-gap semiconductors, thin films of zinc oxide have piezoelectric capabilities. Potential applications of these films include transparent electrodes [1], solar cells [2,3], surface acoustic wave devices [4] and pressure/vibration detectors [5]. Several methods have been used to deposit high quality thin films of zinc oxide, including rf sputtering [6], chemical vapor deposition [7,8] laser ablation [9], conventional spray pyrolysis [10,11,12] and spray pyrolysis with ultrasonic nebulization [13,14,15]. In this study, it is demonstrated that the production of transparent thin films of zinc oxide is possible via a new spray pyrolysis technique using supercritical CO_2-assisted nebulization.

2. Supercritical CO_2-assisted Nebulization

Supercritical CO_2-assisted nebulization utilizes the properties of supercritical carbon dioxide (CO_2 that has been pressurized above its critical pressure (1070 psi) and heated above its critical temperature (31°C)) to assist in the production of aerosols of aqueous solutions. One of the most relevant properties is the solubility of carbon dioxide in water, with up to one to two mole percent of CO_2 dissolving in water at temperatures between ambient and 40°C and at equilibrium pressures of 1070 to 2000 psi. A diagram of the system used for supercritical CO_2-assisted nebulization is shown in **Figure 1**. Supercritical or near critical CO_2 is pumped into one side of a low-dead volume tee, while an aqueous precursor solution containing metal salts or other dissolved species is simultaneously pumped into another leg of the tee. The intimate mixing of the two streams generates an emulsion of aqueous droplets with dissolved CO_2 surrounded by supercritical or near-critical CO_2. The emulsion is not resident in the tee long enough to reach solubility equilibrium,

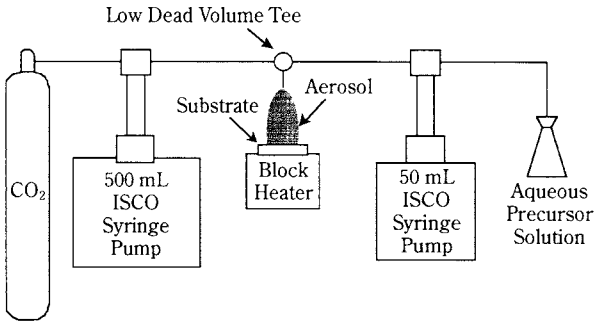

Fig. 1 Schematic for the supercritical CO_2-assisted nebulization system used for thin film deposition.

* To whom correspondence should be directed
† Received: May 16, 2000

but pH indicator studies have shown that significant amounts of CO_2 become dissolved in the aqueous droplets. The resultant emulsion is then allowed to expand out of a fused silica or stainless steel capillary pressure restrictor with a very narrow diameter (50−150 μm i.d.). Upon decompression into a heating chamber containing air at atmospheric pressure, shear forces and the rapidly expanding CO_2 (CO_2 that is dissolved in the aqueous droplets and the gaseous CO_2 surrounding the droplets) produce a dense aerosol plume of very fine droplets containing the dissolved metal salts. The water droplets rapidly dehydrate to form fine particles in dry air with diameters of approximately 1 μm. The aerosol is directed toward a heated substrate, under ambient pressure, where water evaporation and pyrolysis and/or oxidation of the metal precursors occur to form the desired metal oxide thin film.

The supercritical CO_2-assisted nebulization method used for thin film deposition permits the formation of films that are chemically different from the precursors used. A wider variety of films can be formed using this method, which does not require that the precursors be volatile. Any metal-containing precursor compound or mixture of compounds that is soluble in the supercritical fluid or can form a heterogeneous emulsion in the supercritical fluid can be used as a thin film precursor. CO_2 is the supercritical fluid of choice since it is less expensive than any organic solvent, avoids the emission of organic solvent vapors, is nonflammable, and is relatively non-toxic. Sievers and coworkers have been issued several patents for this technology and have employed these methods to form thin films and powders that are potentially useful as phosphors, optical coatings, high temperature protective materials, superconductors, and electronic materials. [16] Whether one forms fine particles or thin films as a final product depends on the experimental apparatus, and heating and diluent gas dynamics. In tube heaters, with gas sheath flow to reduce particle contact with the walls of the dehydration/pyrolysis/oxidation chamber, fine particles (often spherical) are generated rather than films. [16g]

3. Experimental System and Procedure

The precursor solution was transported to the low-dead-volume stainless steel mixing tee (Valco) by an automated ISCO syringe pump set to a constant flow rate (0.3 to 2 mL/min). Carbon dioxide (Scott Specialty Gases, SFE grade) was added to a separate ISCO syringe pump, pressurized above the critical pressure (1100 psi), and then set to deliver at a constant pressure. The third leg of the mixing tee was fitted with either a fused silica capillary restrictor (Alltech, 50 and 75 μm i.d.), or 1/16″ stainless steel tubing (100 and 170 μm i.d.) approximately 4 cm in length. The tip of the restrictor was positioned approximately 8 cm from the center of a ceramic hotplate which was used to heat the silicon substrates. Soda lime glass substrates were heated inside a horizontally mounted tube furnace in order to prevent substrate cracking. The angle of the flow restrictor tubing with the surface was varied between 90 and 180°, and the expected differences in substrate cooling and deposition shapes were noted. The details of the system used to deposit onto glass substrates are shown in **Figure 2**. Substrate temperatures ranged from 350 to 500°C for both silicon and glass. Common parameters and settings for this system are summarized in **Table 1**.

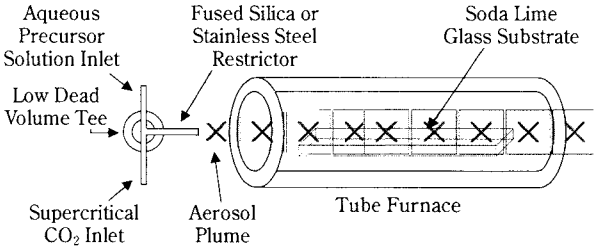

Fig. 2 Detail of nebulization and tube furnace used for soda lime glass substrates.

Table 1 Common system parameter settings for the deposition of zinc oxide thin films using supercritical CO_2-asssisted nebulization.

Parameter	Typical Setting
CO_2 Pressure	1100 psi
Precursor Flow Rate	0.3−2.0 mL/min
Substrate Temperature	350−500°C
i.d. of Restrictor	50−170 μm
Restrictor Tip to Substrate Distance	8 cm
Deposition Time	2−10 min

4. Analysis

The optical transparency of the films was measured with a Perkin Elmer Lambda 9 UV/Vis/NIR spectrophotometer. Coated substrates were mounted perpendicular to the light source and referenced against uncoated substrates of the same composition. Surface morphology and grain size were observed by scanning electron microscopy (SEM) and atomic force microscopy (AFM). Micrographs were taken with an

ISI-SX-30 Scanning Electron Microscope. Samples were coated with a thin film of gold (Polaron SEM Coating System) just prior to imaging. AFM images were taken with a Digital Instruments atomic force microscope set to contact mode using silicon nitride AFM tips (Digital Instruments). Crystal phases were identified with a Scintag PADV diffractometer using CuK_α raradiation. Substrates were cut to the appropriate size of 3 cm×3 cm and mounted in the diffractometer without further preparation.

5. Results and Discussion

5.1 Deposition of ZnO films onto Glass and Silicon Substrates

Precursor solutions (0.05 M) were made using zinc acetate (99.99%, Aldrich) dissolved in deionized water with a few drops glacial acetic acid (Aldrich) to prevent precipitation. Soda lime glass substrates (Ford Glass) were placed inside a cylindrical tube furnace in order to heat the substrate uniformly and prevent substrate cracking. The aerosolized zinc acetate solution was then directed into the tube furnace for a period of 5−20 minutes. Thin films of zinc oxide deposited on glass had good adhesion and were quite transparent. Concentric birefringence rings were visible when the films were viewed perpendicularly to white light, as shown in **Figure 3**. The optical data shown in **Figure 4** indicate 80−90% optical transparency in the region between 500 and 800 nm. A sharp decrease in transmission occurs at 380 nm indicative of a band gap of approximately 3.27 eV. This value is consistent with the literature value reported for bulk ZnO. [17]

Polished silicon substrates were heated with a ceramic block heater to approximately 450°C during the deposition. The aerosolized zinc acetate was directed onto the substrates for 5−20 minutes. The powder diffraction pattern of ZnO deposited onto silicon is shown in **Figure 5**. The absence of a halo in the powder pattern indicates a crystalline thin film with no observable amorphous character. One sample was deliberately broken, and a cross-sectional SEM image of the relatively thick film (>10 μm), shown in **Figure 6**,

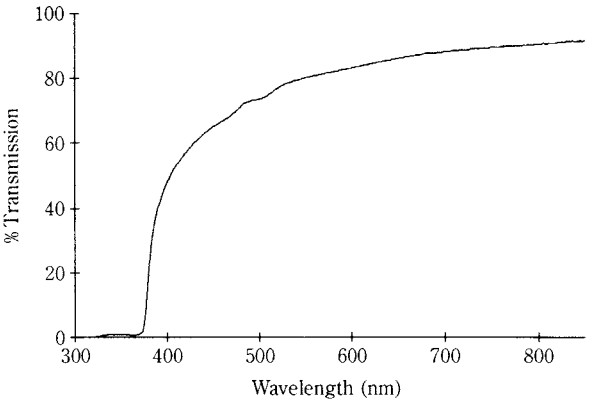

Fig. 4 Optical spectrum for thin film of ZnO deposited onto soda lime glass substrate.

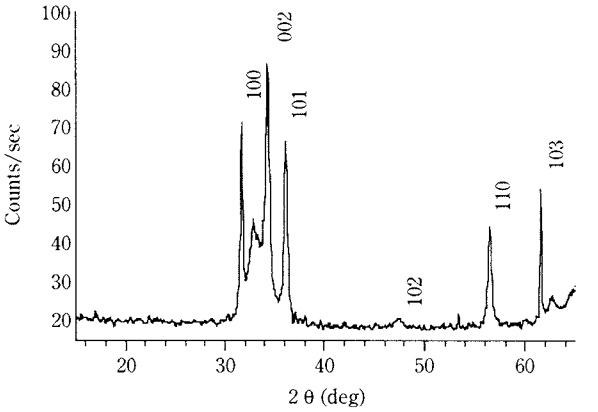

Fig. 5 X-ray powder diffraction pattern for a thin film of ZnO deposited onto a silicon substrate.

Fig. 3 Thin film of ZnO deposited on glass using supercritical CO_2-assisted aerosolization and pyrolysis.

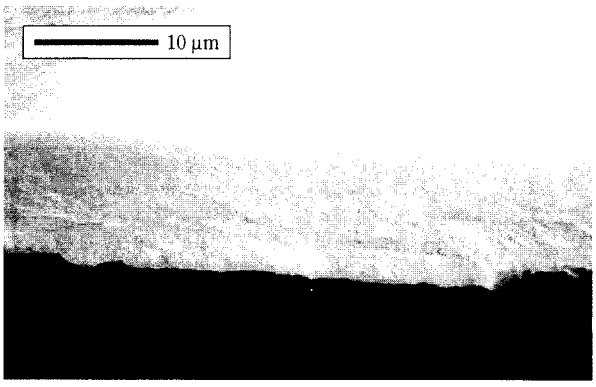

Fig. 6 SEM micrographs of thick film of zinc oxide deposited onto a glass substrate and then cleaved.

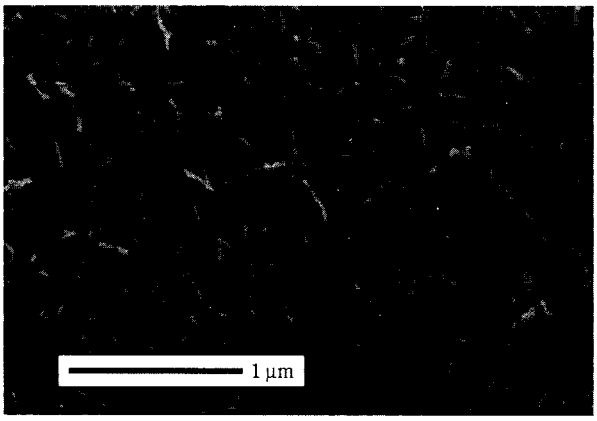

Fig. 7 SEM micrograph of the surface morphology of a thin film (<1 μm) of zinc oxide deposited onto a polished silicon surface.

indicated a structure of layered, approximately 1 μm-thick ZnO plates. Surface features of the very smooth ZnO films are not apparent with the SEM until very high magnification (60,000X), shown in **Figure 7**. The surface features appear to be less than 100 nm across.

5.2 Deposition of $ZnGa_2O_4$ Films onto Silicon Substrates

Precursor solutions were made by mixing zinc acetate ($Zn(CH_3COO)_2$, 99.99%; Aldrich) dissolved in deionized water, and an equal volume of gallium acetylacetonate ($Ga(acac)_3$, 99%; Aldrich) dissolved in isopropanol resulting in a 1:1 water : isopropanol single-phase solution containing 0.0125 M zinc acetate and 0.025 M gallium acetylacetonate. The precursor solution was aerosolized and directed toward a heated silicon substrate using the same parameters as with the deposition of ZnO. As deposited, the zinc gallate films are amorphous as indicated by powder X-ray diffraction. Annealing the films after deposition had the effect of increasing the crystallinity of the film, as shown in **Figure 8**, due to crystallization of the amorphous film or phase change. The surface morphology of the films appeared very smooth and uniform at all magnifications that could be examined in the SEM micrographs (**Figure 9**). An AFM image of a partially coated polished silicon substrate is shown in **Figure 10**. This image indicates that supercritical CO_2-assisted aerosolization and pyrolysis produces very small grain sized (60 nm) $ZnGa_2O_4$ films upon deposition.

The photoluminescence emission spectra of $ZnGa_2O_4$ films deposited on silicon had a maximum emission of approximately 435 nm, the characteristic blue emission band of zinc gallate arising from the $^4T_2$-$^4A_2$ transition. [16] Spectral intensity ranged up to 8.7×10^{-4} ($W/sr\cdot m^2$) (**Table 2**) for samples between one and

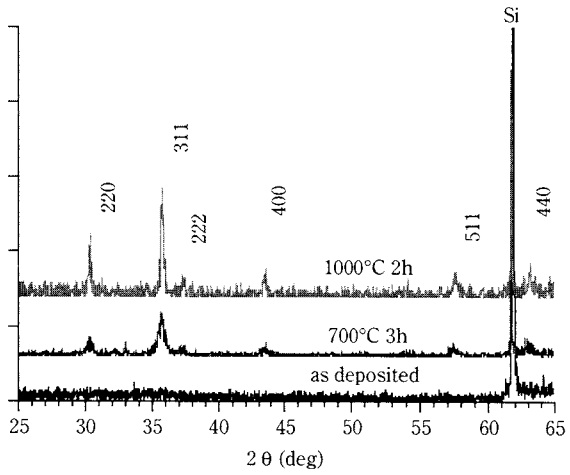

Fig. 8 X-ray powder diffraction of a thin film of zinc gallate deposited at 350°C, annealed at 700°C for 3 hours, and annealed at 1000°C for 2 hours.

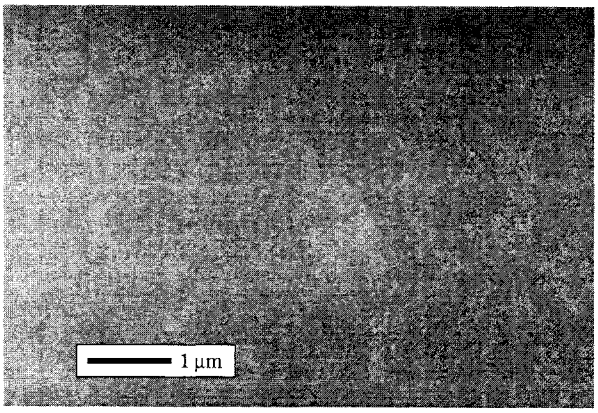

Fig. 9 SEM micrograph of zinc gallate deposited onto polished silicon substrate.

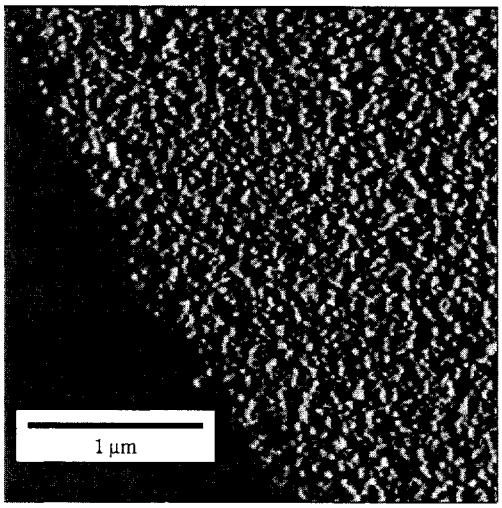

Fig. 10 AFM image of a thin film of zinc gallate deposited onto a polished silicon surface using supercritical CO_2-assisted nebulization and pyrolysis.

Table 2 Film thickness, Ga:Zn molar ratio, peak maximum and intensity for four films of zinc gallate prepared by supercritical CO_2-assisted deposition.

Thickness (μm)	Ga:Zn molar ratio	λ_{max} (nm)	Intensity (W/sr·m^2)
0.5–1	2.08	424	1.8×10^{-4}
1–5	2.27–2.65	444	8.7×10^{-4}
>5	1.65–1.79	428	5.6×10^{-4}

five microns thick. EDS measurements on the samples indicated a Ga:Zn molar ratio close to 2, with little variance across the surface of the film. These data indicate that the stoichiometry of the deposited films is in good agreement with the stoichiometry of the premixed precursor solution.

Five samples of $ZnGa_2O_4$ deposited on silicon and alumina substrates were sent to Spire Corporation for cathodoluminescence testing. The electron beam energy was 8 kV at 200 mA total current with a 3 mm estimated spot size. The cathodoluminescence data were similar for all samples and corresponded to the blue emission attributed to zinc gallate. The variation in relative intensity across the surface of each sample was too small to be detected by the eye. The sample-to-sample luminescence intensity ranged from 2.42 cd/m^2 for the thinnest film to 17.5 cd/m^2 for the thickest film measured. It should be noted that the thicker films were rougher, and it remains unclear whether brighter films are a result of differences in film thickness or surface morphology.

5.3 Manganese-doped Zinc Gallate Thin Films

In order to investigate the possibility of producing ion-doped thin films, manganese-doped zinc gallate ($Mn_xZn_{1-x}Ga_2O_4$, with x=0.006) were deposited onto polished silicon substrates. Mn:$ZnGa_2O_4$ precursor solution was made by the addition of the correct volume of an aqueous stock solution of manganese (II) acetate (25 mg/100 mL) to the zinc acetate/gallium acetylacetonate solution previously described. Films were sprayed using the conditions stated for the ZnO thin films. Films were deposited onto silicon and textured silicon substrates obtained from Spire Corporation. **Figure 11** shows an SEM image of a textured silicon substrate coated with Mn:$ZnGa_2O_4$. The substrate was masked during the deposition to determine the degree of surface coverage of the deposition (i.e., to determine whether the thin zinc gallate film would mimic the rough silicon surface upon deposition). As seen by the SEM, the films appears to have mimicked the surface perfectly with only a slight change in intensity to indicate the area of deposition.

It was determined that Mn:$ZnGa_2O_4$ could be deposited by the supercritical CO_2-assisted nebulization method. Unfortunately, the films appeared to have identical photoluminescence to the undoped films when viewed under a UV lamp. The expected result of doping manganese into the films was an increased intensity of the photoluminescence and a shift in the observed emission. It was determined that deposition in the presence of air could potentially lead to oxidation of the desired manganese (II) ions to manganese (III) (which did not produce the desired enhancement of the intensity of the luminescence), and that the addition of an annealing step (in a reducing atmosphere) might be required. The Spire collaborator was able to confirm this hypothesis by conducting the annealing experiments (for 60 sec at 800°C) and determining that the photoluminescence of the Mn:$ZnGa_2O_4$ films was much brighter after the annealing step. The spectral data for the best of the Mn:$ZnGa_2O_4$, after annealing in forming gas, appears in **Figure 12**. The peak of the spectrum is at 508 nm and luminance (based on eye's spectral sensitivity) was estimated to be 16.75 candella/m^2.

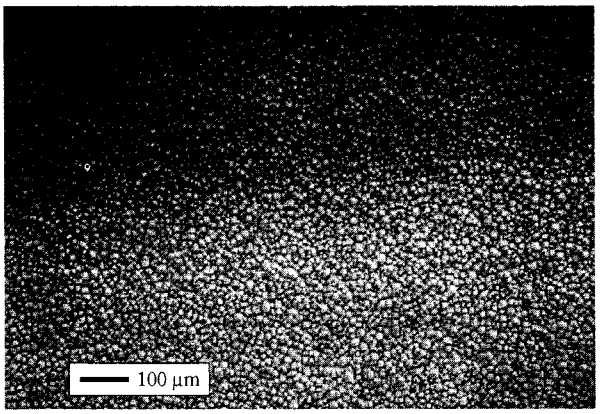

Fig. 11 Manganese-doped zinc gallate deposited onto textured silicon, lighter portion of image indicates the film coating.

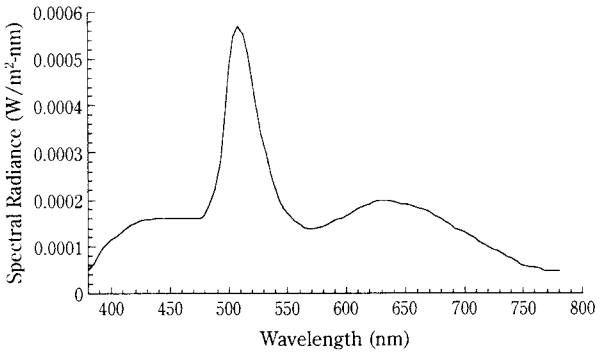

Fig. 12 Spectral radiance for Mn:$ZnGa_2O_4$ deposited by supercritical CO_2-assisted nebulization and pyrolysis followed by annealing in forming gas at 800°C for 60 sec.

6. Conclusion

Supercritical CO_2-assisted aerosolization and pyrolysis has been used to deposit smooth metal oxide films from water-soluble metal precursors. Transparent crystalline films of zinc oxide were deposited onto soda lime glass and polished silicon substrates. This study demonstrated that high quality metal oxide films can be rapidly deposited from non-volatile, as well as volatile, precursors by CO_2-assisted nebulization coupled with pyrolysis and oxidation. The deposition process is conducted at atmospheric pressure. The very fine aerosol droplets formed are rapidly dehydrated to form particles predominantly in the 0.1 to 5 μm diameter range, which decompose at heated (300−700°C) substrate surfaces. Crystallinity of deposited films can be increased by annealing at elevated temperatures. If annealing is conducted in the presence of a reducing gas such as forming gas, the oxidation state of metal ions can be changed; for example manganese doped in zinc gallate is reduced to Mn (II). These results indicate the ease at which multi-component thin metal oxide films and doped metal oxide films may be produced with supercritical CO_2-assisted nebulization and pyrolysis from water (or alcohol/water) soluble precursors.

Acknowledgements

The authors would like to thank Spire Corporation, DARPA (Grant No. DAAL01-96-K0093), NSF (Phase II SBIR Grant No. DMI-9615987), and NSF/EPA (Grant No. DMI-9615987) for their financial support of this work.

References

1) Igasaki, Y. and H. Saito: J. Appl. Phys., 70, 3613 (1991).
2) Aranovich, J., A. Ortiz and R. Bube: J. Vac. Sci. Technol., 16, 994 (1979).
3) Major, S., A. Banerjee, K.L. Chopra and K.C. Nagpal: Thin Solid Films, 143 (1986).
4) Lee, C.T., Y.K. Su and S.L. Chen: J. Cryst. Growth, 96, 785 (1989).
5) Polla, D.L., H. Yoon, T. Tamagawa and K. Voros: IEEE Int. Electron. Dev. Mtg., Washington DC, p. 495 (Dec 1989).
6) Foster, N.F.: J. Vac. Sci. Technol., 6, 111 (1969).
7) Maruyama, T. and J. Shionoya: J. Mater. Sci. Lett., 11, 170 (1992).
8) Kim, J.S., H.A. Marzouk, P.J. Reucroft and C.E. Hamrin Jr.: Thin Solid Films, 217, 133 (1992).
9) Hiramatsu, M., K. Imaeda, N. Horio and M. Nawata: J. Vac. Sci. Technol. A, 16, 669 (1998).
10) Gibbons, C.S., A. Vecht and D.W. Smith: Journal of the SID, 5, 151 (1997).
11) Ambia, M.G., M.N. Islam and M.O. Hakim: Sol. Energy Mater. & Sol. Cells, 28, 103 (1992).
12) Goyal, D.J., C. Agashe, M.G. Takwale, B.R. Marthe and V.G. Bhide: J. Mater. Sci., 27, 4705 (1992).
13) Wu, P., Y-M. Gao, J. Baglio, R. Kershaw, K. Dwight and A. Wold: Mat. Res. Bull., 24, 905 (1989).
14) Studenikin, S.A., N. Golego and M. Cocivera: J. Appl. Phys., 83, 2104 (1998).
15) Ma, T.Y., S.H. Kim, H.Y. Moon, G.C. Park, Y.J. Kim, and K.W. Kim: Jpn. J. Appl. Phys., 35, 6208 (1996).
16) (a) "Methods for Fine Particle Formation," R.E. Sievers, U. Karst, US Patent 5,639,441 (June 17, 1997); (b) "Methods and Apparatus for Drug Delivery Using Supercritical Solutions" R.E. Sievers, B.M. Hybertson and B.N. Hansen, European Patent No. 627,910 (October 1, 1997); (c) "Formation of Aqueous Small Droplet Aerosols Assisted by Supercritical Carbon Dioxide," R.E. Sievers, U. Karst, P.D. Milewski, S.P. Sellers, B.A. Miles, J.D. Schaefer, C.R. Stoldt, and C.Y. Xu, *Aerosol Science and Technology*, 30: 3-15 (1999); (d) "Supercritical CO_2-Assisted Methods for the Production and Pulmonary Administration of Pharmaceutical Aerosols," R.E. Sievers, P.D. Milewski, S.P. Sellers, K.D. Kusek, P.G. Kleutz, and B.A. Miles, *J. Aerosol Sci.*, **29**, pp. S1271-S1272 (1998); (e) "Supercritical Carbon Dioxide-assisted Aerosolization for Thin Film Deposition, Fine Powder Generation, and Drug Delivery," C.Y. Xu, R.E. Sievers, U. Karst, B.A. Watkins, C.M. Karbiwnyk, W.C. Andersen, J.D. Schaefer, and C.R. Stoldt in *Green Chemistry: Frontiers in Benign Chemical Synthesis and Processing*, Oxford Press, Oxford, pp. 312-335 (1998); (f) "Supercritical Submicron Phosphor Particles of Europium-Doped Yttrium Oxide and Terbium-Doped Yttrium Aluminum Gallium Oxide Synthesized by CO_2-Assisted Aerosolization," submitted to: Proceedings of the *Third International Conference on the Science and Technology of Display Phosphors*, Soc. For Info. Display (1998); (g) "Submicron Sized Spherical Yttrium Oxide Based Phosphors Prepared by Supercritical CO_2-assisted Aerosolozation and Pyrolysis," C. Xu, B.A. Watkins, and R.E. Sievers, *Appl. Phys. Lett.*, **71**, 1643 (1997).
17) Hsieh, I.J., K.T. Chu, C.F. Yu and M.S. Feng: J. Appl Phys., 76, 3735, (1994).

Author's short biography

Scott P. Sellers

Scott Sellers received his BS degree in Chemistry from the University of Southern California in 1991 and his PhD. in Inorganic Chemistry in 1997 at the University of Colorado studying molecular magnetic materials. His postdoctoral research at the Cooperative Institute for Research in Environmental Sciences in Boulder, CO included the development of supercritical CO_2-assisted aerosolization technology. Dr. Sellers is currently a research scientist at Coulter Pharmaceutical, Inc. (So. San Francisco, CA).

Robert E. Sievers

Professor Bob Sievers is a Professor of Chemistry and is the Director of the Environmental Program at the University of Colorado at Boulder. After completing his undergraduate work at Tulsa and his Ph.D. studies at the University of Illinois, Professor Sievers served as an officer of the U.S. Air Force and conducted research for 15 years at the Aerospace Research Lab at Wright-Patterson AFB, Ohio. He accepted a professorship at the University of Colorado in 1975, and served as Dean of the Graduate School, 1986-7. Professor Sievers has authored or co-authored approximately 190 publications dealing with powders, thin films, materials chemistry, aerosols, chromatography, and various aspects of trace analysis and environmental chemistry. In 1973, he was chosen as a Distinguished Alum by the University of Tulsa in recognition of his scientific studies, including the analysis of lunar rocks. Professor Sievers has been granted 28 U.S. and foreign patents. His most recent interests have focussed on pulmonary drug delivery and thin films produced by pyrolysis of aerosols. He has developed new patented processes for forming dense plumes of fine aerosols using supercritical carbon dioxide. He is a co-founder of Sievers Instruments, Inc., a company manufacturing innovative detectors for chemical analysis, particularly for environmental measurements, which was acquired by Ionics, Inc., in 1996.

Ward Halverson

Ward Halverson holds S.B. (1956) and Sc.D. (1965) degrees in Geophysics from the Massachusetts Institute of Technology. A post-doctorate appointment at the Centre d'Etudes Nucleares de Fontenay-aux-Roses, France, was on plasma physics and controlled thermonuclear fusion. He was a research scientist at the NASA Electronics Research Center, Cambridge, MA, for 3 years, and was then on the research staff at the Francis Bitter National Magnet Laboratory at the Massachusetts Institute of Technology in basic and applied plasma physics. Since 1978 he has been a Senior Scientist at Spire Corporation in Bedford, Massachusetts, where he performs applied research on thin films and surface modification of materials. He is a member of the American Physical Society and American Association for the Advancement of Science.

Challenges in Pneumatic Conveying†

George E. Klinzing
*Chemical and Petroleum Engineering Department, University of Pittsburgh**

Abstract

Challenges in pneumatic conveying have been explored in an attempt to provide the researcher and practicing engineer with a realistic view of the topic. While much has been achieved in the field in both modeling and experimental understanding, one can not rely totally on these predictions for complete design reliability. The most difficult topic is the individual properties of the various materials that are attempted to be conveyed. These material properties place limitations on the designer sometime because of their finest and others because of delicate nature in requiring that no change in the product occurs during the conveying operation. Unusual applications of pneumatic conveying are reviewed including such conditions as electrostatic generation, temperature and pressure effects.

Introduction

Pneumatic transport sometimes is the forgotten sister of many solids handling and processing operations. The general philosophy has been to worry about the design of the processing unit and then tack on the transport aspect of the operation. Often times, one finds that the transport section is the limiting aspect of the design. The conditions that are carefully controlled in the process can be completely upset by transfer, for example, in the plugging of coal transport lines to blast furnaces. One of the crucial elements of a transport operation is the properties of the materials. If one has developed studies using spherical Geldart type A materials, false confidences can be built such that a simple change in shape or surface characteristics of the particles cause an inoperative transport operation. Solids that are particularly difficult to transport are fine, cohesive materials such as carbon black and titanium oxide. Polymers can be easy to transport when their surface properties do not interfere with the pipe wall. A sticky, bouncy polymer that interacts intensely with the pipe wall has shown unique challenges for transport.

When it comes to the dense phase, one is faced with other kinds of challenges that do not come to light in a dilute phase transport systems. In dense phase conveying the contact between the wall and the particles is intimate and unique. Because piping can vary with surface roughness a system can change its degree of transportability as time proceeds in running the process.

Examples of the challenging materials in dilute and dense phase conveying can be cited:

- Granulated Sugar – This material is particularly sensitive to temperature effects. One can experience local temperature rises at impact points in the transport line. In addition the attrition of the sugar due to wall impacts often causes the product to be unacceptable for the customer. If one is able to address the temperature and attrition effects, care must be concentrated then on the moisture content of the sugar. High humidities can cause caking of the sugar and with this conveying problems arise. These effects of temperature, attrition and moisture of the sugar can change with time and the transport position in the line. One often fines that food stuffs can present the designer with unit material properties that require novel conveying operations.
- Carbon Black – Very fine materials such a carbon black are always challenging to convey or handle due to their cohesive nature. The use of flexible piping in the conveying process can help eliminate the deposits that tend to build upon the walls of systems that have rigid piping. The natural vibrations of the transport line can keep the pipe wall free from these deposits.
- Fine Coal – Coal Liquids – In the conveying of certain materials such a coal there is a high potential for deposits to build up on the bend due to the local temperature rise that occurs due to the impact of the solids with the wall. These

* Pittsburgh, PA 15260
† Received: May 16, 2000

deposits can grow and in a very short period of time block the total pipeline. Coal liquids which are solids at ambient temperatures can soften and cause deposits to build as they are conveyed also due to the local temperature changes caused by impact of the particles and the wall.

- Titanium Dioxide – This fine material also presents conveying challenges. The biggest problem with titanium dioxide conveying is fluctuations in pressure drop. A system can periodically spike in pressure when dilute phase conveying conditions are present. It can be conjectured that these spikes are due to wall deposits in the transport line.
- Tacky Solids – Many polymer have unusual properties. The most challenging are those that have tacky surfaces. It some respects this material may be well not convey pneumatically because of the "glue" that exists between individual particles and the high potential for plugging.

Even if one recognizes the unique properties of materials sometimes one encounters unanticipated behavior for a conveying operation. One of these occurred in the vertical conveying of particles when reducing the conveying velocity at a constant solids flow rate. As one would expect, the pressure drop per unit length decreased as the velocity decreased but at a certain point the pressure rose reaching a local maximum and then fell before reaching a non conveying condition. This experiment was done both with increasing and decreasing velocities obtaining the same results. Upon close analysis with a simplified model one finds that at the larger velocities if one conjectures that the particles are behaving in a clustering manner with a larger effective particle size upon lowering the velocity instabilities are increased to break apart the cluster having the system behavior as if the particles are individual. **Figure 1** shows this behavior and indicates the size of the proposed clusters and their component particles, (Klinzing et al., 1987). This effect has since been observed by others in the conveying of vastly different materials in the same pipeline, for example, in the conveying of diamonds with much heavier rock.

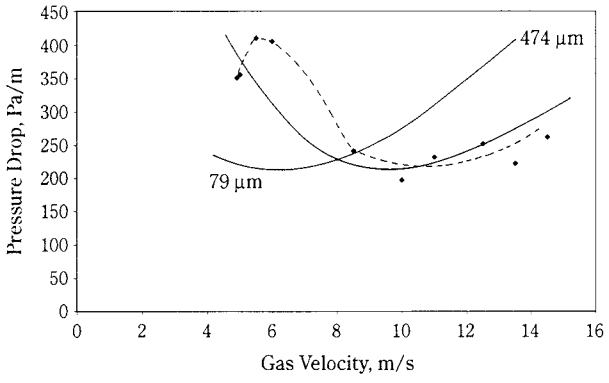

Fig. 1 Double Pressure Drop Minimum Attributed to Clustering

Property Effects

The ideal situation would be a series of basic tests that could be carried on the powder materials that will give the designer the ability to design out or around the problems or make decisions on which material would be more likely to succeed in pneumatic conveying.

One test for powders that has received much attention is that of the shear stress under various load conditions, Jenike type testing. These tests have proved invaluable in the design of bins and hoppers but have not been used as extensively in pneumatic conveying design. Such results are particularly applicable for dense phase conveying systems were intimate particle-particle and particle-wall interactions occur. The analysis of Konrad et al. (1980) first pointed to the importance of the shear stresses in powders to dense phase conveying operations. Other who have explored these avenues have been Aziz and Klinzing (1988) and Mi (1994).

Some interesting measurements that have been made by Molerus and Nywlt (1984) show the effective angle of friction of particle systems have on varying degrees of fines present in the material. As the fines content increases to about 40 percent fines, one sees a decrease in the effective angle of friction. Conjectures can be made that this biomodal distribution provides a ball bearing type lubrication to the powder by the presence of fines. This finding should be helpful in the analysis of dense phase plug systems and permit one to try to optimize plug transport with less energy being expended.

The shape of the particle being conveyed can also increase the pressure loss as shown comparing crush glass with rounded particles, Klinzing (1984).

The conveying of sodium bicarbonate in a crytalline form has showed some yet unresolved challenges. In the production of two lots of this material one was found to convey and other would not. Upon close inspection of the material properties including size and shape no differences were discernible. Since the conveying lines were the same, it is conjectured that some surface chemical difference although slight has an effect on the conveying properties, Rizk (1985).

An unusual conveying operation that can present some challenges is that of conveying crush iced. The bond that is produced between a metal surface and

the transported ice can cause considerable friction. While the plugs formed in the lines in these cases ultimately melt, a considerable disruption of the conveying operation can occur. The use of plastic pipe for the conveying of the crushed ice has proved to be superior since a thin film of melted water lubricates the ice as it is transported in the pipeline, Sheer (1991).

One of the most abrasive materials know to conveying is feldspar. In designing such conveying systems the number of geometry changes should be minimized in order to reduce pipe erosion especially in bends, Solt (1984). Another abrasive material is broken glass chars from fluorescence lights. Conveying this material can erode away the pipeline in very short order, Solt (1984).

Smokeless gun powder has been handled using dilute phase transport at a number of powder manufacturing facilities. The difficult property of this material is that it carries its own oxidant and as such conveying in a non oxygen atmosphere will not eliminate explosions. Care is taken in such operations to have dilute phase conveying be sure that no build up of powder in the transport line occurs where a hot spot can develop.

Uranium oxide powder is a very dense material that does not behave as normal powders. The dispersitivity of this powder is almost like that of a large rocks with integrity. One important aspect of this powder in conveying and processing is its particle size distribution. Good conveying can be obtained when there is a biomodal distribution of particles. The fines again are suspected of lubricating these mixtures.

Fibrous materials can change size and shape as they are conveying in a transport line. In the conveying of shredded tobacco a dog leg in the transport line is sometimes used in order to break apart the agglomerated fibrous ball that can grow in the system. Fiber glass can also show unique behavior with transport distances usually breaking down into fine fibers from cotton balls geometries.

Challenging and Unusual Conveying Conditions

Particulate materials placed in certain conveying environments respond by causing problems for the designer. Geometry is one of these environments that are crucial for an operative conveying system. The straighter the conveying line with few bends the more reliable the system. A good rule of thumb states that one should never place more than two bends in close repetition. The distances should be greater than about 20 feet between bends if possible. Water and air can go through such bend geometries easily although expending more energy but particles have added difficulties due to the excessive particle wall contacts seen in these arrangements. Another phenomenon seen in bends that can cause problems in conveying applications is the splitting of the streams in the vicinity following a bend arrangement. As the particle go around a bend, roping of the flow is seen due to the secondary flows caused in bends. Particles concentrate in a rope like form causing difficulty in the equal splitting of the solids.

Inclined flows can also show some unique behaviors. One observes that the horizontal pressure drop per unit length is less than that of the vertical pressure drop but as the angle of inclination varies between the horizontal to the vertical one notes that at about 75 to 80 degrees of inclination there is a large increase in the pressure drop per unit length over that of the vertical value. One finds that this phenomenon is due to the interaction of the particles with the pipe wall which can sometimes cause a refluxing of the particles, **Figure 2**. One sees that the bottom half of the pipeline carries the majority of the particles often causing refluxing. **Figure 3** shows this pressure drop

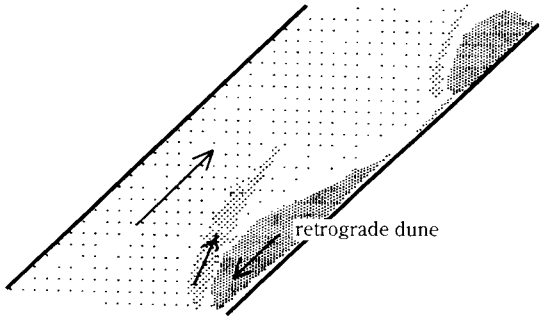

Fig. 2 Retrograde dunes in inclined flow.

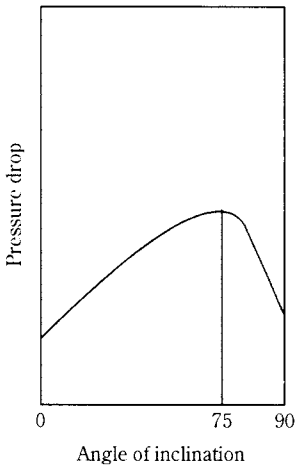

Fig. 3

behavior as the angle of inclination varies, Klinzing et al. (1997).

Electrostatic Phenomenon

If one has a relative humidity of 75% or more electrostatic or triboelectric effects will seem strange as a concern in pneumatic conveying. Lower relative humidities trigger triboelectric effect by the contacting of particles of different surface properties. If a system is not well grounded such as plastic and glass piping, one finds very large and dangerous forces produced by the rubbing of materials with the wall of different surface conditions. In the generation of electrostatic forces pneumatic conveying ranks highest among all such operations.

Kleber (1994) made a fascinating review of the history of electrostatic effects at a meeting concentrating on this topic sponsored by the Nisshin Flour Mill Corporation. **Figure 4** shows the concept of electrostatic charging applied to the spraying in the 1700's.

One of the earliest observation of the effect of electrostatics on pressure drop was shown by Richarsdson and McLean (1960). Using a system that would recycle the solid particles one sees as time proceeds the overall pressure drop increases. This pressure drop growth is attributed to the increased energy required to overcome the electrostatic forces generated on the particles being conveyed.

Electrostatics influences the flow patterns that are seen in horizontal conveying. With the non electrostatic condition one sees a rather gradual transitions from the dilute phase flow to the condition where the particles have all deposited on the bottom of the pipeline due to insufficient transport gas. **Figure 5** shows this behavior along with the electrostatic influences which changes the flow patterns with a dominance of wall interactions due to charging, Dhodapkar (1990).

For vertical flow the electrostatic effect was found to build to a point were clustering of particles occurs until discharge occurs. At the discharge point the particle are dispersed into a homogeneous flow pattern from whence the whole process begins again. **Figure 6** portrays this behavior, Plasynski (1991).

Under the same conditions ones sees rather dramatic changes in the pressure drop and its fluctuations shown in **Figure 7**, Klinzing (1994). This shows the intense wall interactions that occur when electrostatic forces are present.

The electrostatic effects in pneumatic conveying can produce some very unusual behaviors. In one horizontal conveying system the particles were being

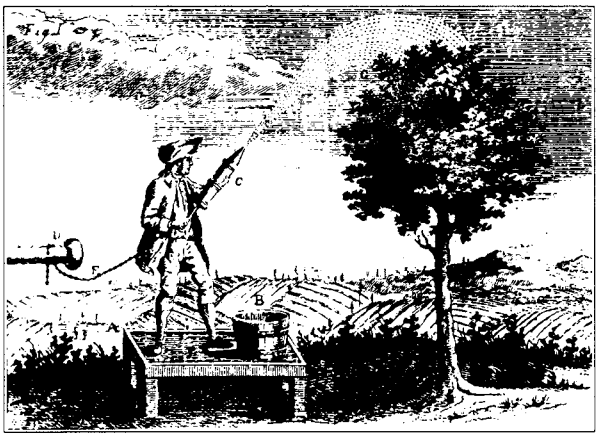

Fig. 4

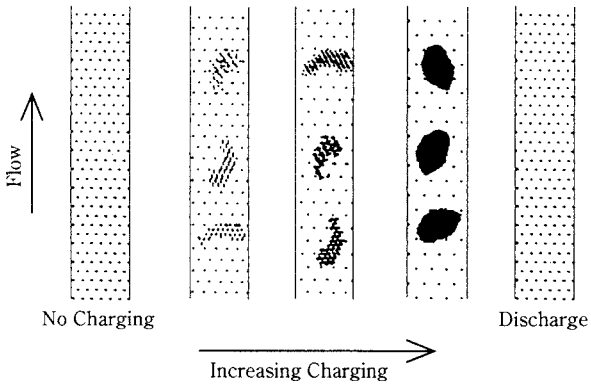

Fig. 6

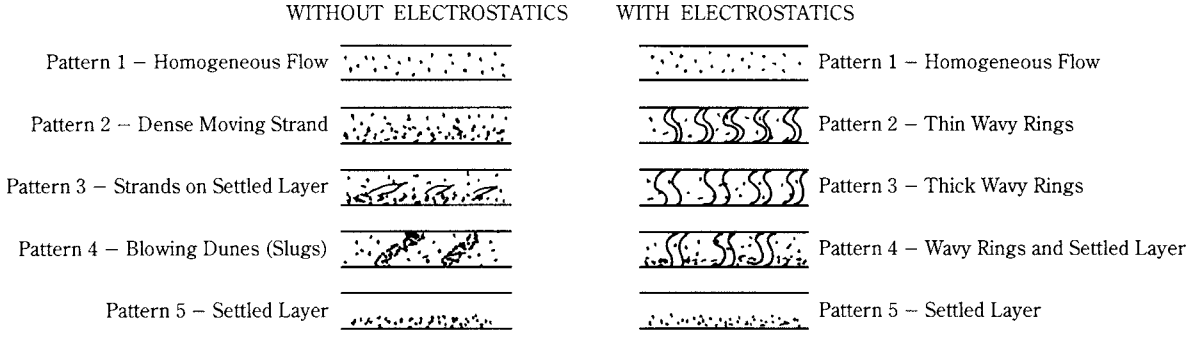

Fig. 5 Flow Patterns for PVC with Electrostatic Charging

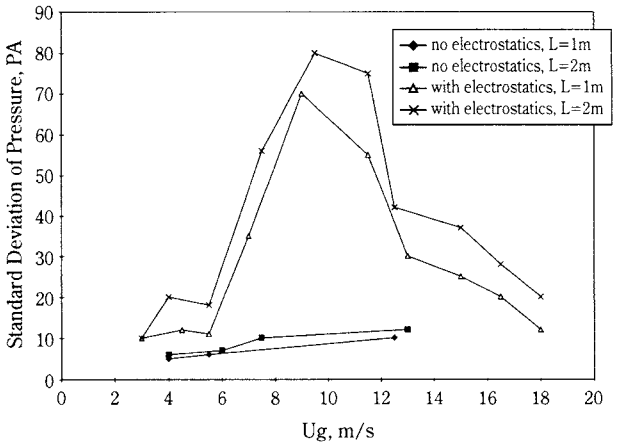

Fig. 7 Effect of Electrostic Charging on Standard Deviation of Pressure Drop for PVC Particles in 0.0245 m System – Ws=1.14 kg/min

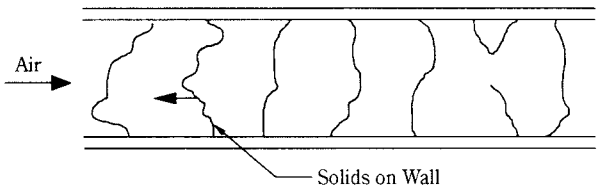

Fig. 8

conveyed with air of varying relative humidities. A 6 foot section of glass pipe separated two copper pipes producing a large section of non conductive transport. As the humidity was decreased, one would see the particles migrate to the wall of the glass section in a rather abrupt fashion and then begin to flow again the main air flow along the wall section of the pipe. Increasing the relative humidity caused a reversal of the phenomenon, Myler (1988). **Figure 8** depicts this flow reversal phenomenon that was observed.

The relative humidity of the air transporting the solids has an effect to increase the pressure loss in a vertical transfer line as shown in **Figure 9**. At the same time the pressure fluctuations seen when the relative humidities are low is also significantly increased. It was been found that the solids loading at the minimum pressure drop point in vertical flow can be presented by relationship

$$R = \frac{F\gamma^x}{10^\delta}$$

The relative humidity also affects the values of this expression. Joseph and Klinzing (1983)

Relative Humidity	x	δ
55%	2.51	1.97
16%	4.38	4.96

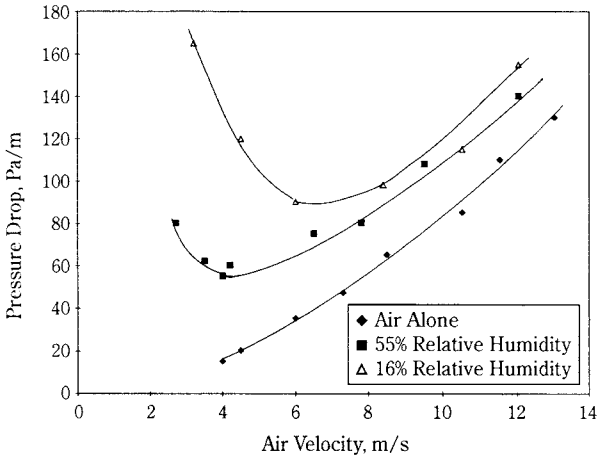

Fig. 9 Effect of Relative Humidity on Pressure Drop

Joseph and Klinzing also found under the presence of electrostatics increased pressure drop due in the choking region was present.

Temperature Effects

Some interesting observations have been seen in conveying material that is affected by temperature at high temperatures. Using a coal slag material it was found that this material softens with temperature cutting down its ordinarily abrasive characteristics at the low temperature. **Figure 10** shows this decreased erosion of a ceramic pipe liner seen for the material as the temperature of conveying is increased. One can also see that as a pipe roughens in time as in the case

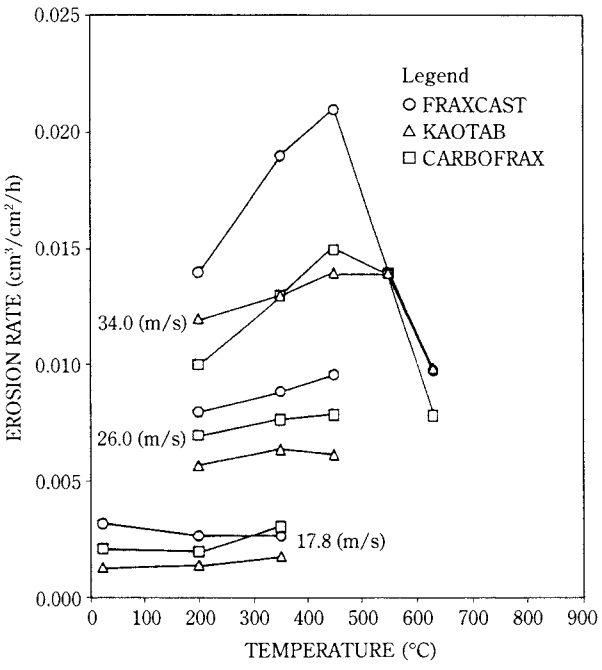

Fig. 10 Effect of temperature on the erosion rate by slag.

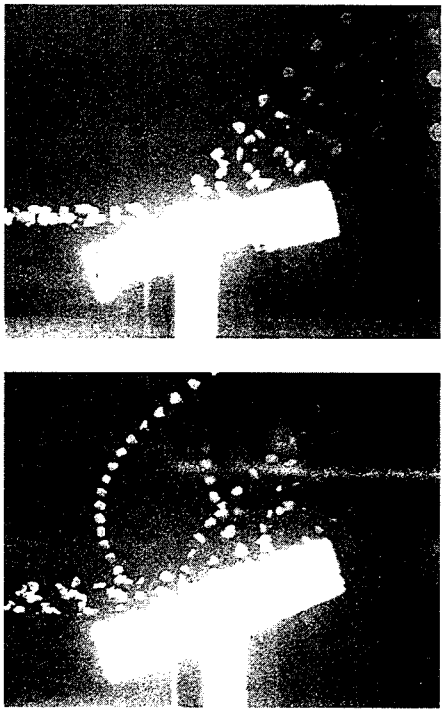

Fig. 11 Solids dispersion upon impact. (a), Smooth wall; (b) rough wall

of a ceramic pipe liner that the pressure drop in the pipe will increase dramatically. This is due to the increased friction between the gas and the solids walls but also by the increased friction experience between the conveying particles and the pipe wall. Rebound angles change dramatically for rough pipes and can be seen in **Figure 11**, Borzone and Klinzing (1990)

Pressure Effects

Some interesting behaviors are seen when the pressure is increased in a pneumatic conveying system. While the pressure is not enough to cause a liquid phase the interaction between the particles and gas up to pressure of 4238 kPa show a more sluggish behavior. For small particles about 100 microns in size slugging rather than choking was observed in vertical transport. Large size particles did choke. There appears to be a non linear relationship at high pressure between the gas friction and solids friction while at lower pressures these effects are linear in nature and can be combined to obtain the overall pressure loss. Using an expression suggested by Weber one can represent the frictional terms for the gas and solid as

$$f_g = 0.1/Re^{0.151}[1/1+\mu^{0.7}]$$

$$f_s = 0.7848\mu^{0.966}Fr^{-1.02}$$

This indicates that there is more solids friction contribution in a high pressure system that in the a lower pressure system.

Reduced Gravity Flows

There has been interest by NASA is the possibility of conveying particulate matter namely illemite of the moon's surface. This material which contains oxygen exists is a dust format on the surface of the moon. Reducing this ore with hydrogen can release oxygen which is needed for life support. In addition titanium metal is recovered which can be used on building of structures. Mechanical devices do no fare well in dusty environments thus the use of pneumatic conveying has been suggested. The differences between conveying on the moon and earth are that the gravitation field is 1/5 of that on earth and there is no atmosphere to draw upon. Conveying of solids under reduced gravity has been explored by two investigators in order to try to understand the conveying operation at reduced gravity which also provides an opportunity to explore the effect purely frictional forces in pneumatic conveying. Nemecek (1986) designed and built a facility to test our reduced gravity conditions proposing to probe the pure frictional effect seen under zero gravity. Sullivan et al. (1992) performed a number of experiments under reduced gravity. The choking velocity for 150 micron glass spheres were determined to be 1/2 to 1/3 the velocity at 1 g when the gravity was 0.16 to 0.38 g. The pressure drops were also seen to be reduced by a similar amount under reduced gravity conditions. Using the Rizk expression for saltation velocity the saltation velocity is seen with vary with the square root of the gravity term. This finding compared favorably with the results obtained under reduced gravity conditions.

Literature

1) Aziz, Z.B., Klinzing, G.E., Powder Technology, Vol. 55, (1988), pp. 97-105
2) Borzone, L.A., and Klinzing, G.E., Powder Technology, Vol. 62, (1990) pp. 277-290
3) Dhodapkar, S.V., Ph.D. Dissertation, University of Pittsburgh (1990)
4) Joseph, S., and Klinzing, G.E., Powder Technology, Vol. 36 (1983) pp. 79-87
5) Kleber, W., NEPTIS 3, Kyoto (1994)
6) Klinzing, G.E. J. of Pipelines, Vol. 4 (1984) pp. 95-102
7) Klinzing, G.E., The Third Nisshin Engineering Particle Technology International Seminar, NEPTIS-3, Kyoto, Japan Nov (1994)

8) Klinzing, G.E., Rohatgi, N.D., Zaltash, A., Myler, C.A., Powder Technology, Vol. 51 (1987) pp. 135-149
9) Klinzing, G.E., Rizk, F., Marcus, R.D., Leung, L.S., "Pneumatic Conveying of Solids," Chapman and Hall, (1997)
10) Konrad, K., Harrison, D., Nedderman, R.M., Davidson, J.F., Pneumotransport 5, April (1980) pp. 225-244
11) Mi, B., Ph.D. Dissertation, U. of Wollongong (1994)
12) Molerus, O. and Nywlt, M, Powder Technology, Vol. 37 (1984) pp. 145-154
13) Myler, C.A., Zaltash, A., Klinzing, G.E., J. of Powder and Bulk Solids Technology, Vol. 10 (1986) pp. 5-12
14) Myler, C.A., Ph.D. Dissertation, University of Pittsburgh (1988)
15) Nemecek, F., Forschungsbericht W 86-009, Bundesministerium fur Forschung und Technologie, July (1986)
16) Plasynski, S.I., Klinzing, G.E., Mathur, M.P., Powder Technology, Vol. 79, (1984) pp. 95-109
17) Richardson, J.F., McLean, M., Trans. Instn. Chem. Engr., Vol. 38 (1960) 257
18) Rizk. F. (1985) Personal Communication
19) Sheer, T.J., Ph.D. Dissertation, Witwatersrand University, Johannesburg, S.A. (1991)
20) Smeltzer, E.E., Weaver, M.A., Klinzing, G.E., Ind. Eng. Chem. Process Devel. Vol. 21 (1982) pp. 390-394
21) Solt, P. (1984) Personal Communication
22) Sullivan, T.A., Koenig, E, Knudsen, C.W., Gibson, A., AIAA 92-1667, AIAA Space Programs and Technologies Conference, March 24-27, 1992 pp.
23) Wildman, D.J., Ekmann, J.M., Mathur, M.P, Klinzing, G.E., A.I.Ch.E. Symposium Series No. 255, Vol. 83 (1987) pp. 58-63

Author's short biography

George E. Klinzing

Professor Klinzing is in the Chemical and Petroleum Engineering Department of the University of Pittsburgh where he does research and teaching in the area of solids processing with an emphasis on pneumatic conveying. He has studied several facets of pneumatic conveying from electrostatic generation to dense phase conveying operations. Most of his research has explored experimental phenomena using this as a basis to develop modeling and design procedures. He has written three books on pneumatic conveying along with a sizeable series of peer-reviewed articles.

Fundamentals of Size Separation†

Peter T. Luckie and Mark S. Klima
*The Pennsylvania State University, Department of Energy and Geo-Environmental Engineering**

Abstract

Screening and classification are used to separate particles based on differences in size. Industrially, these processes are done on a continuous basis to produce two (or more) product streams of varying degrees of fineness. Screening involves the separation of particles based on the probability of passage through a series of apertures of uniform size. Variables such as the number of presentations per second, size of the particle relative to aperture size, and retention time on the screen all are important in determining the probability of passage through the screen. In classification, the separations are determined by the movement of particles in a fluid, typically water or air. In this case, the probability of a particle reporting to the coarse or fine stream depends on the relative effect of gravity and fluid drag. This paper describes the factors affecting both screening and classification, the types of devices used in the separations, and the effects of staging to improve process performance.

Introduction

Size separation involves the partitioning of particles on the basis of size. Industrially, this process is done on a continuous basis, producing a coarse stream and a fine stream. However, in some applications, multiple streams of varying degrees of fineness are produced. The separations are performed using a wide range of devices, which generally can be grouped into one of two categories – screening or classification. Screening involves the separation of particles based on the probability of passage through a series of apertures of uniform size. Variables such as the number of presentations per second, size of the particle relative to aperture size, and retention time on the screen all play a major role in determining the probability of passage. In classification, the separations are determined by the movement of particles in a fluid, typically water or air. In this case, the probability of a particle reporting to the coarse or fine stream depends on the relative effect of gravity and fluid drag.

Screening and classification devices are both used industrially, and their application depends on the separation size of interest. Dry screening with a reciprocating motion is often used to separate particles at sizes greater than about 12 mm, while wet screening is generally employed for particle sizes down to about 0.5 mm. Dry, fine screening is usually performed with a gyratory motion. For finer size separations, classification devices are generally used. Wet classification is primarily carried out with hydrocyclones to separate particles down to about 10 μm, while solid-bowl centrifuges can be used for separations down to several micrometers. Dry classification is typically performed using one of the many types of commercially available mechanical classifiers for separating at sizes down to several micrometers.

In order to improve the performance of a given sizing operation, staging can be used. This involves reprocessing one of the product streams, with or without circulation. This not only improves separation efficiency, but it also can be used to decrease (or increase) the separation size of the circuit and to decrease the apparent bypass of fines to the coarse stream.

Screening

One method of size separation is on the basis of the probability of a particle passing through an aperture. For example, consider a flat screen plate having square openings of dimension s and centers of dimension c, hence a bar dimension of c−s. Ideally, the chance of a spherical particle, having a diameter d, passing through an opening would be 100% for all particles of relative size $d/s<1$, and 0% for all particles of relative size $d/s>1$ (see column I in **Table 1**). So obviously the relative size of the particle to the aperture is a factor affecting whether a particle passes through an aperture deck. However, the chance of such a particle

* 110 Hosler Building, University Park, PA 16802
† Received: May 16, 2000

Table 1 Variation in the probability of passage (expressed as a percentage) of a particle through a screen.

d/s	I	II	III	IV	V	VI	VII	VIII	IX	X
0	100	25.0	64.0	100.0	40.0	36.3	29.5	100.0	100.0	100.0
0.1	100	20.25	51.8	81.0	35.1	30.8	27.0	100.0	100.0	100.0
0.2	100	16.0	41.0	64.0	30.4	25.7	23.0	100.0	100.0	100.0
0.4	100	9.0	23.0	36.0	21.6	16.15	12.0	100.0	100.0	100.0
0.6	100	4.0	10.2	16.0	13.6	8.15	4.0	98.3	100.0	98.3
0.8	100	1.0	2.5	4.0	6.4	2.35	0.2	63.4	100.0	18.1
0.9	100	0.25	0.6	1.0	3.1	0.6	0	22.1	91.8	0
0.95	100	0.05	0.15	0.25	1.525	0.2	0	5.8	45.1	0
0.99	100	0.00	0.0	0.0	0.3	0.0	0	0.25	2.5	0
1	0	0	0	0	0	0	0	0	0	0

passing when approaching the deck normally without reflecting off the bar is given by [Gaudin, 1939]

$$p(d) = 100\left(\frac{1-d/s}{c/s}\right)^2 \quad (1)$$

Column II gives the values for the chance of reporting to the fine stream where c/s=2; i.e., if the dimension of the bar equals the dimension of the square opening. As can be readily seen, these values are much different from those of a perfect separation. This is because the screen deck only has 25% open area. Therefore, there is a 75% chance of a particle whose dimension is d/s<1 impacting a bar. If the bar dimension is 1/4 of the dimension of the square opening, i.e., c/s=1.25, or 64% open area, then the chances increase as shown in column III because there is now only a 36% chance of such a particle impacting a bar, but still do not match the perfect separation values. Thus, the % open area is a factor in the chances of a particle of dimension d/s<1 passing. Even if c/s→1, i.e., approaching 100% open area, the probabilities of passing will not match the perfect separation values as shown in column IV. If particles become lodged in an aperture (blinding), this also reduces the % open area.

Note in column II that the chance of a particle of zero size passing is 25% or a 75% chance of not passing! This "not passing" value is given a unique symbol, a, because it represents the apparent bypassing of the separation process; that is, the process behaves as if it split or sent 75% of the feed directly to the coarse stream and only 25% had an opportunity to pass. Thus, there is a need to correct the chance of passing values for this bypassed material to determine how the device separated the apparent non-bypassed material. This is done by dividing the p(d) values by 1−a/100. These corrected values, p′(d), are the same as those for 100% open area, shown in column IV.

The size modulus and shape modulus of the plot of these corrected values are used to characterize the separation. The size modulus, d_{50}, is defined as the particle size that has a 50% chance of passing (hence not passing). The shape modulus, κ, is defined by the particle size that has a 75% chance of passing divided by the particle size that has a 25% chance of passing, and is called the sharpness index. The d_{50} value for column IV, actually d_{50}/s, is 0.3; the κ value is 0.265. Note that for a perfect separation the d_{50} value is s and the κ value is 1 (and a is zero). Apparent bypassing, i.e., $a>0$, is commonly observed in industrial screening. In fact, the industry only guarantees "95% efficiency" which means, given the way they define efficiency, that they expect a 5% apparent bypass. It is interesting that if the values in column III are corrected, they are identical to the values in column IV, meaning that the chance of passing is the same for particles not striking the bars.

Effects of Aperture Design on Separation

If the aperture is rectangularly shaped, say the length is 4 times the width, s, then the chance of a spherical particle approaching the deck normally without reflecting off the bar is [Gaudin, 1939]

$$p(d) = 100\left(\frac{1-d/s}{c/s}\right)\left(\frac{4-d/s}{3+c/s}\right) \quad (2)$$

As can be seen in column V, the chance of passing values for c/s=2 (or 40% open area) are greater than for the square apertures (column II) with 25% open area, and, the corrected values are greater than the values in column IV, but still do not match the perfect values (column I). Thus the aperture geometry is also a factor affecting passage.

If the square openings are created by woven round wire rather than punched flat plate, and if the reflectance of the particle into the aperture after striking the wire is taken into account, then the chance of

a spherical particle approaching normally a deck of square apertures is

$$p(d)=100\left[1-\frac{(c/s-1+d/s)\left(1+\sqrt{1+8m^2}\right)}{4(c/s)m}\right]^2 \qquad (3)$$

where $m=\frac{c/s+1-d/s}{c/s-1+d/s}$, [Gaudin, 1939]. As can be seen in column VI, the chance of passing values for c/s=2 are greater than for non-reflective, normal incidence (column II) and so are the corrected values. If the angle of incidence is less than 90%, i.e., oblique incidence, then the chance of passing values for c/s=2 are lower, as shown in column VII for a spherical particle striking the deck at 45° [Gaudin, 1939], however the corrected values are greater. Thus the trajectory of approach to the aperture for a particle is a factor affecting passage.

Effects of Operating Variables on Separation

If a particle of relative size d/s<1 that did not pass is given other opportunities, then the chance of that particle passing after n opportunities is $100(1-(q(d)/100)^n)$ where q(d) is the chance of reporting to the coarse stream, or 100−p(d). Whiten [1972], using Equation 1, predicts the probability of a particle of size x reporting to the screen oversize as $q(x)=(1-p(x))^n$. The value of n is related to the load and length of the screen. Column VIII contains the chance of passing values for non-reflective, normal incidence square apertures with c/s=2 after 100 opportunities, which should represent a very good industrial screen operation. As can be seen, the values have improved immensely over the values in column II, but have not achieved the perfect values in column I. Column IX contains the values after 1000 opportunities, which should represent test screening conditions in the laboratory. While these values have improved even more, they still do not equal the perfect values. Notice that it is particles near d/s=1 that have a finite chance of not passing. Thus, the number of presentations, hence stratification of particles and the speed of the particle across the deck, is a factor affecting passage. Screening research [Brereton and Dymott, 1973] has shown that both the d_{50} and κ values increase as the length of the screen is increased.

Column X contains the chance of passing values for reflective, 45° oblique incidence square apertures with c/s=2 after 100 opportunities. What is interesting about these values is that they actually represent a better separation than column VIII. And because the d_{50} is less, larger size screens can be used, reducing screen blinding. This is the basis for so called probability screening.

Screen Selection

Obviously, there are other factors affecting the passage of the particles such as the amount of surface moisture, hence aggregation of the particles. Consequently, because of the multitude of factors acting individually and interactively, it is not possible to establish the chance of passage of each size particle based on first principles. Instead, manufacturers employ a design loading methodology whereby the feed rate/screen area that will produce acceptable chance of passing values is estimated. In addition, there are aperture systems that are not as easily analyzed as screen decks. For example, consider a "rotating probability" screen. The "screen deck" is created by fitting rods to a vertical rotating shaft. The rods, radiating from the central hub, create a horizontal circular deck. The "apertures" are the space between the radial rods, which progressively enlarge and have no supporting members. These "apertures" are typically larger than the feed. If the "deck" is not rotating, then all the feed particles will pass through the "apertures". If the "deck" is rotated at very, very high speeds, then essentially none of the feed material will pass through the "apertures". Thus, by controlling the speed of rotation, the "aperture size" is regulated.

Because the probability of collision between the particles and the rotating rods is not readily derivable, it is necessary to obtain the chances of passing via other means. For example, the values can be obtained by sampling around the device while it is operating at steady state. Then the chances of passing can be calculated from the size analysis of the feed stream, F, the oversize stream, T, and the undersize stream, Q, as

$$p_i=\frac{100\,q_i}{f_i(1+C)} \qquad (4)$$

where $C=\frac{\sum_{i=1}^{n-1}\left|f_i-q_i\right|}{\sum_{i=1}^{n-1}\left|t_i-f_i\right|}$ and the interval values, such as $f_i=F(x_i)-F(x_{i+1})$ are calculated for $x_i/x_{i+1}=\sqrt{2}$, where $F(x_i)$ is the cumulative fraction finer than size x_i in the feed stream, and n is the number of size intervals.

If this is done for a number of different operating conditions, then perhaps a systematic pattern in the changes in the chance of passing values, and consequently in *a*, d_{50} and κ, may occur that can be used to predict the separation process. And since the size consist of the undersize stream does not depend upon the *a* value, hence, only on the corrected values, there is a unique d_{50} value for a particular κ value that will

produce a fine stream analyzing 95%<a particular size.

For example, consider the results reported by Rogers and Brame [1985] for the high frequency screening of limestone slurries. They found, using a 0.35 m^2 pilot-plant Derrick machine that gave comparable performance to a 2.10 m^2 full size Derrick machine, that the slurry feed rate had no affect on the chance of passing values as long as the slurry feed rate did not exceed a maximum rate, which varied with the volumetric feed concentration, Cv_F, and aperture size. They found that $d_{50}=1.08s-50\ Cv_F \exp(0.00925s)$, $0.2<Cv_F<0.5$, and $\kappa=0.93\ d_{50}/s$. Using a functional form for the corrected values

$$p_i' = \frac{100}{1+(x_i/d_{50})\exp\{g[(x_i/d_{50})^3-1]\}} \tag{5}$$

where $g \simeq 0.08 \exp(4.25 d_{50}/s)$, one can search for the d_{50} value that will produce an undersize stream with the desired % passing a particular size by solving the algebraic relationship

$$Q_{i^*} = \sum_{i=n}^{i^*} p_i' f_i / \sum_{j=1}^{n} p_j' f_j \tag{6}$$

They also found that

$$a = 125\frac{Cv_F}{1-Cv_F} - 24.3, \quad 0.2<Cv_F<0.5 \tag{7}$$

and that the apparent bypass essentially equaled the water split, the percentage of the water in the feed stream that reports to the coarse stream or $100T'/F'$, where the prime represents the mass flowrate of the water in the slurry (thus the feed slurry mass flowrate, F'', equals $F+F'$). Then, the mass flowrate of the solids in the undersize stream can be calculated as

$$Q = F(1-a/100)\sum_{j=1}^{n} p_j' f_j \tag{8}$$

and the solids concentration of the undersize stream can be calculated as

$$Cv_Q = \frac{1}{1+\dfrac{1}{(1-Cv_F)\sum_{j=1}^{n} p_j' f_j}} \tag{9}$$

Obviously, the mass flowrate of the oversize stream is

$$T = F-Q \tag{10}$$

and the solids concentration of the oversize stream can be calculated as

$$Cv_T = \frac{Cv_Q Cv_F (T/Q)}{Cv_Q (F/Q) - Cv_F} \tag{11}$$

Classification

Size separations can also be carried out according to differences in the settling velocities of particles of various sizes, densities, and shapes. That is, the probability of a particle reporting to one of the product streams is a function of its settling velocity.

Consider the cylindrical device shown in **Figure 1** containing a polydisperse particle system. If particles are moving within the cylinder as the result of settling (convection) and mixing (diffusion), it is possible to account for their movement into and out of an element (i.e., dz) within the device. Moreover, under conditions where the particles move independently of each other, then their settling velocity does not depend on solids concentration, i.e., free-settling conditions prevail. Since the separation occurs primarily in the vertical (z) direction, then the separating force (gravity) and the level of mixing must only be considered in this direction. If mixing is characterized by a single eddy-diffusion coefficient, then the rate of accumulation in an element z to z+dz can be given by

$$\frac{\partial c(x,\rho,z,t)}{\partial t} = D\frac{\partial^2 c(x,\rho,z,t)}{\partial z^2} - v(x,\rho)\frac{\partial c(x,\rho,z,t)}{\partial z} \tag{12}$$

where $c(x,\rho,z,t)$=concentration of particles of size x and density ρ at depth z and time t; D=eddy diffusion coefficient; $v(x,\rho)$=free settling velocity for particles of size x and density ρ. The free-settling velocity can be calculated using Stokes equation for fine particles (i.e., particle Reynolds numbers less than ~0.1) or Newton's equation for coarser particles (i.e., particle Reynolds numbers greater than ~1000). However, it is often convenient to use Concha's equation to calculate the particle settling velocity, which can be used over the range of particle Reynolds number from about 0.1 to 10,000 [Concha and Almendra, 1979]. Equation 12 can then be used to describe particle movement under free settling conditions.

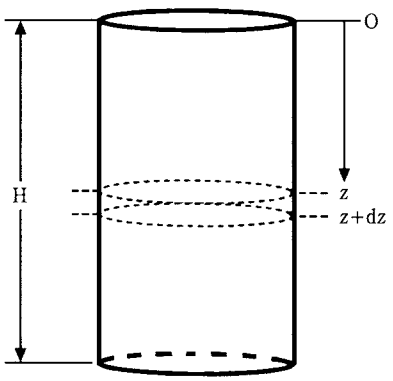

Fig. 1 Cylindrical batch settling device.

Rather than calculate the particle concentration at various points in the separation device, it is more convenient to determine the fractional recovery of particles in a given product stream. The initial amount of material of a given size and density in a separation device of height, H, is

$$f(x,\rho)F = c_0(x,\rho)\int_0^H A(z)\,dz \tag{13}$$

where $f(x,\rho)$=fraction of feed material of size x and density ρ; F=mass of feed material; $c_0(x,\rho)$=initial concentration of particles of size x and density ρ; A(z)=cross sectional area of the device at any vertical (z) direction.

If the particles are allowed to settle for some time, t, and the cylinder is "cut" at some height (z'), then the amount of material remaining in the upper compartment of the device is

$$q(x,\rho,t)Q = \int_0^{z'} c(x,\rho,z,t)A(z)\,dz \tag{14}$$

where $q(x,\rho,t)$=fraction of product material of size x and density ρ; Q=mass of product material. The fraction of feed particles of size x and density ρ that remain in the upper compartment (i.e., probability of reporting to the fine stream) after time t is

$$p(x;\rho,t) = \frac{q(x,\rho,t)Q}{f(x,\rho)F} = \frac{100}{HA_m}\int_0^{z'} \frac{c(x,\rho,z,t)A(z)\,dz}{c_0(x,\rho)} \tag{15}$$

where A_m is the mean value of the cross-sectional area. In the case of a cylindrical device, the cross-sectional area is constant and $A(z)=A_m$. A solution for Equation 15 can be obtained by solving Equation 12 under the appropriate initial and boundary conditions [Klima and Luckie, 1989].

For size separations involving single density particles, the upper compartment would contain only fine particles, while the lower compartment would contain primarily coarse particles. However, since the feed was uniformly dispersed prior to separation, some fine particles will be found in the lower compartment. This fraction represents the apparent bypass of feed to the coarse stream and is typical of many wet size classification devices, e.g., hydrocyclones.

As is common in industry, the fraction of feed material of a given size reporting to the coarse stream (i.e., the size selectivity value) is generally desired. This is given by

$$s(x;\rho,t) = \frac{t(x,\rho,t)T}{f(x,\rho)F} \tag{16}$$

where $t(x,\rho,t)$=fraction of non-specification (i.e., coarse) material of size x and density ρ in the lower compartment after time t; T=mass of coarse material. Obviously,

$$s(x;\rho,t) = 1 - p(x;\rho,t)/100 \tag{17}$$

The above treatment was derived for a batch settling system. However, Equation 15 can also be used to simulate continuous separations assuming that a lumped-parameter approach applies. For example, if it is assumed that no axial back-mixing occurs such that all particles remain in the device for the same amount of time and that the batch separation time is equivalent to the mean retention time, then the batch separations would be equivalent to continuous separations under plug flow conditions. In this case, after separation, the particles are split into two product streams, analogous to "cutting" of the batch device as shown in **Figure 2**. This situation is analogous to the wet classification pulp partition model discussed by Schubert and Neesse [1973]. However, in their case, a steady-state solution of the convection-diffusion equation (Equation 12) was used.

For a device as shown in **Figure 2**, separation occurs because particles of different sizes have different settling velocities, resulting in different trajectories. For example, consider a dispersed feed of particles of different sizes entering the device. Once in the device, large particles settle rapidly below the split point, ending up in the coarse product stream. On the other hand, finer particles that enter in the upper compartment may not have sufficient time to settle into the lower compartment and thus report to the fine product stream. Fine particles that enter into the lower compartment cannot reach the upper compartment and end up misplaced to the coarse product stream. These particles are often considered as bypass material, since they did not have the opportunity to make it to the fine product stream.

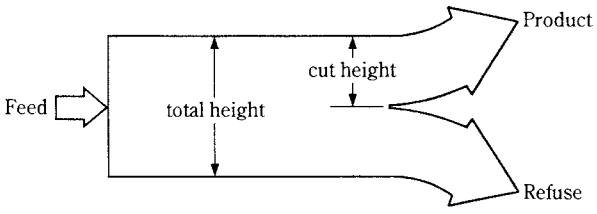

Fig. 2 Continuous settling device.

Effect of Process Variables on Separation

In order to examine the effects of the different fundamental parameters on size separation, a series of simulations can be performed using Equation 15 to generate size selectivity values. The particles are as-

sumed to be settling in water, in a device 12 cm high. Simulations are performed for particle sizes in a $\sqrt{2}$ series, i.e., 150, 105, 75, etc. down to 0.84 μm. The baseline conditions include the following: cut height=10.8 cm, settling time=30 s, particle density=2.65 g/cm^3, diffusion coefficient=1 cm^2/s, number of g's=1. Simulations are then performed by changing each variable, while holding the other variables constant, a process that cannot be performed in actual devices because of the confounding of variables.

In order to determine the characteristic parameters (cut size, sharpness index, and apparent bypass) for each simulation, the corrected size selectivity values are fitted to an appropriate mathematical function, i.e.,

$$c(x;\rho,t) = \frac{s(x;\rho,t) - a/100}{1 - a/100} \tag{18}$$

where a=apparent bypass of feed material to the coarse stream and

$$c(x;\rho,t) = \frac{1}{1 + (x/d_{50})^{2.1972/\ln \kappa}} \tag{19}$$

where d_{50}=cut size, i.e, size at which $c(x;\rho,t)=0.5$; κ=sharpness index, i.e., size at which $c(x;\rho,t)=0.25$ divided by the size at which $c(x;\rho,t)=0.75$. The simulation results are given in the following sections.

Settling Time – Figure 3 shows the variation of the size selectivity curves for retention times of 5, 10, 30, 60, 120, and 240 seconds. The corresponding parameters are given in **Table 2**. At very short times, the curve corresponds closely to the fraction remaining in the lower compartment, i.e., 10% in this case. This corresponds to a value of 1-z'/H. This is expected since at very short times, the particles will have settled only a short distance, giving a splitting action. Hence, the particle size distribution in both compartments would be expected to be similar to that of the feed, which would be represented by a horizontal line through 0.1 at time=0.

As the separation time increases, the cut size and sharpness index decrease (**Table 2**). The decrease is significant up to 30 seconds, after which time very little change occurs. At long times, a limiting condition is reached in which there is a balance between the settling and mixing of the particles, i.e., steady-state condition. This condition will also result using the steady-state solution indicated previously [Schubert and Neesse, 1973]. The limiting curve will change, depending on the operating conditions and the level of mixing present.

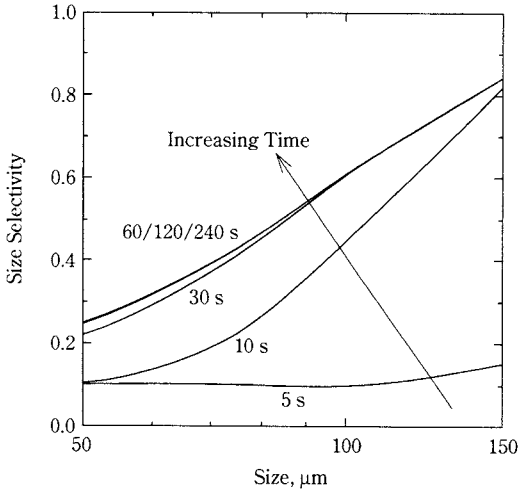

Fig. 3 Effect of settling time on the size selectivity curves.

Table 2 Variation of size selectivity parameters with settling time.

Settling Time, s	d_{50}, μm	κ	a
5	177.1	0.88	0.10
10	111.3	0.63	0.10
30	91.9	0.49	0.10
60	90.0	0.46	0.10
120	89.9	0.46	0.10
240	89.9	0.46	0.10

Level of Mixing – Figure 4 shows the variation of the size selectivity curves with the level of mixing. As expected, increased mixing results in a worsening of the separation as shown by the flatter curves, which correspond to lower sharpness indices and much higher cut sizes (**Table 3**). In fact, at the highest level of mixing, the curve is very flat, indicating that very

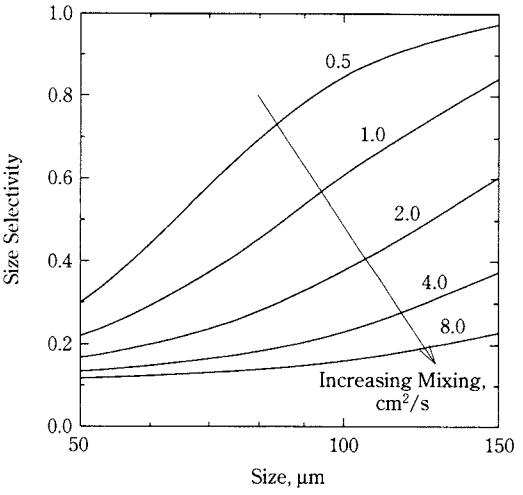

Fig. 4 Effect of mixing on the size selectivity curves.

Table 3 Variation of size selectivity parameters with level of mixing.

Mixing Coefficient, cm^2/s	d_{50}, μm	κ	a
0.5	67.9	0.59	0.10
1.0	91.9	0.49	0.10
2.0	136.9	0.42	0.10
4.0	215.0	0.38	0.10
8.0	352.6	0.35	0.10

little separation occurs. At even higher levels of mixing, no separation will occur and the final products will have the same composition as the feed, i.e., the feed stream is split into two product streams. Obviously, minimizing the level of mixing is critical to improving separator performance.

Cut Height – Figure 5 shows the variation of the size selectivity curves for cut heights of 1.2 (10%), 3.0 (25%), 6.0 (50%), 9.0 (75%), and 10.8 cm (90%). As can be seen, the curves shift downward and to the right as the cut height increases. This results in coarser cut sizes as more of the coarser material is split to the fine stream (**Table 4**). Moreover, at the fine sizes, each curve approaches the value of 1-z'/H, which is equal to the apparent bypass for each curve. Interestingly, the sharpness indices are approximately constant at about 0.5 over the range of cut heights. This trend has been observed for industrial classifiers. The implication is that by changing the fraction of feed slurry that is split to the fine product stream (e.g., through changes in the geometry or operating conditions of the separator) the cut size can be varied without affecting the sharpness index. However, such changes will also produce an uncontrollable change in the apparent bypass, which may be detrimental to the overall separation.

Number of G's – Figure 6 shows the variation in the size selectivity curves as a function of the number of g's. It can be seen that the cut size decreases from 92 to 12 μm as the number of g's increases from 1 to 50 (**Table 5**), while the sharpness indices remain constant at about 0.5. In all cases, the curves approach the limiting value of 0.1, i.e., the expected apparent bypass. **Figure 7** is a log-log plot of cut size versus the number of g's. It can be seen that it becomes increasingly difficult to achieve very fine cut sizes because of the large number of g's required.

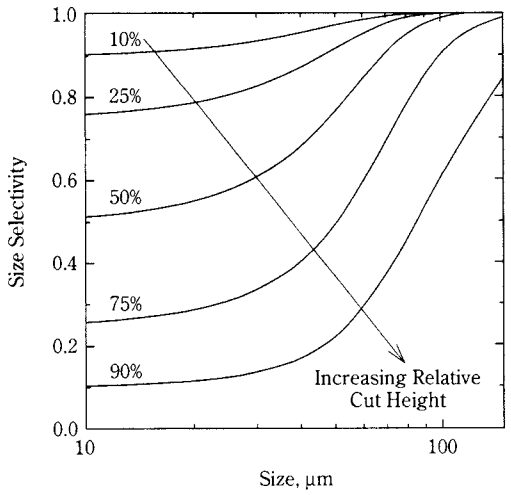

Fig. 5 Effect of cut height on the size selectivity curves.

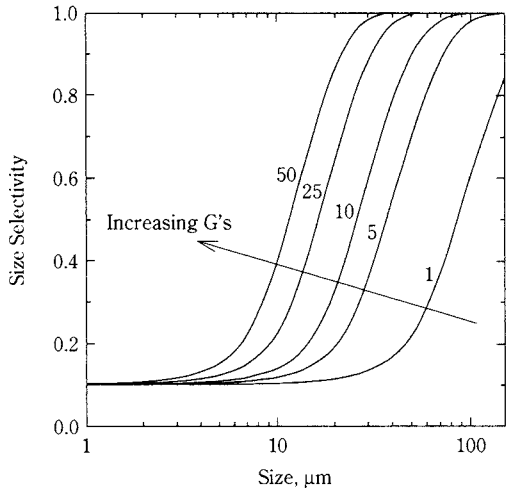

Fig. 6 Effect of the number of g's on the size selectivity curves.

Table 4 Variation of size selectivity parameters with cut height.

Relative Cut Height, z'/H	d_{50}, μm	κ	a
0.10	36.2	0.49	0.90
0.25	39.2	0.50	0.75
0.50	46.3	0.52	0.50
0.75	61.1	0.53	0.25
0.90	91.9	0.49	0.10

Table 5 Variation of size selectivity parameters with number of g's.

Number of G's	d_{50}, μm	κ	a
1	91.9	0.49	0.10
5	39.7	0.51	0.10
10	19.7	0.49	0.10
25	17.4	0.52	0.10
50	12.2	0.53	0.10

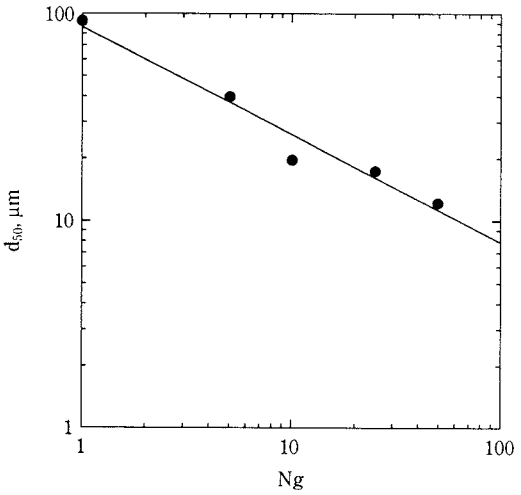

Fig. 7 Variation of cut size with the number of g's.

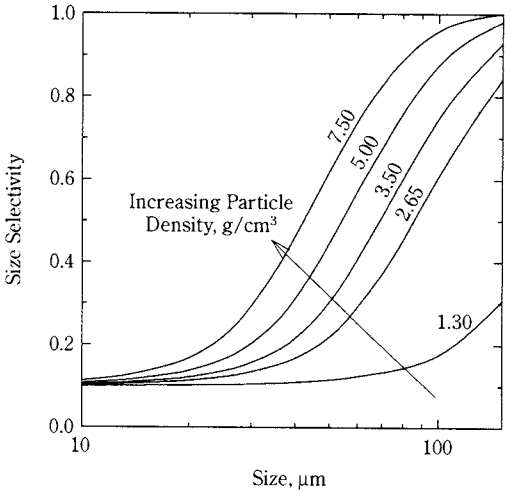

Fig. 8 Effect of particle density on the size selectivity curves.

Particle Density – Figure 8 shows the variation in the size selectivity curves for different particle densities. As expected, the curves shift to the left with increasing particle density, indicating that denser particles separate at finer sizes (**Table 6**). The separation of the lightest particles is minimal. Since a constant cut height of 90% is used, the apparent bypass for all particles approaches 0.1, independent of density. As is the case for some of the previous runs, the sharpness indices are approximately constant at about 0.5.

Table 6 Variation of size selectivity parameters with particle density.

Particle Density, g/cm³	d_{50}, μm	κ	a
1.30	233.8	0.45	0.10
2.65	91.9	0.49	0.10
3.50	73.8	0.50	0.10
5.00	57.7	0.51	0.10
7.50	44.9	0.51	0.10

Hindered-Settling Conditions

The above treatment was considered for free-settling conditions in which particle concentration did not impact the particle settling velocity. However, in many cases, separations are carried out under sufficiently high solid concentrations that hindered-settling conditions prevail. Such separations can be modeled in a manner similar to that for free-settling conditions. In this case, the rate of accumulation for particles of size x to x+dx and density ρ to ρ+dρ in an element z to z+dz is given by

$$\frac{\partial \phi(x,\rho,z,t)}{\partial t} = D\frac{\partial^2 \phi(x,\rho,z,t)}{\partial z^2} - \frac{\partial (V(x,\rho,z,t)\phi(x,\rho,z,t))}{\partial z} \quad (20)$$

where $\phi(x,\rho,z,t)$ = volume fraction of particles of size x to x+dx and density ρ to ρ+dρ in element z to z+dz at time t; $V(x,\rho,z,t)$ = velocity of particles of size x to x+dx and density ρ to ρ+dρ in an element z to z+dz at time t, with respect to the wall of the container; $\phi(z,t)$ = total volume fraction occupied by the solids in element z to z+dz at time t.

As the particles settle, they displace liquid. For higher solids concentrations, the liquid displacement is significant. Thus the rate of accumulation for the liquid in element z to z+dz is given by

$$\frac{\partial [1-\phi(z,t)]}{\partial t} = -\frac{\partial [U_f(z,t)(1-\phi(z,t))]}{\partial z} \quad (21)$$

where $1-\phi(z,t)$ = volume fraction occupied by the liquid in element z to z+dz at time t; $U_f(z,t)$ = velocity of the liquid in element z to z+dz at time t, with respect to the wall of the container.

Solving Equations 20 and 21 requires an equation to calculate the hindered-settling velocity for particles of various sizes and densities. One such equation is a modification of Concha's equation containing empirical factors to account for the effect of solids concentration on slurry viscosity. A description of this equation can be found elsewhere [Lee, 1989].

Equations 20 and 21 can then be solved using a finite difference technique to give the solids concentration at any point within the cylinder [Lee, 1989]. However, as with the free-settling equation, it is more convenient to calculate the size selectivity values. These values are given by

$$s(x;\rho,t) = \frac{\int_{z'}^{H} \phi(x,\rho,t)\,dz}{\phi_0(x,\rho)} \quad (22)$$

where $\phi_0(x,\rho)$ = initial volume fraction of particles of size x and density ρ. Equation 22 has been used to evaluate the variation of size selectivity curves under hindered-settling conditions [Austin et al., 1992]. Very similar trends were obtained as given in the previous figures. This model has also been used to generate partition curves to evaluate density sorting separations [Cho and Klima, 1994; Klima and Cho, 1995].

Wet Classification Devices

Several types of devices are used to classify particles finer than about 100 μm. The wet devices include hydrocyclones and centrifuges and dry devices include mechanical air separators, counter-flow classifiers, and transverse-flow classifiers. The selection of the specific device depends on the desired cut size and production rate.

Hydrocyclones – Classifying hydrocyclones are used extensively in a wide range of industries including mineral, chemical, food, and pulp/paper to process materials in the size range from about 500 μm to 10 μm. A schematic showing the mode of operation of a hydrocyclone is given in **Figure 9**. Essentially, a hydrocyclone consists of hollow, cylindrical and conical sections, into which slurry is admitted, tangentially, at high velocity setting up a highly rotational flow, which imparts centrifugal forces to the particles. Slurry exits the device at the apex (the underflow) and through a central "vortex finder" at the hydrocyclone overflow. The larger and denser particles are concentrated close to the walls of the cone and exit primarily through the apex. Finer and lighter particles, together with the bulk of the carrier fluid, are forced to exit through the vortex finder.

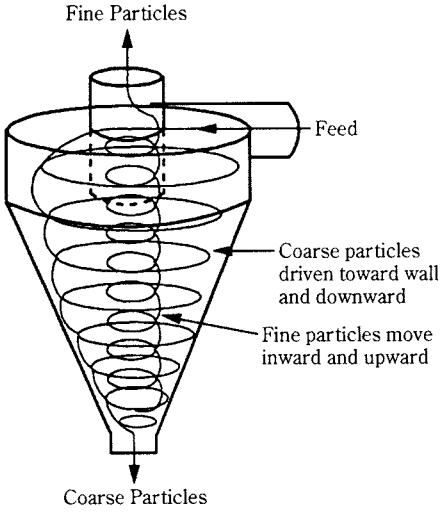

Fig. 9 Typical flow pattern of a hydrocyclone.

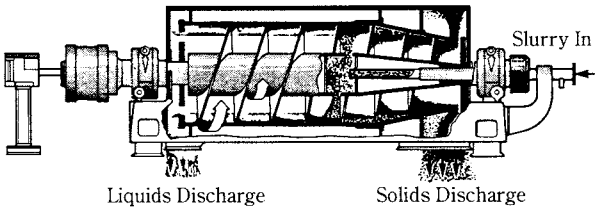

Fig. 10 Schematic of a solid-bowl (decanter) centrifuge.

Centrifuges – Solid-bowl (decanter) centrifuges can also be used for size classification of ultrafine particles (**Figure 10**). The slurry enters through the feed tube and is discharged radially onto the bowl. The (coarse) solids are collected on the bowl and are carried to the discharge end by a scroll, which rotates at a speed slightly slower than the bowl. The liquid and fines are carried hydraulically to the opposite end where they exit over an adjustable weir.

Unlike hydrocyclones, which are limited to separation sizes greater than about 10 μm, solid-bowl centrifuges can be used to separate particles finer than 5 μm. In a solid-bowl centrifuge, the gravity force can be changed by varying the rotational speed of the bowl, while keeping the flow rate constant. The result is the ability to classify at finer sizes, without a decrease in production capacity compared to a hydrocyclone, which requires smaller diameter (and lower capacity) units for finer separations. Moreover, the ability to regulate the centrifuge bowl speed (number of "g's"), flow rate (retention time), scroll speed, and weir height (water split), independently provides a high degree of control of the product size and separation efficiency. Solid-bowl centrifuges can produce more than 3000 g's and can treat a wide range of particulate slurries such as zirconia, alumina, calcium carbonate, and kaolin at sizes down to approximately 1 μm [Williamson and Bacon, 1977; Scheffler and Zahr, 1980]. They can be used either in stand-alone applications or as part of closed grinding circuits [Hennicke and Stein, 1989].

Dry Classification Devices

The vane classifier (**Figure 11**) is an example of a free-vortex counterflow classifier. The solids to be classified enter the outer cone dispersed and entrained in a gas stream. A cyclonic flow pattern is imparted on the feed stream before it passes through the adjustable vanes into the inner cone. As the vanes are closed down, an increase in the centrifugal motion causes more of the larger particles to strike the inner wall of the inner cone and drop out. The finer particles remain in the gas stream, exiting through the cen-

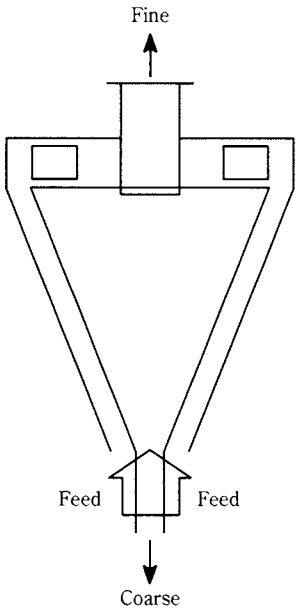

Fig. 11 Schematic of a vane classifier.

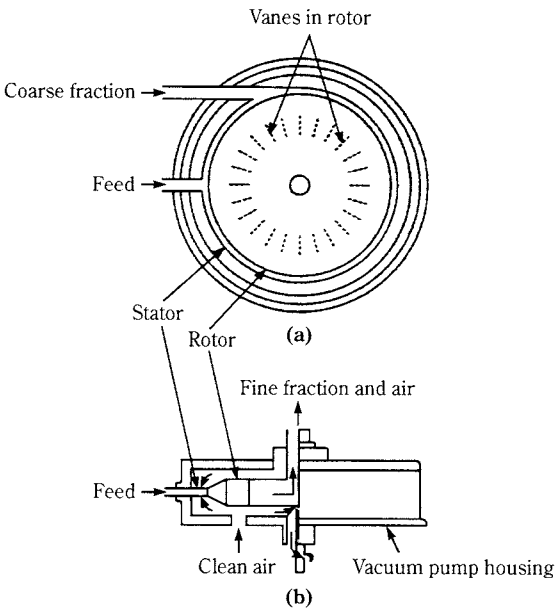

Fig. 12 Schematic of a Mikropul Acucut classifier: a) cross section; b) side view.

trally located exit conduit. For a pilot-scale twin-cone classifier, the sharpness index was constant for a set vane position [NAS, 1981]. As the vanes were adjusted from 100% (an expansion classifier) to 50% to 25% (a pneumatic cyclone) open, the sharpness index increased from 0.3 to 0.5 but then decreased to 0.3. At the lowest air rate, the d_{50} value decreased with vane settling from 120 μm at the 100% open vane settling to 50 μm to 20 μm. Increasing the air rate, thereby also increasing the feed rate, caused an increase in the cut size for each vane setting but a decrease in the apparent bypass at vane settings of 50% and 25% open area.

The free-vortex principle has been extended to fine classification. A built-in fan in the second chamber of the two-chamber Alpine Mikroplex Spiral classifier draws the classifying air into the classifier chamber while the feed is metered in separately. Adjustable vanes control the angle of air-flow approach to the center of the chamber where the fines flow out. The coarse particles are thrown to the outside and removed mechanically from the casing of the chamber. The sharpness index varies between 0.65 and 0.7, decreasing as the feed rate and hence solids loading increases. The cut sizes range between 10 μm and 80 μm, depending on the vane setting and the fan speed. No apparent bypass has been reported, but it is appropriate to assume about 5%. This value increases as the feed rate increases.

An alternative design is that of the forced-vortex in which the vanes are rotated. The Mikropul Acucut classifier (**Figure 12**) draws air in via a vacuum pump. The fines pass through the rotor, discharging out the center. The coarse particles are removed at the outer periphery. The sharpness index varies between 0.6 and 0.8, decreasing as the solids loading increases. The cut sizes range between 2 μm and 30 μm, depending on the rpm of the rotor. The d_{50} is inversely proportional to the rpm to the 1.4 power. Whereas, no apparent bypass has been reported by the manufacturer, values of approximately 5% have been measured. The forced vortex is less sensitive to solids loading than the free vortex.

The use of a rotor has been the cornerstone of the mechanical air classifier design. Rotor design has changed from blades to the multivane or post design (**Figure 13**). In this device, the feed material is dispersed in the airstream drawn through the rotor. Whether or not a particle exits in the central fine particle discharge depends on the force balance between the drag force of the particle being conveyed and the centrifugal force created by the rotor against it or the probability of collision, similar to the Ro-Pro screening device. The cut size is proportional to the rpm of the rotor and the square root of the relative density of the feed material. Values range between 5 μm and 150 μm. Operating sharpness indices can reach 0.75.

Data for a pilot device using a blade rotor design gave a constant sharpness indices of 0.6 [Austin and Luckie, 1976]. There are several responses common to classifiers employing rotors. Increasing the feed rate without any other changes reduces the d_{50} value, the efficiency of the separation, and the yield. The

data demonstrated a consistent pattern, in all cases, of the d_{50} value decreasing to a minimum with increasing feed rate. Moreover, the efficiency of the classification is reduced with increasing feed rate because the apparent bypass value increases. The fine product yield also decreases with increasing feed rate, because the increased quantity of feed is merely bypassing to the coarse stream. Assuming the air flow rate to be proportional to fan speed, then the data for a rotor rpm of 1000 gave d_{50} proportional to the air-flow rate to the 1.2 power. The 800 and 1400 rotor rpm data show that the d_{50} value is inversely proportional to the rotor rpm. Industrial versions of this separator come in sizes up to 10 m in diameter.

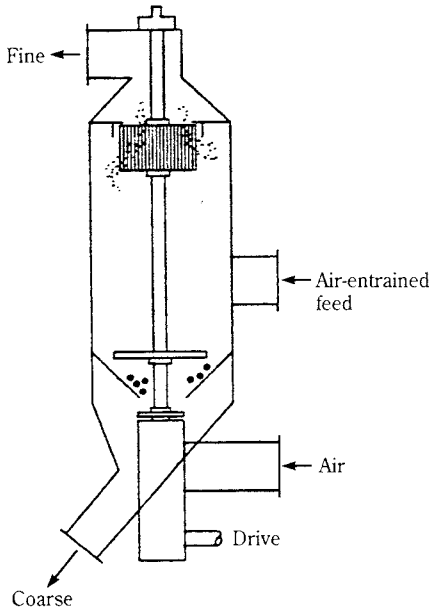

Fig. 13 Schematic of a tank through-flow mechanical air separator.

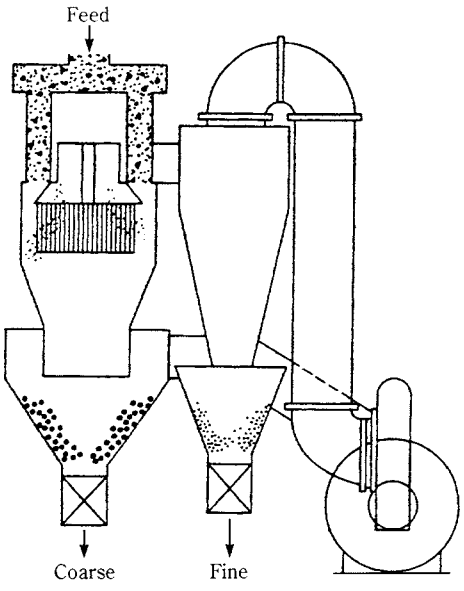

Fig. 14 Schematic of a recirculating mechanical air separator.

A recirculation design (**Figure 14**) returns the gas to the classifier through the fan after the fine particles are removed from the gas stream. Such an arrangement requires an excellent solid/gas separator; otherwise the classification becomes less efficient. Interestingly, a perfect solid/gas separator would be a device having an apparent bypass of one. If the recirculated gas is entered through a secondary coarse stream classification section, then the classification is not less efficient unless the secondary classification is very inefficient.

It is quite common in the designs for fine classification to recontact the coarse stream transversely or in counterflow with air before discharging it (see **Figure 13**). This removes dry fine particles not removed in the primary classification. That is, these particles are swept back into the feed and given another chance to exit with the fine particles. Such an arrangement increases the overall sharpness index and reduces the overall apparent bypass. Another variation is to reenter the air from the solid/gas separation of the coarse stream.

The Matsuzaka Elbow-Jet classifier (**Figure 15**) is based on a transverse flow principle [Rumpf and Leschonski, 1967]. The stream of feed particles are accelerated to minimize the effect of gravity, and introduced into an air jet at right angles. The particles are fanned out in the classification zone with the trajectories for particles of the same hydrodynamic behavior, i.e., size and shape, being the same. Classification is achieved by mounting one or more cutters in the classification zone, thus dividing the feed into two or more fractions. A stream of fine particles of less than 5 μm can be produced in this manner.

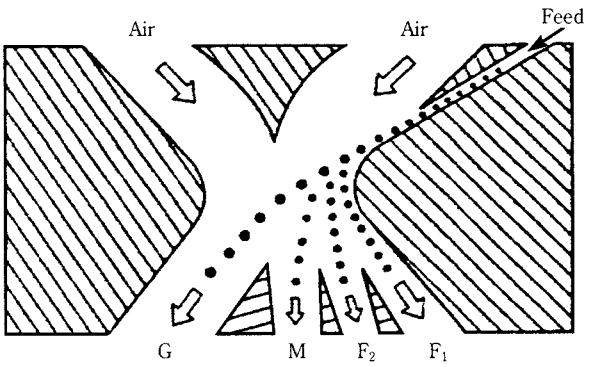

Fig. 15 Schematic of a Matsuzaka Elbow-Jet classifier (G=coarse particles, M=medium particles, F_2=fine particles, F_1 = ultrafine particles).

Staging

The practice of recontacting a stream and the subsequent return to the feed is called stage classification. Based on the linear nature of the classification process, it is possible to calculate the overall chance of a particle reporting to a particular stream for any arrangement. For example, consider the arrangement where the coarse stream from the first stage is reclassified and the fine streams from both stages blended –

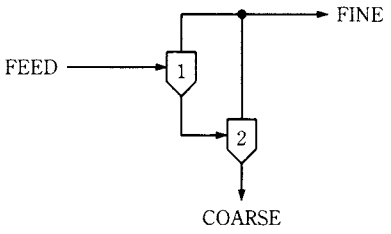

The overall chance of a particle reporting to the coarse stream based on the individual chances, is

$$s(x) = s_1(x)\, s_2(x) \tag{23}$$

Thus the overall apparent bypass is

$$a = a_1 a_2/100 \tag{24}$$

and hence will be reduced, thereby increasing the efficiency. In addition, the overall sharpness index will increase, but, unfortunately, the overall cut size will increase. The latter may not be critical since the 95% passing size in the fine stream is approximately equal to $d_{50}/(\kappa+0.16)$.

Consider instead the arrangement where the fine stream from the first stage is reclassified and the coarse streams from both stages blended –

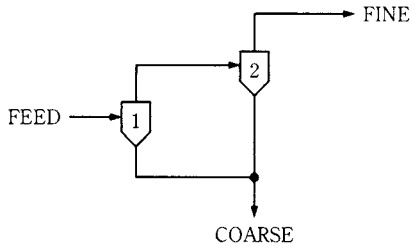

The overall chance of a particle reporting to the fine stream, based on the individual chances, is

$$1-s(x) = (1-s_1(x))\,(1-s_2(x)) \tag{25}$$

While the sharpness index may increase and the cut size decrease, the overall apparent bypass, given by

$$a = a_1+a_2-a_1 a_2/100 \tag{26}$$

will increase, reducing any efficiency increase.

An alternative arrangement is, after reclassifying the coarse stream from the first stage, to blend the fine stream from the second stage with the feed to the first stage –

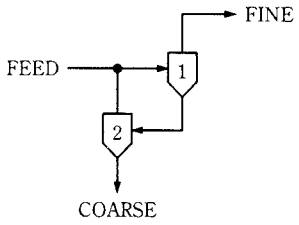

The overall chance of a particle reporting to the fine stream, based on the individual chances, is now

$$1-s(x) = \frac{1-s_1(x)}{1-s_1(x)\,(1-s_2(x))} \tag{27}$$

The overall sharpness index is increased, the overall cut size increases and the overall apparent bypass, given by

$$a = \frac{a_1 a_2}{100-a_1+a_1 a_2/100} \tag{28}$$

decreases, resulting in a much more efficient separation.

Likewise, blending the coarse stream from the second stage which reclassified the fine stream from the first stage with the feed to the first stage, i.e., –

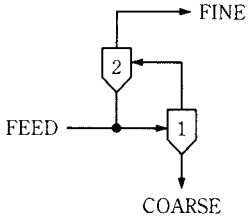

gives the overall chance of a particle reporting to the fine stream, based on the individual chances,

$$s(x) = \frac{s_1(x)}{1-(1-s_1(x))\,s_2(x)} \tag{29}$$

The overall sharpness index may increase, the overall cut size decreases, but the overall apparent bypass, given by

$$a = \frac{100\,a_1}{100-a_2+a_1 a_2/100} \tag{30}$$

increases, reducing any overall efficiency increase, or perhaps making the separation overall efficiency less.

For example, consider the results for a 25 mm diameter hydrocyclone producing a 95%<10 μm fine product. A vortex finder/apex diameter combination produces a cut size of 6 μm, sharpness index of 0.6, but

an apparent bypass of 50%! Any attempt to lower the apparent bypass in order to improve the efficiency results in an increase in the cut size, coarsening the product. However, by staging two of these hydrocyclones such that the underflow from the first becomes the feed to the second, after proper dilution, and the overflow from the second is blended into the feed to the first, it is possible by appropriate selection of vortex finder/apex diameter combinations to produce a 95%<10 μm product with an overall cut size of 7 μm, an overall sharpness index of 0.67 and an overall apparent bypass of 10%!

Conclusions

The separation of particles based on differences in size are carried out using either screening or classification. Screening relies on the probability of passage of a particle through a series of apertures of uniform size and depends on variables such as the number of presentations per second, size of the particle relative to aperture size, and retention time on the screen. In classification, the probability of a particle reporting to the coarse or fine stream depends on the relative effect of gravity and fluid drag as the particles move in a fluid. Staging can be used to improve process performance through changes in cut size, sharpness index, and apparent bypass.

References

1) Austin, L.G., Lee, C.H., Concha, F., and Luckie, P.T., 1992, "Hindered Settling and Classification Partition Curves," *Minerals and Metallurgical Processing*, **9**(4), 161-168.
2) Austin, L.G. and Luckie, P.T., 1976, "An Empirical Model for Air Separator Data," *Zement-Kalk-Gips*, **29**, 452.
3) Brereton and Dymott, 1973, "Some Factors Which Influence Screen Performance," *10th International Mineral Processing Congress*, London, 181-194.
4) Cho, H. and Klima, M.S., 1994, "Application of a Batch Hindered-Settling Model to Dense-Medium Separations," *Coal Preparation*, **14**, 167-184.
5) Concha, F. and Almendra, E.R., 1979, "Settling velocities of Particulate Systems, I. Settling Velocities of Individual Spherical Particles," *International Journal of Mineral Processing*, **5**, 349-367.
6) Gaudin, A.M., 1939, *Principles of Mineral Dressing*, McGraw-Hill, New York.
7) Hennicke, H.W. and Stein, J., 1989, "Process of Fine Milling for Ceramic Materials," *Materials Science and Engineering*, **A109**, 3-7.
8) Klima, M.S. and Cho, H., 1995, "Use of a Batch Hindered-Settling Model to Investigate Variable Interactions in Dense-Medium Cyclone Separations," *Coal Preparation*, **15**, 129-148.
9) Klima, M.S. and Luckie, P.T., 1989, "Application of an Unsteady-State Pulp-Partition Model to Dense-Medium Separations," *Coal Preparation*, **6**, 227-240.
10) Lee, C.H., 1989, Modeling of Batch Hindered Settling, Ph.D. Thesis, The Pennsylvania State University.
11) National Academy of Sciences, 1981, Committee on Comminution and Energy Consumption, National Academy Sciences Report No. 364.
12) Rogers, R.S.C. and Brame, K., 1985, "Analysis of the High-Frequency Screening of Fine Slurries," *Powder Technology*, **42**, 297-304.
13) Rumpf, H. and Leschonski, K., 1967, *Chem. Ing. Tech.*, **39**, 1231.
14) Scheffler, P. and Zahr, P., 1980, "Wet Classification at Cut Points Below 10 Microns," *World Mining*, March, 50-53.
15) Schubert, H. and Neesse, T., 1973, "The Role of Turbulence in Wet Classification," *10th International Mineral Processing Congress*, London, 213-240.
16) Whiten, W.J., 1972, "The Simulation of Crushing Plants with Models Developed using Multiple Spline Regression," *J. South African IMM.*
17) Williamson, J.T. and Bacon, F.C. "Classification of Kaolin Using Decanter Centrifuges," *Physical Separations*, Freeman and Fitzpatrick, eds., Engineering Foundation, New York, 353-371.

Author's short biography

Peter T. Luckie

Peter T. Luckie is Professor of Mineral Engineering in the Department of Energy and Geo-Environmental at The Pennsylvania State University. He received his B.S. in Fuel Engineering in 1960, his M.S. in Mineral Preparation in 1969 and his Ph.D. in Mineral Processing in 1972 from Penn State. Dr. Luckie is a member of Sigma Gamma Epsilon, Sigma Xi, Phi Kappa Phi and A.I.M.E. He has co-authored more than 50 technical articles in the mineral processing field. In addition he has been an invited lecturer at short courses and The Engineering Foundation Conferences.

Mark S. Klima

Mark S. Klima received a B.S. degree in Mining Engineering and M.S. and Ph.D. degrees in Mineral Processing from The Pennsylvania State University. His research interests center on the evaluation and simulation of physical beneficiation processes, especially in the area of fine particle separations. He is a registered Professional Engineer in Pennsylvania and is currently Associate Professor of Mineral Processing and GeoEnvironmental Engineering at Penn State.

Solvent Effects in the Deaggregation of Titania Nanoparticles[†]

Danijela Vorkapic
*Air Products and Chemicals, Inc.**
Themis Matsoukas
*Department of Chemical Engineering, Pennsylvania State University***

Abstract

We report on the effect of alcohols in the acid peptization of aggregated titania nanoparticle produced from alkoxides. Peptization was studied in the presence of each one of the following alcohols: methanol, ethanol, propanol and isopropanol. We find that the final particle size is correlated to the dielectric constant of the peptizing medium. Kinetic measurements reveal that the rate of deaggregation is not affected by the presence of alcohol; however, the tendency for reaggregation of the peptized colloid increases significantly. We conclude that alcohols prevent the full redispersion of the aggregates by decreasing the colloidal stability of the suspension. This conclusion is supported by the measured zeta potential of the peptized particles, which is found to decrease when alcohol is present.

I. Introduction

The novel optical, electronic, chemical, and structural properties of materials fabricated from nanoparticle precursors have motivated a substantial research effort in the synthesis of ultrafine particles [1-5]. A common problem is that such particles are often obtained in highly aggregated form, primarily due to the difficulty in stabilizing nanometer size particles against aggregation. With some systems it is possible to reverse the effect of aggregation and redisperse the aggregates by peptization in a suitable chemical environment. A characteristic example is the formation of titania nanocolloids from the hydrolysis and polycondensation of titanium alkoxides. This reaction produces large aggregates composed of ultrafine primary particles (3 to 5 nm) which can be redispersed through acid peptization. The degree to which redispersion is achieved varies widely. The size of the peptized particles is reported in the literature to range from about 15 nm [6] to more than 100 nm [7], which implies that the degree of redispersion is highly variable depending on the experimental conditions.

In our previous studies we have shown that the degree of redispersion has a strong dependence on the type and amount of alcohol present in the peptization medium [6]. Often, alcohol is added to the reaction mixture to provide uniform mixing of the alkoxide and water, which react rapidly upon contact. Even if no alcohol is added during synthesis, some amount is unavoidably present as a product of the hydrolysis reaction. The effect of alcohols in titania precipitation is summarized in **fig. 1** which shows that the final particle size increases substantially as the concentration of the alcohol is increased. This effect is stronger in isopropanol, weaker in butanol, and intermediate in propanol (only two experimental points are given for

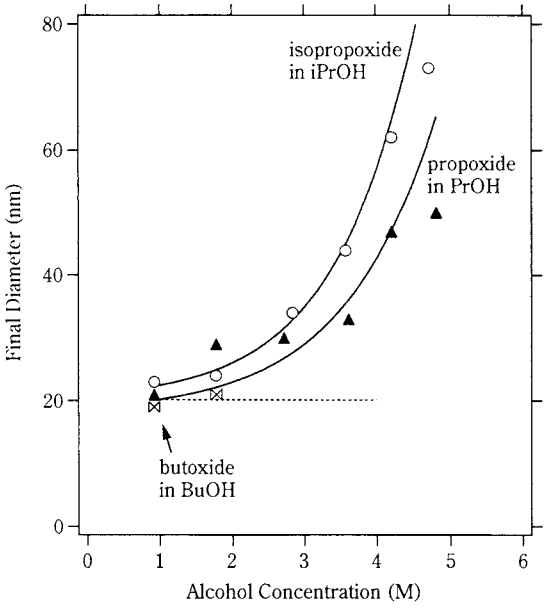

Fig. 1 Size of peptized aggregates as a function of the concentration of alcohol in the peptizing medium.

* 7201 Hamilton Boulevard, Allentown, PA 18195-1501
**University Park, PA 16802
† Received: May 16, 2000

the butoxide/butanol system because of the limited solubility of butanol in water). This trend can be attributed to two possible effects: the alcohol may inhibit the peptization of the aggregated colloid, or/and it may enhance the reaggregation of the dispersed particles. Both mechanisms would result in larger final particles. We have recently proposed a kinetic model of peptization based on the idea that redispersion is the result of competition between the peptization of aggregated particles and the reaggregation of the peptized colloid, and have shown that the model provides a quantitative description of the peptization of titania [8]. This model allows us to measure experimentally the rate constants for peptization and reaggregation and to correlate them to the process parameters. The goal of the present study is to elucidate the mechanism by which alcohols inhibits the full peptization of titania nanocolloids by measuring the peptization and reaggregation rate constants in the presence of various low-molecular weight alcohols.

II. Experimental

Titania nanoparticles were synthesized by reaction between titanium isopropoxide and water in the presence of nitric acid. The concentration of the alkoxide was 0.23 M and the amount of acid corresponds to [H+]/[Ti] molar ratio of 0.5. A specified amount of nitric acid (J.T. Baker) was mixed with distilled water in a glass bottle and the solution was placed in a temperature controller bath maintained at 50°C. Titanium isopropoxide (supplied by Aldrich) was added dropwise as the solutions were constantly stirred at 300 RPM. Titania is formed according to the reaction

$$Ti(iPrO)_4+2H_2O \rightarrow TiO_2+4iPrOH$$

The precipitation of particles is immediately manifested by the formation of a highly turbid suspension. This suspension was divided into 5 equal samples and was let to stand for five minutes. The samples were then mixed with a specified volume of an aqueous solution containing either methanol, ethanol, propanol, isopropanol, or water only (no alcohol). Within a few hours a white-blue solution was observed indicating the progress of peptization. After 6 h of continuous stirring, intermittent stirring was applied (20 s of stirring followed by 10 s of rest) to minimize shear-induced aggregation. After 10 h, the stirring was turned off and the temperature was set to 25°C. Under these conditions peptization continues for several days as indicated by the decrease of the measured particle size and by the increased transparency of the solution. All measurements and theoretical analyses in this paper are for this slow part of the process.

Particle sizes were analyzed by withdrawing samples from the peptization medium, diluting them in water, and measuring the hydrodynamic diameter by light scattering (2030AT Brookhaven model using a He-Ne laser operating at λ=632.8 nm). The reported sizes represent the average of 3 measurements. Zeta potential measurements were performed in a Zeta PALSE model by Brookhaven Instruments.

III. Peptization model

Our interpretation of the peptization experiments is based on a reversible aggregation/deaggregation model. The model has been described in detail elsewhere [8] and its salient features are summarized here. The basic premise is that while deaggregation produces smaller particles (fragments) from a cluster of primary particles but the fragments are subject to reaggregation, as shown schematically in **fig. 2**. In this picture a "particle" is a cluster of aggregated primary particles and the size of the cluster is determined by the competition between deaggregation and reaggregation. Steady-state is reached when the rates of the two processes are balanced. This condition defines the final size and the degree of redispersion that can be achieved. This model provides a simple interpretation of the observed final particle size without explicit reference to the mechanisms responsible for the peptization of the aggregates, and allows the calculation of the rate constants from kinetic experiments. Treating the deaggregation rate as a first-order process in the concentration of particles, the aggregation rate as second-order process, and equating the rate of the two processes we obtain the following expression for the cluster size, D_∞, at steady state [8]:

$$\frac{D_\infty}{D_0}=\left(\frac{3C}{\pi\rho D_0^3}\frac{K_a}{K_d}\right)^{1/d_f} \quad (1)$$

where D_0 is the size of the primary particles, C is the mass concentration of titania, ρ is the material density,

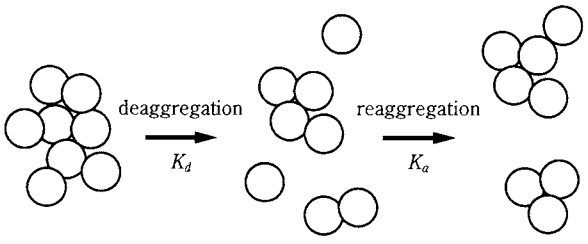

Fig. 2 Schematic representation of the deaggregation/reaggregation model of peptization.

K_a, K_d, are the aggregation and deaggregation (peptization) rate constants, respectively, and d_f is the fractal dimension ($d_f=3$ for compact particles, $d_f<3$ for fractal clusters). If we neglect the dependence of the rate constants on size, we find that the approach to the final steady-state size is given by [8]

$$\frac{D}{D_\infty}=1+Ae^{-K_d t} \tag{2}$$

where A is constant. Equations (1) and (2) provide the basis for interpreting the peptization experiments. According to Eq. (2), the deaggregation rate constant can be obtained from the slope of a semilog plot of $D/D_\infty-1$ versus time. Once K_d is known, the aggregation rate constant, K_a, is calculated from Eq. (1). In this manner we can obtain the rate constants for deaggregation and reaggregation from measurements of the size as function of time. Detailed tests and discussion of the validity of this model for the peptization of titania can be found in Ref. [8].

IV. Results and Discussion

In our previous work [6], the alcohol was added along with all the other reactants and thus was present during precipitation as well as during peptization. To remove any possible effect of the alcohol on the size of the primary particles and the structure and cohesiveness of the precipitates, in all of the experiments reported here the alcohol was added after the precipitation of titania. This ensures that the precipitate is formed under identical conditions and that any subsequent differences are solely due to effects during peptization. The particles were prepared by reacting titanium isopropoxide and as a result, 0.92 M of isopropanol is present in all of our samples during peptization (assuming complete hydrolysis of the alkoxide). This amount is in addition to 3 M of the selected alcohol that is mixed after precipitation and is the same in all samples. The following alcohols were included in this study: methanol, ethanol, propanol and isopropanol. Butanol is not part of this list because it has limited solubility in water (approximately 0.5 M at room temperature). In addition, one sample was peptized without adding alcohol. An equivalent volume of water was added to this sample to bring the concentration of titania to the same level as that of the alcohol-containing samples. This adjustment is necessary in order to obtain the same concentration of titania in all samples (recall that according to Eq. (1) the final size is also function of the concentration of titania). Therefore, all samples contain the same concentrations of titania and acid but differ in the type of alcohol that is present.

The kinetic experiments are summarized in **fig. 3** which shows the size (hydrodynamic diameter) of the peptizing aggregates as a function of time over a period of one week. In support of our previous findings, the presence of alcohol results in larger final sizes, thus lower degree of redispersion of the aggregated nanoparticles. The alcohol effect is most pronounced at the early stages of peptization. For example, after one day of peptization the size in water/isopropanol is about 90 nm compared 30 nm in water. The difference among various alcohols decreases with peptization time but even so the final size clearly reflects the environment in which peptization took place. The ranking of the solvents in terms of dispersion efficiency is: water>methanol>ethanol>propanol>isopropanol. The dielectric constant of the corresponding liquids at 25°C is 78.5, 32.6, 24.3, 20.1 and 18.1, for water, methanol, ethanol, propanol and isopropanol, respectively [9]. Thus, the quality of the solvent in terms of dispersion efficiency is in the order of increasing dielectric constant. This order is preserved even after the dielectric constant of the medium is adjusted for the amount of water that is present (see **table I**).

From these experiments we extract the rate constants for deaggregation and reaggregation. The deaggregation rate constant was obtained by fitting Eq. (2) to the data of **figure 3** and the solid lines in that figure represent these fits. The reaggregation K_a is calculated from Eq. (1) with $d_f=1.72$ and $\rho=3.84$ g/cm^3

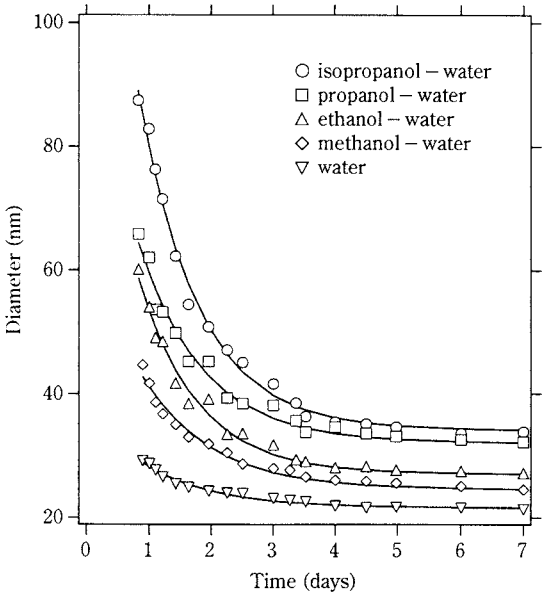

Fig. 3 The hydrodynamic diameter of peptizing particles as function of time. The lines are fits based on Eq. (2).

Table I Summary of results

	water	water/ MeOH	water/ EtOH	water/ PrOH	water/ iPrOH
D (nm)	21.5	24.5	27	32	34
ε of solution (25°C)	78.54	74	70.3	67.4	66.8
zeta potential (mV)	20	15	9.5	8.0	7.5
$K_a \times 10^{21}$ (cm^2/s)	3.90	5.00	7.05	8.72	10.5
K_d (1/day)	0.890	0.905	1.07	0.976	1.05

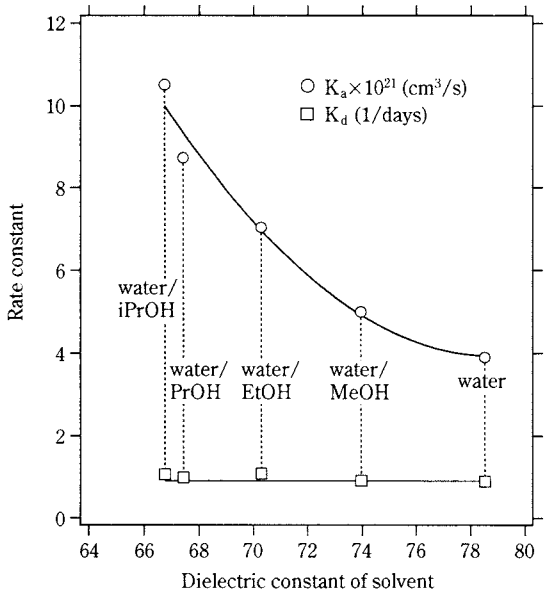

Fig. 4 Aggregation and deaggregation rate constants in various alcohol/water solutions at concentration 3 M.

[8]. The results are shown in **fig. 4** where we plot the rate constants as a function of the dielectric constant of the solvent. The aggregation rate constant decreases significantly, by a factor of more than 2, as we go from the low-dielectric constant solvent (isopropanol/water) to the high-dielectric constant solvent (water). By contrast, the deaggregation rate constant remains unaffected.

The correlation between rate of aggregation and dielectric constant is strong evidence that the observed behavior is due to reduced colloidal stability. To explore this hypothesis we performed measurements of the zeta potential of the peptized particles and the results are reported in **table 1**. The measured potential follows the same trend as the aggregation rate constant, namely, it decreases with decreasing dielectric constant of the solvent. The decrease of the surface potential is analogous to that observed in other colloids and is attributed to the adsorption of the alcohol on the oxide surface and the subsequent reduction in the number of the ionized surface sites [10,11].

Both the zeta potential and the dielectric constant of the medium are important for stability against aggregation. In a simplified picture, the stability factor, W, of the suspension can be expressed as [12]

$$W \approx \exp(V_{max}/k_B T)/\kappa R \tag{3}$$

where V_{max} is the maximum repulsive potential, approximately equal to the electrostatic repulsion between the zeta potentials of two particles,

$$V_{max} \approx 2\pi\varepsilon\varepsilon_0\psi_\zeta^2 R \tag{4}$$

In the above, κ is the inverse screening length, T is the temperature, k_B is Boltzmann's constant, ε is the dielectric constant of the solvent, ε_0 is the permittivity of free space, R is the particle radius and ψ_ζ is the zeta potential. In the presence of alcohols the zeta potential is found to be lower by as much as a factor of 2.5, resulting in poor colloidal stability. In addition, the decrease of the dielectric constant of the solvent further decreases the stability through Eq. (4) and also through the inverse screening length, κ, which scales as $1/\sqrt{\varepsilon}$ [12]. Even though the rate of deaggregation is not affected by the alcohol, the colloidal fragments produced by peptization are insufficiently stabilized and their reaggregation explains the larger sizes observed.

A correlation between alcohol (amount and type) and final particle size has been reported in other related oxide systems as well. Moon and coworkers synthesized monodisperse, spherical zirconia powders by the thermal hydrolysis of $ZrOCl_2 \cdot 8H_2O$ in an alcohol/water solution [13]. These authors showed that the presence of alcohols greatly influences the morphology and the size of final zirconia particles. Particles obtained in ethanol/water solution have soft aggregates made of ultrafine primary particles. In case of the tert-BuOH/water solution, the particles were large and spherical with a broad size distribution whereas the particles obtained from propanol/water and isopropanol/water solutions were small and spherical with a narrow size distribution. Similar observations were reported for titania synthesized under low water-to-titanium ratios [10, 14, 15] and for silica precipitated from alkoxides [16, 17]. In all of these systems, spherical, or almost spherical, particles grow by accretion of precursor units – oligomers or small particles – to final sizes considerably larger than the ones obtained in the present study. Despite differences between these systems and the peptizing environment of our study, our results provide direct evidence that the rate of aggregation is indeed higher in the presence of alcohols and that the size increase

can be attributed entirely to colloidal destabilization brought about the alcohol.

A second important finding of this study is that alcohols have no effect in the deaggregation process itself, as demonstrated by the constant value of K_d in all samples. Therefore, neither the type nor the amount of alcohol interferes with the breakage of aggregates. This result supports the notion that the mechanism of deaggregation is not electrostatic but rather chemical in nature, involving the breakage of chemical bonds between adjacent primary particles [8].

V. Conclusions

The degree of redispersion of titania precipitates formed by the aggregation of nanometer-size primary particles is affected by the presence of alcohols in the peptizing solution. Alcohols hinder the dispersion of the aggregated particles and result in larger particle sizes. This effect can be attributed entirely on the reduced colloidal stability of the suspension which enhances the reaggregation of the peptized aggregates. The peptization mechanism itself is not affected by the presence of the alcohol and its rate constant remains the same regardless of the amount or type of alcohol present.

Acknowledgements

This work was supported by the National Science Foundation under grant CTS#9702653.

References

1) Lafait and S. Berthier, in Nanophase Materials: Synthesis-Properties-Applications (NATO ASI Series, Kluwer Scientific, Boston, 1993), p. 449.
2) L. E. Brus, in *Nanophase Materials: Synthesis-Properties-Applications* (NATO ASI Series, Kluwer Scientific, Boston, 1993), p. 433.
3) O. Koper and K. J. Klabunde, in *Nanophase Materials: Synthesis-Properties-Applications* (NATO ASI Series, Kluwer Scientific, Boston, 1993), p. 789.
4) A. Tschope and J. Y. Ying, in *Nanophase Materials: Synthesis-Properties-Applications* (NATO ASI Series, Kluwer Scientific, Boston, 1993), p. 781.
5) R. W. Siegel and G. E. Fougere, in *Nanoparticles in Solids and Solutions*, edited by J. Fender and I. Dekany (NATO ASI Series, Kluwer Scientific, Boston, 1996), p. 233.
6) D. Vorkapic and T. Matsoukas, J. Am. Cer. Soc. **81**, 2818 (1998).
7) C. Lijzenga, V. T. Zaspalis, K. Keizer and A. J. Burrgraaf, Key Engineering Materials **61-62**, 379 (1991).
8) D. Vorkapic and T. Matsoukas, J. Colloid Interface Sci. **214**, 283 (1999).
9) *Handbook of Chemistry and Physics*, edited by R. C. Weast (CRC Press, Boca Raton, 1974).
10) H. K. Park, D. K. Kim, and C. H. Kim, J. Am. Ceram. Soc. **80**, 743 (1997).
11) P. Hesleitner, N. Kallay, and E. Matijevic, Langmuir **7**, 178 (1991).
12) R. J. Hunter, *Zeta Potential in Colloid Science* (Academic Press, New York, 1981).
13) Y. T. Moon, H. K. Park, D. K. Kim, and C. H. Kim, J. Am. Ceram. Soc. **78**, 2690 (1995).
14) M. T. Harris and C. H. Byers, J. of Non-Crystalline Solids **103**, 49 (1988).
15) M. T. Harris, O. A. Basaran, and C. H. Byers, Mat. Res. Soc. Symp. Proc. **271**, 291 (1992).
16) W. Stober and A. Fink, J. Colloid Interface Sci. **26**, 62 (1968).
17) T. Matsoukas and E. Gulari, J. Colloid Interface Sci. **124**, 252 (1988).

Author's short biography

Danijela Vorkapic

Danijela Vorkapic was born in Yugoslavia and received her B.S. degree in chemical engineering from the University of Belgrade. During her undergraduate studies she joined North Carolina State University, Department of Material Science, for three months and worked as an undergraduate research assistant while helping design and conduct experiments on the atomic layer epitaxy of Si, SiC, and GaN. After receiving her B.S. degree, she worked in "Duga", a paints and varnishes company in Belgrade, as a junior engineer of process development optimizing processes of coatings technology. Later, she joined Penn State University to pursue her Ph.D. under the guidance of Dr. Themis Matsoukas. For her Ph.D. dissertation she conducted studies on the kinetics and colloidal stability of nanosize titania formation for the qualitative and quantitative understanding of process mechanisms. After completing her Ph.D. she joined Air Products and Chemicals Inc where she is now a senior research engineer.

Themis Matsoukas

Themis Matsoukas received his undergraduate degree in Chemical Engineering from the National Technical University in Athens, Greece, and his Ph.D. from the University of Michigan. He was a postdoctoral researcher at UCLA and later joined the Pennsylvania State University where he is now Associate Professor of Chemical Engineering. He has conducted experimental and theoretical research in particulate systems, including synthesis and characterization of nanocolloids, modeling of particle growth in liquid and gas-phase media, the sol-gel synthesis of silica and titania colloids and gels, numerical methods for the solution of population balances, and the plasma processing of particulate materials.

Particle Breakage and Attrition†

H. Kalman
Department of Mechanical Engineering
*Ben-Gurion University of the Negev**

Abstract

The attrition of particulate materials during their handling and processing may result in losses of material, poor product quality, poor flowability and environmental pollution caused by the generation of dust. It is not surprising therefore that so much research has been devoted to studying the breakage mechanism of particles, in order to reduce the attrition in conveying and handling systems. In this paper, an extensive literature review on the above topics is presented. The literature review also covers the experimental systems that are commonly used to evaluate these phenomena. Moreover, some new experimental results are presented to clarify future trends, to better understand the complex mechanisms at work, to reduce the required number of 'standard indices' and to enable better engineering design.

1. Introduction

Particle breakage is a common occurrence in science as well as in engineering. Depending on the situation, the same phenomenon is referred to as crushing, grinding, fracture, partition, division, disintegration, shattering, scission, fragmentation, degradation, and abrasion. However, while "comminution" is used to describe the desired breakage of particles, "attrition" is the undesirable damage of particles. Both comminution and attrition are a result of either impact, compression, frictional or shear forces, or sometimes a combination of these forces.

In the chemical processing industry, breakage can strongly influence the operation and economics of a manufacturing process [1]. Particle breakage can occur in a variety of modes depending on material characteristics and the level of applied stress. Such stresses are encountered in nearly all handling and processing systems and lead to attrition, which, physically, is identical to comminution except that it represents losses due to undesired particle breakage. Attrition is not restricted to any particular type of process, even though there are some processes where it occurs more readily or where its effects are quite serious. The effects of attrition can be a loss of product by removal of undersized particles from the process streams, the need for recycling lost products, the requirement for additional filtration, loss of flowability and environmental pollution caused by large quantities of dust. Conveying systems that increase attrition are: free fall systems, chutes, screw conveyors, pneumatic and hydraulic conveyors, fluidised bed systems, cyclones, silos, etc. [3].

Massive fracture usually occurs when the overall stress acting on a particle exceeds a critical value, and results in disintegration of the particle into a large number of fragments, all significantly smaller than the parent. Degradation is probably associated with smaller applied stresses for which the critical value is only exceeded locally – at the edges, for example. Here, the original particle retains its identity but experiences a slow, more or less continuous loss of mass. At the same time, there is a continuous production of fragments much smaller than the parent [4]. Damage to the particles can occur immediately or after repeated loadings below the critical value, a phenomenon known as fatigue [5].

In chemical engineering practice, attrition may be an important factor in the design of plants with solids processing steps [6,7]. However, a complete mechanistic understanding of solids breakage is not yet available despite numerous fundamental studies [8,9]. To quantify breakage for process design and optimisation, three pieces of information are needed – the stress distribution, the rate at which breakage occurs, and the number and sizes of the "daughter" particles resulting from breakage of a parent particle. The problem is further compounded by the fact that breakage may be history-dependent, with the solid fracturing along existing cracks [1]. This may par-

* P.O. Box 653, Beer Sheva 84105, ISRAEL
† Received: August 8, 2000

tially explain the complexity of the problem that involves simultaneous fractures growing within a large number of interacting particles. As the breakage proceeds, the stress distribution and load transfer between particles changes significantly. Detailed theoretical studies are mostly limited to the propagation of single cracks inside a single particle, and studies that are more global are largely statistical in nature. Experimental studies provide only very superficial data such as fragment size distributions. The existing continuous numerical schemes such as finite element methods can also handle only the propagation of one or two cracks inside a single particle, and do not appear to be able to handle massive fracture [2].

Since a theoretical or numerical analysis of comminution or attrition processes up to a level that could be applied to practical design is impossible, it is common to evaluate the strength of particles and their damage (breakage and degradation) by measuring various indices of friability in a variety of standard systems. Another approach is to conduct simulation experiments with the system in question or a similar one. Many different types of tests have been described by the British Materials Handling Board [3] and in studies such as those by Bemrose and Bridgwater [10] to assess the breakage and attrition tendency of particulate materials.

In this paper, some recently published papers concerning both experimental and theoretical approaches to the breakage and attrition of particles are reviewed. The discussion is limited to compression of individual particles and particulate beds and to impact loads. Examples of comminution and attrition systems are given to emphasise the practical application. Throughout the paper, the fatigue phenomenon is emphasised. Some original experimental results by the present author are also shown.

2. Compression Strength

2.1 Compression of single particles

It is often necessary to monitor the strength of a product rapidly and reproducibly. This is particularly important if the breakdown of particles in subsequent handling is to be avoided. The conventional method is the so-called 'Brazilian test', in which single particles are crushed between two platens and the load required for fracture is recorded. However, in any batch of particles formed under nominally identical conditions, there is always a wide variation in the fracture loads measured in this way. Consequently, many particles must be tested before a reliable average can be

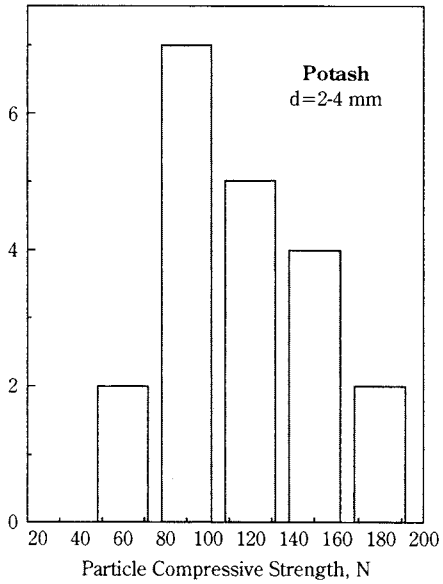

Fig. 1 Compressive strength distribution of single particles of potash.

obtained [11]. An example of compressive strength measurements is shown for potash in **Figure 1**. For only 20 measured particles, the strength range was found to be from 59 to 175 N.

Many researchers conducted experiments to evaluate the compressive strength of single particles of various materials: Shipway and Hutchings [12] tested brittle spheres, Adams et al. [11] tested agglomerates, and Kalman and Goder tested potassium sulphate [5]. It has been shown that the fracture behaviour of a single grain depends generally on its size, shape, material properties and the loading conditions [13]. Danjo et al. [14] measured the particle diameter and compressive load for 140 particles individually, and then the single particle strength was calculated. They found that the compressive strength decreased exponentially with an increase in particle diameter up to about 500 μm, and thereafter showed a constant value. The breakage behaviour of fine single brittle particles of five minerals and two coals in a size range from 88 μm to 1 mm was investigated by Sikong et al. [15]. They found that the relation between the particle strength and the particle size of these fine particles is similar to that of coarser particles.

Gundepudi et al. [16] studied brittle spheres using a different compression method, namely three-point in-plane loading. They found that there are maximum tensile stresses that correlate well with failure, and which are partially responsible for attrition in particulate systems. In the case of tablets, axial and radial compression yields compressive and tensile stresses. However, Kalman et al. [17] showed that the two stresses

are correlated for large tablets (2.5 cm in diameter).

The fracture of brittle materials is controlled by the propagation of a primary crack in a tensile field. Many research studies were conducted to develop theoretical models for crack propagation. Mecholsky et al. [18] found three local maximum tensile stress regions in particle-particle or particle-wall contact situations. The first is the region just outside the contact circle, the second is far-field surface stresses near the meridian of the sphere relative to the contact point, and the third is a region of internal stress below the contact surface and the compressive zone. Tsoungui et al. [13] proposed a theoretical model to define the failure criterion on an individual grain subjected to an arbitrary set of contact forces. The model is implemented in a two-dimensional computer simulation code based on the molecular dynamics method to study the crushing mechanisms of grains inside a granular material under compression. Song et al. [19] proposed a direct stochastic simulation method, which is applicable for general population balances with particle break-up, based on the analysis of the dynamic break-up process of particles in particulate systems. They suggested two steps: 1) to determine whether a particle breaks up using the breakage frequency function; and 2) to determine the volume of daughter particles for one breakage event using the probability distribution function. Another method for generating theoretical breakage distribution functions for multiple particle breakage is presented by Hill and Ng [1]. Mecholsky et al. [18] also found a correlation between the numbers of pieces generated during fracture, the stress at fracture and the fractal dimension for a particular loading geometry. However, in the case of an individual grain with an arbitrary number of contact forces, the calculation of the stress distribution inside the grain and the prediction of its fracture condition remains a difficult task [13].

However, before making any attempt to use these models in practical systems, several further steps should be defined and developed:

1. Crack propagation is a stochastic phenomenon that depends on the structure of the particle, pores, stresses and contaminant distributions. The breakage models should therefore be developed to a stage where a reasonable average for further practical use can be defined despite the variety in the structure of individual particles.
2. The models should be suitable for irregular particle shapes and various sizes.
3. Since particles in the size order of a few millimetres and lower are usually not crushed as single particles, the model should relate the breakage to multiple contact points with variations of stress distribution at the boundaries being accounted for.
4. Finally, the crack propagation models should yield the number and size of daughter particles. In a particulate bed, the daughter particles of a broken particle will affect the remainder of the unbroken particles by increasing the contact points and changing the stress distribution at the particle boundaries.

Since the above requirements are quite complex, more research effort should be devoted to developing empirical or semi-empirical correlations.

2.2 Compression of particulate beds

A simple alternative method to the single particle compression test consists of replacing the single particle with a confined bed of similar particles and then inferring an average single particle strength parameter from the behaviour of the whole bed under compression. This is most easily achieved experimentally using a piston in a cylinder, in which the test becomes one of uniaxial confined compression [11]. Kanda et al. [20] studied the compressive crushing of powder beds (quartz) for a roller mill application. They studied the effect of applied load, the mass of the feed and the particle size on the probability of crushing and on the crushing resistance. Holman [21] showed – for these and similar handling systems – that the percolation theory in combination with the principles of mechanics adequately describes the relationship between the normalised solids fraction and the logarithm of the applied pressure. According to this theory, the materials can be classified by their softness or rigidity on the one hand, and their flexibility or brittleness on the other, depending whether a rigidity threshold, a brittle-ductile transition or a percolation threshold is exceeded.

The pragmatical approach used by Liu and Schönert [22] for modelling interparticle breakage has proved its ability of predicting the size reduction of an arbitrary feed distribution within a technically reasonable range and with a good degree of accuracy. It should therefore be possible to use it for modelling closed-circuit comminution systems with high-pressure roller mills. In an additional experimental study, this application was tested and it was found that model calculations were able to predict the experimental results well [22].

By carrying out confined uniaxial compression tests with monosized materials, the percentage of broken particles versus the pressure can be determined. A

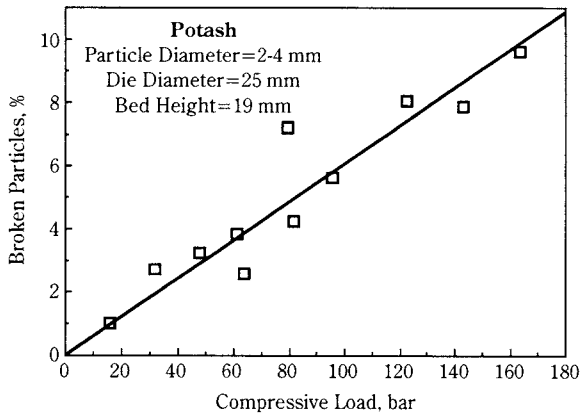

Fig. 2 Confined uniaxial compression of potash.

compression test of potash is presented in **Figure 2**. The experiment was conducted up to a pressure where bonds between particles were observed. The percentage of broken particles was determined by the ratio of undersized particles to the initial weight during sieving, without any distinction being made between fragmentation and degradation. At the presented range of compression loads, the percentage of broken particles is linearly dependent on the compression load. However, for other materials and higher compression loads, the breakage was found to level off at a certain load [5].

3. Impact Strength

Impact tests are common and are aimed at subjecting materials to forces that are similar to those they would encounter during handling (dilute-phase pneumatic conveying, chutes, etc.) and during comminution in a jet mill. It is believed that by performing tests on either single particles or groups of particles that collide with walls or with other particles, a representative measure of the particle friability can be obtained [3]. Therefore, much effort has been devoted to improving the test rigs and the measuring systems. Guigon et al. [23] presented a comprehensive literature survey of studies that investigate the impact of particles on various targets. The reported experimental velocities varied from 1.1 up to 600 m/s. Tavares et al. [24] and Tavares [25] used sophisticated measurement equipment. The test rig consists of a long steel rod equipped with strain gauges on which a single particle or a bed of particles is placed and then impacted by a falling steel ball. Until now, this system has been used to investigate the deformation and fracture of single particles subject to impact crushing.

According to many investigations, the following parameters were found to affect the attrition rate due to impact:

1. Particle Velocity – The fundamental studies of Salman et al. [26-29] and Ghadiri and Papadopoulos [30] demonstrate that the attrition rates increase with increasing velocity. Gorham and Salman [31] found that at the lowest velocities, fracture is mainly due to a brittle-elastic response. At higher velocities, inelastic deformation under the impact site leads to characteristic patterns of fragmentation arising from radial, lateral and meridian cracks.

2. Particle Size – The particle strength decreases as the particle size increases [24,32,33] because larger particles have more micro-cracks and impurities. Nevertheless, the length and number of micro-cracks may vary; therefore, some results showed that particle attrition is independent of particle size [34,35].

3. Particle Shape – Vervoorn and Scarlett [33] found that particle shape is an important factor in attrition, especially when the presence of sharp edges and corners allows large local stresses to be created that easily cause particle attrition. Tavares et al. [24,25] also showed the effect of particle shape on the particle fracture energy, the particle strength and the particle stiffness.

4. Target Rigidity – Salman et al. [26-29] and Mebtoul et al. [36] established the influence of target nature, thickness and orientation on the attrition rate of particles colliding with targets.

5. Particle Orientation – Cleaver et al. [32] found that the attrition mechanism depends also on particle orientation. For impacts on sharp corners and edges, particle damage appears to result from semi-brittle failure at all velocities tested. For impacts on crystal faces, however, a threshold velocity was identified, above which brittle fracture occurred, and below which no visible damage was detected.

6. Impact angle – The studies of Salman et al. [26-29] showed that the probability of particle failure varies only slightly from normal impact to about 50^0.

The mechanical strength of agglomerate materials under impact was investigated by means of computer simulation using Distinct Element Analysis. The breakage of agglomerates upon impact is shown to increase with impact velocity until a certain limit is reached, beyond which the damage seems to approach an asymptote [37]. An examination of the mechanisms that lead to the pattern of impact breakage in two-dimensional discs was presented by Potatov and Campbell [38].

It should be noted at this stage that most of the experiments reported above with high velocities were conducted with systems where the particles are accelerated in an air stream (air gun) and oriented towards

a target. These experimental systems are limited to large particles with high densities. Otherwise, the particles tend to follow the air stream, and do not collide with the target, or are deflected by the air stream to collide at a different angle. These systems should, therefore, be modified to enable fine powders to also be tested.

4. Comparison Between Methods

Comparison between the various methods of measuring particle strength is very important. Although during the years, similarities have been found between the comminution and attrition behaviour in practical systems and some strength measurement methods, all methods relate, in one way or another, to the strength of the particles. Reliable theoretical models or empirical correlations relating the strengths measured by various methods could significantly reduce the number of required measurements and strength indices in current use. Therefore, research and investigation for comparing various strength measurement methods is very important.

4.1 Compression of individual particles and particulate beds

The bulk crushing test is commonly used in industrial applications to assess the attrition resistance of particles. A small quantity of particles is placed in a rigid container and loaded quasi-statically by a piston to a pre-specified level of stress. The extent of breakage is then analysed after the unloading stage. However, despite the simplicity of the test procedure, the analysis of particle breakage is very difficult because the test is carried out on an assembly in which not all particles are uniformly loaded. It is therefore difficult to relate the test results to particle properties; a task that is highly desirable for the optimisation of production as it enables the particle properties to be tailored for improved performance [39]. A full solution to this problem would require the formulation of an assembly model relating the distribution of contact stresses to the distribution of single particle failure stress within the bed. In practice, this problem is so complex that it can only be addressed by computer simulation [11].

Danjo et al. [14] found experimentally that a linear relationship existed between the compressive load and the number of particles. The average particle strength was found to be lower than the single particle strength in every sample. This is due to a variety of factors such as the distributions of particle size, shape, and compressive strength in multiple particle systems. They also examined the particle strength evaluated from the inflection of the compression curve of a particulate bed. Particle strengths obtained from the inflection points were closely related to the single particle strength.

Adams et al. [11] presented a simple theory that provides a means by which the average shear strength of a single agglomerate can be obtained by experiments on a bed of agglomerates, and this value is related to the single particle crushing strength through a single empirical proportionality factor. Such numerical methods as the Distinct Element Method [39] and Distinct Elements Analysis [40,41] were also applied to find the relationship between bulk compression and single particle compressive strengths. Single particle mechanical properties such as Young's modulus and compressive strength distribution have been characterised by Couroyer et al. [39] and used in the simulation to predict the bulk crushing behaviour. The results show that an increase in the value of Young's modulus and the coefficient of friction leads to a significant increase of breakage in the assembly, and that a decrease in the loading rate leads to a lower extent of breakage. The strength of three samples with different levels of macroporosity was compared under quasi-static loading by Couroyer et al. [41]. The experimental data were used to test the DEA.

In order to develop a reliable model, the individual particle compressive strength should be related to particulate bed experiments through the distribution of contact points that transfer the loads and the compression level. The distribution of contact points depends on the size distribution of particles and their orientation and structure in the bed. The problem then becomes more complicated since at low loads and low bed-compaction, particles fracture when the area-averaged load exceeds their single-particle fracture strength. At higher loads and degrees of compaction, fine particles begin to transmit force, and distribute the force flux over the surface of large particles [42].

All of the above-described models assume the compression stress within the die to be constant. However, preliminary results obtained by the present author show that the pressure varies along the die height and sometimes also radially at the pressing piston. The single particle load at the die walls was measured by indentation. In order to increase the indentation sensitivity, a thin copper plate was used to replace the die walls. In these tests, very hard zirconium spheres of 1-1.2 mm in diameter were used in a

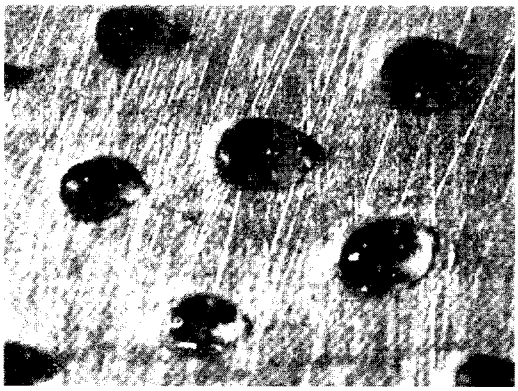

Fig. 3 Indentation of hardened zirconium spheres of 1-1.2 mm in diameter. The die diameter is 25 mm and bed height 35 mm. Compression pressure=3000 kg. The picture shows the indentation at a height of 32 mm from the static piston.

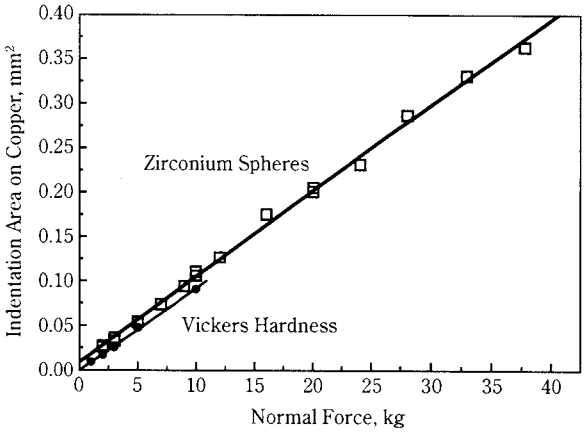

Fig. 4 Calibration of indentation area with individual particle compression.

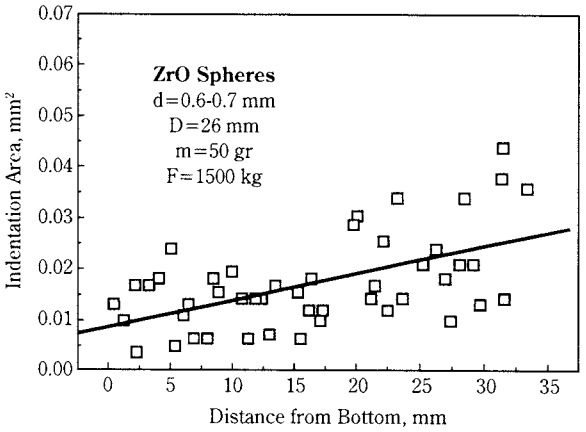

Fig. 5 Indentation distribution along the die wall.

25-mm-diameter die. An example of the indentation at the die walls is shown in **Figure 3**. The indentations have a "droplet" shape which indicates that the bed deforms during application of the load. The indentation area is, however, proportional to the force that presses the spherical particle against the die wall. The force and indentation area were calibrated in a similar way for the hardness measurement of surfaces, and some typical results are shown in **Figure 4**.

Figure 5 is presented to show the indentation area at the die wall as a function of height from the bottom surface (the bottom surface was kept stationary while the load was applied through the upper surface). It is clear that the average indentation area, and consequently the pressure, increase towards the upper surface. This emphasises the need to describe the pressure distribution within the die in a more accurate way prior to any attempt to relate it to the stress experienced by individual particles within the die for their breakage analysis.

4.2 Compression and impact

Shipway and Hutchings [12] presented results of a theoretical and experimental study of the fracture of single brittle spheres by uniaxial compression between opposed platens and by free impact against plane targets. They found that the stress distributions in elastic spheres are broadly similar under both types of loading, with significant tensile components inside the sphere on the axis of the system and on the surface of the sphere, around the equator for the case of compression. Salman et al. [26] have also found similarities in the features of failure of aluminium oxide particles subject to static compression and normal impact. Gorham and Salman [31] carried out impact and compression tests and described the forms of failure and their variation with diameter and impact velocity. Shipway and Hutchings [43] tested glass and sapphire spheres. They reported that the fracture depended strongly on the properties of the platen or target. Shipway and Hutchings [44] derived numerical values for the elastic stress fields in spheres under conditions of quasi-static compression and free impact against plane targets.

5. Fatigue Strength

In most of the handling and conveying systems involving attrition, each particle experiences more than one event of loading. The loading might be of compression and shear force, as in silos, or of impact force, as in pneumatic conveying systems. Many research studies related the attrition rates to the residence time in continuous systems or to the test time in batch systems [45]. However, their tests should be related to the number of loading events, which is a more fundamental parameter as it relates to fatigue [5]. The kinetics of batch milling was proposed to be

expressed with respect to energy instead of time [46]. Moreover, Potapov and Campbell [47] noted that the attrition rate is simply related to the total work performed on the system. This appears to be independent of the mechanisms of breakage, how the work is applied, and even whether the material is experiencing quasi-static or rapid flow behaviour.

Comminution processes involve a combination of discrete breakage events by particle fracture and continuous degradation. A simplified model for a mathematical description of the overall process, as well as process simulations as used to illustrate the effects of the different mechanisms on grinding kinetics and product size distribution, are described by Hogg [4]. He also pointed out that product size distributions assume an increasingly bimodal character as the relative contribution from degradation increases. In order to evaluate a continuous grinding process, a model is proposed which combines experimentally determined breakage kinetics [48]. Berthiaux and Dodds [49] developed a methodology for characterising grinding kinetics based on a new criterion, the so-called "residual fraction" to represent the performance of a grinding process. Similar analyses could be applied to attrition in the handling and processing of particulate materials.

5.1 Compression

Although in storage and handling systems, particles may experience repeated compressive loadings, almost no previous reports concerning fatigue behaviour were found. Experimental results concerning the repeated compressive loading of particulate beds were reported by Kalman and Goder [5,50,51]. They used a testing rig that is shown in **Figure 6**.

A sample of the tested material is compressed in a cylindrical die under repeated compressive forces. Both rate and maximum value of the compressive force are adjustable. The number of cycles is pre-set for every test. The test rig was designed in such a way as to enable the application of compressive stresses to a bulk material inserted into a cylindrical die. After filling, the matrix is tapped to achieve better repeatability of the initial conditions. The upper piston is loaded by a pneumatic piston through a beam that compresses the material. By varying the location of the pneumatic piston, its air pressure, and the die dimensions, one is able to control the compression stress. A pressure switch controls the load of the pneumatic piston between the pre-set upper and lower pressures. The frequency of operation is controlled by a needle valve. With this arrangement, the pneumatic piston increases the load until the upper set point of pressure is reached and then the pressure is reduced to zero, and so on. The frequency was set to very low values to avoid impact effects. An electrical counter that enables long experimentation overnight for thousands of pre-set cycles was incorporated into the system. After each test was terminated, the percentage of material under a certain size was measured.

For engineering use, a fatigue curve is useful. The "fatigue curve" is a term taken from mechanical engineering, and which is applied to metals to describe the load versus the loading cycles for damage to a standard specimen. Since the tested material is a single specimen, a single curve is plotted for any probability of occurrence. In fatigue experiments of particulate assemblies, however, many specimen particles exist in a single test. It would be impossible to plot a single curve. However, several curves can be plotted to describe an amount of damage by each curve as shown in **Figure 7**. From an engineering point of view, the compression load and the number of loading cycles can be found for a postulated amount of dam-

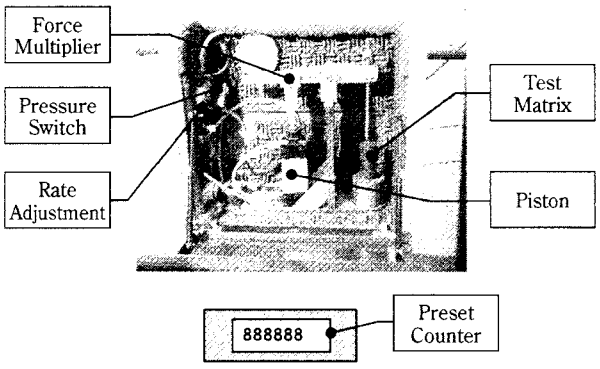

Fig. 6 Experimental apparatus for repeated compression cycles.

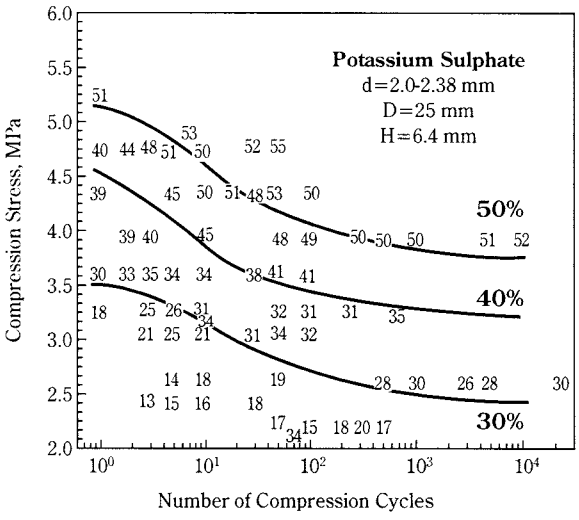

Fig. 7 Fatigue curve of potassium sulphate.

age from such curves. Each curve is expected to stabilise, as mentioned earlier, because the stress distribution on each undamaged particle is moderated due to the broken particles that provide more contact points.

The fatigue curve of potassium sulphate is shown in **Figure 7**. The percentage of undersize particles is an uncontrolled parameter in the experiments. It is a result of the compression stress and number of cycles and is measured only after the test is terminated. Therefore, it was impossible to conduct experiments with a constant amount of damage. The percentage of undersize particles is indicated in the figure for each experiment. From these, the fatigue curves were estimated and plotted manually. As expected, the amount of damaged particles increases with both the compression stress and number of cycles. As expected, the curves also stabilise after a certain number of compression cycles.

In order to complete the insight into the fatigue behaviour, many more tests with various materials must be conducted. Furthermore, new experiments on the fatigue of individual particles subjected to repeated compression loads will be conducted. Finally, a correlation between single particle strength and particulate bed strength during cycled loading can be determined based on the modified or existing empirical models that relate the single particle and particulate bed strength in a single static compression.

5.2 Impact

Most experiments published in the literature and the standard available equipment are related to repeated impact loads. Salman et al. [27-29], Cleaver et al. [32] and Ghadiri and Papadopoulos [30] showed that attrition rates increase sharply with the number of impacts. Also experiments conducted in fluidised beds, which are common test rigs for attrition measurements [34,52], show that attrition rates increase with time. The time of fluidised bed operation can be converted, although in a very complex manner, to the number of impacts. A new test method that allows the characterisation of granules by their attrition resistance, fatigue lifetime and breaking mechanism was presented recently by Beekman et al. [53].

The following sections describe impact strength measurements in various experimental rigs and their relation to attrition in industrial systems. The impact velocity is divided into two ranges: low velocity (1-10 m/s) that is applicable in chutes, dense-phase pneumatic conveying, fluidised beds and some processes conducted in rotating drums such as coating and granulation; and medium velocity (10-40 m/s) that is applicable in dilute-phase pneumatic conveying. A high impact velocity (80-300 m/s) may occur in comminution systems such as jet mills and pin mills.

5.2.1 Low velocity – rotating drum

Rotating drums are used as a means of conducting some processes such as coating, granulation and mixing, as well as for characterising the attrition and strength of particles. This apparatus is widely used in the pharmaceutical industry to characterise the strength of tablets. This method was also used for large tablets (1 inch in diameter) by Kalman and Targan [22]. They found that the attrition rate of tablets is well correlated to the compression or tensile strengths.

Figure 8 presents an example of several results obtained by Grant and Kalman [54] with a rotating drum made of steel of 285 mm in length and 265 mm in diameter. One shelf of 40 mm in width was used. The multiplication of the rotation speed by the period of operation provided the number of rotations. After a predetermined period of operation, the sample was sieved to provide a size distribution, and in some cases the strength of the particles was measured by a Crush Strength Analyser. An example of the size distribution variation during a test with potash is shown in **Figure 8**. The test was conducted at 30 rpm with a sample weight of 100 gr. The initial size of the sample was in a narrow range between 2 and 4 mm, so the sample could be considered monosize material. The figure shows the total weight percentage under the size indicated at each line (cumulative undersize). The upper line, showing the cumulative weight under 2 mm, shows the total weight percentage of the particles that were found to be smaller in size than the initial lower limit. As expected, the percentage of damaged particles increases as the number of rotations

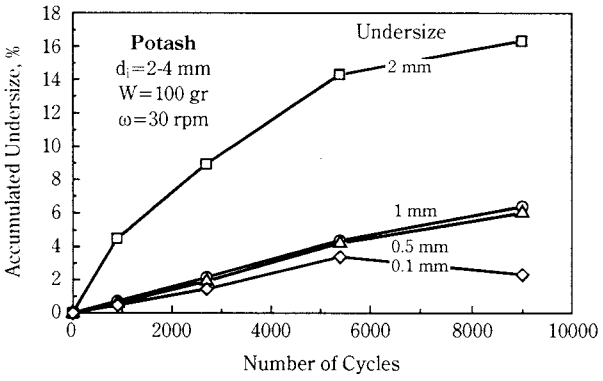

Fig. 8 Attrition of potash in a rotating drum versus the number of rotations.

increases. This is probably due to fatigue. However, it seems that the rate of attrition of the particles decreases.

In order to gain an insight into the breakage mechanism, the compressive strength of the particles was also measured. In these experiments, the sample was sieved after a postulated number of rotations and the compressive strength of the surviving particles at the initial size range was measured. Each average compressive strength shown in **Figure 9** is an average of at least 20 particles and in some cases even more than 60 particles. Although the compressive strength distribution of any shown point was significant, the average values make the attrition mechanism somewhat clearer. The initial particles are the strongest, and become weaker after experiencing some impact loads in the drum test. The decrease in the compressive strength due to the number of rotations creates a minimum, then increases slightly to a local maximum, and finally decreases again until the strength stabilises. The behaviour is too complicated to permit a complete explanation at this stage, but could be the result of two different effects:

1. The strength of each particle could decrease due to fatigue. Thus, repeated impact loadings enlarge the micro cracks within the particle until it breaks.
2. Since there is initially a strength distribution of particles, the weaker ones break first. Therefore the average strength of the remainder increases.

If we also take into account that different materials display different sensitivity levels to repeated loading, then we might have an explanation for the strange behaviour shown in **Figure 9**. The micro cracks grow faster than the breakage during the first rotations, and result in a decrease in strength. Then, most particles that were initially weak or suffered from fatigue are damaged, which results in an increase of the compressive strength of the surviving particles. At the end of the process (after 2000 rotations), fatigue slightly influences the breakage until both effects stabilise to a steady-state condition, i.e. the rate of fatigue equals the rate of attrition.

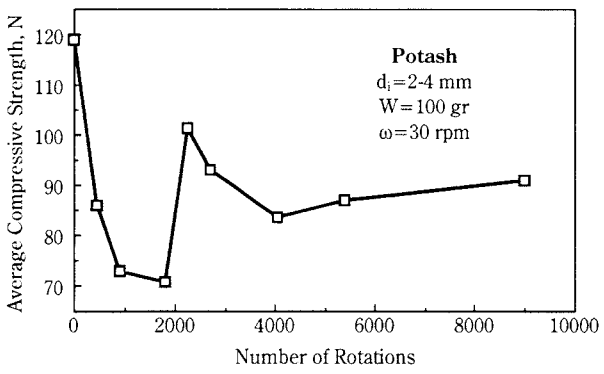

Fig. 9 Compressive strength of surviving potash particles versus the number of rotations.

5.2.2 Medium velocity – dilute-phase pneumatic conveying

The main parameters affecting the breakage and chipping of particles in pneumatic conveying systems are air and particle velocities, loading ratio and particle properties such as size distribution, shape and material. Since it was noticed a long time ago that the main attrition occurs at the bends, most studies were dedicated to flow and attrition mechanisms at various bends. Mckee et al. [55] showed that particle breakage is described to be inversely related to the solids loading factor.

Hilbert [56] examined three bends experimentally: a long-radius bend, a short-radius elbow and a blind-tee. He found that regarding wear, the blind-tee is the best device (less attrition), with the short-radius elbow coming a close second and the long-radius bend coming in third. A comprehensive study was carried out by Agarwal et al. [57] on a long-radius bend. They studied the acceleration length **due to bends** (caused by bends?) and the effects of phase density, conveying velocity and the use of inserts on the wear of the bends, particle degradation and depth of penetration. Vervoorn [45] carried out pneumatic conveying experiments for dilute-phase alumina flow, changing some parameters such as particle velocity and bend structure. Recently, Bell et al. [58] and Papadopoulos et al. [59] presented attrition experiments with salt in which the size distribution was measured on-line. They have also shown that the air velocity has a prime effect on the attrition rate, although the effect of loading ratio and the bend structure cannot be ignored. Kalman and Goder [60] measured the pressure drop, attrition rate, wear of the bend and build-up on the bend walls for four types of bends: long-radius (three construction materials), short-radius elbow, blind-tee, and a turbulence drum. Aked et al. [61] showed that even fine powders (15 μm) suffered significant attrition under certain conditions. Kalman and Aked [62] presented a comparison between different attrition measurement methods and analysed the attrition of various materials. Kalman [63] discussed the possibilities of controlling the attrition rate and of using it for useful processes such as particle rounding, consequently reducing the dust generation during the downstream handling and conveying stages. Most of the parameters affecting attrition in pneumatic con-

veying pipelines for a variety of materials were summarised by Kalman [64].

As for dense-phase flow, measurements were made of the specific energy consumption and particle attrition for a limited range of particulate materials by Taylor [65]. Coppinger et al. [52] presented experimental evidence to show that a fluid bed attrition test performed on small amounts of a wide variety of powders and granules gives a very good indication of both total attrition and bulk density changes for the materials transported in dense-phase conveying loops. The standard compression test did not yield additional information beyond that gathered from the fluid bed attrition test as far as particle breakability was concerned. It was also found that there is a good correlation between attrition in the dilute-phase conveying system and the mechanical sieving test, which seems to indicate that breakage and attrition in the two systems is somewhat similar.

New results of the attrition of potash at 30 m/s in a 1-inch pipe diameter **due to only one bend** (caused by only one bend?) of different type is presented in **Figure 10**. The results are shown in terms of the decrease of the weight median size. It is clear that different bends cause different attrition rates, although in the presented results, the difference is not significant. However, the effect of the number of times that the material passed through the bend significantly affects the attrition rate.

5.2.3 Fatigue curve

By analysing **Figures 8** and **10**, it looks as though a fatigue curve for impact might be developed. Disregarding other effects, the impact velocity defines the impact load for a certain particle and a certain target, i.e. higher impact velocities reflect higher impact loads. Therefore, at lower impact velocities, more collisions cause the same damage as fewer collisions at higher impact velocities. A further investigation and analysis should be conducted in order to develop a fatigue curve, similar to the one shown in **Figure 7**. This could have a significant benefit, since it might unify a number of practical comminution and attrition systems into a common class. Obviously, the picture should be completed with tests with jet mills that give the highest range of impact velocities. In order to enable the comparison of results gained in various systems, other influencing parameters such as the collision angle and target rigidity, should be converted to the effect of normal impact load.

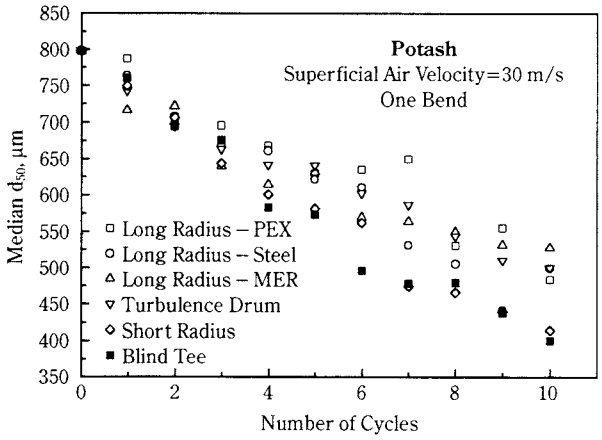

Fig. 10 Attrition by a single bend in pneumatic conveying pipeline.

5. Conclusions

A literature review concerning breakage models in comminution and attrition systems is presented. The common strength characterising systems for compression and impact are reviewed in detail. The difficulties concerning the application of theoretical models for crack propagation to practical problems is discussed. The review and the results presented in the paper can be summarised as follows:

1. In order to reduce the number of required testing and strength indices, future investigations should be devoted to developing empirical correlations between various measurements such as: individual and particulate bed compression, particle compression and impact, etc.
2. The stress distribution in the die used for particulate bed compression should be taken into account for comparison with single particle compressive strengths. The indentation method shown in this paper might give the required means of measurement.
3. Fatigue curves for compression and impact loads could improve design tools for comminution and attrition systems.
4. Industrial impact systems such as rotating drums, ball mills, pneumatic conveying, pin and jet mills might be incorporated as an integral part of a common fatigue curve to characterise most systems where degradation and breakage occur.

6. References

1) P.J. Hill and K.M. Ng: *Statistics of Multiple Particle Breakage*, AIChE Journal 42(6) (1996) pp. 1600-1611.
2) A.V. Potapov and C.S. Campbell: *Computer Simulation of Particle Breakage*, Proceedings of the First Int. Particle Technology Forum, Denver, USA (1994) pp. 225-230.

3) British Materials Handling Board: *Particle Attrition: State-of-the-Art Review*, Trans. Tech. Publications, Germany (1987).
4) R. Hogg: *Breakage Mechanisms and Mill Performance in Ultrafine Grinding*, Powder Technology 105 (1999) pp. 135-140.
5) H. Kalman and D. Goder: *Design Criteria for Particle Attrition*, Advanced Powder Technol. 9 (1998) pp. 153-167.
6) S. Rajagopal, K.M. Ng and J.M. Douglas: *A Hierarchical Procedure for the Conceptual Design of Solids Processes*, Comput. Chem. Eng. 16 (1992) 675 p.
7) B.J. Ennis, J. Green and R. Davies: *Particle Technology: the Legacy of Neglect in the US*, Chem. Eng. Prog. 90 (1995) 32 p.
8) S.Y. Yashima, Y. Kanda and S. Sano: *Relationship Between Particle Size and Fracture Energy or Impact Velocity Required to Fracture as Estimated from Single Particle Crushing*, Powder Technology 51 (1987) 277 p.
9) M. Ghadiri, K.R. Yuregir, H.M. Pollock, J.D.J. Ross and N. Rolfe: *Influence of Processing Conditions on Attrition of NaCl Crystals*, Powder Tech. 65 (1991) 311 p.
10) C.R. Bemrose and J. Bridgwater: *A Review of Attrition and Attrition Test Methods*, Powder Technol. 49 (1987) pp. 97-126.
11) M.J. Adams, M.A. Mullier and J.P.K. Seville: *Agglomerate Strength Measurement Using a Uniaxial Confined Compression Test*, Powder Technology 78 (1994) pp. 5-13.
12) P.H. Shipway and I.M. Hutchings: *Attrition of Brittle Spheres by Fracture Under Compression and Impact Loading*, Powder Technology 76 (1993) pp. 23-30.
13) O. Tsoungui, D. Vallet and J-C Charmet: *Numerical Model of Crushing of Grains Inside Two Dimensional Granular Materials*, Powder Technology 105 (1999) pp. 190-198.
14) K. Danjo, H. Kato, A. Otsuka and K. Ushimaru: *Fundamental Study on the Evaluation of Strength of Granular particles*, Chem. Pharm. Bull. 42(12) (1994) pp. 2598-2603.
15) L. Sikong, H. Hashimoto and S. Yashima: *Breakage Behavior of Fine Particles of Brittle Minerals and Coals*, Powder Technology 61 (1990) pp. 51-57.
16) M.K. Gundepudi, B.V. Sankar, J.J. Mecholsky Jr. and D.C. Clupper: *Stress Analysis of Brittle Spheres Under Multiaxial Loading*, Powder Technology 94 (1997) pp. 153-161.
17) H. Kalman, D. Goder and S. Targan: *Preliminary Investigation on the Effect of Production Parameters on the Strength of Large Tablets*, Part. Part. Syst. Charact. 15 (1998) pp. 150-155.
18) J.J. Mecholsky Jr., D.C. Clupper, B. Sankar and M. Gundepudi: *Fracture Mechanics, Fractals and Failure Analysis as Tools for Understanding Attrition and Comminution of Particles*, World Congress on Particle Technology 3, Brighton, UK, Paper 127 (1998).
19) M. Song, B.M. Li, A. Steiff and P.M. Weinspach: *Stochastic Simulation of Particulate Dynamic Breakup*, Journal of Chemical Engineering of Japan 31(2) (1998) pp. 201-207.
20) Y. Kanda, S. Takahashi, Y. Hata and T. Honma: *The Compressive Crushing of Powder Bed*, Kona 7 (1989) pp. 37-42.
21) L.E. Holman: *The Compaction Behavior of Particulate Materials. An Elucidation Based on Percolation Theory*, Powder Technology 66 (1991) pp. 265-280.
22) J. Liu and K. Schönert: *Modeling of Interparticle Breakage*, Int. J. Miner. Process 44-45 (1996) pp. 101-115.
23) P. Guigon, A. Thomas and J. Dodds: *Experimental Study of a Jet Impacting on a Plate*, Proceedings IFPRI Annual Meeting, Goslar (1994).
24) L.M. Tavares and R.P. King: *Single-Particle Fracture Under Impact Loading*, Int. J. Miner. Process. 54 (1998) pp. 1-28.
25) L.M. Tavares: *Energy Absorbed in Breakage of Single Particles in Drop Weight Testing*, Minerals Engineering 12 (1999) pp. 43-50.
26) A.D. Salman, D.A. Gorham and A. Verba: *A Study of Solid Particle Failure Under Normal and Oblique Impact*, Wear 186-187 (1995) pp. 92-98.
27) A.D. Salman, M. Szabo, I. Angyal, A. Verba and D. Mills: *The Design of Pneumatic Conveying Systems to Minimise Product Degredation*, In: Proc. 13th Powder and Bulk Solids Conf., Chicago, IL (1988).
28) A. Verba, A.D. Salman and M. Szabo: *Particle Degredation in Dilute Pneumatic Conveying*, In: Proc. 5th Conf. On Applied Chemistry Unit Operations and Processes, Budapest, Hungary (1989).
29) A.D. Salman, A. Verba and D. Mills: *Particle Degredation in Dilute Phase Pneumatic Conveying Systems*, In: Proc. 18th Powder and Bulk Solids Conf., Chicago, IL (1992).
30) M. Ghadiri and D.G. Papadopoulos: *Influence of Material Properties on Attrition and Comminution of Particulate Solids*, In: Proc. IFPRI Annual Meeting, Goslar (1994).
31) D.A. Gorham and A.D. Salman: *The Fracture of Glass Spheres*, The 9th European Symposium on Comminution, 8-10, Albi, France (1998).
32) J.A.S. Cleaver, M. Ghadiri and N. Rolfe: *Impact Attrition of Sodium Carbonate Monohydrate Crystals*, Powder Technology 76 (1993) pp. 15-22.
33) P.M.M. Vervoorn and B. Scarlett: *The Attrition Behaviour of Alumina Extrudates in Pneumatic Transport and Fluidized Beds*, Proc. of the Powder and Bulk Solids Conf., Chicago, USA (1987).
34) J.J. Pis, A.B. Fuertes, A. Artos, A. Suarey and F. Rubiera: *Attrition of Coal Ash Particles in a Fluidized Bed*, Powder Technology 66 (1991) pp. 41-46.
35) S. Veesler and R. Boistelle: *Attrition of Hydrargillite ($Al(OH)_3$): Mechanism and Quantification of Particle Fragility by a New Attrition Index*, Powder Technology 76 (1993) pp. 49-57.
36) M. Mebtoul, J.F. Large and P. Guigon: *High Velocity Impact of Particles on a Target -- an Experimental Study*, Int. Miner. Process. 44-45 (1996) pp. 77-91.
37) J. Subero, Z. Ning, M. Ghadiri and C. Thornton: *Effect of Interface Energy on the Impact Strength of Agglomerates*, Powder Technology 105 (1999) pp. 66-73.
38) A.V. Potatov and C.S. Campbell: *The Two Mechanisms of Particle Impact Breakage and the Velocity Effect*, Powder Technology 93 (1997) pp. 13-21.
39) C. Couroyer, Z. Ning and M. Ghadiri: *Distinct Element Analysis of Bulk Crushing: Effect of Particle Proper-*

ties and Loading Rate, Powder Technology 109 (2000) pp. 241-254.
40) C. Couroyer, Z. Ning, F. Bassam and M. Ghadiri: *Bulk Crushing Behaviour of Porous Alumina Particles Under Compressive Loading*, World Congress on Particle Technology 3, Brighton, UK, Paper 61 (1998).
41) C. Couroyer, Z. Ning, M. Ghadiri, N. Brunard, F. Kolenda, D. Bortzmeyer and P. Laval: *Breakage of Macroporous Alumina Beads Under Compressive Loading: Simulation and Experimental Validation*, Powder Technology 105 (1999) pp. 57-65.
42) O. Gutsche and D.W. Fuerstenau: *Fracture Kinetics of Particle Bed Comminution – Ramifications for Fines Production and Mill Optimization*, Powder Technology 105 (1999) pp. 113-118.
43) P.H. Shipway and I.M. Hutchings: *Fracture of Brittle Spheres Under Compression and Impact Loading. II. Results for Bead-Glass and Sapphire Spheres*, Philosophical Magazine A 67(6) (1993) pp. 1405-1421.
44) P.H. Shipway and I.M. Hutchings: *Fracture of Brittle Spheres Under Compression and Impact Loading. I. Elastic Stress Distribution*, Philosophical Magazine A, 67(6) (1993) pp. 1389-1404.
45) P.M.M Vervoorn and L.G. Austin: *The Analysis of Repeated Breakage Events as an Equivalent Rate Process*, Powder Technology 63 (1990) pp. 141-147.
46) A.S. Kheifets and I.J. Lin: *Energetic Approach to Kinetics of Batch Ball Milling*, Int. J. Miner. Process 54 (1998) pp. 81-97.
47) A.V. Potapov and C.S. Campbell: *Computer Simulation of Shear-Induces Particle Attrition*, Powder Technology 94 (1997) pp. 109-122.
48) H. Berthiaux, C. Chiron and J. Dodds: *Modeling Fine Grinding in a Fluidized Bed Opposed Jet Mill Part II: Continuous Grinding*, Powder Technology 106 (1999) pp. 88-97.
49) H. Berthiaux and J. Dodds: *Modelling Fine Grinding in a Fluidized Bed Opposed Jet Mill Part I: Batch Grinding Kinetics*, Powder Technology 106 (1999) pp. 78-87.
50) D. Goder and H. Kalman: *Fatigue Characteristics of Particles*, World Congress on Particle Technology 3, Brighton, UK, Paper 130 (1998).
51) D. Goder, O. Eskin and H. Kalman: *Fatigue Characteristics of Granular Materials*, The Third Israeli Conference for Conveying and Handling of Particulate Solids 1, Eds. H. Kalman, A. Levy and M. Hubert, Dead Sea, Israel (2000) pp. 3.32-3.38.
52) E. Coppinger, L. Discepola, G.I. Tardos and G. Bellamy: *The Influence of Granule Morphology on Attrition During Fluidization and Pneumatic Transport*, Advances Powder Technol. 3(3) (1992) pp. 201-218.
53) W.J. Beekman, G.M.H. Meesters and B. Scarlett: *Measurement of Granule Impact Strength Distributions in a Vibrating Container*, World Çongress on Particle Technology 3, Brighton, UK, Paper 131 (1998).
54) Q-Q Zhao, S. Yamada and G. Jimbo: *The Mechanism and Grinding Limit of Planetary Ball Milling*, Kona 7 (1989) pp. 29-36.
55) S.L. Mckee, T. Dyakowski, R.A. Williams, T.A. Bell and T. Allen: *Solids Flow Imaging and Attrition Studies in a Pneumatic Conveyer*, Powder Technology 82 (1995) pp. 105-113.
56) J.D. Hilbert: *Alternatives in Pneumatic Conveying Bends*, The Best of Bulk Solids Handling, Pneumatic Conveying of Bulk Powders, Vol. D/86, Trans Tech Publications (1984) pp. 107-110.
57) V.K. Agarwal, D. Mills and J.S. Mason: *Some Aspects of Bend Erosion in Pneumatic Conveying System Pipelines*, The Best of Bulk Solids Handling, Pneumatic Conveying of Bulk Powders, Vol. D/86, Trans Tech Publications (1985) pp. 111-116.
58) T.A. Bell, A. Boxman and J.B. Jacobs: *Attrition of Salt During Pneumatic Conveying*, Proceedings of The 5th World Congress of Chemical Engineering V (1996) pp. 238-243.
59) D.G. Papadopoulos, C.S. Teo, M. Ghadiri and T.A. Bell: *Attrition of Common Salt*, World Congress on Particle Technology 3, Brighton, UK, Paper 156 (1998).
60) H. Kalman and D. Goder: *Pressure Drop, Wear and Attrition in Various Bends for Pneumatic Conveying Pipelines*, Proceedings of the 5th World Congress of Chemical Engineering VI (1996) pp. 411-416.
61) K. Aked, D. Goder, H. Kalman and A. Zvieli: *Attrition of Very Fine Powders During Pneumatic Conveying*, Powder Handling and Processing 9 (1997) pp. 345-348.
62) H. Kalman and K. Aked: *Attrition of Fine Powders and Granules at Various Bends During Pneumatic Conveying*, World Congress on Particle Technology 3, Brighton, UK, Paper 154 (1998).
63) H. Kalman: *Attrition Control by Pneumatic Conveying*, Powder Technology 104 (1999) pp. 214-220.
64) H. Kalman: *Attrition of Powders and Granules at Various Bends During Pneumatic Conveying*, Powder Technology 112 (2000) pp. 244-250.
65) T. Taylor: *Specific Energy Consumption and Particle Attrition in Pneumatic Conveying*, Powder Technology 95 (1998) pp. 1-6.

Author's short biography

Haim Kalman

Haim Kalman is a senior lecturer at the Department of Mechanical Engineering at Ben-Gurion University of the Negev, from which he received all his degrees, B.Sc. (1982), M.Sc. (1984) and Ph.D. (1989). Since graduation he initiated research and education in the field of Particle Technology at BGU. He is the Head of the Laboratory for Conveying and Handling of Particulate Solids, Chair of the University Center for Particle Technology, Chair and Founder of the Israeli Forum for Handling and Conveying of Particulate Solids. His international activities include serving in the scientific advisory committees of many conferences and served as the chair of the first, second and third Israeli Conferences for Conveying and Handling of Particulate Solids. The two last ones were actually international conferences with participants from more than 24 countries. He editted the proceedings of the conferences as for the last one it contained over than 1000 pages in two volumes. Haim is also a member of the European Working Party on Mechanics of Particulate Solids and the International Freight Pipeline Society. His research interests involve many topics in Particle Technology, as: Characterization, Pneumatic Conveying, Comminution and Attrition, Strength of Particles, Two-Phase Flow, Heat and Mass Transfer with Particles and Environmental Aspects.

Fluid Mechanics and Heat Transfer in Fluidized Beds†

O. Molerus
Lehrstuhl für Mechanische Verfahrenstechnik
*Universität Erlangen-Nürnberg**

Abstract

Heat transfer between submerged surfaces and gas-fluidized beds depends on fluid mechanics and particle dynamics. Therefore, reliable prediction of the heat transfer coefficient must be based on the observation of particle motion towards and from solid surfaces. Experiments with luminescent particles reveal a rather broad particle residence time distribution at solid surfaces. This broad residence time distribution gives rise to a smearing-out effect of the two different heat transfer mechanisms, namely particle convective and gas convective, respectively. Well-defined residence times can be realized by means of a rudimentary variant of fluidized bed heat transfer in the form of moving bed heat transfer. Experimental and theoretical results obtained from moving bed heat transfer allow the sound modeling of the two "pure" mechanisms (particle convective and gas convective). A predictive equation is derived which may be seen as a safe interpolation between the two extremes. The comparison with a large number of experiments proves the reliability of the prediction with respect to any feature of fluidized bed heat transfer.

1. Introduction

Textbooks on fluid mechanics, or on heat and mass transfer, describe two different modes for the generation of dimensionless groups, namely

- listing the influencing factors and finding out the necessary number of basic units. Through Buckingham's theorem, a distinct number of dimensionless groups is evident, the actual definitions depending on the investigator's taste, or alternatively
- derivation of dimensionless groups from the inspection of the underlying partial differential equations.

Both approaches suggest a quasi automatic definition of the relevant dimensionless groups and work quite well, e.g. in the case of single-phase flow.

Particle technology, however, is a different story. In order to demonstrate the peculiarities of that discipline of chemical engineering, the heat transfer between submerged tubes and bubbling fluidized beds is discussed in detail. This variant of the heat transfer results from complex interactions between fluid and solid material properties, particle size, fluid mechanics and particle dynamics. In other words: The derivation of reliable predictive equations built up from relevant dimensionless groups is not found in any textbook, but instead is the result of an arduous step-by-step process which in retrospect can be likened to piecing together a puzzle.

* Cauerstrasse 4, 91058 Erlangen, Germany
† Received: August 8, 2000

2. Reynolds number and Archimedes number

Particle technology is a discipline in the broader field of chemical engineering. Stationary fluidized beds, for example, are in use with exothermic catalytic gas-phase reactions with particle sizes in the range of $d_p \approx 50$ µm, or with combustion of coal in pressurized fluidized beds with particle sizes up to 5 mm. In both cases, heat removal takes place by means of submerged tubes.

For Reynolds numbers $Re = (\rho_F v d_p)/\mu \leq 10^5$, a reasonable estimate for the aerodynamic resistance of a single sphere is given by the equation

$$c_D \equiv \frac{R^*}{\frac{\pi d_p^2}{4}\frac{\rho_g}{2}v^2} = \frac{24}{Re} + \frac{4}{\sqrt{Re}} + 0.4 . \qquad (1)$$

With the aerodynamic resistance defined by weight minus buoyancy ($R^* = (\pi/6)(\rho_s - \rho_f) d_p^3 g$), Equation (1) rearranges to

$$Ar \equiv \frac{\rho_g(\rho_p - \rho_g) d_p^3 g}{\mu^2} \equiv \frac{3}{4} c_D Re^2 = 18Re + 3Re\sqrt{Re} + 0.3Re^2 \qquad (2)$$

Figure 1 shows Equation (2) and indicates the regimes of the different types of flow.

Equation (2) defines a monotonic function. This means that in the case of fluidization fluid mechanics, the state of flow is defined alone by the Archimedes number, i.e. laminar flow for $Ar \leq 10^2$, the transitional regime for $10^2 \leq Ar \leq 10^5$, and the turbulent regime

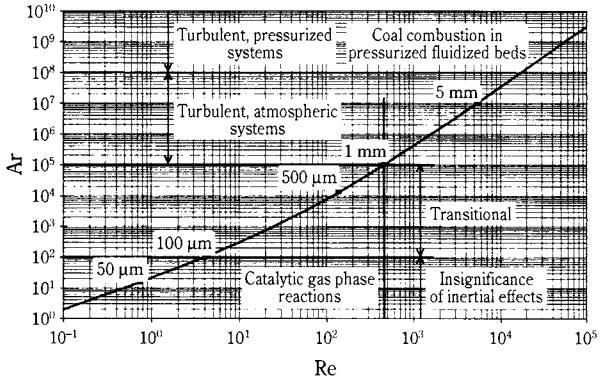

Fig. 1 Archimedes number Ar versus Reynolds number Re, particle sizes represent glass spheres in air under standard conditions

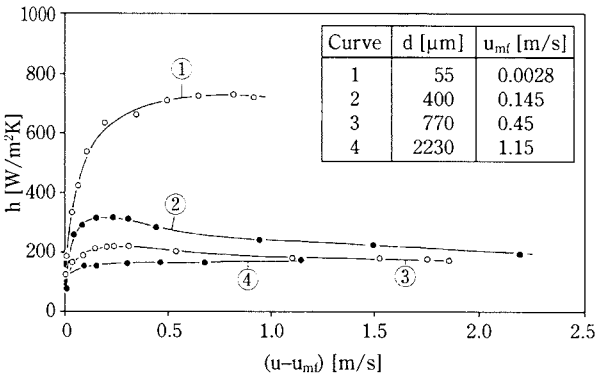

Fig. 2 Heat transfer coefficient versus $u-u_{mf}$ using glass beads as the solid material; measurements from Wunder [2]. The fluidizing agent was air under standard conditions.

for $Ar \geq 10^5$; Archimedes numbers $Ar > 10^8$ are attained only in pressurized systems. These drastic changes in the state of flow must also be reflected in corresponding changes in the heat transfer mechanisms. **Figure 2** shows measured heat transfer coefficients versus the excess gas velocity $u-u_{mf}$ (superficial gas velocity minus minimum fluidization velocity). Obviously, the maximum heat transfer coefficient decreases significantly with increasing particle size. This behavior corresponds to that described by Botterill ([1] Fig. 5.8, p. 241)

The aim of the present paper is to elucidate the physical background of the observed phenomena. In order to limit the length of the paper, details of many experimental procedures or of the underlying theoretical considerations are not given, but instead significant graphs and plausible arguments are preferred.

3. Particle migration at solid surfaces

In particular with fine-grained particles, heat transfer between bubbling fluidized beds and submerged tubes is drastically higher in comparison with the corresponding fixed bed situation, in other words: particle mobility largely enhances the heat transfer.

Mickley and Trilling [3] were the first to appreciate the implications of the unsteady nature of the heat transfer process between a submerged surface and a gas-fluidized bed.

A reliable theory of fluidized bed heat transfer, must therefore be based on quantitative information about the particle migration at submerged solid surfaces. The particles are swept away from the solid surfaces by rising gas bubbles. Spatial bubble distribution and rise velocities are more or less random, so only experiments will provide a useful answer. The basic principle for the detection of particle motion at

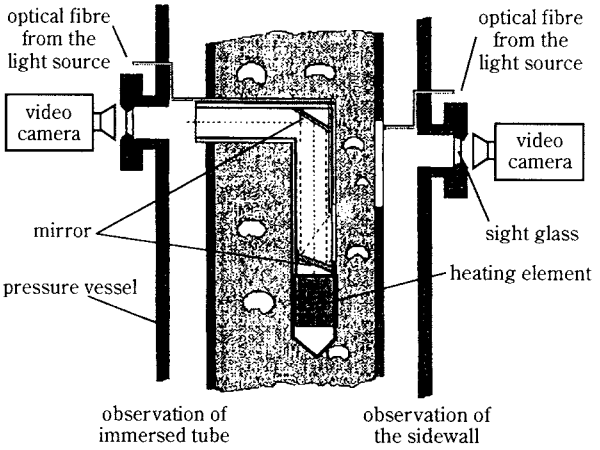

Fig. 3 Experimental set-up for observing particle motion close to solid surfaces.

solid surfaces is quite simple. Transparent side walls allow direct observation of particle migration (**Fig. 3**, right side). The observation of particle motion close to immersed surfaces (**Fig. 3**, left side), e.g. heat exchanger tubes inside a fluidized bed, is realized by using a periscopic mirror arrangement installed in a dummy tube.

Particle motion at the solid surfaces is visualized by using luminous particles. A luminescent pigment (ZnS crystals doped with copper) was available in the form of particles with a mean particle size of $d_p=50$ µm. Larger particles were produced in a fluidized bed by spraying clear varnish onto the bed surface. Subsequent sieving provided different fractions of luminescent lacquer particle fractions with mean particle sizes up to $d_p=300$ µm. After illumination by a pulse of light transmitted via fiber optics to the transparent wall area, these particles show an afterglow for several seconds. The illuminated spot shifts along the solid surface, whereby its shape deforms and its overall luminosity decreases, but the illuminated particles

themselves stay in a close proximity. In other words, the illuminated spot remains as a single identifiable object during its lifetime. Digital image analysis can therefore be applied. In this way a cluster of particles can be passively marked for subsequent observation and tracking.

Particle migration to and from the solid surface is a random process. Simple theoretical considerations [4] yield for the probability W(t) that a particle marked at time t=0 is in contact with the wall up to the present time t

$$W(t) = e^{-t/\tau}. \quad (3)$$

In Equation (3), τ defines the mean particle residence time at the wall. According to the underlying experimental procedure, the probability W is given by the ratio of the actual to the initial luminosity, i.e. it should follow that (compare **Fig. 4**).

$$\ln (L/L_0) = -t/\tau \quad (4)$$

According to Equation (4), the mean particle residence time is found from the slope of curve in semi-logarithmic representation. **Table 1** shows typical mean residence times for two particle sizes and for different static pressures at maximum heat transfer.

4. The contact resistance

Two different experimental results described in the preceding section define the strategy for finding out the mechanisms of the heat transfer:

- The mean particle residence time at the wall is of the order of one second (**Table 1**)
- For given operational conditions, the distribution of the particle residence times is rather broad (**Fig. 4**).

The second feature largely impedes any direct evaluation of fluidized bed experiments because it introduces a smearing-out effect with respect to different mechanisms. This dilemma can be avoided by the evaluation of heat transfer experiments with a given particle residence time in the order of seconds. This situation is experimentally realized by particle beds moving along heat transfer surfaces of given length. Moving bed heat transfer has been investigated by several authors [5, 6], occasionally with the intention

Table 1 Mean residence times of illuminated particles at vertical solid surfaces in a fluidized bed at maximum heat transfer

Particle size	1 bar (0.1 MPa)	5 bar (0.5 MPa)	10 bar (1.0 MPa)	20 bar (2.0 MPa)
d_p=50 μm	1.28 s	0.35 s	0.52 s	0.45 s
d_p=250 μm	1.54 s	1.31 s	0.91 s	0.77 s

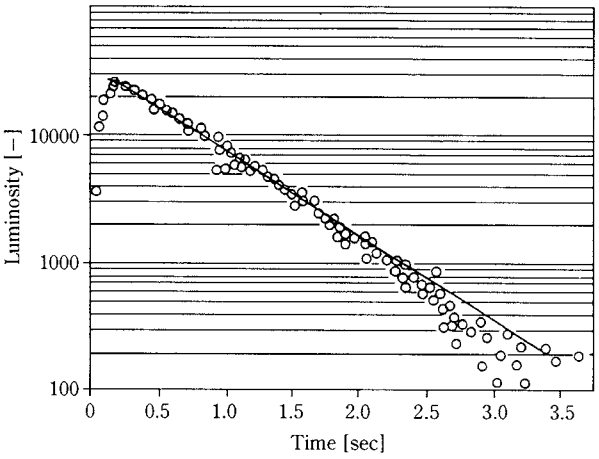

Fig. 4 Decay of dimensionless computer output luminosity L in a fluidized bed

of understanding the fluidized bed heat transfer phenomena [7, 8]. However, instead of providing valuable insights with respect to fluidized bed heat transfer, these investigations have posed fundamental questions which still remain contentious.

With usual gas/solid systems, the particle thermal conductivity k_p is high in comparison to the gas thermal conductivity k_g, i.e. $k_p \gg k_g$. As an asymptotic limit, one can thus assume that particle bed heat transfer is governed by a contact resistance (**Fig. 5**). Heat transfer between a heating surface and an adjacent particle (**Fig. 5**, left side) as well as between two adjacent particles (**Fig. 5**, right side) takes place in the form of a sudden and steep temperature gradient in the gap between the two particles, which results in the case of heat transfer from left to right with a temperature difference $T_1 > T_2$.

In the literature, two different physical reasons are given for the contact resistance observed with particle beds. For perfect spherical particles in contact with a plane wall, Schlünder [9] attributes the contact resistance to a diminished heat transfer rate in the gas in the region where the distance between the particle and the surface is less than the mean free path of the interstitial gas. Glosky et al. [10] attribute it to the

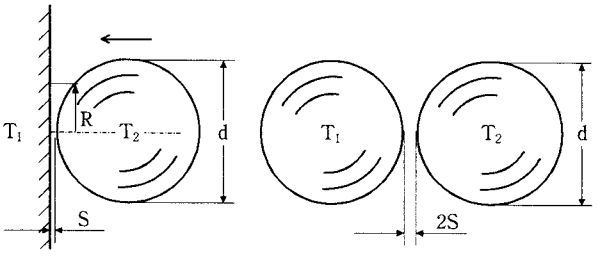

Fig. 5 Contact resistance with particle bed heat transfer, left side: short contact time, right side: steady-state heat conduction in packed beds.

surface roughness. Both approaches, however, are not contradictory, but instead complementary.

That part of the energy which is transferred within the surface area with the radius $0 \le R \le d_p/2$ (**Fig. 5**, left side) in terms of a Nusselt number is

$$Nu\left[(2R/d_p)^2\right] = \pi\left\{\left(1+\frac{2S}{d_p}\right)\ln\left[1+\frac{d_p}{2S}\left(1-\sqrt{1-(2R/d_p)^2}\right)\right]-\left[1-\sqrt{1-(2R/d_p)^2}\right]\right\}. \quad (5)$$

The details of the derivation of Equation (5) can be read in [11].

The heat transfer per particle is defined by $2R/d_p \to 1$, i.e. by the maximum Nusselt number for short contact time

$$Nu_{max} \equiv \frac{h_{max} d_p}{k_g} = \pi\left[\left(1+\frac{2S}{d_p}\right)\times \ln\left(1+\frac{d_p}{2S}\right)-1\right]. \quad (6)$$

According to Schlünder's approach, for ideal geometries

$$S_{min} = 2\ell_0 \frac{2-\gamma}{\gamma} \quad (7)$$

where

$$\ell_0 = \frac{16}{5}\sqrt{\frac{\tilde{R}T}{2\pi\tilde{M}}}\times\frac{\mu}{p} \quad (8)$$

designates the mean free path of the gas molecules and γ the accommodation coefficient. The accommodation coefficient γ defines that fraction of the gas molecules which are not reflected when hitting a solid surface. Equation (7) reveals that the physics of gases yields a minimum effective roughness S_{min}, below which particles can be considered thermodynamically smooth. Thus, Schlünder's approach provides an upper limit for the maximum Nusselt number.

As a by-product, an estimate for the effective thermal conductivity k_e of particle beds is obtained as follows (compare **Fig. 5**, right side): For two adjacent spheres in a cubic array in the main direction of heat flux, the relevant distance for the heat conduction is the particle diameter, so the distance in the model must simply be doubled to yield the gap between particles. The relevant cross-section for the heat flux is the particle equatorial area $(\pi d_p^2)/4$. Thus, the ratio of effective to gas thermal conductivity is also given in the form of a clear function of $2S/d_p$ (see **Fig. 6**)

$$k_e/k_g = (2/\pi)Nu_{max} = 2\left[\left(1+\frac{2S}{d_p}\right)\ln\left(1+\frac{d_p}{2S}\right)-1\right]. \quad (9)$$

Both equations (6) and (9) indicate that the heat transfer in a particle bed is exclusively a function of the length ratio S/d_p. The inherent concept is that the sole physical reason for short contact time resistance between a heating surface and a particle bed as well as for steady-state heat conduction inside the bed is almost exclusively the contact resistance in the gap between the contacting solid bodies.

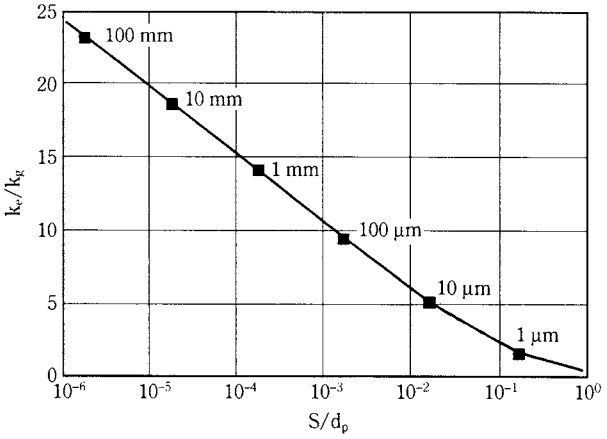

Fig. 6 Effective thermal conductivity in particle beds according to Eq. (9). Numerical values of diameter represent ideal spheres in air (nitrogen) at ambient conditions.

5. Heat transfer in moving beds with a stagnant interstitial gas

The most striking manifestation of the role of the length ratio S/d_p is observed with the heat transfer between a heated solid surface and a particle bed sliding over it. With a short contact time, a maximum Nusselt number according to Equation (6) is observed, whereas with progression of the temperature front inside the bulk of the bed, a long contact time variant of the heat transfer is attained, characterized by gradual heating up of the bed. **Figure 7** shows Nu/Nu_{max}

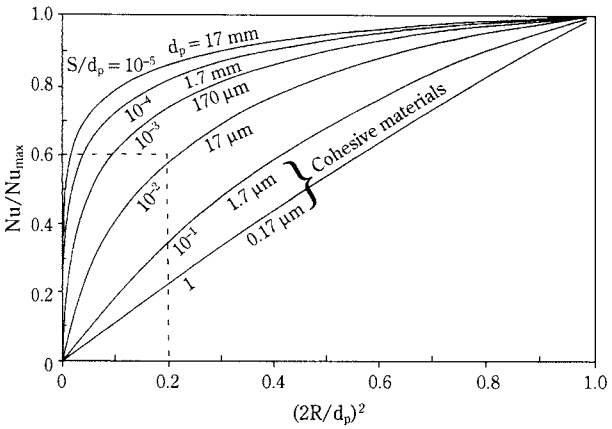

Fig. 7 Relative contribution of the area with radius R to the total heat transfer per particle according to Eq. (5). Particles are smooth spheres in air under standard conditions.

according to Equations (5) and (6) for different values of S/d_p.

Due to the cohesiveness of extremely fine-grained particles, efficient fluidization is restricted to particle sizes $d_p \geq 20$ μm. According to **Figure 7**, $d_p \geq 20$ μm means length ratios $S/d_p < 10^{-2}$ and, hence, concentration of the heat transfer to a region close around the contact point. This fact influences the gradual heating up of moving beds as follows: heat transfer between adjacent particles is not defined by the nominal particle size, but instead by the size S of the effective (due to the mean free path effect) or real (due to surface roughness) distance. The capacity of a particle to store thermal energy on the other hand is defined by the nominal particle size d_p. A dimensionless contact time Co is thus reasonably defined by the ratio of the heat conduction between two adjacent particles to the gain of thermal energy per particle up to the time t

$$Co \equiv \frac{C(k_g/S_{min})S_{min}^2}{(\rho_p c_p d_p^3)/t} = \frac{k_g C \times S_{min} t}{\rho_p c_p d_p^3}. \qquad (10)$$

In Equation (10), a factor $C > 1$ defines the significance of surface roughness for the heat transfer ($S > S_{min}$). In practice, the term $C \times S_{min}$ must be seen as a constant which has to be determined from experiments. Experiments throughout evidence the insignificance of the particle size for the heat transfer, when the heating up proceeds into the bulk of bed. The insignificance of the particle size requires for the actual Nusselt number at time t

$$Nu \times \sqrt[3]{Co} \equiv \frac{h d_p}{k_g} \times \sqrt[3]{\frac{k_g C \times S_{min} t}{\rho_p c_p d_p^3}} = \text{const}, \qquad (11)$$

i.e. $Nu \sim Co^{-1/3}$ (compare **Fig. 8**).

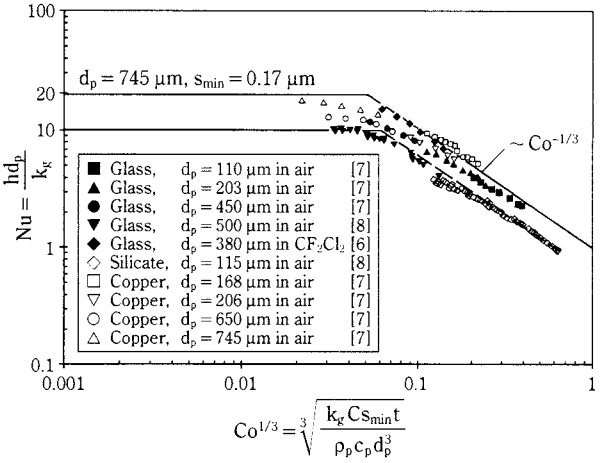

Fig. 8 Nusselt number as a function of the cube root of the dimensionless contact time; $C \times S_{min} = 6.5$μm. Measurements taken from [6, 7, 8].

6. Particle convective heat transfer at Archimedes numbers $Ar \leq 10^2$

According to the two-phase theory of fluidization, the emulsion phase remains more or less in the minimum fluidization state, i.e. the excess gas velocity $u - u_{mf}$ is that part of the total gas throughput which passes the bed in the form of bubbles. With fine-grained particles, viscous resistance balances weight minus buoyancy, i.e.

$$\mu d_p u_{mf} \sim (\rho_p - \rho_g) d_p^3 g. \qquad (12)$$

Equation (12) rearranges to

$$\frac{u_{mf}}{\sqrt{d_p g}} \sim \left(\frac{d_p}{\ell_1}\right)^{3/2} \qquad (13)$$

with a laminar flow length scale

$$\ell_1 = \left[\frac{\mu}{\sqrt{g}(\rho_p - \rho_g)}\right]^{2/3}. \qquad (14)$$

Further rearrangement yields the final result

$$\frac{u_{mf}}{\sqrt{\ell_1 g}} \sim \left(\frac{d_p}{\ell_1}\right)^2. \qquad (15)$$

Equation (15) provides a clear message: according to its definition, Equation (14), the laminar flow length scale ℓ_1 is constant for a given combination of gas and solid material.

Thus, Equation (15) predicts a sharp decrease in the gas velocity in the emulsion phase with decreasing particle size.

From **Figure 2**, for example, one reads for fine-grained particles, i.e. curve 1, maximum heat transfer at $u - u_{mf} \approx 0.7$ m/s and $u_{mf} = 2.8 \times 10^{-3}$ m/s, i.e. $u_{mf}/(u - u_{mf}) \approx 4 \times 10^{-3}$.

This means that with fine-grained particles, the emulsion-phase permeability becomes so small that the system can be seen as a homogeneous particle/gas mixture percolated by rising bubbles. In other words: the particle size becomes irrelevant for the fluid mechanics, and the emulsion phase is close to moving bed conditions with a stagnant interstitial gas.

According to the definition of the dimensionless contact time Co, Equation (10), decreasing particle size means increasing numerical values of Co. From **Figure 8** together with the definition of Co, Equation (11), we thus conclude that with fine-grained particles, the particle size is not only insignificant for the fluid mechanics, but also for the heat transfer mechanism.

The slope of curve 1 in **Figure 2** suggests the following procedure: at first an equation for the maxi-

mum heat transfer coefficient is derived, thereafter a normalized equation is deduced, which fits the slope of curve 1. The maximum heat transfer coefficient must be a clear function of only the relevant material properties and the particle size. As dimensionless groups, we thus have the length ratio

$$\frac{d_p}{\ell_1} \tag{16}$$

which defines the fluid mechanics, a ratio which combines the relevant thermal properties (c_p and k_g)

$$\frac{c_p \mu}{k_g}, \tag{17}$$

the maximum heat transfer coefficient in terms of a Nusselt number

$$Nu_{max} \equiv \frac{h_{max} d_p}{k_g} \tag{18}$$

and the solids volume concentration $1-\varepsilon_{mf}$ in the emulsion phase.

The insignificance of the particle size d_p for the fluid mechanics and the heat transfer reduces the number of dimensionless groups, i.e.

$$\frac{h_{max} \ell_1}{k_g} = f\left(\frac{c_p \mu}{k_g}, 1-\varepsilon_{mf}\right). \tag{19}$$

Evaluation of measurements [12] yields to

$$\frac{h_{max} \ell_1}{k_g}\left(1+\frac{k_g}{2c_p\mu}\right) \sim 1-\varepsilon_{mf}. \tag{20}$$

with the void fraction ε_{mf} at minimum fluidization. Equation (20) predicts $h_{max} \to 0$ for $k_g \to 0$ as well as for $c_p \to 0$, i.e. for the so-called particle convective heat transfer, the gas thermal conductivity k_g as well as the solid material specific heat c_p are relevant. The dependence of the heat transfer on the excess gas velocity is taken into account as follows: the heat transfer from the heating surface takes place in the form of heated particles being swept away from the heating surface by rising bubbles. Swept-away particles come to rest again in the gravitational field after a distance

$$\ell \sim \frac{(u-u_{mf})^2}{g}.$$

The term $\rho_p c_p (u-u_{mf})$ (units $Wm^{-2} K^{-1}$) defines a heat transfer by particle migration. The product of these two terms yields an effective thermal conductivity

$$k_{eff} \sim \frac{\rho_p c_p (u-u_{mf})^3}{g} \quad (Wm^{-1} K^{-1}) \tag{21}$$

The dimensionless excess gas velocity

$$\sqrt[3]{\frac{\rho_p c_p}{k_g g}}(u-u_{mf}), \tag{22}$$

therefore relates the two relevant transfer mechanisms, namely particle transfer and gas thermal conductivity. The efficiency of the particle transfer is also defined by the ratio of bubble gas flow rate to emulsion gas flow rate, i.e. by $(u-u_{mf})/u_{mf}$. The above considerations result in a normalized function

$$n_{pc}(u-u_{mf}) = \frac{1}{1+P\left[\sqrt[3]{\frac{u-u_{mf}}{u_{mf}}}\sqrt[3]{\frac{\rho_p c_p}{k_g g}}(u-u_{mf})\right]^{-1}} \tag{23}$$

with a constant P to be determined from experiments. Obviously, Equation (23) predicts $n_{pc} \to 0$ for $u-u_{mf} \to 0$ and $n_{pc} \to 1$ for $u-u_{mf} \to \infty$. (Compare curve 1, **Fig. 2**.)

The combination of Equations (20) and (23) together with evaluation of experiments yields the final result for the particle convective heat transfer

$$\frac{h_{pc} \ell_1}{k_g} = \frac{0.19(1-\varepsilon_{mf})}{1+\frac{k_g}{2c_p\mu}} \times \frac{1}{1+25\left[\sqrt[3]{\frac{u-u_{mf}}{u_{mf}}}\sqrt[3]{\frac{\rho_p c_p}{k_g g}}(u-u_{mf})\right]^{-1}} \tag{24}$$

The comparison of Equation (24) with the experimental results in **Figure 9** confirms that the influence of the relevant material data (gas thermal conductivity: air and helium; particle specific heat: glass and bronze) is correctly taken into account.

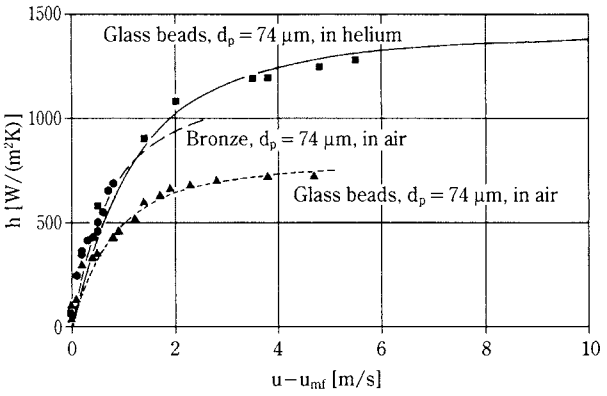

Fig. 9 Comparison of own measurements (symbols) with predictions of Eq. (24) (lines); experiments carried out under standard conditions.

7. Gas convective heat transfer at Archimedes numbers $10^5 \leq Ar \leq 10^8$

In comparison with particle convective heat transfer, gas convective heat transfer in the regime of $10^5 \leq Ar \leq 10^8$ is a simple affair. Starting again from

the rudimentary variant of fluidized bed heat transfer, the moving bed, **Figure 8** tells us that for a given contact time t, an increasing particle size d_p shifts the dimensionless contact time Co towards smaller values. Finally the regime Nu=const. is attained, where the contact time is far too short for significant heating up of the particles at the heating surface. On the other hand, one reads from **Figure 1** that $Re > 5\times10^2$ for $Ar > 10^5$. This means that boundary layer effects dominate the heat transfer. Further valuable information can be deduced from **Figure 2**. Gas convective heat transfer is represented by curve 4, which indicates the maximum heat transfer attained at $u-u_{mf} \approx 0.5$ m/s, whereas the minimum fluidization velocity is 1.15 m/s. From these two figures, it follows that the gas flow rate is higher in the emulsion than in the bubble phase.

All these facts together indicate a single-phase-type of heat transfer in the form of Nu=Nu (Re, Pr). **Figure 1** shows a single valued function Ar=Ar (Re). This fact legitimates the replacement of the Reynolds number by the Archimedes number. According to Baskakov and Filippovski [13], the maximum heat transfer coefficient is given by

$$Nu_{max} \sim (ArPr)^{1/3} \qquad \text{for } 10^5 \le Ar \le 10^8. \tag{25}$$

According to the definitions of Nu and Ar, Equation (25) predicts that the particle size does not affect the heat transfer. The insignificance of the particle size is easy to understand from the following considerations: at higher Reynolds numbers, the heat transfer is defined by the laminar boundary layer thickness δ_l with $\delta_l/d_p \sim Re^{-1/2}$ as indicated by the Ranz equation [14] for the heat transfer from a single particle

$$Nu \sim Re^{1/2} Pr^{1/3}. \tag{26}$$

From Equation (2), for the regime of intermediate Reynolds numbers, $Ar \sim Re^{3/2}$ and, hence, $Re^{1/2} \sim Ar^{1/3}$. Substitution of this relation into Equation (26) yields to Baskakov's statement, Equation (25).

The irrelevance of the particle size d_p, however, requires its elimination from Equation (25). A turbulent flow length scale ℓ_t follows from

$$Ar^{1/3} \equiv \frac{d_p}{\sqrt[3]{\dfrac{\mu^2}{\rho_g(\rho_p-\rho_g)g}}},$$

i.e.

$$\ell_t \equiv \sqrt[3]{\frac{\mu^2}{\rho_g(\rho_p-\rho_g)g}}. \tag{27}$$

Substitution of ℓ_t into Equation (25) yields

$$\frac{h_{max}\ell_t}{k_g} Pr^{-1/3} = \text{const.} \tag{28}$$

It is worth noting that the independence of the particle size in the regime of $10^5 \le Ar \le 10^8$ has a completely different physical background in comparison with that observed at $Ar \le 10^2$. The dependence on the excess gas velocity according to curve 4 of **Figure 2** is given by the normalized function

$$n_{g.c.} = \frac{1}{1+G\left(\dfrac{u-u_{mf}}{u_{mf}}\right)^{-1}} \tag{29}$$

with a constant G to be determined from experiments. Equation (29) predicts $n_{g.c.} \to 0$ for $u-u_{mf} \to 0$ and $n_{g.c.} \to 1$ for $u-u_{mf} \to \infty$.

The combination of Equations (28) and (29) together with evaluation of experiments yields the final result for gas convective heat transfer (compare **Fig. 10**)

$$\frac{h_{g.c.}\ell_t}{k_g} = \frac{0.165Pr^{1/3}}{1+0.05\left(\dfrac{u-u_{mf}}{u_{mf}}\right)^{-1}} \quad \text{for} \quad 10^5 \le Ar \le 10^8 \tag{30}$$

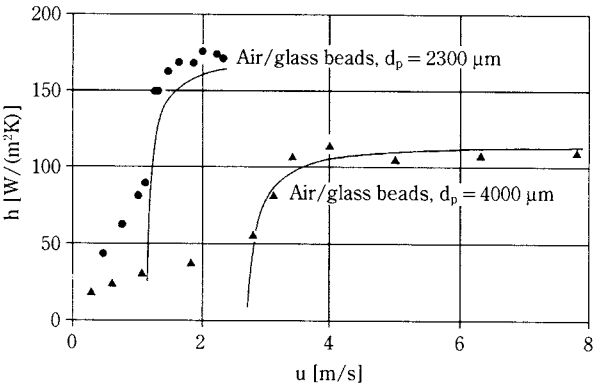

Fig. 10 Comparison of measurements by Wunder [2] (symbols) with predictions of Eq. (30) (lines), pressure varied.

8. Heat transfer in the regime $10^2 \le Ar \le 10^5$

With two well-understood end points, namely purely particle convective heat transfer at $Ar \le 10^2$ and purely gas convective type at $Ar \ge 10^5$, a predictive equation for the intermediate regime can be derived in the form of an interpolation between the two extremes. A successful strategy can be derived from **Figures 4** and **2**. **Figure 4** evidences a rather wide particle residence time distribution. This means that in the intermediate regime of Archimedes numbers, short residence times result in a "gas convective" behavior, whereas long residence times favor the "particle convective" behavior. An increase in the

excess gas velocity $u-u_{mf}$ increases the bubble frequency which, for its part, reduces the mean particle residence time at the heating surface. All these features are evident from **Figure 2**: an increase in particle size d_p, and, hence, in the minimum fluidization velocity u_{mf}, shifts the behavior from particle convective towards gas convective (compare curves 1, 2, 3 and 4). The above-mentioned considerations also explain the humps observed in curves 2 and 3. These curves start more "particle convective" and end more "gas convective". In particular, curve 3 approaches the purely gas convective curve 4 from top. All these considerations taken together, a damping function must be implemented in the formula for the particle convective heat transfer which reflects two features: the particle convective heat transfer must decrease with increasing u_{mf} as well as with increasing $u-u_{mf}$. The final result of a prolonged trial-and-error procedure in the form of the comparison with all available well-documented experiments resulted in the formula [15]

$$\frac{h\ell_l}{k_g}=\frac{0.125(1-\varepsilon_{mf})\left(1+33.3\left\{\sqrt[3]{[(u-u_{mf})/u_{mf}]}\sqrt[3]{(\rho_p c_p/k_g g)(u-u_{mf})}\right\}^{-1}\right)^{-1}}{1+(k_g/2c_p\mu)\left\{1+0.28(1-\varepsilon_{mf})\sqrt{}\left[\rho_g/(\rho_p-\rho_g)\right]^{0.5}\left[\sqrt[3]{(\rho_p c_p/k_g g)(u-u_{mf})}\right]^2 u_{mf}/(u-u_{mf})\right\}}$$

$$+0.165\mathrm{Pr}^{1/3}\left(\frac{\rho_g}{\rho_p-\rho_g}\right)^{1/3}\left[1+0.05\left(\frac{u-u_{mf}}{u_{mf}}\right)^{-1}\right]^{-1} \qquad (31)$$

which fits all situations for $\mathrm{Ar}\leq 10^8$. Its complexity is justified by comparison with experimental data in **Figures 11** to **15**, which reflect all variations in the relevant data (**Fig. 11**: particle size together with particle shape in the form of ε_{mf}; **Figure 12**: particle density and particle specific heat; **Figure 13**: gas thermal conductivity; **Figure 14**: gas density; **Figure 15**: bed temperature).

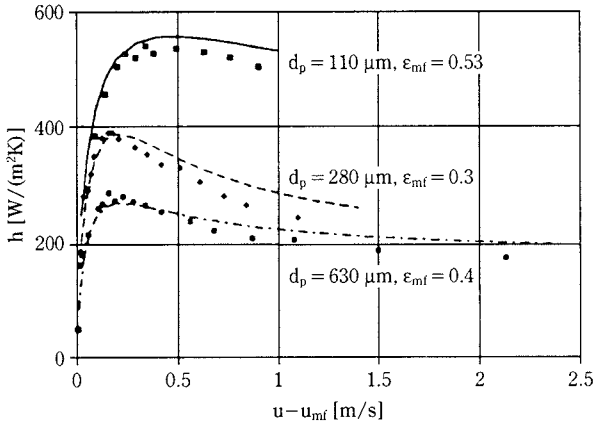

Fig. 11 Measurements (symbols) with mullite-air at ambient conditions, heat transfer surface: single vertical immersed tube, data from Wunder [2], prediction (lines) according to Eq. (30)

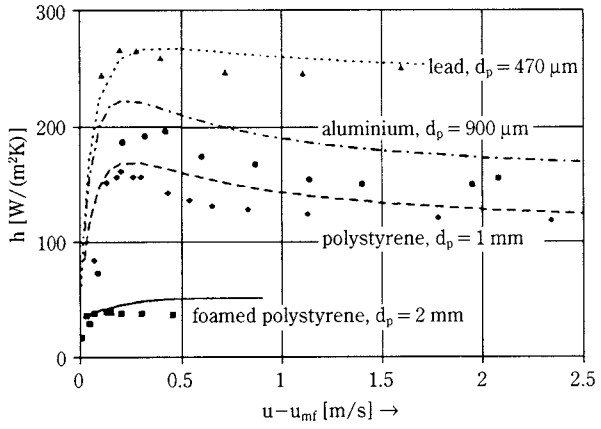

Fig. 12 Measurements (symbols) with different solids – air at ambient conditions, heat transfer surface: single vertical immersed tube, data from Wunder [2], prediction (lines) according to Eq. (30).

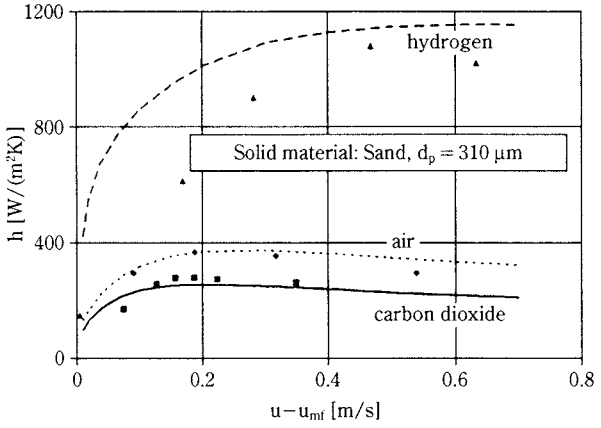

Fig. 13 Measurements (symbols) with sand – different gases at ambient conditions, heat transfer surface: single vertical immersed tube, data from Wicke and Fetting [16], prediction (lines) according to Eq. (30).

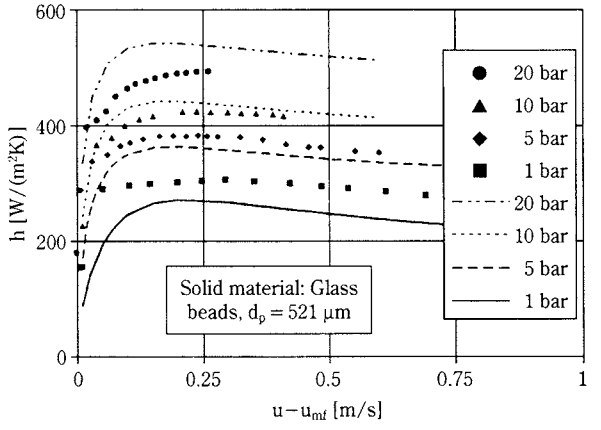

Fig. 14 Own measurements (symbols) with glass beads – air, pressure varied, heat transfer surface: single vertical immersed tube, prediction (lines) according to Eq. (30).

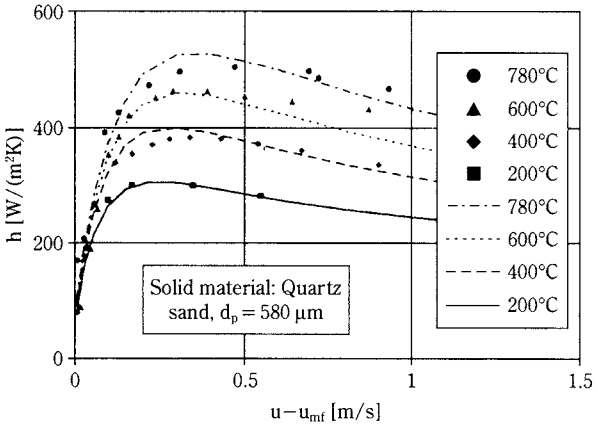

Fig. 15 Measurements (symbols) with sand–air, bed temperature varied, heat transfer surface: horizontal tube, data from Janssen [17], prediction (lines) according to Eq. (30).

From the viewpoint of chemical engineering practice, the most important result is depicted in **Figure 15**. At Archimedes numbers $Ar < 10^5$, the cooling down of hot particles at cooling surfaces results in an effective shielding against radiative effects – even at elevated temperatures up to 780°C. On the other hand, with purely gas convective heat transfer at $Ar \geq 10^5$, only marginal cooling down or heating up of the particles at the cooling or heating surface is observed. Therefore, at $Ar \geq 10^5$, the radiative component of the heat transfer gives a significant contribution for temperatures > 500°C.

9. Additional remarks

Fluidization ceases with the dominance of adhesion forces in comparison with aerodynamic resistance and weight minus buoyancy [18] usually observed at particle sizes of $d_p \leq 10$ µm. The then observed particle immobility manifests itself in a sharp breakdown of the heat transfer.

With coarse-grained particles and elevated pressures, Archimedes numbers $Ar > 10^8$ are attained. As can be read from **Figure 1**, Archimedes numbers $Ar > 10^8$ result in Reynolds numbers $Re > 10^4$, which means an effective heat transfer even in fixed beds. The by-pass effect of gas bubbles in fluidized beds then results in even a decrease of the heat transfer in fluidized beds in comparison with fixed beds (for details see [19]).

10. Conclusions

Heat transfer in gas-fluidized beds is the result of complex mutual interactions of fluid mechanics, particle dynamics and the thermal properties of the involved media. The derivation of a predictive equation for the reliable prediction of the heat transfer in bubbling fluidized beds thus involves a step-by-step procedure which takes into account all relevant aspects of the problem in question. Due to the large number of influencing factors (altogether eleven) with four basic units (K, kg, m, s), the resulting equation, Equation (30) must be complex, namely built up from seven different dimensionless groups.

List of Symbols

C	: constant	
c_p	: specific heat of particle material	[Ws kg^{-1} K^{-1}]
d_p	: particle diameter	[m]
G	: constant	
g	: gravitational acceleration	[ms^{-2}]
h_{gc}	: gas convective heat transfer coefficient	[Wm^{-2} K^{-1}]
h_{pc}	: particle convective heat transfer coefficient	[Wm^{-2} K^{-1}]
h, h_{max}	: heat transfer coefficient, maximum value	[Wm^{-2} K^{-1}]
k_e	: effective thermal conductivity	[Wm^{-1} K^{-1}]
k_g	: gas thermal conductivity	[Wm^{-1} K^{-1}]
k_p	: solid material thermal conductivity	[Wm^{-1} K^{-1}]
L, L_0	: digital luminosity, initial value	
ℓ	: length	[m]
ℓ_0	: mean free path of gas molecules	[m]
$\tilde{M}$	: molar mass	[kg mol^{-1}]
ℓ_l	: laminar flow length scale	[m]
ℓ_t	: turbulent flow length scale	[m]
n_{gc}	: normalized gas convective heat transfer function	
n_{pc}	: normalized particle convective heat transfer function	
p	: pressure	[Nm^{-2}]
P	: constant	
R	: radius	[m]
R'	: aerodynamic resistance force	[N]
$\tilde{R}$	: gas constant	[Nm mol^{-1} K^{-1}]
r	: integration variable	[m]
S	: size of surface asperities	[m]
S_{min}	: minimum effective surface roughness	[m]
T	: absolute temperature	[K]
t	: time	[s]
u	: superficial gas velocity	[ms^{-1}]
u_{mf}	: superficial gas velocity at minimum fluidization condition	[ms^{-1}]
v	: fluid velocity	[ms^{-1}]
W	: probability	

Greek letters

ε_{mf}	: minimum fluidization void fraction	
γ	: accommodation coefficient	
φ	: angle	
ρ_g	: gas density	[kg m^{-3}]
ρ_p	: solid density	[kg m^{-3}]
τ	: mean residence time	[s]

Dimensionless groups

$Ar \equiv \frac{d_p^3 g(\rho_p - \rho_g)\rho_g}{\mu^2}$	Archimedes number
$Co = k_g C S_{min} t/\rho_p c_p d_p^3$	Dimensionless contact time
$c_D \equiv R^*/[(\pi d_p^2/4)](\rho_f/2)u^2$	Drag coefficient
$Nu, Nu_{max} \equiv \frac{hd_p}{k_g}$	Nusselt number
$Pr \equiv \frac{c_g \mu}{k_g}$	Prandtl number
$Re \equiv \rho_g v d_p/\mu$	Reynolds number

References

1) Botterill, J.S.M.: Fluid-bed heat transfer, Academic Press, 1975
2) Wunder, R.: Dr.-Ing. Dissertation, München, 1980
3) Mickley, H.S. and Trilling, C.A.: Ind. Eng. Chem. **41**, 1135, 1949
4) Molerus, O., Burschka, A. and Dietz, S.: Chem. Engng. Sci. **50**, 871, 1995
5) Ernst, R.: Chem.-Ing.-Techn. **32**, 17, 1960
6) Harakas, N.K. and Beatty, K.O. Jr.: Chem. Engng. Symp. Ser. **59** (41), 122, 1963
7) Botterill, J.S., Butt, M.H.D., Cain, G.L. and Redish, K.A.: in Proceedings of the International Symposium on Fluidization, June 6-9 Eindhoven (edited by A.A. Drinkenburg) 442-57, Amsterdam, 1967
8) Barreto, G.F., Lancia, A. and Volpicelli, G.: Powder Technol. **46**, 155, 1986
9) Schlünder, E.U.: Chem. Engng. and Processing, **18**, 97-106, 1984
10) Glosky, D., Glicksman, L. and Decker, N.: Intern. Journal of Heat and Mass Transfer, **27**, 599-610, 1985
11) Molerus, O.: Int. J. Heat and Mass Transfer **40**, 4151, 1997
12) Dietz, S.: Dr.-Ing. Dissertation, Erlangen, 1994
13) Baskakov, A.P. and Filippovsky, N.F.: in Fluidization VI (edited by J.R. Grace, L.W. Schemilt and M.A. Bergougnou) 695, Engineering Foundation, New York, 1988
14) Ranz, W.E.: Chem. Engng. Progr. **40**, 247, 1952
15) Molerus, O., Burschka, A. and Dietz, S.: Chem. Eng. Sci. **50**, 879-885, 1995
16) Wicke, E. and Fetting, F.: Chem.-Ing.-Techn. **6**, 301, 1954
17) Janssen, K.: Dr. Dissertation, Bonn, 1973
18) Molerus, O.: Principles of Flow in Disperse Systems, Chapman & Hall, London, 1993
19) Molerus, O.: Chem. Engng. Sci. **53**, 4, 753-759, 1998

Author's short biography

O. Molerus

Dr. Molerus is Professor of Particle Technology (Mechanische Verfahrenstechnik) at the University of Erlangen-Nürnberg, were he has been since 1968.
He was the Dean of the Engineering Faculty (Technische Fakultät) from August 1971 – August 1972. He received his Dipl.-Ing. and his Dr.-Ing. from Karlsruhe University – both in Mechanical Engineering. He received several awards: Award for Excellence in Particle Technology Research at the Second World Congress on Particle Technology in Kyoto, the Hans-Rumpf Medal for the Excellence in the Field of Particle Technology and the Max-Planck-Forschungspreis, together with John C. Chen from the Lehigh University in Bethlehem.
He has published over 200 technical articles – many of them are of the subject of solid gas flow and several books. Two are in English language – "Principles of Flow in Disperse Systems" and "Heat Transfer in Fluidized Beds" (co-author K.-E. Wirth). Both books are from Chapman & Hall.

Interaction between Feeding and Compaction During Lactose Compaction in a Laboratory Roll Press†

O. Simon., Pr. P. Guigon
Université de Technologie de Compiègne
Département de Génie Chimique
*Centre de Recherche de Royallieu**

Abstract

Experimental work was carried out to determine the influence of operating parameters on the roll press compaction of lactose and the interactions between feeding and compaction. A laboratory roll press was specially instrumented. The press and instrumentation are described. The first part of the experimental work deals with the adjustment of the roll press parameters in order to produce compacts with good mechanical strength and aspect for several roll press throughput. The measured normal stresses applied to the powder, the roll gap variations and the roll press throughput are correlated with the ratio between the speed of the rollers and the screw feeder speed, also called work coefficient. The roll press throughput is principally governed by the screw feeder speed. The second part of the experimental work deals with characterisation of the influence of the feeding conditions on the compaction. The single screw feeder produces locally a periodic disturbance which is responsible for compact heterogeneity. The normal stress measured on the rollers was correlated with the period of the screw. A minor variation of the feeding pressure produces a great variation of the compaction stress.

1. Introduction

Roll press compaction is an agglomeration process for particulate solids. It was developed to produce coal briquets at the end of the 19th century. Today, large numbers of other powders are compacted using a roll press – generally in mass production industries, but also in the pharmaceutical or speciality chemical industries [1]. The primordial principle of compaction is that many particulate materials become a compact when they are subjected to high pressure. Such materials are compressible. The roll pressing process consists if squeezing compressible particulate materials between two rolls rotating in opposite directions (**figure 1a**). Due to the large pressure exerted in the roll gap, the particulate material is transformed into a compact. The compact can vary in shape. With smooth or pocketed rolls, either a strip of compacted material or briquets are produced, respectively. The strip of compacted material can also be crushed in order to produce granules.

The space between the rolls is commonly divided into three areas, each of which is shown in (**figure 1b**): the feeding, the compaction and the ejection areas. In the feeding area, the material slips along the surface of the rolls and the bulk density of the material increases by virtue of particle rearrangement. In the compaction area, the material is driven by the rolls and very high pressures are applied to the material. In this area, the density increases by virtue of particle fracture and plastic deformation. Finally, in the ejection area, the compact can re-expand as a result of elasticity.

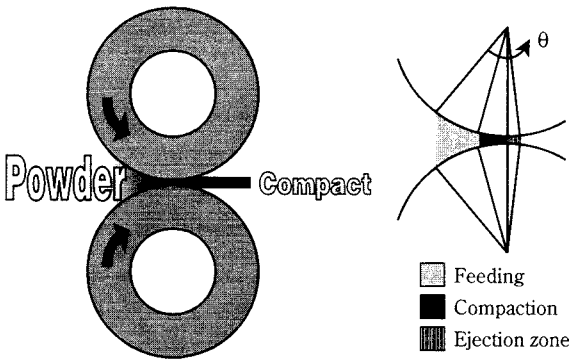

Fig. 1 (a) Roll pressing process. (b) Feeding, compaction and ejection areas in the space between rolls.

* B.P. 649, F-60206 Compiègne, France
† Received: August 8, 2000

When fine powders are compacted, feeding is often a problem [2,3]. First, because fine powders often have a poor de-aeration ability. The air squeezed between the particles has difficulty in leaving the mass of powder being compacted and counteracts the feeding of the press. Secondly, because fine powders exhibit poor flowability and this impedes the use of gravity feeding. Screw feeders are therefore employed. In which case the roll press parameters are not only the speed of the rollers and the roll gap, but also the screw feeder parameters. Moreover, the screw feeder interacts with the compaction process [4,5].

This paper presents the influence of the operating parameters of a laboratory roll press on the compaction of lactose as well as a characterisation of the interactions between the feeding and the compaction process.

2. Experimental set-up and materials

2.1 Laboratory roll press

Experiments were carried out on a laboratory roll press (Komarek® B100QC) shown in (**figure 2**) [6].

The roll press is equipped with smooth rolls of 130 mm in diameter and 50 mm in width that are vertically arranged. The initial roll gap is 0.8 mm. The powder is fed from a feed hopper (7) and is stirred by a paddle mixer (6) which prevents the occurrence of arches at the feed inlet. Feeding is achieved by a screw feeder (5). Between the screw and the rolls, there is a feed adapter with a Plexiglas® cheek plate (8). The upper roll is vertically moveable and is supported by a hydraulic system (4). The pressure in the hydraulic system is monitored.

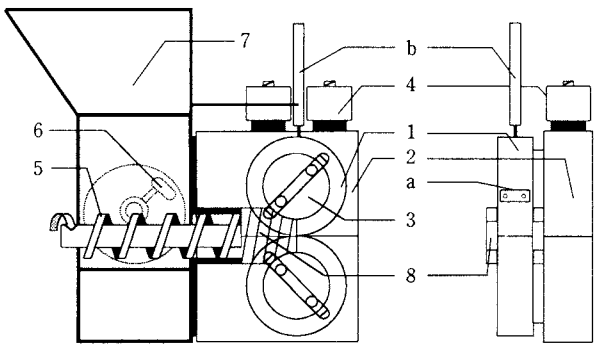

Fig. 2 The laboratory roll press [1. Roll, 2. Bearing block, 3. Roll shaft, 4. Supporting hydraulic system, 5. Screw feeder, 6. Paddle mixer, 7. Feed hopper, 8. Cheek plate. (a) Piezoelectric transducers, (b) Displacement transducer]

2.2 Instrumentation

The laboratory roll press was specially instrumented in order to permit measurement of the compaction conditions. The upper roll is fitted with two flush-mounted piezoelectric transducers (a) [3,7] which measure the normal stress (0−200 MPa) exerted on the surface at 15 mm from both sides of the roll. The signals of the transducers are transmitted by means of a high-precision slip ring to the charge amplifier, which is connected to a computer via a direct memory access A/D converter card. The position of the piezoelectric transducers is detected once a roll rotation by a photoelectric cell. Displacement of the moveable upper roll is measured by a displacement transducer (b) and is recorded. The roller speed, the screw feeder speed and the hydraulic pressure are also measured and recorded. The acquisition frequency of the recorded values is 1000 Hz for the normal stress measured by the piezoelectric transducers and 2 Hz for the other data.

The laboratory roll press parameters are:

- the roller speed that can be set from 2 to 16 rpm (0.013-0.108 $m.s^{-1}$),
- the screw feeder speed that can be set from 7.5 to 300 rpm,
- the hydraulic pressure that can be set from 80 to 150 bar (1-10 tons on 5 cm roll width).

For the experimental study, the hydraulic pressure was set to the minimum (80 bar) in order to protect the piezoelectric transducers from overload.

2.3 Material

The material compacted during the study is pharmaceutical monohydrate lactose. It could not be compacted without internal lubrication because it stuck to the rolls. It was therefore mixed with 0.5 percent of magnesium stearate. The characteristics of the monohydrate lactose+0.5% magnesium stearate are the following:

- mean diameter (d_{50}): 70 µm (without magnesium stearate)
- bulk density: 548 $kg.m^{-3}$
- tapped density: 865 $kg.m^{-3}$
- true density: 1530 $kg.m^{-3}$
- internal friction angle: 39° +/−2 (0.68 rad), wall friction angle (polished stainless steel): 9° +/−2 (0.157 rad)

The particle size was measured by laser granulometry (granulometer Malvern® Mastersizer). The true density was measured by helium picnometry. The friction angle was measured using a Peschel shear cell.

3. Experimental study

3.1 Adjustment of the roll press parameters

3.1.1 General information

The roll press throughput is principally limited by two factors. On one hand, the feeding speed is limited by the powder de-aeration ability. On the other hand, the compaction speed is limited by the elasticity of the particles. Generally speaking, a poor-quality compaction takes place when a critical throughput is reached. In that case, either the air flow generated by compaction disturbed the feeding (bad de-aeration), or the compaction was too fast [1]. All experiments of the study were carried out below this critical throughput. In other words, when no strip of compacted powder was produced or when the strip was of poor quality, the problem was not caused by poor de-aeration or an excessively high roller speed (too short a compaction time).

3.1.2 Compaction rates, good compaction settings

A wide range of roller speeds and screw feeder speeds can be set on the laboratory roll press. We therefore investigated the condition of roller speed and screw speed that enables the formation of a compacted strip of lactose mixed with 0.5% magnesium-stearate. The screw feeder speed was fixed and the roller speed was set in order to visually detect the high and low limit of roller speed that enables the compaction. At low roller speed, over-compaction occurs, and at high roller speed, no strip was formed.

Three operating rates have been defined as follows:

- the sub-feeding corresponds to the operating rate of the roll press when the amount of powder provided by the screw feeder is too small. In that case, the particulate material is not compacted.
- the overfeeding corresponds to the operating rate of the roll press when the amount of powder provided by the screw feeder is too large. The compact is extruded between the rolls and the roll gap increase is important. In that case, the compacted material is of poor quality and the powder loss is very important.
- the "good compaction rate" is an operating rate between sub-feeding and overfeeding. It corresponds to the production of a strip of compacted material that exhibits sufficient cohesion and mechanical strength.

For a fixed screw speed, the limits of "good compaction rate" are the lower and the higher roller speed that enable the production of compacts. These limits were detected visually for the four following screw feeder speeds: 7.7 rpm, 15,7 rpm, 22.7 rpm, 25.7 rpm. They are represented in (**figure 3**).

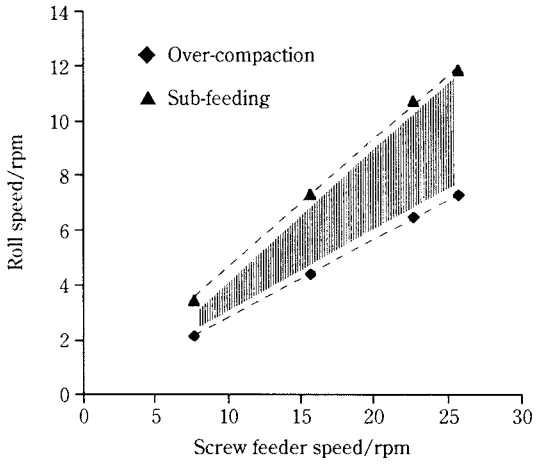

Fig. 3 Roller speed versus screw feeder speed corresponding to the limit of overfeeding and sub-feeding.

As the limits of the "good compaction rate" are straight lines on the graph representing roller speed versus screw speed, the limit of sub-feeding or overfeeding corresponds to a constant ratio between the roller speed and screw speed. This ratio (roller speed: screw speed) is called the work coefficient [8]. We established that the work coefficient must be greater than 0.28 and less than 0.49 for a satisfactory compaction of monohydrate lactose on our roll press. The work coefficient is therefore an indication of the compaction rate. For example, overfeeding occurs for a work coefficient greater than 0.28, regardless of the roller speed.

3.1.3 Roll press throughput

The roll press throughput was measured at the following screw feeder speeds: 7.7 rpm, 15.7 rpm, 22.7 rpm, 25.7 rpm. The roller speed was set to obtain the limits of sub-feeding and overfeeding and then to a value corresponding to an average value between sub-feeding and overfeeding. The results are shown in (**figure 4**).

The results of these experiments are very interesting. At a constant screw speed, the roll press throughput is constant. For example: at a screw feeder speed of 22.7 rpm, the roll press throughput is 268 +/−4 $g.min^{-1}$ for any roller speed set from 6 rpm to 10 rpm. So as long as compacts are produced, the roll press throughput does not depend on the roller speed. To sum things up, the influence of the roller speed on the roll press feeding is negligible. The roll press

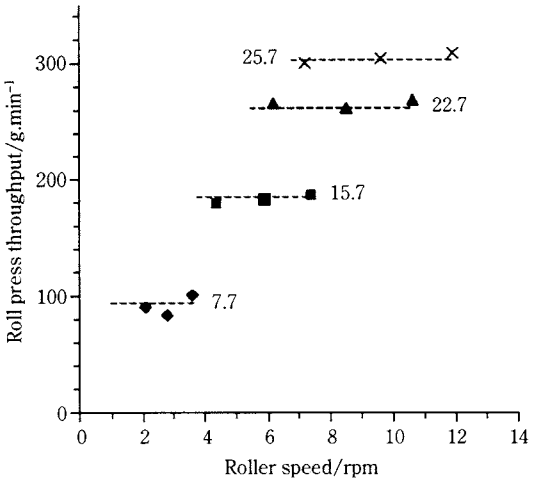

Fig. 4 Roll press throughput versus roller speed at fixed screw speeds indicated on the figure in rpm.

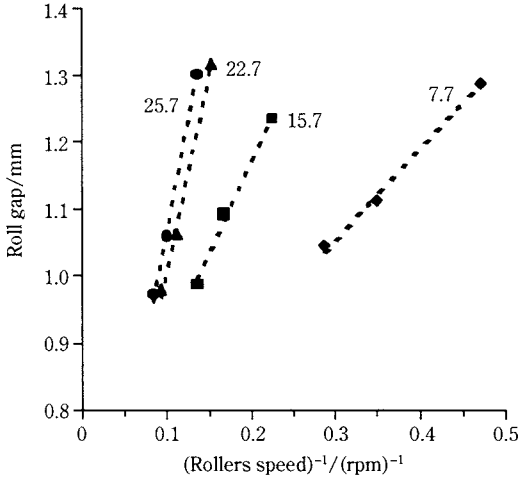

Fig. 5 Roll gap versus the inverse of the roller speed at fixed screw speeds indicated on the figure in rpm.

throughput is governed only by the screw feeder speed, regardless of the roller speed.

3.1.4 Roll gap variation

As the upper roll can move vertically, the roll gap increases from its initial value to an equilibrium value when the powder is compacted. This equilibrium value is a function of the mean stress applied by the rolls to the compacted material. It is also a function of the roller speed V_r, the roll press throughput Q_c, the density of the compacted material δ_s, the roll width, and the slipping of the compacted material on the roll surface ζ_s:

$$e = \frac{Q_c}{L.V_r.\delta_s.(1-\zeta_s)} \tag{1}$$

At a fixed screw feeder speed, the roll gap increases linearly with $(1/V_r)$ (**figure 5**). Because the variation of the density of the compacted material δ_s and of the slip between the compact and the rolls ζ_s is negligible in relation to variation of the roller speed, this result confirms that the roll press throughput Q_c is constant at a fixed screw speed V_v.

Furthermore, the roll gap increases linearly with the ratio screw feeder speed/roller speed $(1/C_w)$ (**figure 6**).

$$e = K_2.\frac{V_v}{V_r} = \frac{K_2}{C_w} \tag{2}$$

The screw feeder throughput is then proportional to the screw feeder speed:

$$Q_s = K_1.V_v. \tag{3}$$

The screw feeder throughput Q_s can be calculated as follows [9,10]:

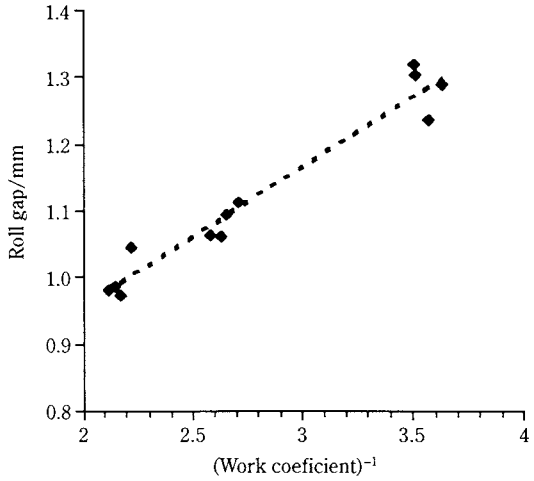

Fig. 6 Roll gap versus the ratio screw feeder speed/roller speed

$$Q_s = k\delta_S A_s V_{ax},\ A_s = \frac{\pi}{4}.(D_S^2 - D_{ss}^2),$$

$$V_{ax} = \pi.D_s.n_s G(\psi,\phi),\ G(\psi,\phi) = \frac{\tan\phi.\tan\psi}{\tan\phi+\tan\psi}. \tag{4}$$

k: filling ratio of the screw, δ_S: relative bulk density at the outlet, Ds: screw barrel diameter, Dss: screw shaft diameter, n_s: number of screw revolutions, Φ: screw helix angle, ψ: transportation angle.

k, δ_S and ψ are process data and have to be measured. As the screw feeder throughput is proportional to the screw feeder speed, the variations of k, δ_s and ψ are negligible for the range of screw feeder speeds investigated [10].

3.1.5 Normal stress

The normal stress is recorded once a roll rotation by the two piezoelectric transducers. Due to the

screw feeding, the normal stress fluctuates greatly per rotation. Therefore, a mean normal stress profile has to be calculated from a great many normal stress profiles. Fourteen normal stress profiles were used in our case. Some of the calculated average profiles corresponding to various roll press settings are shown in (**figures 7** and **8**). When a constant work coefficient is set, the normal stress profile does not change, regardless of the roll speed or the screw speed (**figure 7**). But when different work coefficients are set, then the profiles are also different (**figure 8**). For example, at a constant roller speed, the stress applied to the powder increases when the screw feeder speed is increased. This phenomenon can be explained by the increase of the feed pressure when the screw speed is increased and the roll speed remains constant. As demonstrated by Johanson [11], the stress exerted during compaction is in relation with the mean feed pressure. Therefore, identical compaction conditions exist for many different parameter settings.

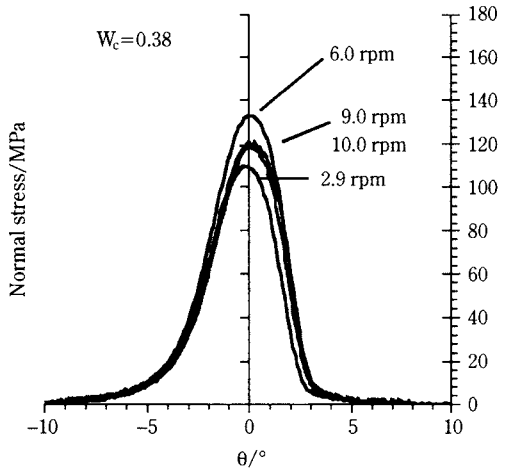

Fig. 7 Mean normal stress profile measured at a constant work coefficient C_w=0.38.

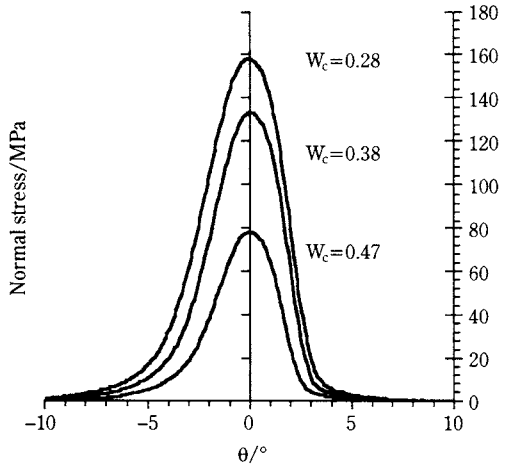

Fig. 8 Mean normal stress profile measured at a constant screw feeder speed (7.7 rpm) for three work coefficients indicated on the figure.

By integrating the mean stress profile and assuming that this profile is exerted across the entire roll width, the separating force of the upper roll can be estimated (the tangential stress is not considered).

$$F_v = L.\frac{D}{2}\int \sigma_n(\theta)\cos(\theta).d\theta. \quad (5)$$

F_v was correlated with the roll gap variation in (**figure 9**). The roll gap and the separating force are proportional. This result is due to the elasticity of the upper bearing block. As the roll gap is easier to measure than the normal stress, it is a very good process control variable.

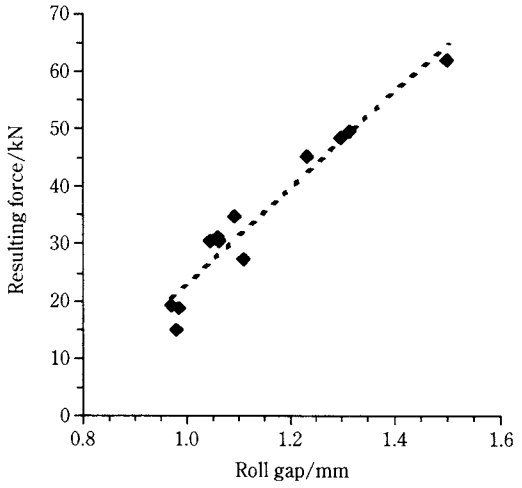

Fig. 9 Estimated separating force versus roll gap variation

3.2 Characterisation of the influence of the feeding conditions

3.2.1 Fluctuations of the measured normal stress

Normal stress profiles are measured once a roll revolution. For reproducibility reasons, fourteen consecutive measurements (14 revolutions) were recorded by both piezoelectric transducers. The variations of the measured profile between consecutive revolutions (**figure 10**) would be much more important than expected if the stress distribution in the roll gap were not dependent on time. In fact, the stress applied locally to the powder by the rolls (maximum of the profile) σ_n^{max} fluctuates over time. Moreover, the stress measured simultaneously by the left and the right transducer is not similar even though the transducers are symmetrically mounted. In fact, when a major stress is measured by the left transducer, a minor one is measured by the right one and vice versa. The stress

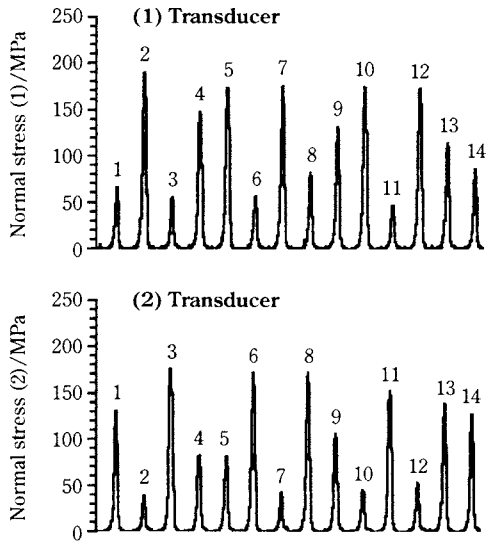

Fig. 10 Profiles of normal stress recorded simultaneously by both piezoelectric transducers (1) and (2) during fourteen turns (screw speed: 22.7 rpm, roller speed: 9.0 rpm)

distribution in the roll gap is thus not homogeneous across the roll width. As a conclusion, the stress applied to the powder in the roll gap depends on both time and position across the roll width.

3.2.2 Heterogeneity of the compacted strip

In order to determine the heterogeneity of the stress applied during compaction, the following method was employed. Five percent of coal measuring 200-400 μm particle size was added to the lubricated monohydrate lactose before compaction. During compaction, the coal particles are fragmented locally and crushed by the applied stress. The higher the stress, the larger the quantity of fine particles. Assuming that the distribution of the coal particles is homogeneous across the roll width at feeding, then after compaction, the number of particles is greater in

Fig. 11 Strip of a mix (monohydrate lactose+0.5% magnesium stearate+5% [200-400 μm] coal particles) compacted with a screw speed of 7.7 rpm and a roller speed of 2.2 rpm. Rolling is from left to right.

the zones that have endured the highest stress. As can be seen in (**figure 11**), these zones appear darker. The darkest zones of the strip of compacted material are therefore representative of the maximum applied stress. The localisation of this maximum stress applied to the compacted material looks like a sinusoidal curve. This curve represents the localisation across the roll width of the maximum stress applied to the powder versus the time. Assuming no slip occurs between the rolls and the strip during ejection of the compacted material, then the time period of the sinusoidal curve is:

$$p = \frac{60.l}{\pi.D.V_r} \tag{6}$$

where l is the length [mm] of the period measured on the compacted strip.

This period has been found to be the same as the screw feeder period ($p_s=60/V_v$). The origin of the fluctuations is definitely the screw feeder. In fact, the feed pressure heterogeneity is linked with the geometrical properties of the screw extremity. As the screw turns, the feeding heterogeneity also moves, and that is the reason why we observe a sinusoidal curve.

3.2.3 Interpretation of the heterogeneity of the strip in terms of fluctuations of the measured normal stress

The stress applied to the powder is a periodic phenomenon (**figure 11**) but it is sampled once a roller revolution (408 mm) and only on two small sites across the roll width. The collecting period (period of roll rotation) is also much larger than the period of phenomenon (period of screw rotation). That is the reason why the periodicity of the stress is not easy to demonstrate.

Localisation (x,y) of compacted strip zones that have endured a higher stress are simulated as follows. The value of (y) is calculated as a function of the length of the strip (x) using the following relation:

$$y = 0.02\text{m}\cdot\sin\left(\frac{2.V_v}{D.V_r}.x\right) \tag{7}$$

Three portions of the 'simulated compacted strip' are shown in (**figure 12**). The stress is measured by the transducers (1) and (2) every roll revolution, that corresponds to every 408 mm (roll circumference). An example of this sampling is shown in (**figure 11**). An arbitrary initial localisation of the transducers is chosen for the first roll revolution and represented for the second and the third one. As we can see, the

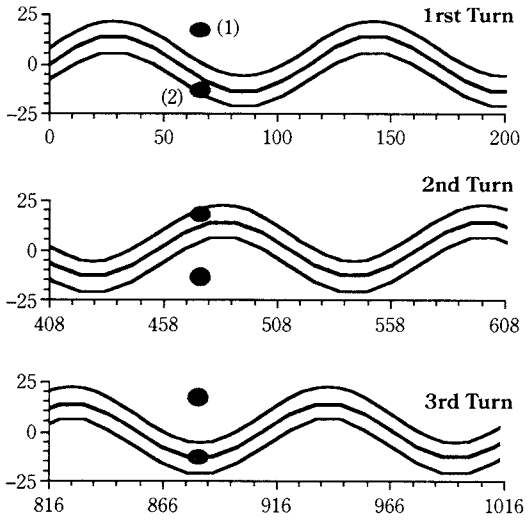

Fig. 12 Representation of the sampling of the normal stress by the transducers (1) and (2), coordinates (x,y) are represented in mm, localisation of the higher stress zone is represented by a sinus curve (screw speed: 22.7 rpm, roller speed: 9.0 rpm)

transducer (1) measures first a low stress, then a higher stress, then a low stress again. Transducer (2) measures exactly the opposite. This phenomenon is exactly what can be observed in (**figure 10**). So the heterogeneity of the strip can be estimated by measuring the normal stress applied by the rolls using the piezoelectric transducers over many roller revolutions. For this purpose, the roller period should not be a multiple of the screw feeder period.

4. Conclusion

The feeding of a roll press is a complex process that interacts with the compaction process. When a screw feeder is used, the compaction process is not only controlled by the roller speed but also by the screw feeder speed. Therefore, there are many possibilities to set the roll press parameters. For example, the adjustment of the screw feeder speed can modify the stress applied to the powder. Moreover, we showed that the throughput of the press is governed only by the screw feeder speed, regardless of the roller speed (as long as compacted material is produced). When a constant screw feeder speed is set, a modification of the roller speed induces a variation of the roll gap and of the applied mean stress. The normal stress applied to the powder or the roll gap variation can be correlated with the ratio between the roller speed and the screw feeder speed, also called the work coefficient. In fact, the work coefficient is characteristic of the compaction rate. Another consequence for using a screw feeder is the heterogeneity of the feeding. We showed that the single screw feeder is responsible for fluctuations of the stress applied during compaction. These fluctuations can be measured using piezoelectric transducers and correlated with the heterogeneity of the stress applied to the strip of compacted material. As the difference between the highest and the lowest stress measured is important, we conclude that the feeding disturbances caused by the screw feeder have a large influence on the compaction conditions.

Nomenclature

A_s	: area between the screw shaft and screw barrel	[m^2]
C_w	: work coefficient	
D	: roll diameter	[m]
D_s	: screw barrel diameter	[m]
D_{ss}	: screw shaft diameter	[m]
e	: roll gap	[m]
F_v	: separating force exerted on the upper roll	[N]
$G(\Phi,\psi)$	: screw transportation coefficient	
k	: filling ratio of the screw	
K_1	: proportionality constant between Q_s and V_v	
K_2	: proportionality constant between e and $(Cw)^{-1}$	
l	: length of the measured period of the compacted strip	[m]
L	: roll width	[m]
n_s	: number of screw revolution	
p	: time period of the fluctuation of the localisation of the maximum applied stress across the roll width	[s]
p_s	: screw feeder period	[s]
Q_c	: roll press throughput	[$kg.s^{-1}$]
V_{ax}	: transportation speed of the particulate solid in the screw	[$m.s^{-1}$]
V_r	: roller speed	[$rad.s^{-1}$]
V_v	: screw feeder speed	[$rad.s^{-1}$]
x	: length coordinate for the localisation of the maximum stress	[m]
y	: width coordinate for the localisation of the maximum stress	[m]
Φ	: screw helix angle	[rad]
δ_s	: density of the compacted material	[$kg.m^{-3}$]
θ	: rolling angle	[rad]
σ_n	: normal stress	[Pa]
σ_n^{max}	: maximum of the normal stress profile	[Pa]
ψ	: angle of direction of solid movement	[rad]
ζ_s	: slipping of the compacted material on the roller surface	

Bibliography

1) Pietsch W.: Size enlargement by agglomeration. Wiley Publishers, 1991
2) Dec R.T.: Problems with processing of fine powders in roll press. Komarek® internal communication, 1997
3) Petit-Renaud, A.: Compaction des poudres en presse à rouleaux lisses alimentée par une vis horizontale, PhD Thesis, Université de Technologie de Compiègne, 1998
4) Johanson, J.R.: Feeding roll press for stable operation. Proc. 18th Biennial Conference for Briquetting and Agglomeration, 1981, 209-227
5) Dec R.T.; Komarek R.K.: Experimental simulator of roll press feed system. International Meeting on Chemical Engineering and Biotechnology, ACHEMA, 1994
6) Dec R.T.; Komarek R.K.: Benefits of using small laboratory roll press for research and development of compaction process. Powder & Bulk Solids, 1997, Conference-Exhibition.
7) Michel B.: Contribution à l'étude de l'agglomeration des poudres en presse à rouleaux lisses, PhD Thesis, Université de Technologie de Compiègne, 1994
8) Goidin-Jerôme E.; A. Delacourte; J.C. Guyot; Dehont F.; Hervieu P.: Modification des propriétés d'une poudre à l'aide d'un compacteur granulateur. Influence des différents réglages. S.T.P. Pharma Sciences, 1992, 2 (4), 320-324
9) Darnel W.H.; Mol E.A.J.: Solids Conveying in Extruders. SPE Journal, 1956, 20-29
10) Sander U.; Schönert K.: Operation conditions of a screw feeder equipped high pressure roller mill, 9th European Symposium On Comminution, 1998, 485-492

Author's short biography

O. Simon

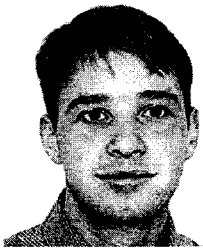

Olivier Simon graduated in chemistry from Ecole Superieure de Chimie Organique et Minérale, France 1996. He is currently in a third year Ph.D. program at the Université de Technologie de Compiègne in the powder technology group of Pr. Pierre Guigon, the subject of his thesis is: Study of the interactions between feeding and compaction in a laboratory roll press.

P. Guigon

Pierre Guigon is a Chemical Engineer from ENSIGC Toulouse (France 1971). Master of Engineering Science, UWO London Ontario, (Canada 1974), Docteur Ingénieur UTC Compiègne (France 1976), Docteur es Science UTC Compiègne (France 1987), Fellow of the Institution of Chemical Engineers and head of the Chemical Engineering Department at the University of Compiègne. His research is in the field of particle suspensions (fluidization, pneumatic transport) and particle technology (commination and agglomeration).

Tracking Single Particles in Process Equipment or Probing Processes Using Positrons†

R.N. Forster[a], J.P.K. Seville[b], D.J. Parker[a] and Y. Ding[b]
[a] *Positron Imaging Centre, School of Physics and Astronomy*
[b] *School of Chemical Engineering*

Abstract

In Positron Emission Particle Tracking (PEPT), a single positron-emitting tracer particle is placed within the bulk of particles in the device of interest. The tracer will typically be of the same material as the bulk, or comparable with it in size and density. A positron emitted from the tracer annihilates with an electron, leading to the production of two near collinear 'back-to-back' gamma rays. The detection of these and subsequent pairs of gamma rays enable the tracer to be located in three dimensions by simple triangulation. Typically, a particle moving at 1 ms^{-1} can be located to within 1 mm 500 times a second, whilst at 0.1 ms^{-1} the spatial resolution is improved to 0.5 mm for a location calculated 50 times a second. The tracer particle position data can then be processed to yield information such as particle velocity, the residence time distributions within specified zones, and the frequency of entering these zones. A real time visualisation of the tracer motion enables the technique to be used for rapid diagnostic and development studies.

In the current work, PEPT is being applied in the investigation of a wide range of Particle Technology unit operations including mixing, gravity driven flows, rotary kilns and fluidisation. In each case, detailed trajectories have been obtained, enabling new insights into particle behaviour. In mixing, for example, it has been possible to obtain dispersion coefficients relating to each volume element of the bed, so enabling the separate contribution of each part of the mixer to be distinguished.

Introduction

The ability to map the flow of fluids and the movement of particles within engineering processes has long been sought, and has historically often relied upon the use of glass or perspex models with optically visible tracer particles. Such techniques however prohibit investigation of process systems within opaque apparatus, and also do not permit investigation of the material behaviour deep within the bulk. The use of radioactive isotopes in medicine for diagnosis or therapy has however become a recognised medical speciality named nuclear medicine, and sophisticated equipment for imaging tracer distributions by detecting the emitted radiation is commercially available.[3,12]

Radioisotope emission tomography is based on the use of a γ-ray emitting isotope as a flow tracer. External detectors are used to measure the number of γ-rays emerging from the system along each line of sight, thus providing the information needed to reconstruct the tracer distribution inside by the standard tomographic approach. These techniques are particularly useful for the study of multi-phase flow, where one component can be labelled and its behaviour observed. In medical applications, radioactive tracers that mimic natural metabolic substances are used *in vivo* to investigate whether organs are functioning normally. Two types of emission tomography have been developed in medicine. Single Photon Emission Computed Tomography (SPECT) is based on measuring the number of single γ-rays emitted by the tracer along each line of sight through the system, using collimated detectors. Alternatively, Positron Emission Tomography (PET) uses tracers that decay by positron emission. The emitted positron subsequently annihilates with an electron, resulting in the emission of a pair of back-to-back γ-rays which are detected in coin-

[a,b] University of Birmingham, Edgbaston, Birmingham, B15 2TT, United Kingdom.
† Received: August 8, 2000

cidence, thus defining the line of sight without the need for collimation. In addition, the pair of 511 keV γ-rays produced from the positron/electron annihilation are quite penetrating (50% are transmitted through 11 mm of steel) and thus in principle PET offers greater potential for industrial process tomography.[13]

In medicine, PET has been extensively developed since the mid 1970s and although the cost of the detector system has restricted its routine use, a considerable number of PET systems are in use worldwide. However, only a few limited attempts have been made to use such systems for non-medical imaging, partly because a fixed geometry designed for medical imaging is unsuited for many industrial applications. At the University of Birmingham, a positron camera designed for industrial PET has been in use since 1984, consisting of a pair of multi-wire proportional chambers (MWPC) operating in coincidence. This camera (as shown in **Figure 1**), which was designed and built at the Rutherford Appleton Laboratory, is still operating reliably, its principal limitation remaining a low quantum efficiency for detecting 511 keV photons. Though the efficiency is unacceptably low for medical applications, this is not necessarily true for industrial applications where, generally, the exposure time and/or the radionuclide inventory may be increased as needed to provide adequate statistics to separate the true signal from background in the resulting images. However due to dead time limitations, the useful coincidence event rate for the MWPC camera is restricted to less than 5000 counts per second (5 kcps), and there exists a maximum limit to the activity which can be seen by the camera. With such a limit to the number of events recorded per second, less positional information can therefore be obtained per tracer 'step interval' for faster moving particles.[13]

In June 1999, the Positron Imaging Centre took delivery of a new, commercially available positron camera (ADAC Forte) which has been funded under the UK Joint Research Equipment Initiative. This camera, as shown in **Figure 2**, consists of a pair of sodium iodide gamma camera heads (with >20 times greater coincidence efficiency than the MWPC) operated in coincidence. It is fully digital, and is thus capable of count rates of up to 200 kcps. Both of these improvements result in a detection system of much greater capability, allowing tracers of smaller size, moving at higher velocities, to be tracked to greater levels of precision.[11]

This paper is intended to provide a brief description of the techniques employed within the Positron Imaging Centre for the investigation of industrial processes, and also to provide a number of examples where particle tracking techniques have been successfully employed.

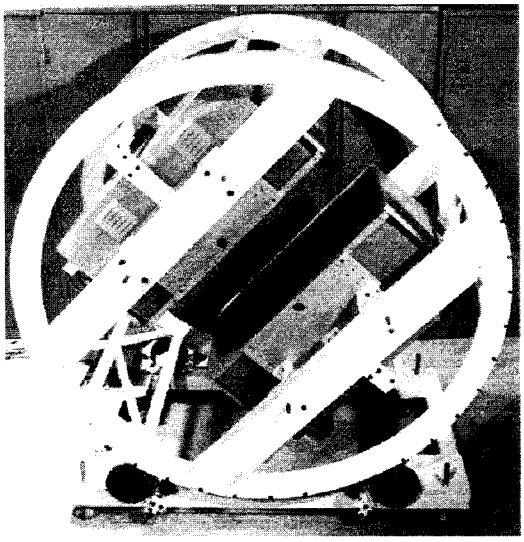

Fig. 1 Original Birmingham Positron Camera

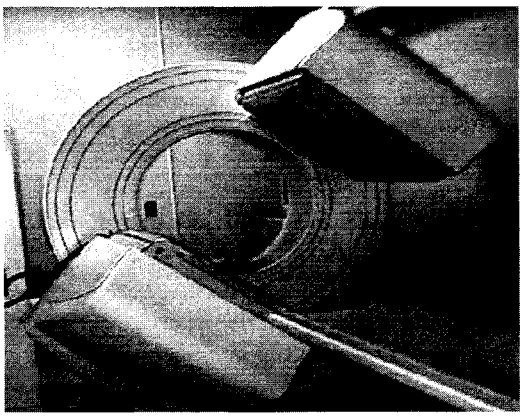

Fig. 2 ADAC Forte Gamma Camera

Positron Emission Tomography for Process Applications

For 2D imaging, the two stationary detectors act as a camera, and measure a single 2D projection of the distribution of positron emitting tracer within the volume between them. If two coincident 511 keV γ-rays are detected at particular points on the detectors, it may be inferred that the positron annihilation occurred somewhere along the line or path joining these points. On obtaining a series of such coincidences, a 2D image may then be obtained which quantitatively represents the tracer concentration across the system. Interpretation of the images is particularly simple if the system under investigation is relatively thin and thus can be considered in essence two dimensional.

Three-dimensional images are obtained by rotating the two detectors around the object under investigation. The series of projections obtained from the collection of the paths measured at many angles are then processed by the standard tomographic methods of backprojection followed by deconvolution, or filtered backprojection. An extremely large amount of data is required to achieve reasonable signal/noise ratios however and thus for rapidly evolving flow systems, such a timescale is too long and typically a 2D image only is obtained. In Birmingham, the MWPC has been used over the last 16 years for the investigation of the distribution of oil within operating aero-engines and gearboxes[1], the extrusion of doughs and pastes[19], the flow of liquid through fractured rocks[2], the displacement of oil from porous rock by brine[13], and the uptake of water into building material by capillary action[5],[12,13]

As an example of the application of PET imaging, **Figure 3** below shows results from a study of a stirred slurry of sand and water. Some of the sand grains were activated within the University cyclotron, generating the positron emitter ^{18}F from the activation of oxygen within the silica. The left hand image is for slurry containing only coarse grains of sand and has been normalised so as to represent the volume fraction of sand in each voxel. The right hand image is for a slurry containing the same mass of sand and stirred at the same speed, but in this case 20% of the sand was in the form of much finer grains. Only coarse grains were irradiated and so the distribution of the coarse grains has been selectively measured in the presence of the fine grains (the scale now represents the volume fraction of coarse grains in each voxel). This example demonstrates the application of emission tomography to the selective imaging of one component in a multi-component system.[13]

Positron Emission Particle Tracking

Though the new camera has provided a major increase in tomographic capability, tomography in general does not provide the most effective method for investigation of process operations. The technique of Positron Emission Particle Tracking (PEPT) which was developed at The University of Birmingham provides an alternative method for the investigation of a process operation.[10]

If it is known that only a single positron-emitting particle is present within the system of interest, it becomes relatively straightforward to calculate its position. This is done on the basis that the paths of

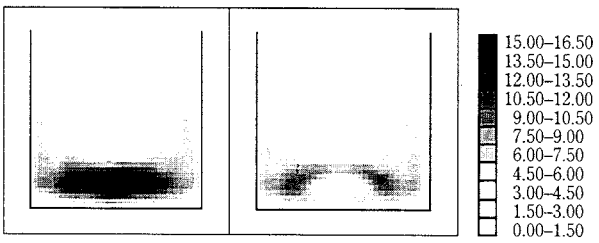

Fig. 3 Centre line tomographs of radioactive sand within a stirred slurry.

the detected γ-rays should all intersect in one location, that location being the tracer position. Given a set of detected events, each specified by the co-ordinates of the detected events on the two detectors, then there is an analytical expression for the co-ordinates of the point closest to which the paths all pass. This position is obtained by the intersection of these events as shown schematically in **Figure 4** below. In theory, only two such paths are required to triangulate the tracer position, but in practice, however, many of the detected events have been corrupted and more are in fact required.

Corruption may occur when one or both of the γ-rays are scattered prior to detection, or due to a recorded coincidence being a random event. The degree of scattering will depend on the nature and quantity of material the γ-ray must pass through to reach the detector – for a process material enclosed within a steel walled container for example, the number of events that are rejected increases. An iterative algorithm is therefore employed to reject corrupted events whose γ-ray paths do not pass close to the others. This algorithm automatically adjusts the number of events used to calculate a specific location, with an optimum number of events chosen so that statistics are adequate without the tracer having moved too far in this time period. Optimising this allows more accurate locations to be determined for a very slow mov-

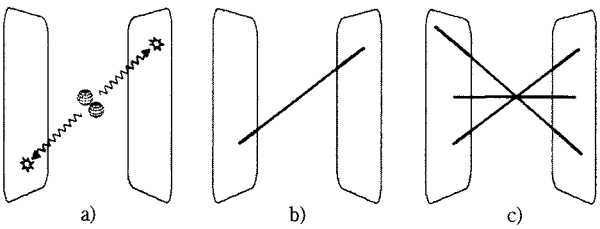

Fig. 4 Principles of PEPT
Detection of gamma rays occurs via two large position sensitive detectors (a).
Two events detected in coincidence define a line, along which the tracer particle lies (b).
After several such coincidences are recorded, the tracer may be located via geometric triangulation (c).

ing particle, and more frequent calculation of position (with an associated increase in positional error) for fast moving particles. Typically, a particle moving at 1 ms^{-1} can be located to within 1 mm 500 times a second, whilst at 0.1 ms^{-1} the spatial resolution is improved to 0.5 mm for a location calculated 50 times a second. The processed data from a PEPT analysis therefore consists of a sequence of typically hundreds of thousands of particle locations.[10,11]

Each results file, consisting of a long list of consecutive particle locations, may then be analysed with a user code, or a suite of software developed at the University of Birmingham. This software, *Track*, allows a range of basic analyses to be carried out on the data. The motion of the particle can be followed in real time in three dimensions, and positions plotted against time. **Figure 5a** below, represents approximately five seconds of track data for a tracer particle located within a spouted fluidised bed. From the list of tracer locations and time, other quantities can be deduced. From the variation of tracer location with time, a tracer particle's instantaneous velocity can be calculated, where typically the best estimate is obtained by taking the difference between every fifth location, and averaging over a series of such locations. A velocity vector plot may be produced, and a typical example is shown below in **Figure 5b**, which shows the velocity distribution for the same spouted fluidised bed as shown in **Figure 5a**.

For a closed circulating system in which the tracer particle explores all possible types of motion, PEPT is particularly useful not only in obtaining average velocity maps but also in determining the probability of the tracer being located in specific parts of the process domain. This probability or occupancy, is defined as the ratio of time spent by the tracer in a designated volume element to the total experimental run time. The occupancy plot for the spouted bed is shown below in **Figure 5c**, where red indicates regions of high occupancy and blue low occupancy. The occupancy can be especially useful in the investigation of segregation and maldistribution as may be seen in some of the examples described subsequently, and it can also be related to the bulk density of a well mixed process.

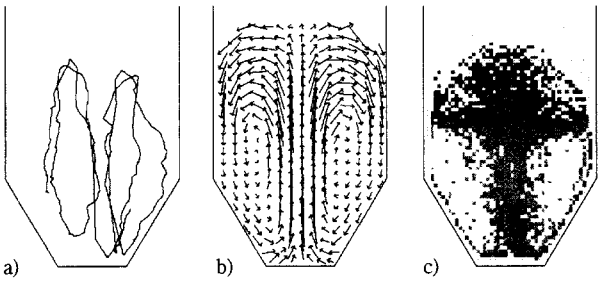

Fig. 5 Typical particle track (a), velocity vector plot (b), and occupancy plot (c) for a spouted fluidised bed.

Radioactive tracers are produced within the University cyclotron by either of the following methods. Typically a particle selected from the bulk may be directly irradiated, with the activation of ^{16}O already present within the particle forming ^{18}F. The activity produced is a function of cross-sectional area of the particle, with tracer particles down to a size of 500 μm being routinely employed. Alternatively, a solution of activated water is produced, with the activity transferred onto resin beads via an ion-exchange method. This allows production of tracers of sizes down to 150 μm. More complex tracers have been produced (generally for tomographic work) containing isotopes of carbon, sodium and copper.

Application of PEPT to Industrial Processes

Descriptions of some of the applications of PEPT to industrial process systems as carried out at the University of Birmingham are given in the following paragraphs.

1. Fluidised Beds

Previous research into fluidisation has always been limited by inability to measure the motion of particles in the bed without seriously disturbing the system. Data obtained generally have limited validity as measurements have often been taken near the boundary of the system or in a 'two-dimensional' fluidised bed. Much of previous research has in addition been directed towards the motion of the rising bubbles. PEPT however, allows the possibility of tracking a single particle (often identical in physical properties to the bulk material) within the bed in a totally non-invasive manner, with the penetrating nature of the γ-rays emitted allowing fluidised beds to be studied which are operated under high pressure and/or temperature.[15,16]

The particle tracks which are produced allow detailed analysis of the particle motion within the bed, in particular the frequency and duration of the distinct, rapid vertical movements ("jumps") which are interspersed with periods of virtual inactivity, before the particle descends slowly to the distributor region and completes a cycle. This circulation frequency can be measured directly and thus serves as an important validation tool in the validation of circulation models.

Principles of scale-up have also been investigated, with experiments carried out on a range of columns with different diameters and charged with materials differing in size and density, so as to keep the relevant dimensionless numbers for scale-up constant. It was found that within the experimental range, the results were consistent with the theoretical prediction that cycle frequency is proportional to excess gas velocity and that the Glicksman/Horio scale-up criteria were sufficient to ensure similarity in cycle time[17]. The range of applicability of circulation frequency models has been investigated through subsequent experiments on shallow (aspect ratio less than one) fluidised beds, which have previously been studied less extensively[8]. **Figure 6** below shows the circulation frequencies for a series of fluidising velocities and a number of bed heights and compares the results with those predicted by Geldart circulation theory. It can be seen that theory tends to give a poor prediction for shallow beds and is successful only for those taller beds at low excess gas velocities [8,15,16,17,18]

Circulation frequency was also found to be affected greatly by the presence of immersed objects within the bed. The presence of one to three immersed cylinders, representative of heat exchanger tubes as present in a fluidised combustor, was found to reduce significantly the overall circulation frequencies by a factor of two or more. Particle velocities in the vertical direction towards the tubes were found to be higher than they would be in the absence of such obstructions, a finding broadly consistent with previous studies on local heat transfer rates and erosion of immersed tubes in fluidised bed combustors.[18]

More complex fluidised bed processes have been investigated with PEPT, including granulation processes, multi-compartment beds, associated attrition problems and coating applications. In an investigation of a four-compartment fluidised bed used for the combustion of biomass, PEPT allowed quantitative investigation of the detailed circulation behaviour between the compartments, with results indicating that control of the material circulation rate could be achieved either by varying the excess gas velocity within the two 'fast' compartments, or the aeration rate in the two slow ones, with the latter option being the better. Mixing could in addition be investigated, and it was found the fast compartments acted as ideal mixers, whilst little mixing took place in the slow ones at the aeration rates used. A series of investigations into attrition were made on a bed of low-density porous glass particles, which tended to suffer continual abrasive wear rather than breakage. By experimentally measuring the elutriation rate, it was possible to estimate the rate of attrition, which primarily occurs when an individual particle enters the jet region. In turn, PEPT allowed the paths of entry into the jet region to be identified, and thus the rate of attrition could be directly related to the frequency of a particle entering the jet.[14,15]

As part of a series of investigations into fluidised granulation processes, the velocity of the tracer before and after it had been through a zone of liquid addition could be compared, with a clear deceleration being observed. Further investigations were concerned with the effects of addition of liquid layers. The non-solidifying Polyethylene Glycol (PEG) 600 was gradually added to a fluidised bed, and the effect on the motion within the bed was investigated through application of PEPT. **Figure 7** shows the velocity of the tracer for both wet and dry beds and clearly shows the velocity of the tracer particle decreasing as the liquid layers built up (to a maximum of 4 μm), leading to a more sluggish bed. Circulation frequencies similarly decreased dramatically.[8]

PEPT was also used to characterise those coating applications that use fluidised beds, for instance in

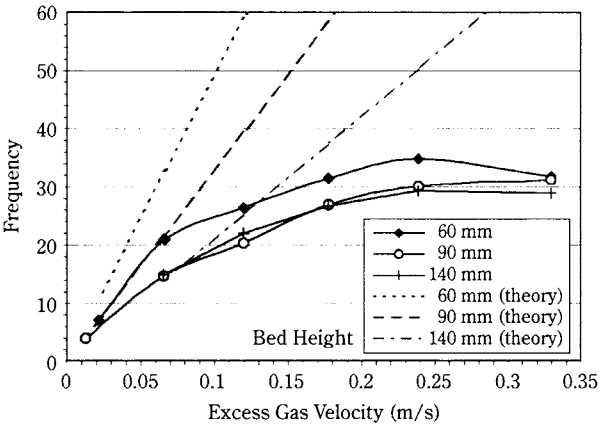

Fig. 6 Circulation frequency for a number of bed heights.

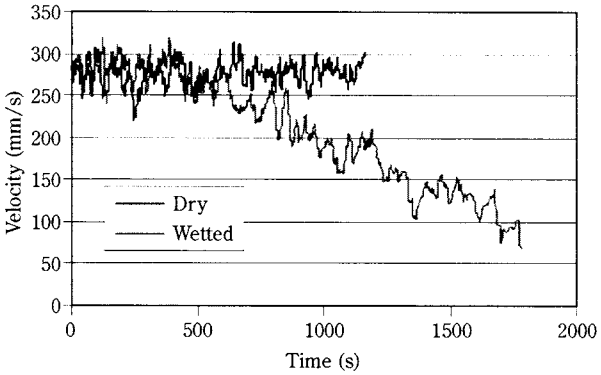

Fig. 7 Tracer velocity within gradually de-fluidising bed.

the pharmaceutical and food industries. In such beds, the coating material is sprayed upwards from the base of a spouted fluidised bed, the particles are coated, and then dried before circulating around to be re-coated. Similarly to the investigation of attrition, it is useful to identify when the particle was within a certain region of the bed, or specifically in this case, for how long and how often an individual particle entered the spray region. This information could be obtained from PEPT (see spouted bed examples in **Figure 5**) and therefore it was possible to develop a model of the coating process which was able to predict successfully the quality of the coating on a batch of bulk material.

2. Mixing Applications

Powder mixing is a common unit operation widely used in industry, especially in the manufacture of pharmaceuticals, ceramics, food, and polymers and PEPT has been used in a number of ways to study the behaviour of powder in mixers. As PEPT allows the position of the tracer particle to be determined very accurately and frequently, it has been possible to characterise and investigate the individual interactions between a particle of the bulk and for instance a blade or paddle used to mix the bulk material. Likely trajectories of particles as they move off the paddle can be determined, and also regions of inactivity can be identified. The particle tracking facilities at the University of Birmingham also allow additional information to be recorded alongside the tracking data, for instance by simultaneously logging the position of the impeller or paddle and also the applied torque. The motion of the bulk material can therefore be separated or binned according to the angular position of the paddle. In the case of a cylindrical paddle mixer, **Figure 8** below shows the bulk material behaviour as the blade passes through the bed, moving anti-clockwise. The angular interval of the paddle position is denoted by the wedge. The material can be seen to be lifted by the paddle, the bed distorted, and finally the lifted material falls off the paddle at relatively high velocities towards the lower end of the bed. Active and inactive regions of the bed could be identified, and trajectories obtained of material passing off the blade may prove a useful tool in blade design.[6]

In mixing devices, it is often of interest to evaluate the effectiveness of the mixing process. This has traditionally been done by charging the system, mixing for a set length of time and then analysing the whole as it is emptied, or spot samples taken at random throughout the mixture. Drawbacks of these methods may include possible degradation of the mixture upon emptying, or the influence of sampling technique upon results. Though such drawbacks may perhaps be accounted for, and some information about the mixing effectiveness may therefore be obtained, neither method enables the mechanisms at work within the mixer to be investigated.

The PEPT occupancy distribution measured after a limited time interval provides some indication of the mixing effectiveness within a complex system. For a steady state system, a more detailed measure of dispersion produced in each volume element can be obtained by following each pass of the tracer through

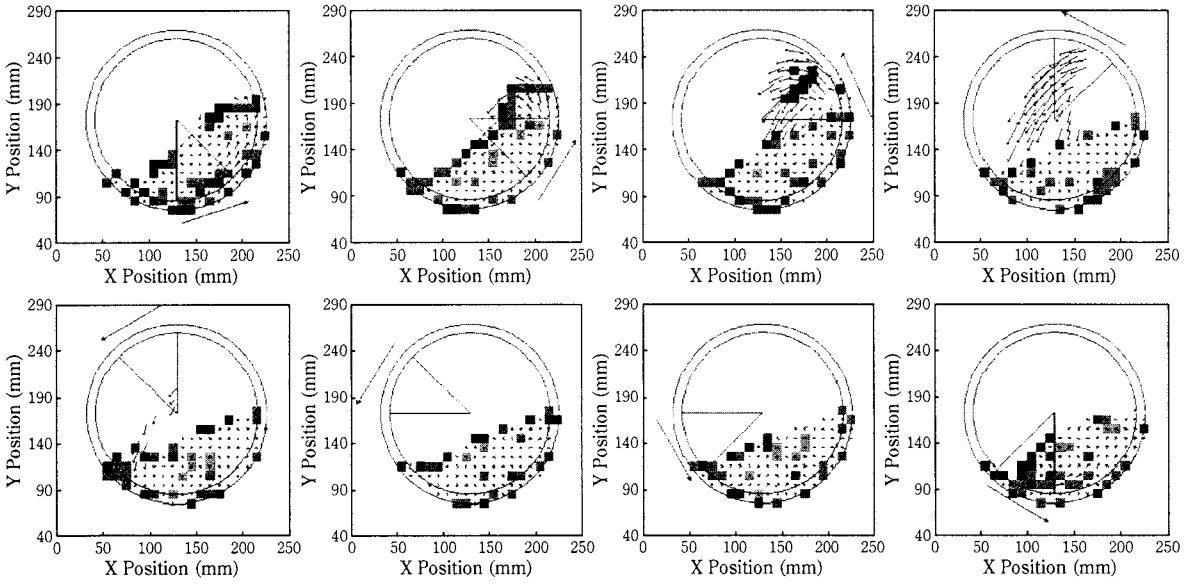

Fig. 8 Occupancy and Velocity Plots for Cylindrical Paddle Mixer.

this element, finding its location a specified time interval later (see **Figure 9**), and determining the dispersion of these endpoints (displacement vectors $\underline{r}_1$, $\underline{r}_2$ etc.) about the mean endpoint (mean displacement vector $\underline{r}$). In this way the value of the dispersion coefficient can be determined for each volume element by selecting a suitably short time interval. Alternatively a figure for the mixing effectiveness of the entire system may be obtained by multiplying the dispersion coefficient at each point by the local occupancy.[7]

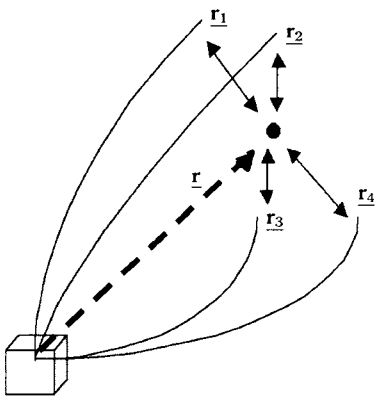

Fig. 9 Definition of Dispersion

3. Rotary Drums

Various aspects of the operation of rotary kilns have been extensively studied and modelled by a number of groups, but a detailed understanding of the mixing processes (such as is required to predict heat exchange through the bed) is still lacking. PEPT analysis of rotary drums provides detailed velocity measurements without the need for invasive measurement techniques such as for example optical probes. These velocity measurements allow the quantified characterisation of both the active layer and the passive or solid body rotation layer. Experimental measurements obtained have served to validate continuum models of granular motion within the drum.

The rate of surface renewal is of great importance and the residence time of material on the bed surface affects heat transfer from the freeboard in, for example, the case of rotary kilns or the quality of coating or flavour addition processes. The motion of granular material within a rolling drum is often classified as a function of rotation speed into one of six categories[4]. Most industrial processes are operated either in the slumping mode, in which the material is periodically lifted up the wall before sliding down again, or in rolling mode, which is a steady state motion of the entire bed where the lower part rotates with the drum and constantly feeds a sliding surface layer. The bed surface residence time will be determined by the characteristic mode of rotation, where for example rolling mode will promote good mixing of particles along with rapid surface renewal. Transition from a slumping to a rolling mode occurs when the upper shear wedge is replenished with solids by the rotating bed in less time than the time taken for the solids to fall. PEPT has proved useful in studying the transition between slumping and rolling modes, with bed surface velocity characteristics allowing identification of the mode. A typical particle track for a particle moving up through the passive layer before avalanching n times down the active layer is shown for a rolling mode drum and one operated at the transition between rolling and slumping in **Figures 10** and **11** respectively. As can be seen in **Figure 10**, the particle travels down the bed surface in one continuous, uninterrupted movement for a rolling mode drum, whereas a series of well defined discrete steps are observed for the slumping mode drum as shown in **Figure 11**. The onset of rolling can therefore be readily identified as occurring at that rotational speed where n=1.

Segregation within rolling drums has been investigated through the selection of appropriately sized tracers, with the findings broadly consistent with previous studies. After just a few rotations, particles were classified in radial position according to their size, with larger particles circulating at high radial displacements. In addition the 3D structure of axial

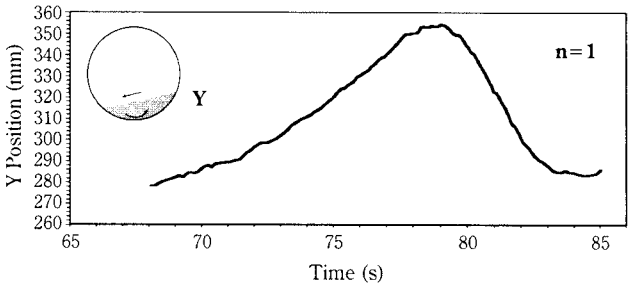

Fig. 10 Rolling mode particle surface movement

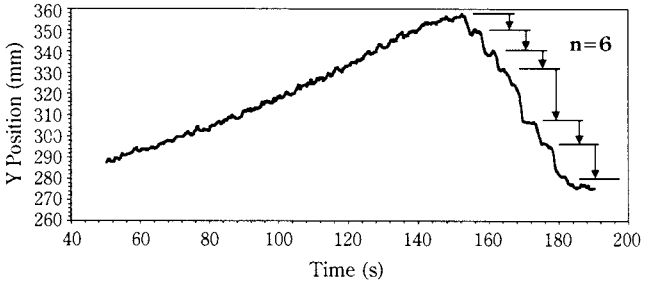

Fig. 11 Slumping/Rolling Transition particle surface movement.

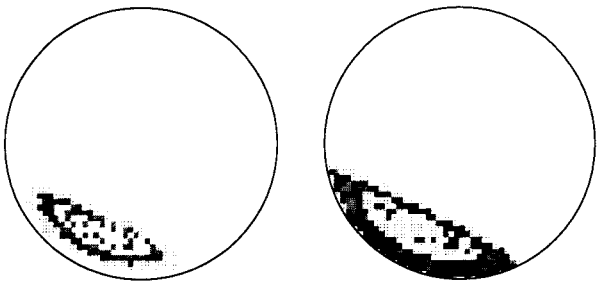

Fig. 12 Segregation within a Rolling Drum.

bands of fines could be observed. **Figure 12** above shows occupancy plots for a binary mixture of 20% fines (1.5 mm glass ballotini) and 80% coarse particles (3 mm glass ballotini). The structure of the segregated core can clearly be seen.

4. Other Applications

PEPT has been applied to a wide range of other processes including fundamental studies of vibrating beds, heat exchangers and stirred tanks. Tracer particles have been used as neutrally buoyant tracers in order to characterise flow patterns within liquid systems. Gravity driven flows have been investigated, and it has been possible to determine flow fields during hopper discharge. A wide range of external collaborators have used PEPT to increase their knowledge of powder mixers, distribution of foodstuffs within suspensions, milling processes and other varied applications.

Conclusions

PEPT has been employed for sixteen years at the University of Birmingham's Positron Imaging Centre. PEPT can provide detailed information on material behaviour within a process, thus aiding in development of novel processes, refinement of existing systems, and as an aid in the solution of process problems. PEPT has allowed the investigation of *real* equipment of a laboratory scale operating under realistic conditions. The MWPC has proved extremely reliable within this time and has exclusively been available for the study of industrial systems. With the arrival of the new ADAC Forte Gamma Camera, the capabilities for particle tracking have increased dramatically. Particles for tracking can now be smaller ($>150\,\mu$m), be moving at speeds of 10 ms^{-1} and can be located to a greater precision.

PEPT continues to provide new insights into established unit processes and to provide essential validation for the development of Discrete Element and Continuum Models of granular flow.

Bibliography

1) Allen M J, Fowles P, Hawkesworth M R, O'Dwyer M A, Rogers J D, Salter PL, Skelton R T and Stewart P A E.; Positron Emission tomography in gas turbine engine development; Proc. Conf. Modern Techniques and Development in Engine and Component Testing, Bath, UK, April 1989, Royal Aeronautical Society, London 1989 pp1301-1318 ISBN 09033409359
2) Gilling D, Jefferies N L, Hawkesworth M R, Parker D J and Fowles P.; The application of positron emission tomography to the study of mass transfer in fractured rocks.; The Scientific Basis for Nuclear Waste Disposal: Proc. Conf. XIV, Boston, USA, Nov. 1990, Abrajano T A Jr. and Johnson L H (Eds.), Materials Research Society, Pittsburg, 1991, pp551-558
3) Hawkesworth M R, Parker D J, Fowles P, Crilly J F, Jefferies N L and Jonkers G.; Non-medical applications of a positron camera.; Nucl. Instrum. & Meth. A310 1991 pp423-434
4) Heinen H, Brimacombe J K, Watkinson A P.; Experimental study of transverse bed motion in rotary kilns.; Metall. Trans. 14B 1983 pp191-205
5) Hoff W D, Wilson M A, Benton D M, Hawkesworth M R, Parker D J, Fowles P.; The use of positron emission tomography to monitor unsaturated water flow within porous construction materials.; J. Mat. Sci. Lttrs 15 1996 pp1101-1104
6) Kuo H P; PhD Thesis, (to be submitted Oct. 2001), University of Birmingham.
7) Martin T W, Seville J P K.; Dispersion of Particulate Materials in Mixers.; Proc. World Cong. on Particle Technol. IchemE, No.331 1998
8) McCormack A.; A Study of Melt Binder Granulation in fluidised Beds; PhD Thesis (to be submitted Aug. 2000), University of Birmingham.
9) McKee S L, Parker D J, Williams R A.; Visualisation of size-dependent particle segregation in slurry mixers using positron emission tomography.; Frontiers in Industrial Process Tomography, Scott D M and Williams R A (Eds.), Engineering Foundation 1995 pp249-259 ISBN 0939204525
10) Parker D J, Broadbent C J, Fowles P, Hawkesworth M R, McNeil P A.; Positron emission particle tracking – a technique for studying flow within engineering equipment.; Nucl. Instrum. & Meth. A326 1993 pp592-607
11) Parker D J, Forster R N, Fowles P, Takhar P S.; Positron emission particle tracking using the new Birmingham positron camera; Nuclear Instruments and Methods (submitted Oct 1999)
12) Parker D J, Hawkesworth M R, Beynon T D.; Process applications of emission tomography; The Chemical Engineering Journal 56 1995 pp109-117
13) Parker D J, McNeil P A.; Positron emission tomography for process applications; Measurement Science and Technology 7 1996 pp287-296
14) Snieders F F, Hoffmann A C, Cheesman E, Yates J G, Stein M, Seville J P K.; The Dynamics of Large Particles

in a Four-Compartment Interconnected Fluidized Bed. Powder Technol. 101 1999 pp229-239
15) Stein M, Martin T W, Seville J P K, McNeil P A, Parker D J.; Positron emission particle tracking: particle velocities in gas fluidised beds, mixers and other applications; Non-invasive monitoring of multiphase flows, Chaouki J et al (Eds.) Elsevier 1997 pp 309-334 ISBN 0444 825215
16) Stein M, Seville J P K, Benton D M, McNeil P A, Parker D J.; Particle movement and segregation in gas fluidised beds; 'Proc 1996 I Chem E Research Event, I Chem E, Rugby, 1996, pp 1060-1062
17) Stein M, Seville J P K, Parker D, Allen D.; Scale-Up of Particle Motion in Fluidised Beds Using Positron Emission Particle Tracking; Fluidization IX, Fan L S and Knowlton T M (eds), Engineering Foundation, New York 1998 pp77-84.
18) Stein M, Seville J P K, Parker D J, Allen D, Dee P R.; Solids Motion in Fluidised Beds in the Presence of an Immersed Cylinder; Proc. World Cong on Particle Technol., IChemE 1998, No. 206
19) Wildman R D, Blackburn S, Benton D M, McNeil P A, Parker D J.; Investigation of paste flow using positron emission particle tracking; Powder Technol. 103 (1999) 220-229

Author's short biography

R.N. Forster

Robin Forster graduated with a BSc. in Astronomy and Astrophysics from the University of St. Andrews in 1993, and completed an MSc. in Radiation and Environmental Protection at the University of Surrey, Guildford, and the University of Linköping, Sweden in 1994. At Surrey, he then joined the Department of Chemical and Process Engineering where he obtained a PhD in Computational Fluid Dynamics Modelling of High Swirl Combustors. In January 1999, he joined the Positron Imaging Centre, University of Birmingham as a Research Fellow. His interests include developmental work in the particle tracking technique, and also granular motion within rotary drums.

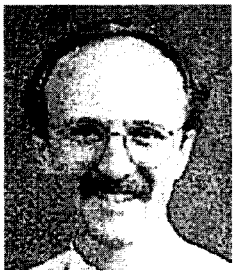

J.P.K. Seville

Jonathan Seville has been Professor of Chemical Engineering at the University of Birmingham since April 1994, and Editor-in-Chief of Powder Technology since 1995. He is a past Chairman of the UK Institution of Chemical Engineers Particle Technology Group and a member of the European Federation of Chemical Engineers Working Party on Agglomeration. His research interests include particle formation and breakage processes, fluidisation and other fluid solid contacting methods, particle characterisation, and gas filtration, particularly at high temperatures. Amongst his publications are two books on Gas Cleaning at High Temperatures, and a general text on Particle Technology

D.J. Parker

David Parker graduated in Mathematics from Cambridge University in 1979, and was then employed for 10 years as an experimental nuclear physicist at the UKAEA's Harwell Laboratory. During this period he was awarded his DPhil from Oxford University for studying nuclear reaction mechanisms by observing the distribution of the radioactive products, and was also involved in industrial applications of nuclear physics, including studying the wear of components by observing the removal of radioactive layers. Since 1989 he has been in the School of Physics and Astronomy at the University of Birmingham, responsible for the development of the PET and PEPT techniques. He is currently Director of the Positron Imaging Centre.

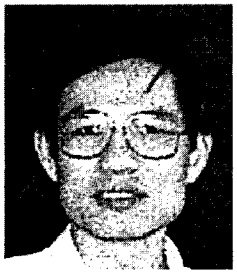

Y. Ding

Yulong Ding received his BSc. (1985) and MSc. (1988) from the University of Science and Technology Beijing (USTB), and his PhD (1997) from the University of Birmingham. He spent 6 years at the UTSB as a lecturer and 2 years at Imperial College of the University of London as a research associate. He is currently with the Solids Processing Group of the University of Birmingham. His research interests include fixed beds, moving beds, fluidisation, pure granular flows and heat transfer, sorption enhanced chemical reaction processes, solids processing, mathematical modelling and environmental engineering such as C02 abatement.

Granular Motion in a Rotary Kiln: the Transition from Avalanching to Rolling†

J.F. Davidson, D.M. Scott, P.A. Bird, O. Herbert, A.A. Powell and H.V.M. Ramsay
University of Cambridge,
*Department of Chemical Engineering**

Abstract

We report measurements of flow transitions, from avalanching to rolling, for granular material in rotary kilns. In the avalanching mode, the surface slips periodically; in the intervals between avalanches, all particles rotate with the kiln. In the rolling mode, the surface particles slide down continuously; the material underneath the surface rotates with the kiln.

Our measurements give Froude numbers ($R\omega^2/g$) for transitions, which are significantly different for sand and TiO_2 powder.

For the avalanching mode, we measured cycle times and deduced t_{12}, the avalanche time; t_{12} was also measured directly by video photography. For kilns of diameters 0.2–0.5 m, both methods give t_{12}, of order 1–2 sec and it appears to be proportional to $\sqrt{l}$, l being the chord length of the granular bed, the maximum distance of fall for avalanche material.

Simple theory, assuming the avalanche particles slide down a frictional surface, gives fair estimates of t_{12} and may be a basis for predicting avalanche-to-rolling transitions in large industrial kilns.

1. Introduction

A rotary kiln for processing granular material is usually a cylinder rotating slowly about its axis, inclined at a few degrees to the horizontal. Granular material is fed continuously at the top end of the cylinder. Within the cylinder, the material forms a bed which may occupy about one third of the cylinder volume. The bed surface is inclined to the horizontal at about the angle of repose for the granular material. A full-size industrial kiln is typically about 3 m diameter and 50 m long and rotates once in 5–10 minutes. At these slow rotation speeds, the flow regime of the granular material may be in one of two alternative modes, as follows.

(1) The bed may be in *"avalanching"* mode, otherwise described as *slumping*: for most of the time, the whole bed rotates at the same angular velocity, ω, as the kiln, thus undergoing *"solid body"* rotation. Then there is an avalanche, starting when the bed surface reaches the *static angle of repose* γ_s: during the avalanche, material from the upper part of the bed surface slides rapidly down; when the avalanche stops, the bed surface is inclined at a lesser angle γ_d, the *dynamic angle of repose*. Solid body rotation of the whole bed ensues, until the surface inclination again reaches angle γ_s, when avalanching occurs and the cycle is repeated.

(2) At higher kiln speeds, the motion of near-surface particles is continuous, the *"rolling"* mode. Most of the bed rotates with the kiln in *solid body* rotation, but the surface and near-surface particles fall continuously down the slope, whose inclination is approximately γ_d.

This paper is concerned with the transition from *avalanching* to *rolling*. In all cases centrifugal accelerations are small, i.e., the Froude number $Fr << 1$, where $Fr = R\omega^2/g$, R being the kiln radius and g the acceleration of gravity. The surface of the bed is essentially flat. The avalanching/rolling transition was addressed by Henein et al [1, 2] who proposed the Froude number as a suitable parameter to define the transition from avalanching to rolling. Their experiments showed that very low values of Fr, less than 10^{-5}, are consistent with avalanching. Then there is a transition region where $10^{-5} < Fr < 10^{-4}$; values of Fr above 10^{-4} are consistent with the rolling mode.

The use of Froude number is important for scale-up. If the transition from avalanching/slumping to rolling were uniquely described by Fr, then large

* Pembroke Street, Cambridge CB2 3RA, UK
† Received: August 8, 2000

kilns would have the transition at lower speeds than small kilns.

The work described here was a study of the transition from avalanching/slumping to rolling in drums of diameters 194, 288 and 500 mm, to test the effect of scale-up, albeit over a small range of R. Experiments were done with two granular materials, namely (i) sand in the size range 300−500 μm and (ii) titanium dioxide powder as discharged from a rotary kiln. The sand was chosen as a free-flowing granular material. The titanium dioxide powder represented the powder near the kiln discharge: it had a wide range of particle sizes, with a mean particle size of about 250 μm and a very wide size distribution with particle diameters up to about 10 mm; the powder was somewhat cohesive.

The results from observations of avalanching to rolling transitions for the three drum diameters and the two powders are presented in terms of Froude number.

There were also observations of cycle time for the avalanching mode, this being the time interval between one avalanche and the next, the form of the powder bed being identical at the beginning and end of each cycle: for example a cycle could be assumed to begin when the inclination of the powder bed is a maximum. Analysis of the relation between cycle time and rotation speed, ω, casts light on the mechanism of avalanching, particularly the time for an avalanche, which is finite. While this does not yet give a new criterion for scale-up, it suggests how an improved criterion might be developed.

2. Experimental

2.1 Apparatus

The experiments used a cylindrical steel drum of internal diameter 500 mm, length 300 mm, with a horizontal axis. The drum was flanged at one end: mounted on the flange was a flat vertical transparent Perspex plate, diameter 600 mm, so that the granular bed in the drum could be viewed from the front. This plate contained a small opening port, with a Perspex lid forming a flush internal face; the port was used to load powder into the drum and to unload. The other end of the drum was vertical steel plate, welded to the cylindrical part and connected to a shaft at the back: this shaft supported the drum and was driven by a variable speed motor with speed control and interchangeable gearbox. Thus the drum could be rotated at speeds from 0.1 to 6 revolutions per minute. The cylindrical part of the drum was lined with sandpaper.

To study the effects of varying drum diameter, two cylindrical Perspex inserts were made, of diameters 194 and 288 mm. Each was closed at the front end by a 600 mm diameter Perspex plate that replaced the above mentioned 600 mm diameter plate on the drum. The two cylindrical Perspex inserts were each closed at the back end to give a (length/diameter) ratio=3/5, as for the 500 mm drum, and the cylindrical parts were lined with sandpaper. When the drum operated with an inserted cylinder, the granular bed was contained entirely within the insert.

In this way, there were three alternative rotary drums of diameters 194, 288 and 500 mm with the capability of viewing the slumping or rolling granular bed through a transparent end plate.

2.2 Experiments: slumping/rolling observations

A number of experiments were performed to test the effect of the nature of the granular material and the percentage fill of the drum on the bed behaviour i.e., whether it was (i) slumping, (ii) transition or (iii) rolling. Sand of size range 300−500 μm and TiO_2 particles discharged from a kiln were used. These TiO_2 particles were in two forms namely (i) raw calciner discharge with a wide size range, up to 10 mm, or (ii) with the larger particles sieved out, so that there was still a wide size range, but up to 1 mm.

The following experiments were made with the objective of plotting bed behaviour diagrams, such as **Figures 1** and **2**, which were suggested by Henein et al. [1]. The steps in the experiments were as follows:

(1) An amount of granular material was introduced into the cylinder, which was then rotated to give a bed with a flat surface, albeit inclined. With the drum rotation stopped, the chord length of the surface was measured and from thence the percentage fill calculated; the percentage fill is the ratio (area of the crescent-shaped cross section of the bed)/πR^2.

(2) With the drum rotating steadily, the angular speed was measured by timing one revolution. The bed behaviour was classified as slumping, transitional or rolling, using the following definitions:

(i) In the *slumping* or *avalanching* mode, there was a clearly cyclical motion: over a distinct period, the whole bed rotated with the drum, in solid body rotation; then there was an avalanche. The times for these separate parts of the cycle were the subject of further measurements, see below.

(ii) In the *rolling* mode, the surface layer of particles moved down continuously. Below this surface layer, which was only a few millimetres thick, the

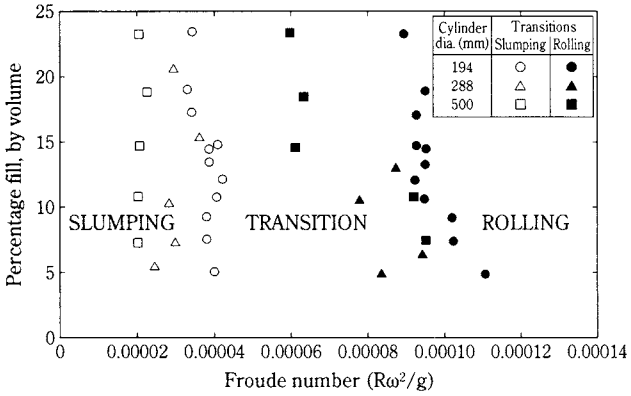

Fig. 1 Bed behaviour diagram: transition from slumping (avalanching) to rolling for sand

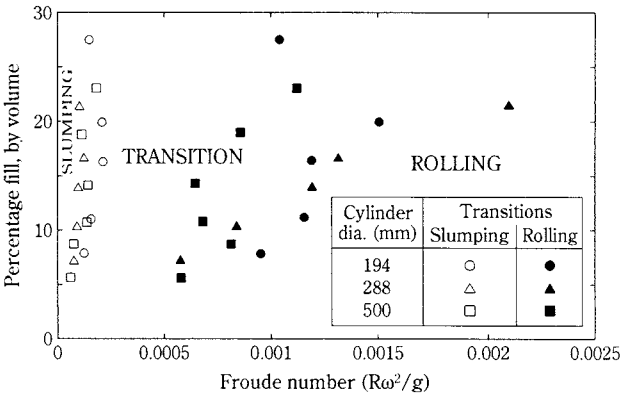

Fig. 2 Bed behaviour diagram: transitions from slumping and to rolling for raw TiO_2

main part of the bed moved with the drum, in solid body rotation.

(iii) There was a rather ill-defined *transition region*, in which some parts of the surface were falling continuously: other parts were subject to cyclical motion. As will be evident from the results, the transitional region included an appreciable range of drum speeds.

2.3 Experiments: cycle time in the slumping mode

With the drum speed slow enough to give well-defined slumping, the cycle time was measured for a range of drum speeds, for each of the three drum diameters. Two methods of observation were used, as follows.

(i) The time for ten slump cycles was recorded. This measurement was repeated nine times, so there were ten recordings of the time for ten slump cycles. The drum rotation speed was measured by simply timing a revolution. These observations gave the total cycle time t_{13}. From analysis of these results, given below, the duration of the avalanche, t_{12}, could be deduced.

(ii) Direct measurements of the avalanche duration, t_{12}, were obtained from video pictures of the cyclical motion. The video camera was set up to observe the granular bed through the transparent front wall of the drum. The video picture included a digital stopwatch. The video was played back at a low framing rate: the tape was stopped at the beginning and end of an avalanche; from the stopwatch readings, the time t_{12} for the avalanche was obtained. The kiln speed and the chord length of the particle bed were measured as before, giving the percentage fill. For each speed/percentage fill combination, the video photography and analysis were repeated five times, to give an average value of t_{12}.

3. Results and discussion

3.1 Bed behaviour diagrams: Froude number as a scaling parameter

Henein et al. [1] used the *bed behaviour diagram*, plotting either bed depth or percentage fill against Froude number, Fr, and delineating areas of the diagram as *slumping, transition* or *rolling*. **Figures 1** and **2** show our data plotted in this form as percentage fill against Fr, the plotting points indicating transitions, measured in the way described above.

Figures 1 and **2** show bed behaviour diagrams for our data, respectively for sand and raw TiO_2 calciner discharge. For sand, **Figure 1**, it appears that the slumping/transition boundary is in the region $0.00002 < Fr < 0.00004$; the transition to rolling is less well defined, in the region $0.00006 < Fr < 0.0001$. **Figure 2** shows the results for raw TiO_2 calciner discharge: here the slumping/transition boundary is in the region $0.0001 < Fr < 0.0002$; the transition to rolling is in the region $0.0006 < Fr < 0.0015$.

From these results, the following conclusions may be drawn:

(1) The Froude number gives a rough guide to transitions in the flow regimes. But the transition Froude numbers are markedly different between sand and raw TiO_2. Thus the boundary for slumping is about five times higher for TiO_2 as compared with sand; the boundary for transition to rolling is about ten times higher for TiO_2 as compared with sand.

(2) With regard to the effect of drum diameter, the data in **Figure 1** show that the Froude numbers for

the two transitions tend to increase as the drum diameter decreases; the same effect is approximately true of the data in **Figure 2**.

The overall conclusion is that although the Froude number is a very rough guide to behaviour, there is certainly not a unique Froude number for each of the two observed transitions. There must therefore be grave doubts about the use of these transition Froude numbers for industrial sized rotary kilns.

With this in mind, the measurements of cycle times in the slumping mode were undertaken, with the objective of understanding the mechanism of the slumping/avalanching mode.

3.2 Cycle time results and analysis

Figure 3 shows the sequence observed at slow rotation speeds with clearly defined avalanching or slumping giving a sequence of bed states 1, 2 and 3 shown in the diagram. An avalanche starts at state 1, when the bed surface is at maximum angle γ_s (degrees), the static angle of repose. Then a finite quantity of granular material slides down the surface. At time t_{12}, the avalanching material comes to rest, relative to the drum, when the inclination of the bed surface is γ_d (degrees), the dynamic angle of repose; this is condition 2 in **Figure 3**. Between conditions 2 and 3, the granular bed rotates with the drum in *solid body* motion at angular velocity ω. At condition 3, the bed is in the same state as at 1. Subsequently the cycle repeats itself, with a cycle time t_{13}, measured in the experiments.

As the angular speed, ω, varies, it is assumed that the avalanche time t_{12} is constant, plausible because t_{12} is usually much less than t_{13}, so the drum rotation during time t_{12} is small. During the 2–3 sequence, there is solid body rotation, so it follows that $\gamma_s-\gamma_d=\omega(t_{13}-t_{12})180/\pi$ and hence

$$t_{13}=t_{12}+(\gamma_s-\gamma_d)\,\pi/180\omega \qquad (1)$$

Figures 4, **5** and **6** show our data for sand, plotted as t_{13} against $1/\omega$: from equation (1), this should be a linear relationship for a given powder-in-drum combination. Each of **Figures 4**, **5** and **6** does indicate a linear relationship between t_{13} and $1/\omega$; extrapolation to $1/\omega=0$ gives values of t_{12}, the avalanche time, shown in **Table 1**. This analysis neglects the change in path length of the avalanche, TB in **Figure 3**, as

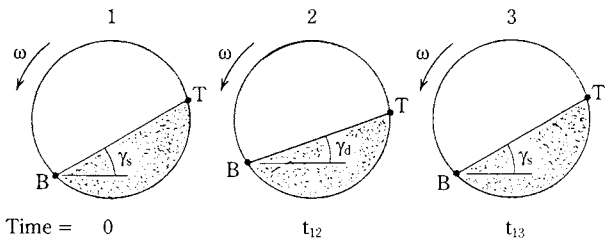

Fig. 3 Cyclical slumping or avalanching
(1) Start of slump at angle γ_s
(2) End of slumping at angle γ_d
(3) Start of next slump at angle γ_s

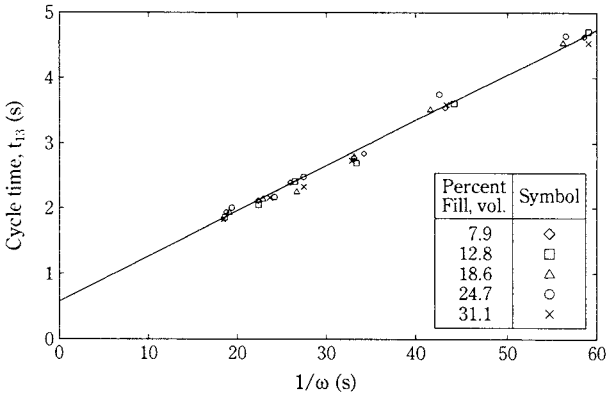

Fig. 4 Slump cycle time against 1/(angular speed) for sand in 194 mm dia. drum

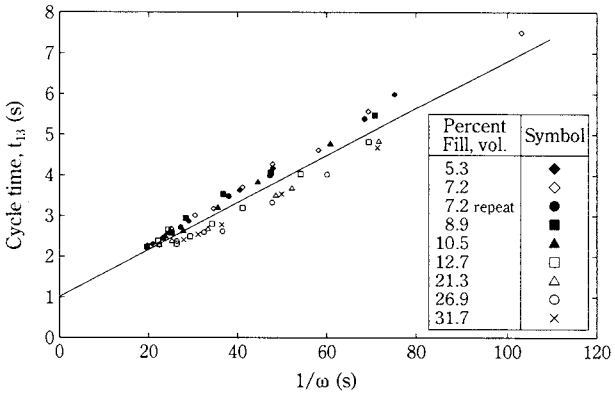

Fig. 5 Slump cycle time against 1/(angular speed) for sand in 288 mm dia. drum

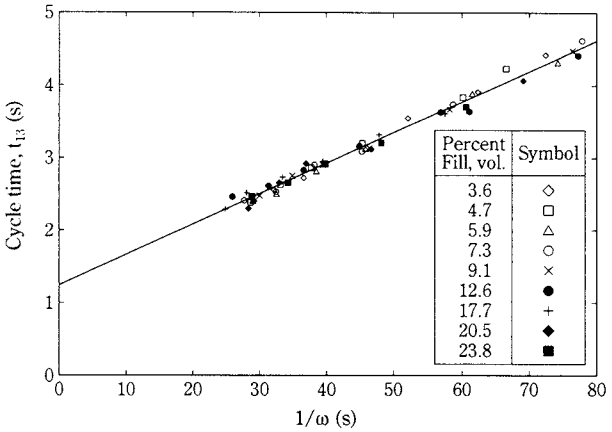

Fig. 6 Slump cycle time against 1/(angular speed) for sand in 500 mm dia. drum

Table 1 Avalanche times t_{12} for sand from Figures 4–6 on the basis of Equation (1)

Figure Number	Drum diameter (mm)	Avalanche time t_{12} (sec)	$\frac{180}{\pi} \times \text{slope} = \gamma_s - \gamma_d$ (degrees)
4	194	0.6	3.9
5	288	1.0	3.4
6	500	1.2	2.4

the percentage fill changes. The effect of path length, TB, on avalanche time t_{12} is considered further in Section 3.3 below.

Table 1 also shows the slope of the best fit line in each diagram, **Figures 4**, **5** and **6**. From equation (1) the slope should be $(\gamma_s-\gamma_d)\pi/180$, the difference between static and dynamic angles of repose. There appears to be a size effect, $(\gamma_s-\gamma_d)$ diminishing as drum size increases. The bed inclinations (i) just before an avalanche and (ii) just after an avalanche, were measured for sand by Powell and Ramsay [5, 6], using photography. Their results suggested $\gamma_s=33°$ and $\gamma_d=30°$: thus $\gamma_s-\gamma_d=3°$, in good agreement with **Table 1**.

Figure 7 shows the corresponding data for TiO_2, both the raw calciner discharge (sizes up to 10 mm) and the calciner discharge with large particles sieved out, leaving sizes up to 1 mm. The data are much more scattered than for sand, but t_{13} is still roughly linear against $1/\omega$, and the deduced values of avalanche time $t_{12}=1-2$ sec, are of the same order as with sand. The slopes of the two fitted lines are: (i) 7.2° for raw TiO_2 and (ii) 5.0° for sieved TiO_2. These angles, representing $(\gamma_s-\gamma_d)$ the difference between static and dynamic angles of repose, are greater than the values for sand, given in **Table 1**. The higher values of $\gamma_s-\gamma_d$ for TiO_2 are entirely plausible, the TiO_2 powder being somewhat cohesive.

Henein *et al.* [1] report experimental measurements of slumping frequency N (min^{-1}) against kiln rotation speed, n, in revolutions per minute (rpm) for two drum sizes and a variety of granular materials. Their most complete data set, for limestone particles, is shown in **Figure 8**. Now $1/t_{13}$ is the slumping frequency, and $\omega=2\pi n/60$ so equation (1) can be transformed, with appropriate conversion of units, to give

$$N = 60/[t_{12}+(\gamma_s-\gamma_d)/6n] \qquad (2)$$

Curve fitting of Equation (2) to the data in **Figure 8** gives values of $(\gamma_s-\gamma_d)$ and t_{12}: the value of $(\gamma_s-\gamma_d)$ is obtained from the slope at the origin, because $dN/dn=360/(\gamma_s-\gamma_d)$ at $n=0$ and t_{12} is obtained by curve fitting at finite n. This procedure gives $\gamma_s-\gamma_d=6$ degrees for both kiln diameters, and $t_{12}=1.13$ sec for

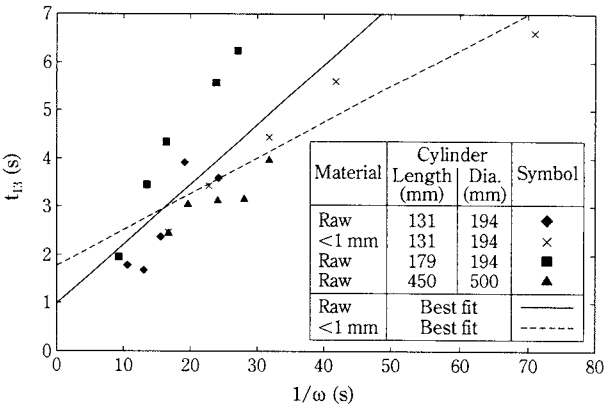

Fig. 7 Slump cycle time against 1/(angular speed) for Titanium Dioxide powder of wide size range

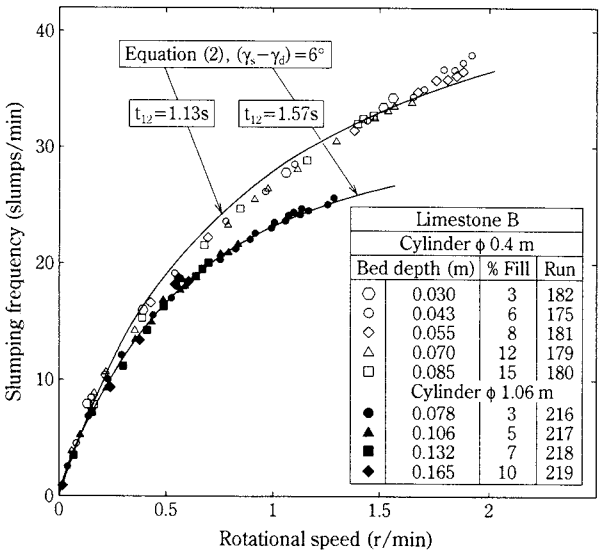

Fig. 8 Slumping frequency data of Henein et al [1]. The curves are from Equation (2) with $(\gamma_s-\gamma_d)$ and t_{12} chosen to give best fit to the data.

kiln diameter D=0.4 m and $t_{12}=1.57$ sec for D=1.06 m. These parameters were used to give the plots of Equation (2) shown in **Figure 8**: the curves are in remarkably good agreement with the data. Henein et al. [1] report values of static and dynamic angle of repose: for the limestone of **Figure 8** they give $\gamma_s=40.3°$ and $\gamma_d=39.6°$ or 36.5°, so their values of $\gamma_s-\gamma_d$ range from 0.7° to 3.8°. However, their values of γ_d were for rolling motion in the kiln, whereas ours are values of γ_d at the end of an avalanche, likely to be smaller than the value of γ_d for continuous rolling motion.

3.3 Avalanche times t_{12}

Bird [3] and Herbert [4] plotted their data for sand as in **Figures 4–6**. For each drum diameter, they fitted a straight line to the data; by extrapolation to

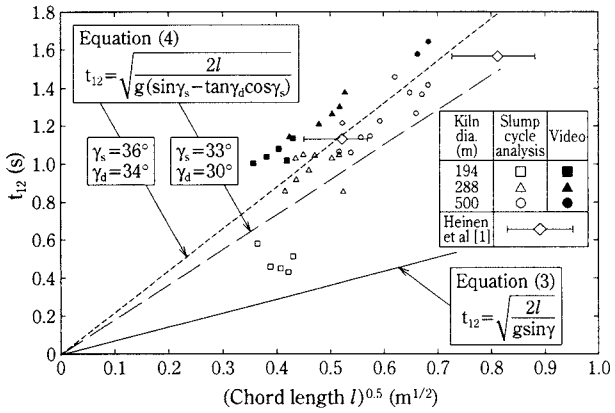

Fig. 9 Avalanche duration t_{12} against (chord length l)$^{1/2}$ for sand. The chord length l is the maximum length of travel for avalanche particles.

$1/\omega=0$, they obtained values of avalanche time t_{12}, plotted in **Figure 9** as the open points. The solid points are from their direct measurements of avalanche times, using video photography as described above. The chord length, l, is the length TB shown in **Figure 3**, the distance from the top to the bottom of the particle bed.

Also shown in **Figure 9** are data points from fitting Equation (2) to the data of Henein *et al.* [1] in **Figure 8**. These data are for a range of values of l, the chord length; hence a range of values of $\sqrt{l}$ is shown for each of Henein *et al's* data points in **Figure 9**. Bearing in mind the differences of granular material, Henein *et al's* [1] results agree remarkably well with ours.

The reason for plotting t_{12} against $\sqrt{l}$ is for comparison with the time taken for a single particle to slide down a smooth surface of length l. The slope being γ, it is readily shown that with no friction,

$$t_{12}=(2l/g\sin\gamma)^{1/2} \qquad (3)$$

Figure 9 shows a plot of Equation (3), with $\gamma=34°$, from which it is clear that the avalanche times are much greater than the time for free fall down a slope of length l.

An alternative is to consider a single particle sliding down a slope with surface friction. Assume that the inclination of the slope is γ_s: the normal force between the slope and the particle, per unit mass, is $g\cos\gamma_s$. We assume the friction coefficient, between the particle and the slope, to be $\tan\gamma_d$; the dynamic friction is relevant because the particle is in motion. The frictional force on the particle, parallel to the slope, is thus $g\tan\gamma_d\cos\gamma_s$: this acts against the gravity component $g\sin\gamma_s$, so the net force causing acceleration is $g(\sin\gamma_s-\tan\gamma_d\cos\gamma_s)$ in place of $g\sin\gamma$ in deriving Equation (3). It follows that the flight time, with friction, is

$$t_{12}=[2l/g(\sin\gamma_s-\tan\gamma_d\cos\gamma_s)]^{1/2} \qquad (4)$$

Bird [3] and Herbert [4] used, for sand, $\gamma_s=36°$ and $\gamma_d=34°$, giving the line plotted in **Figure 9**, in fair agreement with most of the data. However, Powell [5] and Ramsay [6] give $\gamma_s=33°$, $\gamma_d=30°$ from video measurements, so $\gamma_s-\gamma_d=3°$, in fair agreement with the results in **Table 1**. **Figure 9** shows a plot of Equation (4), using Powell and Ramsay's values of γ_s and γ_d.

In spite of the fair agreement between Equation (4) and the data in **Figure 9**, there must be reservations about its validity for scale-up, as follows:

(1) The range of values of $\sqrt{l}$ in **Figure 9** is small. Data are needed for much larger cylinders.
(2) There is the unexplained difference between the data in **Figure 9** from the video records compared with the data from **Figures 4–6**.
(3) Attempts to plot t_{12} against $\sqrt{l}$ for TiO_2, from **Figure 7**, gave very wide scatter, although the values of t_{12} were of the same order as those in **Figure 8**.

4. Conclusions

1. The Froude number $Fr=R\omega^2/g$, provides a rough guide to flow regime transitions in a rotary kiln. But the Froude numbers for transition vary from one granular material to another. Our results for kiln diameters from 194 to 500 mm show
   (i) For sand, there is avalanching (otherwise described as slumping) for $Fr<0.00002-0.00004$, and rolling for $Fr>0.00006-0.0001$.
   (ii) For TiO_2 powder, calciner discharge with a wide size range, the corresponding values are: avalanching for $Fr<0.0001-0.0002$; rolling for $Fr>0.0006-0.0015$.
2. It is by no means certain that these transition Froude numbers are independent of kiln diameter. Hence the transitions for large industrial kilns may be at very different Froude numbers.
3. For the avalanching mode, the granular material moves cyclically: the bed rotates with the kiln in solid body motion till its surface reaches a maximum inclination, the static angle of repose γ_s. Then there is an avalanche, of duration t_{12}: when the avalanche terminates, the inclination is γ_d, the dynamic angle of repose. The avalanche time was measured in two ways.
   (i) Measuring the total cycle time t_{13} and plotting it against 1/(rotation speed ω) gave, by extrapolation to $1/\omega=0$, values of t_{12}; these are of order 1–2 sec for our cylinders, 198–500 mm

dia.

(iii) Video photography gave direct measurements of t_{12}.

The values of t_{12} from method (i) are somewhat lower than from method (ii).

4. The avalanche time t_{12} is approximately proportional to $\sqrt{l}$; here l is the chord length of the sloping granular bed, the maximum length of fall for avalanche material. The times t_{12} are much greater than the time for a particle to fall down a smooth slope of length l. But t_{12} is reasonably well predicted by theory for a particle falling down a frictional slope of inclination γ_s, the static angle of repose: between the falling particle and the slope, the coefficient of friction is $\tan\gamma_d$, γ_d being the dynamic angle of repose. The results suggest that for sand, the values are: $\gamma_s=36°$ with $\gamma_d=34°$, or $\gamma_s=33°$ with $\gamma_d=30°$.
5. The cycle time analysis suggests that for sand, $(\gamma_s-\gamma_d)$ is between 2.4 and 3.9°; for TiO_2 particles $(\gamma_s-\gamma_d)$ is about 5°−7°; for Henein *et al's* [1] limestone B, $(\gamma_s-\gamma_d)$ is about 6°.
6. The analysis of cycle times and the mechanism of avalanching may lead to an improved scale-up method for predicting flow regimes in large kilns.

Acknowledgement

The authors are grateful to Huntsman Tioxide for loan of the apparatus for this work and for constructive discussions.

Nomenclature

D	: Kiln diameter	(m)
Fr	: Froude number=$R\omega^2/g$	
g	: Acceleration due to gravity	(m/s^2)
l	: Chord length of granular bed	(m)
R	: Kiln radius	(m)
N	: Slumping frequency	(min^{-1})
n	: Kiln revolutions per minute	(min^{-1})
t_{12}	: Avalanche time	(sec)
t_{13}	: Complete cycle time for avalanching bed	(sec)
t_{23}	: Duration of solid body rotation	(sec)
γ	: Angle of repose for granular material	(degrees)
γ_d	: Dynamic angle of repose	(degrees)
γ_s	: Static angle of repose	(degrees)
ω	: Angular speed of kiln rotation	(rad/sec)

References

1) Henein, H., J.K. Brimacombe and A.P. Watkinson. Experimental Study of Transverse Bed Motion in Rotary Kilns. Metallurgical Transactions **14B**, 191-205 (1983).
2) Henein, H., J.K. Brimacombe and A.P. Watkinson. The Modeling of Transverse Solids Motion in Rotary Kilns. Metallurgical Transactions **14B**, 207-219 (1983).
3) Bird, P.A. Particle Dynamics in Rotary Cylinders. Research Project Report for the Chemical Engineering Tripos, Part II, Cambridge (1996).
4) Herbert, O. Particle Dynamics in a Rotary Cylinder. Research Project Report for the Chemical Engineering Tripos, Part II, Cambridge (1996).
5) Powell, A.A. Particle Dynamics in Rotary Kilns. Research Project Report for the Chemical Engineering Tripos, Part II, Cambridge (1997).
6) Ramsay, H.V.M. A Study of Particle Dynamics in Rotary Kilns. Research Project Report for the Chemical Engineering Tripos, Part II, Cambridge (1997).

The Chemical Engineering Tripos Part II is the final examination of the four year course. The Project Reports are available in the Library of the Department of Chemical Engineering.

Authors' short biography

J.F. Davidson

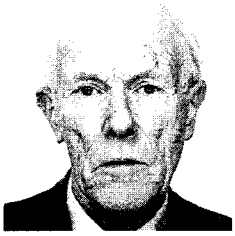

John Davidson was a Faculty Member in the Department of Chemical Engineering, Cambridge, from 1952 until he retired in 1993; he was Head of Department 1975–1993.
Since 1993 he has worked in the Department on research, in collaboration with other Faculty Members, helping to supervise students working for the PhD degree and students undertaking research projects during the final year of the MEng degree course. The paper here given is the outcome of two such final year projects.

D.M. Scott

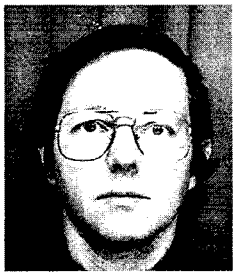

David Scott has been a Faculty Member in the Department of Chemical Engineering, Cambridge, from 1983. He received his B.A. in Mathematics in 1970 and Ph.D. in Theoretical Physics in 1974, both from the University of Cambridge. From 1974 to 1983 he carried out research in Theoretical Physics at the Rutherford Laboratory, the University of Wisconsin-Madison, and in Cambridge. His research interests include granular materials, adsorption and fluid mechanics.

Paul Bird, Oliver Herbert, Andrew Powell and **Helen Ramsay** were students whose project work for the MEng course in Cambridge is reported here. Their work follows a long tradition in the Department: 40 years of research on fluidization began with MEng projects involving limited funding and no forward planning.

Particle Adhesion Fundamentals and Bulk Powder Consolidation†

Jürgen Tomas
*The Otto-von-Guericke-University Magdeburg, Mechanical Process Engineering**

Abstract

The fundamentals of particulate solids consolidation and flow behaviour using a reasonable combination of particle and continuum mechanics are explained. By means of the model "stiff particles with soft contacts" the combined influence of elastic, plastic and viscoplastic repulsion in particle contacts is derived. Consequently, contact normal force displacement $F_N(h_K)$ and adhesion force models $F_H(F_N)$ are presented to describe the stationary, instantaneous and time consolidation behaviour in particle contacts as well as in the bulk. On this particle mechanical basis, the stationary, instantaneous and time yield loci as well as uniaxial compressive strength $\sigma_c(\sigma_1)$, effective angle of internal friction $\varphi_e(\sigma_1)$, bulk density $\rho_b(\sigma_1)$ are derived and shown for a very cohesive sub-micron titania powder. Finally, these models in combination with accurate shear cell test results are used as constitutive functions for computer aided silo design for reliable flow and pressure calculations.

1. Introduction

The well-known flow problems of cohesive particulate solids in storage and transportation containers, conveyors or process apparatuses leads to bridging, channelling, oscillating mass flow rates and particle characteristics with feeding and dosing problems as well as undesired effects like widely spread residence time distribution, fertiliser time consolidation process or caking, chemical conversions, food deterioration and finally insufficient element and system reliability of solid processing plants. Taking into account this list of selected technical problems and hazards, it is really necessary to deal with the fundamentals of particulate solids consolidation and flow behaviour, namely from using a reasonable combination of particle and continuum mechanics.

2. Particle Contact Constitutive Model

The well-known failure hypotheses of Tresca, Coulomb-Mohr (3) and the yield locus concept of Jenike (1, 2) and Schwedes (4, 5) as well as the Warren-Spring-Equations (6) to (10) were specified from Molerus (11 to 14) by the cohesive steady-state flow criterion. The consolidation and non-rapid flow of fine and cohesive particulate solids (size $d<100$ µm, flow or deformation rate $v<1$ m/s, therefore shear stress $\tau_v<\rho\cdot v^2/2\approx 1$ kPa, pressure $\sigma\approx 0.1-100$ kPa) was explained by acting adhesion forces in particle contacts, Molerus (11).

On principle, there are four essential mechanical deformation effects in particle surface contacts and their physical behaviour – influenced namely by mechanical, optical and electromagnetic material characteristics of bulk phase – can be distinguished as follows:

(1) reversible elastic (Hertz (15), Huber (16), Mindlin (17), Dahneke (19), DMT theory from Derjagin et al. (20) and JKR theory from Johnson et al. (21, 22), Thornton (27)) without deformation rate and consolidation time effects, valid for all particulate solids;
(2) irreversible plastic (Krupp (18), Schubert (23), Molerus theory (11, 12), Maugis (26) and Thornton (28)), deformation rate and consolidation time invariant, e.g. mineral powders;
(3) reversible viscoelastic (Hsuin (24) and Rumpf et al. (25)), deformation rate and consolidation time variable, e.g. cut post-consumer waste particles;
(4) irreversible viscoplastic (Rumpf et al. (25)), deformation rate and consolidation time variable, e.g. fine particle fusion.

If an external compressive normal force F_N is acting on a *soft contact* of two isotropic, *stiff*, linear elastic, mono-disperse spherical particles the previous contact point is deformed to a contact area and the adhesion force between these two partners is increasing, see **Fig. 1**.

* Universitätsplatz 2, D-39106 Magdeburg, Germany, Phone: ++49 391 67 18783, Fax: ++49 391 67 11160, e-mail: juergen.tomas@vst.uni-magdeburg.de
† Received: November 9, 2000

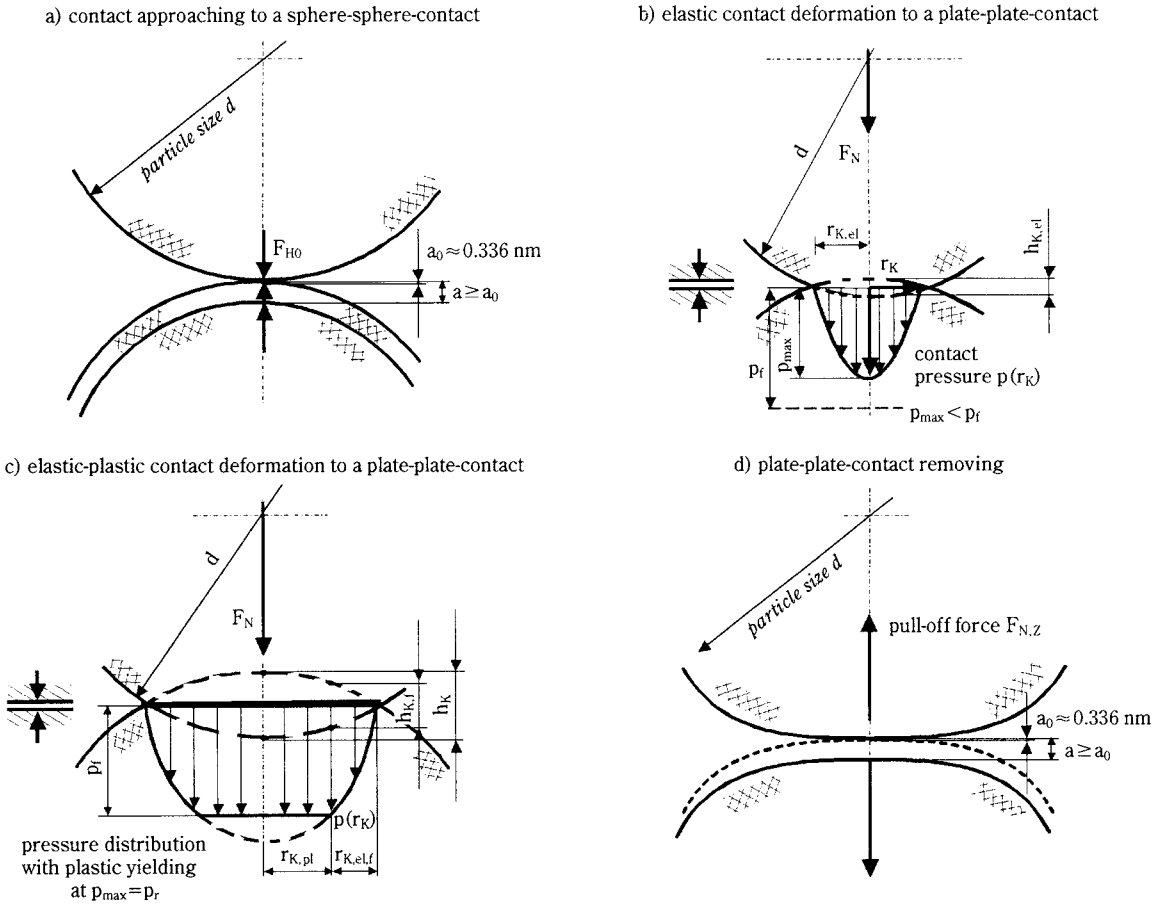

Fig. 1 Particle contact approaching, elastic, elastic-plastic deformation and removing

First of all, Rumpf et al. (25) have developed a constitutive model approach for describing the linear increasing of adhesion force F_H, mainly for plastic contact deformation:

$$F_H = \left(1 + \frac{p_{VdW}}{p_f}\right) \cdot F_{H0} + \frac{p_{VdW}}{p_f} \cdot F_N \qquad (1)$$

With another prerequisite and derivation Molerus (12) obtained an equivalent formula:

$$F_H = F_{H0} + \frac{p_{VdW}}{p_f} \cdot F_N = F_{H0} + \kappa_p \cdot F_N \qquad (2)$$

The adhesion force F_{H0} without additional consolidation ($F_N = 0$) can be approached as a single sphere-sphere-contact, see **Fig. 1a)**. This soft particle contact is flattening by the external normal force F_N to a plate-plate-contact, **Fig. 1c)**. The coefficient κ_p describes a dimensionless ratio of attractive Van Der Waals pressure p_{VdW} for a plate-plate model to repulsive particle micro-hardness p_f (resistance against plastic deformation)

$$\kappa_p = \frac{p_{VdW}}{p_f} = \frac{C_{H,sls}}{6 \cdot \pi \cdot a_{F=0}^3 \cdot p_f} \qquad (3)$$

and is to be called here as a plastic repulsion coefficient. The characteristic adhesion separation distance lies in a molecular scale (atomic centre to centre distance) and amounts to about $a = a_{F=0} \approx 0.3 - 0.4$ nm. It depends mainly on the properties of liquid-equivalent packed adsorbed layers and can be estimated for a molecular force equilibrium or interaction potential minimum $-dU/da = F = 0 = F_{attraction} + F_{repulsion}$. The Hamaker constant solid-liquid-solid $C_{H,sls}$ acc. to Lifschitz theory is related to continuous media, dependent on their permittivities (dielectric constants) and refractive indices, see Israelachvili (29).

If the contact radius r is small compared with the particle size d, an elliptic pressure distribution $p_{el}(r)$ is found, see Hertz (15). Schubert (23) has combined the elastic and plastic contact strain expressed with the annular elastic A_{el} and circular plastic A_{pl} contact area:

$$F_H = F_{H0} + \frac{p_{VdW}}{p_f \cdot (1 + 2 \cdot A_{el}/(3 \cdot A_{pl}))} \cdot F_N \qquad (4)$$

Taking into account these Eqs. (1), (2), (4) as well as the model from Thornton (28) and superposition pro-

vided, the particle contact force equilibrium between attraction (−) and elastic as well as plastic repulsion or force response (+)

$$\sum F = 0 = -F_{H0} - p_{VdW} \cdot \pi \cdot r_C^2 - F_N + p_f \cdot \pi \cdot r_{pl}^2 + 2 \cdot \pi \cdot \int_{r_{pl}}^{r_C} p_{el}(r) \cdot r \, dr \quad (5)$$

delivers a very useful linear force displacement model for $\kappa_A \approx$ const. with the particle centre approach of both partners h_K (32), **Fig. 2**:

$$F_N + F_{H0} = \frac{\pi}{4} \cdot d \cdot p_f \cdot [\kappa_A - \kappa_p] \cdot h_K \quad (6)$$

Thus, the contact stiffness decreases with smaller size especially for cohesive fine powders and nanoparticles, predominant plastic yielding behaviour provided (32):

$$k_{N,pl} = \frac{dF_N}{dh_K} = \frac{\pi}{4} \cdot d \cdot p_f \cdot (\kappa_A - \kappa_p) \quad (7)$$

But if we consider Eq.(9) a slightly nonlinear (progressively increasing) curve is obtained.

The dominant linear elastic-plastic deformation range between really tested yield loci levels YL1 to YL 4 is to be demonstrated in **Fig. 2**. The origin of this diagram $h_K=0$ is equivalent to the characteristic adhesion separation for a direct contact (atomic centre to centre distance) and can be estimated for a molecular force equilibrium $a=a_0=a_{F=0}$. Provided that these molecular contacts are stiff enough compared with the *soft mesoscopic particle contact behaviour* influenced by mobile adsorption layers due to molecular rearrangement, this separation $a_{F=0}$ is assumed to be constant during loading and unloading in the interesting macroscopic pressure range of $\sigma=0.1-100$ kPa. After loading 0−Y the contact is elastically compacted with an approximated circular contact area, see **Fig. 1b)** and starts at the yield point Y at $p_{max}=p_f$

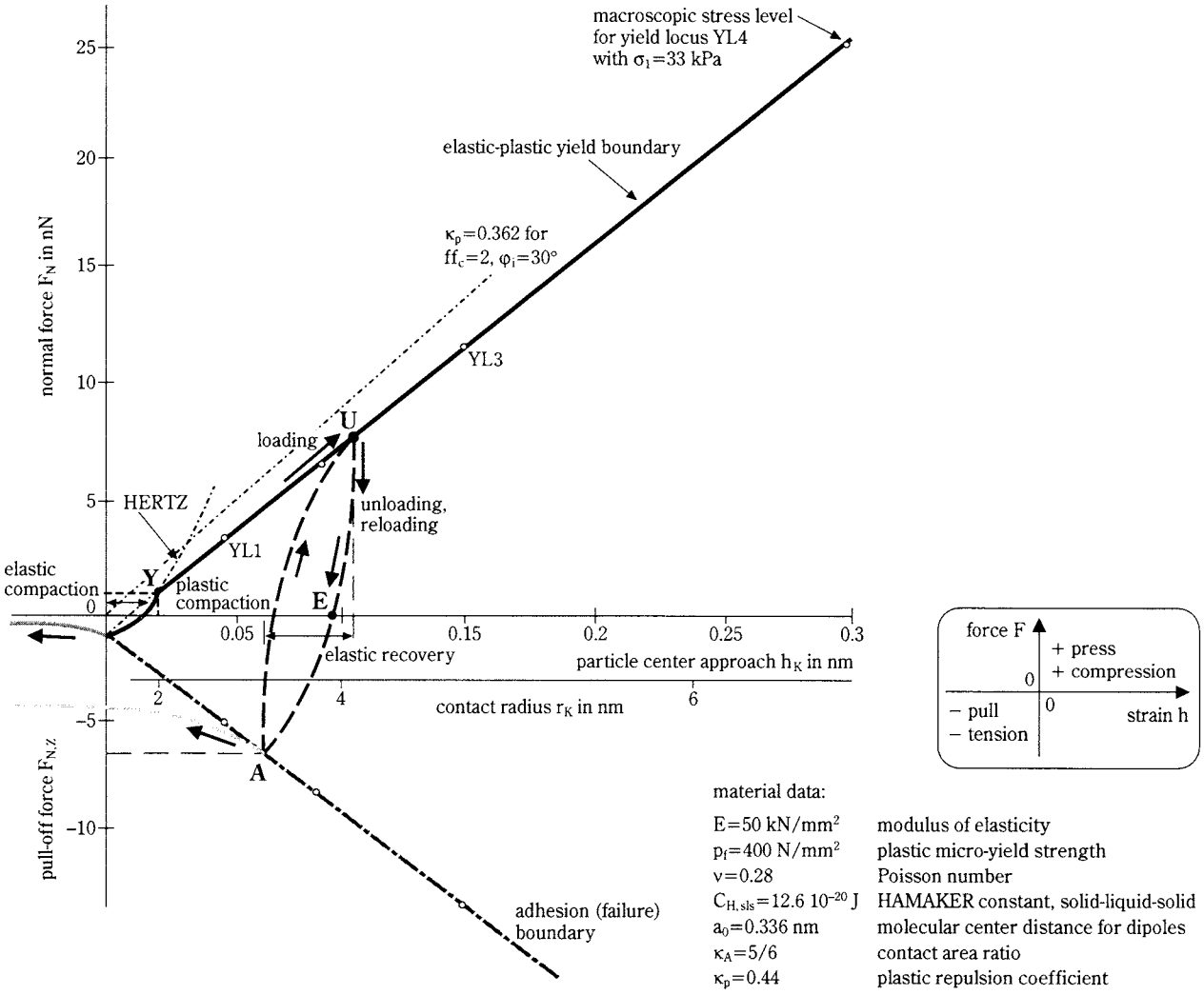

Fig. 2 Recalculated characteristic contact deformation acc. to Fig. 1 of very cohesive titania particles, median particle size $d_{50,3}=610$ nm, moisture $X_W=0.4\%$.

with plastic yielding, see **Fig. 1c)**. Now, the combined elastic-plastic yield boundary of the plate-plate contact is achieved, see Eq.(6). This displacement is to be expressed with the annular elastic A_{el} (thickness $r_{K,el}$) and circular plastic A_{pl} (radius $r_{K,pl}$) contact area, see **Fig. 1c)**. For comparison, a dashed line for the flowability limit $ff_c=2$ (very cohesive acc. to Jenike (2)) is plotted additionally (32), see **Fig. 2**. After unloading U−E the contact recovers elastically in the compression mode and remains with an perfect plastic displacement $h_{K,E}$. Below point E left the tension mode begins. Between U−E−A the contact recovers probably elastically along a supplemented Hertzian parabolic curvature up to a displacement $h_{K,A}$. Along A−U the contact could be reloaded. If we apply a certain pull-off force $F_{N,Z}=-F_{H,A}$, here negative, the adhesion (failure) boundary at point A is reached and the contact plates are failing and removing with the increasing distance $a=a_{F=0}+h_{K,A}-h_K$. This actual particle separation is to be considered for the calculation by means of a hyperbolic adhesion force curve $F_{N,Z}=-F_{H,A}\propto a^{-3}$ with the plate-plate model, see Eq.(3). These new models in **Fig. 2** follow Molerus' (11), Schubert's (23), Maugis' (26) and especially Thornton's (28) example.

The slopes of plastic curves are a measure of irreversible particle contact stiffness or softness, resp. Thus the dimensionless contact consolidation coefficient (strain characteristic) κ is read here as the slope of adhesion force, **Fig. 3**, influenced by predominant plastic contact failure.

$$\kappa=\frac{\kappa_p}{\kappa_A-\kappa_p} \tag{8}$$

The elastic-plastic contact area coefficient κ_A represents the ratio of plastic particle contact deformation area A_{pl} to total contact deformation area $A_K=A_{pl}+A_{el}$

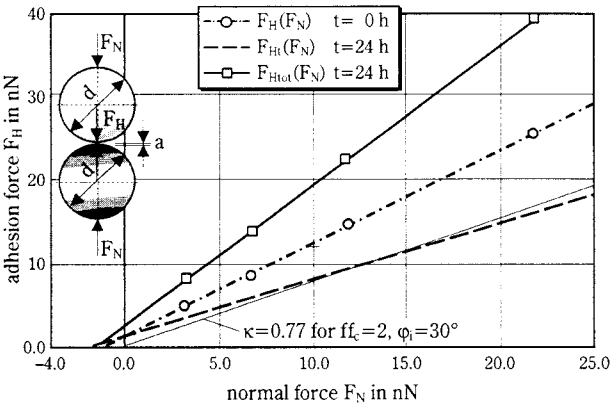

Fig. 3 Recalculated variable particle adhesion force of titania acc. to, median particle size $d_{50}=0.61$ µm, moisture $X_W=0.4\%$ accurately analysed with Karl Fischer titration

including a certain elastic displacement (32)

$$\kappa_A=\frac{2}{3}+\frac{1}{3}\cdot\frac{A_{pl}}{A_K}=1-\frac{1}{3}\cdot\sqrt[3]{\frac{h_{K,f}}{h_K}}, \tag{9}$$

with the centre approach $h_{K,f}$ for incipient yielding at $p_{el}(r=0)=p_{max}=p_f$:

$$h_{K,f}=d\cdot\left(\frac{\pi\cdot p_f}{2\cdot E^*}\right)^2 \tag{10}$$

The pure elastic contact deformation $A_{pl}=0$, $\kappa_A=2/3$, has no relevance for fine cohesive particles and should be excluded here. Commonly, for pure plastic contact deformation $A_{el}=0$ or $A_K=A_{pl}$, $\kappa_A=1$ is obtained. From Eq.(5), a linear model for the adhesion force F_H as function of normal force F_N is obtained again (32):

$$F_H=\frac{\kappa_A}{\kappa_A-\kappa_p}\cdot F_{H0}+\frac{\kappa_p}{\kappa_A-\kappa_p}\cdot F_N=(1+\kappa)\cdot F_{H0}+\kappa\cdot F_N \tag{11}$$

The contact consolidation coefficient κ is a measure of irreversible particle contact stiffness or softness as well, see **Fig. 3**. A small slope stands for low adhesion level $F_H\approx F_{H0}$ because of stiff particle contacts, but a large inclination means soft contacts or consequently, a cohesive powder flow behaviour, see **Fig. 6** as well.

This model considers additionally the flattening of soft particle contacts caused by acting an adhesion force $\kappa\cdot F_{H0}$. Herewith, the adhesion force F_{H0} for $F_N=0$ considers an essential characteristic micro roughness height $h_r<d$ particle size (Schubert (30)):

$$F_{H0}=\frac{C_{H,sls}\cdot(2\cdot h_r)}{24\cdot a_{F=0}^2}\cdot\left[1+\frac{d/h_r}{2\cdot(1+h_r/a_{F=0})^2}\right]\approx\frac{C_{H,sls}\cdot h_r}{12\cdot a_{F=0}^2} \tag{12}$$

The intersection of function (11) with abscissa ($F_H=0$) in the negative extension range of consolidation force F_N, **Fig. 3**, is surprisingly independent of the Hamaker constant $C_{H,sls}$:

$$F_{N,Z}=-\frac{\pi}{2}\cdot a_{F=0}\cdot h_r\cdot p_f\cdot\kappa_A\cdot\left[1+\frac{d/h_r}{2\cdot(1+h_r/a_{F=0})^2}\right]$$

$$\approx-\frac{\pi}{2}\cdot a_{F=0}\cdot h_r\cdot p_f \tag{13}$$

Considering the model prerequisites for cohesive powders, this minimum normal (tensile) force limit $F_{N,Z}$ combines the influences of a particle contact hardness or micro-yield strength $p_f\approx3\cdot\sigma_f$ (σ_f yield strength in tension) and particle separation distance distribution characterised by a particle roughness height h_r as well as molecular centre separation distance $a_{F=0}$. Obviously, this value characterises the *contact softness* with respect to a small asperity height h_r as well, compare Eq.(7). It corresponds to an

abscissa intersection $\sigma_{1,Z}$ of the constitutive consolidation function $\sigma_c(\sigma_1)$, see **Fig. 6** and **Fig. 8** below.

A term for deformation rate influence on adhesion force in a particle contact is to be inserted

$$F_{Ht} = \kappa_t \cdot F_{H0} + \kappa_t \cdot F_N \tag{14}$$

with a viscoplastic contact consolidation coefficient κ_t=attraction/repulsion force ratio as a dimensionless combination of attractive contact strength $\sigma_a \equiv p_{VdW}$ and repulsive particle contact viscosity $\eta_V/t \equiv p_f$, i.e. viscoplastic stiffness, analogous to plastic deformation, **Fig. 3**.

$$\kappa_t = \frac{\sigma_a}{\eta_V \cdot \dot{\varepsilon}_V} = \frac{\sigma_a}{\eta_V} \cdot \frac{d \cdot dt}{dr_{vis}} \tag{15}$$

For example, the driving potential in the main case of viscoplastic contact deformation or particle fusion resp., is given by means of free surface energy σ_{ss}. On the one hand, the influence of the pre-consolidation normal force F_N on the contact circle radius ratio r_{vis}/d was derived from Rumpf et al. (25):

$$\left(\frac{r_{vis}}{d}\right)^2 = \frac{2 \cdot t}{5 \cdot \eta_s} \cdot \left(\frac{2 \cdot \sigma_{ss}}{d} + \frac{1}{\pi} \cdot \frac{F_N}{d^2}\right) \tag{16}$$

The adhesion force F_{Ht} is set proportional to the tensile strength of flowing material. This is created either by means of liquid-equivalent adsorption layer bridges with Van Der Waals and hydrogen bondings or by Van Der Waals solid bridges $\sigma_{Zs} \equiv \sigma_a$ and $\eta_s \equiv \eta_V$, with small melting point $(0.75-0.9) \cdot T_m$ for particle fusion in the contact zone:

$$F_{Ht} = \pi \cdot r_{vis}^2 \cdot \sigma_{Zs} = \frac{4 \cdot \pi \cdot \sigma_{Zs} \cdot \sigma_{ss} \cdot d \cdot t}{5 \cdot \eta_s} + \frac{2 \cdot \sigma_{Zs} \cdot t}{5 \cdot \eta_s} \cdot F_N$$
$$\equiv \kappa_t \cdot F^*_{H0} + \kappa_t \cdot F_N \tag{17}$$

Generally, this corresponds to linear particle contact constitutive model, Eq.(14), with the viscoplastic repulsion or contact consolidation coefficient κ_t as a slope of adhesion force when a normal force F_N acts in the deformed contact (33, 34, 35, 36):

$$\kappa_t = \frac{2 \cdot \sigma_{Zs}}{5 \cdot \eta_s} \cdot t \tag{18}$$

The particle viscosity η_s decreases with temperature increasing. This is to be described with a typical thermal kinetic expression for particle fusion with 3 parameters ($E_{\dot{\gamma}}$ molar fusion activation energy for shear rate gradient $\dot{\gamma}$, T_r=(200...400) K temperature parameter for polymers with $0K < T_r < T_G$ glass transition point, R universal gas constant). The viscosity parameter $\eta_s = \eta_{s,min}$ for $T >> T_m$ depends here on molecular mass, chain length and number of cross-links for polymers (31).

$$\eta_s = \eta_{s,min} \cdot \exp\left[\frac{E_{\dot{\gamma}}}{R \cdot (T - T_r)}\right] \tag{19}$$

The median adhesion forces F^*_{H0} and F_{H0}, see Eq.(12), of a direct spherical contact

$$F_{H0,t} = 2 \cdot \pi \cdot d \cdot \sigma_{ss} \cdot \kappa_t(t) \equiv F^*_{H0} \cdot \kappa_t(t) \quad \textbf{and} \tag{20}$$

$$F^*_{H0} = 2 \cdot \pi \cdot \sigma_{ss} \cdot d \equiv F_{H0} \tag{21}$$

correspond each other if the so-called Derjaguin approximation (29) is valid ($a_{F=0} << d$)

$$\sigma_{ss} = -\frac{1}{2 \cdot A_C} \cdot \int_{a_{F=0}}^{\infty} F_{H0}(a)\,da = -\frac{1}{2} \cdot \int_{a_{F=0}}^{\infty} p_{VdW}(a)\,da$$
$$= \frac{C_{H,svs}}{24 \cdot \pi \cdot a^2_{F=0}} \tag{22}$$

and the particle bondings are comparatively weak, e.g. Van Der Waals interaction ($C_{H,svs}$ Hamaker constant solid-vacuum-solid). But, these bonds are strong enough to disturb essentially reliable flow of particulate solids.

In opposition to time invariable plastic contact deformation, all parameters depend on time. Therefore superposition provided, the total adhesion force F_{Htot} consists of a instantaneous F_H and a time influenced component F_{Ht}, **Fig. 3**:

$$F_{Htot} = F_H + F_{Ht} = (1 + \kappa + \kappa_t) \cdot F_{H0} + (\kappa + \kappa_t) \cdot F_N \tag{23}$$

In this context, the total adhesion force F_{Htot} is a function of adhesion force F_{H0} without any deformation or pre-consolidation in a very closed sphere-sphere contact plus a consolidation term $(\kappa + \kappa_t) \cdot (F_N + F_{H0})$ with a normal force in the flattened plate-plate particle contact. Finally, this Eq.(23) can be interpreted as a general linear particle contact constitutive model, i.e. linear in forces and stresses, but non-linear concerning material characteristics, **Table 1**. Generally, this adhesion force level, see **Fig. 3**, amounts up to 10^5-10^6 fold of particle weight for very cohesive fine particles. Additionally, for moist powders, the liquid bridge bonding forces are strength determined (33, 38, 39).

3. Particle contact Failure and cohesive Powder Flow criteria

Regarding the formulation of failure conditions at the particle contacts, we can obviously follow the Molerus theory (14), but here with a general supplement for the particle contact constitutive models Eqs.(11), (14) and (23), see in detail (32). The inclina-

tion of radius and centre contact force components F_R, F_M and normal vectors are described with an angle α, see contact failure conditions in **Table 1**. It should be noted that the stressing pre-history of a cohesive powder flow is stationary (steady-state) and delivers significantly a *cohesive* stationary yield locus in radius – centre-stress coordinates,

$$\sigma_{R,st} = \sin\varphi_{st} \cdot (\sigma_{M,st} + \sigma_0) \tag{24}$$

with the isostatic tensile strength σ_0 obtained from the adhesion force F_{H0}, see Eq.(12).

$$\sigma_0 = \frac{1-\varepsilon_0}{\varepsilon_0} \cdot \frac{F_{H0}}{d^2} \tag{25}$$

From it, the stress dependent effective angle of internal friction φ_e acc. to Jenike as a slope of *cohesionless* effective yield locus follows obviously, see **Fig. 4**:

$$\sin\varphi_e = \sin\varphi_{st} \cdot \left(\frac{\sigma_1 + \sigma_0}{\sigma_1 - \sin\varphi_{st} \cdot \sigma_0} \right) \tag{26}$$

If the major principal stress σ_1 reaches the stationary uniaxial compressive strength $\sigma_{c,st}$,

$$\sigma_1 = \sigma_{c,st} = \frac{2 \cdot \sin\varphi_{st} \cdot \sigma_0}{1 - \sin\varphi_{st}} \tag{27}$$

the effective angle of internal friction amounts to $\varphi_e = 90°$ and for $\sigma_1 \to \infty$ follows $\varphi_e \to \varphi_{st}$, see **Fig. 4**.

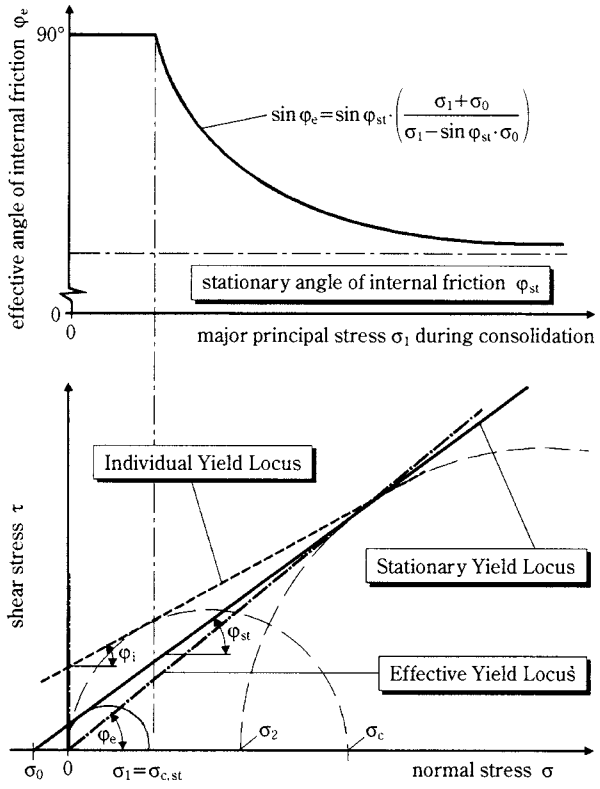

Fig. 4 Stationary yield locus (33) and effective yield locus acc. to Jenike (2)

For the relation between the angle of internal friction φ_i (slope of instantaneous yield locus) and the stationary angle of internal friction φ_{st} following relation is used (12):

$$\tan\varphi_{st} = (1+\kappa) \cdot \tan\varphi_i \tag{28}$$

The softer the particle contacts, the larger the difference between these friction angles are and consequently the more cohesive the powder behave. Therefore considering Eq.(23), the new relation between the time dependent angle of internal friction φ_{it} (slope of time yield locus) and the time invariable stationary angle of internal friction φ_{st} (slope of stationary yield locus) is defined as **Fig. 5**:

$$\tan\varphi_{st} = (1+\kappa+\kappa_t) \cdot \tan\varphi_{it} = \text{const.} \neq f(t) \tag{29}$$

Now, the angle of internal friction of a time consolidation φ_{it} is to be expressed (33):

$$\tan\varphi_{it} = \frac{\tan\varphi_i}{1+\frac{\kappa_t}{1+\kappa}} = \frac{\tan\varphi_i}{1+\frac{\kappa_t \cdot \tan\varphi_i}{\tan\varphi_{st}}} = \frac{\tan\varphi_i}{1+\frac{2\,\sigma_{Zs}\tan\varphi_i}{5\,\eta_s \tan\varphi_{st}} \cdot t} \tag{30}$$

First of it, with this Eq.(30) following predictions are possible (33, 34, 35, 36, 37), **Fig. 5**:

(1) If no time consolidation occurs t=0, both friction angles are equivalent $\varphi_{it} = \varphi_i$. The non-linear and linear instantaneous yield loci in radius-centre-coordinates are obtained:

$$\sigma_R = \sin\varphi_i \cdot (\sigma_{M,st} + \sigma_0) \cdot \left[\sqrt{\left(\frac{\tan\varphi_{st}}{\tan\varphi_i} - \frac{\sigma_{M,st} - \sigma_M}{\sigma_{M,st} + \sigma_0} \right)^2 - \frac{\tan^2\varphi_{st} \cdot \sin^2(\varphi_{st} - \varphi_i)}{\tan^2\varphi_i}} - \tan\varphi_{st} \cdot \sin(\varphi_{st} - \varphi_i) \right] \tag{31}$$

$$\sigma_R = \sin\varphi_i \cdot \left[\sigma_M + \left(\frac{\sin\varphi_{st}}{\sin\varphi_i} - 1 \right) \cdot \sigma_{M,st} + \frac{\sin\varphi_{st}}{\sin\varphi_i} \cdot \sigma_0 \right] \tag{32}$$

(2) But if t>0 the angle of internal friction during time consolidation decreases $\varphi_{it} < \varphi_i$ and the non-linear and linear time yield loci in radius-centre-coordinates are:

$$\sigma_{R,t} = \sin\varphi_{it} \cdot (\sigma_{M,st} + \sigma_0) \cdot \left[\sqrt{\left(\frac{\tan\varphi_{st}}{\tan\varphi_{it}} - \frac{\sigma_{M,st} - \sigma_{M,t}}{\sigma_{M,st} + \sigma_0} \right)^2 - \frac{\tan^2\varphi_{st} \cdot \sin^2(\varphi_{st} - \varphi_{it})}{\tan^2\varphi_{it}}} - \tan\varphi_{st} \cdot \sin(\varphi_{st} - \varphi_{it}) \right] \tag{33}$$

$$\sigma_{R,t} = \sin\varphi_{it} \cdot \left[\sigma_{M,t} + \left(\frac{\sin\varphi_{st}}{\sin\varphi_{it}} - 1 \right) \cdot \sigma_{M,st} + \frac{\sin\varphi_{st}}{\sin\varphi_{it}} \cdot \sigma_0 \right] \tag{34}$$

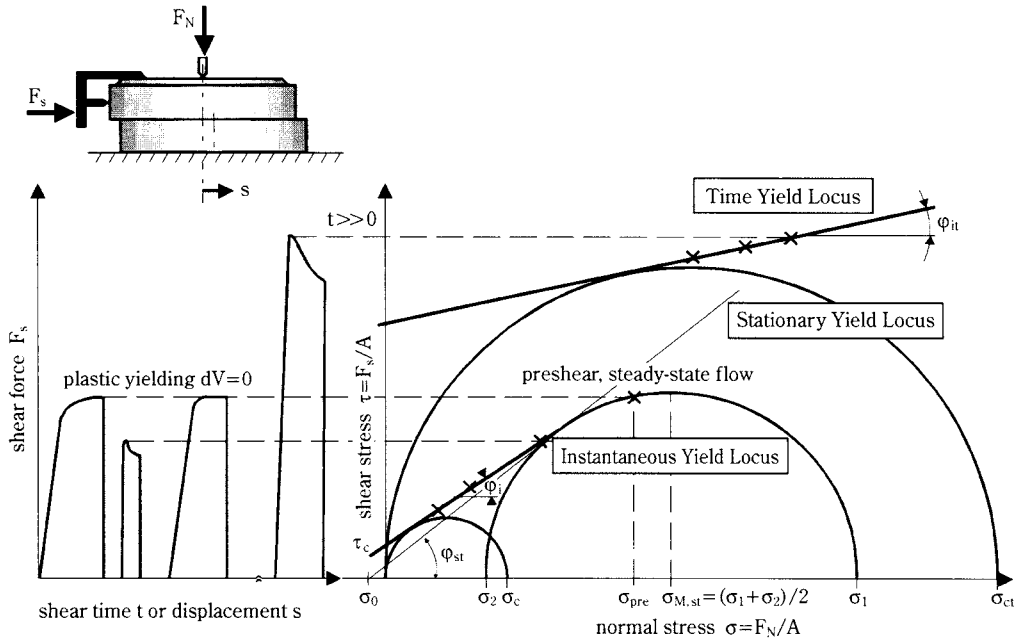

Fig. 5 Characteristics of instantaneous, stationary and time yield locus

(3) For $t\to\infty$ follows $\varphi_{it}\to 0$, that means, the time yield locus is a parallel line to the σ-axis, i.e. failure criterion of ideal plasticity by Tresca. The bulk material is hardening to a complete solid state with plastic failure conditions as a limitation.

The non-linear and linear yield loci in τ-σ-coordinates are shown in **Table 1** and **Fig. 5**. These instantaneous yield loci, complementary consolidation loci and the stationary yield locus are completely described only with three material parameters plus the characteristic pre-consolidation (average pressure) influence (32):

(1) φ_i – incipient particle friction of failing contacts, i.e. Coulomb friction;

(2) φ_{st} – steady-state particle friction of failing contacts, increasing adhesion by means of contact flattening expressed with the contact consolidation coefficient κ, or by friction angles $\sin(\varphi_{st}-\varphi_i)$ and $(\sin\varphi_{st}-\sin\varphi_i)$ see Eqs.(31), (32) and (36). The softer the particle contacts, the larger the difference between these friction angles are and consequently the more cohesive the powder behave;

(3) σ_0 – isostatic tensile strength of unconsolidated particle contacts, characteristic cohesion force in an unconsolidated powder, see Eq.(37);

(4) $\sigma_{M,st}$ – previous consolidation influence of an additional normal force in a particle contact, characteristic centre stress of Mohr circle of pre-consolidation state directly related to powder bulk density. This average pressure influences the increasing isostatic tensile strength of yield loci by means of cohesive steady-state flow as the stressing pre-history of a powder.

With the derivation of time yield locus the uniaxial compressive strength (unconfined yield strength) σ_{ct} is found as function of the major principal stress σ_1 comparable with a linear bulk material constitutive model, **Table 1**:

$$\sigma_{ct}=\frac{2\cdot(\sin\varphi_{st}-\sin\varphi_{it})}{(1+\sin\varphi_{st})\cdot(1-\sin\varphi_{it})}\cdot\sigma_1+\frac{2\cdot\sin\varphi_{st}\cdot(1+\sin\varphi_{it})}{(1+\sin\varphi_{st})\cdot(1-\sin\varphi_{it})}\cdot\sigma_0=a_{1,t}\cdot\sigma_1+\sigma_{ct,0} \qquad (35)$$

The slope $a_{1,t}$ and the intersection of σ_c-axis $\sigma_{ct,0}$ are time dependent, Eq.(30). The abscissa intersection $\sigma_{1,Z}$ of linear consolidation constitutive function $\sigma_c(\sigma_1)$, corresponds to the $F_{N,Z}$ value of contact consolidation function acc. to Eq.(13) and **Fig. 3**.

Again, the following predictions are to be advanced,:

(1) If no time consolidation occurs, both angles are equivalent $\varphi_{it}=\varphi_i$ and the linear constitutive model for plastic contact deformation is obtained $\sigma_c=a_1\cdot\sigma_1+\sigma_{c,0}$

$$\sigma_c=\frac{2\cdot(\sin\varphi_{st}-\sin\varphi_i)}{(1+\sin\varphi_{st})\cdot(1-\sin\varphi_i)}\cdot\sigma_1+\frac{2\cdot\sin\varphi_{st}\cdot(1+\sin\varphi_i)}{(1+\sin\varphi_{st})\cdot(1-\sin\varphi_i)}\cdot\sigma_0 \qquad (36)$$

Table 1 Yield characteristics from Particle Mechanics point of view (37)

	instantaneous consolidation	time consolidation
adhesion force	$F_H = (1+\kappa)\cdot F_{H0} + \kappa \cdot F_N$	$F_H = (1+\kappa+\kappa_t)\cdot F_{H0} + (\kappa+\kappa_t)\cdot F_N$
contact consolidation coefficient	$\kappa = \frac{\kappa_p}{\kappa_A - \kappa_p} = \frac{p_{VdW}/p_f}{2/3 + A_{pl}/(3\cdot A_K) - p_{VdW}/p_f}$	$\kappa_t \propto \frac{\sigma_a}{\eta_V \cdot \dot{\varepsilon}_V} = \frac{\sigma_a}{\eta_V}\cdot\frac{d\cdot dt}{dr_{vis}} \approx \frac{2\cdot\sigma_{Zs}}{5\cdot\eta_s}\cdot t$
contact failure condition for stationary flow	$\frac{F_R \sin 2\alpha}{(1+\kappa)\cdot F_{H0} + (1+\kappa)\cdot(F_M + F_R\cos 2\alpha)} \le \tan\varphi_i$	$\frac{F_R \sin 2\alpha}{(1+\kappa+\kappa_t)\cdot F_{H0} + (1+\kappa+\kappa_t)\cdot(F_M + F_R\cos 2\alpha)} \le \tan\varphi_{it}$
stationary angle of internal friction	$\tan\varphi_{st} \equiv (1+\kappa)\cdot\tan\varphi_i = \text{const.}$	$\tan\varphi_{st} \equiv (1+\kappa+\kappa_t)\cdot\tan\varphi_{it} = \text{const} \neq f(t)$
effective angle of internal friction	$\sin\varphi_e = \sin\varphi_{st}\cdot(\sigma_1+\sigma_0)/(\sigma_1 - \sin\varphi_{st}\cdot\sigma_0)$	$\sin\varphi_e = \sin\varphi_{st}\cdot(\sigma_1+\sigma_0)/(\sigma_1 - \sin\varphi_{st}\cdot\sigma_0)$
stationary yield locus	$\tau_{st} = \tan\varphi_{st}\cdot(\sigma_{st}+\sigma_0)$	$\tau_{st} = \tan\varphi_{st}\cdot(\sigma_{st}+\sigma_0)$
particle contact failure condition	$\frac{F_R\cdot[\sin 2\alpha - (1+\kappa\cdot F_{HR}/F_R)\cdot\tan\varphi_i\cdot\cos 2\alpha]}{(1+\kappa)\cdot F_{H0} + F_M + \kappa\cdot F_{HM}} \le \tan\varphi_i$	$\frac{F_R\cdot[\sin 2\alpha - (1+(\kappa+\kappa_t)\cdot F_{HR}/F_R)\cdot\tan\varphi_{it}\cdot\cos 2\alpha]}{(1+\kappa+\kappa_t)\cdot F_{H0} + F_M + (\kappa+\kappa_t)\cdot F_{HM}} \le \tan\varphi_{it}$
failure angle $\alpha = \pi/4 + \beta/2$	$\tan\beta \equiv (1+\kappa\cdot\sigma_{R,st}/\sigma_R)\cdot\tan\varphi_i$	$\tan\beta \equiv (1+(\kappa+\kappa_t)\cdot\sigma_{R,st}/\sigma_R)\cdot\tan\varphi_{it}$
angle of internal friction	$\tan\varphi_i = \text{const.}$	$\tan\varphi_{it} = \tan\varphi_i\cdot\left(1+\frac{2\cdot\sigma_{Zs}\cdot\tan\varphi_i}{5\cdot\eta_s\cdot\tan\varphi_{st}}\cdot t\right)^{-1}$
non-linear yield locus	$\tau = \tan\varphi_i\cdot(\sigma_{M,st}+\sigma_0)\cdot\frac{\tan\varphi_{st}}{\tan\varphi_i}\cdot\left[\sqrt{\left(1-\frac{\tan\varphi_i}{\tan\varphi_{st}}\cdot\frac{\sigma_{M,st}-\sigma}{\sigma_{M,st}+\sigma_0}\right)^2 - \sin^2(\varphi_{st}-\varphi_i)} - \tan\varphi_i\cdot\sin(\varphi_{st}-\varphi_i)\right]$	$\tau_t = \tan\varphi_{it}\cdot(\sigma_{M,st}+\sigma_0)\cdot\frac{\tan\varphi_{st}}{\tan\varphi_{it}}\cdot\left[\sqrt{\left(1-\frac{\tan\varphi_{it}}{\tan\varphi_{st}}\cdot\frac{\sigma_{M,st}-\sigma}{\sigma_{M,st}+\sigma_0}\right)^2 - \sin^2(\varphi_{st}-\varphi_{it})} - \tan\varphi_{it}\cdot\sin(\varphi_{st}-\varphi_{it})\right]$
linear yield locus	$\tau = \tan\varphi_i\cdot\left[\sigma+\left(\frac{\sin\varphi_{st}}{\sin\varphi_i}-1\right)\cdot\sigma_{M,st}+\frac{\sin\varphi_{st}}{\sin\varphi_i}\cdot\sigma_0\right]$	$\tau_t = \tan\varphi_{it}\cdot\left[\sigma+\left(\frac{\sin\varphi_{st}}{\sin\varphi_{it}}-1\right)\cdot\sigma_{M,st}+\frac{\sin\varphi_{st}}{\sin\varphi_{it}}\cdot\sigma_0\right]$
uniaxial compressive strength	$\sigma_c = \frac{2\cdot(\sin\varphi_{st}-\sin\varphi_i)}{(1+\sin\varphi_{st})\cdot(1-\sin\varphi_i)}\cdot\sigma_1 + \frac{2\cdot\sin\varphi_{st}\cdot(1+\sin\varphi_i)}{(1+\sin\varphi_{st})\cdot(1-\sin\varphi_i)}\cdot\sigma_0$	$\sigma_{ct} = \frac{2\cdot(\sin\varphi_{st}-\sin\varphi_{it})}{(1+\sin\varphi_{st})\cdot(1-\sin\varphi_{it})}\cdot\sigma_1 + \frac{2\cdot\sin\varphi_{st}\cdot(1+\sin\varphi_{it})}{(1+\sin\varphi_{st})\cdot(1-\sin\varphi_{it})}\cdot\sigma_0$

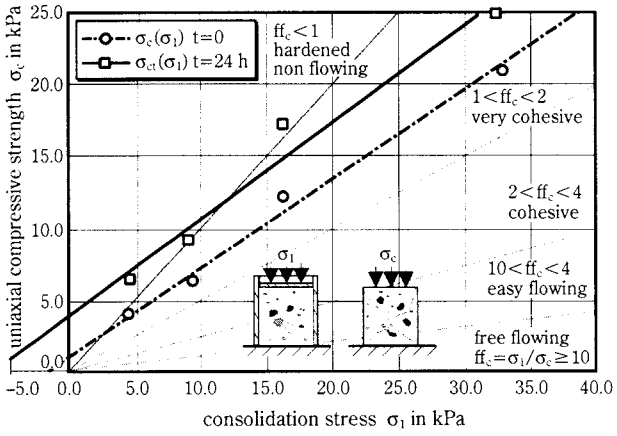

Fig. 6 Consolidation function of titania, d_{50}=0.61 µm, moisture X_W=0.4%

and with Eqs.(12) and (21) the isostatic tensile strength is expressed $\varepsilon_0 = 1-\rho_{b,0}/\rho_s$:

$$\sigma_0 = \frac{1-\varepsilon_0}{\varepsilon_0}\cdot\frac{F_{H0}}{d^2} = 2\cdot\pi\cdot\frac{1-\varepsilon_0}{\varepsilon_0}\cdot\frac{\sigma_{ss}}{d}$$
$$= \frac{1-\varepsilon_0}{\varepsilon_0}\cdot\frac{C_{H,sls}}{12\cdot a_{F=0}^2\cdot d}\cdot\left[\frac{h_r}{d}+\left(1+\frac{h_r}{2\cdot a_{F=0}}\right)^{-2}\right] \quad (37)$$

(2) But if $t>0$ the angle of internal friction during time consolidation decreases $\varphi_{it}<\varphi_i$ and the slope $a_{1,t}$ increases.

(3) For $t\to\infty$ is $\varphi_{it}\to 0$, that means, the slope follows $a_{1,t}\to 1$. This is the largest slope considering the model prerequisites of an only viscoplastic flow. If the first derivative is greater then one $a_{1,t}=d\sigma_{ct}/d\sigma_1>1$ a non-linear relation of particle contact deformation and consequently other physico-chemical effects of irreversible bulk material consolidation should be considered.

(4) Notice that for $t\to\infty$ the intersection of σ_{ct}-axis $\sigma_{ct,0}$ achieves a upper limit, which is only dependent on surface energy σ_{ss} and particle size and not from time and viscosity:

$$\sigma_{ct,0} = \frac{2\cdot\sin\varphi_{st}\cdot(1+\sin\varphi_{it})}{(1+\sin\varphi_{st})\cdot(1-\sin\varphi_{it})}\cdot\sigma_0$$
$$\underset{\varphi_{it}\to 0}{\cong} 4\cdot\pi\cdot\frac{1-\varepsilon_0}{\varepsilon_0}\cdot\frac{\sin\varphi_{st}}{1+\sin\varphi_{st}}\cdot\frac{\sigma_{ss}}{d} \quad (38)$$

4. Powder Flowability and Compressibility

Assessing the flow behaviour of a powder, Eq.(35) shows that the flow function acc. to Jenike (2) is not constant and depends on the consolidation stress level σ_1:

$$ff_{ct} = \frac{\sigma_1}{\sigma_{ct}} = \frac{1}{2} \cdot \frac{(1+\sin\varphi_{st})\cdot(1-\sin\varphi_{it})}{\sin\varphi_{st}-\sin\varphi_{it}+\sin\varphi_{st}\cdot(1+\sin\varphi_{it})\cdot\sigma_0/\sigma_1} \quad (39)$$

But roughly we can write for a small intersection with the ordinate $\sigma_{c,0}$, i.e. isostatic tensile strength $\sigma_0 \to 0$ near zero, the stationary angle of internal friction is equivalent to the effective angle $\varphi_{st} \approx \varphi_e$ and Jenike's (2) formula is obtained in order to demonstrate the general model validity:

$$ff_c \approx \frac{(1+\sin\varphi_e)\cdot(1-\sin\varphi_i)}{2\cdot(\sin\varphi_e-\sin\varphi_i)} \quad (40)$$

Thus, the semi-empirical classification by means of the flow function introduced by Jenike (2) is adopted here with a certain particle mechanical sense completion, **Table 2**:

The class "non flowing" is characterised by the fact that the unconfined yield strength σ_{ct} is higher than the consolidation stress σ_1 and thus in case of time consolidation, caking, cementation or hardening the powder has been agglomerated to solid state (38).

Obviously, the flow behaviour is mainly influenced by the difference between the friction angles, Eq.(40), as a measure for the adhesion force slope κ in the general linear particle contact constitutive model, Eq.(23). Therefore we can recalculate these coefficients from flow function measurements:

$$\kappa = \frac{1+(2\cdot ff_c-1)\cdot\sin\varphi_i}{\tan\varphi_i\cdot(2\cdot ff_c-1+\sin\varphi_i)} \cdot \sqrt{\frac{1}{1-\left(\frac{1+(2\cdot ff_c-1)\cdot\sin\varphi_i}{2\cdot ff_c-1+\sin\varphi_i}\right)^2}-1} \quad (41)$$

Table 2 Flowability assessment and elastic-plastic contact consolidation coefficient $\kappa(\varphi_i=30°)$

flow function ff_c	κ-values	φ_{st} in deg	evaluation	examples
100–10	0.01006–0.1068	30.3–33	free flowing	dry fine sand
4–10	0.1068–0.3	33–37	easy flowing	moist fine sand
2–4	0.3–0.77	37–46	cohesive	dry powder
1–2	0.77–∞	46–90	very cohesive	moist powder
<1	∞	–	non-flowing, hardened (ff_{ct})	moist powder, hydrated cement

A characteristic value $\kappa=0.77$ for $\varphi_i=30°$ of a very cohesive powder is included in the force displacement, **Fig. 2**, as well as adhesion force diagram, **Fig. 3**, and shows directly the correlation between strength and force enhancement with pre-consolidation, **Table 2**. Due to the consolidation function in **Fig. 6**, a small slope stands for a free flowing particulate solid with very low adhesion level because of stiff particle contacts, but a large inclination means a very cohesive powder flow behaviour because of soft particle contacts, **Fig. 3**.

Obviously, the finer the particles the "softer" the contacts and the more cohesive the powder (33, 42). Köhler (43) has experimentally confirmed this thesis for alumina powders (α-Al_2O_3) down to the submicron range ($\sigma_{c,0} \approx$ const.=2 kPa, d_{50} median particle size in µm):

$$ff_c \approx 2.2\cdot d_{50}^{0.62} \quad (42)$$

Analogously to adiabatic gas law $p\cdot V^{\kappa_{ad}}=$const., a differential equation for isentropic compressibility of a powder dS=0, i.e. remaining stochastic homogeneous packing without a regular order in the continuum, is to be derived:

$$\frac{d\rho_b}{\rho_b} = n\cdot\frac{dp}{p} = n\cdot\frac{d\sigma_{M,st}}{\sigma_{M,st}+\sigma_0} \quad (43)$$

The total pressure including particle interaction $p=\sigma_{M,st}+\sigma_0$ should be equivalent to a pressure term with molecular interaction (V_m molar volume)

$$(p+a_{VdW}/V_m^2)\cdot(V_m-b) = R\cdot T \quad (44)$$

in Van Der Waals equation of state to be valid near gas condensation point. A loose powder packing is obtained $\rho_b=\rho_{b,0}$, if only particles are interacting without an external consolidation stress $\sigma_{M,st}=0$, e.g. particle weight compensation by a fluid drag, and Eq.(43) is solved:

$$\frac{\rho_b}{\rho_{b,0}} = \left(\frac{\sigma_0+\sigma_{M,st}}{\sigma_0}\right)^n \quad (45)$$

Therefore, this physically based compressibility index $n \equiv 1/\kappa_{ad}$ lies between n=0, i.e. incompressible stiff bulk material and n=1, i.e. ideal (gas) compressibility index, see **Fig. 7** above.

For hopper design purposes in powder mechanics the major principle stress σ_1 during preconsolidation is used instead of the centre stress $\sigma_{M,st}$. Hence we replace the total pressure $p=\sigma_1+\sigma_{1,Z}$ with the new abscissa intersection $\sigma_{1,Z}$ in the negative tensile or pull-off range of the consolidation function $\sigma_c=f(\sigma_1)$, Eq.(36) and **Fig. 7**, and obtain this function:

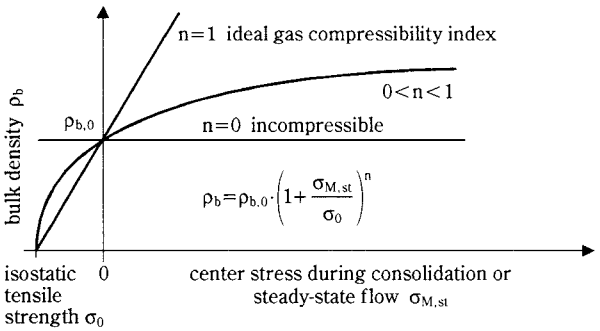

Fig. 7 Compressibility index n of powders

$$\frac{\rho_b}{\rho_{b,0}} = \left(\frac{\sigma_1+\sigma_{1,Z}}{\sigma_{1,Z}}\right)^n \tag{46}$$

Considering the predominant plastic and viscoplastic particle contact deformation and rearrangement in the stochastic homogeneous packing of a cohesive powder, following values of compressibility index are to be suggested, **Table 3**:

Table 3 Compressibility index of powders, semi-empirical estimation for $\sigma_1 = 1-100$ kPa

index n	evaluation	examples	flowability
0–0.01	incompressible	gravel	free flowing
0.01–0.05	low compressibility	fine sand	
0.05–0.1	compressible	dry powder	cohesive
0.1–1	very compressible	moist powder	very cohesive

5. Design Consequences for Reliable Flow

Mainly for functional silo design purposes in Mechanical Process Engineering, these fundamental models can be applied by means of a characteristic apparatus dimension function, here a minimum hopper opening width $b_{min,t}$ avoiding cohesive bulk material arches (g gravitational acceleration, ff flow factor acc. to Jenike, m=1 conical hopper, m=0 wedge hopper, φ_w angle of wall friction, θ hopper angle versus vertical, ρ_b bulk density):

(1) If no time consolidation occurs t=0, both friction angles are equivalent $\varphi_{it}=\varphi_i$ and the linear bulk material constitutive model for plastic contact deformation is obtained. Consequently it is:

$$b_{min} = \frac{2\cdot(m+1)\cdot\sin 2(\varphi_w+\theta)\cdot(1+\sin\varphi_i)\cdot\sin\varphi_{st}\cdot\sigma_0}{\rho_b\cdot g\cdot[1-\sin\varphi_{st}\cdot\sin\varphi_i-(\sin\varphi_{st}-\sin\varphi_i)\cdot(2\cdot ff-1)]} \tag{47}$$

(2) For the general case t>0 the angle of internal friction during time consolidation decreases $\varphi_{it}<\varphi_i$, the slope $a_{1,t}$ and $b_{min,t}$ increase:

$$b_{min,t} = \frac{2\cdot(m+1)\cdot\sin 2(\varphi_w+\theta)\cdot(1+\sin\varphi_{it})\cdot\sin\varphi_{st}\cdot\sigma_0}{\rho_b\cdot g\cdot[1-\sin\varphi_{st}\cdot\sin\varphi_{it}-(\sin\varphi_{st}-\sin\varphi_{it})\cdot(2\cdot ff-1)]} \tag{48}$$

(3) Often a technological unreasonable time independent limit $b_{min,t}(t\to\infty)$ follows for an extreme hardening or agglomerating particle material:

$$\lim_{t\to\infty} b_{min,t\to\infty} = \frac{4\cdot\pi\cdot(m+1)\cdot\sin 2(\varphi_W+\theta)\cdot\sin\varphi_{st}}{\rho_s\cdot\varepsilon_0\cdot g\cdot[1-\sin\varphi_{st}\cdot(2\cdot ff-1)]}\cdot\frac{\sigma_{ss}}{d} \tag{49}$$

This approach should express the enormous problems concerning reliable flow of powders which are tending to time consolidation, hardening and caking. Consequently, discharging aids should be applied in handling practice (33).

The essential consolidation functions necessary for reliable design are collected in **Fig. 8**. For the cohesive steady-state flow $\sigma_1=\sigma_{c,st}$, **Fig. 4** and Eq.(27), the flow factor is ff=1 and a minimum outlet width $b_{min,st}<b_{min}$ (instantaneous flow) is obtained which prevents bridging during the stationary hopper operation.

$$b_{min,st} = \frac{2\cdot(m+1)\cdot\sin 2(\varphi_W+\theta)\cdot\sin\varphi_{st}\cdot\sigma_0}{\rho_b\cdot g\cdot(1-\sin\varphi_{st})} \tag{50}$$

As starting value, $b_{min,st}$ should be used for numerical calculation (33) of both functions $\varphi_e(\sigma_1)$ and $\rho_b(\sigma_1)$ as

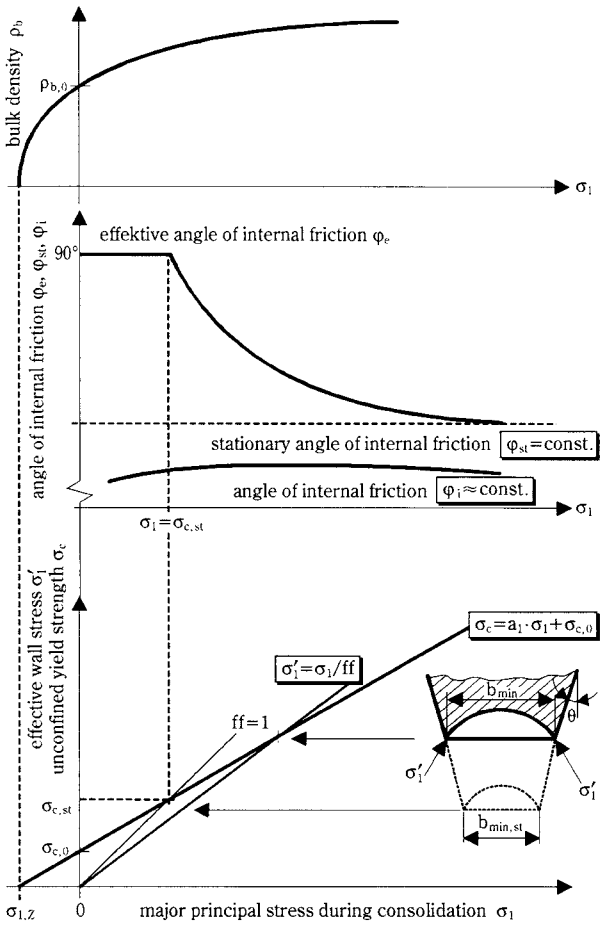

Fig. 8 Consolidation functions of a cohesive powder for reliable design

well as the flow factor (1, 2) ff ($\varphi_e(\sigma_1), \varphi_W$). Before that the hopper angle $\theta(\varphi_e(\sigma_1), \varphi_W)$ has properly to be selected (1, 2, 4, 5, 13).

For the sub-micron titania powder ($d_{50,3}$=610 nm, σ_0=0.327 kPa, $\rho_b \approx 800$ kg/m^3, friction angles φ_i=33°, φ_{st}=54°, φ_W=31°, θ=11°, ff≈1.3) practically reasonable $b_{min,st}$=0.7 m for steady-state flow, but b_{min}=1.52 m for incipient yield and incredible $b_{min,t}$=8.4 m for gravitational flow (without flow promotion) after time consolidation at rest (t=24 h, φ_{it}=31°) are determined for a conical hopper.

Both, shear test results – accurate measurements provided – evaluated with these combined particle and continuum mechanical approach, are used as constitutive functions for computer aided silo design for reliable flow (37) on the one hand. On the other hand a supplemented slice-element standard method (41, 42) is used for pressure calculations. Considering the reliable physical basis of the $\rho_b(\sigma_1)$ and $\varphi_e(\sigma_1)$ functions for example, these can be suitably extrapolated using pressure calculations for large silos with more than 1000 m^3 storage capacity (44).

6. Conclusions

Taking into consideration all the different properties of cohesive to very cohesive powders tested (particle size distribution, moisture content, material properties etc.), the model fit can be characterised as satisfactory to good. Thus, the model has proved its effectiveness and can be accordingly applied in reliable silo design for flow and pressure calculation.

Obviously, recommendations are to be elaborated with respect to the powder product design for processing, logistics, transportation, distribution and consumption, see Borho et al. (45) as well.

7. Acknowledgements

The author would like to acknowledge his co-workers Dr. S. Aman, Dr. T. Gröger, S. Schubert, B. Reichmann and Th. Kollmann for their experimental contributions, relevant information and theoretical tips.

Symbols

a	: separation	[m]
a_1	: slope of $\sigma_c(\sigma_1)$ consolidation function	[−]
A	: area, particle contact area	[m^2]
b	: outlet width	[m]
C_H	: Hamaker constant	[J]
d	: particle size	[μm]
E	: modulus of elasticity	[kN/mm^2]
F	: force	[N]
ff	: flow factor acc. to Jenike	[−]
ff_c	: flow function acc. to Jenike	[−]
g	: gravity acceleration	[m/s^2]
m	: mass, hopper shape factor	[kg, −]
p	: pressure	[kPa]
p_f	: plastic yield strength of particle contact	[MPa]
r	: contact radius	[μm]
α	: failure angle	[deg]
β	: auxiliary failure angle function	[deg]
$\dot{\gamma}$	: shear deformation rate gradient	[s^{-1}]
ε	: porosity	[−]
$\dot{\varepsilon}$	: deformation rate gradient	[s^{-1}]
η	: viscosity	[Pa·s]
η_V	: viscoplastic yield strength of particle contact	[Pa·s]
κ	: contact consolidation coefficient	[−]
θ	: hopper angle	[deg]
φ	: angle of friction	[deg]
ρ	: density	[kg/m^3]
σ	: normal stress	[kPa]
σ_a	: adhesion strength	[kPa]
σ_1	: major principal stress	[kPa]
σ_0	: isostatic tensile strength	[kPa]
τ	: shear stress	[kPa]

Indices

ad	: adiabatic
b	: bulk
c	: compressive
e	: effective
el	: elastic
H	: adhesion (Haft-)
i	: internal
K	: total contact
l	: liquid
m	: molar
M	: centre of Mohr circle
min	: minimum
N	: normal
p	: pressure
pl	: plastic
pre	: pre-shear
R	: radius of Mohr circle
s	: solid
st	: stationary
t	: time dependent
T	: tangential
V	: volume
VdW	: Van Der Waals

vis : viscoplastic
W : wall
Z : tensile (Zug-)
0 : initial, zero point

References

1) A. W. Jenike, "Gravity flow of solids", Engng. Exp. Station Bull. No. 108, Univ. Utah, (1961)
2) A. W. Jenike, "Storage and flow of solids", Engng. Exp. Station Bull. No. 123, Univ. Utah, (1964)
3) F. Ziegler, "Techn. Mechanik der festen und flüssigen Körper", Springer Verlag Wien (1985)
4) J. Schwedes, "Fließverhalten von Schüttgütern in Bunkern", Verlag Chemie Weinheim (1970)
5) J. Schwedes and H. Wilms, "Fließeigenschaften von Schüttgütern", pp. 39-58, edited by P. Martens, "Silo – Handbuch", Ernst & Sohn Berlin (1988)
6) Ashton, M. D., Cheng, D. C. D., Farley, R. and Valentin, F. H. H., Some investigations into the strength and flow of powders, *Rheolog. Acta* **4** 206-218 (1965)
7) Cheng, D. C. H., The tensile strength of powders, *Chem. Engng. Sci.* **23** 1405-1420 (1968)
8) Stainforth, P. T., Ashley, R. C., and Morley, J. N. B, Computer analysis of powder flow characteristics, *Powder Technology* **4** 250-256 (1971)
9) Stainforth, P. T. and Ashley, R. C., An analytical hopper design method for cohesive powders, *Powder Technology* **7** 215-243 (1973)
10) Stainforth, P. T. and Berry, R. E. R., A general flowability index for powders, *Powder Technology* **8** 243-251 (1973)
11) O. Molerus, "Theory of yield of cohesive powders", *Powder Technology* **12** 259-275 (1975)
12) O. Molerus, "Effect of interparticle cohesive forces on the flow behaviour of powders", *Powder Technology* **20** 161-175 (1978)
13) O. Molerus, "Schüttgutmechanik – Grundlagen und Anwendungen in der Verfahrenstechnik", Springer Verlag Berlin (1985)
14) O. Molerus, "Principles of Flow in Disperse Systems", Chapman & Hall London (1993)
15) H. Hertz, "Über die Berührung fester elastischer Körper", *J. reine u. angew. Math.* **92** 156-171 (1882)
16) M. T. Huber, "Zur Theorie der Berührung fester elastischer Körper", *Annal. Physik* **14** 153-163 (1904)
17) Mindlin, R. D. and Deresiewicz, H., Elastic spheres in contact under varying oblique forces, *J. Appl. Mech., Trans. ASME* **20** 327-344 (1953)
18) Krupp, H., Particle Adhesion – Theorie and Experiment, *Advanced Colloid Interface Sci.* **1** 111-239 (1967), in (11)
19) Dahneke, B., The influence of flattening on the adhesion of particles, *J. Colloid and Interface Sci.* **40** 1-13 (1972)
20) Derjagin, B. V., Muller, V. M., Toporov, U. P., Effect of contact deformations on the adhesion of particles, *J. Colloid and Interface Sci.*, **53** 314-326 (1975)
21) Johnson, K. L., Kendall, K. and Roberts A. D., Surface energy and the contact of elastic solids, Proc. Roy. Soc. Lond. **A 324** 301-313 (1971), in (22)
22) K. L. Johnson, "Contact Mechanics", Cambridge University Press (1985)
23) H. Schubert, K. Sommer and H. Rumpf, "Plastisches Verformen des Kontaktbereiches bei der Partikelhaftung", *Chemie Ingenieur Technik* **48** 716 (1976)
24) Wei Hsuin Yang, The contact problem for viscoelastic bodies, *J. Appl. Mech., Trans. ASME* **33** 395-401 (1966)
25) H. Rumpf, K. Sommer and K. Steier, "Mechanismen der Haftkraftverstärkung bei der Partikelhaftung durch plastisches Verformen, Sintern und viskoelastisches Fließen", *Chemie Ingenieur Technik* **48** 300-307 (1976)
26) Maugis, D. and Pollock, H. M., Surface forces, deformation and adherence at metal microcontacts, *Acta Metall.* **32** 1323-1334 (1984)
27) Thornton, C. and Yin, K. K., Impact of elastic spheres with and without adhesion, *Powder Technology* **65** 153-166 (1991)
28) Thornton, C. and Ning, Z., A theoretical model for the stick/bounce behaviour of adhesive, elastic-plastic spheres, *Powder Technology* **99** 154-162 (1998)
29) J. N. Israelachvili, "Intermolecular and surface forces", Academic Press London (1992)
30) H. Schubert, "Kapillarität in porösen Feststoffsystemen", Springer Verlag Berlin (1982)
31) H. Domininghaus, "Die Kunststoffe und ihre Eigenschaften", VDI Verlag Düsseldorf (1992)
32) J. Tomas, Particle Adhesion and Powder Flow Properties – Part I: Instantaneous Elastic-Plastic Particle Contact Consolidation and Yield Loci, *Powder Technology* (2001), (submitted)
33) J. Tomas, "Modellierung des Fließverhaltens von Schüttgütern auf der Grundlage der Wechselwirkungskräfte zwischen den Partikeln und Anwendung bei der Auslegung von Bunkeranlagen", Habilitation, Bergakademie Freiberg (1991)
34) J. Tomas, "Modelling the Time Consolidation Processes of Bulk Materials – Problems and Preliminary Solutions", International Symposium "Reliable Flow of Particulate Solids II" Oslo, Proceedings, 335-372 (1993)
35) J. Tomas, "Zum Verfestigungsprozeß von Schüttgütern – Mikroprozesse, Kinetikmodelle und Anwendungen", *Schüttguttechnik* **2** 31-51 (1996)
36) J. Tomas, "Zur Verfestigung von Schüttgütern – Mikroprozesse und Kinetikmodelle" *Chemie Ingenieur Technik* **69** 455-467 (1997)
37) J. Tomas, Particle adhesion fundamentals and bulk powder consolidation, International Symposium "Reliable Flow of Particulate Solids III", Porsgrunn, 641-656, 1999
38) J. Tomas and H. Schubert, "Modelling of the strength and flow properties of moist soluble bulk materials", International Symposium on Powder Technology Kyoto, Proceedings (1982)
39) J. Tomas and H. Schubert, "Modelling of the strength and the flow properties of moist soluble bulk materials", *Aufbereitungs-Technik* **23** 507-515 (1982)
40) J. Tomas and H. Schubert, "Flow behaviour of moist

bulk materials", *Aufbereitungs-Technik*: **26** 399-404 (1985)
41) TGL 32 274/09, "Lasten aus Schüttgütern in Bunkern, Flachsilos und Silos", (1987)
42) Tomas, J., Graichen, K. and Schubert, H., Influence of Flow Properties of Particulate Solids on Silo Pressure Calculation, *Aufbereitungs-Technik* **31** 475-481 (1990)
43) Köhler, Th. and Schubert, H., Influence of particle size distribution on the flow behaviour of fine powders, *Part. Part. Syst. Charact.* **8** 101-104 (1990)
44) Flügel, R., 6400 t potato starch in a "first in – first out" mode mammoth silo, powder handling & processing **11** 374-375 (1999)
45) Borho, K., Polke, R., Wintermantel, K., Schubert, H. and Sommer, K., Produkteigenschaften und Verfahrenstechnik, *Chem.-Ing.-Techn.* **63** 792-808 (1991)

Author's short biography

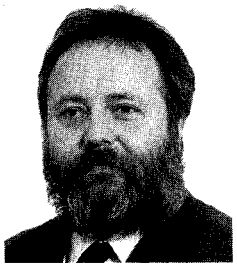

Jürgen Tomas

J. Tomas studied process engineering, special field system engineering, at the Institute of Technology (TH) Merseburg from 1971 to 1975. He finished his studies with Diploma-theses concerning crystallization and particle agglomeration in a liquid fluidized bed reactor. After his research work at the department of Mechanical Process Engineering and Mineral Processing of the Institute of Mining Technology (Bergakademie) Freiberg, he wrote his PhD-theses "Investigations on Flow Behaviour of Moist Soluble Bulk Materials" in 1982. R/D-activities followed this work, e.g. design of silo plants for power stations, cement mills, process industries as well as port installations for ores, consultant for trouble shouting in chemical plants. From 1988 to 1989, he teached as Assistant Professor at the Addis Abeba University (Ethiopia). In 1991 he wrote the ScD-theses (Habilitation) "Modelling the Flow Behavior of Bulk Materials on Particle Interaction Forces Basis and Application in Bunker Plant Design" at the Bergakademie Freiberg. After substituting a professorship in Mechanical Process Engineering at the Bergakademie Freiberg from 1992 to 1993, he was appointed professor at the School of Technology (HTWS) Zittau/Görlitz and, in 1994, full professor at the Otto-von-Guericke-University Magdeburg. From 1995 to 1997, he was chairman of the joint research field 385 (DFG Sonderforschungsbereich) "Building Material Recycling". His principal research activities are in particle characterization, particle and powder mechanics, comminution, solid-solid separation, press filtration, bulk solids storage and handling.

Aerosol Flame Reactors for the Synthesis of Nanoparticles†

Karsten Wegner and Sotiris E. Pratsinis
*Institute of Process Engineering, ETH Zürich**

Abstract

This paper presents an overview of recent basic research on flame aerosol reactors for the gas-phase synthesis of nanoparticles. Emphasis is placed on flame reactor technology as it is widely used in industry for the large-scale manufacture of oxide and carbon nanoparticles. The importance of reactant gas mixing, additives and external electric fields in flame technology is highlighted for the control of product particle properties by affecting the chemistry, temperature and collision histories. Laser-induced fluorescence (LIF), Fourier transform infrared spectroscopy (FTIR) and thermophoretic sampling are addressed as some of the promising diagnostic tools in flame aerosol research and even for on-line process control. Recent work on aerosol dynamics modeling is presented, and the growing importance of computational fluid dynamics (CFD) aimed at better understanding the particle formation and growth mechanisms in flames is emphasized, focusing on the synthesis of non-aggregated nanoparticles.

1. Introduction

Over the last few years, the scientific community has cherished the potential of nanosize clusters or particles [1, 2, 3]. These entities have distinctly different properties to bulk material because the number of atoms or molecules on their surface can become comparable to that inside the particles [4]. Some people even believe that nanosize particles may constitute another state of matter. Laboratory studies in various scientific fields show that especially non-aggregated nanoparticles can be used to develop new materials with unique characteristics such as optical, mechanical, electrical, catalytic, and heat transfer properties. With nanoparticles, the particle melting point decreases [5], light absorption increases, and magnetic, optoelectronic [6] and other material properties change compared with those in the bulk material. Their large surface area to volume ratio and high density of active sites make nanoparticles attractive for applications in catalysis. By reducing the grain size to nanometer scale, the sintering temperature of structural ceramics can be decreased while the plasticity is increased [7]. Nanoparticles can also be used in thin membrane films, for protective glass, metal and polymer coatings, in the production of inorganic/polymeric nanocomposites, as electronic devices and, if assembled in chains or arrays, as novel recording and storage media for digital data.

* CH-8092 Zürich, Switzerland
† Received: August 8, 2000

In general, nanosized powders can be synthesized via the wet chemical route and gas-phase processes. The latter are advantageous for powder manufacture since they do not involve the tedious and expensive steps of solid-liquid separation, washing and drying of wet chemistry processes and they avoid the use of high liquid volumes and surfactants [1]. Today, flame processes are by far the most widely used methods for the gas-phase manufacture of commercial quantities of nanoparticles, the most important of which are carbon blacks and fumed silica, produced for instance by Cabot and Degussa-Hüls, as well as pigmentary titania, made by DuPont, Ishihara, Kerr-McGee, Millenium, Tioxide, and others. The annual production volume of the flame industry is several million metric tons, and aerosol reactors produce nanoparticles at a rate of 100 metric tons per day [8]. Other commercial aerosol processes include hot-wall reactors for the industrial synthesis of filamentary (nanostructured) nickel and iron powders from decomposition of the corresponding metal carbonyls (BASF, INCO). In addition, these reactors have been used for the commercial synthesis of nanostructured carbides, nitrides, borides, and other non-oxide ceramics (Dow, Bayer). More recently, the inert gas condensation technique has been scaled up for the manufacture of rather costly (about $100/kg) nanostructured metals and ceramic powders (Nanophase). Spray pyrolysis technologies are used primarily by small start-up companies (for example, Particle Technology, Nanochem, SSC, and others) for the manufacture of precious metal, ceramic

and especially nanostructured composite ceramic powders from nitrate, organic and other solutions.

Despite the age and significance of industrial gas-phase processes, their design and operation rely heavily on experience and empiricism. As a result, it is nearly impossible for existing industrial units to address the synthesis of nanosize powders without going through the laborious and expensive cycle of Edisonian research that was followed for the development of the current units and processes (e.g. the so-called "chloride" process for TiO_2 synthesis). However, in contrast to the past state of affairs in industry, substantial work has been done on a laboratory scale toward understanding the fundamentals of nanoparticle formation and growth at high temperatures [8, 9], and even the use of computational fluid dynamics for reactor design is actively investigated in industry today [10].

2. Synthesis Methods

2.1 Process Classification

Gas-phase synthesis methods for nanoparticles can be divided into gas-to-particle and droplet-to-particle processes. Gas-to-particle conversion refers to the production of particles from individual atoms or molecules in the gas phase. Product powders generally exhibit small particle size, narrow particle size distribution, non-porous particles and high purity (**Figure 1**). Compared to droplet-to-particle or wet chemical processes, it is more difficult to produce multicomponent materials, and special care has to be taken in handling hazardous off-gases and precursors. Examples of these processes include flame [11], hot-wall [12, 13], evaporation-condensation [14, 15], plasma [16, 17], laser [18] and sputtering [19, 20].

In the droplet-to-particle route, solution droplets are suspended in gases by liquid atomization or by condensation of a superheated vapor. This is followed by the evaporation of solvent from droplets and solute crystallization to form a dried particle undergoing solid-state reactions and sintering upon heating. Compact nanostructured particles can be formed by spray drying of a nanoparticle slurry, as is shown in **Figure 2**. In general, the advantages of droplet-to-particle processes are: the ability to process organic and inorganic materials, to form a variety of multicomponent particles, simplicity, many choices for inexpensive liquid-phase precursors and a low degree of particle aggregation. Porous or hollow particles can be formed under certain conditions. However, the spread of the particle size is limited by the spread of the starting droplets. Spray drying [21] and pyrolysis [22] are typical industrial processes employing droplet-to-powder conversion and can be used for the manufacture of nanoparticles as well as flame spray pyrolysis [23], electrosprays [24, 25] and freeze drying [26]. Recent books give a detailed picture of the field [27, 28].

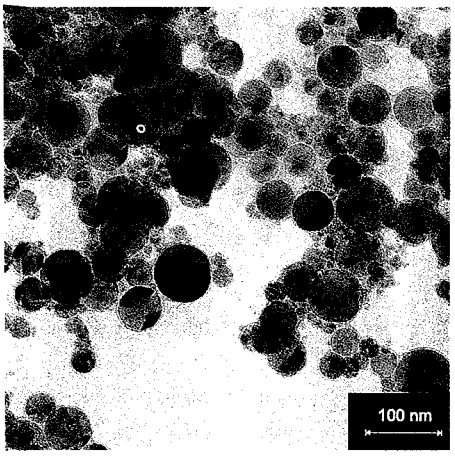

Fig. 1 Spherical, dense titania nanoparticles synthesized in a diffusion flame reactor by oxidation of titaniatetraisopropoxide (d_p, av=35 nm).

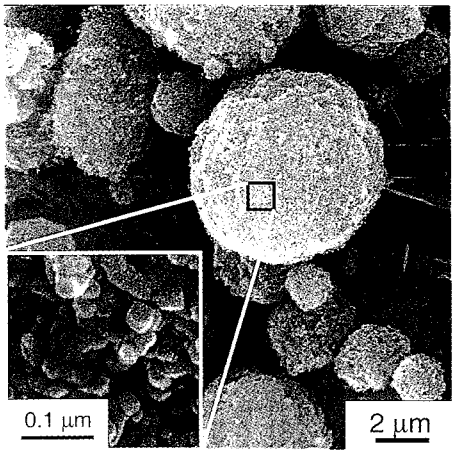

Fig. 2 Granules of nanostructured titania particles built by the re-processing of flame-made TiO_2 (d_p=35 nm) through spray-drying of a slurry (courtesy O. Wilhelm and L. Mädler, ETH Zürich).

2.2 Gas-Phase Synthesis Route

In the gas-to-particle route, nanoparticles are made by "building" them from individual molecules all the

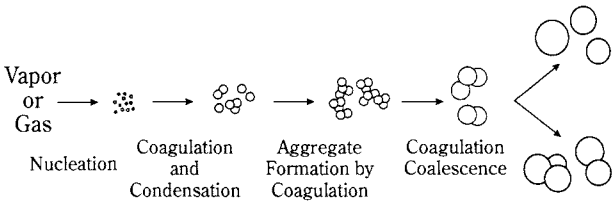

Fig. 3 Gas-to-particle conversion: Schematic of particle formation and growth. Adapted from Kodas and Hampden-Smith [27].

way up to the desired size as is shown in **Figure 3**. The particle formation process is driven by the generation of molecules by chemical reaction from precursor gases or by rapid cooling of a superheated vapor. High temperatures are usually required to accomplish the reaction or to bring the vapor to the superheated state. Depending on the thermodynamics of the process, the product molecules can form particles either by uninhibited collisions (collision-controlled nucleation) or by a balanced condensation and evaporation to and from molecular clusters (condensation-evaporation controlled nucleation). The newly formed particles grow further by collision with product molecules (condensation or reaction on the particle surface) and/or with particles (coagulation). In coagulation, two particles collide and stick to form an aggregate or agglomerate. The particles within this agglomerate can coalesce (fuse) by sintering into a spherical particle of the same volume and mass. However, as coagulation continues, the ratio of the sintering rate (the rate of particle coalescence) and the rate of coagulation determines the morphology of the final product particle. When the rate of coalescence is faster than that of coagulation, spherical particles are obtained. However, as particles grow, the sintering rate decreases and particle coalescence usually becomes slower than coagulation. As a result, irregularly shaped aggregate particles are formed. These are termed hard or soft aggregates (or agglomerates) depending on how easy it is to break the bonds connecting the primary particles [8].

3. Flame Synthesis

In flame reactors, the energy of a flame is used to drive chemical reactions of precursor compounds that result in the formation of product molecules, which then nucleate to form particles following the mechanism described earlier [8]. High flame temperatures of 1200 to 3000 K constitute a self-purifying environment for particle synthesis resulting in high-purity powders, as are needed for the manufacture of optical fiber preforms [29]. Even though non-oxide ceramic powders such as silicon nitride [30] and tungsten carbide [31] have been synthesized in flame reactors, the production of carbon and metal oxide nanoparticles dominates the field. One distinguishes two types of flame reactors: diffusion and premixed. While premixed flames have the advantage of more uniform radial temperature profiles, diffusion flames are safer to operate (no flashback) and offer flexibility in product qualities by controlling the reactant gas composition over broad ranges. Turbulent co-flow diffusion flame reactors are used in industry for the large-scale manufacture of ceramic powders. Counterflow diffusion flame reactors, on the other hand, are often used in laboratory studies [8]. The flow along the axial stagnation streamline of a counterflow diffusion flame can be approximated as one-dimensional, facilitating the use of optically-based diagnostics for the non-intrusive study of nanoparticle formation [9].

A typical laboratory set-up of an aerosol diffusion flame reactor is depicted in **Figure 4**. The co-flow reactor is made of three concentric stainless steel tubes of about 120 mm length. The inner diameter of the center tube is 5 mm, while the o.d. of the outer tube is 18 mm and the width of the two annular ports is about 1.5 mm. Oxygen is delivered through the outer tube while methane flows through the center port. High-purity argon loaded with the precursor vapor is added to the fuel stream prior to entering the burner.

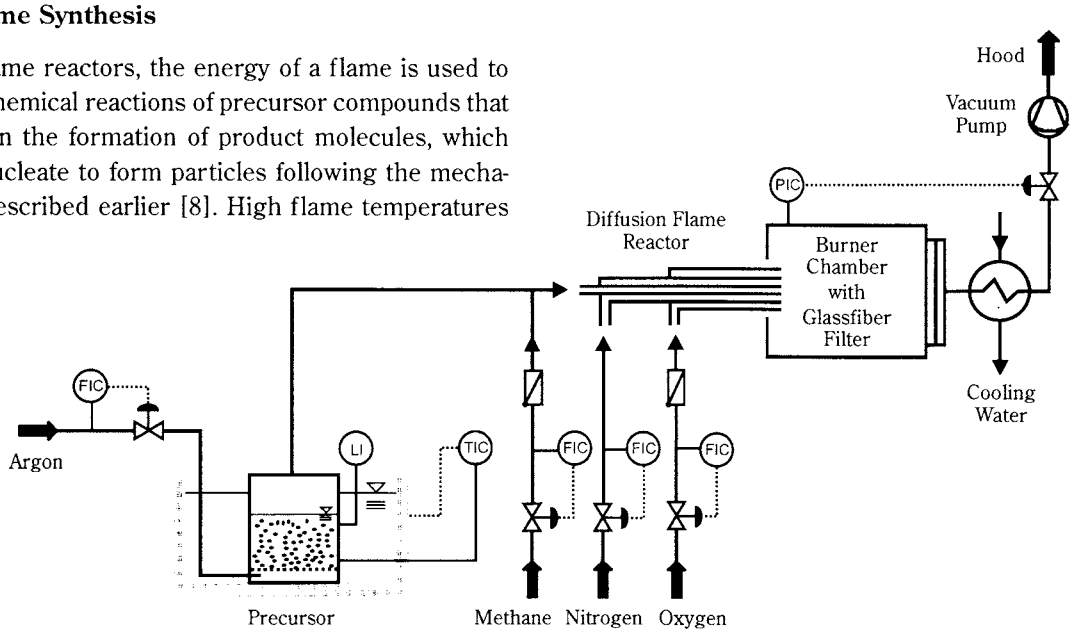

Fig. 4 Diffusion flame reactor set-up for nanoparticle synthesis.

A small stream of nitrogen is introduced between the fuel and oxidant streams to prevent deposition of particles on the burner mouth. An evaporator or a bubbler can be used to load the inert gas stream with the precursor. When a bubbler is used, controlled amounts of precursor can be delivered into the reactor by adjusting the temperature of the liquid compound with the help of a thermostated bath. Evaporators offer the advantage of precise precursor dosing, easier handling of moisture-sensitive chemicals and the evaporation of mixtures. Industrial processes usually operate with halide precursors. In laboratory units, organometallic compounds are preferred to circumvent HCl and chlorine removal from the off-gas and to avoid post-cleaning of the powders. In order to prevent condensation of precursor vapor, the precursor delivery tubes and the reactor are heated above the temperature of the evaporator or bubbler. Product particles are collected on a filter with the aid of a vacuum pump. The flame is surrounded by a quartz glass cylinder in order to achieve stable burning. The outer tube of the reactor can be surrounded by a sheath of nitrogen for flame stabilization.

In diffusion flames, the maximum flame temperature usually occurs at the tip of the cone-shaped flame front, where aggregates fuse [32]. Upon leaving the flame, the temperature drops quickly and particles continue to coagulate while sintering takes place at much lower rates. In many systems, the characteristic time for coalescence is longer or in the same order as the characteristic time for coagulation, resulting in aggregates consisting of a few to many thousands of primary particles [33]. The characteristics of the product particles such as the morphology, crystallinity and size strongly depend on the precursor concentration, temperature profile and residence time distribution in the flame.

3.1 Current State of Research

The current state of research in this field has been recently reviewed by Pratsinis [8] and Wooldridge [9] so that here only the keypoints are reported. Fumed silica became industrially important in the 1940s as a substitute for carbon black [11] and was first marketed under the name "Aerosil" by Degussa AG [34]. Flame technology was soon also applied in the manufacture of titanium dioxide from $TiCl_4$ as precursor (chloride process) to replace the wet-chemistry-based sulfate process [11]. The manufacture of uranium dioxide by oxidation of uranium hexafluoride in a flame became the third industrially important flame process with high potential to replace its wet precipitation counterpart [11]. The flame generation of UO_2, as described by Federer et al. [35], yields powders of high purity which can be pressed and sintered to form fuel pellets for nuclear reactors.

Paralleling the growing industrial importance of the flame processing of chemicals in the mid-20th century, research in this field was first led by industrial laboratories. Emphasis was placed on burner design and use of additives [8]. The early patent race in flame technology for the synthesis of TiO_2 and SiO_2 was superbly summarized by Mezey [36].

The establishment of flame technology in industry stimulated a number of research issues in academia. Especially Ulrich and co-workers [37, 38, 39, 40] along with Formenti et al. [41] pioneered research on flame synthesis of ceramic powders. The group of Ulrich studied the synthesis of SiO_2 by $SiCl_4$ oxidation in premixed laminar and turbulent jet flames. Thereby, they recognized that coagulation rather than nucleation was the dominant particle formation mechanism and that the size distributions of the product particles were self-preserving [42]. These early studies revealed that the appearance of aggregates of primary particles results from the competition between particle collision and sintering [39].

In the mid-1980s an idea already mentioned in a 1936-patent by Corning Glass Works, New York, [43, 44] further accelerated research in the field: the deposition of flame-generated silica to form transparent articles of high purity led to the introduction of flame reactors in the large-scale manufacture of optical fiber preforms [29]. Today, the production of optical waveguide preforms which are used to draw hair-thin fibers is one of the most profitable processes of Corning Inc. In academia, opposed jet (counterflow) diffusion flame reactors were introduced by Chung and Katz [45] for the synthesis of oxide powders. The flat and stable flame of the burner exhibits uniform temperature and species concentration distributions in the horizontal plane, thus allowing a precise tracing of particle formation. The importance of sintering in oxide particle formation was demonstrated by Helble and Sarofim [46] while investigating fly ash formation during coal combustion. Hurd and Flower [47] introduced fractal concepts to describe the structure of the resulting silica aggregates from a laminar premixed methane flame. Koch and Friedlander [33] presented a simple but elegant model describing the formation of non-spherical particles by coagulation and sintering.

Renewed interest in flame technology for the manufacture of advanced materials intensified research in the field since the early 1990s. Mixed-oxide systems

such as SiO_2-GeO_2, Al_2O_3-TiO_2, and V_2O_5-Al_2O_3 were studied by Hung, Miquel and Katz [48, 49, 50], while Zachariah and co-workers [51, 52] made superparamagnetic nanoparticles in a premixed methane-oxygen flame. When synthesizing submicron $YBa_2Cu_3O_7$ particles in an oxy-hydrogen diffusion flame reactor, Zachariah and Huzarewicz [53] found that the flame configuration may have a profound effect on the product powder properties. Pratsinis et al. [54] observed that by merely altering the position of fuel and oxidant streams in diffusion flame reactors, the average particle size of product titania powders can be changed by as much as a factor of ten.

As a result, great emphasis was placed on determining the role of flame process variables such as flame configuration, temperature, oxidant composition, and precursor type. For example, Lindackers et al. [55] made titania and silica particles in low-pressure, premixed oxy-hydrogen flat flames. This flame configuration resulted in enlarged reaction zones compared to standard-pressure flames and allowed them to observe the formation of titania particles. Of all variables, temperature probably has the most drastic effect on the process and product characteristics. Bautista and Atkins [29] found that hydrolysis is the main route for $SiCl_4$ conversion at low temperatures, while oxidation is the dominating mechanism at high temperatures. Hung and Katz [48] found that increasing flame temperatures resulted in high concentrations of fine particles during the synthesis of SiO_2 and TiO_2 in a counterflow diffusion flame reactor. Large temperature gradients can generate strong thermophoretic forces on the newly formed particles, drastically altering their residence time at the decisive region where nucleation, growth, coagulation and sintering occur, thus affecting the morphology of flame-made particles [56]. Today, oxides such as SiO_2, TiO_2, Al_2O_3, ZrO_2, V_2O_5, and most other oxides of metal elements in the periodic table and their composites have been produced in powder form in hydrocarbon flames on a laboratory scale [8, 27].

3.2 Control of Particle Properties

The size and morphology of flame-synthesized particles depend on the structure and properties of the flame. The most important parameters are the temperature field of the flame, the particle residence time and, for diffusion flame reactors, the mixing of precursor and oxidant. These parameters depend on the reactor geometry and the gas flow rates into the burner.

The advantage of co-flow diffusion flame reactors regarding their flexibility in reactant mixing is illustrated in **Figure 5** by the example of titania synthesis from $TiCl_4$ [54] along with the corresponding temperature fields of the flame calculated by computational fluid dynamics [57]. Different flame configurations referred to as the A, B, C, or D-flame were achieved by introducing the reactants through different ports of the burner. As can be seen from **Figure 5**, the particle size and morphology change drastically with the mode of mixing. Double-diffusion flame A produces the finest TiO_2 particles with an average primary particle diameter of about 10 nm. Here, the precursor stream is diluted with air prior to its oxidation in the flame and the particles experience rather low temperatures [8, 54]. In double-diffusion flame B, the mixing of precursor and air streams takes place further downstream of the burner, resulting in particles larger than those of flame A. In the single-diffusion flame C, mixing of precursor vapor and methane takes place much earlier than in flames A and B [57]. The newly formed particles experience higher temperatures than in flames A and B with the temperature maximum being at the middle of the flame. As a result, sintering is rapid, creating large non-aggregate particles ($\approx$ 80 nm in diameter) as shown by TEM and proven by small-angle X-ray scattering [58]. Titania particles synthesized in single-diffusion flame D are a bit larger than those synthesized in flame C. Flowing methane through the center tube results in a narrow flame front and high flame temperatures, leading to fast sintering rates and large particles with a low degree of

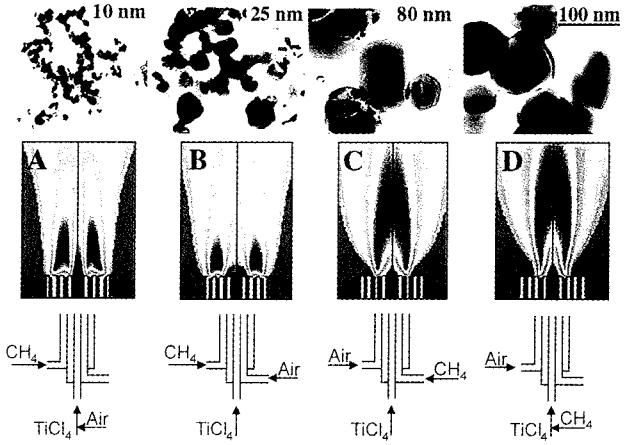

Fig. 5 Influence of the flame configuration on the morphology of titania particles synthesized with a diffusion flame reactor [54]. The center tube diameter of this burner is 4 mm and the spacing between the successive tubes is 1 mm. Temperature profiles of the double-diffusion flames A, B, as well as those of single-diffusion flames C and D are calculated by computational fluid dynamics (CFD) and are adapted from Johannessen [57]. The reactant mixing leads to control of primary particle size up to a factor of 10.

aggregation. By using pure oxygen instead of air as the oxidant, the flame can even produce non-aggregated, perfectly spherical particles [59], as is shown in **Figure 6**.

For a given flame configuration, the oxygen flow rate as well as the choice of the precursor compound affects the size and morphology of flame-generated nanoparticles by altering the temperature field of the flame and gas mixing properties [60]. Our recent work on a diffusion flame reactor operated in C-flame configuration, as in **Figure 5**, shows that the specific surface area of silica particles increases from 40 to about 200 m^2/g when the oxygen flow rate is increased from 1000 to 12000 cm^3/min (**Figure 7**). The average BET-equivalent particle diameters range from 63 to about 13 nm. Also, the degree of aggregation is reduced when the oxygen flow rate is decreased from 8000 to 2000 cm^3/min.

Electric charges offer another tool for the control of the characteristics of flame-made powders. Electric fields applied across a particle-generating flame charge the newly formed nanosized particles. As a result, the coagulation rate of these particles is reduced in the high temperature region of the flame. Furthermore, particles are removed from the flame toward the external electrodes by electrophoresis. In premixed [61, 62] and diffusion flames [63] making titania, tin oxide, silica, and even carbon or silicon-carbon composites [64, 65], the aggregate and primary particle size decrease proportionally to the applied electric field strength. **Figure 8** shows the average primary particle diameter of titania particles as a function of the applied electric field intensity across the flame together with TEM micrographs and pictures of the premixed flame. As can be seen, the average primary and aggregate size of these powders can be narrowly controlled by applying external electric fields across the flame. Recently, it was demonstrated by Kammler and Pratsinis [66] that electric fields can also be applied for the control of fumed silica particle properties when the production rate of a lab-scale burner was increased from a few grams per hour to almost 100 g/h. Kammler and Pratsinis further confirmed that the location of the electrodes with respect to the flame is a decisive factor in electrically-assisted flame aerosol synthesis [63]. Thus, electric fields provide the unique opportunity for making powders of closely controlled size, composition and morphology.

The introduction of additives or dopants in particle-generating flames is widely practiced in industry as they can have a profound effect on particle formation and growth mechanisms and subsequently on the

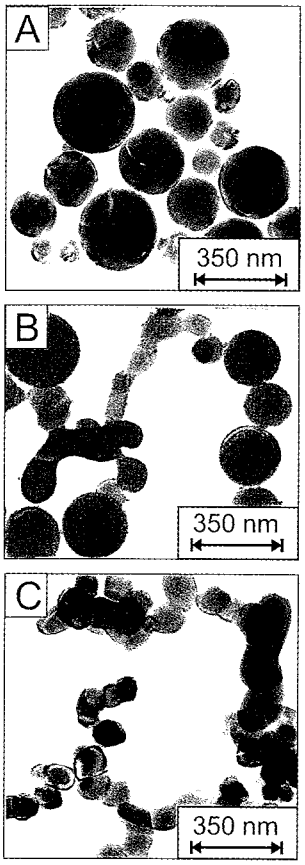

Fig. 6 Influence of oxidant composition on the morphology of flame-synthesized titania particles by $TiCl_4$ oxidation, using: a) pure oxygen, b) 50% nitrogen, c) air as oxidant. Pure oxygen accelerates combustion leading to the highest temperature and synthesis of perfectly spherical non-aggregated particles. Adapted from Zhu and Pratsinis [59].

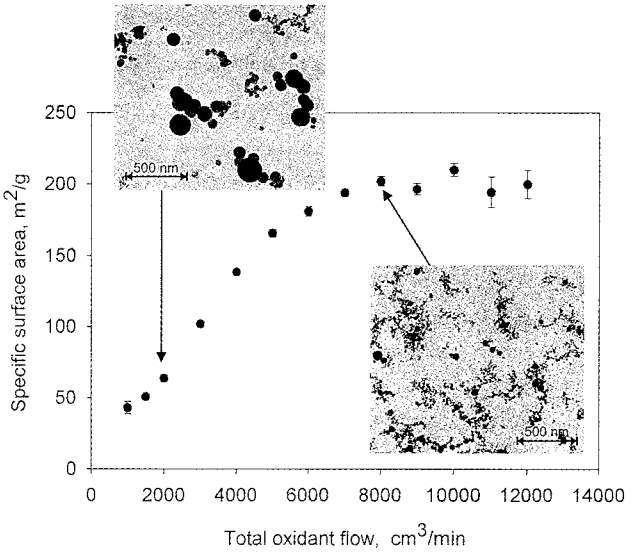

Fig. 7 Specific surface area of fumed silica determined by liquid nitrogen adsorption as a function of oxidant flow rate. TEM micrographs show the effect of oxygen flow rate on product particle morphology. Increasing oxidant flow rate lowers the particle residence time at high temperature leading to smaller nanoparticles.

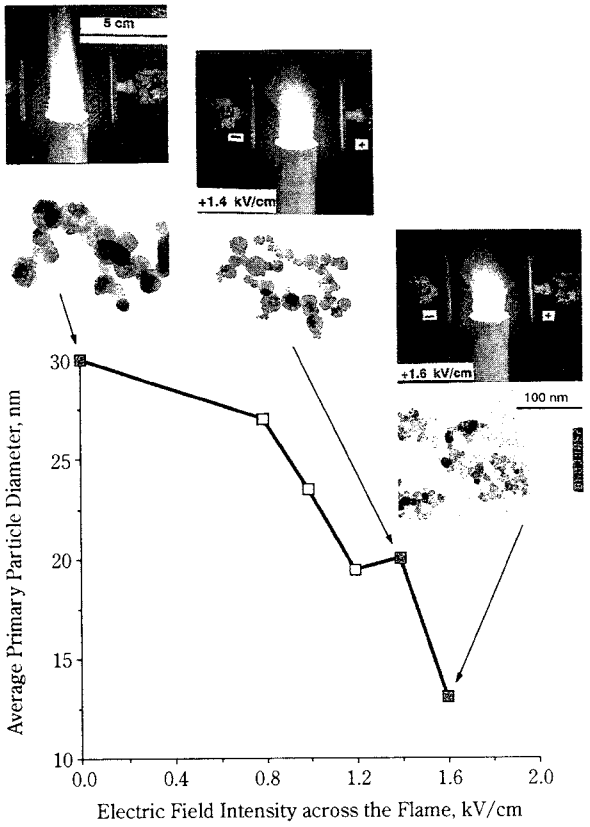

Fig. 8 Influence of the electric field of plate electrodes on the average primary particle diameter and morphology of titania particles made by $TiCl_4$ oxidation. Increasing the electric field strength from 0 to 1.6 kV/cm reduces the primary particle size from 30 to 13 nm as charges slow down coagulation and particle growth. [Pictures courtesy of S. Vemury, Lucent Technologies.]

product particle characteristics. Additives are used as a means to control the crystallinity (e.g. Si or Al in TiO_2 for anatase or rutile) or the morphology (e.g. K in carbon blacks) of the powders. Vemury and Pratsinis [67] added $SiCl_4$, $SnCl_4$, and $AlCl_3$ to a titaniumtetrachloride precursor stream and investigated the effect of these additives on the phase composition, morphology and size of titania particles synthesized in a laminar diffusion flame. They found that the introduction of the silica-precursor inhibits the titania phase transformation from anatase to rutile, decreases the primary particle size, and, as a result, increases the specific surface area. These observations parallel those of Akhtar et al. [68], who had shown how Si, P or B create interstitial defects in the anatase lattice of titania made in a tubular hot-wall reactor. However, when $SnCl_4$ or $AlCl_3$ were used as dopants [67], the phase transformation of anatase to rutile was enhanced and the specific surface area was decreased in agreement with Akhtar et al. [69], who had shown how Al creates substitutional defects in the titania lattice.

Regarding flame synthesis of silica, the role of ferrocene on product particle properties was investigated by Fotou et al. [70]. The presence of ferrocene increased the specific surface area of silica up to 150% and removed the coarse tail of the silica aggregate size distribution. Retardation of coagulation by charging effects was found to be a possible explanation of these results. As was briefly pointed out, the use of additives and dopants in the flame synthesis of ceramic powders provides another means to control particle properties, especially when high purity of the product powders is not a concern.

3.3 Diagnostics

Combustion models and computational fluid dynamics (CFD) as well as state-of-the-art flame diagnostics are powerful tools for better understanding particle formation and growth mechanisms in the flame. Johannessen et al. [71] developed a computational fluid dynamics model of temperature, velocity and gas composition in a diffusion flame and combined it with a simple model for coagulation and coalescence of aerosol particles. By comparing the results with temperature measurements throughout the flame and analysis of alumina product particles and their size distribution, they gained insight into the fundamental flame synthesis mechanisms. Current efforts are toward an integration of particle dynamics models into CFD-codes as indicated in the recent works of Schild et al. [10] and Pyykönen and Jokiniemi [72]. While Schild et al. integrated a monodisperse aerosol dynamics model [73] into fluid mechanics for the simulation of titania formation from $TiCl_4$ in a tubular aerosol flow reactor, Pyykönen and Jokiniemi [72] introduced a computational-fluid-dynamics-based sectional aerosol model to simulate aerosol formation in a laminar flow reactor.

Non-intrusive diagnostic tools for flame temperature, velocity and species concentration provide the means to both verifying the CFD simulations of flames and to providing an accurate and detailed database characterizing the environment for particle formation and growth models. Concerning flame velocities, 3-phase Laser-Doppler Anemometry (LDA) has already been applied extensively to characterize laminar and turbulent flames. The results obtained from non-particle generating flames using micrometer-sized pigmentary titania or zirconia as seeds might be directly applicable to flame reactors, since their low precursor concentrations should not alter the velocity field significantly. Flame temperature measurements are usually done in the absence of precursor (e.g. Chung and

Katz [45]) since particles either deposit on thermocouple probes or, for non-intrusive laser diagnostic methods, the interference of the response signal with particulate matter weakens the signal intensity. The oxidation especially of organometallic precursors, however, is highly exothermic and can constitute a large fraction of the overall combustion enthalpy of the flame [60]. Thus, adding the precursor to a flame is expected to alter its temperature field, making the development of fast and reliable non-intrusive temperature diagnostics for particle-generating flames a necessity in flame aerosol reactor research. In particle-laden low-pressure flames, spatially resolved temperature and OH species concentration were determined by Glumac et al. [74] using laser-induced fluorescence (LIF). One of the few applications of LIF in particle synthesis at atmospheric pressures is the work reported by Zachariah and Burgess [75], who used LIF to measure OH and SiO concentrations and Mie scattering to measure particle distributions during the flame synthesis of silica powders. Such information is of fundamental importance to a better understanding of gas-to-particle conversion processes because gas-phase species determine not only the rate of particle formation, but also the chemical composition of the particles.

Fourier transform infrared (FTIR) spectroscopy has been successfully applied for in-situ temperature and concentration measurements in particle-generating flames operated at atmospheric pressure. Morrison et al. [76] and Arabi-Katbi [77] have shown that FTIR measurements can determine particle temperature and concentrations as well as gas temperatures and concentrations in a premixed methane-oxygen flame for the synthesis of titania powders (**Fig. 9**). The application of FTIR spectroscopy also enables the

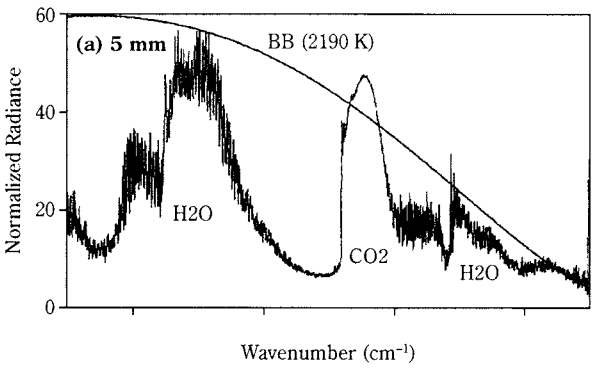

Fig. 9 Normalized radiance spectra of a premixed flame for titania nanoparticle synthesis recorded 5 mm above the burner mouth. The Planck function (blackbody) spectrum (smooth line envelopes) that matches the normalized radiance is also shown. Adapted from Arabi-Katbi [77].

acquisition of in-situ temperatures during flame synthesis of particles in the presence of electric fields as reported by Morrison et al. [76]. Hitherto, process temperatures have not been measured under these conditions since conventional temperature probes such as thermocouples cannot be applied.

Information on the aggregate structure and size of particles during flame growth can be obtained by thermophoretic sampling on transmission electron microscopy (TEM) grids at different flame heights [78]. By rapidly inserting and withdrawing a TEM grid, particles can be collected on the grid by thermophoresis. The method was applied by Arabi-Katbi [77] in a premixed flame, generating titania nanoparticles. **Figure 10a** shows the tip of the sampler through which the grid is inserted into the premixed flame for titania production along the center axis at a height of 3.3 cm above the burner. The corresponding TEM micrograph of titania particles is shown in **Figure 10b**. An average particle size of 42 nm and a standard deviation of 11 nm are obtained by image

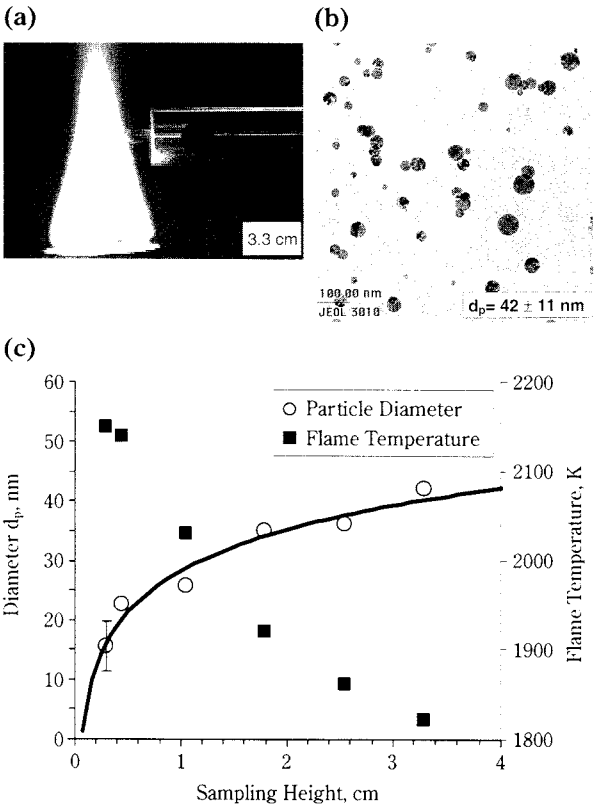

Fig. 10 a), b), c): Thermophoretic sampling in a premixed flame for titania synthesis. The tip of the thermophoretic sampler at a height of 3.3 cm from the burner mouth is presented in Fig. 10a). Fig. 10b) shows a TEM micrograph of particles sampled at this height on the center axis of the flame. The evolution of particle size in the flame is shown in Fig. 10c) together with the centerline temperature profile of the flame. [Pictures courtesy of H.K. Kammler, ETH Zürich.]

analysis. Thermophoretic sampling at different flame heights is perfect for determining the particle growth evolution in this flame (**Figure 10c**).

4. Modeling Particle Dynamics

There is a strong industrial interest in the development of simulators for the aerosol manufacture of nanoparticles. More specifically, mathematical models relating the characteristics of the product powder (size, polydispersity, specific surface area, crystallinity and morphology) to the process variables (reactant state, composition and flow rate as well as reactor geometry) are needed that are based on a sound understanding of particle formation and growth. This is best accomplished by interfacing models for computational fluid dynamics with models for particle dynamics, assuming that the chemistry is fast as it typically is with high-temperature processes dominated by coagulation.

The construction of such a simulator starts with the velocity and temperature profiles in the reactor that can be readily calculated even by commercial software such as CFX or Fluent.

Regarding particle dynamics, moment and sectional representations of the size distribution are employed depending on the required product particle specifications. Moment models make assumptions about the shape of the particle size distribution, allowing the population balance equation to be converted to ordinary differential equations [27]. Lognormal models, for instance, rely on the assumption that the particle size distribution has a lognormal shape throughout the entire system. In sectional models, the particle size distribution is divided into sections in which the characteristics of the particles are described by average values [27]. Typically, the specific surface area (SSA) or an average particle diameter (dp) and polydispersity are key characteristics of the product powder. Assuming that particles are monodisperse further simplifies the population balance equation, making monodisperse models quite attractive for fast calculation of the specific surface area and average particle diameter. For polydispersity, however, either a sectional or lognormal moment model is required. Typically, monodisperse models offer computational simplicity while sectional ones provide detail. Models that distinguish between primary and aggregate particles are attractive such as the one by Kruis et al. [73] that has been widely used. While early models for two-dimensional size (volume-area) distributions [80] required substantial computational time on a supercomputer, recently developed computer codes for sectional models accounting for coagulation and sintering giving both primary and aggregate particle size distribution require far less computational effort and can be run on a personal computer without loss of accuracy [79]. An introduction to particle dynamics models, discussing the advantages and disadvantages of different approaches and giving numerous literature references on the topic, has been recently published by Kodas and Hampden-Smith [27].

The availability of these simulators can break the Edisonian cycle for the process design of aerosol reactor units and can lead to optimal reactor design and operation, because it is possible to achieve better process control for existing products since the models make apparent which process variables most effectively determine the powder characteristics. Second, a simulator can accelerate scale-up for the manufacture of new products as it provides a much better starting point for selection of process conditions. Third, a simulator assists in minimizing the down time of existing production lines as it can reveal process conditions prone to particle deposition on reactor walls. Fourth, simulators can point out conditions for better process yields that translate in money and energy savings. Finally, simulators can assist in the training of new scientists and engineers for research and development as well as engineers and reactor operators at reaction sites, thus contributing to safety and environmental compliance.

Running these simulators can be quite revealing as they can identify problematic regions in the reactors involving either hot spots or dead volumes. As the volume fraction of particles in the suspension is typically up to 0.001, the fluid and particle dynamics can be separated. If chemical reactions are fast, as is usually the case with high-temperature processes, they can be neglected and the particle dynamics can be superimposed on the velocity and temperature profiles calculated by the commercial computational fluid dynamics simulators. This was successfully done for the synthesis of titania in hot-wall reactors [10], in flame synthesis of alumina [71] and titania [57] using a simple monodisperse model for aggregate dynamics by coagulation and sintering [73]. Furthermore, the synthesis of Pd metal nanoparticles by evaporation-condensation in jet flow condensers has been simulated by interfacing Fluent with a monodisperse model for particle dynamics [81]. These models [10] have been quite successful in industry, as was reported by A. Gutsch [82], since they predicted the specific surface area of the product powder within 3%.

The early success of simulators has motivated research in the further development of diagnostic tools for verification as well as more accurate models that account for the full size distribution and the detailed chemistry. This, however, dramatically increases computational demands, motivating research for the efficient design of algorithms for these simulators. Nevertheless, the availability of data describing the detailed evolution of the particle size distribution by thermophoretic sampling, and computerized image analysis coupled with accurate temperature and velocity measurements creates the foundation for rigorous testing of models and hypotheses.

5. Concluding Remarks

Flame aerosol synthesis is a versatile technology to manufacture nanoparticles with well-defined properties. Reactant gas mixing, electric charges or dopants can be used to control the size, morphology, crystallinity and phase composition of product powders. Many diagnostic tools used in combustion research can be adapted for aerosol flame reactors, yielding important information for the understanding of particle formation and growth processes in flames. These data describing the flame environment and the stages of particle synthesis are also of great value for the validation of particle dynamic models. Recent studies show that the combination of flame diagnostics, computational fluid dynamics and particle dynamic models is an effective way to improve the understanding of flame synthesis of nanoparticles and to break the cycle of Edisonian research in this field. Gas-phase combustion technology produces some of the cheapest ceramic powders today and has high potential to provide tailor-made nanoparticles for new and commercially viable applications. Having a low-cost starting material (nanoparticles) will certainly accelerate the development of nanotechnology in the future.

Acknowledgements

Support by ETH-Gesuch Nr. 33/99-2 and Bayer AG (Dr. Claus Riehle, Leverkusen, Germany) is acknowledged.

References

1) Pratsinis, S.E.; Mastrangelo, S.V.R.: "Material Synthesis in Aerosol Reactors", *Chem. Eng. Prog.* **85** (1989), 62-66.
2) Andres, R.P.; Averback, R.S.; Brown, W.L.; Brus, L.E.; Goddard, W.A.; Kaldor, A.; Louie, S.G.; Mascovits, M.; Peercy, P.S.; Riley, S.J.; Siegel, R.W.; Spaepen, F.; Wang, Y.: "Research opportunities on cluster and cluster-assembled materials – A Department of Energy, Council of Materials Science Panel Report", *J. Mater. Res.* **4** (1989), 704-736.
3) Gleiter, H.: "Nanocrystalline materials", *Prog. Mater. Sci.* **33** (1989), 223-315.
4) Ichinose, N.; Ozaki, Y.; Kashu, S.: "Superfine Particle Technology", Springer Verlag, London (1992).
5) Buffat, P.; Borel, J.P.: "Size effect on the melting point of gold particles", *Phys. Rev. A* **13** (1976), 2287.
6) Kruis, F.E.; Fissan, H.; Peled, A.: "Synthesis of nanoparticles in the gas phase for electronic, optical and magnetic applications – a review", *J. Aerosol Sci.* **29** (1998), 511-535.
7) Siegel, R.W.; Ramasamy, S.; Hahn, H.; Gronsky, R.; Li, Z.Q.; Lu, T.: "Synthesis, characterization, and properties of nanophase TiO_2", *J. Mater. Res.* **3** (1988), 1367-1372.
8) Pratsinis, S.E.: "Flame aerosol synthesis of ceramic powders", *Prog. Energy Combust. Sci.* **24** (1998), 197-219.
9) Wooldridge, M.S.: "Gas-phase combustion synthesis of particles", *Prog. Energy Combust. Sci.* **24** (1998), 63-87.
10) Schild, A.; Gutsch, A.; Mühlenweg, H.; Pratsinis, S.E.: "Simulation of nanoparticle production in premixed aerosol flow reactors by interfacing fluid mechanics and particle dynamics", *J. Nanoparticle Res.* **1** (1999), 305-315.
11) Ulrich, G.D.: "Flame synthesis of fine particles", *Chem. Eng. News* **62** (1984), 22-29.
12) Alam, M.K.; Flagan, R.C.: "Controlled nucleation aerosol reactors – production of bulk silicon", *Aerosol Sci. Technol.* **5** (1986), 237-248.
13) Akhtar, M.K.; Xiong, Y.; Pratsinis, S.E.: "Vapor synthesis of titania powder by titanium tetrachloride oxidation", *AIChE J.* **37** (1991), 1561-1570.
14) Yatsuya, S.; Kasukabe, S.; Uyeda, R.: "Formation of ultrafine metal particles by gas evaporation technique. I. Aluminium in helium", *Jap. J. Appl. Phys.* **12** (1973), 1675-1684.
15) Granqvist, C.G.; Buhrman, R.A.: "Ultrafine metal particles", *J. Appl. Phys.* **47** (1976), 2200-2219.
16) Girshick, S.L.; Chiu, C.P.; Muno, R.; Wu, C.Y.; Yang, L.; Singh, S.K.; McMurry, P.H.: "Thermal plasma synthesis of ultrafine iron particles", *J. Aerosol Sci.* **24** (1993), 367-382.
17) Vissokov, G.P.; Stefanov, B.I.; Gerasimov, N.T.; Oliver, D.H.; Enikov, R.Z.; Vrantchev, A.I.; Balabanova, E.G.; Pirgov, P.S.: "Plasmachemical technology for high-dispersion products", *J. Mater. Sci.*, **23** (1988), 2415-2418.
18) Bauer, R.A.; Becht, J.G.M.; Kruis, F.E.; Scarlett, B.; Schoonman: "Laser synthesis of low-agglomerated submicrometer silicon-nitride powders from chlorinated silanes", *J. Am. Ceram. Soc.* **74** (1991), 2759-2768.

19) Johnston, G.P.; Muenchausen, R.; Smith, D.M.; Fahrenholz, W.; Foltyn, S.: "Reactive laser ablation synthesis of nanosize alumina powder", *J. Am. Ceram. Soc.* **75** (1992), 3293-3298.
20) Hahn, H.; Averback, R.S.: "The production of nanocrystalline powders by magnetron sputtering", *J. Appl. Phys.* **67** (1990), 1113-1115.
21) Lukasiewicz, S.J.: "Spray-drying of ceramic powders", *J. Am Ceram. Soc.* **72** (1989), 617-624.
22) Messing, G.L.; Zhang, S.C.; Jayanthi, G.V.: "Ceramic powder processing by spray pyrolysis", *J. Am. Ceram. Soc.* **76** (1993), 2707-2726.
23) Bickmore, C.R.; Waldner, K.F.; Treadwell, D.R.; Laine, R.M.: "Ultrafine spinel powders by flame spray pyrolysis of a magnesium aluminum double alkoxide", *J. Am. Ceram. Soc.* **79** (1996), 1419-1423.
24) Borra, J.P.; Camelot, D.; Marijnissen, J.C.M.; Scarlett, B.: "A new production process of powders with defined properties by electrohydrodynamic atomization of liquids and post-production electrical mixing", *J. Electrostat.* **40** (1997), 633-638.
25) Mahoney, J.F.; Taylor, S.; Perel, J.: "Fine powder production using electrohydrodynamic atomization", *IEEE Trans. Ind. Appl.* **23** (1987), 197-204.
26) McGrath, P.J.; Laine, R.M.: "Theoretical process-development for freeze-drying spray-frozen aerosols", *J. Am. Ceram. Soc.* **75** (1992), 1223-1228.
27) Kodas, T.T.; Hampden-Smith, M.: "Aerosol Processing of Materials", Wiley-VCH, New York, (1999).
28) Friedlander, S.K.: "Smoke, Dust and Haze", 2nd ed., Oxford University Press, New York, (2000).
29) Bautista, J.R.; Atkins, R.M.: "The formation and deposition of SiO_2 aerosols in optical fiber manufacturing torches", *J. Aerosol Sci.* **22** (1991), 667-675.
30) Calcote, H.; Felder, W.; Keil, D.G.; Olson, D.B.: "A new flame process for synthesis of Si_3N_4 powders for advanced ceramics", *23rd Int. Symposium on Combustion*, The Combustion Institute, Pittsburgh (1990), 1739-1744.
31) Zhao, G.Y.; Revankar, V.V.S.; Hlavacek, V.: "Preparation of tungsten and tungsten carbide submicron powders in a chlorine-hydrogen flame by the chemical vapor-phase reaction", *J. Less Common Metals* **163** (1990), 269-280.
32) Zhu, W.; Pratsinis, S.E.: "Synthesis of SiO_2 and SnO_2 particles in diffusion flame reactors", *AIChE J.* **43** (1997), 2657-2664.
33) Koch, W.; Friedlander, S.K.: "The effect of particle coalescence on the surface area of a coagulating aerosol", *J. Colloid Interface Sci.* **140** (1990), 419-427.
34) Kloepfer, H.: "Verfahren zur Herstellung von feinverteilten Oxyden", German Patent DE 830,786 (1949).
35) Federer, J.I.; Robinson Jr., W.C.; Patterson, F.H.: "Conversion of UF_6 to UO_2 in a flame reactor", *Nuclear Appl.* **6** (1969), 298-306.
36) Mezey, E.J.: "Pigments and reinforcing agents" in *Vapor Deposition,* C.F. Palmer, J.H. Oxley, J.M. Blocher Jr. (Eds.), John Wiley & Sons, New York (1966).
37) Ulrich, G.D.: "Theory of particle formation and growth in oxide synthesis flames", *Combust. Sci. Technol.* **4** (1971), 47-57.
38) Ulrich, G.D.; Milnes, B.A.; Subramanian, N.S.: "Particle growth in flames. II: Experimental results for silica particles", *Combust. Sci. Technol.* **14** (1976), 243-249.
39) Ulrich, G.D.; Subramanian, N.S.: "Particle growth in flames. III. Coalescence as a rate-controlling process", *Comb. Sci. Technol.* **17** (1977), 119-126.
40) Ulrich, G.D.; Riehl, J.W.: "Aggregation and growth of submicron oxide particles in flames", *J. Colloid Inter. Sci.* **87** (1982), 257-265.
41) Formenti, M.; Juillet, F.; Meriaudeau, P.; Teichner, S.J.; Vergnon, P.: "Preparation in a hydrogen-oxygen flame of ultrafine metal oxide particles", *J. Colloid Interface Sci.* **39** (1972), 79-89.
42) Friedlander, S.K.; Wang, C.S.: "The self-preserving distribution for coagulation by Brownian motion", *J. Colloid Interface Sci.* **22** (1966), 126.
43) Corning Glass Works, "Verfahren zur Herstellung von durchsichtigen Gegenständen aus Kieselsäure", German Patent #638 955 (1936).
44) Hyde, J.F.: "Method of making a transparent article of silica", US-Patent 2272342 (1942).
45) Chung, S.L.; Katz, J.L.: "The counterflow diffusion flame burner: A new tool for the study of the nucleation of refractory compounds" *Combust. Flame* **61** (1985), 271-284.
46) Helble, J.J.; Sarofim A.F.: "Factors determining the primary particle size of flame-generated inorganic aerosols", *J. Colloid Interface Sci.* **128** (1989), 348-362.
47) Hurd, A.J.; Flower, W.L.: "In-situ growth and structure of fractal silica aggregates in a flame", *J. Colloid Interface Sci.* **122** (1988), 178-192.
48) Hung C.H.; Katz, J.L.: "Formation of mixed oxide powders in flames: Part I. TiO_2-SiO_2", *J. Mater. Res.* **7** (1992), 1861-1869.
49) Hung, C.H.; Miquel, P.F.; Katz, J.L.: "Formation of mixed oxide powders in flames: 2. SiO_2-GeO_2 and Al_2O_3-TiO_2", *J. Mater. Res.* **7** (1992), 1870-1875.
50) Miquel, P.F.; Hung, C.H.; Katz, J.L.: "Formation of V_2O_5-based mixed oxides in flames", *J. Mater Res.* **8** (1993), 2404-2413.
51) Zachariah, M.R.; Aquino, M.I.; Shull, R.D.; Steel, E.B.: "Formation of superparamagnetic nanocomposites from vapor-phase condensation in a flame", *Nanostruc. Mat.* **5** (1995), 383-392.
52) McMillin, B.K.; Biswas, P.; Zachariah, M.R.: "In-situ characterization of vapor phase growth of iron oxide-silica nanocomposites: 1. 2-D planar laser-induced fluorescence and Mie imaging", *J. Mater. Res.* **11** (1996), 1552-1561.
53) Zachariah, M.R.; Huzarewicz, S.: "Aerosol processing of YBaCuO superconductors in a flame reactor", *J. Mater. Res.* **6** (1991), 264-269.
54) Pratsinis, S.E.; Zhu, W.; Vemury, S.: "The Role of Gas Mixing in Flame Synthesis of Titania Powders", *Powder Technol.* **86** (1996), 87-93.
55) Lindackers, D.; Strecker, M.G.D.; Roth, P.: "Particle formation behavior in H_2/O_2 low pressure flames doped with SiH_4 and $TiCl_4$", *NanoStructured Mater.* **4** (1994), 545-550.

56) Gomez, A.; Rosner, D.E.: "Thermophoretic effects on particles in counterflow laminar diffusion flames", *Combust. Sci. Technol.* **89** (1993), 335-362.
57) Johannessen, T.: "Synthesis of nanoparticles in flames", Ph.D. Thesis, Dept. Chem. Eng., Technical University of Denmark, 2800 Lyngby, Denmark (1999).
58) Hyeon-Lee, J.; Beaucage, G.; Pratsinis, S.E.; Vemury, S.: "Fractal analysis of flame-synthesized nano-structured silica and titania powders using small angle X-ray scattering", *Langmuir* **14** (1998), 5751-5756.
59) Zhu, W.; Pratsinis, S.E.: "Flame synthesis of nanosize particles: Effect of flame configuration and oxidant composition" in *Nanotechnology*, ACS Symposium Series, G.-M. Chow and K.E. Gonsalves Eds., **622** (1996), 64-78.
60) Briesen, H.; Fuhrmann, A.; Pratsinis, S.E.: "The effect of precursor in flame synthesis of SiO_2", *Chem. Eng. Sci.* **53** (1998), 4105-4112.
61) Vemury, S.; Pratsinis, S.E.: "Charging and coagulation during flame synthesis of silica particles", *J. Aerosol Sci.* **27** (1996), 951-966.
62) Vemury, S.; Pratsinis, S.E.; Kibbey, L.: "Electrically-controlled flame synthesis of nanophase TiO_2, SiO_2 and SnO_2 powders", *J. Mater. Res.* **12** (1997), 1031-1042.
63) Vemury, S.; Pratsinis, S.E.: "Corona-assisted flame synthesis of ultrafine titania particles", *Appl. Phys. Lett.* **66** (1995), 3275-3277.
64) Artelt, C.; Sanders, S.; Pratsinis, S.E.; Jenkins, R.G.: "Flame aerosol synthesis of carbon nanoparticles in the presence of electric fields", Proc. Symp. Innovative Processing and Synthesis of Ceramics, Glasses, and Composites, Amer. Ceram. Soc., *Ceram. Trans.* **85** (1997), 27-39.
65) Spicer, P.T.; Artelt, C.; Sanders, S.; Pratsinis, S.E.: "Flame synthesis of composite carbon black – fumed silica nanostructured particles", *J. Aerosol Sci.* **29** (1998), 647-659.
66) Kammler, H.K.; Pratsinis, S.E.: "Electrically-assisted flame aerosol synthesis of fumed silica at high production rates", *Chem. Eng. Process.* **39** (2000), 219-227.
67) Vemury, S.; Pratsinis, S.E.: "Dopants in flame synthesis of titania", *J. Am. Ceram. Soc.* **78** (1995), 2984-2992.
68) Akhtar, M.K.; Pratsinis, S.E.; Mastrangelo, S.V.R.: "Dopants in vapor phase synthesis of titania powders", *J. Am. Ceram. Soc.* **75** (1992), 3408-3416.
69) Akhtar, M.K.; Pratsinis, S.E.; Mastrangelo, S.V.R.: "Vapor phase synthesis of Al-doped titania powders", *J. Mater. Res.* **9** (1994), 1241-1249.
70) Fotou, G.P.; Scott, S.J.; Pratsinis, S.E.: "The role of ferrocene in flame synthesis of silica", *Combust. Flame* **101** (1995), 529-537.
71) Johannessen, T.; Pratsinis, S.E.; Livbjerg, H.: "Computational fluid-particle dynamics for the flame synthesis of alumina particles", *Chem. Eng. Sci.* **55** (2000), 177-191.
72) Pyykönen, J.; Jokiniemi, J.: "Computational fluid dynamics based sectional aerosol modelling schemes", *J. Aerosol Sci.* **31** (2000), 531-550.
73) Kruis, F.E.; Kusters, K.A.; Pratsinis, S.E.; Scarlett, B.: "A simple model for the evolution of the characteristics of aggregate particles undergoing coagulation and sintering", *Aerosol Sci. Technol.* **19** (1993), 514-526.
74) Glumac, N.G.; Chen, Y.J.; Skandan, G.; Kear, B.: "Scalable high-rate production of non-agglomerated nanopowders in low pressure flames", *Mater. Lett.* **34** (1998), 148-153.
75) Zachariah, M.R.; Burgess Jr., D.R.F.: "Strategies for laser-excited fluorescence spectroscopy measurements of gas-phase species during particle formation", *J. Aerosol Sci.* **25** (1994), 487-497.
76) Morrison Jr., P.W.; Raghavan, R.; Timpone, A.J.; Artelt, C.P.; Pratsinis, S.E.: "In situ Fourier Transform Infrared characterization of the effect of electrical fields on the flame synthesis of TiO_2 particles", *Chem. Mater.* **9** (1997), 2702-2708.
77) Arabi-Katbi, O.I.: "Flame synthesis of titania nanoparticles: Analysis using in situ Fourier Transform Infrared (FTIR) Spectroscopy and thermophoretic sampling", M.S. Thesis, Dept. Chem. Eng., University of Cincinnati, Cincinnati, OH., (1999).
78) Dobbins, R.A.; Megaridis, C.M.: "Morphology of flame-generated soot as determined by thermophoretic sampling", *Langmuir* **3** (1987), 254-259.
79) Tsantilis, S.; Pratsinis, S.E.: "Evolution of primary and aggregate particle size distributions by coagulation and sintering", *AIChE J.* **46** (2000), 407-415.
80) Xiong, Y.; Pratsinis, S.E.: "Formation of agglomerate particles by coagulation and sintering: I. A two-dimensional solution of the population balance equation", *J. Aerosol Sci.* **24** (1993), 283-300.
81) Tsantilis, S.; Pratsinis, S.E.; Haas, V.: "Simulation of synthesis of Pd powders in a jet aerosol flow condenser", *J. Aerosol Sci.* **30** (1999), 785-803.
82) Gutsch, A.; Schild, A.; Riemenschneider, H.; Pratsinis, S.E.: 1997 AIChE Meeting, Los Angeles, CA.

Author's short biography

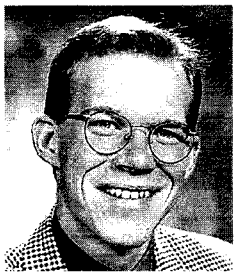

Karsten Wegner

Karsten Wegner graduated in Process Engineering at the University of Karlsruhe, Germany, in 1998, majoring in thermal and mechanical process technology. After carrying out his Diploma thesis on zeolite membranes for isomer separation at the University of Cincinnati, USA., he started working on a Ph.D project in Prof. Pratsinis' group for fine particle research at the Swiss Federal Institute of Technology in Zürich. His project deals with the synthesis of metal and ceramic nanoparticles in hot wall and flame reactors. The emphasis of the work is placed on formation of metal oxide nanoparticles in aerosol flame reactors.

Sotiris E. Pratsinis

Prof. Pratsinis received his Diploma in Chemical Engineering (1977) from the Aristotle University of Thessaloniki, Greece and his M.S. (1982) and Ph.D. (1985) from University of California, Los Angeles, USA. He joined the faculty of Chemical Engineering at the University of Cincinnati as Assistant Professor in 1985. There he was promoted to the rank of Associate Professor with tenure in 1989 and to the rank of Professor in 1994 and served as Interim Head until 1998. Then he was elected Professor of Process Engineering at the Department of Mechanical and Process Engineering at ETH Zurich where he is leading a research program on Particle Technology focusing on synthesis and processing of fine powders (http://www.ivuk.ethz.ch/staff/pratsinis/). He has published 100+ refereed papers, book chapters and three patents licensed to Dow Chemical and Hosokawa. His program has been funded largely by the U.S. National Science Foundation, Swiss National Science Foundation and ETH-Projekte as well as by DuPont, Dow Chemical, W.R. Grace, ICI-Tioxide [England], Degussa and Bayer [Germany], Royal Gist Brocades [Netherlands], Genencor, Procter & Gamble, Particle Technology Inc. and Advanced Fuel Co.

Some of the highlights of Prof. Pratsinis' research include the measurement of a fundamental reaction rate for oxidation of $TiCl_4$ vapor for synthesis of titania powder. He and his students developed the first simulator for manufacture of optical fiber preforms that is used now by Lucent Technologies (former AT&T Bell Labs) in manufacture of optical fiber preforms for telecommunications. Prof. Pratsinis and his students also developed, for the first time, algorithms for agglomerate formation and growth relating product particle characteristics to material properties and process conditions through rigorous population balances in particle mass and surface area accounting for gas phase reaction and sintering. Recently he has focused on synthesis of nanoparticles where he has shown how to precisely control the size and structure of these particles from perfectly spherical ones to highly ramified aggregates. Prof. Pratsinis' contributions have been recognized by the 1988 *Kenneth T. Whitby Award* of the American Association for Aerosol Research, the 1989 *Presidential Young Investigator Award* by the U.S. National Science Foundation and the 1995 *Marian Smoluchowski Award* by the Gesellschaft fur Aerosolforschung for his research on Aerosol Reactor Engineering. Since 1991 he is on the Editorial Board of the *Journal of Aerosol Science*, since 1998 in the Editorial Board of the journal of *Powder Technology*, since 1994 a consultant to the *International Fine Particle Research Institute* on Particle Formation and since 1998 Associate Editor of the *Journal of Nanoparticle Research*.

Prof. Pratsinis has received teaching awards at the University of Cincinnati and has taught courses at the Technical University of Delft in the Netherlands, at the University of Queensland in Australia, at the University of Karlsruhe in Germany, at the University of New Mexico, USA. He has given also a number of short courses to industrial and academic audiences. Currently he is teaching Mass Transfer, Particle Technology and Particulate Processes at ETH Zurich in Switzerland.

On-line Characterisation of Aerosols – Comparability and Combination of Selected Measuring Devices†

R. Friehmelt
*Degussa-Hüls AG, Germany**
H. Büttner and F. Ebert
*University of Kaiserslautern, Germany***

Abstract

A scanning mobility particle sizer (SMPS, TSI Model 3934) and a white-light optical particle counter (OPC, as described by Umhauer 1983) are combined. With these two instruments, fast and non-intrusive on-line measurements of particle size distributions in a range of 15 nm up to 15 μm are possible. A filter provides the possibility of taking samples in order to analyse the morphology and chemical composition of the aerosol. Both liquid and solid airborne particles in diluted suspensions can be measured. The complete system is able to cope with particle concentrations of up to 10^7 particles/cm^3 without dilution of the aerosol. Since the measuring principles of the combined devices are based on different physical properties, careful calibration is necessary. Both theoretical calculations and experimental methods are used for calibration purposes. The measuring results of different devices are compared during simultaneous characterisation of several aerosols. The performance of the combined measuring system is demonstrated by means of comparison with a common cascade impactor in the laboratory as well as during industrial application.

Introduction

Particulate emissions are often still characterised solely by mass concentration. In modern environmental technology and with regard to particle separation, however, more detailed data are necessary. Health hazards cannot be quantified solely by respireable mass, but by the physical and chemical properties of the inhaled particles. Fibrous particles of certain dimensions and aspect ratios, for example, are suspected of being carcinogenic with little influence of the bulk material. On the other hand, very fine particles that neither consist of dangerous bulk material nor have a critical shape are able to adsorb relatively high amounts of hazardous substances due to their relatively high specific surface area. Thus, dangerous components can be transported by harmless particles into the deepest regions of the human lung where they may become injurious to health.

Detailed information on particle size distributions and chemical composition is of growing interest, not only concerning human health. The latest developments in particle technology increasingly show the tendency to operate in the submicron and nanometer size range. Especially with new materials, e.g. ceramics, nanoparticles have interesting qualities. The production and handling of nanoparticles as well as the characterisation and design of separators and qualified description of emissions, however, call for high-performance measuring systems.

Optical particle counters that determine particle sizes and concentrations by analysing scattered light have become a common tool in aerosol measurement technology. Devices of the type described by Umhauer (1983) are able to measure particle sizes and concentrations fast, non-intrusively, and on-line. The measurable range of concentrations amounts to between 10 and 10^7 cm^{-3}, which means for spheres of unit density and a diameter of 1 μm, mass concentrations of between approximately 0.005 mg/m^3 and 5 g/m^3.

An important reason not to use white-light optical particle counters in modern emission control systems and during material processing is their relatively high detection limit of approximately 0.5 μm. However, in many emissions most of the emitted particles are

* Process Technology, Postfach 1345, D-63403 Hanau, Germany
**Particle Technology and Fluid Mechanics, Postfach 3049, D-67653 Kaiserslautern, Germany
† Received: August 8, 2000

smaller than this limit. Under environmental aspects especially, these small particles are dangerous to human health.

The goal of our work was to develop a measuring system which is suitable for measurements over a wide range of both particle sizes and concentrations. In order to meet these requirements, the white-light optical particle counter was combined with a scanning mobility particle sizer, the detection limit of which amounts to 15 nm. Thus, a size range from 15 nm up to 15 µm is covered by the combination of the chosen devices.

The main problem with this combined system is uniform calibration. As the scattered light intensity depends on both the bulk material and the particle shape, the optical particle counter had to be calibrated carefully.

Experimental results, e.g. for polystyrene latices and glycerine droplets, were confirmed by *Mie* calculations for spherical particles (Sachweh, 1991). Calibration methods for "aerodynamic" size measurements (Büttner, 1983, 1990; Heidenreich et al., 1995; Friehmelt and Heidenreich, 1999) were applied for non-spherical particles such as quartz dust. The non-sphericity of particles severely affects the shape of the calibration curve.

Experimental results show that the scattered light intensities depend on particle shape as well as on particle orientation (Bottlinger, 1989). Zerull and Killinger (1987) found that the forwards and sideways scattering of larger particles is enhanced by a non-spherical particle shape in comparison with spheres. Experiments with quartz particles have shown that the enhancement of scattered light intensity by particle shape starts at equivalent volume diameters of around 0.5 µm (Friehmelt and Heidenreich, 1999).

The scattered light intensities caused by non-spherical particles in a 90° white-light optical particle counter are simulated by means of a discrete dipole approximation (DDA) code (DDSCAT, Draine, 1998). Calculations were carried out for particle diameters ranging from 0.1 µm to 2 µm in order to cover the size range in which particle shape becomes important to light scattering. DDA simulations with spherical particles were verified by *Mie* calculations which proved the method to be applicable.

A compact and mobile calibration unit was developed in order to be able to calibrate measuring devices on-line. The separation characteristics of the cyclone configurations, which are used in this calibration unit, were determined experimentally with glycerine droplets. A universal grade efficiency curve was specified by applying the dimensionless representation proposed by Büttner (1999). Thus, the calibration unit is applicable to any aerosol.

In order to verify the counting and sizing performance as well as the resolution of the measuring devices used in the combined system, simultaneous measurements were carried out with several aerosol analysers such as an aerodynamic particle sizer, a laser diffraction device, a laser aerosol spectrometer, a condensation particle counter, and a cascade impactor.

The mobility analyser and optical particle counter proved to have high resolution and good classification accuracy. The decreasing counting efficiency of the optical particle counter is taken into account when measuring in combination with the mobility analyser.

Instrumental set-up

The complete system for the characterisation of aerosols is shown in **figure 1**. The collection probe includes a cyclone in order to separate coarse particles which are larger than the upper detection limit of the measuring devices. With the help of an optional ejection dilution system, the sample can be conditioned. Thus, condensation can be avoided and concentrations adapted to meet the requirements of the individual measuring devices.

The optical particle counter used in our investigations is of the type that was first described by Umhauer (1983). The aerosol is illuminated by a white light source. The scattered light intensity of single particles that pass the sensing volume is collected around a scattering angle of 90° and is converted to an electrical pulse by a photomultiplier tube. The pulse height depends on particle size, shape and bulk material, especially the refractive index of the particles, and is used to determine the particle size. Since the

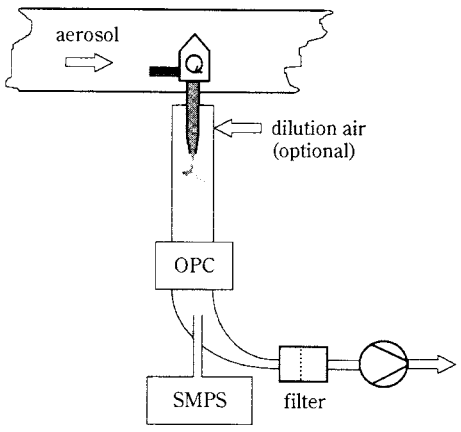

Fig. 1 Schematic of the instrumental set-up of a combined measuring system.

sensing volume is optically defined and the aerosol is not aerodynamically focused, high concentrations can be measured without any dilution (Sachweh et al. 1998). However, the measurable concentration is limited by the counting principle, which rules out the possibility of more than one particle being present in the sensing volume at the same time.

The lower detection limit of the OPC is 0.2−0.5 µm, depending on the specific device. Therefore the scanning mobility particle sizer (SMPS, TSI Model 3934) was chosen to extend the lower detection limit of the combined system down to 15 nm. In the SMPS, the aerosol is electrostatically classified. The concentration in the individual size classes is then determined by a condensation particle counter.

The aerosol sample stream is taken isokinetically and completely drawn through the OPC. Downstream of the OPC, another sample is taken and fed to the SMPS. A filter provides the possibility to either determine the total mass concentration or to take samples for the scanning electron microscope or the X-ray diffractometer in order to analyse the morphology and chemical composition of the aerosol.

The whole set-up was designed to be variable to permit adaptation of the complete system to a wide field of applications as described above. Before the designed set-up could be applied, a lot of problems had to be investigated carefully. The different sensors had to be calibrated uniformly and their accuracy has to be controlled constantly. Concentration measurements had to be verified, and especially the influence of coincidences and the counting efficiency of the optical particle counter was considered (Sachweh et al. 1998). The applicability of the concept was evaluated by means of simultaneous measurements with different sensors both in laboratory and industry.

Calibration

The different measuring devices and varying calibration techniques lead to size distributions which are related to different equivalent diameters. A uniform particle size distribution for the combination of the measuring devices is derived from calculating the equivalent volume diameter d_e of both the mobility diameter d_m and the aerodynamic diameter d_a. The equivalent volume diameter is given by Hinds (1982):

$$d_e = \frac{d_m Cu(d_e)}{\chi Cu(d_m)} \qquad d_e = d_a \left[\frac{\chi Cu(d_a)\rho_o}{Cu(d_e)\rho_p} \right]^{0.5}$$

where Cu is the slip correction, ρ_p is the particle density, ρ_o is unit density (1g/cm^3), and χ is the dynamic shape factor which is defined as the relation of the drag force acting on a particle to the drag force on a volume equivalent sphere of the same velocity.

In a first step, both measuring devices were calibrated by monodisperse fractions of polystyrene latex (PSL) spheres. The accuracy of the SMPS is improved by choosing longer scanning times and depends on the correct determination of the so-called delay time, which takes into account the residence time of the aerosol particles between the classifier and the condensation particle counter.

In the case of the OPC, the experimental results were compared to *Mie* calculations. The transfer characteristic of all optical and electronic components of the OPC proved to be linear. This means that the differential scattering cross-section, which is calculated from *Mie* theory, can be converted to a representative pulse height by multiplication with a constant. If this constant has been determined once, the OPC can be calibrated without any further experiment for any spherical particles of known refractive index (Friehmelt and Heidenreich 1999).

Figure 2 shows the results of experimentally derived and calculated calibration curves for PSL-spheres and glycerine droplets. For spherical particles, good agreement between *Mie* theory and experiment is achieved.

In the case of the experimental calibration with PSL spheres, several monodisperse fractions of PSL were measured and the mode of the intensity distribution was correlated to the given particle size.

With the glycerine droplets, an experimental calibration method was applied which had been proposed by Heidenreich et al. 1995. The particle size distribution of an aerosol, for which the measuring device is to be calibrated, is determined by an aerodynamic particle sizer (APS, TSI Model 3310) and the measur-

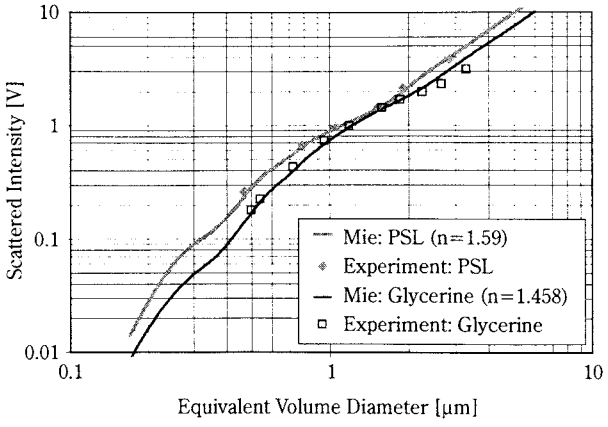

Fig. 2 Experimental calibration of the OPC for PSL spheres and glycerine droplets in comparison with theoretical calibration curves.

ing device itself. The comparison of the different cumulative distributions leads to a calibration curve for aerodynamic particle sizes. This method is also suitable to calibrate the OPC for non-spherical particles. However, since the results of the APS are also influenced by particle shape, the APS has to be calibrated as well.

Figure 3 shows the calibration of the APS for quartz particles. For calibration purposes, a quartz standard (BCR) with certified size distribution was used. By reference, the given and measured cumulative mass were compared and the measured diameter is plotted against the correlating reference diameter. In comparison with our experimental results, some calculated data of Cheng et al. (1990) and measurements published by Marshall et al. (1991) are plotted, which are both valid for a dynamic shape factor of around $\chi=1.19$, while the dynamic shape factor of quartz is approximated by $\chi=1.36$. Our experimental results seem to be in reasonable agreement with literature. The error bars are caused by experimental uncertainties:

- The quartz standard has to be dispersed prior to the measurement. If this redispersion is not complete, the certified size distribution will not be reached.
- The sample includes particles smaller than the lower detection limit of the APS, which may cause "phantom particles".
- The counting efficiency of the APS decreases towards its lower detection limit.
- The certified size distribution of the quartz standard itself includes some variation.

Another method of calibrating measuring devices for "aerodynamic" size measurements is calibration by means of sampling cyclones (Büttner 1983, 1990), which is based on the fact that the median of the grade efficiency of a cyclone is uniquely related to the aerodynamic diameter. The comparison of measured medians of grade efficiency curves with the known separation characteristic of the particular cyclone yields the calibration curve. This method is of special interest because it is mobile and measuring devices can be calibrated on-line. A schematic diagram of a portable calibration unit and a photo of our technical design is shown in **figure 4**.

The results of a calibration of the OPC for quartz dust are shown in **figure 5**. Both calibration methods yield similar results. However, the calibration curve gained by the characterisation of cyclones seems to be shifted to smaller particle sizes.

Irregularly shaped monodisperse particles will cause an intensity spectrum when measured by the OPC, since the scattered light intensity depends on particle

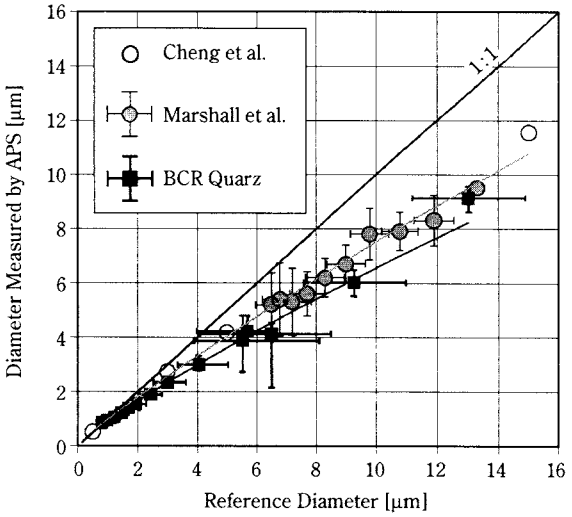

Fig. 3 Calibration of the APS for quartz particles.

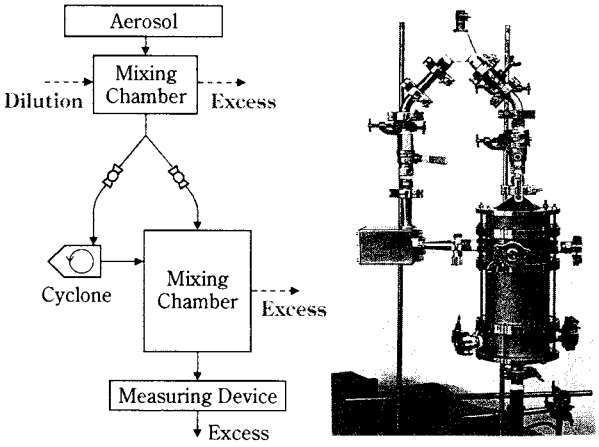

Fig. 4 Portable calibration unit – diagrammatic set-up and technical design.

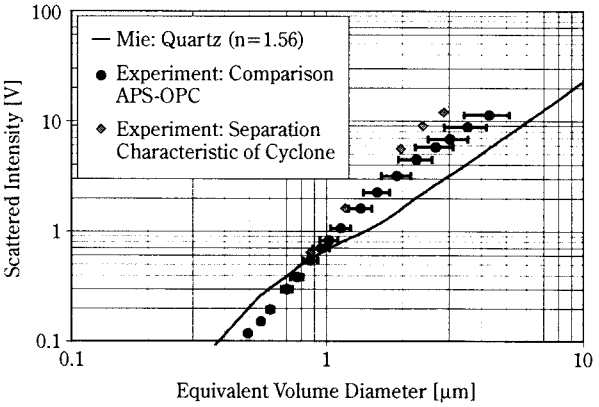

Fig. 5 Calibration of the OPC for quartz particles.

orientation in the sensing volume. In the case of quartz particles, this intensity spectrum will be asymmetric (Bottlinger 1989). These asymmetric intensity spectra lead to a broadening and a shift of measured grade efficiencies (Friehmelt 2000). In the case of

symmetric spectra, the median of the grade efficiency would be measured correctly, and perfect agreement between the different calibration techniques would be achieved.

Due to the irregular particle shape, the scattered light intensity when compared to the calculations for quartz particles under the assumption of spherical shape is increased for larger particles and reduced for smaller particles. In contrast to spherical particles (see **figure 2**), the use of theoretical calibration curves derived by *Mie* calculations will severely falsify the measured size distributions of irregularly shaped particles. In order to simulate the scattered intensities caused by non-spherical particles, numerical methods have to be applied. In our investigations, a discrete dipole approximation code (DDSCAT, Version 5a9, by Draine 1998) was used.

Discrete dipole approximation means that the investigated particle is replaced by an array of point dipoles. Any particle can thus be approximated by a finite number of discrete dipoles. The scattering problem for this array of dipoles is then solved exactly (Draine and Flatau 1994).

The number of dipoles was approximated according to the guidelines given in the user guide for DDSCAT (Draine and Flatau 1998) and checked for each investigated symmetry. The scattered intensity at the detectors of the OPC was calculated from the results for 289 scattering directions which were chosen according to the detection aperture of the OPC. Calculations were carried out under the assumption of parallel incident light. All calculations have to be performed with one discrete illuminating wavelength. The white-light source was approximated by the superposition of seven wavelengths between 300nm and 600nm. The spectral composition of the light source and the spectral sensitivity of the photomultiplier tubes were taken into account when calculating the detected intensity. Using 13 instead of 7 wavelengths with a cube of 1 µm effective diameter leads to a difference in averaged intensity of less than one percent.

Calculations were carried out for particle diameters in the range of 0.1 µm up to 2 µm and for 125 orientations of the particles relative to the incident light beam. In **figure 6**, theoretical calibration curves for some model particles are plotted. The data points are derived from the scattered light intensity averaged over all orientations as an approximation for random orientation of the particles in the sensing volume. Discrete dipole approximation (DDA) with spherical particles is verified by *Mie* calculations. Both scattering calculations lead to the same result. Cubes and rectangular prisms with square cross-section and a ratio of length to width of two to one ("short prism") and five to one ("long prism") served as non-spherical particles. In the case of the prisms, 250 orientations were averaged. From **figures 5** and **6** it is obvious that the tendency of enhanced scattered intensities is modelled correctly by DDA for larger non-spherical particles. No significant difference in scattered intensities between cubes and short prisms was detected. For the long prisms, the scattered intensity seems to be reduced in comparison with cubes and spheres with small particle sizes, which correlates to the observations with quartz particles and calibration by comparison of cumulative size distributions.

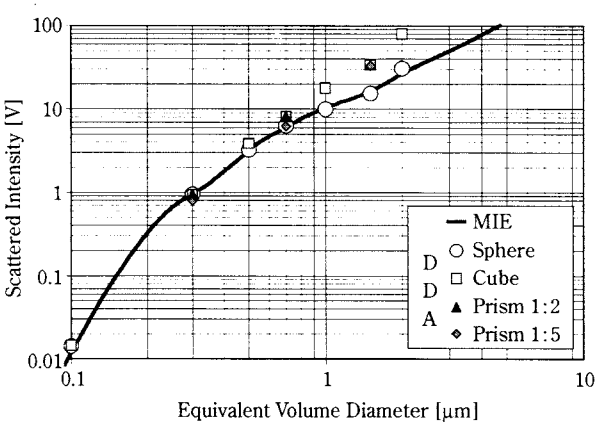

Fig. 6 Calibration of the OPC for regular non-spherical particles gained by DDA calculations.

Another important quality of particle sizing devices is resolution. A single non-spherical particle may cause different scattered intensities depending on its orientation. Instead of a monodisperse size distribution, a broad distribution will be measured. Bottlinger (1989) showed that the relative standard deviation (standard deviation normalised by mean value) of such broadened distributions increases with particle size and growing deviation from spherical shape. **Table 1** shows the relative standard deviations of the model particles, calculated by means of DDA. The relative standard deviations of spheres remains below 0.1 and exhibits no systematic tendency, which confirms that the simulation method yields reasonable results. The

Table 1 Relative standard deviation of intensity spectra caused by regular non-spherical particles in an OPC, simulated by means of DDA.

Volume Equivalent Diameter [µm]	0.1	0.3	0.5	0.7	1	1.5	2
Sphere	0.0014			0.063	0.036	0.082	
Cube	0.013	0.18	0.49	0.69	0.84	1.32	1.82
Prism 1:2		0.63		1.36		1.60	
Prism 1:5	0.79	1.26		1.64	1.78	1.94	

small differences in scattered intensities of a sphere under varying orientations are caused by the incomplete approximation of the spherical shape by a finite number of dipoles. The calculations for non-spherical particles confirm Bottlinger's findings. Relative standard deviations increase with growing particle size and from cube to prism and from the short prism to the longer one (see **table 1**).

DDA calculations with varying detector apertures showed that averaged intensities should not be influenced by neglecting the illumination aperture. However, relative standard deviations of the intensity spectra will be slightly increased by the assumption of parallel illumination.

All the calibration experiments and calculations show that a proper calibration is absolutely essential if different particle sizers are to be compared. Another problem is that size distributions of non-spherical particles are adulterated by the sensing characteristic of almost any aerosol measuring device. Errors caused by the sensing characteristic can be corrected by a suitable inversion algorithm provided that the systematic falsification of measuring results is known. The OPC simulations showed that DDA can serve as a tool to model systematic errors such as the broadening of size distributions caused by non-spherical particles.

Comparison of different measuring devices

Simultaneous measurements with different instruments were carried out both in the laboratory and in industry. In **figure 7** the detection limits of the devices used in our investigations are illustrated. The cascade impactor (Andersen Inc., Type M III) covers a wide size range but has a weak size resolution, and the gravimetric determination of size distributions is time-consuming, and it is restricted to a narrow concentration range and is susceptible to errors. Due to its robust design and the fact that it yields mass concentrations, which are important in emission control, it is often used in industry. Since the size ranges of APS and OPC are very similar and the APS has a high sizing accuracy and resolution (Friehmelt 2000), it is suitable for the experimental calibration of the OPC as described above. A high-sensitivity laser aerosol spectrometer (HS-LAS, PMT GmbH) was applied to check the performance of OPC and SMPS near their detection limits. The SMPS itself was chosen to cover the submicron size range. All measuring devices except for the impactor provide measuring results on-line within seconds (at most three minutes).

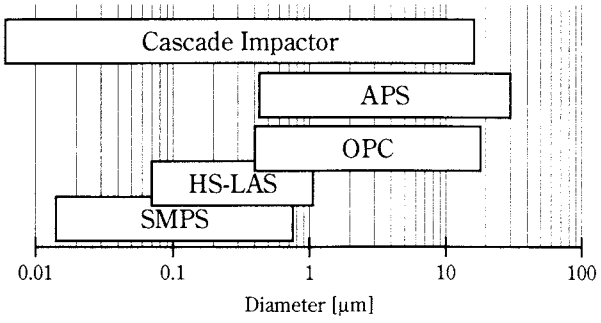

Fig. 7 Detection limits of the investigated measuring devices.

Performance of OPC and SMPS near their detection limits.

The size ranges of OPC and SMPS overlap reasonably. However, especially around the detection limits of the measuring devices, systematic errors may occur. The upper detection limit of the SMPS and the lower detection limit of the OPC were investigated within simultaneous measurements with the HS-LAS. The measurement of particles in ambient air, carried out with OPC, HS-LAS and SMPS simultaneously, are plotted in **figure 8**. In the case of the SMPS, no systematic error was detected – as **figure 8** clearly shows. After proper calibration, HS-LAS and SMPS yield the same result. Good agreement was also achieved with the measuring results of the OPC. In the case of the OPC, however, some additional effects have to be taken into account when optical particle counters are compared with other measuring devices – as **figure 9** shows.

Different monodisperse fractions of polystyrene latex (PSL) spheres were investigated in the overlapping size range between OPC and HS-LAS. The measuring results of three discrete fractions are plotted in **figure 9**. The particle size distributions support agreement and systematic errors. For example, excellent conformity of the particle size distributions measured by OPC and HS-LAS was achieved with 0.356 µm

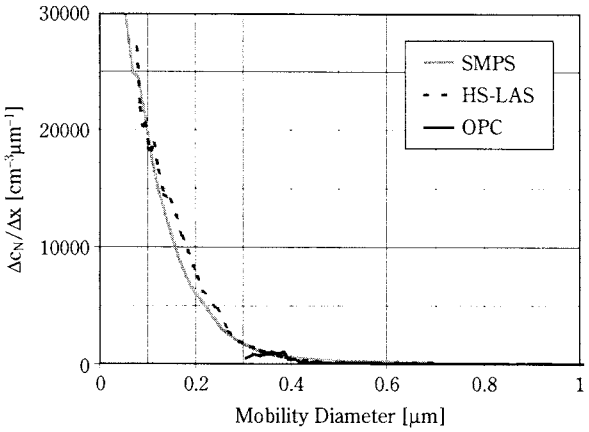

Fig. 8 Simultaneous measurements of particles in ambient air with SMPS, HS-LAS and OPC.

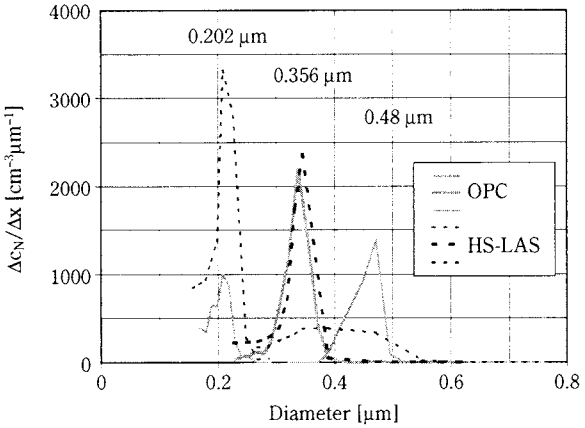

Fig. 9 Simultaneous measurements of three monodisperse fractions of PSL spheres with OPC and HS-LAS.

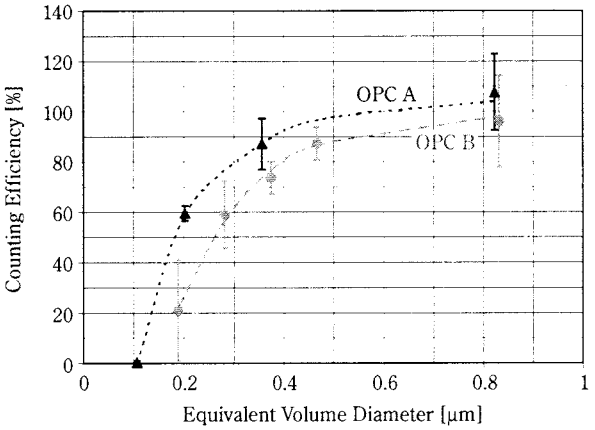

Fig. 10 Counting efficiency of two different OPCs in comparison with a CPC.

latex spheres. Near the detection limits of the sensors, however, measured distributions are adulterated. The upper detection limit of the HS-LAS is given by its calibration curve. For particles larger than d=0.4 µm ambiguities appear and measured distributions are broadened, as measurements of 0.48-µm latex spheres in **figure 9** show. The lower counting efficiency of the OPC can be observed for the 0.2-µm spheres. In order to quantify the counting efficiency of the OPC, the concentrations of monodisperse aerosols were measured with an OPC and a condensation particle counter (CPC) simultaneously. **Figure 10** shows the counting efficiency of two different OPCs compared with the CPC. Type A has a higher illumination intensity, higher detection aperture and lower working distance than type B (Sachweh et al. 1998). As **figure 10** shows, the lower detection limit, which is defined as the 50% counting efficiency, varies for different OPCs. If OPC measurements are to be combined with other measuring devices, the counting efficiency of the specific OPC has to be determined and taken into account when concentrations are compared.

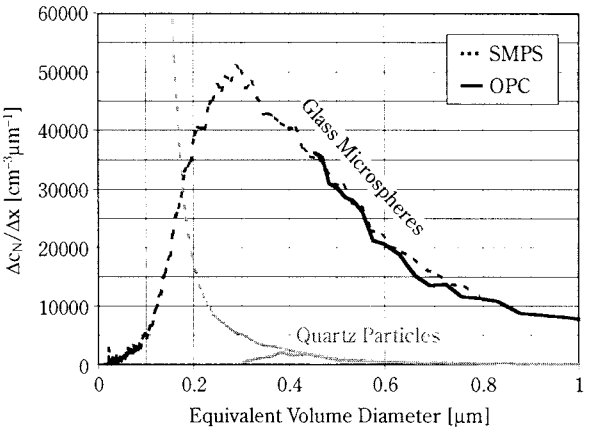

Fig. 11 Simultaneous measurements of glass microspheres and quartz particles with SMPS and OPC.

Combination of OPC and SMPS

After having verified the performance of OPC and SMPS in the size range where both instruments overlap, several simultaneous measurements were carried out with these two devices and different aerosols. As an example, the results for glass microspheres and quartz particles are plotted in **figure 11**. The measured number concentrations in the overlapping size range agree well, provided that the OPC is properly calibrated and the counting efficiency of the OPC is taken into account. The results of the two measuring devices can be combined to a continuous size distribution which covers a size range of three decades.

Combination of OPC and SMPS versus cascade impactor

The advantages of the combined measuring system comprising OPC and SMPS are high resolution both in time and particle size. Reasonable measuring times range from 1 to 3 minutes for the combined system, while an impactor measurement may take hours, depending on the total concentration of the aerosol. Furthermore, results of the combined system are available on-line, while the gravimetric evaluation of impactor measurements is not possible at all on-line. **Figure 12** illustrates the resolution in time for an aerosol of glass microspheres with moderately changing concentration. Changes in concentration can be observed on-line with the combined system, while the impactor yields a mean concentration with an additional delay caused by the evaluation procedure. The mass density of the same glass aerosol is plotted in **figure 13** and demonstrates the higher resolution in particle size of the combined system. In principle, the mass density distribution and total mass concentration agree well, in this case for spherical particles.

Even in the case of non-spherical particles such as

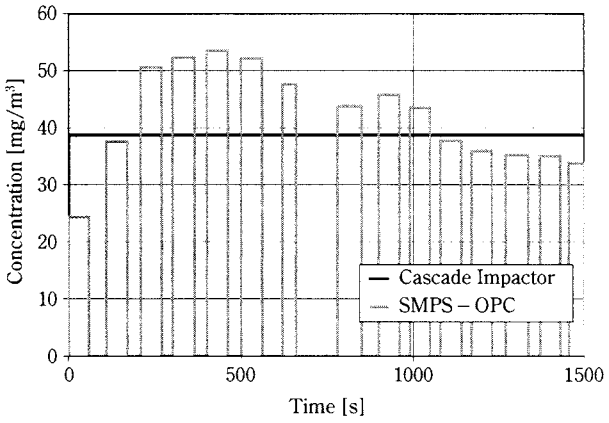

Fig. 12 Resolution in time of cascade impactor in comparison with the combination of SMPS and OPC

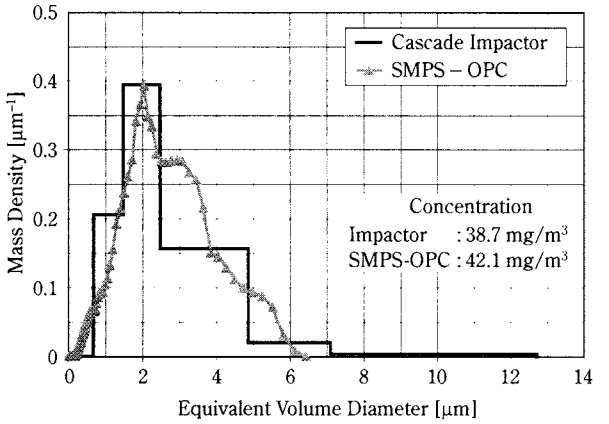

Fig. 13 Resolution in particle size of cascade impactor in comparison with the combination of SMPS and OPC

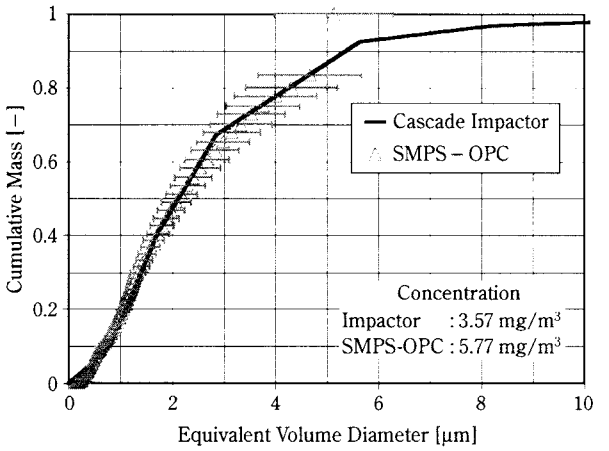

Fig. 14 Simultaneous measurements of quartz particles with combination of SMPS and OPC and cascade impactor.

quartz, good agreement between the combined measuring system and the cascade impactor are achieved as demonstrated in **figure 14**. For the combined system the range of probable size distributions is estimated because of the uncertainty with the calibration of the OPC as described by **figure 5**. When comparing the total mass concentration, it has to be mentioned that particle losses in the cascade impactor have not been taken into account. For the combined measuring system, the concentration range described by the error bars amounts to 3.49–9.0 mg/m³.

Industrial application

The measurement of the blow-by aerosol from an Otto engine shall serve as an example of the industrial application of the combined particle characterisation system. During ignition the pressure inside the piston of an Otto engine increases rapidly. Although the piston is sealed, the pressure difference between piston and crankcase will cause a leak flow which drags along oil droplets. For environmental reasons, this so-called blow-by aerosol has to be drawn off the engine housing, recirculated and injected again with the combustion air. In order to avoid losses of oil and interference with the combustion process caused by oil droplets, the aerosol has to be separated before injecting the recirculated blow-by gas. The task was to characterise the blow-by aerosol at different locations all around the engine housing in order to find a suitable position to draw off the aerosol and to design the separation step properly.

The experimental set-up is shown in **figure 15**. The blow-by aerosol is routed to a chamber which helps to dampen pressure pulsations, unify concentration and size distribution and separate coarse particles. From this chamber, the aerosol is fed to the combined measuring system as described above or to the cascade impactor in alternation. The volume flow through the measuring devices is metered and controlled.

The OPC was calibrated for the oil droplets by means of the mobile calibration unit described above. Additionally, a theoretical calibration curve was gained by *Mie* calculations, since the refractive index n of the

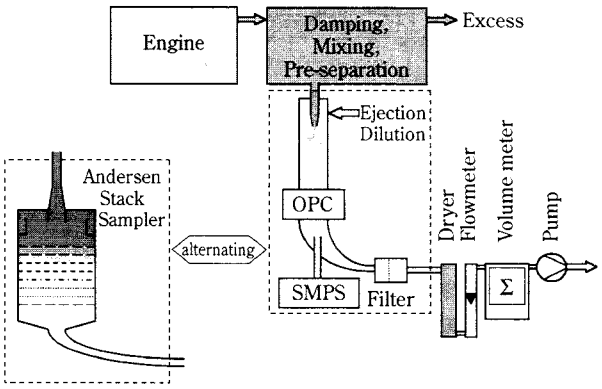

Fig. 15 Diagrammatic view of the experimental set-up for blow-by measurements.

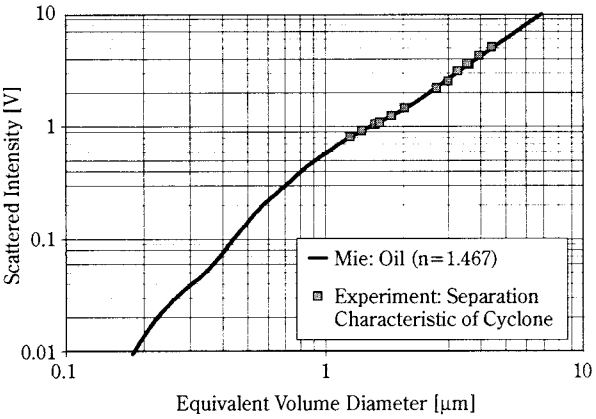

Fig. 16 Calibration of the OPC for oil droplets.

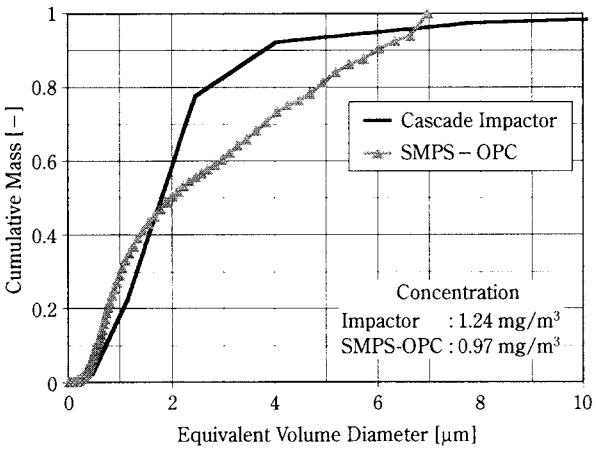

Fig. 17 Simultaneous measurement of blow-by aerosol with combination of SMPS and OPC and cascade impactor.

specific oil could be determined. Both coinciding calibration curves are plotted in **figure 16**. Again, both cascade impactor and the combined measuring system lead to comparable results as demonstrated by **figure 17**.

However, a set of measurements at seven locations around the engine housing was carried out within less than half a day with the combined system, whereas it took about a week with the impactor. In addition, defects such as a leak in the measuring system will be obvious at once with the combined system, since measuring results are available on-line. Troubleshooting and repetition of the measurement will cause no significant loss of time. If using the cascade impactor, it may take days to become aware of any defects.

The measurements revealed increasing mass concentration with growing speed and load, which could be expected, and significant changes in mass concentration and size distribution depending on the location in the engine housing. However, the investigated locations could be divided into two groups as illustrated in

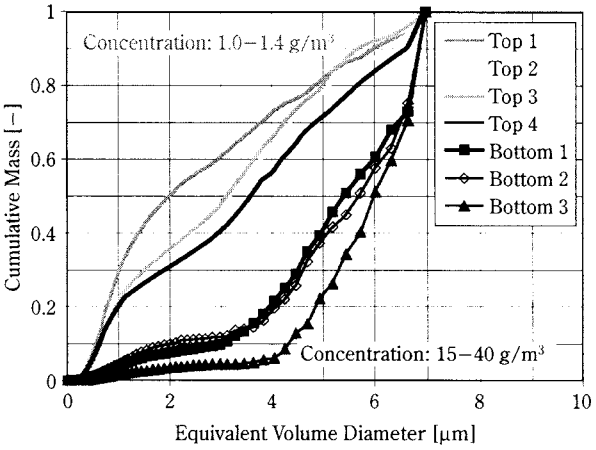

Fig. 18 Blow-by aerosol at different locations of the engine housing of an Otto engine.

figure 18. Mass concentration and size distribution at several locations near the top of the engine housing are similar as well as at three locations near its bottom, inside or near the crankcase. At the bottom locations, concentrations are higher and the size distribution is shifted to larger particles compared with the top locations. However, the total mass concentration for submicron droplets, which are difficult to separate, is nearly constant throughout the engine.

Conclusion

A measuring system was presented that covers a size range from 15 nm up to 15 µm. The different measuring devices were calibrated uniformly. For spherical particles, the calibration curves of the scattered light detectors can be derived from *Mie* calculations, whereas for non-spherical particles, empirical aerodynamic calibration is applied. Measurable concentrations exceed $5 \cdot 10^6$ particles/cm^3.

The combination of an optical particle counter and mobility analyser on the one hand and a common cascade impactor on the other hand were compared under ideal conditions in the laboratory as well as with demanding industrial applications. Reasonable agreement between both measuring systems was achieved in terms of both size distributions and aerosol concentrations. Compared with the cascade impactor, measurements with an optical particle counter are much faster, measuring results are obtained on-line, and a higher resolution both in time and in particle sizes can be achieved.

The limitations of the described combined measuring system are primarily given by the effects of irregular particle shape. Like all common aerosol analysers, especially the optical particle counter is affected

by non-sphericity and surface structures of the investigated aerosol particles. With experimental calibration methods some uncertainties have to be taken into account. However, a powerful simulation method could be established, which already improved the understanding of shape effects in optical particle sizing and may serve as a basis for further investigations.

Symbols and Abbreviations

c_N	: number concentration	[cm^{-3}]
Cu	: slip correction	[−]
d_a	: aerodynamic diameter	[μm]
d_e	: equivalent volume diameter	[μm]
d_m	: mobility diameter	[μm]
n	: refractive index	[−]
χ	: dynamic shape factor	[−]
ρ_o	: unit density	[1 kg/m^3]
ρ_p	: particle density	[kg/m^3]
APS	: aerodynamic particle sizer	
CPC	: condensation particle counter	
HS-LAS	: high sensitivity laser aerosol spectrometer	
OPC	: optical particle counter	
PSL	: polystyrene latex	
SMPS	: scanning mobility particle sizer	

References

1) Bottlinger, M.: "Quantifizierung und Eliminierung des Einflusses von Partikelform und -struktur auf das Ergebnis der Streulicht-Partikelgrößen-Zählanalyse." Ph.D. Dissertation, Universität Karlsruhe, Germany (1989).
2) Büttner, H.: "Dimensionless representation of particle separation characteristic of cyclones." J. Aerosol Sci. 30. 1291-1302 (1999).
3) Büttner, H.: "Measurement of the size of fine nonspherical particles with a light-scattering particle counter." Aerosol Sci. Technol. 12. 413-421 (1990).
4) Büttner, H.: "Messung von Partikelgrößenverteilungen im gasgetragenen Zustand mit einem Optischen Partikelzähler." Chem.-Ing.-Tech. 55. 733 (1983).
5) Draine, B.T.: "DDSCAT.5a9." http://www.astro.princeton.edu/~draine (1998).
6) Draine, B.T. and Flatau, P.J.: "User Guide for the Discrete Dipole Approximation Code DDSCAT (Version 5a9)." Princeton Observatory Preprint POPe-695 (URL ftp://astro.princeton.edu/draine/scat/ddscat/ver5a9/UserGuide. ps.gz) (1998).
7) Draine, B.T. and Flatau, P.J.: "Discrete Dipole Approximation for Scattering Calculations." J. Opt. Soc. Am. A 11. 1491-1499 (1994).
8) Friehmelt, R.: "Aerosol-Meßsysteme: Vergleichbarkeit und Kombination ausgewählter on-line Verfahren." Fortschritt-Berichte Mechanische Verfahrenstechnik und Strömungsmechanik, Universität Kaiserslautern, Band 1, ISBN 3-925178-47-3 (2000).
9) Friehmelt, R. and Heidenreich, S.: "Calibration of a white-light/90° optical particle counter for "aerodynamic" size measurements – experiments and calculations for spherical particles and quartz dust." J. Aerosol Sci. 30. 1271-1280 (1999).
10) Heidenreich, S., Büttner, H. and Ebert, F.: "Investigations on the Behaviour of an Aerodynamic Particle Sizer and its Applicability to Calibrate an Optical Particle Counter." Part. Part. Syst. Charact. 12. 304-308 (1995).
11) Hinds, W.C.: "Aerosol Technology." John Wiley & Sons, New York (1982).
12) Killinger, R.T. and Zerull, R.H.: "Effects of Shape and Orientation to be Considered for Optical Particle sizing." In: International Symposium on Optical Particle Sizing: Theory and Practice, Rouen, France, 419-429 (1987).
13) Sachweh, B., Umhauer, H., Ebert, F., Büttner, H. and Friehmelt, R.: "*In situ* optical particle counter with improved coincidence error correction for number concentrations up to 10^7 particles cm^{-3}." J. Aerosol Sci. 29. 1075-1086 (1998).
14) Sachweh, B.: "Erweiterung des Meßbereichs eines Optischen Partikelzählers durch moderne, digitale Signalverarbeitungstechniken." Ph.D. Dissertation, Universität Kaiserslautern, Germany (1991).
15) Umhauer, H.: "Particle size distribution analysis by scattered light measurements using an optically defined measuring volume." J. Aerosol Sci. 14. 765-770 (1983).

Author's short biography

Rainer Friehmelt

R. Friehmelt graduated in Chemical Engineering from the University of Karlsruhe (TH) (1994). He became Research Assistant at the University of Kaiserslautern in the field of Mechanical Process Technology. His major activities have been in the field of Particle Characterisation (especially light scattering techniques) and Particle Separation (sampling cyclones). Doctoral Dissertation 1999. He has already published around 20 papers, several of them discussed at international conferences.
Since 2000 he has been employed in the Department of Process Technology of Degussa-Huels AG in the field of Particle Technology.

Helmut Büttner

H. Büttner graduated in Process Technology from the Rheinisch Westfälische Technische Hochschule Aachen (1967). He started his carreer at Bayer AG, Leverkusen, in the field of Reaction Technology. Afterwards he became Research Assistant in Mechanical Process Technology, first at the Technical University of Stuttgart and then at the University of Kaiserslautern; Doctoral Dissertation 1977; Habilitation 1984; venia legendi for the subject of Particle Technology (Mechanical Process Technology).
Research and teaching activities in the field of Particle Separation / Gas Cleaning, Particle Characterisation, Waste Treatment, and Correlation Theory. He has been author of more than 90 papers dealing with these topics. H. Büttner is appointed member of the GVC committees of experts for "Particle Characterisation" and "Gas Cleaning".

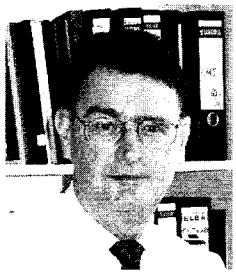

Fritz Ebert

F. Ebert graduated in Mechanical Engineering from the University of Karlsruhe (TH) (1962), where he also got his Ph. D. (1967). Activities in the period from 1967 to 1975 were related to BASF, Ludwigshafen, and University of Erlangen-Nürnberg, where he habilitated in Chemical Engineering.
Then, F. Ebert became Professor of Particle Technology and Fluid Mechanics at the University of Kaiserslautern. His main interests involve turbulent flows, multiphase flow, particle separation and flow of granular media. Approximately 200 papers concerning these fields have been published so far.

Impact Milling of Printed Circuit Board Waste for Resource Recycling and Evaluation of Liberation using Heavy Medium Separation[+]

Shigeki Koyanaka[1], Hitoshi Ohya[1], Jae-chun Lee[2], Hiroyuki Iwata[1] and Shigehisa Endoh[1]

[1] *National Institute for Resources and Environment*

[2] *Korea Institute of Geology, Mining and Materials*

Abstract

The authors evaluated the degree of liberation of printed circuit boards ground by impact milling to recover valuable materials. Wastes of two board types were ground with a swing-hammer-type impact mill. Heavy medium separation using tetrabromoethane was employed to separate the ground materials into the sink product, containing mainly copper, and the float product, consisting mainly of epoxy resin and glass fiber. The degree of liberation was evaluated with heavy medium separation. The sink product was larger than the float product. When processing boards whose surfaces are fully plated with copper foil we attained a degree of liberation for copper in the sink of up to 95%, which was higher than the degree of printed circuit board liberation. By contrast, the copper content of the float product was quite low at less than 1%. Thus, non-copper materials are easily liberated, and non-copper materials with few impurities can be obtained from printed circuit board wastes.

1. Introduction

Factory shipments of personal computers and other kinds of electronic information equipment are increasing at a blistering pace, which is indicative of the fast-growing information society, and it is anticipated that the amounts of discarded equipment will likewise increase rapidly. The 1997 quantities have been calculated at 1,230,000 desktop computers and 430,000 laptop computers, while the weight of PCs discarded in 2002 is anticipated to be about 200,000 tons for the year.[1,2] Electronic information equipment contains many valuable materials, but a characteristic of such equipment is that they consist of about 10% printed circuit boards, which are made by copper foil wiring on epoxy reinforced with material like glass fibers, and resins such as phenol, combined in a laminated structure. Because copper accounts for about one-third to one-half, it is apparently possible to recover from electronic appliances an amount of copper equal to several percent of that used in the printed circuit boards.[2] Furthermore, the electronic components mounted on circuit boards use gold, platinum, and other precious metals, which can also be recovered.[3,4] Major computer makers are setting up their own recovery and resource reclamation systems for discarded PCs and other items, but overall most junked equipment is disposed in landfills.[5] This gives rise to concerns about soil contamination by the lead and other hazardous substances in circuit boards, making it urgent to set up systems for resource reclamation.

In view of the foregoing, the authors tried applying the shape separation technique in a process for recovering the copper from scraps produced when manufacturing printed circuit boards, and from discarded boards.[6-10] In this attempt we focused on the nature of materials used in printed circuit boards, i.e., metals, consisting primarily of copper, become spherical particles when impact milled because of their great ductility and malleability, while the plastics and glass fibers making up the boards become non-spherical particles because they undergo brittle fracturing. This demonstrated that the efficient recovery of copper can be accomplished. And because the composition ratio of recovered materials is important for the reuse of copper, we also examined the recovered copper's liberatability and the dependence on milling conditions of the amount of solder contained in the recovered materials.[10]

Therefore, to increase the reclamation of materials other than copper, such as plastics and glass, this

[1] 16-3 Onogawa, Tsukuba-shi, Ibaragi 305-8569
TEL 0298-61-8468

[2] 30 Kajung-dong, Yusong-gu, Taejon, 305-350, KOREA
TEL +82-42-868-3613

[+] This report was originally printed in J. Soc. Powder Technology, Japan. **36**, 479-483 (1999) in Japanese, before being translated into English by KONA Editorial Committee with the permission of the editorial committee of the Soc. Powder Technology, Japan.

report explores the liberation of plastics and glass, and the relationship between impact milling and the intermixing of plastics and glass with metals.

2. Experimental Apparatus and Method

2.1 Experiment Samples

Our experiment used the two types of circuit boards described in **Table 1** as samples. Sample 1 was glass fiber-reinforced unpatterned scrap from the printed circuit board manufacturing process. This sample therefore had no electronic components mounted. Copper content was about 60%.

Table 1 Copper Printed Circuit Boards Used in Experiment

	Sample 1	Sample 2
	Unpatterned board	Board without electronic components mounted
Cu content	60 wt%	24 wt%
Board thickness	1.5 to 1.8 mm	1.8 mm
Copper film and board	Copper films plated on both sides of glass/epoxy resin board	Laminated glass/epoxy resin board with four copper film layers

2.2 Experimental Method

Fig. 1 illustrates the experiment procedure. Samples were milled as described in previous reports.[6-10] They were first cut into 2- or 3-cm pieces by hand, then coarse cut to under 3 mm with a cutting mill (a model VM16 vertical cutting mill made by Orient Co., Ltd.). These pieces were milled with a swing-hammer type impact mill (high-speed hammer mill 1018-LA made by Tokyo Atomizer Co., Ltd.) under appropriate milling conditions (1 mm mesh, 4,000 to 10,000 rev. min^{-1}), and the product was used as the analysis sample.

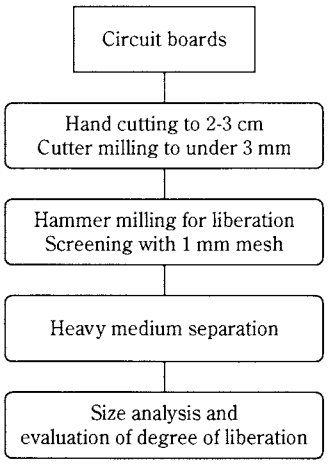

Fig. 1 Experimental Procedure

We used a Ro-Tap to screen the product for 10 min, and then we checked the particle size distribution. Tetrabromoethane with a density of 2,960 kg/m^3 was used to perform dense media separation, thereby separating the product into a sink product, containing mainly copper, and a float product, consisting mainly of non-copper components.[6] Concentrated nitric acid was used to dissolve only the copper from both particle groups. We then measured the amount of copper in both groups with induced-coupled plasma-mass (ICP) analysis, and evaluated the degree of liberation.[1]

3. Results and Discussion

3.1 Particle Size Characteristics of Milled Product

Figs. 2 and **3** show the particle size distributions of the milled circuit board products. All have about the same distributions, and the faster the hammer speed

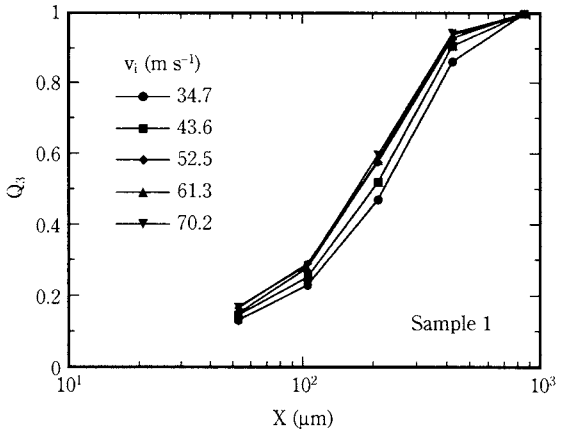

Fig. 2 Particle Size Distribution of Milled Sample 1

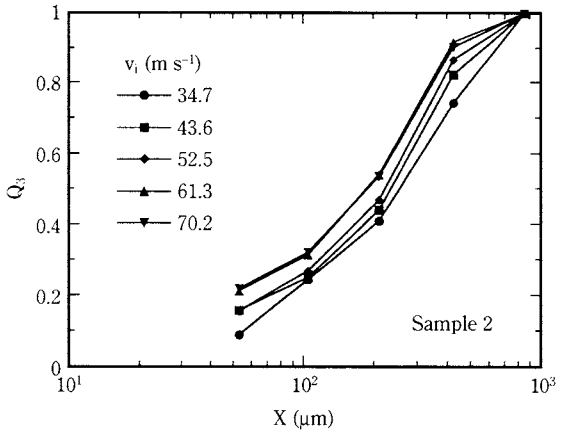

Fig. 3 Particle Size Distribution of Milled Sample 2

[1] In addition to copper, sample 2 contained 2.5% solder, 2% iron, and 0.6% aluminum, but our ICP analysis quantified only copper. Therefore the following liberatability evaluation likewise focuses on copper.

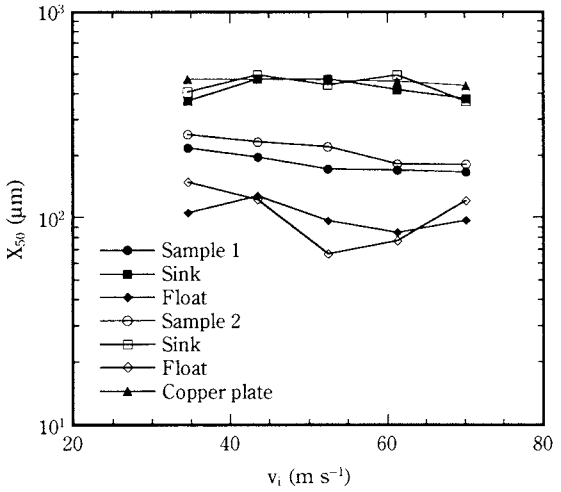

Fig. 4 Relationship Between Milled Product Median Diameter and Milling Conditions

v_i, the finer the particles we obtained. **Fig. 4** plots the relationship between hammer speed and the median diameter X_{50} (weight-based) of the sink and float products obtained with heavy medium separation of milled products. There were no appreciable differences in median diameter between samples, and just as we previously reported,[6,10] in all cases the float products, consisting mainly of resin and glass fibers, had smaller particle sizes than the sink products. This shows that glass fiber-reinforced epoxy resin undergoes brittle fracturing more readily than copper, and that the copper particles became large spherical particles because of their ductility and malleability. In connection with dependence on hammer speed, the graph clearly shows that the particle distribution of the milling product as a whole becomes finer as the impact increases, but distributions tended to differ somewhat between metal and resin/glass. Specifically, we observed that copper tended to become fine particles under low impact, whereas resin/glass tended to become coarse particles at high speed.[6] For the purpose of comparison the figure includes the milling results[8] for copper plate from our previous report. Although no large differences in values were discerned, we did note a tendency, when milling copper plate, for a simple value decrease in response to increasing impact. We conjecture that this is because the milling of copper that is combined with other materials differs from the milling of copper foil alone in that copper is affected by the milling characteristics of glass and plastic.

3.2 Liberatability

Fig. 5 shows the degree of copper liberation α from sink product subjected to heavy medium separation using tetrabromoethane with a specific gravity of 2.96. Here the degree of liberation α is defined by the following equation.

$$\alpha = W_{m,Cu} / W_m \quad (1)$$

Where:
W_m is the particle weight recovered as sink product by heavy medium separation, and
$W_{m,Cu}$ is the copper content of W_m obtained by quantitative analysis.

It is evident from the definition that α is the apparent degree of liberation. In other words, the sink product conceived here is those particles with a specific gravity of 2.96 or higher, which are judged to be sink product even when nonmetals adhere to them. Accordingly, α will have a lower value than the true degree of liberation. As in **Fig. 5**, an 80 to 90% degree of liberation was achieved with sample 1 circuit board material for particles that were 100 μm or larger. Especially under high-impact milling, this particle size yielded a high liberation degree of at least 95%. Additionally, although it appears that the degree of liberation suddenly drops when particles are under 53 μm, it would seem this is for the following reasons: In general the finer the particles, the better the liberation, but when evaluating liberatability by means of heavy medium separation as in this instance, one cannot ignore the bias of dense media separation when separating fine particles. In other words, when separating comparatively large particles, the adherence of a slight bit of metal to nonmetals can be ignored, and the particles can be recovered as float product, but when particles are smaller than 100 μm, the adherence of even a little metal will make particle density relatively large, causing nonmetals to sink and be intermixed with the sink product. And as we shall discuss below, it is thought that because of a decline in the precision of

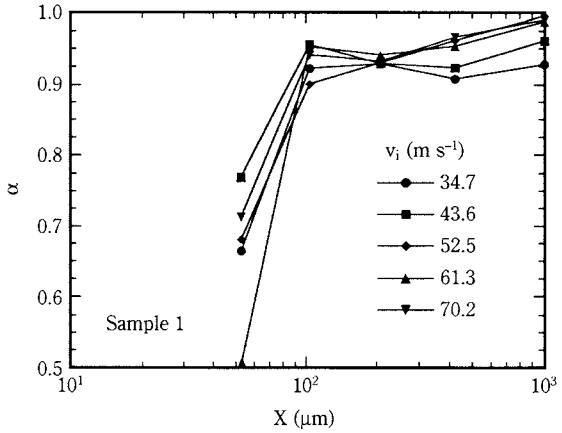

Fig. 5 Relationship Between Apparent Degree of Liberation and Particle Size

dense media separation, the degree of liberation apparently dropped.

Fig. 6 shows the relationship between the liberation degree for each sample as a whole and milling conditions. The degree of liberation increased in both samples as hammer speed increased. With sample 1 we achieved a liberation degree of over 95%, showing that impact force is effective for liberation. On the other hand, circuit boards with resist-processed surfaces had a somewhat lower liberation degree of about 80% owing to factors such as the complexity of their laminated structure.

Fig. 7 shows the relationship between float product liberatability and milling conditions. In accordance with Eq. 1, the following equation defines the parameter β of float product liberatability.

$$\beta = 1 - W_{n,Cu} / W_n \quad (2)$$

Where:

W_n is the particle weight recovered as float product with heavy medium separation, and

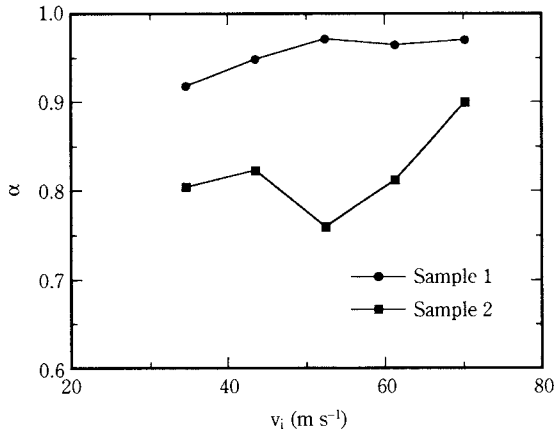

Fig. 6 Relationship Between Apparent Degree of Liberation and Milling Conditions

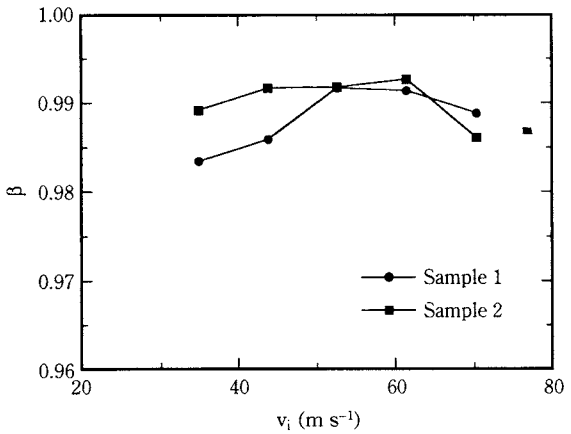

Fig. 7 Relationship Between Apparent Liberation Degree of Non-copper Materials in Float Product and Milling Conditions

$W_{n,Cu}$ is the copper content of W_n obtained by quantitative analysis.

Just as in Eq. 1, β is the apparent degree of liberation, but the float product was a particle group with a particle density of under 2.96, and the resin and glass with a slight amount of metal adhering were recovered as float product. This means that β had a higher value than the true degree of liberation. Because the float product was a mixture of resin and glass fibers, $1-\beta$ here is the percentage of intermixed copper. Although liberation is facilitated more as impact force increases, β was 0.98 or higher in comparison with the liberatability of the copper component, and very little copper was mixed into the float product. Thus when reclaiming resin and glass, one obtains high-purity substances with little metal, which holds forth the possibility that their uses could be expanded.

Fig. 8 plots the relationship between $1-\beta$ and particle size. Unlike the sink product, the copper intermixing rate increased as particle size grew. As noted previously, large resin and glass particles are recovered as float product even if slight amounts of metal adhere to them, indicating that liberation is inadequate. But when particles are small, those with metal adhering to them will sink, so the floating product's degree of liberation does not decrease. The reason that $1-\beta$ increases somewhat for fine particles is thought to be slight metal intermixing in the float product, which is because small metal particles sink with difficulty.

An evaluation of liberation and heavy medium separation used for printed circuit boards can be diagrammed as in **Fig. 9**. As the float product, resin and glass rather well liberated from copper are recovered, while the sink product is a mixture of well-liberated

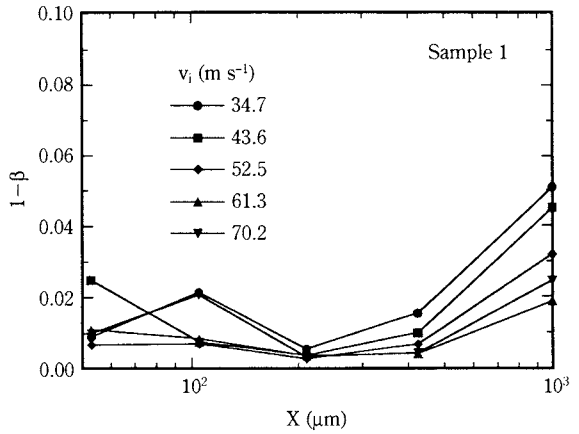

Fig. 8 Relationship Between Extent of Copper Intermixing in Float Product and Particle Size

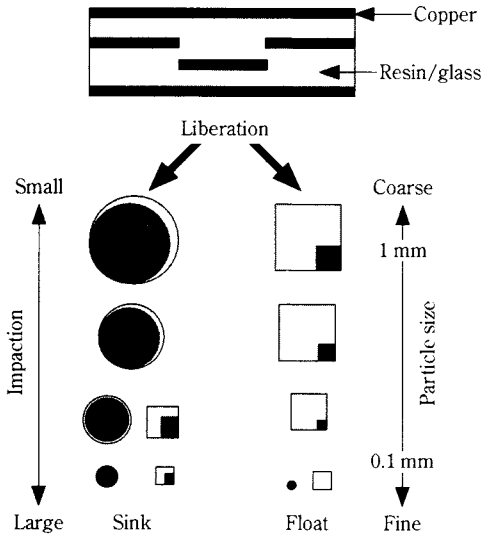

Fig. 9 Liberation of Printed Circuit Board Materials by Impact Milling and Heavy Medium Separation

copper, as well as resin and glass to which copper has adhered, thereby giving their particles specific gravity of over 2.9. This results in the decline of apparent liberatability α, with the effect being especially apparent in fine particles.

4. Conclusion

In anticipation of the recovery of valuable materials from printed circuit boards, whose disposal amount is expected to increase rapidly, this paper has explored the liberation characteristics of such boards when using impact milling. We sought the apparent liberation degree of sink and float products which had undergone heavy medium separation in a dense liquid whose density was 2.96, and determined the relationship with milling conditions and other parameters. Our results produced the following conclusions.

1) Resin and glass became finer particles, and had higher liberatability, than copper. Thus even when the resin and glass are to be recycled, it is possible to recover them with very little metal mixed in.

2) Copper has a liberatability of 80% or more even from circuit boards such as those with electronic components actually mounted on them, and we demonstrated that liberatability of 90% or more is obtainable if one adjusts particle size by controlling impact force.

Acknowledgments

The authors wish to express their appreciation to Masato Miyake (who at the time of the experiment was a senior at Shibaura Institute of Technology) for this great cooperation.

Nomenclature

Q_3 : Cumulative undersize distribution (mass base) (−)
v_i : Hammer speed (m s^{-1})
$W_{m,Cu}$: Mass of sink product obtained by heavy medium separation using tetrabromoethane and mass of copper in the sink product measured by ICP analysis (g)
$W_{n,Cu}$: Mass of the float product obtained by heavy medium separation using tetrabromoethane and mass of copper in the float product measured by ICP analysis (g)
X : Particle diameter (μm)
X_{50} : Median diameter (μm)
α : Apparent degree of liberation of copper in the sink product defined by Eq. 1 (−)
β : Degree of liberation of non-copper materials in the float product defined by Eq. 2 (−)

References

1) Endoh, S. "Recovery of valuable metal from spent printed circuit boards by the shape separation technique," *Kinzoku*, **68**, 883-888 (1998).
2) "Report on resource recycling techniques of advanced wastes – Separation of metal and plastics," Clean Japan Center (1996).
3) Rokukawa, N., M. Tanaka, and H. Sakamoto. "Properties of printed wiring boards with electronic components in relation to the effective recovery of metals," *Shigen to Kankyo*, **1**, 209-217 (1992).
4) Saito, I., M. Tanaka, and H. Sakamoto. "Research on waste treatment of advanced technology products – Recovery of valuable metals from printed wiring board wastes," *Shigen to Kankyo*, **4**, 397-404 (1995).
5) Iji, M., S. Yokoyama, and Y. Nakahara. "Development of recycling technology of plastic wastes for electronic computers," *NEC Giho*, **46**, no. 9, 55-61 (1993).
6) Koyanaka, S., S. Endoh, and H. Iwata. "The recycling of printed wiring board scraps using a shape sorting technique – Recovering copper components by the inclined vibrating method," *J. Soc. Powder Technol., Japan*, **32**, 385-391 (1995).
7) Izumikawa, C., H. Sasaki, H. Ohya, S. Endoh, and H. Iwata. "Copper recycling from printed circuit board scrap by shape separation – Application of the inclined conveyor method," *J. Soc. Powder Technol., Japan*, **32**, 378-384 (1995).
8) Koyanaka, S., S. Endoh, H. Ohya, and H. Iwata. "Particle shape of copper milled by swing-hammer type impact mill," *Powder Technol.*, **90**, 135-140 (1997).

9) Ohya, H., S. Koyanaka, S. Endoh, H. Iwata, C. Izumikawa, H. Sasaki, and P. Ditle. "Analysis of trajectory for ground printed wiring boards using shape separation," *Shigen Shori Gijutsu*, **44**, 3-8 (1997).

10) Lee, J. C., S. Koyanaka, M. Y. Lee, H. Ohya, and S. Endoh. "Recovery of copper, tin, and lead from spent printed circuit boards (PCBs) by the shape separation method," *Shigen to Sozai*, **113**, 357-362 (1997).

Author's short biography

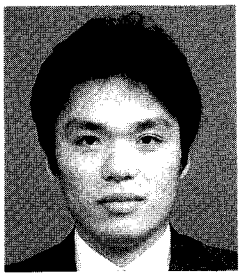

Shigeki Koyanaka

Shigeki Koyanaka is a researcher at National Institute for Resources and Environment (NIRE), Japan. He received his bachelor of engineering (BE) and master of engineering (ME) in Mining Engineering from Kyoto University. He joined the Materials Handling and Characterization Division in 1993. His major research interest is physical separation of particulate solids for resource recycling. He works presently to develop new particle separation method by using laser radiation pressure. E-mail: koyanaka@nire.go.jp

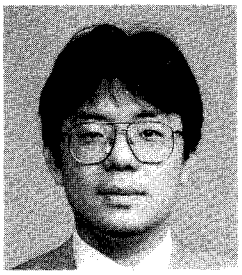

Hitoshi Ohya

Hitoshi Ohya received his BE and ME degrees in Chemical Engineering from Kyoto University. He has been at NIRE since 1986. He earned his doctor of engineering (DE) in 1997 from Kyshyu University for a thesis entitled "Study on shape separation of particulate materials". He works presently for environmental impact assessment of resource recycling process. E-mail: ohya@nire.go.jp

Jae-chun Lee

Jae-chun Lee, Ph.D. is a senior researcher at Korea Institute of Geology, Mining & Materials. He stayed at NIRE as a research fellow in 1996. His main area of interest is refining of metallic and non-metallic materials by hydrometallurgical process.

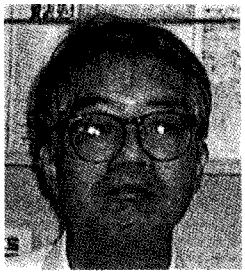

Hiroyuki Iwata

Hiroyuki Iwata earned his DE degree in Mining Engineering in 1976 from Waseda University. He was the former leader of the Materials Handling and Characterization Division in NIRE. His major research interests are size reduction, characterization and separation of particulate solids. He works presently for international research cooperation program with eastern European countries.

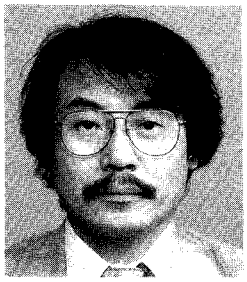

Shigehisa Endoh

Shigehisa Endoh has been the leader of the Materials Handling and Characterization Division in NIRE since 1995. He received his BE and ME degrees in Chemical Engineering from Kanazawa University. He earned his DE degree in Chemical Engineering in 1984 from Osaka Prefecture University. His major research interest are characterization of particular materials and resource recycling of solid waste. E-mail: endoh@nire.go.jp

On-line Monitoring of Electrostatic Charge in Powder Pneumatic Transportation Process†

Satoru Watano, Teruo Suzuki and Kei Miyanami
*Department of Chemical Engineering, Osaka Prefecture University**

Summary

This paper describes a novel system for continuous monitoring of powder electrostatic charge in pneumatic transportation process. An electrostatic detecting system based on the electrostatic field strength measurement, together with a purge air system for preventing powder adhesion, has been newly developed. Performance of the system has been confirmed in a powder pneumatic transportation process under various kinds of powder materials and operating conditions. Specific charge of powder and the induced current at the transportation pipe were simultaneously measured. The relationship between the electrostatic field strength and the space charge density and the measured induced current were investigated. It is found that the electrostatic filed strength has linear relationship between the space charge density and the induced current. This proves that our newly developed system is a very effective and simple device for continuously measure the electrical charge of powder. A model for the powder charge in the pneumatic transportation process has also been proposed here to understand the powder charge mechanism.

1. Introduction

Recently, powder technology tackles the electrostatic disasters and troubles, which have now developed into a social problem because they cause explosion and fire in the worst case [1-3]. For example, in the process of powder pneumatic transportation, powders are tremendously charged due to the collision between powders and inside wall of the transportation pipe. In the case such charged powders are fed into a silo, a lightning discharge (atmospheric discharge) in the upper space of the silo or cone discharge along with the accumulated powder surface are frequently observed, which sometimes induce explosion and fire [4-6]. In order to prevent these hazards beforehand, continuous motoring of powder electrical charge is required.

So far, a Faraday cage [4-6] has been well used to statically measure the electrical charge of powders. However it is not available for the continuous measurement, though several sampling devices have already been developed. A surface electrical potential sensor with a vibrating electrode [7] has also been developed and applied for detecting the surface potential of a flat sheet of paper and nylon film. Since this sensor requires calibration of distance between sensor and object, it cannot be used for powder handling processes in which powders randomly and furiously move.

In this study, a novel electrostatic detecting system based on the measurement of electrostatic field strength has been developed. Performance of the system has been confirmed in a powder pneumatic transportation process under various kinds of powders and operating conditions.

2. Measurement Principle of Electrostatic Field Strength

Figure 1 illustrates the concept of electrostatic field around a charged sphere. The characteristics of electrical charge can be evaluated by the electrostatic field strength because the electrical charge and the electrostatic field strength are correlated by a Gauss's theory. Suppose that a charged sphere is placed in a space generating electrostatic field around it. The electrostatic field strength at a distance of r from the center of the charged sphere (the amount of charge is

* 1-1, Gakuen-cho, Sakai, Osaka 599-8531, Japan
Tel: +81-722-58-3323 Fax: +81-722-54-9911
Email: watano@chemeng.osakafu-u.ac.jp

† This report was originally printed in J. Soc. Powder Technology, Japan. **34**, 778-784 (1997), **35** 846-855 (1998) in Japanese, before being translated into English by KONA Editorial Committee with the permission of the editorial committee of the Soc. Powder Technology, Japan.

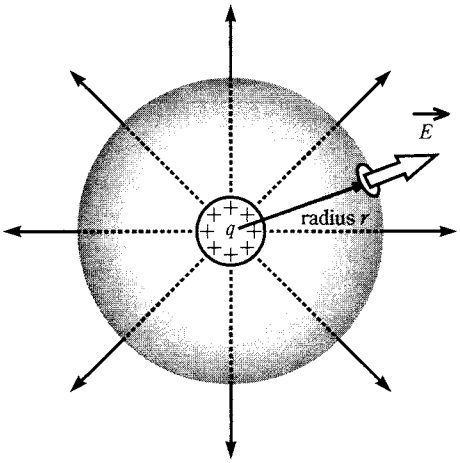

Fig. 1 Schematic diagram of electrostatic field

assumed to be q) can be described as Eq. (1).

$$\int_0^S E_0 \cdot \mathrm{d}s = q/\varepsilon_0 \tag{1}$$

where ε_0 and $\mathrm{d}s$ represent an air dielectric constant and an infinitely small area on the surface of a virtual sphere where electrostatic filed is functioning at a distance of r from the center, respectively.

Integrating the both sides obtains Eq. (2)

$$E_0 = q/(4\pi\varepsilon_0 r^2) \tag{2}$$

Therefore, as far as distance r is known, measurement of E_0 obtains electrical charge q.

Figure 2 illustrates measurement principle of electrostatic field strength. A developed sensor measures electrostatic field strength as an alternating voltage which is induced at an electrode by periodically chopping the electrostatic field.

Assuming that the chopping cycle is ω (=500 Hz), area of the electrode where electrostatic field flows in is S_0, and the one which changes periodically due to the electrode vibrating is S_1, then the effective area of the electrode S can easily be written as:

$$S = S_0 + S_1 \sin\omega t \tag{3}$$

The Gauss's law calculates an electrical charge q, which is induced by the electrostatic field periodical change,

$$q = ES\varepsilon_0 \tag{4}$$

where E shows an electrostatic field.

A current I_s running through an electric resistance R_s which connects the electrode and ground is calculated as,

$$\begin{aligned} I_s &= \mathrm{d}q/\mathrm{d}t \\ &= E\varepsilon_0\omega\, S_1 \cos\omega t \end{aligned} \tag{5}$$

The voltage between the electric resistance is thus:

$$\begin{aligned} V_s &= R_s I_s \\ &= R_s E\varepsilon_0\omega\, S_1 \cos\omega t \end{aligned} \tag{6}$$

Finally, the electrostatic field strength E can be detected by measuring the voltage V_s of the electric resistance R_s.

3. Electrostatic Field Strength Detecting System

Figure 3 is a schematic diagram of the detecting sensor. The sensor consists of a chopper, an electromagnet and a driving gear composed of a tuning fork and an electric magnet. The driving gear activates the chopper at a constant chopping cycle. The sensor is originally designed to miniaturize as small as possible (i.d.7×H50 mm) without any decrease in sensor sensibility by means of amplifying and transmitting signal with a high S/N ratio.

Figure 4 illustrates the sensor extremity. The sensor is setup in a double-walled cylinder, and purge air is blowing inside of each cylinder. Due to this air purge system, powder cannot reach to the detecting sensor. The double-walled cylinder is connected with the main

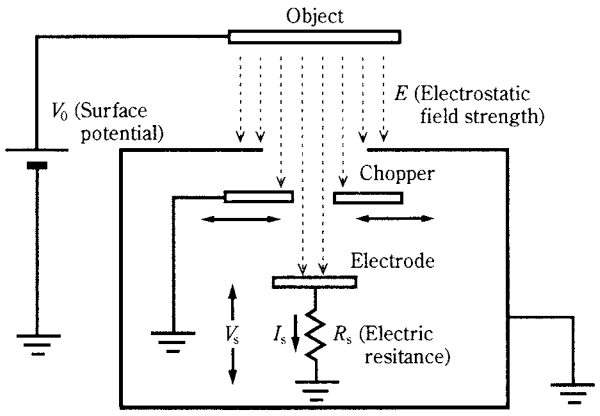

Fig. 2 Measurement principle of electrostatic field strength

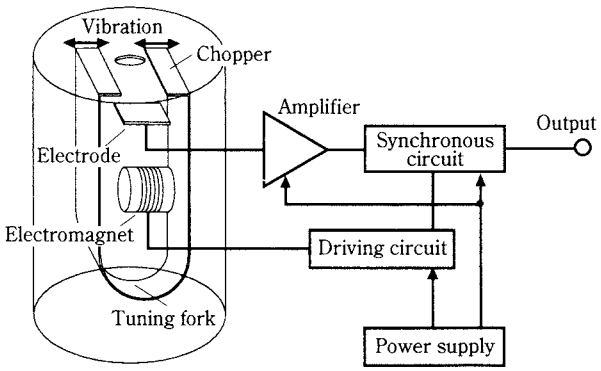

Fig. 3 Schematic diagram of electrostatic detecting sensor

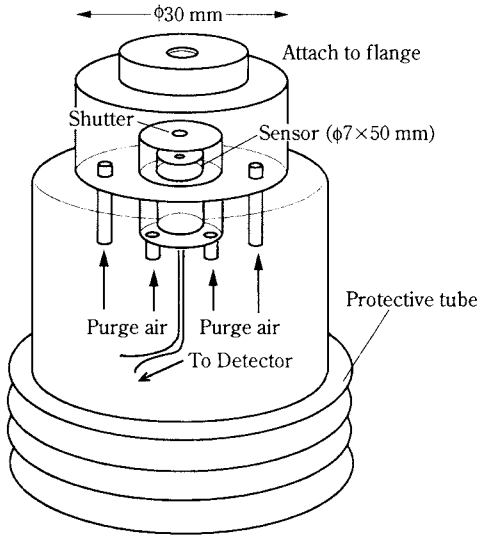

Fig. 4 Schematic diagram of the sensor extremity

body of the system (detector) by using a flexible protective tube (2 m in length), which enhances operational flexibility. Shock absorbing rubber is also placed between the sensor extremity and a flange mounted on the wall of powder handling equipment. This shock absorbing rubber is able to remove the effect of vibration, such as knocking, air blasting, and etc.

4. Monitoring of Electrostatic Charge in Pneumatic Transportation Process

Figure 5 describes a schematic diagram of a pneumatic transportation system. The system consists of a transportation pipe, a measuring pipe made of stainless steel, an electrostatic filed sensor, a Faraday cage, electrometers and a personal computer. Powders are fed into the transportation pipe (inner diameter is 28 mm, 2 m in length) through a stainless funnel and

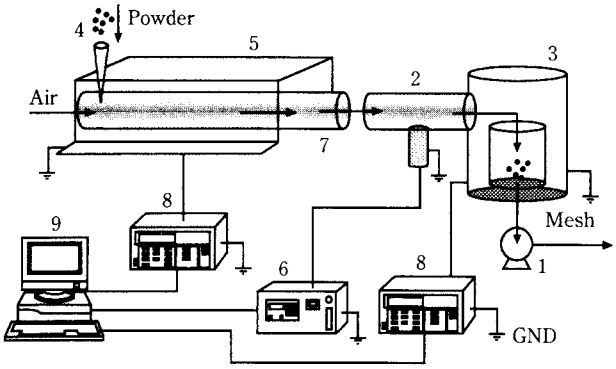

Fig. 5 Experimental set-up for powder pneumatic transportation
1. Exhaust blower; 2. Measuring pipe; 3. Faraday cage;
4. Powder feed funnel; 5. Wire shield;
6. Electrostatic field sensor; 7. Transportation pipe;
8. Electrometer; 9. Personal computer

then charged by collisions between powders and the pipe wall while a suction blower conveys them through the pipe. The tail end of the pipe attaches so called "a measuring pipe" that has a flange connecting the electrostatic sensor. Since the measuring pipe and the transportation pipe are both grounded, the sensor can only measure electrostatic field strength arisen by the charged powders. After passing through the measuring pipe, the Faraday cage collects powders; at the bottom of the cage, wire mesh is placed, so that the powders remain inside the cage and only air passes through the mesh. Through the electrometer, amount of charge (specific charge) is measured.

During the transportation, the generation of powder charge also induces electrical charge on the outside wall of the transportation pipe. Since the transportation pipe is grounded through the electrometer, the induced charge can also be measured as an induced current by the electrometer (the transportation pipe is not only for the powder transportation but also for the induced electrode). The transportation pipe having a function of the induced electrode is covered by a wire shield; it is the same structure as the Faraday cage.

Here, we assume that, 1) flow of uniformly charged powders is laminar and uniform, 2) there is no electrostatic generation neither relax inside the measuring pipe, 3) direction of electrostatic field strength generated by the charged powders inside the measuring pipe is radial direction and 4) direction of a current flows into the transportation pipe is defined as positive.

Figure 6 illustrates a model for the powder charge in the pneumatic transportation system. When the charged powders (I_1) flow into the transportation pipe, the charge is induced at the pipe, as well. Since the transportation pipe (work as the induced electrode) is grounded through the electrometer, transient charge

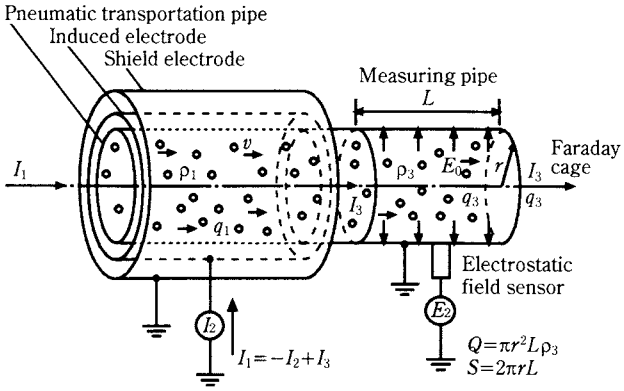

Fig. 6 The powder charge model for pneumatic transportation process

is generated to eliminate the induced charge. At the same time, powders flow with colliding each other or with transportation pipe wall, the powder and the wall are charged with different sign, respectively. When the powders flow out of the pipe, induced current (I_2) and charge of powders (I_3) are observed.

Therefore, the balance of the current should be

$$I_1 = -I_2 + I_3 \tag{7}$$

Here, the current of charged powders (I) can be described by the powder feed rate (v) and the powder specific charge (q) as follows,

$$I = q \cdot v \tag{8}$$

The powder feed rate can be replaced by the product of air flow rate (u) and powder space density (m), Also, the product of the specific charge (q) and the powder space density (m) should be the space charge density (ρ),

$$I = q \cdot mu = \rho u \tag{9}$$

If Eq.(8) is applied to the current of powder (I_3), I_3 can be expressed by the product of the space charge density and the air flow rate.

$$I_3 = q_3 \cdot mu = \rho_3 u \tag{10}$$

According to the Gauss's theory, total charge Q is expressed by using electrostatic field strength E, dielectric constant of air ε_0 and cross sectional area of the pipe S

$$Q = ES\varepsilon_0 \tag{11}$$

Thus,

$$E = \frac{Q}{2\pi r \varepsilon_0 L} \tag{12}$$

where r and L show radius and length of the pipe, respectively. Since total charge Q can also be written by the space charge density ρ_3,

$$Q = \pi r^2 L \rho_3 \tag{13}$$

Following Eq. (14) can be obtained from Eqs.(12) and (13)

$$E = \left(\frac{r}{2\varepsilon_0}\right)\rho_3 \tag{14}$$

Assume that the initial powders have no electrical charge (I_1=0),

$$I_2 = I_3 = \left(\frac{2\varepsilon_0 u}{r}\right)E \tag{15}$$

Total electrical charge of powders Q can also be obtained by integrating the induced current I over the moving time t,

$$\int_0^t I \, dt = Q \tag{16}$$

The specific charge can be obtained by dividing the electrical charge Q by the total mass of powder M,

$$q = \frac{Q}{M} \tag{17}$$

Figure 7 investigates the effect of measuring pipe materials on the electrostatic filed strength measurements. In case of using acrylic for the measuring pipe, glass beads charge to negative while the pipe to positive. However, the electrostatic field strength sensor shows that the charge is positive and it remains after the glass beads pass away from the pipe. This phenomenon is originated from the fact that the insulted acrylic pipe is tremendously charged to positive and the sensor measures its electrostatic filed strength not by the glass beads. Therefore in case of using insulated materials for the measuring pipe, the electrostatic field strength measurement is impossible.

Contrary to the acrylic pipe, a measuring pipe made of stainless steel can measure the electrostatic field strength properly. This is because the pipe is grounded so that the charge of the pipe is eliminated, and the electrostatic field strength arisen from only the charged glass beads can be measured. The metal such as stainless steel is thus required for the measuring pipe.

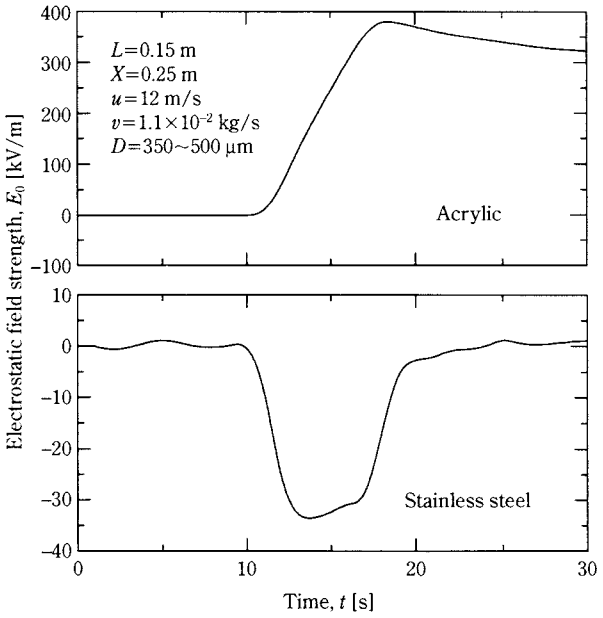

Fig. 7 Effect of measuring pipe materials on the electrostatic field strength measurement.

Figure 8 shows the temporal change in electrostatic field strength and induced current at various transport distances, X. With an increase in transport distance (X), both the electrostatic field strength and the induced current become larger. It is because the number of collisions between glass beads and wall and glass beads themselves increase awfully as the transport distance increases, leading to the simultaneous increase in electrical charge.

Figure 9 illustrates the relationship between the electrostatic field strength E and space charge density ρ_3. Here, PMMA (polymethylmethacrylate) particles, grass beads and cellulose spherical granules having different sizes were used. During the experiments, the space charge density is obtained by the induced current measurement.

All experimental data points in **Fig. 9** are well expressed by the theoretical value (Eq. (14)), showing that space charge density theoretically determines the electrostatic filed strength, regardless of the particle property and size.

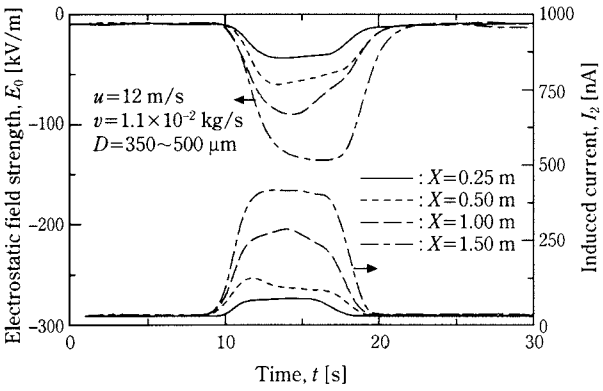

Fig. 8 Temporal change in electrostatic field strength and induced current at various transportation distances

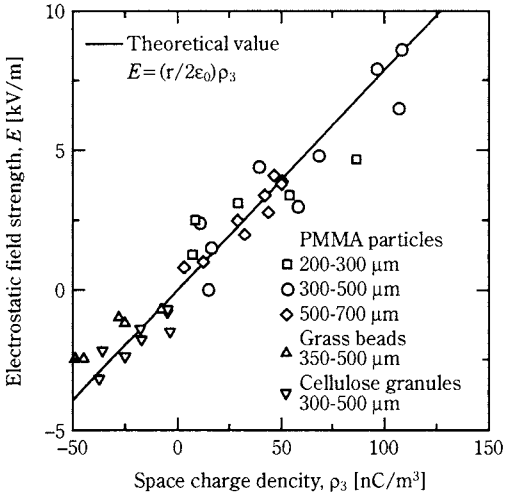

Fig. 9 Relationship between electrostatic field strength and space charge density

Figure 10 investigates the relationship between electrostatic field strength and induced current. Fairly good linearity can be obtained between the two measurements. The induced current measurement method being used for a long time can be replaced by the electrostatic measurement. In addition, since the induced current method is not available when powders have their initial charge, the electrostatic field detecting method has more merit because it is not affected by the initial charge.

Figure 11 also describes relationship between induced current (I_2) and current (I_3) calculated from the Faraday cage measurement. Both results suggest good linearity. This confirms a theoretical formula of $I_2=I_3$ (Eq.(15)). Also, this implies that the Faraday cage method can be replaced by the electrostatic method.

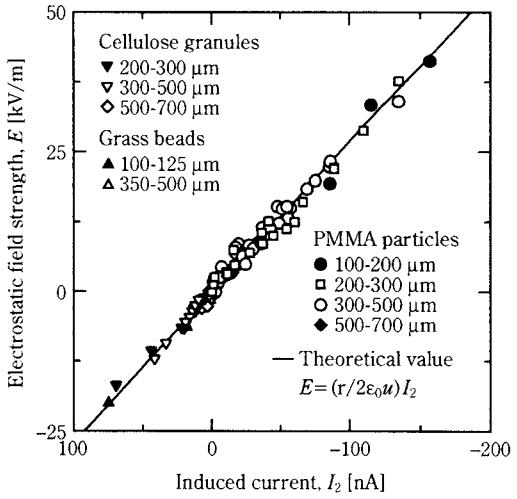

Fig. 10 Relationship between electrostatic field strength and induced current

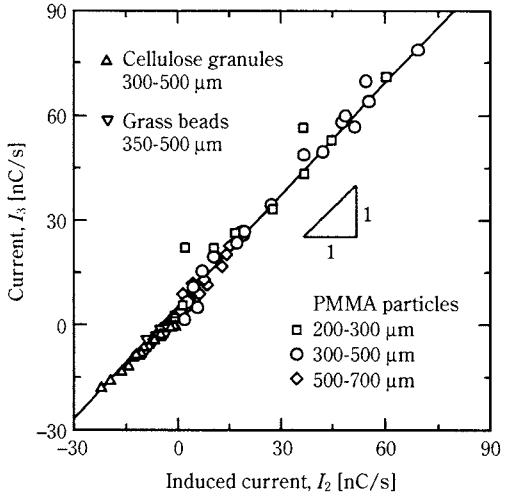

Fig. 11 Relationship between induced current I_2 and I_3

As a result, the validity of our newly developed electrostatic detecting system can be experimentally and theoretically confirmed. Since the electrostatic method is not affected by the powder initial charge nor requires no sampling devices, it can continuously monitor powder charge in any powder handling processes with high accuracy.

5. Conclusions

In this contribution, a novel system for detecting electrostatic field strength of charged powders has been developed. The performance of the system has been investigated in the powder pneumatic transportation process where powders are enormously charged due to the collision between powders and the pipe wall. It is found that the developed system could continuously monitor the electrostatic charge with high accuracy. It is theoretically and experimentally proved that the electrostatic field strength can be used to evaluate the power charge in powder pneumatic transportation process.

Acknowledgement

The authors wish to thank Mrs. T. Taira, T. Numa and T. Kurooka for their assistance in part of the experimental work.

References

1) Jones, T. B. and J. L. King, "Powder Handling and Electrostatics", Lewuis Publisher (1991).
2) Van Larr, G. F. M., "How to Protect a Brewery against Dust Explosions", *Powder Handling & Processing*, **10**, 55-59 (1988).
3) Bours, R., "Dust Explosion Protection: A Difficult Choice?" *Powder Handling & Processing*, **10**, 191-192 (1998).
4) Glor, M. and K. Schwenzfeuer, "Occurrence of Cone Discharge in Production Silos", *J. Electrostatics*, **40** & **41**, 511-516 (1997).
5) Schwenzfeuer, K. and M. Glor, "Tests to determine the ignition of dust by brush discharges", *J. Electrostatics*, **30**, 115-122 (1993).
6) Glor, M., "Ignition Tests with Discharges from Bulked Polymeric Granules in Silos (Cone Discharges)", *J. Electrostatics*, **30**, 123-134 (1993).
7) Yamada, H. and T. Kobayashi, "Vibration Type Surface Potential Sensor", *J. Inst. Electrostatics Japan*, **10**, 213-216 (1986).
8) Watano, S., Y. Ito, T. Suzuki and K. Miyanami, "The On-line Monitoring of the Electrostatic Field Strength in Fluidized Bed Granulation and Drying Using a Newly Developed Electrostatic Field Detecting System", *J. Soc. Powder Technol., Japan*, **34**, 32-38 (1997).
9) Watano, S., T. Suzuki, T. Taira and K. Miyanami, "Continuous Monitoring and Mechanism of Electrostatic Charge of Powder in Fluidized Bed Process", *Chem. Pharm. Bull.*, **46**, 1438-1443 (1998).
10) Suzuki, T., S. Watano, T. Numa, T. Taira and K. Miyanami, "On-line Monitoring of Electrostatic Field Strength in Powder Pneumatic Transportation Process Using Newly Developed Electrostatic Field Detecting System", *J. Soc. Powder Technol., Japan*, **35**, 846-855 (1998).
11) Watano, S., T. Suzuki, T. Taira and K. Miyanami, "Monitoring of Electroststic Charge in Powder Pneumatic Conveying Processes", *Powder Handling & Processing*, **11**, 431-434 (1999).

Author's short biography

Satoru Watano

Satoru Watano received his B.S., M.S. and Ph.D. degrees in chemical engineering from Osaka Prefecture University. Currently, he is an associate professor at the department of chemical engineering, Osaka Prefecture University. He is also a visiting professor at Particle Technology Center, New Jersey Institute of Technology (U.S.A.) sine 1997. His major research interest lies in measurement, control, optimization, computer simulation and scaling up of powder handling processes. Now, he is an editor of Journal of the Society of Powder Technology, Japan and Journal of Advanced Powder Technology.

Teruo Suzuki

Teruo Suzuki graduated from the Tokyo Denki University in 1979 and received his Ph.D. in chemical engineering from Osaka Prefecture University. He has been active in the filed of electrostatics for the past 20 years. Currently, he is working at Kasuga Denki Inc. and responsible for the design and development of novel devices for detecting and eliminating electrostatics in powder handling processes. He is an editor of the Journal of Electrostatics, Japan.

Kei Miyanami

Kei Miyanami graduated in Chemical Engineering from Osaka Prefecture University (OPU). After four years research on computer control of chemical plants at Hitach, Ltd, he obtained faculty position at Chemical Engineering, OPU in 1965. He obtained Ph.D. degree in Chemical Engineering from OPU in 1971. In 1979, he became Professor of Chemical Engineering at OPU. Currently he is the Emeritus Professor. He was at the position of former editor in chief of KONA Journal of HOSOKAWA Foundation in the past seven years. Now he is working as members of many councils and committees in local governments for environmental assessment-protection-affairs and wastes management.

Dechlorination of PVC by Mechanochemical Treatment†

Qiwu Zhang, Fumio Saito,
*Institute for Advanced Materials Processing, Tohoku University**
Kaoru Shimme, Seiichi Masuda
*Sumitomo Metal Industries, Ltd., HQ Center***

1. Introduction

Polyvinyl chloride (PVC) is an important material for industrial plastics, having excellent resistance to corrosion and rotting. Adding plasticizers to PVC is endowed with over 170 different characteristics such as elasticity, rigidity, transparency, multiple colors, good workability, heat resistance, and chemical stability. And owing to its light weight and low manufacturing cost, PVC finds wide application in construction materials, industry, agriculture, medical equipment, and other fields. Japan's 1997 annual PVC production was about 2.5 million tons, which corresponds to about 17% of total plastics.[1] PVC products produced in large quantities are discarded owing to breakage and other reasons, but the recycling rate is only about 6%. While PVC wastes were once disposed by simple incineration, disposal is currently dependent on properly managed incineration and landfilling owing to the formation of dioxins. But for reasons including the rising costs of incineration facilities and operation, and the limits to landfill space, it is urgent to develop PVC processing and recycling technologies that can replace incineration and landfilling in the future. New PVC processing methods currently being proposed and tried are (1) blast furnace feed material,[2] (2) eco-cement fuel conversion,[3] (3) and liquefaction technology.[4,5] Each of these methods, however, has difficulties such as economy and restriction to certain regions. Further, because they basically rely on heating, they also present hazards from toxic gas emissions and the risk of fire, as well as the environmental burden of CO_2 emissions. Badly needed, therefore, is the development of PVC processing and recycling methods that are simple, flexible, inexpensive, and eco-friendly.

The authors' research group has made proposals for mechanochemical (MC) waste processing methods, and methods for recovering resources from wastes.[6-8] In MC methods frictional heat arises from comminution, but the operation basically does not use heating (at least heat is not actively applied from outside). Instead, MC method breaks the bonds of solids, modify their structures, and activate them. When other substances are added to a material, the method makes the mutual interface area to increase, and force solid-state reactions to proceed. The MC method is thereby useful as pretreatment prior to chemical processing such as solvent extraction of reaction products to extract them at room temperature. It is therefore possible to easily recover certain components contained in wastes. Our research explored the extent to which MC methods can be used to dechlorinate PVC at room temperature.

2. Samples and Experimental Method

The PVC used in our experiment was a special-grade reagent (60 to 400 μm particle size [133 μm average particle size]; 1100 mean degree of polymerization; noncrystalized) made by Wako Pure Chemical Industries, Ltd. As the dechlorinating agent added to the PVC when comminuting we chose powdered CaO reagent (made by Wako, 9.7 μm particle size). We set three PVC-CaO mixing ratios based on the PVC chlorine amount: We mixed in amounts of Ca for equimolar reactions, and two and four times those amounts of Ca.

MC treatment of these mixed powder samples used a small planetary mill (Fritsch, Pulverizete-7)[6-8] and an experimentally made TS (Tohoku University-Sumitomo Metal Industries, Ltd.)-type MC reactor (made by Nisshin, Ltd.). The small planetary mill had two 50-ml stainless steel pots mounted on a horizontally rotating disk so that their rotation radius was 70 mm. It was structured to allow the clockwise revolution of

* 2-1-1 Katahira, Aoba-ku, Sendai 980-8577
TEL 022-217-5135
**3-5, Hikaridai, Seika-cho, Souraku-gun, Kyoto 619-0237
TEL 0774-98-2130

† This report was originally printed in J. Soc. Powder Technology, Japan. **36**, 468-473 (1999) in Japanese, before being translated into English by KONA Editorial Committee with the permission of the editorial committee of the Soc. Powder Technology, Japan.

the disk and the rotation of the pots themselves at the same speed. Owing to this arrangement, powerful compression and shearing forces arise among the balls put into the mill, and between the balls and the mill wall. Both the pots and the disk rotated at 700 rpm. Into each pot were placed seven stainless steel balls each 15 mm in diameter and 3 g of the PVC-CaO powder mix. MC treatment was performed in air. We stopped the mill every 15 minutes to let it cool naturally for 30 minutes so as to prevent the excessive rise of internal mill temperature. We set total MC treatment time to up to 5 h. The TS-type MC reactor is horizontal with an inner cylinder and an outer cylinder that rotate together, but in opposite directions. The outer cylinder's surface-based diameter is 400 mm, and its length is 600 mm. The inner cylinder's axis-based outside diameter is 200 mm. Fin-like projections are attached to both cylinder surfaces. Into the reactor we put about 172 kg of steel balls 10 mm in diameter (about a 50% fill rate), and 1 kg of PVC-CaO powder mix. MC treatment was accomplished by rotating the inner cylinder at 300 rpm and the outer cylinder at 70 rmp. **Fig. 1** shows a drawing of the reactor.

After MC treatment using the mill and reactor, we took 0.5 g of the comminuted substance for each processing time, suspended it in 25 ml of distilled water, stirred with a magnetic stirrer for 30 min, filtered, and separated solid from liquid. For each MC-processed sample we measured particle size distribution (Seishin, LMS-30) and observed its shape with a scanning electron microscope (SEM; Hitachi S-430), as well as analyzing composition/crystallization state with powder x-ray diffraction (XRD; Rigaku, RAD-B System) and the state of surface functional groups with a Fourier transform infrared spectrophotometer (FT-IR; BIO-RAD, FTS-40A). The washed and filtered residue was likewise analyzed and assessed by XRD and FT-IR, and we also used the combustion method to analyze the remaining amount of chlorine. The washed filtrate was analyzed with a liquid chromatograph (made by Shimadzu Corporation) to measure and assess dissolved chlorine.

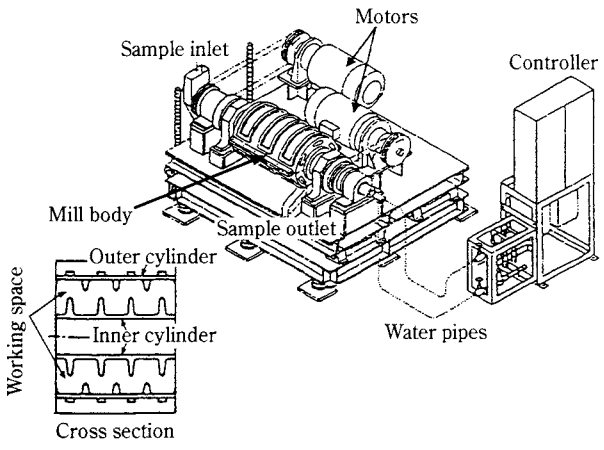

Fig. 1 TS-Type Mechanochemical Reactor

3. Results and Discussion

3.1 Shape Change and Reactivity Assessment of Processed Substances (Results of Small Planetary Mill Processing)

Fig. 2 shows the change in particle size for MC treatment times of 0.5 to 5 h for equimolar mixtures of PVC and CaO. The graph shows that the mixtures' particle size distributions become finer as processing time increases, that comminution of the samples proceeds smoothly, and that, assessed by average particle size, particles are about 110 μm at 0.5 h, 45 μm at 3 h, and down to 30 μm at 5 h treatment time. The decrease in particle size of the powder mix with MC treatment can be observed also in the SEM photomicrographs in **Fig. 3**. Especially in the initial powder mix photograph there is a great difference between the sizes of the PVC and CaO particles, making it easy to tell them apart, but the PVC and CaO powders are kneaded together in the post-MC treatment photos, and they can be observed growing smaller with time. It is likely that MC treatment of a PVC-only sample affords no hope of a particle size decrease owing to PVC's caking capacity, but when mixing it with CaO both powders are subjected to a powerful shearing action owing to the effects of external forces,

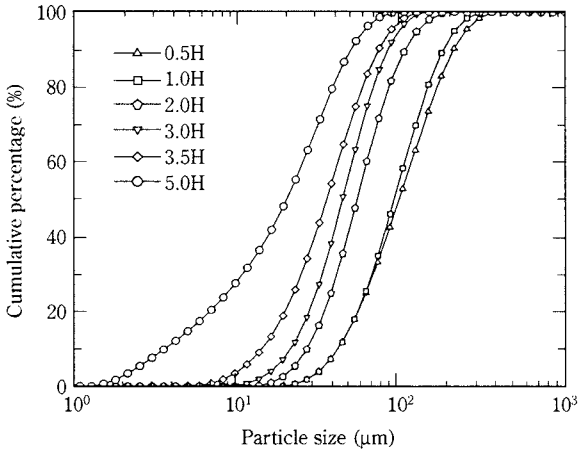

Fig. 2 Size distribution curves of the mixture (Cl in PVC : Ca in CaO = 1 : 1) milled for different periods of time by a planetary mill

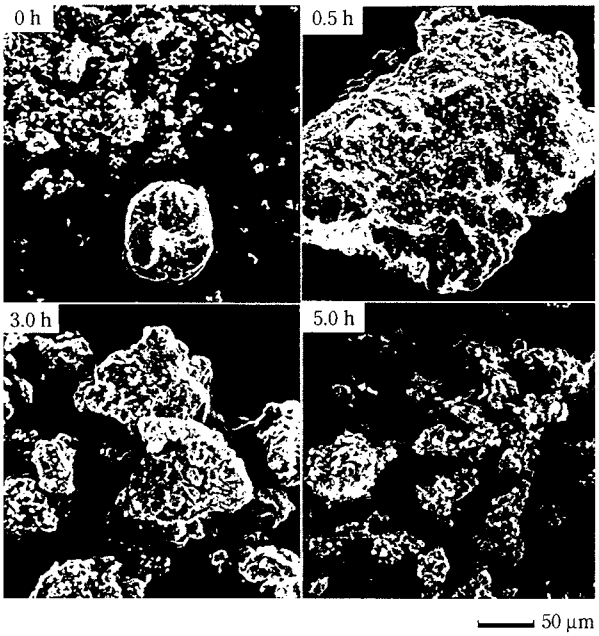

Fig. 3 SEM photographs of the mixture (Cl in PVC : Ca in CaO = 1:1) milled for different periods of time by a planetary mill

because of which the particles become smaller as their interface area increases.

Fig. 4 shows XRD patterns of an MC-treated mixture. In the untreated powder mix (0 h) the CaO displays high diffraction peaks, but as MC treatment time lengthens, peaks for $Ca(OH)_2$ appear while those for CaO become smaller. $Ca(OH)_2$ is thought to be formed when CaO absorbs moisture in the air either during MC treatment or during the XRD analysis after MC treatment. Further, after 3.5 h or more of MC treatment, the CaOHCl peaks become apparent. FT-IR spectra for each MC-treated batch are shown in **Fig. 5**. The results correspond to those of **Fig. 4** in that as MC treatment time increases, the infrared absorption peak of CaOHCl at about 1210 cm^{-1} gradually heightens, indicating the progression of a solid-state reaction. At the same time, when MC treatment time exceeds 3 h a peak showing the existence of C=C bonds becomes evident at about 1700 cm^{-1}. These results suggest that the following reaction occurs. Here n and x are the mean degrees of polymerization of, respectively, the initial PVC sample and post-treatment PVC. In our experiment n was about 10,000, while after 8 h of treatment x was about 800, showing that MC treatment decreased the degree of polymerization (mean molecular weight decreased). This result showed the same tendency as experimental results by Yasue et al.[9]

$$-[CH_2CHCl]n- + CaO = -[CH=CH]x- + CaOHCl,\ n>x \quad (1)$$

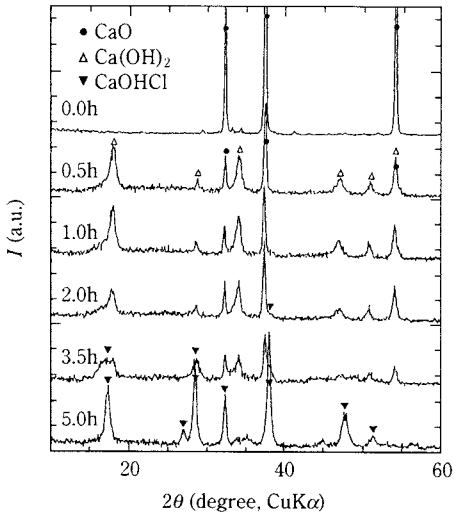

Fig. 4 XRD patterns of the mixture (Cl in PVC : Ca in CaO = 1:1) milled for different periods of time by a planetary mill

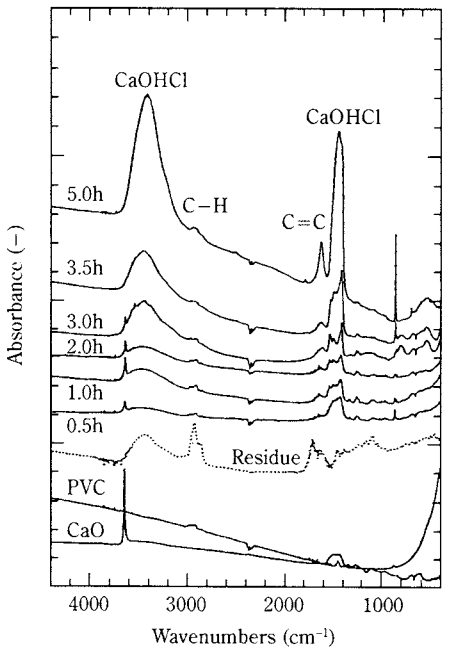

Fig. 5 FT-IR patterns of the mixture (Cl in PVC : Ca in CaO = 1:1) milled for different periods of time by a planetary mill

3.2 Dechlorination Rate (Results Obtained with the Small Planetary Mill and the TS-Type MC Reactor)

First let us examine the small planetary mill results. **Fig. 6** shows the XRD patterns of solid residues separated out by washing and filtering after MC treatment for various times. Residues from the untreated sample exhibited peaks for $Ca(OH)_2$ and $CaCO_3$, and as treatment time increased, the peaks for $Ca(OH)_2$ diminished while only those for $CaCO_3$ remained. And it is likely that the diminishing stature of $Ca(OH)_2$

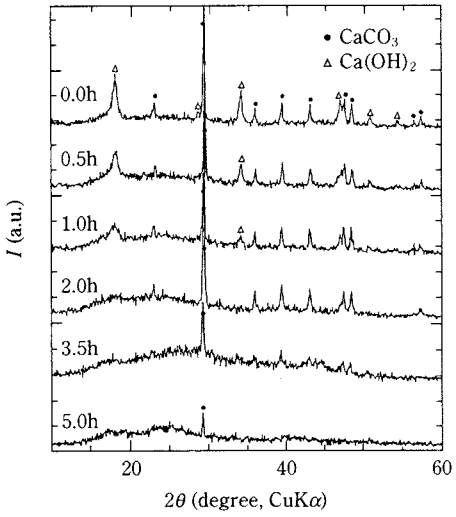

Fig. 6 XRD patterns of the washed mixture after MC treatment for different periods of time by a planetary mill

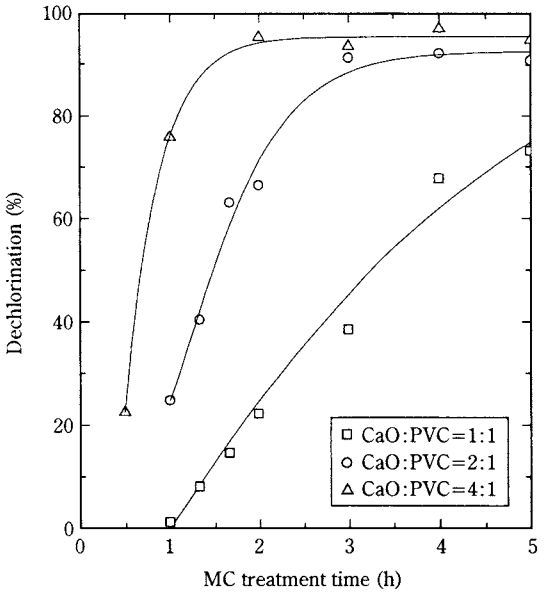

Fig. 7 Dechlorination yield of PVC as a function of MC treatment time (Cl in PVC:Ca in CaO=1:1, 1:2 and 1:4) by a planetary mill

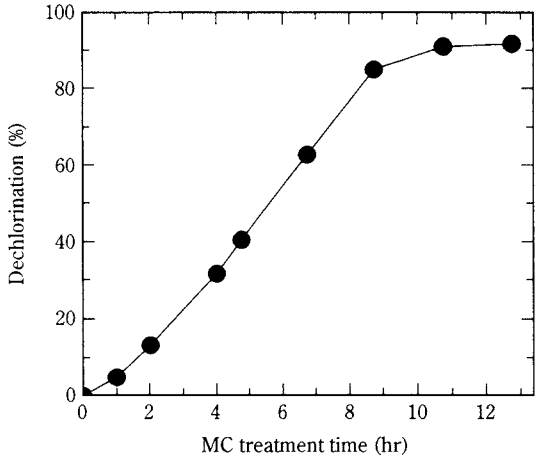

Fig. 8 Dechlorination yield of PVC as a function of MC treatment time. (Cl in PVC:Ca in CaO=1:4) by a TS-type mechanochemical reactor

peaks, which occurred with lengthening MC treatment time, signifies the transformation of CaO in the powder mix to CaOHCl, while the existence of $CaCO_3$ diffraction peaks appeared either because, during MC treatment, the $Ca(OH)_2$ in the powder mix reacts with CO_2 in the air, or, during the washing process, reacts with CO_3^{2-} ions dissolved in the washing solution. $CaCO_3$ diffraction peaks diminish as MC treatment time lengthens, but even after 5 h treatment some of the compound remained, suggesting that the CaO in the powder mix did not react completely with the PVC. **Fig. 7** shows the relationship between dechlorination rate and MC treatment time for three different CaO:PVC mixing ratios. Focusing first of all on the equimolar ratio shows that dechlorination after 5 h of MC treatment was about 70%. Up to 3 h treatment time the dechlorination rate rose slowly, and thereafter increased sharply, showing that the solid-state reaction rate depends on processing time. It probably means that a short MC treatment time made it difficult for the two substances to be finely comminuted, and that this is perhaps a region in which a great deal of mechanical energy (corresponding to MC treatment time) is expended to increase the interface area of the two substances. On the other hand, with a long MC treatment time the particles became fine to an extent, and solid-phase diffusion was facilitated, which we believe happened because after a time the MC reaction proceeded smoothly. By contrast, results obtained by MC treatment when excess CaO has been added show that the addition of excess CaO contributes not only to raising the final dechlorination rate, but also to shortening the reaction starting time and increasing the reaction speed.

Next we used the TC-type MC reactor, added four times the equivalent CaO amount of chlorine in the PVC, and performed MC treatment. **Fig. 8** shows the relationship between the dechlorination rate and MC treatment time. The graph shows that as MC treatment time lengthens, the dechlorination rate increases linearly, attaining over 90% after about 10 h of treatment. We calculated the power required per unit weight of sample for both the small planetary mill and the TS-type MC reactor to achieve 90% dechlorination under our experimental conditions. The former ran on 200 V, used an average 17 A current, and required MC treatment time of 10 h/kg to attain 90% dechlori-

nation (based on **Fig. 8**), coming to about 34 kWh/kg. By contrast, the mill ran on 100 V, used an average 10 A current, and required MC treatment time of 1.5 h/3 g to attain 90% dechlorination (based on **Fig. 7**), coming to about 500 kWh/kg. This comparison of the two devices' capabilities by power required per unit weight shows that the TS-type MC reactor is about 15 times better than the small planetary mill. Calculating efficiency, however, necessitates ascertaining the amount that each device can effectively treat, its optimum operating conditions, and other qualities, which we intend to do in future research.

4. Conclusion

For the purpose of developing a safe, economical, and effective technology for treating and recycling PVC wastes, we examined non-thermal dechlorination methods using a planetary mill and an experimentally made TS-type MC reactor. We arrived at the following conclusions.

(1) PVC reacts with CaO in MC treatment, yielding polyethylene and CaOHCl. However, the two substances do not react completely, leaving some unreacted. In this reaction process the powders' particle sizes gradually become smaller as MC treatment time lengthens.

(2) Washing and filtering MC reaction products divides them into polyethylene and chlorides. Basically the former is a solid residue, while the latter are filtrates. The residue, however, contains unreacted substances or $Ca(OH)_2$, the latter of which contains solubilized $Ca(OH)_2$. In any event, this method can be used to dechlorinate PVC to an extent.

(3) The more CaO added to excess in relation to PVC, the higher the dechlorination rate, the faster the speed of dechlorination, and the shorter the reaction starting time.

(4) The TS-type MC reactor, like the small planetary mill, was able to dechlorinate PVC, and the experiment suggested the possibility of enlarging its treatment scale from gram- to kilogram-sized batches (large-scale treatment).

Acknowledgement

The authors are grateful to Dr. G. Mi and Mr. T. Aoyagi for their assistance of this work. The TS-type MC reactor was made by Nisshin, Ltd. under the financial support from Sumitomo Metal Industries, Ltd. The authors wish to thank these people and institution.

References

1) VEC (Enbi-Kougyo/Kankyou-Kyoukai), ed. *Seisan/Shukka Tokei Data*, no. 9 (1998).
2) Fukumoto, T. *Haikibutsu-Syori-Gijyutsu*, Kyoritsu Syuppan Co., Ltd. pp. 53-77 (1977).
3) Furubayashi, K. "Disposing Technologies by Means of RDF (Refuse Derived Fuel)," *Kagaku-Kogaku*, **61**, no. 7, pp. 502-505 (1997).
4) Adschiri, M. "Recovery of Terephthalic Acid by Decomposition of PET in Supercritical Water," *Kagaku-Kogaku-Ronbunsyu*, **23**, no. 4, pp. 505-511 (1997).
5) Murata, K. "Technologies for Liquefying Waste Plastics," *Kagaku-Kogaku*, **61**, no. 7, pp. 510-512 (1997).
6) Sanchez, E. Cruz, F. Saito and H. Horita. "Enhancement of Magnesium and Nickel Extraction from Garnierite by Mechanochemical Treatment," *Shigen-to-Sozai (MMIJ)*, **113**, pp. 35-38 (1997).
7) Zhang, Q., K. Sugiyama and F. Saito. "Enhancement of Acid Extraction of Magnesium and Silicon from Serpentine by Mechanochemical Treatment," *Hydrometallurgy*, **45**, pp. 323-331 (1997).
8) Zhang, Q. and F. Saito. "Non-thermal Extraction of Rare Earth Elements from Fluorescent Powder by Means of Mechanochemical Treatment", *Shigen-to-Sozai (MMIJ)*, **114**, pp. 253-257 (1998).
9) Yasue, T., T. Aizawa and Y. Arai. "Influence of Silicon Dioxide Addition on Mechanochemical Degradation of Poly (vinyl Chloride) by Grinding," *Nippon-Kagaku-Kaishi*, no. 3, pp. 415-421 (1976).

Author's short biography

Qiwu Zhang

Qiwu Zhang received his bachelor's and master's degrees in Mineral Processing from Wuhan University of Technology, China in 1984 and 1987, respectively. He has worked at Zhengzhou Institute of Multipurpose Utilization of Mineral Resources, China in 1987 to 1992. He joined Prof. Saito's group in 1992 and received his Ph.D degree at Tohoku University, Japan in 1997. He is working at IAMP, Tohoku University as a Research Associate, and has been assigned to research on mechanochemistry for application to engineering field.

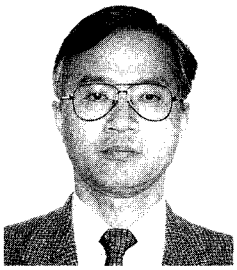

Fumio Saito

Fumio Saito received his bachelor's and master's degree in Chemical Engineering from Yamagata University, Japan in 1970 and 1972, respectively. He got his Ph.D in Mining and Minerals Engineering from Tohoku University, Japan in 1982. He has been a full-time professor since 1993, followed by his career of Associate Professor at Yokohama National University. His interests cover mechanochemical engineering for human life, molecular design by grinding, nano-technology in comminution and nano-structural control by an arc-plasma method.

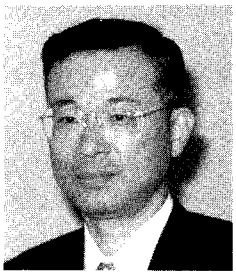

Kaoru Shimme

Kaoru Shimme received his Ph.D degree in Metallurigical Engineering from Kyoto University, Japan in 1993. He has worked at Sumitomo Metals Co. Ltd since 1974, in the field of iron and steel making and its purification. He has devoted to work on environmental protection since 1997 at the same company, and is now collaborating on dehalogenation of organic materials and on effective utilization of wastes emitted from industries with Prof. Saito, Tohoku University. He is now a senior researcher at Sumitomo Metals, Co. Ltd, Japan as well as a guest lecturer at Kyoto University.

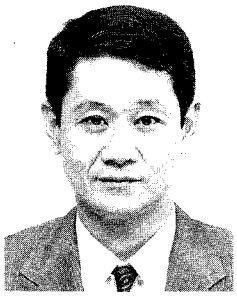

Seiichi Masuda

Seiichi Masuda received his bachelor's and master's degrees in Metallurigical Engineering from Osaka University, Japan in 1973 and 1975, respectively. He has worked at Sumitomo Metals Co. Ltd, Japan since 1975. Since then, he has devoted the research on purification of iron and steel at the company. Since 1997 he joined to the group headed by Dr. Shimme, and supporting Dr. Shimme' activity intensively.

Behavior of Fine Particles on a Plate under Ultrasonic Vibration†

Shuji Matsusaka, Shiro Nakamura and Hiroaki Masuda
*Dept. of Chem. Eng., Kyoto Univ.**

Abstract

The behavior of particles on a vibrating plate was investigated both theoretically and experimentally. Ultrasonic vibration of 39 kHz was applied, and the mass median diameters of test powders were in the range of D_{p50}=0.5 to 46 μm. Experimental results showed that all particles moved randomly on the vibrating plate. Fine particles, approximately 10 μm or less in mass median diameter, formed many small agglomerates, which also vibrated with their shapes and sizes intact. The size distribution of agglomerates could be represented by a log-normal distribution. Adhesion and separation stresses in an agglomerate were used to theoretically analyze the agglomeration mechanism. The analysis showed that agglomerate diameter was inversely proportional to primary particle diameter. Furthermore, it was shown that compressive breaking load could be estimated from the analysis.

1. Introduction

Although powders of micrometer- and submicrometer-size are widely used by industry, such fine particles have strong adhesiveness, so that when using them in powder operations they tend to lose fluidity and dispersibility, or have problems such as bridging or choking. External vibration is employed in various kinds of operations to collapse the bridged structures caused by adhesion, or to increase fluidity,[1-3] and many findings have been obtained on the behavior of particles in vibration fields by means of experiments[4-6] or numerical calculations.[7-10] However, most of that work has been on coarse particles highly subject to gravity, while there has been little research on fine particles with strong adhesiveness, in which the movement of individual particles is highly limited. We performed research in which random movement arose near a vibrating wall even in fine particles when a high-frequency vibration field was used, and we reported that the force of interaction between interior powder and the pipe wall decreased markedly.[2,3] To utilize this phenomenon for various purposes, it is necessary to elucidate the behavior of fine particles in high-frequency vibration fields. Here we used powders with different median diameters, from submicrometer sizes to several tens of μm, to examine the effect of particle size on behavior and agglomeration/dispersion when placing a particle bed on a flat plate and applying ultrasonic vibration.

2. Experimental Apparatus and Method

Fig. 1 shows the experimental apparatus for forming a thin powder bed on a flat plate[11]. An ejector (model DN-154 by Nisshin Engineering) was used to inject sample powder for a very short time into a cylindrical container 300 mm in diameter and 600 mm high, and the powder was allowed to settle onto a flat

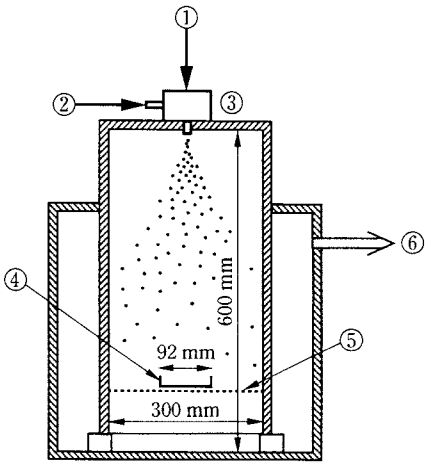

① Powder ④ Flat plate
② Compressed air ⑤ Wire mesh
③ Ejector ⑥ Bag filter

Fig. 1 Experimental Apparatus for Particle Deposition

* Yoshida-honmachi, Sakyo-ku, Kyoto 606-8501
TEL. 075-753-5585

† This report was originally printed in J. Soc. Powder Technology, Japan. **36**, 16-22 (1999) in Japanese, before being translated into English by KONA Editorial Committee with the permission of the editorial committee of the Soc. Powder Technology, Japan.

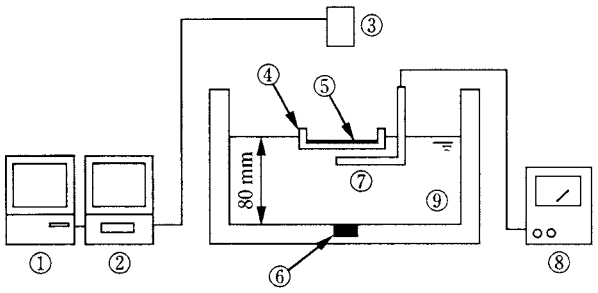

① Computer
② Video and Monitor
③ Microscope camera
④ Flat plate
⑤ Particle bed
⑥ Piezoelectric transducer
⑦ Sensor
⑧ Ultrasonic meter
⑨ Water

Fig. 2 Experimental Apparatus for Particle Vibration

plate stainless steel container with a 92 mm inside diameter placed at the bottom center of the cylinder. Captured powder ranging between 30 and 40 mg was used in the ultrasonic vibration experiment. **Fig. 2** is a diagram of the ultrasonic vibration device. The flat plate with powder bed was placed in the device and subjected to vibration from below via a water medium. The device's characteristic vibration frequency was 39 kHz, and when using an ultrasonic meter (model UTK32 by NGK Spark Plug Co., Ltd.) to measure vibration intensity directly under the flat plate, we found it to be 1.5×10^5 Pa. We used a video microscope (model OVM1000N by Olympus) to record and observe the behavior of fine particles on the vibrating flat plate, and we analyzed the video images to determine the size distribution of agglomerated particles formed on the plate. A microcompression tester (model MCTM-500 by Shimadzu) was used to measure the strength of agglomerated particles. For the compressing tip we used a flat type 500 μm in diameter, which found the compressive load and displacement between itself and the lower plate. The sample powders used in this experiment were nine kinds of antimony trioxide with different mass median diameters (D_{p50}=0.5 to 13 μm; particle density: ρ_p=5.2×10^3 kg·m^{-3}) and seven kinds of alumina (D_{p50}=5 to 40 μm; ρ_p=4.0×10^3 kg·m^{-3}). Spherical glass beads (D_{p50}=46 μm; ρ_p=4.3×10^3 kg·m^{-3}) with excellent dispersibility was also used for a control experiment.

3. Results

3.1 Observation of Particles on Vibrating Flat Plate

Fig. 3 shows the state of three sample powders with very different median diameters after they had been vibrated. The glass beads (D_{p50}=46 μm) had

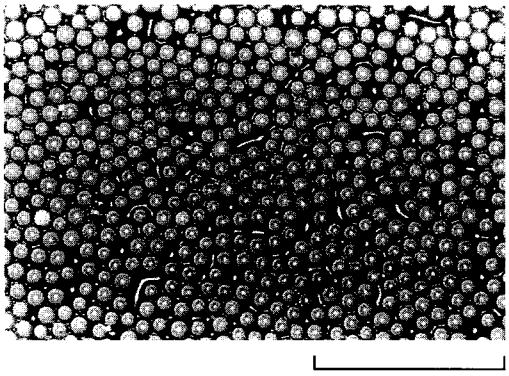

(a) Glass beads D_{p50}=46 μm

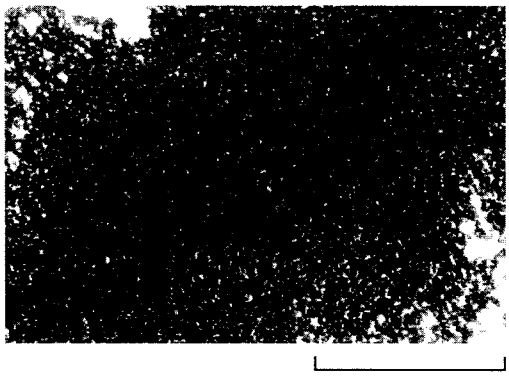

(b) Antimony trioxide D_{p50}=13 μm

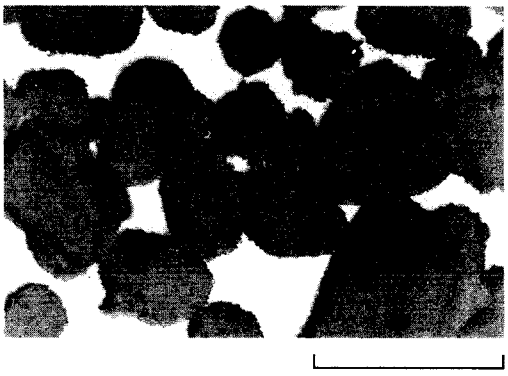

(c) Antimony trioxide D_{p50}=0.7 μm

Fig. 3 Particles on Vibrating Plate (1800 s)

good fluidity and displayed energetic random movement on the stainless steel plate. Photo **(a)** shows the result after affixing a film of polymer to the plate as a vibration damper. It is evident from the photograph that by adjusting vibration intensity it is possible to make a uniform particle bed. On the other hand, antimony trioxide (D_{p50}=13 μm) was formed into agglomerates of several tens of μm that covered the plate like a film (**Fig. 3 (b)**, particles look black), while the fine particles (D_{p50}=0.7 μm) formed comparatively large agglomerates measuring several hundred μm (**Fig. 3 (c)**).

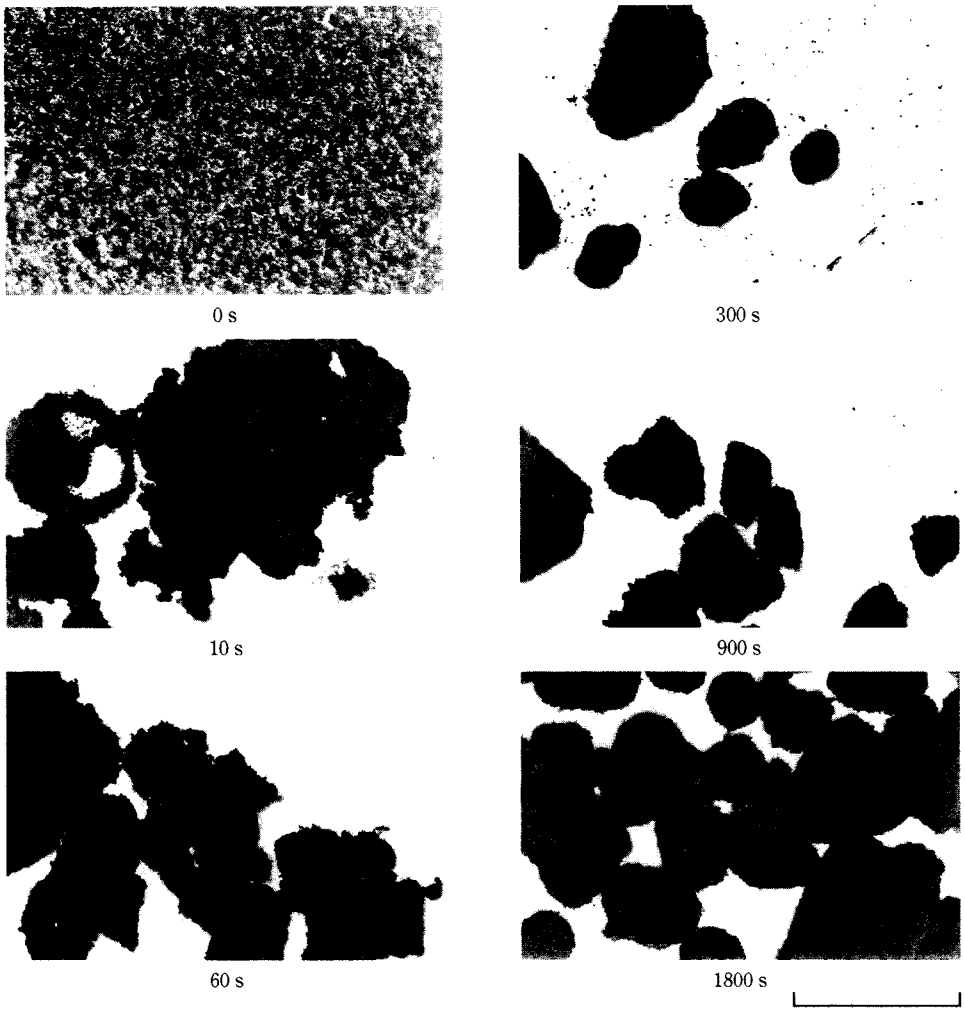

Fig. 4 Agglomerates Formed by Vibration (D_{p50}=0.7 μm)

Fig. 4 shows the process by which fine particles (D_{p50}=0.7 μm) form agglomerates. The camera position is fixed and the particles move randomly, so the number of agglomerates fluctuates; one's attention here focuses on the variation in agglomeration shape and size. Since the fine particles were dispersed in a gaseous phase and allowed to naturally settle onto the flat plate, the initially accumulated particle bed was formed more or less uniformly; when vibration was applied to the plate, the particles immediately began moving, and large agglomerates were formed by the contact and adherence between particles. After one minute the final agglomerate size was determined as the particles underwent repeated agglomeration and disintegration, and after five minutes the agglomerates assumed slightly rounded shapes. Subsequently they continued moving randomly while maintaining their shapes. Although agglomerate sizes differ according to differences in the sample powders' median diameters, in all cases the agglomerates attained their final and constant sizes in several minutes.

3.2 Agglomerate Size Distribution

Fig. 5 shows the agglomerate size distribution on a count basis as determined by image analysis, and **Fig. 6** shows the same data plotted in a log-normal distribution. In the latter plots the curves are nearly straight lines, and the geometric standard deviation is in the range of 1.3 to 1.8. In **Fig. 7** the ratio of

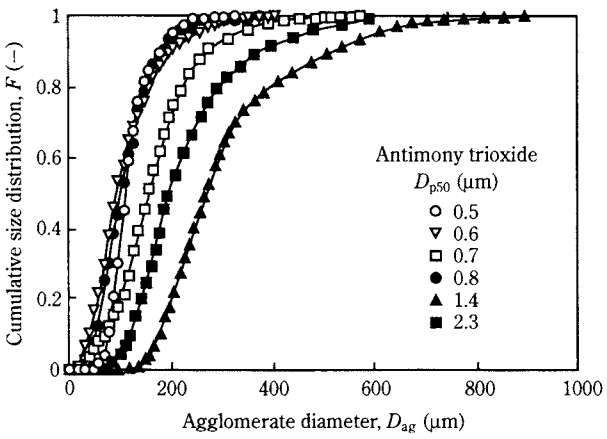

Fig. 5 Cumulative Size Distribution of Agglomerates on Count Basis

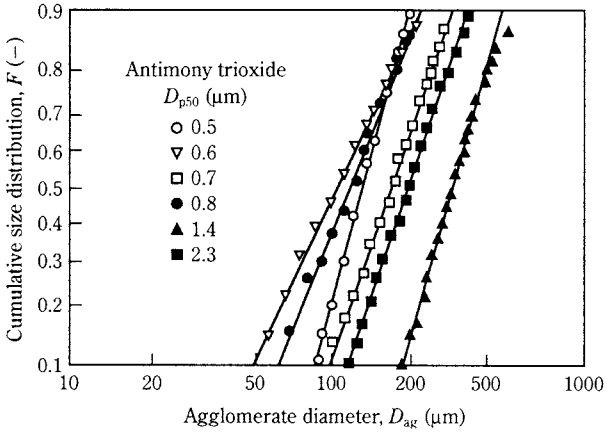

Fig. 6 Cumulative Size Distribution of Agglomerates on Count Basis Plotted on a Log-Normal Scale

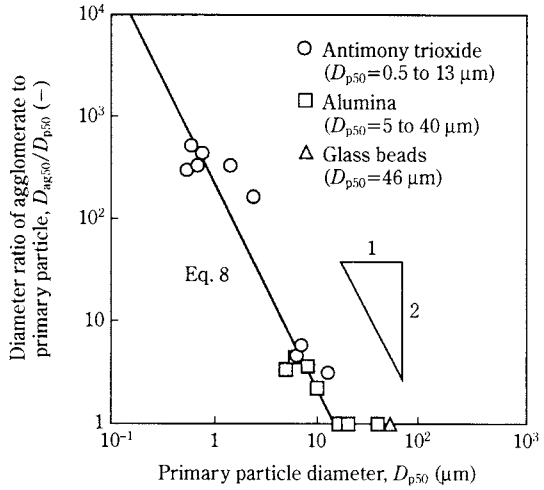

Fig. 7 Ratio of Agglomerate Diameter to Primary Particle Diameter

agglomerate diameter to primary particle diameter (D_{ag50}/D_{p50}) is shown as the degree of agglomeration converted to a mass basis. Particles with a mass median diameter of about 10 μm became small agglomerates several tens of μm in diameter and gathered in a film configuration (see **Fig. 3(b)**), which made it difficult to discern the diameter of individual agglomerates with image processing. We therefore used an optical microscope and the focal depth method to determine the particle film height (except for places where agglomerates were stacked), and put the value in **Fig. 7**. With a certain particle diameter as the boundary, we found that above that boundary particles tended to disperse as primary particles, while below it particles tended to agglomerate more as primary particle diameter decreased. We shall discuss the theoretical line of **Fig. 7** in detail below (Section 4).

3.3 Compressive Breaking Load of Agglomerates

Fig. 8 shows the result of a representative compression test on an agglomerate formed of submicrometer

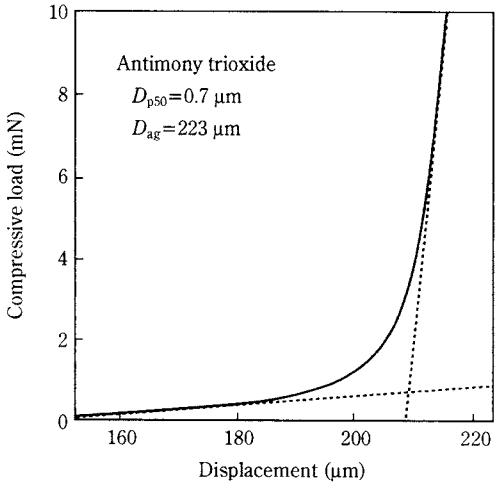

Fig. 8 Compression Test on an Agglomerate

particles (D_{p50}=0.7 μm). Since the agglomerate was rather soft, displacement increased in tandem with load, and we found no distinct breaking point, but the graph shows a large change in load where relative displacement in relation to agglomerate diameter exceeds 90%. Here the intersection (a value slightly smaller than 1 mN) of the two tangential lines is seen to be a yardstick for breaking load.

4. Analysis of Adhesive Force and Separation Force of Agglomerates

The formation of agglomerates on the vibrating plate is controlled by the adhesive force of particles and the separation force generated by vibration. This can be represented as follows when the adhesive force of primary particles is proportional to particle diameter D_p (see Appendix).

$$F_a = c_1 D_p \tag{1}$$

Where:

c_1 is a constant determined by adhesion characteristics.

On the other hand, the separation force F_s of primary particles in the vibration field is given by the product of particle mass ($\rho_p(\pi/6)D_p^3$) and vibration acceleration ($a\omega^2$).

$$F_s = \rho_p \frac{\pi}{6} D_p^3 a\omega^2 \tag{2}$$

Rumpf's equation[12] is used for the intra-agglomerate adhesion stress σ_t (i.e., it is equivalent to tensile breaking strength), which is based on inter-particle adhesive force.

$$\sigma_t = \frac{(1-\varepsilon) k_n F_a}{\pi D_p^2} \tag{3}$$

Where:
ε is the void fraction in an agglomerate, and
k_n is the coordination number.
At the same time, agglomerates are constantly colliding with the vibrating wall. The following equation is used for separation stress σ_t' (i.e., tensile breaking strength), which is based on the compression load when collisions occur.[13,14]

$$\sigma_t' = \frac{c_2 F_{ags}}{\pi D_{ag}^2} \tag{4}$$

Where:
c_2 is an experimental constant, and
F_{ags} is compressive breaking load.

In the initial stage of agglomerate formation in the vibration field, agglomeration and disintegration occur repeatedly, and as time passes change in agglomerate size is no longer observed. The likely reason is that a balance is reached between adhesion stress and separation stress, which contribute to adhesion and disintegration, upon which a steady state is achieved. That is to say:

$$\sigma_t = \sigma_t' \tag{5}$$

Here the compressive breaking load F_{ags} in Eq. 4 is yielded by replacing the particle density in Eq. 2 with agglomeration bulk density ρ_{ag} $(=(1-\varepsilon)\rho_p)$, and replacing particle diameter D_p with agglomerate diameter D_{ag}. I.e.,

$$F_{ags} = (1-\varepsilon)\rho_p \frac{\pi}{6} D_{ag}^3 a\omega^2 \tag{6}$$

The following equation is obtained from Eq. 1 and Eqs. 3 through 6.

$$D_{ag} = \frac{6k_n c_1}{\pi c_2 \rho_p a\omega^2} \times \frac{1}{D_p} \qquad (D_{ag} \geq D_p) \tag{7}$$

This equation can be rewritten as follows if for agglomerates we put in D_{pc} as a critical particle diameter that is the same diameter as a primary particle.

$$D_{ag} = \frac{D_{pc}^2}{D_p} \tag{8}$$

Here the critical particle diameter D_{pc} can also be expressed as follows.

$$D_{pc} = \sqrt{\frac{6k_n c_1}{\pi c_2 \rho_p a\omega^2}} \tag{9}$$

Since D_{pc} is also particle diameter when the separation force acting on primary particles exceeds adhesive force, it is necessary to satisfy the following equation.

$$F_a(D_{pc}) = F_s(D_{pc}) \tag{10}$$

Thus, the following equation can be derived from Eqs. 1, 2, 9, and 10.

$$c_2 = k_n \tag{11}$$

To compare the results of the preceding analysis with experimental results we put the relationship according to Eq. 8 in **Fig. 7**. We assumed that critical particle diameter D_{pc} was 15 μm (see Appendix). Eq. 8 agrees with our experimental results, showing that the relationship between primary particle diameter and agglomerate diameter can be expressed by a simple equation. To show in an easily understood manner the relationship with the main equations used in the analysis, **Fig. 9** presents the adhesive force between primary particles, F_a; the separation force generated by vibration, F_s; the intra-agglomerate adhesion stress, σ_t; and the separation stress, σ_t'. Here we used these values: 15 μm for critical particle diameter D_{pc}; 0.8 (experimental value) for agglomeration void fraction

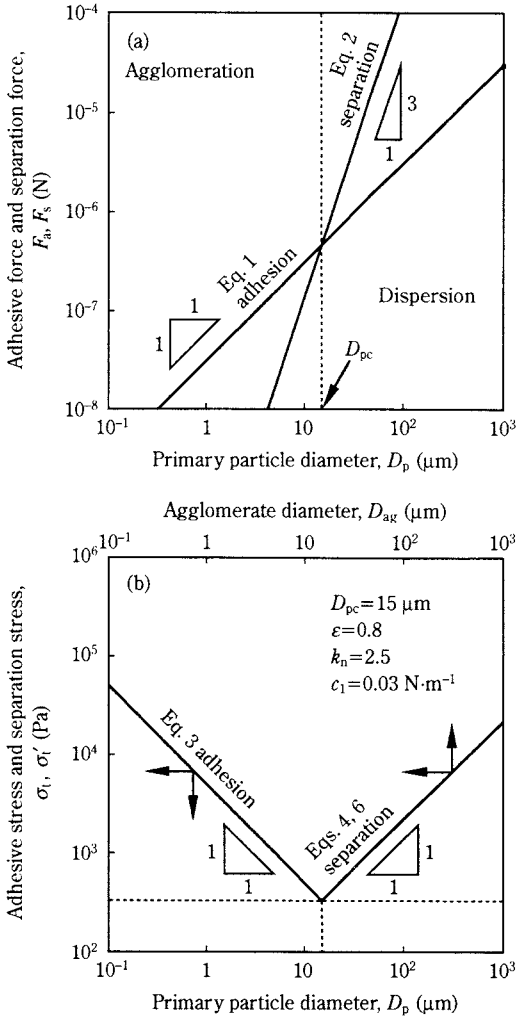

Fig. 9 Adhesive Strength and Separation Strength

ε; 2.5 for coordination number k_n; and 0.03 $N \cdot m^{-1}$ for adhesion characteristic constant c_1. When particle diameter is smaller than the critical value, adhesive force is stronger than separation force, and when it is larger, separation force is dominant (**Fig. 9 (a)**). Additionally, adhesion stress is determined from primary particle diameter, and agglomerate diameter can be found from its corresponding separation stress (**Fig. 9 (b)**).

Compressive breaking load F_{ags} can be derived in the following way from Eqs. 6, 8, 9, and 11.

$$F_{ags} = (1-\varepsilon)\frac{D_{pc}^4}{D_p^3} c_1 \tag{12}$$

If we substitute the value used above into Eq. 12 and perform a calculation with 0.7 μm as the particle diameter D_p, the compressive breaking load is 0.9 mN. Since this is nearly equal to the value obtained from the compression test in section 3.3, it shows that these analyses can be used to estimate the compressive breaking load.

5. Conclusion

We experimentally and theoretically investigated the behavior of particles (0.5 to 46 μm mass median diameter) on a flat plate when applying ultrasonic vibration, and arrived at the following conclusions.

1) Coarse particles move randomly in a primary particle state, but particles of about 10 μm become agglomerates of several tens of μm and form a film-like particle layer. Particles smaller than several μm form still larger agglomerates, which continue to move randomly on the vibrating plate.
2) The size distributions of agglomerates formed of particles under several μm in diameter could be approximated with log-normal distributions, and the median diameter was several hundred μm.
3) By analyzing the adhesive force and separation force of primary particles, and the adhesion stress and separation stress of agglomerates, it is possible to estimate agglomerate diameter and compressive breaking load. When adhesive force is proportional to primary particle diameter, agglomerate diameter is inversely proportional to primary particle diameter.

Acknowledgment

The authors express their appreciation to NIHON SEIKO Co., Ltd. for providing the antimony trioxide of various particle sizes for this experiment.

Appendix

1) Inter-particle adhesive force, F_a

We assume that inter-particle adhesive force can be approximated with van der Waals force, which is given by the following equation.

$$F_a = \frac{AD_p}{24z^2} \tag{a-1}$$

For the Hamaker constant A we used 1×10^{-19} J as a value representative of mineral powders in a gaseous phase, and for the distance between particle surfaces z we used 4×10^{-10} m, thereby yielding:

$$F_a = c_1 D_p \tag{a-2}$$

$$c_1 \fallingdotseq 0.03\ N \cdot m^{-1} \tag{a-3}$$

2) Particle coordination number, k_n

The particle coordination number is found with the Ridgway-Tarbuck experimental equation[15].

$$k_n = 13.8 - \sqrt{232\varepsilon - 57} \tag{a-4}$$

When the void fraction ε (0.8, an experimental value) is substituted in, $k_n \fallingdotseq 2.5$.

3) Critical particle diameter, D_{pc}

Critical particle diameter is derived from Eqs. 9 and 11, i.e.,

$$D_{pc} = \sqrt{\frac{6c_1}{\pi\rho_p a\omega^2}} \tag{a-5}$$

Thus when the adhesive force and separation force that act on primary particles are known, it is possible to estimate the critical particle diameter D_{pc}, however, since we had difficulty in accurately finding the vibrating plate's amplitude a in experiments, our analysis in section 4 used 15 μm for D_{pc}, based on observation results for agglomeration and disintegration. The value 0.8 μm will be obtained for amplitude a when calculating in reverse by substituting these values into Eq. a-5: c_1=0.03 $N \cdot m^{-1}$; ρ_p=5.2×10^3 $kg \cdot m^{-3}$; and ω ($=2\pi f$) $\fallingdotseq 2.5\times10^5$ $rad \cdot s^{-1}$.

Nomenclature

A	: Hamaker constant	(J)
a	: amplitude of vibration	(m)
c_1	: constant in Eq. 1	($N \cdot m^{-1}$)
c_2	: constant in Eq. 4	(−)
D_{ag}	: diameter of agglomerate	(m)
D_{ag50}	: mass median diameter of agglomerate	(m)
D_p	: primary particle diameter	(m)

D_{pc} : critical (maximum) particle diameter able to agglomerate (m)
D_{p50} : mass median diameter of primary particles (m)
F : cumulative size distribution of agglomerates on a count basis (−)
F_a : inter-particle adhesive force (N)
F_{ags} : compressive breaking load (N)
F_s : separation force (N)
f : vibration frequency (Hz)
k_n : particle coordination number (−)
z : effective inter-particle distance (m)
ε : void fraction (−)
ρ_{ag} : bulk density of agglomerate ($kg \cdot m^{-3}$)
ρ_p : particle density ($kg \cdot m^{-3}$)
σ_t : tensile strength (adhesion stress) (Pa)
σ_t' : tensile strength (separation stress) (Pa)
ω : vibrational angular velocity ($=2\pi f$) ($rad \cdot s^{-1}$)

References

1) Kage, H., M. Oba, H. Ishimatsu, H. Ogura, and Y. Matsuno. "The Effects of Frequency and Amplitude on the Powder Coating of Fluidizing Particles in Vibro-Fluidized Bed," *J. Soc. Powder Technol., Japan*, **33**, 711-716 (1996).
2) Matsusaka, S., K. Yamamoto, and H. Masuda. "Micro-Feeding of a Fine Powder Using a Vibrating Capillary Tube," *J. Soc. Powder Technol., Japan*, **32**, 83-88 (1995).
3) Matsusaka, S., M. Urakawa, and H. Masuda. "Micro-Feeding of Fine Powders Using a Capillary Tube with Ultrasonic Vibration," *Advanced Powder Technol.*, **6**, 283-293 (1995).
4) Akiyama, T. and H. Yamaboshi. "Behaviour of Vibrating Beds of Irregular Particles" Powder Technol., **69**, 163-169 (1992).
5) Akiyama, T., K. M. Aoki, and Y. Tsuruta. "Bistability of Particle Bed Surface Levels in Single Tubes Immersed in Vibrating Particle Beds," Papers of 3rd World Congress on Particle Technology, 346 in CD-ROM, Brighton (1998).
6) Yubuta, K., K. Gotoh, and H. Masuda. "Size Segregation of Polydispersed Particles Caused by Vertical Tapping," *J. Soc. Powder Technol., Japan*, **32**, 89-96 (1995).
7) Taguchi, Y. "Numerical Modeling of Convective Motion in Granular Materials," *J. Soc. Powder Technol., Japan*, **30**, 173-177 (1993).
8) Yoshida. J. "A Numerical Study on Convection of Particles in a Bin during Vertical Vibration," *J. Soc. Powder Technol., Japan*, **33**, 279-286 (1996).
9) Nakanishi, Y., S. Hashimoto, H. Fujimoto, and K. Gotoh. "The Packing Characteristics of Equal Spheres in Vertically Oscillating Cylinders," *J. Soc. Powder Technol., Japan*, **33**, 788-794 (1996).
10) Matsusaka, S., M. Furutate, and H. Masuda. "Distinct Element Simulation of Vibrating Behavior of Adhesive Fine Powder." *J. Soc. Powder Technol., Japan*, **35**, 168-173 (1998).
11) Matsusaka, S., K. Mizumoto, M. Koumura, and H. Masuda. "Evaluation of Adhesive Strength Distribution Based on Reentrainment Phenomena – Discrimination between Particle-particle and Particle-wall Interaction," *J. Soc. Powder Technol., Japan*, **31**, 719-725 (1994).
12) Rumpf. H. "Zur Theorie der Zugfestigkeit von Agglomeraten bei Kraftübertragung an Kontakt-punkten," *Chemie. Ing. Techn.*, **42**, 538-540 (1970).
13) Hiramatsu, Y. and Y. Oka. "Determination of the Tensile Strength of Rock by a Compression Test of an Irregular Test Piece," *Int. J. Rock. Mech. Min. Sci.*, **3**, 89-99 (1966).
14) Iwadate, Y., H. Kamiya, and M. Horio. "The Characterization of Agglomerates from Pressure Swing Granulation with Surface Treatment," *J. Soc. Powder Technol., Japan*, **33**. 722-727 (1996).
15) Ridgway, K. and K. J. Tarbuck. "The Random Packing of Spheres," *Br. Chem Eng.*, **12**, 384-388 (1967).

Author's short biography

Shuji Matsusaka

After graduating from Hiroshima University in 1981, and completing his masters degree at the same university two years later, Mr. Matsusaka worked at Toray Engineering Company from 1983-1989. Offered a research associate position at Kyoto University in 1989, he decided to study powders and aerosols, and obtained his Ph.D. from Kyoto University in 1993. In 1996 he was appointed a lecturer at Kyoto University, and the following year he was promoted to associate professor. One success since joining Kyoto University was winning the Iinoya Award from the Japanese Association of Aerosol Science and Technology in 1995. His research interests are in particle deposition and re-entrainment, particle electrification and its applications, particle interactions, and assembly mechanics.

Hiroaki Masuda

Professor Masuda obtained his B.Sc. and M.Sc. degrees from Hiroshima University in 1966 and 1968, respectively. In 1973 he obtained his Ph.D. from Kyoto University, which appointed him a research associate that same year. In 1979 he accepted a post as an associate professor at Hiroshima University and then took a chair in 1986. He returned to Kyoto University in 1989 as a full professor, where he has remained ever since. Among the numerous awards that Professor Masuda has won are the Excellent Paper Awards from the Society of Chemical Engineers (1980), the Society of Powder Technology (1985), and the Society of Aerosol Science and Technology (1991). He was also presented with the Iinoya Award from the Society of Aerosol Science and Technology (1995), the Distinguished Achievements Award from the Institute of Electrostatics Japan (1996), the Naito Award from the Society of Chemical Engineers, Japan (1998), and the KONA Award from Hosokawa Powder Technology Foundation (1998). Professor Masuda's current research interests are in the electrostatic phenomena and characterization of particles, the deposition and re-entrainment of fine particles, dry dispersion of powder particles, and classification of submicrometer particles.

Shiro Nakamura

Mr. Nakamura has recently joined the group after having graduated from Kyoto University in 1998.

Particle Classification of Fly Ash Using a Modified Louver-type Separator and Reduction of Unburned Carbon Amount†

Hideto Yoshida and Kunihiro Fukui
*Dept. of Chem. Eng., Hiroshima Univ.**
Hideki Morizaki
*Chugoku Electric Co., Inc., Technical Research Center***

Abstract

Experimental and theoretical studies have been conducted on the classification of fly ash particles using a bench-scale louver separator. A new type of louver blade based on Joukowski's theory demonstrated classification performance superior to that of the plane-type blade. Classification performance changed with the angle of louver blades, the optimum blade angle being 50° for the Joukowski type and 70° for the plane type.

The finite element method was used to solve the Navier-Stokes equations. Calculated partial separation efficiency agreed with the experimental results.

The unburned carbon amount on the classified fine particle decreased about 20 to 30 wt%.

1. Introduction

In recent years, most of thermal power plants use pulverized coal, but because coal combustion produces large amounts of fly ash as a by-product, it is important to find out effective usage of the fly ash. Because fly ash particles are spherical, mixing the fly ash particles into cement improves qualities such as the product's strength, fluidity, and airtightness. For that reason it has been used in cement for some cases. In particular, the effect of fly ash particles in cement becomes even better when its particle sizes are small and it has a low percentage of unburned carbon. Thus as one of the means of increasing the effect of fly ash in cement usage, size separation is effective when the feed fly ash particles include much unburned carbon. For separating coarse particles in feed fly ash, a louver separator with cut sizes of 10 to 100 μm is appropriate. However, research papers reported[1-3] the performance of the separator by use of comparatively small devices. It is necessary to know the performance of large scale louver separator.

In our research we conducted bench-scale separation experiments by use of a louver-type separator having a new kind of Joukowski-type blade[5] or a plane-type blade. Experimental and simulation studies have been conducted on the performance of the bench-scale louver-type separator, and its optimum operating conditions. Additionally, we experimentally examined the amount of unburned carbon in the separated small particles by use of the louver-type separator. Here, we report some of the interesting results regarding the bench-scale louver separator.

2. Experimental Separator

Fig. 1 shows the experimental apparatus we used, and **Fig. 2** is a photograph of the louver unit. Experiments have been conducted with the bench-scale louver-type separator capable of separating compara-

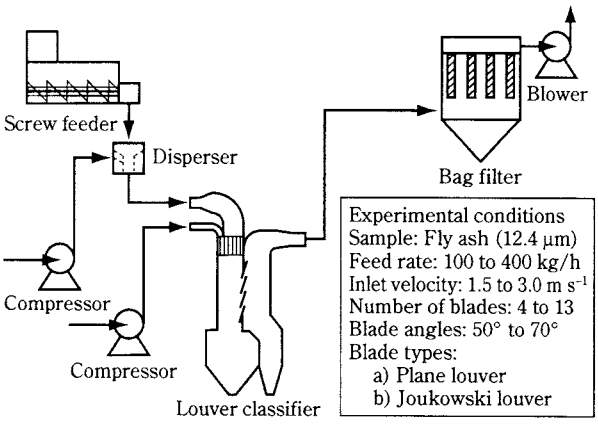

Fig. 1 Experimental Apparatus

* 1-4-1 Kagamiyama, Higashi-hiroshima, 739-8527
**3-9-1 Kagamiyama, Higashi-hiroshima, 739-8527
† This report was originally printed in J. Soc. Powder Technology, Japan. **36**, 454-461 (1999) in Japanese, before being translated into English by KONA Editorial Committee with the permission of the editorial committee of the Soc. Powder Technology, Japan.

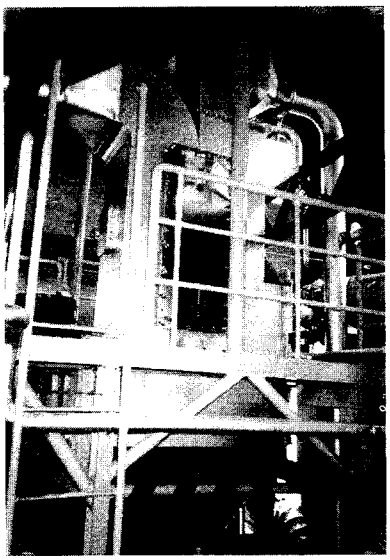

Fig. 2 Photograph of Louver Classifier

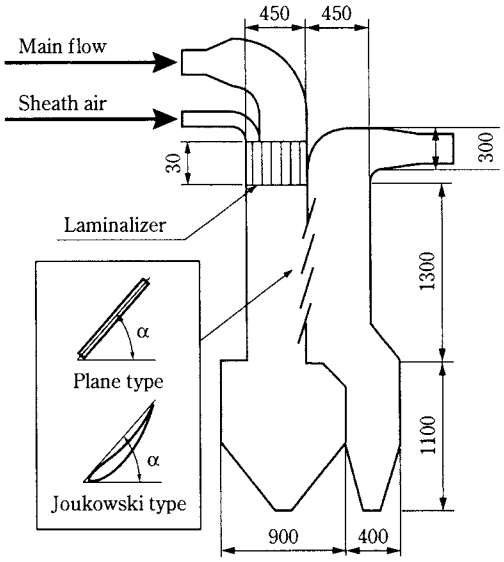

Fig. 3 Structure of Louver Classifier

tively large amounts of fly ash particles. Its characteristics are:

(1) A row of louver blades used are shown in the center of **Fig. 3**. In addition to the conventional plane-type blades, we also used new Joukowski-type blades based on blade theory[4] to improve separation performance.

(2) It allows the broad-range study of louver blade angle, number of blades, and inlet velocity on the reduction amount of the unburned carbon in the classified particles.

(3) It employs the clean air method at the louver inlet, and allows experiments to be conducted with either the blow-up or blow-down method.

Experimental conditions:

Powder feed rate	100 to 400 kg/h
Air flow rate	27 m^3/min
Blow-down rate	0 to 10%
Blow-up rate	0 to 10%
Velocity at louver inlet	0.5 to 3 m s^{-1}
Blade angle	50 to 70°
Number of blades	3 to 13

Fly ash particles with mass median diameter of 12.4 μm formed as a by-product at Chugoku Electric's Shin-Onoda Power Station were used. Separation performance was evaluated using the partial separation efficiency curve calculated with the following equation.

$$\Delta\eta(D_p) = \frac{m_a f_a(D_p)\Delta D_p}{m_a f_a(D_p)\Delta D_p + m_b f_b(D_p)\Delta D_p} \quad (1)$$

Where:

m_a and m_b are the masses of large and small particles, respectively, and $f_a(D_p)$ and $f_b(D_p)$ are the size distributions of those particles.

Particle size distribution measurements were conducted with a centrifugal settling method (Shimadzu SA-CP4L) and a laser diffraction analyzer (Horiba Mfg. Co. LA-720).

3. Results of Separation Performance Experiment

3.1 Joukowski-type Blades

As the blades in the louver-type separator, we used the usual plane-type blades and newly developed Joukowski blades. We used Joukowski blades because the previously reported[5] results of an experiment with a small scale separator showed that Joukowski blades had good separation performance.

Figs. 4 through **7** present experimental results by use of the Joukowski blades. Effects of blade angle are shown in **Fig. 4**. Compared with 40°, 50° and 60°, the 50° angle shows smaller 50% cut size, and the slope of the partial separation efficiency curve is larger, thus yielding high performance. These findings coincide with those of our previous report[5]. When the blade angle was 40°, performance dropped because the horizontal separation effect is the dominant particle separation mechanism. In case of 60°, separation performance dropped due to the increased air flow turbulence inside the louver. Effective blade spacings between the louver blades become smallest for the blade angle of 60°.

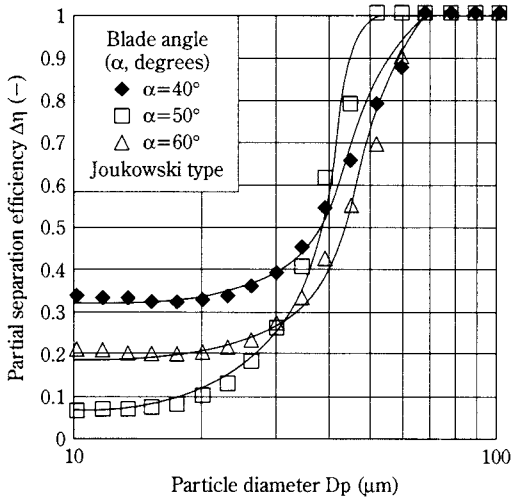

Fig. 4 Effect of Blade Angle on Partial Separation Efficiency (n=4, u_0=2 m s^{-1}, W=100 kg/h)

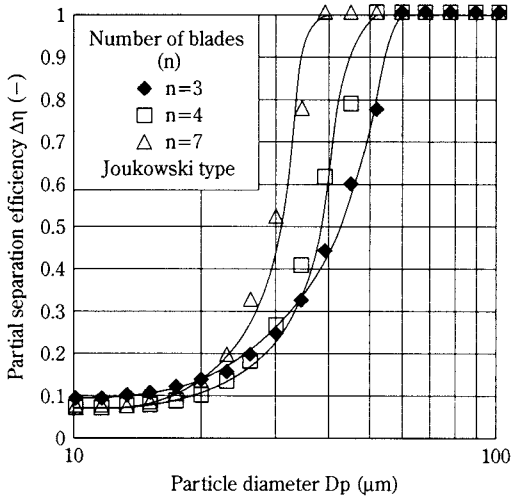

Fig. 5 Effect of Number of Blades on Partial Separation Efficiency (u_0=2 m s^{-1}, α=50°, W=100 kg/h)

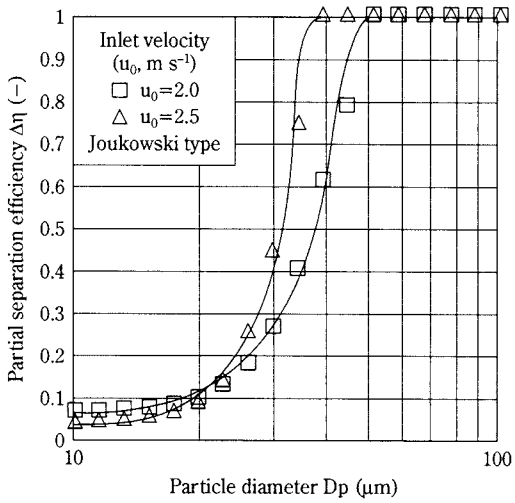

Fig. 6 Effect of Inlet Velocity on Partial Separation Efficiency (n=4, α=50°, W=100 kg/h)

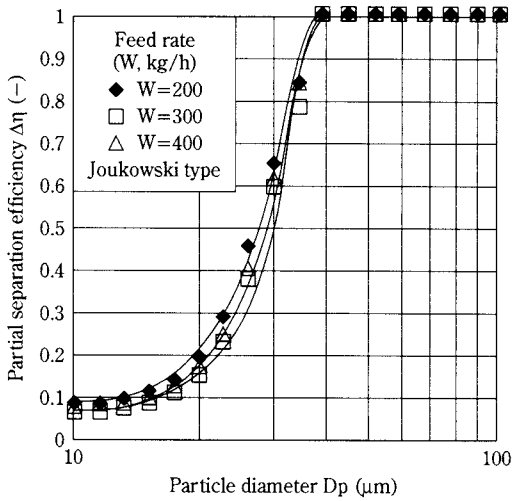

Fig. 7 Effect of Feed Rate on Partial Separation Efficiency (n=4, α=50°, u_0=2.5 m s^{-1})

Fig. 5 shows the effect of the number of blades with the 50° blade angle. Increasing the number of blades decreased the cut size. This is due to the following reasons. Increasing the number of blades gives particles more opportunity to be separated out. Because increasing the number of blades indicate that they occupied a greater volume of space, thereby reducing the effective flow passage area and increasing the flow velocity between louver blades. The results that the cut size becomes smaller when the number of blades increases coincide with our previously reported experimental data.

Fig. 6 shows the effect of louver inlet velocity on the partial separation efficiency. We observed separation performance at the two inlet velocities of 2 and 2.5 m s^{-1} under the constant conditions of four blades, blade angle of 50°, and powder feed rate of 100 kg/h. For the inlet velocity equals to 2.5 m/s, the cut size becomes small compared to the 2 m s^{-1} velocity, and better separation is realized. Because of a better dispersive effect on agglomerated particles among the louver blades and an increase in the inertial effect of particles, the classification performance becomes better for inlet velocity equals to 2.5 m/s.

Fig. 7 shows the effect of powder feed rate on separation performance. When using the Joukowski blades, the change in separation performance is small even when the powder feed rate increased from 200 to 400 kg/h. Hence the Joukowski blades used in this experiment are considered promising for practical usage.

3.2 Plane-type Blades

Here we discuss the experimental and simulation results for separation performance when using the plane-type blades. Our numerical simulation used are the k-ε turbulence model shown in **Table 1**. We divided the calculation region into small triangular elements and used the relaxation method. In our calculations, we used the stream function-vorticity method. For boundary conditions we used zero flow velocity at the wall. To calculate the stream function at the second or third louver blade, we used the concept that the pressure is a single value function.

Fig. 8 shows the influence of blade angle on separation performance. The blade angle of 70° indicated a smaller 50% cut size compared to the 60° angle, and the slope of its partial separation efficiency curve was large and close to ideal separation. By the velocity distribution of the numerical simulation shown in **Fig. 9**, the particles flow mainly between the third and fourth blades for a 60° angle. For a 70° angle, although the flow is mainly between the third and fourth blades as for a 60° angle, but there is also flow to a certain extent between the first and second, and second and third blades, and flow distortion is small compared to the case of blade angle of 60°. The cut size becomes small with 70° blade angle because particles are more often subjected to the separation effect near the inlet at the tips of the louver blades.

Fig. 10 shows the effect of the number of blades on the separation characteristics. As **Fig. 5** shows, when using the Joukowski blades, the cut size becomes smaller when increasing the number of blades, but

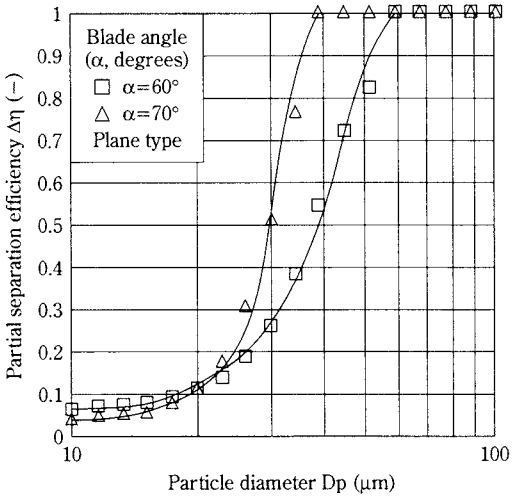

Fig. 8 Effect of Blade Angle on Partial Separation Efficiency (n=4, u_0=3 m s^{-1}, W=100 kg/h)

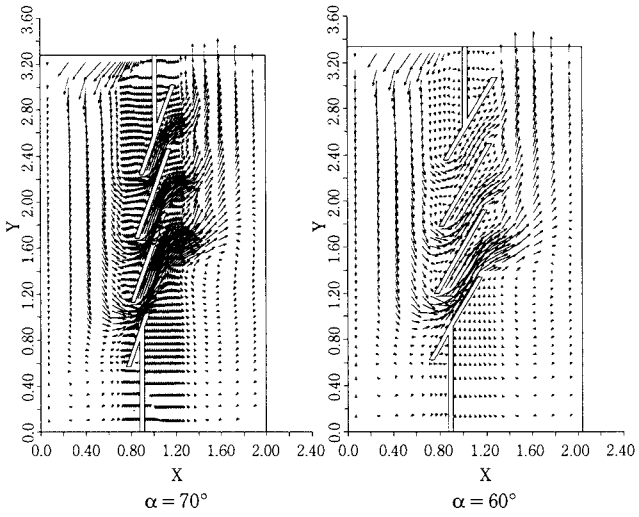

Fig. 9 Calculated Fluid Velocity Distributions (α=70°, α=60°)

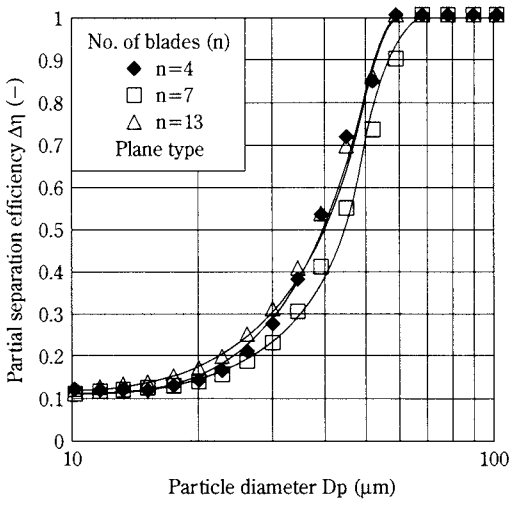

Fig. 10 Effect of Number of Blades on Partial Separation Efficiency (u_0=2 m s^{-1}, α=60°, W=100 kg/h)

Table 1 Turbulence Calculation Equations

$$u\frac{\partial\phi}{\partial x}+v\frac{\partial\phi}{\partial y}=\frac{\partial}{\partial x}\left(\Gamma_\phi\frac{\partial\phi}{\partial x}\right)+\frac{\partial}{\partial y}\left(\Gamma_\phi\frac{\partial\phi}{\partial y}\right)+S_\phi$$

ϕ	Γ_ϕ	S_ϕ
ψ	1	ω
ω	$\frac{1}{Re}+\nu_t$	R
k	$\frac{1}{Re}+\frac{\nu_t}{\sigma_k}$	$\nu_t\Delta-\varepsilon$
ε	$\frac{1}{Re}+\frac{\nu_t}{\sigma_\varepsilon}$	$C_1C_\mu k\Delta-C_2\frac{\varepsilon^2}{k}$

$$R=\omega\left(\frac{\partial^2\nu_e}{\partial x^2}+\frac{\partial^2\nu_e}{\partial y^2}\right)+\frac{\partial\omega}{\partial x}\frac{\partial\nu_e}{\partial x}+\frac{\partial\omega}{\partial y}\frac{\partial\nu_e}{\partial y}$$

$$-4\frac{\partial^2\psi}{\partial x\partial y}\frac{\partial^2\nu_e}{\partial x\partial y}+2\frac{\partial^2\psi}{\partial y^2}\frac{\partial^2\nu_e}{\partial x^2}+2\frac{\partial^2\psi}{\partial x^2}\frac{\partial^2\nu_e}{\partial y^2}$$

$$\Delta=4\left(\frac{\partial^2\psi}{\partial x\partial y}\right)^2+\left(\frac{\partial^2\psi}{\partial y^2}-\frac{\partial^2\psi}{\partial x^2}\right)^2 \qquad \varepsilon=C_\mu\frac{k^2}{\nu_t}$$

$C_\mu=0.09$, $C_1=1.44$, $C_2=1.92$ $\quad\sigma_k=1.0$, $\sigma_g=1.3$

when using the plane type there was not clearly defined tendency, making for little change in cut size.

Experimental results for the effect of powder feed rate on separation performance are shown in **Fig. 11**. The ratio of small particles into the coarse particle side increases with powder feed rate. This is probably because particle dispersion became incomplete as the powder feed rate increased. By contrast, there was not clear influence when using the Joukowski louver as shown in **Fig. 7**, signifying that the Joukowski type is superior to the plane type with regard to separation. The probable reason is that, when using the Joukowski type, flow velocity between louver blades is faster than that with the plane louver even when inlet velocity is the same, because Joukowski-type blades are thicker. Thus when using the Joukowski-type blades, the particle dispersion effect between blades increases, and change of the separation performance becomes small even under high loaded powder flow rate conditions.

Fig. 12 presents experimental and simulation results obtained for louver inlet velocities of 1.5 and 3 m s^{-1} under conditions of four louver blades, 60° blade angle, and powder feed rate of 100 kg/h. The 50% cut size for inlet velocity equals to 3 m/s was small compared to the case of 1.5 m s^{-1} due to the increased inertial effect of particles. The experimental values more or less coincided with calculated values except for particle size less than 20 μm. When inlet velocity becomes high, the separation characteristic is closer to the ideal, this tendency agrees with the results for the Joukowski-type blades shown in **Fig. 6**.

Fig. 13 shows the effect of inlet velocity when blade angle was 70°. Simulation results indicate that, just as when blade angle is 60°, the 50% cut size is small when flow velocity is high, but the experimental values are not clearly indicated. The probable reason is that even though the inertial effect of particles increased as flow velocity between blades increased, reentrainment of particles after they collided with the blades is also facilitated.

Figs. 12 and **13** indicate that when inlet velocity is 1.5 m s^{-1}, the cut size is smaller with a 70° blade angle than that with a 60° angle. Thus the blade angle of 70° is desirable when the louver is to be used as a dust collector.

Separation performance is good with a blade angle of 50° for the Joukowski louver and 70° for the plane louver, so the results of the two cases are compared in **Fig. 14**. The 50% cut size is small, and the slope of the partial separation efficiency curve of the Joukowski louver is larger than that of the plane louver. These

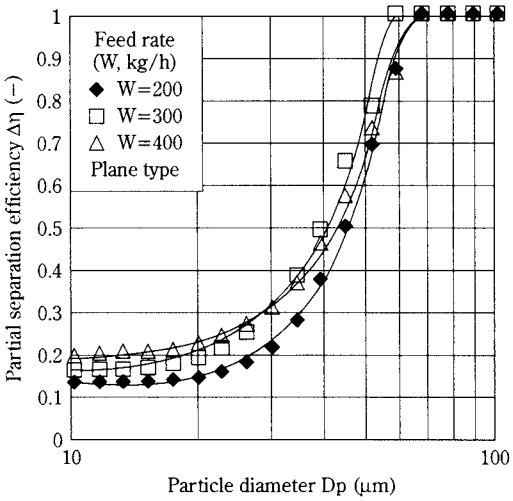

Fig. 11 Effect of Feed Rate on Partial Separation Efficiency (n=4, α=50°, u_0=2 m s^{-1})

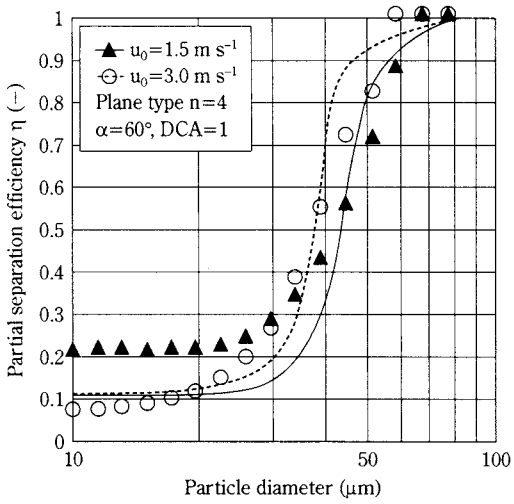

Fig. 12 Effect of Inlet Velocity on Partial Separation Efficiency (n=4, α=60°)

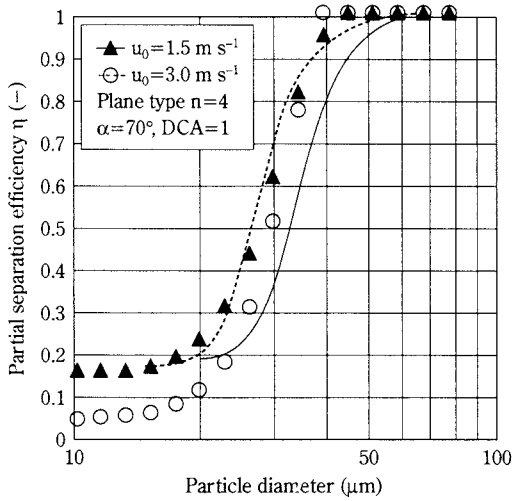

Fig. 13 Effect of Inlet Velocity on Partial Separation Efficiency (n=4, α=70°)

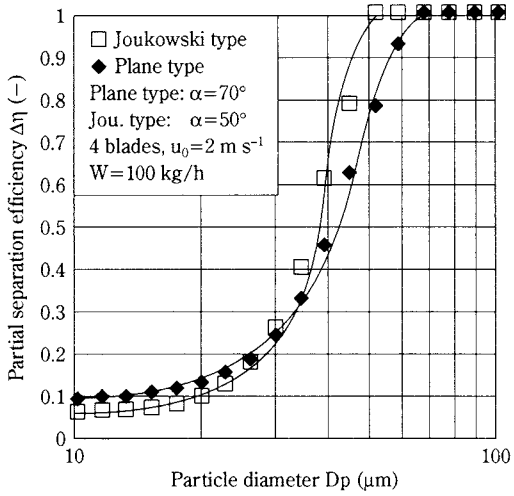

κ value

Joukowski type	Plane type
1.6	2.0

Fig. 14 Experimental Result of Classification Efficiency by Two Blade Types

results coincide with the findings reported by us previously, and the reason is presumed to be that the Joukowski louver creates less turbulence than the plane louver inside the separator.

4. Experimental Results on Reducing Unburned Carbon

Here we shall discuss the results on the reduction rate of unburned carbon in the classified fine powder. The feed fly ash contained an average of 3.0 wt% unburned carbon, the ratio increases with particle diameter. This means that when the louver is used to separate coarse particles having much unburned carbon amount, it is expected that reduction of the unburned carbon amount of fine particle side is possible. **Fig. 15** presents photographs showing the extent to which the unburned carbon amount had been reduced in separated fine powder in comparison with the feed particles. Overall the separated coarse particles are darker in color than the feed particles, indicating the presence of much unburned carbon. To measure the unburned carbon content, we burned the powder at 800°C for 1.5 h and determined that portion from the loss in mass.

Fig. 16 shows the results obtained for reducing unburned carbon with the Joukowski louver while varying louver inlet velocity. When the louver inlet velocity was between 1 and 2 m s^{-1}, we found that the higher the louver inlet velocity, the more unburned carbon was removed, but when the velocity of 2 m s^{-1}

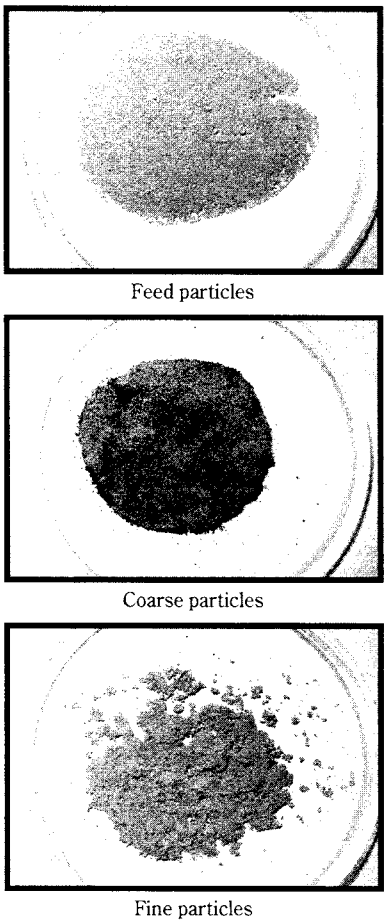

Fig. 15 Photographs of Feed, Coarse, and Fine Particles

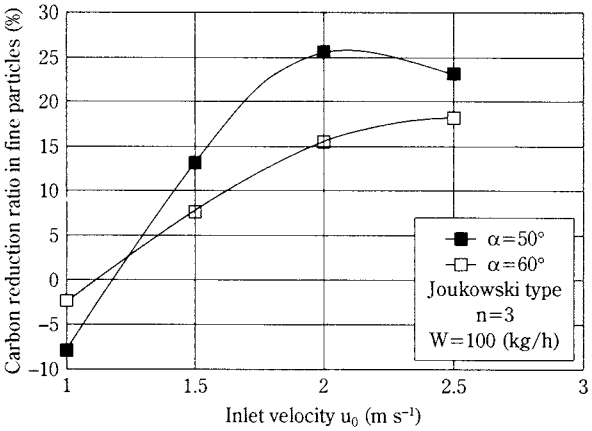

Fig. 16 Relationship Between Carbon Reduction Rate and Inlet Velocity (Joukowski type)

was exceeded, less unburned carbon was removed. The unburned carbon amount of fly ash displays two peaks, for ultra-fine particles and for large particles of about 30 μm and larger, and the proportion of large particles is greater. But as **Fig. 17** shows, the large particles contained many fine particles of 1 to 2 μm in size which contained much unburned carbon. Thus

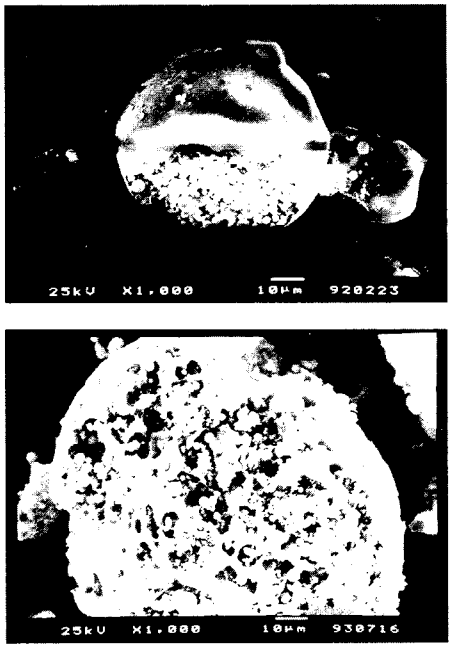

Fig. 17 Photographs of Feed Fly Ash Particles

the probable reasons that unburned carbon amount decreased little for velocities exceeding 2 m s^{-1} are that large particles are reentrained and moved to the fine particle side, and that the thin outer layers making up large particles is broken, thereby releasing and scattering the small particles inside them, which are captured on the fine particle side. For 50° blade angle, which provided good separation performance, unburned carbon amount was reduced more than at a 60° angle. This is probably because the blade angle of 50° provides separation close to the ideal. Also, when the blade angle was 50°, we achieved the unburned carbon reduction rate of about 23% even when increasing the powder feed rate to 400 kg/h. The probable reason that the unburned carbon reduction rate did not decrease even if the powder feed rate was increased using the Joukowski-type blades is that there was an effect by which particles disperse appropriately only to the extent that the fine particles contained inside large particles will not scatter just after passing through the blades.

Experimental results of the plane-type blades are shown in **Fig. 18**. Overall, an increase in inlet flow velocity decreased the unburned carbon amount in fine particles, but the reduction rate of the unburned carbon amount was small for 3 m s^{-1}. This was probably because, just as when using the Joukowski-type blades, in this range the particle dispersion effect in the louver was strong. In other words, it is probably because the fine particles containing much unburned carbon, which are contained in the coarse particles,

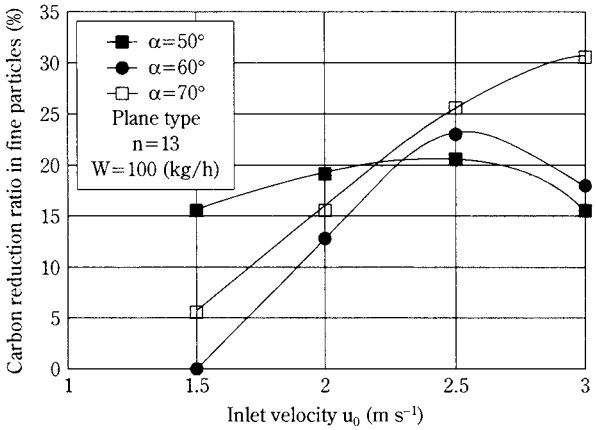

Fig. 18 Relationship Between Carbon Reduction Rate and Inlet Velocity (plane type)

moved to the fine particle side.

Regarding the blade angle, we found that the 70° angle, which gave good separation performance, produced the largest decrease in unburned carbon amount in fine particles. The closer to ideal separation, the more the reduction of unburned carbon amount in fine particles was achieved, and this tendency was the same as that for the Joukowski-type blades. Both blade types were capable of reducing unburned carbon amount by 20 to 30%, suggesting that the louver separator is an effective method to control the amount of unburned carbon amount in the feed fly ash particles.

5. Conclusion

We used a bench-scale louver separator to classify fly ash particles and to reduce the unburned carbon amount, and the following findings are obtained.

(1) In performing separation, a blade angle of 50° for the Joukowski-type and 70° for the plane-type blades yielded a small 50% cut size and a large slope for the partial separation efficiency curve, indicating good performance.

(2) The 50% cut size became smaller when louver inlet velocity was high, but for the optimum blade angle the Joukowski-type blades provided a smaller 50% cut size and a larger slope for the partial separation efficiency curve than plane-type blades.

(3) The Joukowski-type blades yielded a smaller 50% cut size when using a larger number of blades. Even for a powder feed rate of about 400 kg/h, there was a smaller decrease in separation performance compared to the plane-type blades.

(4) With regard to the unburned carbon reduction rate on the fine particle side, we found that both

the Joukowski and plane blades were capable of changing a 20 to 30 wt% decrease of unburned carbon amount in separated fine particles.

Nomenclature

D_p	: particle diameter	(μm)
$f_a(D_p), f_b(D_p)$	: size distribution of large and small particles	(1/μm)
k	: turbulence energy	(−)
n	: number of blades	(−)
m_a, m_b	: masses of large and small particles	(kg)
Re	: flow Reynolds number	(−)
x, y	: coordinates of x and y directions	(m)
u, v	: fluid velocity of x and y directions	(m/s)
u_o	: inlet fluid velocity	(m/s)
W	: powder flow rate	(kg/h)
α	: blade angle	(deg)
υ_t	: kinematic viscosity	(m^2/s)
υ_e	: effective viscosity	(m^2/s)
ρ_p	: particle density	(kg/m^3)
$\Delta\eta$	: partial separation efficiency	(−)
$C_\mu, C_1, C_2, \sigma_k, \sigma_e$	: model parameters	(−)
ϕ	: dependent variable	(−)
Ψ	: stream function	(−)
ω	: vorticity	(−)
ε	: turbulence energy dissipation rate	(−)

References

1) Iinoya, K. "Syuujin Kougaku," p. 86, *Nikkan Kogyou* (1980)
2) Iinoya, K., N. Kimura, and Z. Tanaka. "On the Classification by Cyclone and Louver," *J. of Soc. Powder Technol. Japan*, **1**, 2, pp. 114-119 (1964)
3) Ushiki, K., Z. Tanaka, and K. Iinoya. "On the Performance of the Upper-End Feed Louver Classifier," *Kagaku-Kougaku*, **38**, 2, pp. 151-156 (1974)
4) Ishiwata, R. *Ryuutairikigaku*, pp. 85-87, Morikita-Shuppan (1993)
5) Yoshida, H., K. Fukui, K. Kanagawa, M. Okamoto, Chi-Mun Yun and K. Iinoya. "Particle Classification of a Louver-type Separator," *J. of Soc. Powder Technol. Japan*, **34**, 9, pp. 684-689 (1997)

Author's short biography

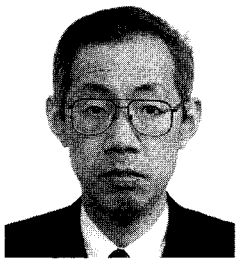

Hideto Yoshida

The author is Professor of Chemical Engineering Department at Hiroshima University since 1994. His major research interests are fine particle classification, numerical simulation of cyclone separator, cut size control of dry and wet cyclones, development of particle size distribution with automatic liquid sedimentation method and recycling of fly ash particles.

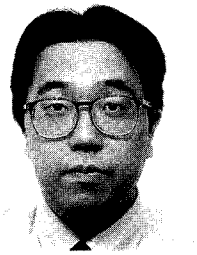

Kunihiro Fukui

The author received his B.S. and M.S. degrees from Kyoto University in 1991 and 1993. He earned his Ph.D. degree in Chemical Engineering in 1998 from Kyoto University. He is Research Instructor of Chemical Engineering Department at Hiroshima University since 1996. His major research interests are accurate size classification of fine particles, measurement of particle size distribution and recycling technology of coal flyash.

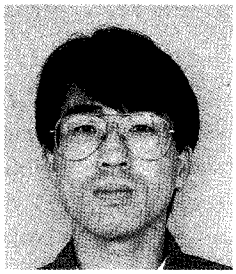

Hideki Morizaki

- The Chugoku Electric Power Co., Inc.
- Technical Research Center 1994-1998
- Shimonoseki Power Station 1999-

Specific Surface Area Measurement by Air Permeability with Consideration for the Molecular Flow Effect†

Akira Suganuma, Yu Matsumoto, Egure Murata and Toshitaka Hamada
*Science University of Tokyo, Department of Industrial Chemistry, Faculty of Science & Technology**

Abstract

Because gas permeation through a powder bed is affected by molecular flow, applicability of the Kozeny-Carman equation, which neglects this effect, is limited to powders coarser than about 10 μm. $\Phi_B = \Phi_V + \delta\Phi_M$ is a general expression in some permeability equations for finer powders, where Φ_B denotes the permeability of a bed, Φ_V is a viscous flow term, and Φ_M is a molecular flow term. δ is a constant that adjusts for the molecular flow effect. It has been more than 40 years since $\delta=0.515$ was proposed by Rigden, 0.97 by Lea and Nurse, and 1.215 by Carman. It is because of these large differences in δ that the Kozeny-Carman equation is still used. In this paper $\delta=0.82$ is proposed as a reasonable value based on a least squares analysis of Rigden's data and with reference to Knudsen's equation of capillary permeation. The use of $\delta=0.82$ allows the more reasonable measurement of powders down to about 1 μm.

1. Introduction

Specific surface area measurement by gas absorption also measures interior surface area including that of cracks, while the air permeability method measures only the surface area of the gas-permeated voids in packed beds. In principle, therefore, it measures the surface area corresponding to particle outlines. As the air permeability and gas absorption measurement methods differ by nature from one another, air permeability is an important means of powder assessment even now when gas absorption has become quick and simple.

When measuring specific surface area by air permeability the limit at which the Kozeny-Carman equation can be applied is about 10 μm, because with finer powders the influence of molecular flow must be taken into account. This fact became evident at about the time the Powder Forum was formed. And yet, even now after the Forum has met 35 times, nearly all introductory texts state that specific surface area measured by air permeability is calculated with the Kozeny-Carman equation. Very few books mention the fact that this equation is an approximation which ignores the influence of molecular flow, and one rarely finds a book which states clearly that its limit of applicability is about 10 μm. Some of the causes of this situation are that formerly there were not as many fine powders under 10 μm as there are now; the simplicity of the Kozeny-Carman equation, which finds specific surface area by square root extraction calculation alone, presented a major practical advantage in the days before pocket calculators; and because it was still difficult to accurately measure the particle size distribution of fine powders, about all people did was compare the specific surface area measured by air permeability to electron microscope photomicrographs of the samples and discuss them. It was under these circumstances that the Kozeny-Carman equation continued to be used, with no conclusion being reached in the controversy over ways to correct for the influence of molecular flow.

In addition to reconfirming that the Kozeny-Carman equation's limit of application is about 10 μm, this report discusses a suitable packed bed permeability equation that takes the influence of molecular flow into account, for the purpose of overcoming this limit and making it possible to use air permeability to measure the specific surface area of fine powders of about 1 μm.

* 2641 Yamazaki, Noda-shi, Chiba 278-8510 Japan
Tel. 0471-24-1501

† This report was originally printed in J. Soc. Powder Technology, Japan. **35**, 649-654 (1998) in Japanese, before being translated into English by KONA Editorial Committee with the permission of the editorial committee of the Soc. Powder Technology, Japan.

2. Knudsen Number (*Kn*) of a Gas Flow Permeating a Powder Bed[1]

The *Kn* of a gas flow through a capillary is defined as the ratio of the mean free path of gas molecules λ to the diameter of the capillary d.

$$Kn \equiv \lambda/d \tag{1}$$

λ can be calculated with Eq. 2, coming to about 0.065 μm at ordinary temperature and pressure.

$$\lambda = 2(\mu/\rho)(\pi M/8RT)^{1/2} \tag{2}$$

In a packed bed with void fraction ε packed with a powder having volume-referenced specific surface area Sv, the hydraulic radius r_h of the voids through which gases penetrate is found with Eq. 3.

$$r_h = \{\varepsilon/(1-\varepsilon)\}/Sv \tag{3}$$

Because the hydraulic radius of a capillary is $d/4$, in this report we defined the packed bed void equivalent diameter d_H with Eq. 4, and the *Kn* gas flow permeating the packed bed with Eq. 5.

$$d_H \equiv 4r_h = (4/Sv)\{\varepsilon/(1-\varepsilon)\} \tag{4}$$

$$Kn \equiv \lambda/4d_H = \lambda(Sv/4)\{(1-\varepsilon)/\varepsilon\} \tag{5}$$

The region $Kn<0.01$ is called the viscous flow region, $0.01<Kn<0.1$ is the slip flow region, $0.1<Kn<10$ is the transitional flow region, and $10<Kn$ is the molecular flow region. Calculating the relationship among S_V, ε, and *Kn* while assuming normal temperature and air pressure (λ=0.065 μm) yields the values in **Table 1**. When measuring specific surface area by air permeability the slip flow region $0.01<Kn<0.1$ and the region around it are important, and permeability flow when using the air permeability method to measure the specific surface area of fine powders 10 to 1 μm in size is found in the slip flow region.

Table 1 *Kn* of Permeating Air (λ=0.065 μm) Through Packed Powder Bed

$D_s=6/S_v$ (μm)	30	10	3	1	0.3
S_v (km²/m³)	0.2	0.6	2	6	20
ε=0.3	0.0076	0.0228	0.0758	0.228	0.758
ε=0.4	0.0049	0.0146	0.0488	0.146	0.488
ε=0.5	0.0033	0.0098	0.0325	0.098	0.325
ε=0.6	0.0022	0.0065	0.0217	0.065	0.217
ε=0.7	0.0014	0.0042	0.0139	0.042	0.139

2. Permeability Equations that Take the Molecular Flow Effect into Account

2.1 Equations for Capillary Gas Flow

The authors shall start by exploring the effect of molecular flow on capillary permeability, the reason being that this paper adopts the capillary aggregate model, which regards a packed particle bed as an aggregate of curved non-circular cross-section capillaries. And to simplify the discussion, the molar flux of a gas flowing through a capillary, j_C, is expressed as Φ_C after having made it nondimensional using the capillary's axial pressure gradient $(dp/dz)_C$, kinetic viscosity (μ/ρ), gas constant R, and absolute temperature T.

$$\Phi_C \equiv j_c RT/\{(dp/dz)c(\mu/\rho)\} \tag{6}$$

In the viscous flow region $Kn<0.01$ it is possible to use the Hagen-Poiseuille law of Eq. 7 by regarding the flow as the viscous flow of a continuous fluid. When $10<Kn$ Eq. 8 can be used by regarding the flow as a perfect molecular flow.

$$\Phi_{C,V} = (\pi/64)\,Kn^{-2} \qquad Kn<0.01 \tag{7}$$

$$\Phi_{C,M} = (2/3)\,Kn^{-1} \qquad 10<Kn \tag{8}$$

When $0.01<Kn<10$ one must take into account the influence of both viscous flow and molecular flow. In the slip flow region ($0.01<Kn<0.1$), which adjoins the viscous flow region, the comparatively small influence of molecular flow allows the use of the permeability equation Eq. 9 of the slip flow model, which incorporates molecular flow influence as a correction term for the slippage effect along capillary walls.

$$\Phi_{C,S} = \Phi_{C,V} + \delta\Phi_{C,M} \qquad 0.01<Kn<0.1 \tag{9}$$

The constant δ in Eq. 9 is the weight coefficient of the molecular flow term. If the entire range of *Kn* is covered instead of limiting δ to the slip flow region, then δ is a function of *Kn*.

$$\Phi_C = \Phi_{C,V} + \delta(Kn)\Phi_{C,M} \tag{10}$$

If Knudsen's half-experimental equation,[2] which is well-known as a capillary permeability equation applicable to the entire range of *Kn*, is expressed in the form of Eq. 10, then

$$\Phi_{C,K} = \Phi_{C,V} + \delta_K(Kn)\Phi_{C,M}$$

$$\delta_K(Kn) = \{Kn + 1.00(\pi/2)^{1/2}\}/\{Kn + 1.235(\pi/2)^{1/2}\} \tag{11}$$

$\delta_K(Kn)$ is the monotone increase function of *Kn*, making the limit value of $Kn\to 0$ about 0.81 and that of $Kn\to\infty$ equal to 1. But because change in $Kn<0.1$ is very slight, it is possible to approximate with a δ_K constant of around 0.82 if the applicable range is lim-

Table 2 Knudsen's Weight Function, $\delta(Kn)$[2]

Kn	$\delta(Kn)$	Kn	$\delta(Kn)$
0.001	0.8098	0.100	0.8213
0.002	0.8100	0.200	0.8315
0.004	0.8102	0.400	0.8488
0.010	0.8109	1.000	0.8844
0.020	0.8121	2.000	0.9170
0.040	0.8145	4.000	0.9469

ited to the slip flow region (**Table 2**).

$$\delta_K(Kn) \doteqdot \delta_K = 0.82 \qquad 0.01 < Kn < 0.1 \tag{12}$$

Below this will be called Knudsen's approximation equation.

2.2 Powder Bed Gas Permeability Equations

Molar permeation flux j_B of a packed bed cross sectional area reference is expressed as Φ_B after having made it nondimensional using the packed bed axial pressure gradient $(dp/dz)_B$, kinetic viscosity (μ/ρ), gas constant R, and absolute temperature T.

$$\Phi_B \equiv j_B RT/\{(dp/dz)_B(\eta/\rho)\} \tag{13}$$

The subscript B signifies the packed bed. Regarding a packed particle bed as an aggregate of curved noncircular cross-section capillaries, capillary equivalent diameter would be, if we adopt the capillary aggregate model supposedly given by Eq. 4,

$$\Phi_B = (2\varepsilon/k)\,\Phi_C \tag{14}$$

Where:

k=5 is the Kozeny-Carman coefficient.

If the capillary permeability equation Eq. 7 for the viscous flow region is substituted in Φ_C, the packed bed permeability equation Eq. 15 for the viscous flow region is obtained, and if the capillary permeability equation Eq. 8 for the molecular flow region is substitution, the packed bed permeability equation Eq. 16 for the molecular flow region is obtained.

$$\Phi_{B,V} = (2\varepsilon/k)\,(\pi/64)\,Kn^{-2} \qquad Kn < 0.01 \tag{15}$$

$$\Phi_{B,M} = (2\varepsilon/k)\,(2/3)\,Kn^{-1} \qquad 10 < \mathrm{Kn} \tag{16}$$

Eq. 15 is the Kozeny-Carman equation. If the applicable range of Eq. 15, $Kn < 0.01$, is converted with $\varepsilon=0.4$ and $\lambda=0.065$ μm, then $S_V < 4\times10^5$ m^2/m^3 and $D_S=6/S_V > 15$ μm. This is the limit of application for the Kozeny-Carman equation.

Based on liquid permeability and air permeability measurement results, Rigden[3] observed that the limit of applicability for the Kozeny-Carman equation, which ignores molecular flow influence, is about 10 μm, and that molecular flow influence must be taken into consideration for finer powders. Lea and Nurse, and Carman et al., published papers saying the same thing almost simultaneously.[4] Rigden adopted the capillary aggregate model and proposed the packed bed permeability equation Eq. 17 which substituted the capillary permeability equation Eq. 9 of the slip flow model for Φ_C in Eq. 14.

$$\Phi_{B,S} = (2\varepsilon/k)\,(\Phi_{C,1} + \delta\Phi_{C,2}) = \Phi_{B,V} + \delta\Phi_{B,M} \tag{17}$$

Below we shall use the term Rigden-type packed bed permeability equations for packed bed permeability equations of this type. Converting the coefficient used by Rigden to δ yields 0.515.

$$\Phi_{B,R} = \Phi_{B,V} + \delta_R\,\Phi_{B,M} \qquad \delta_R = 0.515 \tag{18}$$

Rigden's main point was in the implementation of Eq. 17, and $\delta_R=0.515$ is a value merely quoted from the literature, but it is quite small in comparison with the $\delta_K=0.82$ given in the previous section. Carman et al. claimed that δ_K was too small and proposed $\delta_C=1.215$.[5]

$$\Phi_{B,C} = \Phi_{B,V} + \delta_C\,\Phi_{B,M} \qquad \delta_C = 1.215 \tag{19}$$

The paper released at about the same time by Lea and Nurse proposed $\delta_{LN}=0.97$.[4]

$$\Phi_{B,LN} = \Phi_{B,V} + \delta_{LN}\,\Phi_{B,M} \qquad \delta_{LN} = 0.97 \tag{20}$$

Below, this paper shall refer to Eqs. 18, 19, and 20 as the Rigden, Carman, and Lea and Nurse packed bed permeability equations, respectively. Substituting Eq. 12 for the Φ_C of Eq. 14 yields

$$\Phi_{B,K} = \Phi_{B,V} + \delta_K\,\Phi_{B,M} \qquad \delta_K = 0.82 \tag{21}$$

Below we shall refer to this as the packed bed permeability equation based on Knudsen's approximation equation.

3. Comparison of Powder Bed Permeability Equations

Fig. 1 plots a comparison of the packed bed equations Eqs. 15, 18-21, which have been standardized with the $\Phi_{B,1}$ defined by Eq. 22.

$$\Phi_{B,1} = \Phi_{B,V} + \Phi_{B,M} \tag{22}$$

It stands to reason that the Kozeny-Carman equation, Eq. 15, which ignores molecular flow, has the smallest value, but there are also sizable differences among the packed bed equations Eqs. 18-21, which take the influence of molecular flow into account. This makes it difficult to choose a permeability equation to take the place of the Kozeny-Carman equation.

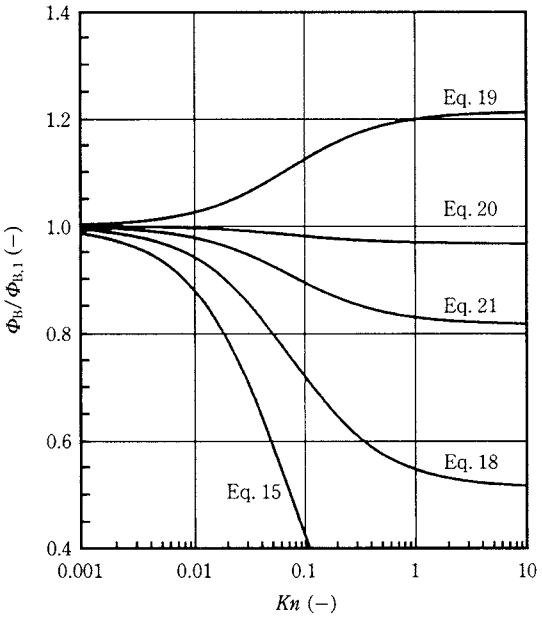

Fig. 1 Comparison of Powder Bed Permeability Equations

Eqs. 18-21 have the same form as the Rigden-type permeability equation Eq. 17 based on the slip flow model, with only the values for δ differing. Below we shall consider an appropriate value for δ. In measuring specific surface area by air permeability, it is calculated from the measured values for sample bed permeability, which corresponds to solving a permeability equation for Kn. If Eq. 17 is solved for Kn,

$$Kn=(A/2\Phi_{B,s})\left[\delta B+\{(\delta B)^2+(4\Phi_{B,s}/A)^{0.5}\}\right] \quad (23)$$

But because

$$A=(\pi/32)(\varepsilon/k), \qquad B=128/\pi \quad (24)$$

once Kn is found, it can then be converted to S_V using Eq. 2. If molecular flow influence were properly assessed in permeability equations, the value of S_V should not be dependent on permeating gas pressure p. Rigden measured the permeability of the same packed powder bed while varying p, and for comparison plotted, as a function of p, the values of S_V calculated with the Kozeny-Carman equation and the Rigden equation. Below we shall call this type of plot a Rigden plot. **Fig. 2** is one of the Rigden plots produced by the authors using Rigden's data. It plots S_V values found with permeability equations 18 through 21, as a function of p. **Fig. 3** [Fig. 2?] results indicate that Rigden plots produced with Rigden-type permeability equations have far superior horizontal linearity than the Kozeny-Carman equation, which ignores molecular flow. But plots according to Rigden equations, for example, are somewhat low at the left end,

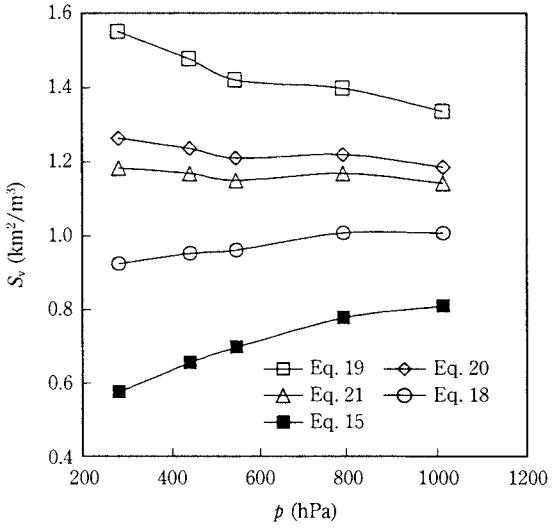

Fig. 2 Examples of Rigden Plots based on Rigden's Data (fine slate powder)[3]

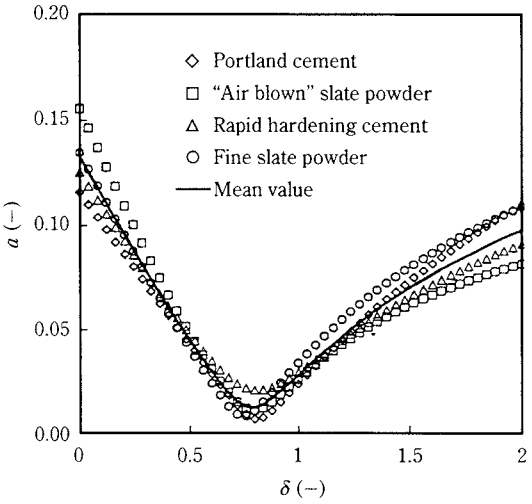

Fig. 3 Rigden Plot Variation Coefficient Based on Rigden's Data[3] and Plotted Against δ

showing that $\delta_R=0.515$ is too small. Variability coefficient a might be one way of numerically evaluating the horizontal linearity of Rigden plots.

$$a=\{\Sigma(S_{Vi}-S_{Vm})^2/(n-1)\}^{0.5}/S_{Vm} \quad (25)$$

Where:

S_{Vi} is the value of the specific surface area measured at permeating gas pressure p_i, and S_{Vm} is the arithmetical mean of n values for S_{Vi}.

In **Fig. 3** a has been calculated for all of the data in four sets of Rigden's data, and plotted against δ. The reason that a becomes smaller as δ increases in the small-δ range is that molecular flow is being properly assessed, while the reason that a increases as δ increases in the large-δ range is that molecular flow is

over-assessed, thereby lowering the horizontal linearity of Rigden plots. Judging by **Fig. 3**, it appears that Rigden's $\delta_R=0.515$ is too small, Carman et al.'s $\delta_C=1.215$ is too large, and Lea and Nurse's $\delta_{LC}=0.97$ is a little too large. The value of δ at which variability coefficient a is smallest is about 0.8, and the $\delta_K=0.82$ obtained with Knudsen's approximation equation is close to that.

If the general form of the Rigden-type permeability equation Eq. 17 is rewritten into a practical, ordinary expression, we obtain

$$Ql/At\Delta p=F_1/k\mu S_v^2+\delta F_2(32/3)(2RT/\pi M)^{0.5}/kpSv \quad (26)$$

Where:

Q is the permeating gas volume converted to the value of mean permeating gas pressure p in a packed bed,
l is packed bed thickness,
A is the packed bed's cross sectional area,
t is required permeation time,
Δp is the difference between front and back pressure of a packed bed,
$k=5$ is the Kozeny-Carman coefficient,
R is a gas constant, and
M is the molecular weight of the permeating gas,

which gives $F_1=\varepsilon^3/(1-\varepsilon)^2$, $F_2=\varepsilon^2/(1-\varepsilon)$. Our investigations show that 0.82 is a reasonable value for δ. Eq. 26 is applicable to the slip flow region ($0.01<Kn<0.1$), but because at Kn$\rightarrow$0 it approaches the Kozeny-Carman equation, in a practical sense that equation falls within the range of applicability, i.e., $Kn<0.01$. Accordingly, it can be considered applicable to all specific surface area measurements using air permeability for powders up to about 1 μm.

Conclusion

It was about the time the Powder Forum was formed when it was found that the applicability limit of the Kozeny-Carman equation, which ignores the influence of molecular flow, is about 10 μm, but until now that equation has continued to be used without having found a way to correct for molecular flow influence, and even while doing nothing about the very necessity for correction.

In this paper we explored Rigden-type packed bed permeability equations that were derived by combining the capillary aggregate model, which regards a packed particle bed as an aggregate of curved non-circular cross-section capillaries, with a capillary permeability equation based on the slip flow model. We obtained $\delta_K=0.82$ as a reasonable value for the weight coefficient of the molecular flow term δ. This value was found using an analysis of Rigden's data with the least squares method, and the slip flow model approximation of Knudsen's capillary permeation equation, which is applicable to the entire range of Kn. It is equivalent to about 8/5 times the weight of the molecular flow term used by Rigden, and about 2/3 the weight of that in Carman's equation.

Using $\delta_K=0.82$ for the weight of the molecular flow term gives rise to hopes that it will be possible to transcend the 10 μm applicability limit of the Kozeny-Carman equation and perform rational air permeation measurements of the specific surface area of fine powders down to sizes of about 1 μm. Important factors when making such measurements, however, include the agglomeration state of samples, and the uniformity of packed beds. Needless to say, these are high on the future research agenda.

Nomenclature

A	: Cross sectional area of packed powder bed	(m^2)
a	: Coefficient of variation in Rigden's plot	(−)
D_s	: Particle diameter of specific surface area	(m)
d	: Capillary diameter	(m)
d_h	: Equivalent diameter of permeation channel	(m)
F_1	: Porosity function, $\varepsilon^3/(1-\varepsilon)^2$	(−)
F_2	: Porosity function, $\varepsilon^2/(1-\varepsilon)$	(−)
j_B	: Molar permeation flux of packed bed	(mol/m^2s)
j_C	: Molar permeation flux of capillary	(mol/m^2s)
k	: Kozeny-Carman constant	(−)
Kn	: Knudsen number	(−)
l	: Thickness of packed bed	(m)
M	: Molar weight of permeating gas	(kg/mol)
p	: Mean pressure of permeating gas in packed bed	(Pa)
Q	: Volume of permeating gas at p during t	(m^3)
R	: Gas constant	(Nm/kmol)
S_V	: Specific surface area	(m^2/m^3)
T	: Absolute temperature of permeating gas	(K)
t	: Permeation time	(s)
δ	: Weight coefficient of molecular flow term	(−)
$\delta(Kn)$	: Knudsen's weight function of molecular flow term	(−)
ε	: Void fraction of packed bed	(−)
λ	: Mean free path of permeating gas molecules	(m)
μ	: Viscosity of permeating gas	(kg/ms)
ρ	: Density of permeating gas	(kg/m^3)
Φ_B	: Dimensionless permeability of packed bed	(−)
Φ_C	: Dimensionless permeability of capillary	(−)

References

1) Society of Chemical Engineers, Japan. *Kagaku-Kogaku-benran*, pp. 158-161, Maruzen (1988).
2) Society of Chemical Engineers, Japan. *Kagaku-Kogaku-benran*, p. 159, Maruzen (1988).
3) Rigden, P. J. "The Specific Surface of Powders. A Modification of the Theory of the Air-Permeability Method," *J.S.C.I.*, **66**, 130-136 (1947).
4) Carman, P. C. and J. C. Arnell. "Surface Area Measurement of Fine Powders Using Modified Permeability Equations," *Candian J. Res.*, **26**, A 128-136 (1948).
5) Carman, P. C. & P. le. R. Malherbe. "Routine Measurement of Surface of Paint Pigment and Other Fine Powders," *J.S.C.I.*, **69**, 134-143 (1950).

Author's short biography

Akira Suganuma

Late emeritus professor Akira Suganuma was a member of the Society of Powder Technology, Japan. He received his Ph.D. degrees in applied chemistry at Tokyo University in 1963. He devoted his life into both teaching and doing research and wrote about 100 papers on powder technology.

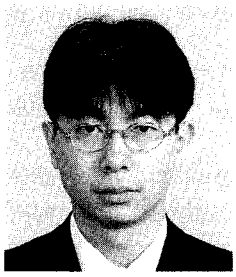

Yu Matsumoto

Yu Matsumoto is now working as a system engineer at NTT Data Corporation. He received his B.S. in 1996 and M.S. in 1998 in chemical engineering at Science University of Tokyo.

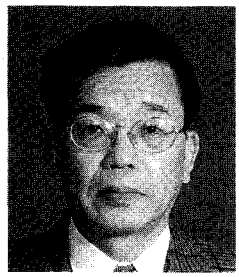

Toshitaka Hamada

Toshitaka Hamada is a research engineer at Science University of Tokyo, Faculty of Science & Technology. He received his B.S. in physics in 1965 and M.S. in 1968 and Ph.D. degrees in applied chemistry at Science University of Tokyo. He is a member of the Society of Powder Technology, Japan.

Structure and Wettability of Various Silica Surfaces: Evaluation on the Nano and Macro Levels†

Masayoshi Fuji, Masakazu Araki, Takashi Takei, Tohru Watanabe and Masatoshi Chikazawa
*Department of Applied Chemistry, Graduate School of Engineering, Tokyo Metropolitan University**

Abstract

Microscopic and macroscopic wettabilities of various silica surfaces modified with trimethylsilyl groups were studied, focusing on the effect of their surface geometrical structures. Micro and macro geometrical structures were investigated by water vapor adsorption. Microscopic wettability was determined by water vapor adsorption, while macroscopic wettability was determined by measuring the contact angle. Microscopic wettability affects the continuous two-dimensional water layer, while macroscopic wettability is influenced by capillary condensation and surface roughness. Surface wettability is essentially governed by microscopic wettability, which is a primary property of various silica surfaces. Capillary condensation and surface roughness enhance wettability as a secondary effect which results from the primary property of microscopic wettability.

1. Introduction

The wettability of solid surfaces is closely related to the characteristics of their surfaces, such as surface energy and roughness. Cassie[1] and many other researchers have performed research on the relationship between surface energy and wettability. Even now a great deal of industrial attention is directed at research on ultrahydrophobic materials that involve the modification of surfaces with fluorine-based polymers and other substances to lower surface energy and obtain a high contact angle.[2-5] Additionally, Wenzel[6] and many other researchers have performed research on the relationship between surface roughness and wettability. Industrially it is known that, for example, roughing the surface of water-repellent materials will produce an even higher contact angle. Thus it is a well-known fact that surface structure affects wettability, but the influence of surface structure, which affects wettability, from the level that is visible to the naked eye to the nano level such as pore and modification groups has been not investigated. Furthermore, there are a few researches about the classification and evaluation of surface roughness from macro level to nano level.

In powder engineering, determining wettability is of great importance because it is related to improving dispersability, endowing surface functions with modifying, controlling the prevention of powder caking and agglomeration, and the like. In our research we therefore used various kinds of silica powder and porous silica glass to assess surface structure on the nano level based on water vapor adsorption experiments. Additionally we compared the macroscopic and nanoscopic wettabilities as determined by measurements of contact angle and water vapor adsorption in order to examine the relationship between surface structure and wettability from the nano level to the macro level.

2. Experimental

2.1 Samples

Three kinds of silica, which were made in different way, were used: nonporous silica powder made by vapor phase synthesis (Aerosil 200 made by Nippon Aerosil Co., Ltd.; 198.5 m^2/g, 2.5-OH/nm^2), porous silica powder made by wet synthesis (Nipsil HD-2 made by Japan Silica Industries Co., Ltd.; 260.0 m^2/g, 4.2-OH/nm^2), and porous silica plate made by phase separation and elution method (#7930 made by Corning; 215.2 m^2/g, 3.1-OH/nm^2). Their surface hydroxyl group densities were determined with Grignard's

* 1-1 Minami-osawa, Hachioji-shi, Tokyo 192-0397
TEL. 0426-77-1111

† This report was originally printed in J. Soc. Powder Technology, Japan. **36**, 528-533 (1999) in Japanese, before being translated into English by KONA Editorial Committee with the permission of the editorial committee of the Soc. Powder Technology, Japan.

reagent method.[7] We used the modification agent hexamethyldisilazane to modify the surfaces of samples. Modification was accomplished with the reflux method, using hexane as the solvent. Modification extent was controlled by adjusting the modification agent concentration according to the amount of hydroxyl groups on the surfaces of unmodified samples and modification conditions involved running the modification reaction for 1 h at the boiling point of hexane. Preprocessing for surface modification consisted of heat treatment at 180°C for 2 h at a reduced pressure of under 10^{-3} torr to remove physically adsorbed water. To quantify modifying groups we used elemental analysis.[8]

Before subjecting samples to measurements we removed their physically adsorbed water by heat treatment at 180°C for 2 h at a reduced pressure of under 10^{-5} torr.

2.2 Water Vapor Adsorption Experiments

The volume method was used to perform water vapor adsorption experiments on samples which had been preprocessed with heat. We measured the amount of adsorbed water vapor at the adsorption temperature of 0°C until relative pressure attained $P/P_0=1$. Water used for adsorption was prepared by bubbling pure water with nitrogen for about 10 min to remove dissolved CO_2, connecting to a vacuum line, and freezing and melting several times to remove dissolved gases. The cross sectional area of water molecules was used 0.105 nm^2, which was calculated from water density.

2.3 Contact Angle Measurements

Contact angle with the sessile drop method was measured using a model CA-X contact angle gauge (Kyowa Surface Science Co., Ltd.) attached with an image processor. Droplets were distilled water of about 2 μl. Samples used in contact angle measurements were preprocessed by heating at 180°C for 2 h at a reduced pressure of under 10^{-3} torr. Measurements were performed under saturated vapor pressure using a sealed cell with an adjustable ambient temperature.

3. Results and Discussion

3.1 Evaluation of Nano-Level Surface Structure and Wettability

Fig. 1 shows the water vapor adsorption isotherms for modified and unmodified Aerosil 200 and #7930. The adsorption isotherms for unmodified samples are IUPAC classification type III for Aerosil 200, and type IV for #7930. Both the Aerosil 200 and #7930 unmodified samples (hydrophilic) rapidly increased their adsorption amounts at a relative pressure of about 1 either among particles or by capillary condensation into mesopores. On the other hand, their hydrophobic modified samples (Aerosil 200 had a 41% modification rate, #7930 a 40% rate) had no increase in their adsorption amounts even at a relative pressure of about 1 either among particles or by capillary condensation into mesopores, and then isotherms did not rise up. However, the adsorption amount for #7930 under extremely low relative pressure was not that much lower. Thus, to investigate the range in which modification brings about no change in adsorption amount, i.e., the adsorption mechanism of the initial adsorption stage, we converted the adsorption isotherms of all samples to the V-V plot proposed in this research. For this purpose our reference adsorption isotherm was the isotherm of unmodified Aerosil 200, whose particles had smooth surfaces.

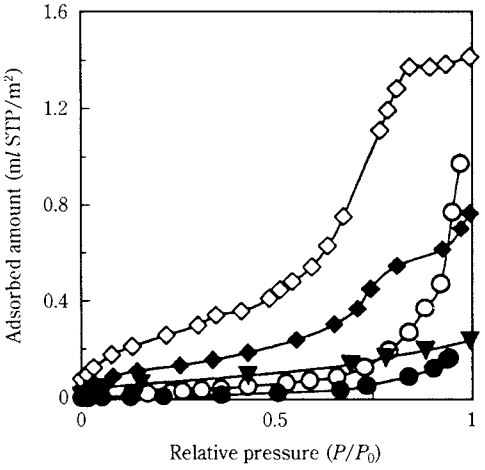

Fig. 1 H_2O Adsorption Isotherms of Unmodified and Modified Silicas
○ Unmodified Aerosil 200
● 41% modified Aerosil 200
◇ Unmodified Corning #7930
◆ 21% modified Corning #7930
▲ 40% modified Corning #7930

Fig. 2 presents V-V plots. As V-t plots[10] and α_s plots,[11] V-V plots evaluate surface structures by comparing, at the same relative pressure, the adsorption amount, which is determined from the reference adsorption isotherm at various relative pressures, with the adsorption amount found for each sample. It is reported[12] that the mechanism by which water molecules are adsorbed onto smooth silica as Aerosil 200, involves the localized adsorption of water molecules by highly hydrophilic surface hydroxyl groups in the low relative pressure region, and those parts then be-

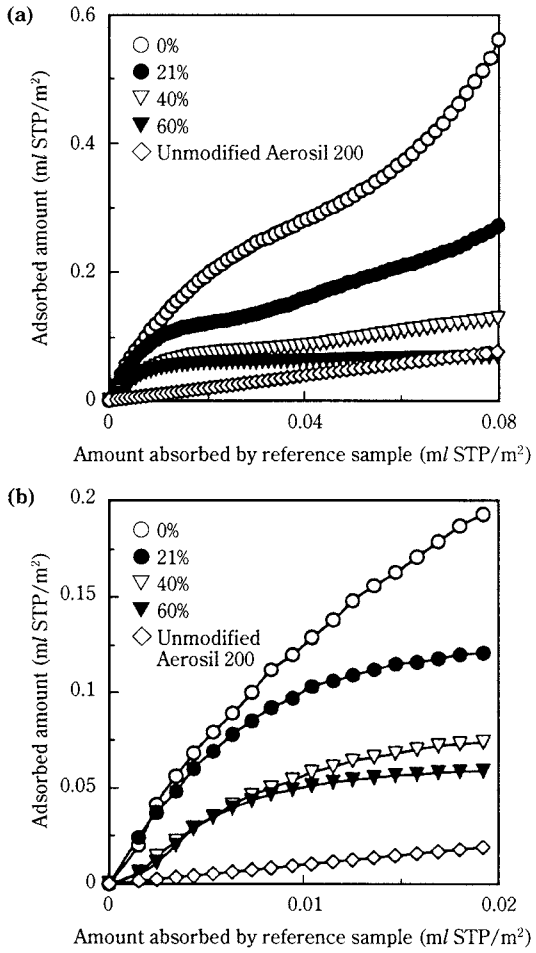

Fig. 2 V-V Plots for Unmodified and Modified Corning #7930 and Unmodified Aerosil 200
(a) Entire plot
(b) Enlarged portion of (a)

come the adsorption sites for ensuing insular adsorption. Thus it seems preferable to use the V-V plot, which can directly evaluate differences in adsorption mechanisms from changes in adsorption amount, instead of the V-t plot, in which t, the thickness of the adsorbing layer, is vague. In this research we therefore decided to use the V-V plot, whose reference sample has a smooth surface. In **Fig. 2 (a)** one can see that after the reference sample's adsorption amount above about 0.02 ml STP/m^2, the V-V plots of #7930, just like that of Aerosil 200, are straight lines. The reason for this straight-line part of the V-V plot is perhaps the same mechanism as that for water vapor adsorption by Aerosil 200, and the curves in the plots can be attributed to changes in the adsorption mechanism. This means, in other words, that after about 0.02 ml STP/m^2, #7930 and Aerosil 200 have more or less the same adsorption mechanism. The curves in the V-V plots of the unmodified and the 21% modified samples, which occur after approximately 0.06 ml STP/m^2 of the reference sample adsorption amount, are likely caused by capillary condensation into mesopores. The existence of mesopores (average diameter of 2.36 nm) in #7930 has been measured by nitrogen adsorption.[13] Before the adsorption amount of reference sample reaches 0.02 ml STP/m^2 (below, "initial adsorption region"), one can tell from the plot curves that the adsorption mechanisms of Aerosil 200 and #7930 differ. Accordingly we investigated the initial adsorption region of #7930. The initial adsorption region in the V-V plot shows that adsorption amount decreases as the modification rate of #7930 increases. But samples of all modification rates had adsorption rates exceeding about 0.005 ml STP/m^2 at their first inflection points (**Fig. 2 (b)**).

It is likely that the following factors are at work in changing adsorption amount in the initial adsorption region when the modification rates are changed. First is the decrease in surface hydroxyl groups when modifying a surface, and the change in the type of surface hydroxyl groups with the decrease of them; second is differences in surface structure. Concerning the first, although different from our experimental conditions, there are reports[8,14,15] that when heat treatment temperature is high, the water vapor adsorption isotherm changes from type II to type III, meaning that when surface hydroxyl groups decrease, the adsorption mechanism changes. In our experiments, however, the adsorption isotherm type did not change even when decreasing surface hydroxyl groups by surface modification. What is more, this cannot explain the result that samples of all modification rates display an adsorption amount exceeding approximately 0.005 ml STP/m^2 at the initially appearing inflection point. This means that change in the amount of surface hydroxyl groups, which are the adsorption sites, is not the only dominant factor. Further, because the plot shows an adsorption amount exceeding about 0.005 ml STP/m^2 at the first inflection point no matter what the modification amount, it would appear that this adsorption amount arose because water molecules were adsorbed by filling the pores not blocked by modification groups (cross sectional area of trimethylsilyl group; 0.55 nm^2). This is also suggested by previous reports[16,17] that up to the inflection point of low-thickness film regions in V-t plots, water molecules fill micropores that are not blocked by modification groups. In other words, the differences in surface structure (the second factor changing adsorption amount, given above) could be highly involved in the adsorption amount differences of the initial adsorption region due to modification rate change. Also, until about 0.005 ml STP/m^2 there

is no change in the slope of the reference sample adsorption amount of the #7930 V-V plot in **Fig. 2**, which allows one to conjecture that wettability is not affected by micropores of a size that does not allow the entry of modification groups.

Just as with #7930, we used Aerosil 200 for the reference adsorption isotherm and assessed the surface structure of Nipsil HD-2 according to the V-V plot. Results showed that Nipsil HD-2 also has micropores.

Based on these evaluations we proposed an adsorption mechanism for silica with micropores.

The nano-level wetting model in **Fig. 3 (a)** shows that at first unmodified samples adsorb water molecules by the filling of ultramicropores into which water molecules enter, but which are inaccessible to modification groups. Later, insular adsorption occurs on the outer surface of ultramicropores. Insular adsorption areas then come into mutual contact and form a two-dimensional water film, bringing about multi-molecular layer adsorption. In hydrophilic modified samples, initially the adsorption of water molecules occurs by the filling of ultramicropores that are not blocked by modification groups. Subsequently, insular adsorption occurs on the outer surface of ultramicropores that are not blocked by modification groups. Owing to the decrease in surface hydroxyl groups, and steric hindrance by modification groups, it is difficult to form a two-dimensional water layer, but this water layer forms by rising over and covering the modification groups, thereby bringing about multi-molecular layer adsorption. The nano-level wetting model in **Fig. 3 (b)** illustrates that in hydrophobic modified samples, at first water molecule adsorption occurs by the filling of ultramicropores that are not blocked by modification groups. Later, insular adsorption occurs on the outer surface around ultramicropores that are not blocked by modification groups, but a two-dimensional continuous large water layer does not form owing to decreasing numbers of surface hydroxyl groups, steric hindrance by modification groups, and the decreased hydrophilic surface area. As a consequence, multi-molecular layer adsorption does not occur.

From the results of our water vapor adsorption experiment we found that wettability on the water molecule level (nanoscopic wettability) is determined by whether a two-dimensional water layer forms over the outside surface of ultramicropores, and that samples on which two-dimensional water layer form become wet because of capillary condensation among particles or in mesopores. Additionally, strong adsorption caused by pore filling does occur in ultramicropores of a size not allowing the entry of modification groups, but it appears this does not affect wettability.

3.2 Evaluation of Macroscopic Wettability

Contact angle measurement was used to evaluate macro-level (macroscopic) wettability. For contact angle measurement we used the porous plate #7930 and the powder Aerosil 200, the latter having been formed into pellets. The diameter of maximum spherical space, which is produced in the gap of the spherical particle 12-coordinated packing model for unmodified Aerosil

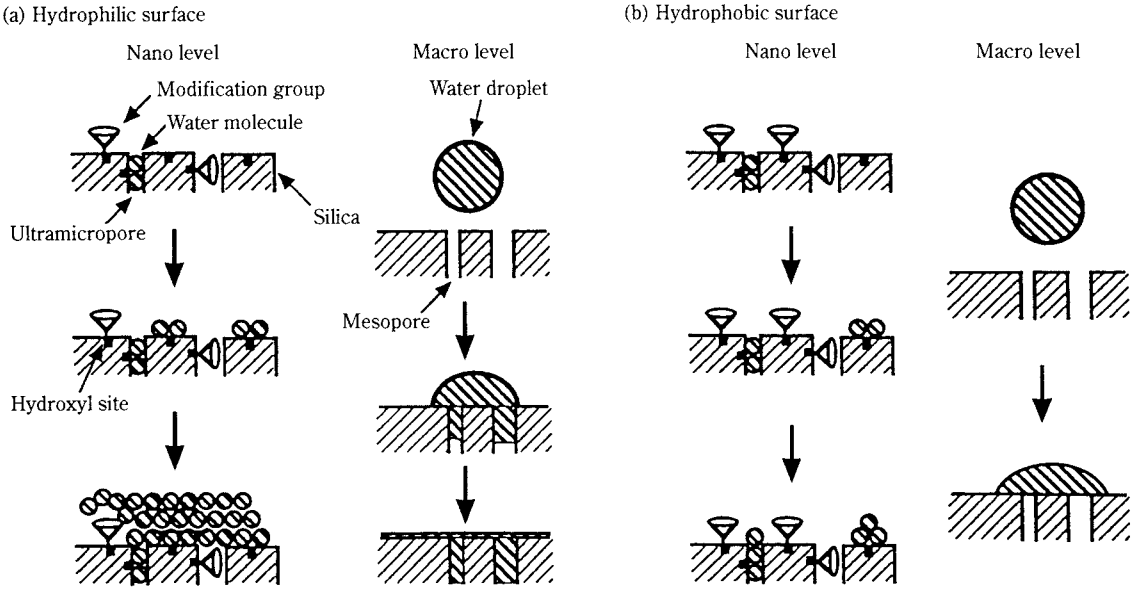

Fig. 3 Macro- and Nano-Level Wetting Model for Porous Silica Sample
(a) Hydrophilic surface (b) Hydrophobic surface

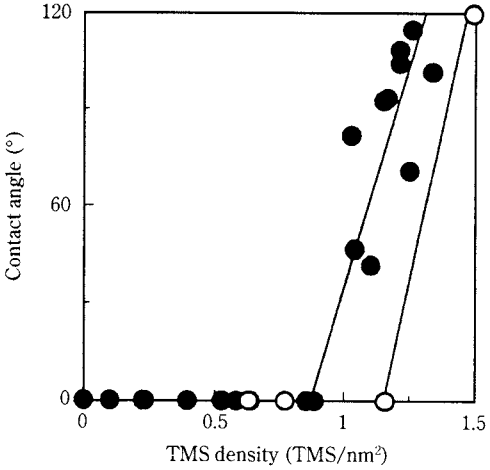

Fig. 4 Relationship Between Contact Angle and TMS Density
● #7930
○ Aerosil 200

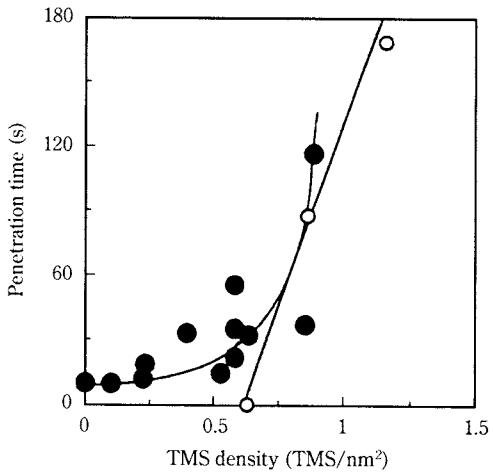

Fig. 5 Relationship Between Penetration Time and TMS Density in Zero Contact Angle Samples
● #7930
○ Aerosil 200

200, is about 3 nm. **Fig. 4** presents the results of contact angle measurements. The figure shows that we obtained finite contact angles when modification group density exceeded 0.9 TMS/nm^2 for #7930 and 1.2 TMS/nm^2 for Aerosil 200. But before the contact angle became a finite value, droplets penetrated into mesopores by capillary condensation, and we observed that the contact angle was 0° apparently. We therefore investigated samples before the appearance of finite contact angles (hydrophilic samples), using as a wettability index the time needed for water droplet penetration to conclude, and noting its relationship to modification group density. **Fig. 5** shows the relationship between penetration time and modification group density, and indicates that the higher the density, the more time was needed for penetration. The likely reason is that capillary condensation in mesopores and among particles became difficult. The section 3.1 water vapor adsorption experiments showed that capillary condensation into the mesopores of #7930 is influenced by the formation of a two-dimensional layer of water molecules. Thus the reason that penetration time lengthens with an increase in modification group density would seem to be that steric hindrance by modification groups made it difficult for a two-dimensional water layer to form, thereby making it hard for capillary condensation to occur (**Fig. 3(a)**). At the same time, the samples exhibiting finite contact angles in **Fig. 4** (hydrophobic samples) show that, despite a modicum of variation, an increase in modification group density is accompanied by an increase in contact angle that is nearly linear. We observed from videotaped images that the volume of water droplets does not change at this time, which means that because water molecules cannot form broad, two-dimensional layer on hydrophobic samples, capillary condensation does not occur, and water droplets do not penetrate (**Fig. 3(b)**). The foregoing investigation leads us to believe that the macroscopic wettability of hydrophobic samples is unrelated to the structure of mesopores that bring about capillary condensation, but is affected by changes in surface energy occurring in conjunction with changes in the amount of modification groups on the surfaces outside mesopores, and by surface roughness outside mesopores.

4. Conclusion

The effects of the surface structure of various silica types on wettability were investigated using water vapor adsorption experiments and contact angle measurements. This yielded the following conclusions.

(1) Nanoscopic wettability is determined by whether or not a two-dimensional water layer is formed on the outside surface of ultramicropores. Although strong water vapor adsorption occurs due to the filling of pores whose size prevents the entry of modification groups, this is unrelated to wettability.

(2) Macroscopic wettability is determined by whether or not capillary condensation occurs in mesopores or among particles, and that, in hydrophilic samples, this is influenced by capillary condensation in mesopores, while in hydrophobic samples it is influenced by the outer surface structure around mesopores.

(3) It is nanoscopic wettability which governs essentially whether a surface will become wet, and that capillary condensation in mesopores and surface structure outside mesopores are factors that constitute secondary influence on wettability.

Acknowledgment

The authors express their appreciation to Hosokawa Powder Technology Foundation for the grant under which this research was partly conducted.

Nomenclature

P	: Equilibrium Pressure	(Pa)
P_0	: Saturated Pressure	(Pa)

References

1) Cassie, A. B. D. and S. Baxter. "Wettability of Porous Surfaces," *Trans. Faraday Soc.*, **40**, 546-551 (1944).
2) Saito, H. and H. Takazawa. "Modifying the Water-Repellent Properties of Surfaces by the Application of Water-Repellent Coatings," *Hyomen Gijutsu*, **47**, 558-561 (1996).
3) Muroi, K. "Development of Water-Repellent Films by the Electrodeposition Method," *Hyomen Gijutsu*, **47**, 562-565 (1996).
4) Hozumi, A. and O. Takai. "Low-Temperature Deposition of Highly Transparent and Water-Repellent Films – Application to Transparent Plastic Substrates," *Hyomen Gijutsu*, **47**, 575-579 (1996).
5) Takada. Y. "Ultrahydrophobic Surfaces Prepared Using Chemical Adsorption," *Hyomen Gijutsu*, **47**, 580-583 (1996).
6) Wenzel, R. W. "Resistance of Solid Surfaces to Wetting by Water," *Ind. Eng. Chem.*, **28**, 988 (1936).
7) Kanazawa, T., M. Chikazawa, T. Takei, and K. Mukasa. "Characterization of Surface OH Groups on Porous Glass," *Yougyo-Kyokai-shi*, **92**, 654-659 (1984).
8) Fripiat, J. J. and J. Uytterhoeven. "Hydroxyl Content on Silica Gel 'Aerosil'," *J. Phys. Chem.*, **66**, 800-805 (1962).
9) "IUPAC Manual of Symbols and Terminology, Appendix 2, Pt. 1 , Colloid and Surface Chemistry," Pure and Appl. Chem., **31**, 578 (1972).
10) Lippens, B. C. and J. H. de boer. "Studies on Pore Systems in Catalysis V. The t Method," *J. Catalysis*, **4**, 319-323 (1965).
11) Sing, K. S. W. *Surface Area Determination*, p. 25, Butterworths (1996).
12) Fuji. M., H. Iwata, T. Takei, T. Watanabe, and M. Chikazawa," The Change in the Water Vapor Affinity of Fine Particles Loaded with Trimethylsilyl Groups," *J. Soc. Powder Technol., Japan*, **32**, 649-654 (1996).
13) Takei, T., A. Yamazaki, T. Watanabe, and M. Chikazawa. "Water Adsorption Properties of Porous Silica Glass Modified by Trimethylsilyl Groups," *J. Colloid Interface Sci.*, **188**, 409 (1997).
14) Naono, H., R. Fujiwara, and M. Yagi. "Determination of Physisorbed and Chemisorbed Water on Silica Gel and Porous Silica Glass by Means of Desorption Isotherms of Water Vapor," *J. Colloid Interface Sci.*, **76**, 74-82 (1980).
15) Taylor, J. A. G. and J. A. Hockey. "Heats of Immersion in Water of Characterized Silicas of Varying Specific Surface Area," *J. Phys. Chem.*, **70**, 2169-2172 (1966).
16) Fuji. M., H. Iwata, T. Takei, T. Watanabe, and M. Chikazawa. "The Change in Wettability and Structure of Silica Powder Surfaces Modified with Hexamethyldisilazane," *J. Soc. Powder Technol., Japan*, **33**, 740-746 (1996).
17) Fuji, M., K. Machida, T. Takei, T. Watanabe, and M. Chikazawa. "Change in Surface Property and Structure of Porous Silica Particles by Hydrothermal Treatments," *J. Soc. Powder Technol., Japan*, **30**, 706-721 (1998).
18) Iler, R. K. *The Chemistry of Silica*, p. 482, Wiley-Interscience (1979).

Information Articles

The 34th Symposium on Powder Technology

The 34th Symposium on Powder Technology was held on Friday, August 25, 2000, at the Hotel Laforet, Tokyo under the sponsorship of the Hosokawa Powder Technology Foundation and with the support of Hosokawa Micron Corporation. The symposium in this year was also very successful with the attendance of more than 283 with about 28 academic people. The main subject of this year was "Powder Technology in the information technology industry".

The 34th Symposium on Powder Technology

Theme: "Powder Technology in the information technology industry"

Session 1 Chairperson: Prof. Jusuke Hidaka (Doshisha Univ.)

- Toner as an imaging material — Mr. Hiroyuki Moriya (Fuji Xerox Co., Ltd.)
- Liquid crystal display for 21st century — Mr. Yutaka Ishii (Sharp Co., Ltd.)
- Material processing related to IT and Powder Technology — Dr. Toyokazu Yokoyama (Hosokawa Micron Corp.)

Session 2 Chairperson: Dr. Yoshitaka Kuwahara (National Industrial Research Institute of Nagoya)

- Material engineering to support the IT industry in the 21st century — Role of nanoparticles and nano-materials — — Prof. Kouichi Niihara (Osaka Univ.)

Session 3 Chairperson: Prof. Kiyoshi Nogi (Osaka Univ.)

- Nanoparticulate design for electron ceramics — Mr. Yukio Sakabe (Murata Mfg. Co. Ltd.)
- Materials of lithium ion battery and their main properties — Mr. Masatake Matsui (Mitsubishi Cable Industries, Ltd.)

Session 4 **KONA Award commemorative lectures**
Chairperson: Prof. Hitoshi Emi (Kanazawa Univ.)

- Behavior of aerosols in the air and their collection — Prof. Chikao Kanaoka (Kanazawa Univ.)
- Review of complex particulate systems — Prof. Yutaka Tsuji (Osaka Univ.)

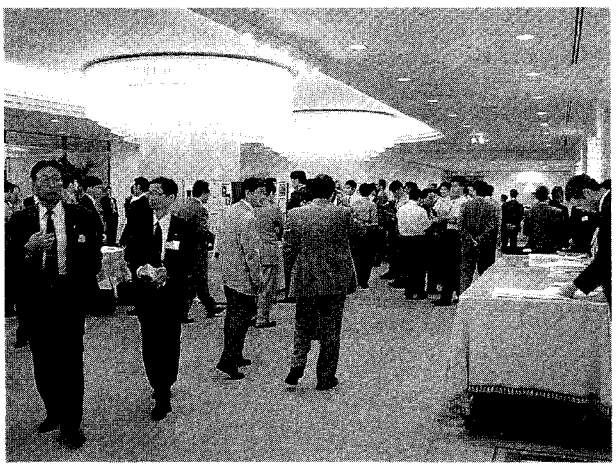

The 8th KONA Award

The 8th KONA Award sponsored by Hosokawa Powder Technology Foundation and given to the scientists or groups who have achieved excellence in the researches related to the basic powder technology, was presented to Professor Yutaka Tsuji of Osaka University and to Professor Chikao Kanaoka of Kanazawa University by Masuo Hosokawa, President of the Foundation on January 25, 2000 at the R&D Center of Hosokawa Micron Corporation in Hirakata.

Prof. Kanaoka's research achievements are related to studies on aerosol behavior and collection efficiency of aerosol.

Prof. Tsuji's research achievements are related to studies on computer simulation in the field of gas-solid flows and in fluidized beds.

In these studies both professors obtained epoch-making results.

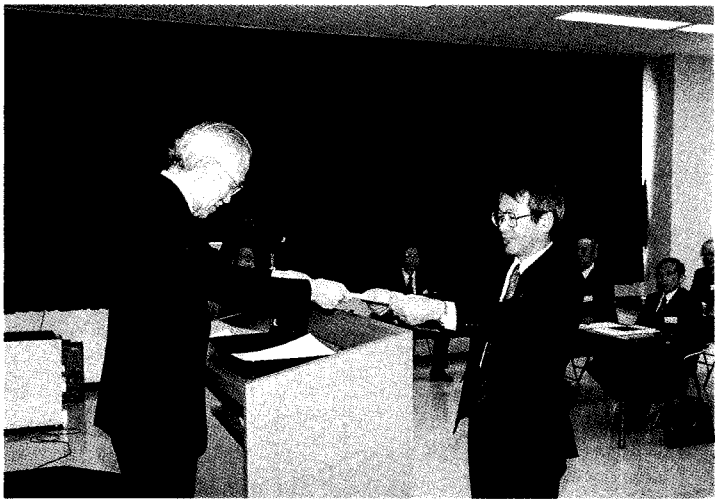

Academic publication concerning powder technology in Japan (1999)

Journal of the Society of Powder Technology, Japan Vol.36 (1999)

Title	Author(s)	Page
〈Research Papers〉		
• Measurements of Thermophoretic Velocity in the Field with Suppressed Natural Convection	R. Dobashi, Y. Ohi, A. Toda and T. Hirano	4–9
• Application of a Tensile Test Method for the Evaluation of Unraveling State of Fibrous Filler in Powder-Fiber Mixtures	Y. Sugai and M. Satoh	10–15
• Preparation of Controlled Release Particles by Suspension Spray Method Using Fluidized Bed Coater with Rotary Disk	N. Takei, K. Unosawa and S. Matsumoto	98–105
• Effect of Spray and Drying Process on the Property of coated Film in Fluidized Bed Granular Coaters	N. Takei, K. Unosawa and S. Matsumoto	106–111
• Particle Shape Separation Utilizing a Gyratory Movement	H. Iwata, H. Ohya, K. Masuda, S. Endoh and S. Koyanaka	112–120
• Influence of the Atmospheric Condition for Tribo-Charging of Powder	T. Nomura, N. Taniguchi and H. Masuda	168–173
• Fractal Dimension of Particle Surface Geometry as a Measure of Surface Roughness and its Relationship to Angle of Repose	T. Sato and Y. Nomura	174–178
• Investigation on the Structure of Surface Hydroxyl Groups on Silica −Chemical Reaction and Molecular Adsorption Method−	T. Takei, M. Ataku, T. Konishi, M. Fuji, T. Watanabe and M. Chikazawa	179–184
• Evaluation of Flow Properties of Aluminium Hydroxide Powder Treated with Stearic Acid	M. Kimata, H. Tsujikawa and K. Matsumoto	258–265
• Stertic Stability of Coal-Oil-Water Mixture Prepared by Disintegration of Deasherd Coal Agglomerates	H. Takase and S. Miyazaki	266–273
• A Study of a Generation Process of Magnetic Ultra Fine Particles with Arc Energy	Y. Endo, Y. Imaraki, M. Kanamaru, T. Araya and S. Hioki	274–279
• I-V Characteristics of Contact Interface in a Semiconductive $BaTiO_3$-In Complex Particle	T. Dan, M. Egashira, J. Kyono, H. Fudouji and N. Shinya	280–285
• Irreversible Adsorption of Methanol Vapor on Silica Surface	S. Shoji, M. Kawaguchi, Y. Hayashi, K. Tokami and H. Yamamoto	352–362
• A Common Expression of Flowability in Strengths Tests of Cohesive Powders	H. Tsunakawa	363–367
• Evaluation of Direct Granulation Method of Liquid Materials with a Fluidized Bed Granulator	H. Tsujimoto, T. Yokoyama and I. Sekiguchi	368–377
• Hot Gas Cleanup Technologies for Coal Burning PFBC System for High Efficient Power Generation	K. Higashi	378–386
• Classification of Flyash Particles with a Modified Louver-type Separator and Reduction of Unburned Carbon Content	H. Yoshida, C. Yun, K. Fukui, M. Etou and H. Morisaki	454–461
• Amorphization of Kaolinite and Media Motion in Grinding by a Double Rotating Cylinders Mill −A Comparison with a Tumbling Ball Mill−	M. Miyazaki, M. Kamitani, T. Nagai, J. Kano and F. Saito	462–467
• Dechlorination of PVC by a Mechanochemical Treatment under Atmospheric Condition	Q. Zhang, F. Saito, K. Shimme and S. Masuda	468–473
• Room Temperature Acid Extraction of Valuable Substances from $LiCo_{0.2}Ni_{0.8}O_2$ Scrap by a Mechanochemical Treatment	Q. Zhang, J. Lu, F. Saito, C. Nagata and Y. Itoh	474–478
• Impact Milling of Printed Circuit Board Wastes for Resources Recycling and Evaluation of the Liberation using Heavy Medium Separation	S. Koyanaka, H. Ohya, J. Lee, H. Iwata and S. Endoh	479–483

Kagaku Kougaku Ronbunnshu Vol.25 (1999)

HOSOKAWA MICRON DRYMEISTER

= Powerful Dispersion Type Flash Dryer suitable for even high wet material =

New mechanism of material dispersion has made possible to dry high wet material such as solution, slurry and paste which are difficult to be dried by the conventional flash dryer.

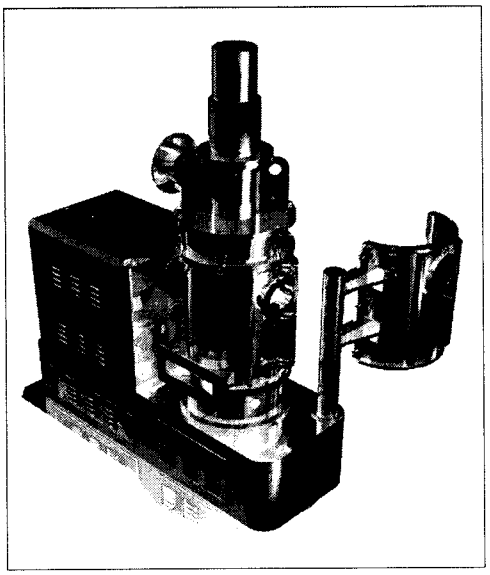

Advantages

- Adhesion Free in the drying chamber even solution and slurry
- Strong Dispersion and Grinding Power
- Compact Design – Smaller than the conventional Micron Dryer
- High Energy Efficiency – even 600°C inlet air temperature is possible
- Big Capacity Model Available – Max. 800 m^3/min
- Easy access

Drying Mechanism

Strong impact force and air turbulence generated by high speed dispersion rotor has made possible better performance of feed material dispersion in the drying chamber. It has also achieved the remarkable drying efficiency. Feed material fed in to the chamber is dispersed by the dispersion rotor into the fine powder, then heated up by the hot air in the strong air turbulence. No adhesion by undried material is observed at the inside wall of drying chamber. By changing of the classifying rotor speed, the moisture content and the particle size of the product can be adjusted and controlled and the desired homogeneous product can be obtained.

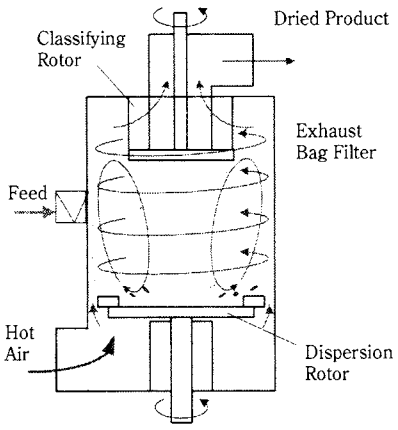

For more information contact; **HOSOKAWA MICRON CORPORATION**
5-14, 2-chome, Kawaramachi, Chuo-ku,
Osaka 541-0048, JAPAN
Telephone : 81-6-6233-3968
Facsimile : 81-6-6229-9267

HOSOKAWA MICRON AGGLOMASTER®

The Agglomaster is a new multifunctional fluidized granulator. This single granulator is capable of various types of particle processing such as crushing damp and caked material into powder, as well as granulating, coating and drying.

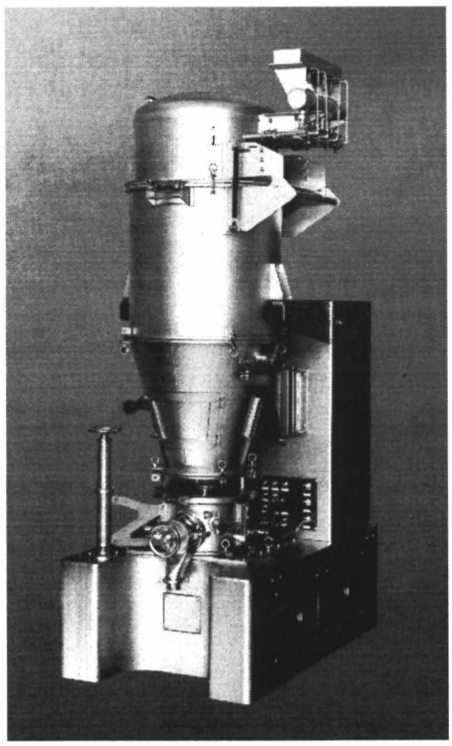

AGGLOMASTER is a multifunctional batch-type fluidized granulator based on the "fluidized bed granulation method". Depending on the diversified needs for granulation, it is able to select either the "agitation granulation principle" using agitation blades or the "tumbling granulation principle" using the unique rotating slit disk. The machine is capable of enhancing the function of the powder through controlling not only the particle size but also its shape, density and other characteristics of the granules.

Coating of the ultrafine particles with the size of about 10 μm:
It has been difficult so far to fluidize and coat the ultrafine particles with the size of about 10 μm. By incorporating the newly developed "opposed flow pulse jet mechanism" in this granulator, however, now it is possible to do so. In addition, this single granulator is capable of such a series of processes that the caked material is first crushed, then the crushed particles are made uniform of the size, and finally the particles are granulated.

Features

- The length of granulation process time can be shortened.
- High-quality granules can be produced with a narrow range of particle size distribution.
- The density (light or heavy) and shape (spherical or irregular) of the granules can be controlled in a wide range respectively.
- This single granulator is capable of performing all of the mixing, crushing, granulating, coating and drying.
- By incorporating the "pulse jet dispersion and crushing mechanism" in the granulator, the ultrafine particles with the size of about 10 μm can be coated with this granulator.
- Better efficiency can be attained in terms of space, energy and cost savings.
- The process control is simplified by **AGGLOGIC**, our exclusive software for automatic operations of AGGLOMASTER.
- **AGGLOGIC** makes it possible to collect, analyze, evaluate and store the test data efficiently, and accordingly it is able to promote efficiently the validation procedures and examine the conditions for optimum granulation process.
- The machine construction allows for easy disassembling, cleaning and re-assembling.
- All processes of the material powder are completed in an air-tight chamber with no contamination or pollution of the environment.

For more information contact; **HOSOKAWA MICRON CORPORATION**
5-14, 2-chome, Kawaramachi, Chuo-ku,
Osaka 541-0048, JAPAN
Telephone : 81-6-6233-3968
Facsimile : 81-6-6229-9267

HOSOKAWA MICRON

Hosokawa Micron Ltd. is a member of the Hosokawa Micron Group, responding to global needs through an emphasis on materials science and engineering. The Group is an international provider of equipment and Technology for powder and particle processing, product recovery, plastics processing and confectionery products. The Group maintains facilities for research, engineering, manufacturing, and service in each of the world's major industrial markets.

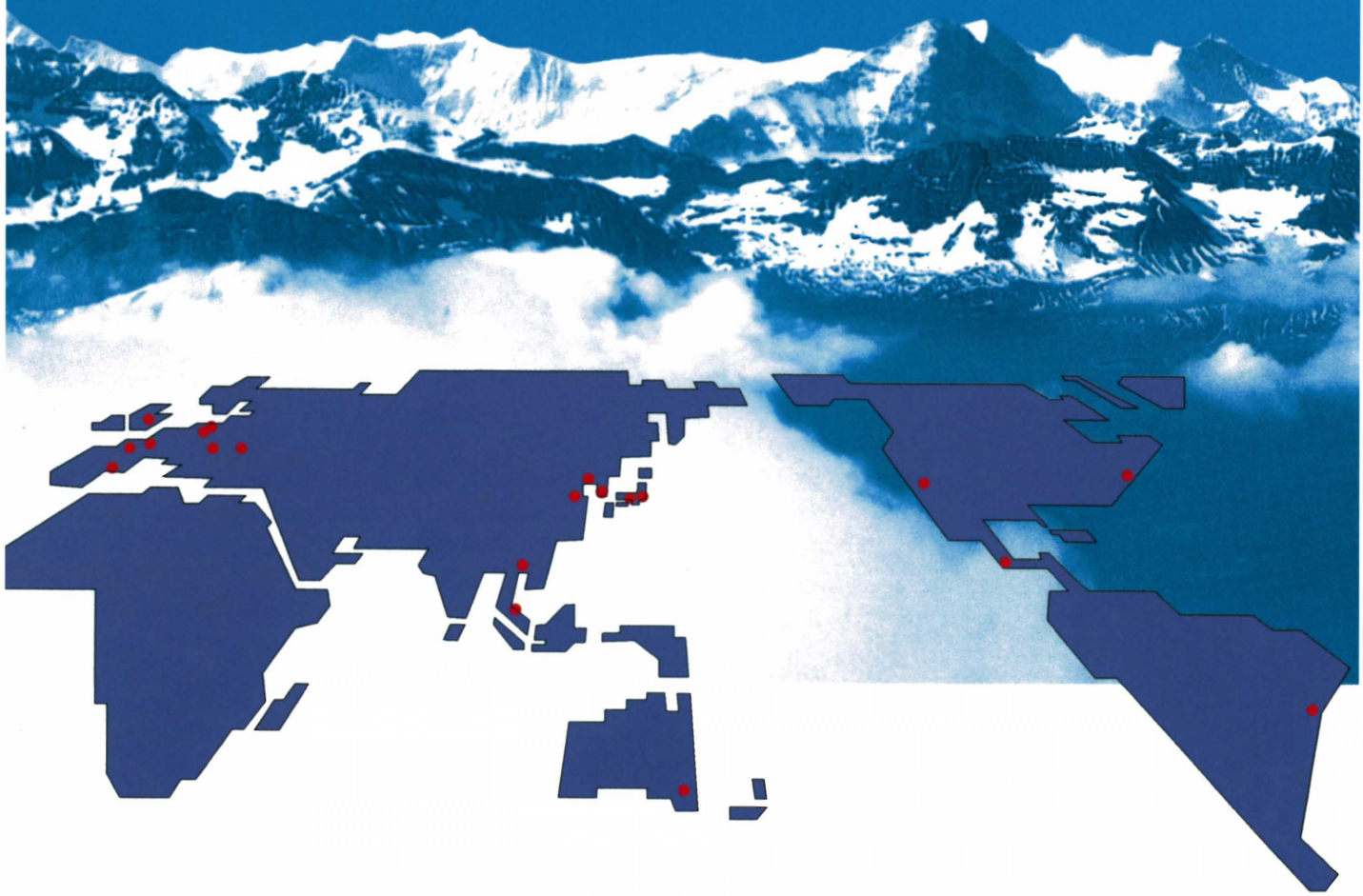

Process Technologies for Tomorrow

HOSOKAWA MICRON

Headquarter Locations;
HOSOKAWA MICRON CORPORATION
5-14, 2-chome, Kawaramachi, Chuo-ku,
Osaka 541-0048, Japan
Tel: 81-6-6233-3968
Fax: 81-6-6229-9267
http://www.hosokawamicron.com/japan